

UNIVERSITY OF CALIFORNIA  
RIVERSIDE

PROBING THE SPIN STRUCTURE OF THE PROTON USING POLARIZED  
PROTON-PROTON COLLISIONS AND THE PRODUCTION OF  $W$  BOSONS

A Dissertation submitted in partial satisfaction  
of the requirements for the degree of

Doctor of Philosophy

in

Physics

by

Michael J. Beaumier

August 2016

Dissertation Committee:

Professor Kenneth Barish, Chairperson  
Professor Rich Seto  
Professor John Ellison

Copyright by  
Michael J. Beaumier  
2016

The Dissertation of Michael J. Beaumier is approved:

---

---

---

Committee Chairperson

University of California, Riverside

## Acknowledgments

I am indebted to my advisor, Ken Barish, whose calm, stoic and unabated support helped guide me through my research. Ken's advising style allowed me the freedom to pursue my own interests while keeping centered on scientific goals.

During my time at Brookhaven National Lab, I was mentored by many inspirational scientists and graduate students. Josh Perry taught me everything I know about PHENIX data acquisition. Martin Leitgab taught me the value of patience and tenacity when solving an intractable problem. Martin Purschke showed me the value of a sense of humor, even in stressful situations. Chris Pinkenburg demonstrated the advantage of doing things the right way, the first time.

Without Joe Seele, I would have never compiled a single line of code - his introduction to Makefiles and the wider world of computer science has been invaluable, and helped kindle my passion for writing software.

Richard Hollis has been a role model of persistance, patience, and good humor – he has always seemed to carve out time from his busy schedule to give me personalized attention and guidance. Even after Richard left my research group for the world of data science, he still made time to read and review this thesis, for which I am very grateful.

Oleg Eyser pushed me to be the best graduate student possible. Even when I wanted to give up or just ‘get the right answer’, he did not lower his standards.

The team of researchers who carried out the ‘W Analysis’ with me comprise some of the most helpful and talented people I’ve ever worked with. Daniel Jumper has been my comrade in analysis since the beginning. Ralf Seidl has provided a constant cross check and push to improve, in addition to his fantastic leadership facilitating the W Analysis for many years. Francesca Giordano made time to explain even the simple things patiently to me, and guided me in my first foray into hardware assembly, with the RPCs. Along with Sangwha Park, Abraham Meles, Ciprean Gal, Chong Kim, and Hideyuki Oide, the W Analysis team has supported all aspects of this analysis with cross-checks, expert advice, and clearly written analysis notes and theses.

Angelika Drees and Amaresh Datta were both instrumental in directing and discussing my progress with the ‘Vernier Analysis’.

I must also acknowledge my dear friends who have supported me emotionally throughout graduate school. Chris Heidt, Behnam Sarvestani, Pat Odenthal, Oleg Mar-

tynov and Corey Kownacki: my experience living, working, dreaming and toiling through graduate school with you guys have been the best years of my life. There will never be another ‘FZX House’ which will rival what we created. Flavia Ruzi, Jackie Hubbard, Alex Natale-Anderson, and the DeGroots—I don’t think anyone could ask for better friends, and I couldn’t have done this without you guys. Thank you to Emily, who put up with me when I was the worst, and helped me be at my best.

Thank you to my mother and father, Bob and Marian, who always made time to support my various interests and encouraged me to find my own way. They never once tried to force me onto one path over another. Instead, they gave me the most valuable gift parents can provide: unconditional love and the tools to become successful. They cultivated my curiosity and my desire to learn, and taught me to be loving and humble before all else. Thank you to my two brothers, Joe and David, who have always had my back. It is difficult to describe the bond that exists between brothers—they are my dear friends, constant comrades, comic relief, and more. Perhaps it can be summed up with: ‘We...ARE BROTHERS!’ I wish that all people could experience what it was to grow up with my family, I can’t think of a better way to come into this world.

*Some say that it takes a village to raise a child. The same can be said of raising a graduate student up to earning a PhD. This thesis is dedicated to the multitude who have helped me become the man I am today, and to students who struggle, and their mentors who do not give up on them.*

## ABSTRACT OF THE DISSERTATION

### PROBING THE SPIN STRUCTURE OF THE PROTON USING POLARIZED PROTON-PROTON COLLISIONS AND THE PRODUCTION OF $W$ BOSONS

by

Michael J. Beaumier

Doctor of Philosophy, Graduate Program in Physics  
University of California, Riverside, August 2016  
Professor Kenneth Barish, Chairperson

This thesis discusses the process of extracting the longitudinal asymmetry,  $A_L^{W\pm}$ , describing  $W \rightarrow \mu$  production in forward kinematic regimes. This asymmetry is used to constrain our understanding of the polarized parton distribution functions characterizing  $\bar{u}$  and  $\bar{d}$  sea quarks in the proton. This asymmetry will be used to constrain the overall contribution of the sea-quarks to the total proton spin. The asymmetry is evaluated over the pseudorapidity range of the PHENIX Muon Arms,  $2.1 < |\eta| < 2.6$ , for longitudinally polarized proton-proton collisions at 510 GeV  $\sqrt{s}$ . In particular, I will discuss the statistical methods used to characterize real muonic  $W$  decays and the various background processes is presented, including a discussion of likelihood event selection and the Extended Unbinned Maximum Likelihood fit. These statistical methods serve estimate the yields of  $W$  muonic decays, which are used to calculate the longitudinal asymmetry.

# Contents

<b>List of Figures</b>	<b>xii</b>
<b>List of Tables</b>	<b>xxxiii</b>
<b>1 Introduction</b>	<b>1</b>
1.1 Scope and Objectives of This Work . . . . .	2
<b>2 History</b>	<b>4</b>
2.1 The Phenomenon of Spin . . . . .	4
2.2 A Brief History of Relevant Physics . . . . .	5
2.3 Ancient Foundations . . . . .	5
2.4 The Scientific Revolution . . . . .	7
2.4.1 Galileo Galilei . . . . .	7
2.4.2 Isaac Newton . . . . .	8
2.5 Atomic Theory . . . . .	9
2.5.1 John Dalton . . . . .	10
2.5.2 J.J. Thompson . . . . .	10
2.5.3 Ernest Rutherford . . . . .	11
2.6 Early Quantum Theory . . . . .	13
2.7 Early Particle Physics and The Eightfold Way . . . . .	16
2.8 Deep Inelastic Scattering, Quantum Chromodynamics and The Parton Model	20
2.9 Modern Deep Inelastic Scattering Experiments . . . . .	26
<b>3 Models and Associated Probes For Proton Spin Structure</b>	<b>28</b>
3.1 Modeling the Proton Structure . . . . .	28
3.1.1 Structure Functions . . . . .	29
3.2 Parton Distribution Functions . . . . .	32
3.2.1 Polarized Parton Distribution Functions . . . . .	33
3.3 Proton Spin Decomposition with the Ellis-Jeffe Sum Rule . . . . .	37
3.4 The Spin Asymmetry: An Experimental Probe . . . . .	37
3.5 $W$ Production . . . . .	40

<b>4 The Relativistic Heavy Ion Collider</b>	<b>45</b>
4.1 Overview . . . . .	45
4.1.1 Experimental Apparatus . . . . .	52
4.2 Production of Polarized Proton Beams . . . . .	54
4.2.1 Polarized Injection . . . . .	54
4.2.2 AGS to RHIC Transfer Line . . . . .	56
4.3 Maintaining Beam Polarization . . . . .	59
4.3.1 Siberian Snakes . . . . .	59
4.3.2 Spin Rotators . . . . .	59
4.3.3 Measuring Beam Polarization . . . . .	59
4.4 The Pioneering High Energy Nuclear Interaction Experiment . . . . .	62
4.4.1 Units . . . . .	63
4.4.2 Subsystems . . . . .	69
4.5 The Forward Upgrade . . . . .	75
4.5.1 The Muon Tracker Electronics . . . . .	76
4.5.2 The Resistive Plate Chambers . . . . .	79
4.5.3 Triggering and Data Acquisition . . . . .	88
<b>5 The Vernier Analysis</b>	<b>95</b>
5.1 Overview . . . . .	95
5.2 Variables and Calculations . . . . .	97
5.3 Data Streams . . . . .	100
5.4 Beam Position Monitors . . . . .	102
5.5 PHENIX Raw Data . . . . .	108
5.5.1 GL1-1P Scalers, ATP Numberand Event Time Stamps . . . . .	108
5.6 Beam Beam Counter Analysis . . . . .	110
5.6.1 BBC Efficiency . . . . .	114
5.6.2 Calculation of $\epsilon_{BBC}$ . . . . .	117
5.7 Wall Current Monitor and Direct-Current Current Transformer . . . . .	123
5.8 Beam Width Extraction . . . . .	128
5.9 Determination of $\beta^*$ and $\theta_{xring}$ . . . . .	131
5.10 Outlook . . . . .	145
<b>6 Data Analysis</b>	<b>146</b>
6.1 Raw Data to Reconstructed Parameters . . . . .	147
6.2 Choosing Analysis Variables . . . . .	148
6.3 Beam Polarization . . . . .	149
6.4 Data Analysis . . . . .	149
6.4.1 Variables Related to Likelihood Selection . . . . .	150
6.4.2 Variables Related to Signal to Background Ratio Extraction . . . . .	153
6.5 Efficiencies . . . . .	156
6.6 Rate Dependence of Detector Response . . . . .	158
6.7 MuID hit efficiency . . . . .	158
6.8 MuTR Hit Efficiency . . . . .	159
6.9 Single Muon Trigger Efficiencies . . . . .	163

6.10	Reference data sets and method . . . . .	164
6.10.1	Rapidity Dependent Efficiencies . . . . .	166
6.10.2	$p_T$ Dependent Efficiencies . . . . .	168
6.10.3	Efficiencies Versus $W_{ness}$ . . . . .	171
6.11	Total Trigger Efficiencies . . . . .	173
<b>7</b>	<b>Feature Engineering</b>	<b>174</b>
7.1	The Basic Cut . . . . .	176
7.2	Simulations . . . . .	177
7.3	$W_{ness}$ : Likelihood Event Tagging . . . . .	180
7.3.1	Naive Bayes Classification . . . . .	180
7.4	Extended Unbinned Maximum Likelihood Selection: The Signal to Background Ratio . . . . .	188
7.4.1	Introduction . . . . .	188
7.4.2	Hadronic Background PDFs . . . . .	189
7.4.3	Muon Background and W-Signal PDFs . . . . .	198
7.4.4	Final PDFs Used in EULMF . . . . .	201
7.5	Systematic Tests . . . . .	210
<b>8</b>	<b>Spin Analysis</b>	<b>211</b>
8.1	Introduction . . . . .	211
8.2	Measured Beam Polarization . . . . .	213
8.3	Spin Patterns . . . . .	215
8.4	Muon Yields . . . . .	220
8.5	Calculation of $\epsilon_L$ and $A_L$ for $W \rightarrow \mu$ . . . . .	224
8.5.1	Defining $A_L^{W\pm}$ , $A_{LL}^{W\pm}$ . . . . .	224
8.5.2	Calculating $A_L^{W\pm}$ , $A_{LL}^{W\pm}$ . . . . .	226
8.5.3	Preliminary Results . . . . .	228
<b>9</b>	<b>Discussion and Conclusion</b>	<b>231</b>
<b>Bibliography</b>		<b>232</b>
<b>A</b>	<b>Tables of Variables Used in Analysis</b>	<b>243</b>
<b>B</b>	<b>Additional Figures</b>	<b>248</b>
<b>C</b>	<b>Trigger Efficiency Studies</b>	<b>254</b>
C.0.4	Azimuthal Dependence of Trigger Efficiencies . . . . .	314
<b>D</b>	<b>Rate Dependence of Trigger Efficiencies</b>	<b>318</b>
<b>E</b>	<b>Systematic Studies–<math>A_L</math></b>	<b>329</b>
E.1	Combined systematic studies . . . . .	329
E.1.1	Asymmetries as function of W selection and deflection angular bands	330

E.1.2	Asymmetries and Signal to BG ratio as a function of rate, time and transverse momentum range . . . . .	332
E.1.3	Addition of artificial MC-based signal and asymmetries . . . . .	341
E.1.4	Checking the relative luminosities between patterns . . . . .	345

# List of Figures

1.1	Left: the naïve quark model, while predicting the correct spin of the proton, does not bear fruit when the quark spin contribution is measured. Right: a more realistic cartoon of the proton as a composite of gluons, valence quarks and sea-quarks [1]. . . . .	2
2.1	Two Greek philosophers, who made important philosophical contributions our understanding of matter. Empedocles (Panel (a)), postulated the precursor to the elemental theory of matter[2] and Democritus (Panel (b)), postulated the precursor to the atomic theory of matter. . . . .	5
2.2	Giants in the age of Empiricism, Newton (Panel (a)) and Galileo (Panel (b)) both made foundational contributions to Physics. Galileo lived in Italy, born in 1564 and dying in 1642. Newton lived in England from 1642 until his death in 1727 . . . . .	7
2.3	Matter at an atomic scale [3] (left), intermediate nuclear scale [4] (center), and the sub-nuclear partonic scale (right) [5] . . . . .	9
2.4	Left: J.J. Thomson, who showed that cathode ray tubes were in fact producing the first observed subatomic particle: the electron. Right: A cartoon of Thomson's cathode ray tube setup. Electrons would be deflected by a magnetic field, sent from cathode to anode. . . . .	10
2.5	Ernest Rutherford, in his lab. [6] . . . . .	11
2.6	Ernest Rutherford's historic experiment, showing (top right) that atoms were composed of a small dense nucleus, in contrast to Thomson's ‘pudding model’ of homogeneous charge (top left). The experiment, (bottom left and right) contrast the expected results (bottom left) against the observed results (bottom right) [7]. . . . .	12
2.7	The attendees of the Solvay Conference in Brussels, 1927 [8]. . . . .	13
2.8	Paul Dirac, next to his original formulation of the Dirac Equation, describing the wave function for an electron with rest-mass $m$ , in terms of its space-time coordinates. Dirac’s equation has been expressed free of any defined basis.	14
2.9	Hideki Yukawa, the first Japanese Nobel Laureate and publisher of influential research on the theory of mesons, and other elementary particles [9]. . . .	17
2.10	An old bubble chamber, once used at Fermilab, [10] . . . . .	18

2.11	An example of the photographs taken with a Bubble Chamber, in 1973. In this picture, we see a $300\text{ GeV}$ proton producing particles as it travels through a hydrogen-filled bubble chamber at Fermilab [11]. . . . .	19
2.12	A schematic [12] of deep inelastic scattering, where the incoming electron inelastically scatters off the proton, producing results $X$ , via virtual photon exchange, $\gamma^*$ . The diagram is split into a perturbative portion (the electron) and a non-perturbative portion. Mathematically, we describe the interaction with kinematic variables summarized in Equations 3.1-3.3 . . . . .	22
2.13	"This diagram displays the structure of the standard model (in a way that displays the key relationships and patterns more completely, and less misleadingly, than in the more familiar image based on a 4x4 square of particles). In particular, this diagram depicts all of the particles in the standard model (including their letter names, masses, spins, handedness, charges, and interactions with the gauge bosons – i.e. with the strong and electroweak forces). It also depicts the role of the Higgs boson, and the structure of electroweak symmetry breaking, indicating how the Higgs vacuum expectation value breaks electroweak symmetry, and how the properties of the remaining particles change as a consequence." [13]. . . . .	25
3.1	Shown: "the proton structure function, $F_2^p$ measured in electromagnetic scattering experiments of electrons and positrons on protons" from experiments including H1+Zeus, BCDMS, E665, NMC and SLAC [14] . . . . .	31
3.2	On the left is the NNPDF calculation of PDFs with world data (width is related to uncertainty) at $10\text{ GeV}$ , while $10\text{ TeV}$ is shown on the right. Note that at low $x$ , the proton is dominated by gluons. [14]. . . . .	32
3.3	Deep Inelastic Scattering Process (Panel (a)) alongside Hadron-Hadron inelastic scattering (Panel (b)). In hadron inelastic scattering, one may try to select initial state with scattering between arbitrary partons in order to probe various proton structures. . . . .	33
3.4	World data used to generate fits to predict the parton distribution functions of various quark flavors in the proton at $10\text{ GeV}$ (left) and $10\text{ TeV}$ (right) [14]	35
3.5	PDFs for polarized parton distribution functions shown at $10\text{ GeV}$ for quarks, anti-quarks, and gluons in the proton. The uncertainties for the gluon and anti-quark PDFs are quite large, warranting experimental investigation [15].	36
3.6	A summary of the various probes for longitudinally polarized protons. The " <b>Reaction</b> " column summarizes the reaction observed experimentally. The " <b>Dom. partonic process</b> " column describes the dominant process at the partonic level. The " <b>probes</b> " column shows which proton spin structure can be measured with the reaction. Finally, the leading order Feynman diagram for the partonic process is drawn [16]. . . . .	39
3.7	Real $W^+$ production as produced at PHENIX. The helicity of the initial state fixes the helicity of the partonic participants due to the relativistic final state of the neutrino + the handedness of the $W$ . $x_1$ and $x_2$ are the momentum fractions of the quarks participating from the participant partons [16]. . .	41

4.1	A diagram of the acceleration process of RHIC is shown in the top panel, and aerial view is shown in thin the bottom panel. RHIC is nearly four miles in circumference and collides a variety of ions at center-of-mass energies between 5 GeV $\sqrt{s}$ and 510 GeV $\sqrt{s}$ . . . . .	48
4.2	Runs 1–3 at RHIC focused on commissioning work for experiments measuring collisions at RHIC. Work was mostly characterized by heavy-ion measurements related to understanding Quark-Gluon Plasma. The spin program began with Run 5. Table produced from data posted at the RHIC run page [17]. . . . .	49
4.3	Though RHIC is currently still running (as of May 9, 2016), I include runs here up to and including the run producing my data set (Run 13). An unprecedented 13.3 cryo-weeks of running was awarded to the W-Physics group. Table produced from data posted at the RHIC run page [17]. . . . .	50
4.4	Upgrades to RHIC’s electron lens have enabled massive improvements to luminosity—seen in the year 2013. The high luminosity was taken advantage of with an extra long proton+proton run. Figure obtained from [17] . . . . .	51
4.5	STAR (a) and PHENIX (b) with cutaways showing the event display for a heavy-ion collision as reconstructed by the detectors’ electromagnetic calorimeters [18]. . . . .	52
4.6	The longitudinal distribution of all bunches in a typical fill are overlaid. The bunches from the blue beam (top) and yellow beam (bottom) are shown for over a 40 nanosecond time period. . . . .	53
4.7	RHIC’s optically pumped polarized ion source. Produces 0.5-1.0 mA current of polarized $H^-$ ions. The optical pumping is pulsed at 400 $\mu s$ , [19] . . . . .	55
4.8	A view of the RHIC polarized injection system. Panel (a) shows a zoomed in technical view of the OPPIS to the booster. Panel (b) shows a zoomed out cartoon of the next step in the polarization injection system, including the AGS, and the feeder line to RHIC. . . . .	57
4.9	A schematic of the geometry of the AGS-to-RHIC transfer line [20]. . . . .	58
4.10	This cartoon illustrates one potential polarization pattern configuration of the beams as they collide at PHENIX’s interaction region. As beams are longitudinally rotated into position for collision, it is crucial to keep careful track of the magnet currents rotating the beams, as well as the overall polarization pattern. . . . .	60
4.11	The shift-crew display output for the Spin Monitor. The upper panel shows the polarization of the blue and yellow beams, and other panels summarize information including magnet currents (needed to understand the spin orientation), issues with data packet loss, the recognized spin-pattern, as well as a large boxed area on the lower left where errors could be shown to the shift crew along with the proper response. . . . .	61

4.12	Shown: The two main arms of the PHENIX Spectrometer. The central arms are shown via the beam-on view of PHENIX (a) and Forward Muon Arms are highlighted via the 90-degree rotated view (b). In both cases, the 2013 configuration is shown. The beams are brought into intersection at the geometric center of each figure (immediately between the BBCs)	64
4.13	The PHENIX coordinate system is shown (RGB arrows) at the center of the nominal interaction point within PHENIX, the origin, in this quarter-cutaway drawing. The small black figures are actually miniaturized human beings, the PHENIX detector is very small–this is a full scale drawing of PHENIX. Shown: the $x$ , $y$ , and $z$ coordinates, as well as the azimuthal coordinate, $\theta$ and polar coordinate $\phi$ [21]	65
4.14	Shown: A flow chart summarizing the PHENIX DAQ [22].	68
4.15	Here, we see a typical BBC z-vertex distribution for one run’s worth of data, over a z-vertex range of -300 cm to 300 cm. The central peak is close to the nominal interaction point of $z = 0$ cm. The peaks to the left and right (at $\pm 144$ cm) are from collisions outside of the BBC.	69
4.16	Shown: a schematic of the exact proportions of the detector as viewed alongside the beam pipe, along with the pseudorapidity and azimuthal coverage [23]	71
4.17	Showers from the primary event vertex impinge on the north and south BBC. The average timing of these particles are used to calculate $T_N$ and $T_S$ , allowing for the calculation of event z-vertex (Equation 4.2)	71
4.18	A schematic of the Forward Vertex Detector, showing the silicon chip layers (light blue wedges), and readout electronics (green). The FVTX was designed to mount directly onto the Silicon Vertex Detector (center) [24]. This configuration allows for a very high density of interleaved chips, in several layers, covering a maximum area around the beam pipe for detection of secondary vertex events. Secondary vertices are expected to occur rapidly after the primary vertex, making the region close to the primary vertex important real-estate to occupy.	72
4.19	Observing the simulated production of muon as a function of $p_T$ , we can see that in the kinematic region of $W$ production that the dominant sources of muons come from other processes. The new PHENIX muon trigger threshold is sensitive at 10 GeV/ $c$ and above. The threshold is still high enough that with other methods, we can record all events which come from the $W$ Boson, with triggering, whereas with the old threshold, this was impossible.	77
4.20	Shown: the muon trigger schematic layout, incorporating information from the Muon Tracker, and MuID. To the left of the dotted lines, we see the Muon Tracker, feeding information to both its front-end electronics module (MuTr FEE) and the analog-to-digital converter, in the MuID. The information is sent to the rack room, a small computing cluster which manages and assembles the data streaming in from the PHENIX interaction region [25].	78
4.21	In 2013 with the final commissioning of the RPCs and the Forward Upgrade complete, we saw a dramatic increase in rejection power, as expected.	79

4.22	As a muon passes through the layers of the RPC (left), the gas in the bakelite gap is ionized. This charge migrates and collects near the highly resistive graphite coating. An image distribution is induced on the overlapping readout strip (right), which is passed along its own channel to the front-end electronics. . . . .	80
4.23	The individual layers of an RPC segment installed at PHENIX. A High Voltage bias is applied to the graphite coating on either side of bakelite gas-filled gaps. Readout strips are positioned between the two bakelite gaps. Finally, the entire double-gap structure is surrounded by a copper grounding cage, and wrapped in insulating mylar [26]. . . . .	81
4.24	Two special tents inside building 912 at Brookhaven National Laboratory, built to house completed RPC octants and the laboratory used to construct and test the octants. . . . .	82
4.25	The North RPC Station 1 is installed on the muon tracker nosecone (left). Similarly we see the installation of the south RPC Station 1 (right). The metal tube in the center is the beryllium beam pipe. . . . .	83
4.26	The chassis is prepared with insulating Kapton tape and mylar sheeting. The grooves along the bottom of the chassis are for routing cabling from the readout strips (shown later). The channels along the side of the chassis is for routing gas flow lines. . . . .	84
4.27	Foam shock insulation is added to the RPC 1 chassis. . . . .	84
4.28	The assembled Bakelite gas gap, ready for leak/pop testing, followed by burn in. . . . .	85
4.29	The egress port of the gas gap is carefully shielded with tape to prevent friction from causing tears, and routed out of the ports machined into the bottom of the chassis (right), with the final position of the first gap shown on the left. . . . .	86
4.30	The copper readout strips are mounted to the chassis. Each readout strip is soldered to a copper wire, which in turn are gathered into readout chips. . . . .	87
4.31	The final Bakelite gas gaps are installed on top of the copper readout strips. Gas lines are routed similarly to 4.29 . . . . .	87
4.32	A completed RPC 1 octant, interior assembly complete, left, and the outer assembly completed on the right. . . . .	88
4.33	Left: the cosmic test stand setup. RPC octants were sandwiched between scintillators to run performance and efficiency tests. An example of the clustering due to a cosmic ray is shown on the right, with a particle (red) activating one or two strips per octant (activation shown in green). . . . .	89
4.34	A schematic of the new muon trigger for recording $W$ Bosons [26] . . . . .	90
4.35	The position of the Front-End Electronics upgrades and new RPCs + Absorber are shown. Muon tracker stations are shown in blue (along with the front-end electronics). The RPCs sandwich the muon tracking stations and the MuID. The absorber material sits just inside of the Muon Arms, before the Forward Vertex Detectors and inner tracking stations of the muon tracker [26] . . . . .	91

5.1	Left Panel: Type 1 scanning pattern. Right Panel: Type 2 scanning pattern. In both panels, we see the mean beam displacement as a function of time since the beginning of the vernier scan.	97
5.2	BPM electronics use a comparator circuit, and the readings from X1,2 and Y1,2 to determine the $x$ and $y$ beam positions.	103
5.3	Shown: the geometric extrapolation of beam displacement at the IR plane.	104
5.4	The horizontal scan is shown in green, with the vertical scan shown in purple. Note that relative scan displacements are shown in both the horizontal and vertical for the horizontal scan and vertical scan. In this case, the blue beam was scanned and the yellow beam was held fixed.	105
5.5	Left: the BBC GL1P scaler plotted as a time series, against an arbitrary time proxy. Right: the CLOCK GL1P scaler, plotted in the same way. Both distributions are histograms.	111
5.6	Shown: the BBC Rate as a function of time since scan start for Run 359711. The stepped distribution is due to changing beam overlap. The rates here are intrinsically live-time corrected, because they were generated from the ratio of the BBC GL1P scaler and the CLOCK scaler.	112
5.7	In each panel, the BBC rate distribution about a manually defined scan step is shown as a histogram. The horizontal is the rate, while the vertical is the number of times that a rate bin was observed in the data. From left to right, top to bottom, the scan steps are shown, starting at the chronologically first step in the top left, and ending with the chronologically last step in the bottom right.	113
5.8	Shown on the left and right are annular cross-sections of the BBC north and south at $\pm 144\text{cm}$ . The integration bounds in $\theta$ (Eqtn 5.5) are labeled, with the distance relative to the BBC N and S labeled as $d$ , with respect to the event collision vertex (the yellow sunburst). Scale is exaggerated to better show the angles.	115
5.9	Top: the BBC solid angle as calculated for all possible solid angles within the BBC $z$ -vertex sensitivity range. Bottom: the solid angle of the ZDC seen from an event vertex for all $z$ -vertices over the BBC $z$ -vertex range. Units on the vertical axis are arbitrary for this qualitative comparison.	116
5.10	Panel(a): the $z$ -vertex distribution for events that trigger the wide BBC trigger. Panel (b): the $z$ -vertex distribution for events that trigger the BBC wide and narrow triggers.	118
5.11	Panel (a) shows the trigger acceptance curve, produced from Figure 5.10. Panel (b) shows the absolute value of the derivative of (a), with two Gaussian fits to the peak, centered at -34.4 cm and 35.8 cm, representing the real trigger turn on.	119
5.12	Panel (a) shows the wide ZDC $z$ -vertex distribution, Panel (b) shows the distribution from trigger coincidences between the BBC wide and ZDC wide triggers.	121

5.13	The BBC $z$ -vertex correction is obtained from the ratio of BBC and ZDC to ZDC yields and fit with a quadratic polynomial. The resulting polynomial is used to correct the yields for the BBC coincidence and BBC wide distributions, before calculating the total efficiency. . . . .	122
5.14	Shown: an insulating ceramic break in the beam pipe, which shunts image wall currents from the beam pipe into the electronics. Magnetic shielding excludes external magnetic fields. [27] . . . . .	124
5.15	The wall current monitor uses an insulating ceramic break in the beam pipe similarly to the DCCT, which forces image wall currents through electronics which measure the current frequencies. The WCM is sensitive only to bunched beams, and can measure longitudinal profiles of bunches [27]. . . . .	125
5.16	Shown: The product of the WCM blue and WCM yellow calibrated data describing the total beam ion distribution, as a function of time. This may be used to estimate the beam losses due to real ion loss, with the slope representing the per-second rate of luminosity loss. In all scans, this amounts to 1% or less for the duration of the scan. . . . .	126
5.17	Distribution of WCM population, corrected by DCCT for each bunch for an example run. Left: blue beam. Right: yellow beam. For both figures, the horizontal axis represents the bunch number. . . . .	127
5.18	The horizontal beam width fit . . . . .	129
5.19	The vertical beam width fit . . . . .	129
5.20	The simultaneous fit to the BBC rate vs beam displacement. . . . .	130
5.21	A cartoon is shown for various potential values of $\beta^*$ , showing the squeezing transverse profile [28]. . . . .	131
5.22	Shown: a simple bunch collision with no crossing angle or beam focusing with Gaussian bunch profiles in $x, y$ , and $z$ , [28]. . . . .	132
5.23	Panel (a) shows the coordinate transformation applied to the bunch profiles which resulting in a crossing angle, with Panel (b) depicting the result. . . . .	134
5.24	A parameterization of the blue beam profile in $z$ is shown in Panel (a), with the yellow in panel (b). Included are the resulting fits by parameterizing the profiles with a triple-Gaussian fit, with parameters 2, 5 and 8 referencing the widths of the distributions. . . . .	136
5.25	Shown: the ZDC $z$ -vertex collision profile for beams colliding at maximum overlap. . . . .	137
5.26	Shown: a cartoon of realistic beam profiles before (Panel (a)) collision, during collision (Panel (b)), and after collision (Panel(c)). . . . .	140
5.27	Shown: With a large displacement in the beams, the hourglass effect can be seen in the ZDC $z$ -vertex profile. . . . .	141
5.28	The least-squares residual is shown to be converging with each successive iteration of the algorithm. Modulation in the parameter within each iteration is a result of the binary search executing and finding the best set of parameters to keep for the next iteration. . . . .	141
5.29	The schematic algorithm for the hourglass simulation. . . . .	142

5.30	Shown: the convergence of the $z$ -profile simulation after 15 iterations for a $65 \mu\text{m}$ beam displacement.	142
5.31	Shown: the convergence of the $z$ -profile simulation after 15 iterations for a $971 \mu\text{m}$ beam displacement.	143
5.32	Shown: the convergence of the $z$ -profile simulation after 15 iterations for a $1105 \mu\text{m}$ beam displacement.	143
5.33	Shown: the convergence of the $z$ -profile simulation after 15 iterations for a $1004 \mu\text{m}$ beam displacement.	144
6.1	Shown: A transverse-view of the FVTX, RPCs, MuTR, and MUID, with variables engineered from track reconstruction (track shown as red arc from yellow collision point on left) [29]	151
6.2	Shown: A beam-view of the MuTR tracking planes with additional variables engineered from track reconstruction [29].	152
6.3	A schematic representation of track-matching variables DG0 and DDG0 at the intersection between the Muon Tracker and Muon Identifier [25].	153
6.4	The top plot shows panel numbering scheme. Each plane has six panels. The bottom plots show the structure of hv groups for each horizontal and vertical plane [30].	158
6.5	MuID hit efficiency of south gap0 horizontal plane, for the 2011 data set (green), the 2012 data set (red) and the 2013 data set (blue) [30].	160
6.6	Panel (a): The probability to have OR hit in a gap. Panel (b): The probability that a gap does not have a hit in one plane when there is OR hit in a gap. Both: The red points are for south arm, and black points are for north arm in both plots [30].	161
6.7	Shown: The correlation plots between gap efficiency and plane efficiency. The red points are for south arm, and black points are for north arm. The blue solid line indicates the full correlation, while the blue dashed line represents there is no correlation between two efficiencies [30].	162
6.8	Shown: Absolute yields in the $W \rightarrow \mu$ candidates separated by arm and charge for various muon triggers as a function of rapidity. Those with substantial contributions are given in the Legend to the right for each arm including their total fraction [30].	163
6.9	Shown: Relative yields in the $W \rightarrow \mu$ candidates separated by arm and charge for various muon triggers as a function of rapidity. Those with substantial contributions are given in the Legend to the right for each arm including their total fraction [30].	164
6.10	Shown: Trigger efficiencies for trigger bit 16 for single $W \rightarrow \mu$ candidates with $p_T$ above 5 GeV. The efficiencies for ERT (blue), MPC (green), MinBias(red) and 1D (purple) triggered data samples are shown as well as a constant fit over the whole range [30].	167

6.11 Trigger efficiencies for trigger bit 17 ((MUIDLL1_N1D  S1D)&BBCLL1(noVtx)) for single $W \rightarrow \mu$ candidates in the rapidity range $1.1 < \eta < 1.4$ as a function of $p_T$ . The efficiencies for ERT (blue), MPC (green), MinBias(red) and 1D (purple) triggered data samples are shown as well as a constant fit over the whole range [30]. . . . .	169
6.12 Left: Trigger efficiencies for trigger bit 25 (MUON_N_SG1&BBCLL1(noVtx)) for single $W \rightarrow \mu$ candidates for the $W_{ness}$ ranges $0 \leq W_{ness} < 0.9$ (left plot) and $W_{ness} > 0.9$ . Right: The triggers are shown as a function of $p_T$ . The efficiencies for ERT (blue), MPC (green), MinBias(red) and 1D (purple) triggered data samples are shown as well as a constant fit over the whole range [30]. . . . .	170
6.13 Trigger efficiencies for trigger bit 17 ((MUIDLL1_N1D  S1D)&BBCLL1(noVtx)) for single $W \rightarrow \mu$ candidates in the rapidity range $1.1 < \eta < 1.4$ as a function of $W_{ness}$ . The efficiencies for ERT (blue), MPC (green), MinBias(red) and 1D (purple) triggered data samples are shown as well as a constant fit over the whole range [30]. . . . .	171
7.1 Shown: stacked cross-sections of all simulated processes as a function of $p_T$ . All data shown has been created from the PISA+PYTHIA framework. Top Left: South $\mu-$ , Top Right: South $\mu+$ , Bottom Left: North $\mu+$ , Bottom Right: North $\mu-$ [31] . . . . .	179
7.2 In panel (a) Correlations are shown between kinematic variables, produced from the signal simulation. In panel (b) correlations are shown for the real data proxy for hadronic background. Variables that are correlated are combined in two dimensional probability distribution functions, i.e. DG0 and DDG0 and $DCA_r$ and $\chi^2$ . . . . .	181
7.3 A cartoon of the decision tree to determine the PDF cocktail to use for quantifying the $W_{ness}$ of a given track. The track's properties are used to traverse the tree, and select the cocktail contents. . . . .	184
7.4 The left panel shows the distribution of $DCA_r$ , the transverse distance of closest approach between the track and the event vertex, for each arm and charge, produced from the PHENIX data set, after the basic cut. The right panel the same distributions from a simulation of the W-Signal. Both panels have the arm and charge data partitions overlaid. . . . .	185
7.5 Distributions of $W_{ness}$ are shown for the recorded data in red, and the simulated data in blue. Note that the vertical is plotted on a log scale. The two distributions have been normalized to total area. . . . .	186
7.6 Shown: the fraction of signal and background remaining (vertical axis) in the total data set with successively higher cuts in $W_{ness}$ (horizontal axis). The inflection point in the blue distribution is chosen as the optimal $W_{ness}$ cut. . . . .	187
7.7 Shown: distributions of the recorded data set for $dw_{23}$ , $\eta$ and $W_{ness}$ . The first column shows $\eta$ as a function of $W_{ness}$ . The middle column shows $dw_{23}$ as a function of $W_{ness}$ , and the right column shows a histogram of the $W_{ness}$ distribution. The rows all correspond to (top to bottom): North, $\mu+$ , North $\mu-$ , South $\mu+$ , and North $\mu-$ . . . . .	191

7.8	Shown: distributions of the simulated $W$ signal data set for $dw_{23}$ , $\eta$ and $W_{ness}$ . The first column shows $\eta$ as a function of $W_{ness}$ . The middle column shows $dw_{23}$ as a function of $W_{ness}$ , and the right column shows a histogram of the $W_{ness}$ distribution. The rows all correspond to (top to bottom): North, $\mu+$ , North $\mu-$ , South $\mu+$ , and North $\mu-$ . . . . .	192
7.9	From left to right the columns show $dw_{23}$ for the full $W_{ness}$ range, $0.1 < W_{ness} < 0.3$ , $0.3 < W_{ness} < 0.7$ , $0.3 < W_{ness} < 0.7$ , $0.7 < W_{ness} < 0.9$ . The columns show the extrapolated shape for $W_{ness} > 0.99$ . The red curve shows the 1D projection of the total 2D parameterization of $dw_{23}$ vs $W_{ness}$ plotted on top of the green curves. The green curve shows the coaxial double Gaussian fit to a slice of $dw_{23}$ in $W_{ness}$ . The final column shows the projected shape of $dw_{23}$ against the signal data region ( $W_{ness} > 0.99$ ). A0 and A1 refer to North or South arms, Q0 and Q1 refer to negatively or positively charged muons. . . . .	193
7.10	The four parameters from the co-axial Gaussian parameterization of $dw_{23}$ as a function of $W_{ness}$ . Rows are arm/charge, labeled on the left, while columns are co-axial Gaussian parameters, summarized in Equation 7.13 . . . . .	194
7.11	Shown: resulting fourth degree polynomial fit to the yield vs $W_{ness}$ representing the hadronic background region $0 < W_{ness} < 0.9$ of the real data. . . . .	195
7.12	Panel (a) shows a red wire-frame representing the resultant fit of to the $dw_{23}$ vs $W_{ness}$ distribution, against the lego-style real data distribution. Panel (b) shows the process of extrapolating the shape of $dw_{23}$ from lower $W_{ness}$ to the signal region to obtain the hadronic background PDF representing $dw_{23}$ . . . . .	197
7.13	Shown: a comparison of four independent extrapolations of $dw_{23}$ into the signal region [31]. . . . .	197
7.14	Left: distribution of number of collisions per crossing $\mu$ for all runs available from the 2013 data set. Right: True and observed BBCnovtx live rates for all runs as a function of the true rate and calculated as described in the text. The green, dashed line represents a perfect accounting of true collisions, while the red curve takes the efficiencies of the two BBC sides into account [31]. . . . .	200
7.15	Left Column: The hadronic background PDFs, Middle Column: The Summed Muon Background PDFs, Right Column: The W-Signal PDF. For South Arm, $\mu+$ . . . . .	201
7.16	Left Column: The hadronic background PDFs, Middle Column: The Summed Muon Background PDFs, Right Column: The W-Signal PDF. For South Arm, $\mu-$ . . . . .	202
7.17	Left Column: The hadronic background PDFs, Middle Column: The Summed Muon Background PDFs, Right Column: The W-Signal PDF. For North Arm, $\mu-$ . . . . .	202
7.18	Left Column: The hadronic background PDFs, Middle Column: The Summed Muon Background PDFs, Right Column: The W-Signal PDF. For South Arm, $\mu+$ . . . . .	203

7.19	Here, we see the preliminary results of the EULMF for the 2013 Run. On the left, $\eta$ is shown. In the middle, $dw_{23}$ . On the right, $dw_{23}$ is subdivided into the three standard $\eta$ bins. In all cases, we see the unbinned data in black (with error bars), and the sum of the three fits in black. In Blue, we can see the fake-muon hadronic background. In Green, the muon background. In blue, we see the W-Signal result. The area under the curves represents the yield, relative to the total. Shown: South Arm, $\mu-$ [31] . . . . .	204
7.20	Here, we see the preliminary results of the EULMF for the 2013 Run. On the left, $\eta$ is shown. In the middle, $dw_{23}$ . On the right, $dw_{23}$ is subdivided into the three standard $\eta$ bins. In all cases, we see the unbinned data in black (with error bars), and the sum of the three fits in black. In Blue, we can see the fake-muon hadronic background. In Green, the muon background. In blue, we see the W-Signal result. The area under the curves represents the yield, relative to the total. Shown: South Arm, $\mu+$ [31] . . . . .	205
7.21	Here, we see the preliminary results of the EULMF for the 2013 Run. On the left, $\eta$ is shown. In the middle, $dw_{23}$ . On the right, $dw_{23}$ is subdivided into the three standard $\eta$ bins. In all cases, we see the unbinned data in black (with error bars), and the sum of the three fits in black. In Blue, we can see the fake-muon hadronic background. In Green, the muon background. In blue, we see the W-Signal result. The area under the curves represents the yield, relative to the total. Shown: North Arm, $\mu-$ [31] . . . . .	206
7.22	Here, we see the preliminary results of the EULMF for the 2013 Run. On the left, $\eta$ is shown. In the middle, $dw_{23}$ . On the right, $dw_{23}$ is subdivided into the three standard $\eta$ bins. In all cases, we see the unbinned data in black (with error bars), and the sum of the three fits in black. In Blue, we can see the fake-muon hadronic background. In Green, the muon background. In blue, we see the W-Signal result. The area under the curves represents the yield, relative to the total. Shown: North Arm, $\mu+$ [31]. . . . .	207
8.1	Shown: the average beam polarization per run over the course of the 2013 data set. All of the runs in the analysis were indexed from 0 to approximately 1000, and plotted in the order that they were taken. The blue open circles are from the blue beam, the yellow open circles are for the yellow beam. . .	214
8.2	Panel (a) shows the yellow beam polarization distribution over all runs in the 2013 data taking period, with an average of about 55.27%. Panel (b) shows the blue beam similarly, with an average polarization of 55.08% polarization.	214
8.3	Shown: the crossing distribution for every run taken for the 2013 data set. We use the typical code for arm/charge. The top row is for the South Arm. The bottom row is for the North Arm. The left column is for negative charge, the right column is for positive charge. Note the characteristic empty abort gap, as well as the change from $109 \times 109$ colliding bunches to $111 \times 111$ colliding bunches about 1/3 of the way through the data taking period. . . . .	217

8.4	Shown: the yield for various crossing combinations as taken from the dataset itself, rather than the database. We see a very consistent distribution between the various possible crossing patterns. In this case, the horizontal axis is the crossing pattern code–0:++, 1:–+, 2:+–, 3:––. Any slight difference between yields for each pattern is well below our experimental precision. . . . .	218
8.5	Shown: the South arm’s yields for each helicity combination of colliding protons, with the polarization of the blue beam and yellow beams color coded in column 2. These yields represent all muons observed in the signal region, and are a combination of signal and background muons. + represents positive helicity beam polarization relative to the blue beam’s momentum, - represents negative helicity, with * representing an unfilled bunch. . . . .	221
8.6	Shown: the North arm’s yields for each helicity combination of colliding protons, with the polarization of the blue beam and yellow beams color coded in column 2. These yields represent all muons observed in the signal region, and are a combination of signal and background muons. + represents positive helicity beam polarization relative to the blue beam’s momentum, - represents negative helicity, with * representing an unfilled bunch. . . . .	222
8.7	Shown: the preliminary longitudinal single spin asymmetries for three distinct bins in $\eta$ per Muon Arm. The red boxed points represent the measured asymmetry from the 2013 analysis. The green points show the central rapidity asymmetries produced from STAR in 2014, with the blue points showing PHENIX’s central asymmetries from 2009-2012. The colored curves are superimposed predicted asymmetries. The top panel shows results for the $W^+$ process, with the bottom panel showing results for the $W^-$ process. . . . .	229
8.8	Shown: the preliminary longitudinal single spin asymmetries for two distinct bins in $\eta$ per Muon Arm. The red boxed points represent the measured asymmetry from the 2013 analysis. The green points show the central rapidity asymmetries produced from STAR in 2014, with the blue points showing PHENIX’s central asymmetries from 2009-2012. The colored curves are superimposed predicted asymmetries. The top panel shows results for the $W^+$ process, with the bottom panel showing results for the $W^-$ process. . . . .	230
B.1	The left panel shows the distribution of DG0, the linear distance between the reconstructed muon track and the road through station zero of the MUID, for each arm and charge, produced from the PHENIX data set, after the basic cut. The Right panel the same distributions from a simulation of the W-Signal. Both panels have the arm and charge data partitions are overlaid.	248
B.2	The left panel shows the distribution of DDG0, the opening angle between the reconstructed muon track and the road to station 0 of the MUID, for each arm and charge, produced from the PHENIX data set, after the basic cut. The right panel shows the same distributions from a simulation of the W-Signal. Both panels have the arm and charge data partitions are overlaid.	249

B.3	The left panel shows the distribution of $\chi^2$ , the reduced $\chi^2$ residual from track reconstruction, for each arm and charge, produced from the PHENIX data set, after the basic cut. The right panel shows the same distributions from a simulation of the W-Signal. Both panels have the arm and charge data partitions overlaid.	250
B.4	The left panel shows the distribution of $DCA_r$ , the transverse distance of closest approach between the track and the event vertex, for each arm and charge, produced from the PHENIX data set, after the basic cut. The right panel shows the same distributions from a simulation of the W-Signal. Both panels have the arm and charge data partitions overlaid.	251
B.5	The left panel shows the distribution of $Rpc3dca$ , the distance of closest approach between the reconstructed muon track and the RPC3 hit cluster, for each arm and charge, produced from the PHENIX data set, after the basic cut. The right panel shows the same distributions from a simulation of the W-Signal. Both panels show the arm and charge data partitions overlaid.	252
B.6	The left panel shows the distribution of $Rpc1dca$ , the distance of closest approach between the reconstructed muon track and the RPC1 hit cluster, for each arm and charge, produced from the PHENIX data set, after the basic cut. The right panel shows the same distributions from a simulation of the W-Signal. Both panels show the arm and charge data partitions overlaid.	253
C.1	MuID hit efficiency of south gap0 horizontal plane, for run11 (green), run12 (red) and run13 (blue).	255
C.2	MuID hit efficiency of south gap0 vertical plane, for run11 (green), run12 (red) and run13 (blue).	256
C.3	MuID hit efficiency of south gap1 horizontal plane, for run11 (green), run12 (red) and run13 (blue).	257
C.4	MuID hit efficiency of south gap1 vertical plane, for run11 (green), run12 (red) and run13 (blue).	258
C.5	MuID hit efficiency of south gap2 horizontal plane, for run11 (green), run12 (red) and run13 (blue).	259
C.6	MuID hit efficiency of south gap2 vertical plane, for run11 (green), run12 (red) and run13 (blue).	260
C.7	MuID hit efficiency of south gap3 horizontal plane, for run11 (green), run12 (red) and run13 (blue).	261
C.8	MuID hit efficiency of south gap3 vertical plane, for run11 (green), run12 (red) and run13 (blue).	262
C.9	MuID hit efficiency of south gap4 horizontal plane, for run11 (green), run12 (red) and run13 (blue).	263
C.10	MuID hit efficiency of south gap4 vertical plane, for run11 (green), run12 (red) and run13 (blue).	264
C.11	MuID hit efficiency of north gap0 horizontal plane, for run11 (green), run12 (red) and run13 (blue).	265
C.12	MuID hit efficiency of north gap0 vertical plane, for run11 (green), run12 (red) and run13 (blue).	266

C.13 MuID hit efficiency of north gap1 horizontal plane, for run11 (green), run12 (red) and run13 (blue) . . . . .	267
C.14 MuID hit efficiency of north gap1 vertical plane, for run11 (green), run12 (red) and run13 (blue) . . . . .	268
C.15 MuID hit efficiency of north gap2 horizontal plane, for run11 (green), run12 (red) and run13 (blue) . . . . .	269
C.16 MuID hit efficiency of north gap2 vertical plane, for run11 (green), run12 (red) and run13 (blue) . . . . .	270
C.17 MuID hit efficiency of north gap3 horizontal plane, for run11 (green), run12 (red) and run13 (blue) . . . . .	271
C.18 MuID hit efficiency of north gap3 vertical plane, for run11 (green), run12 (red) and run13 (blue) . . . . .	272
C.19 MuID hit efficiency of north gap4 horizontal plane, for run11 (green), run12 (red) and run13 (blue) . . . . .	273
C.20 MuID hit efficiency of north gap4 vertical plane, for run11 (green), run12 (red) and run13 (blue) . . . . .	274
C.21 Trigger efficiencies for trigger bit 17 ((MUIDLL1_N1D  S1D)&BBCLL1(noVtx)) for single $W \rightarrow \mu$ candidates with transverse momenta above 5 GeV. The efficiencies for ERT (blue), MPC (green), MinBias(red) and 1D (purple) trig- gered data samples are shown as well as a constant fit over the whole range.	275
C.22 Trigger efficiencies for trigger bit 18 (RPC1+RPC3_S) for single $W \rightarrow \mu$ candidates with transverse momenta above 5 GeV. The efficiencies for ERT (blue), MPC (green), MinBias(red) and 1D (purple) triggered data samples are shown as well as a constant fit over the whole range. . . . .	276
C.23 Trigger efficiencies for trigger bit 19 (RPC1+RPC3_N) for single $W \rightarrow \mu$ candidates with transverse momenta above 5 GeV. The efficiencies for ERT (blue), MPC (green), MinBias(red) and 1D (purple) triggered data samples are shown as well as a constant fit over the whole range. . . . .	277
C.24 Trigger efficiencies for trigger bit 20 (SG3&RPC3&MUID_1D_N  S) for single $W \rightarrow \mu$ candidates with transverse momenta above 5 GeV. The efficiencies for ERT (blue), MPC (green), MinBias(red) and 1D (purple) triggered data samples are shown as well as a constant fit over the whole range. . . . .	278
C.25 Trigger efficiencies for trigger bit 21 (SG1+RPC1(C)&MUIDLL1_N  S) for single $W \rightarrow \mu$ candidates with transverse momenta above 5 GeV. The effi- ciencies for ERT (blue), MPC (green), MinBias(red) and 1D (purple) trig- gered data samples are shown as well as a constant fit over the whole range.	279
C.26 Trigger efficiencies for trigger bit 22 ( MUON_S_SG1_RPC3A&MUID_S1D) for single $W \rightarrow \mu$ candidates with transverse momenta above 5 GeV. The efficiencies for ERT (blue), MPC (green), MinBias(red) and 1D (purple) trig- gered data samples are shown as well as a constant fit over the whole range.	280
C.27 Trigger efficiencies for trigger bit 23 ( MUON_N_SG1_RPC3A&MUID_N1D) for single $W \rightarrow \mu$ candidates with transverse momenta above 5 GeV. The efficiencies for ERT (blue), MPC (green), MinBias(red) and 1D (purple) trig- gered data samples are shown as well as a constant fit over the whole range.	281

C.28 Trigger efficiencies for trigger bit 24 (MUON_S_SG1&BBCLL1(noVtx)) for single $W \rightarrow \mu$ candidates with transverse momenta above 5 GeV. The efficiencies for ERT (blue), MPC (green), MinBias(red) and 1D (purple) triggered data samples are shown as well as a constant fit over the whole range. . . . .	282
C.29 Trigger efficiencies for trigger bit 25 (MUON_N_SG1&BBCLL1(noVtx)) for single $W \rightarrow \mu$ candidates with transverse momenta above 5 GeV. The efficiencies for ERT (blue), MPC (green), MinBias(red) and 1D (purple) triggered data samples are shown as well as a constant fit over the whole range. . . . .	283
C.30 Trigger efficiencies for trigger bit 26 (MUON_S_SG1_RPC3_1_B  C) for single $W \rightarrow \mu$ candidates with transverse momenta above 5 GeV. The efficiencies for ERT (blue), MPC (green), MinBias(red) and 1D (purple) triggered data samples are shown as well as a constant fit over the whole range. . . . .	284
C.31 Trigger efficiencies for trigger bit 27 (MUON_N_SG1_RPC3_1_B  C) for single $W \rightarrow \mu$ candidates with transverse momenta above 5 GeV. The efficiencies for ERT (blue), MPC (green), MinBias(red) and 1D (purple) triggered data samples are shown as well as a constant fit over the whole range. . . . .	285
C.32 Trigger efficiencies for trigger bit 17 ((MUIDLL1_N1D  S1D)&BBCLL1(noVtx)) for single $W \rightarrow \mu$ candidates in the rapidity range $1.4 < \eta < 2.0$ as a function of transverse momentum. The efficiencies for ERT (blue), MPC (green), MinBias(red) and 1D (purple) triggered data samples are shown as well as a constant fit over the whole range. . . . .	286
C.33 Trigger efficiencies for trigger bit 17 ((MUIDLL1_N1D  S1D)&BBCLL1(noVtx)) for single $W \rightarrow \mu$ candidates in the rapidity range $2.0 < \eta < 2.6$ as a function of transverse momentum. The efficiencies for ERT (blue), MPC (green), MinBias(red) and 1D (purple) triggered data samples are shown as well as a constant fit over the whole range. . . . .	287
C.34 Trigger efficiencies for trigger bit 20 (SG3&RPC3&MUID_1D_N  S) for single $W \rightarrow \mu$ candidates in the rapidity range $1.1 < \eta < 1.4$ as a function of transverse momentum. The efficiencies for ERT (blue), MPC (green), MinBias(red) and 1D (purple) triggered data samples are shown as well as a constant fit over the whole range. . . . .	288
C.35 Trigger efficiencies for trigger bit 20 (SG3&RPC3&MUID_1D_N  S) for single $W \rightarrow \mu$ candidates in the rapidity range $1.4 < \eta < 2.0$ as a function of transverse momentum. The efficiencies for ERT (blue), MPC (green), MinBias(red) and 1D (purple) triggered data samples are shown as well as a constant fit over the whole range. . . . .	289
C.36 Trigger efficiencies for trigger bit 20 (SG3&RPC3&MUID_1D_N  S) for single $W \rightarrow \mu$ candidates in the rapidity range $2.0 < \eta < 2.6$ as a function of transverse momentum. The efficiencies for ERT (blue), MPC (green), MinBias(red) and 1D (purple) triggered data samples are shown as well as a constant fit over the whole range. . . . .	290

C.37 Trigger efficiencies for trigger bit 21 (SG1+RPC1(C)&MUIDLL1_N  S) for single $W \rightarrow \mu$ candidates in the rapidity range $1.1 < \eta < 1.4$ as a function of transverse momentum. The efficiencies for ERT (blue), MPC (green), MinBias(red) and 1D (purple) triggered data samples are shown as well as a constant fit over the whole range. . . . .	291
C.38 Trigger efficiencies for trigger bit 22 ( MUON_S_SG1_RPC3A&MUID_S1D) for single $W \rightarrow \mu$ candidates in the rapidity range $1.4 < \eta < 2.0$ as a function of transverse momentum. The efficiencies for ERT (blue), MPC (green), MinBias(red) and 1D (purple) triggered data samples are shown as well as a constant fit over the whole range. . . . .	292
C.39 Trigger efficiencies for trigger bit 22 ( MUON_S_SG1_RPC3A&MUID_S1D) for single $W \rightarrow \mu$ candidates in the rapidity range $2.0 < \eta < 2.6$ as a function of transverse momentum. The efficiencies for ERT (blue), MPC (green), MinBias(red) and 1D (purple) triggered data samples are shown as well as a constant fit over the whole range. . . . .	293
C.40 Trigger efficiencies for trigger bit 23 ( MUON_N_SG1_RPC3A&MUID_N1D) for single $W \rightarrow \mu$ candidates in the rapidity range $1.4 < \eta < 2.0$ as a function of transverse momentum. The efficiencies for ERT (blue), MPC (green), MinBias(red) and 1D (purple) triggered data samples are shown as well as a constant fit over the whole range. . . . .	294
C.41 Trigger efficiencies for trigger bit 23 ( MUON_N_SG1_RPC3A&MUID_N1D) for single $W \rightarrow \mu$ candidates in the rapidity range $2.0 < \eta < 2.6$ as a function of transverse momentum. The efficiencies for ERT (blue), MPC (green), MinBias(red) and 1D (purple) triggered data samples are shown as well as a constant fit over the whole range. . . . .	295
C.42 Trigger efficiencies for trigger bit 26 (MUON_S_SG1_RPC3_1_B  C) for single $W \rightarrow \mu$ candidates in the rapidity range $1.1 < \eta < 1.4$ as a function of transverse momentum. The efficiencies for ERT (blue), MPC (green), MinBias(red) and 1D (purple) triggered data samples are shown as well as a constant fit over the whole range. . . . .	296
C.43 Trigger efficiencies for trigger bit 26 (MUON_S_SG1_RPC3_1_B  C) for single $W \rightarrow \mu$ candidates in the rapidity range $1.4 < \eta < 2.0$ as a function of transverse momentum. The efficiencies for ERT (blue), MPC (green), MinBias(red) and 1D (purple) triggered data samples are shown as well as a constant fit over the whole range. . . . .	297
C.44 Trigger efficiencies for trigger bit 27 (MUON_N_SG1_RPC3_1_B  C) for single $W \rightarrow \mu$ candidates in the rapidity range $1.1 < \eta < 1.4$ as a function of transverse momentum. The efficiencies for ERT (blue), MPC (green), MinBias(red) and 1D (purple) triggered data samples are shown as well as a constant fit over the whole range. . . . .	298

C.45 Trigger efficiencies for trigger bit 27 (MUON_N_SG1_RPC3_1_B  C) for single $W \rightarrow \mu$ candidates in the rapidity range $1.4 < \eta < 2.0$ as a function of transverse momentum. The efficiencies for ERT (blue), MPC (green), MinBias(red) and 1D (purple) triggered data samples are shown as well as a constant fit over the whole range. . . . .	299
C.46 Trigger efficiencies for trigger bit 17 ((MUIDLL1_N1D  S1D)&BBCLL1(noVtx)) for single $W \rightarrow \mu$ candidates in the rapidity range $1.4 < \eta < 2.0$ as a function of $W_{ness}$ . The efficiencies for ERT (blue), MPC (green), MinBias(red) and 1D (purple) triggered data samples are shown as well as a constant fit over the whole range. . . . .	300
C.47 Trigger efficiencies for trigger bit 17 ((MUIDLL1_N1D  S1D)&BBCLL1(noVtx)) for single $W \rightarrow \mu$ candidates in the rapidity range $2.0 < \eta < 2.6$ as a function of $W_{ness}$ . The efficiencies for ERT (blue), MPC (green), MinBias(red) and 1D (purple) triggered data samples are shown as well as a constant fit over the whole range. . . . .	301
C.48 Trigger efficiencies for trigger bit 20 (SG3&RPC3&MUID_1D_N  S) for single $W \rightarrow \mu$ candidates in the rapidity range $1.1 < \eta < 1.4$ as a function of $W_{ness}$ . The efficiencies for ERT (blue), MPC (green), MinBias(red) and 1D (purple) triggered data samples are shown as well as a constant fit over the whole range.	302
C.49 Trigger efficiencies for trigger bit 20 (SG3&RPC3&MUID_1D_N  S) for single $W \rightarrow \mu$ candidates in the rapidity range $1.4 < \eta < 2.0$ as a function of $W_{ness}$ . The efficiencies for ERT (blue), MPC (green), MinBias(red) and 1D (purple) triggered data samples are shown as well as a constant fit over the whole range.	303
C.50 Trigger efficiencies for trigger bit 20 (SG3&RPC3&MUID_1D_N  S) for single $W \rightarrow \mu$ candidates in the rapidity range $2.0 < \eta < 2.6$ as a function of $W_{ness}$ . The efficiencies for ERT (blue), MPC (green), MinBias(red) and 1D (purple) triggered data samples are shown as well as a constant fit over the whole range.	304
C.51 Trigger efficiencies for trigger bit 21 (SG1+RPC1(C)&MUIDLL1_N  S) for single $W \rightarrow \mu$ candidates in the rapidity range $1.1 < \eta < 1.4$ as a function of $W_{ness}$ . The efficiencies for ERT (blue), MPC (green), MinBias(red) and 1D (purple) triggered data samples are shown as well as a constant fit over the whole range. . . . .	305
C.52 Trigger efficiencies for trigger bit 22 ( MUON_S_SG1_RPC3A&MUID_S1D) for single $W \rightarrow \mu$ candidates in the rapidity range $1.4 < \eta < 2.0$ as a function of $W_{ness}$ . The efficiencies for ERT (blue), MPC (green), MinBias(red) and 1D (purple) triggered data samples are shown as well as a constant fit over the whole range. . . . .	306
C.53 Trigger efficiencies for trigger bit 22 ( MUON_S_SG1_RPC3A&MUID_S1D) for single $W \rightarrow \mu$ candidates in the rapidity range $2.0 < \eta < 2.6$ as a function of $W_{ness}$ . The efficiencies for ERT (blue), MPC (green), MinBias(red) and 1D (purple) triggered data samples are shown as well as a constant fit over the whole range. . . . .	307

C.54 Trigger efficiencies for trigger bit 23 ( MUON_N_SG1_RPC3A&MUID_N1D) for single $W \rightarrow \mu$ candidates in the rapidity range $1.4 < \eta < 2.0$ as a function of $W_{ness}$ . The efficiencies for ERT (blue), MPC (green), MinBias(red) and 1D (purple) triggered data samples are shown as well as a constant fit over the whole range. . . . .	308
C.55 Trigger efficiencies for trigger bit 23 ( MUON_N_SG1_RPC3A&MUID_N1D) for single $W \rightarrow \mu$ candidates in the rapidity range $2.0 < \eta < 2.6$ as a function of $W_{ness}$ . The efficiencies for ERT (blue), MPC (green), MinBias(red) and 1D (purple) triggered data samples are shown as well as a constant fit over the whole range. . . . .	309
C.56 Trigger efficiencies for trigger bit 26 (MUON_S_SG1_RPC3_1_B  C) for single $W \rightarrow \mu$ candidates in the rapidity range $1.1 < \eta < 1.4$ as a function of $W_{ness}$ . The efficiencies for ERT (blue), MPC (green), MinBias(red) and 1D (purple) triggered data samples are shown as well as a constant fit over the whole range.	310
C.57 Trigger efficiencies for trigger bit 26 (MUON_S_SG1_RPC3_1_B  C) for single $W \rightarrow \mu$ candidates in the rapidity range $1.4 < \eta < 2.0$ as a function of $W_{ness}$ . The efficiencies for ERT (blue), MPC (green), MinBias(red) and 1D (purple) triggered data samples are shown as well as a constant fit over the whole range.	311
C.58 Trigger efficiencies for trigger bit 27 (MUON_N_SG1_RPC3_1_B  C) for single $W \rightarrow \mu$ candidates in the rapidity range $1.1 < \eta < 1.4$ as a function of $W_{ness}$ . The efficiencies for ERT (blue), MPC (green), MinBias(red) and 1D (purple) triggered data samples are shown as well as a constant fit over the whole range.	312
C.59 Trigger efficiencies for trigger bit 27 (MUON_N_SG1_RPC3_1_B  C) for single $W \rightarrow \mu$ candidates in the rapidity range $1.4 < \eta < 2.0$ as a function of $W_{ness}$ . The efficiencies for ERT (blue), MPC (green), MinBias(red) and 1D (purple) triggered data samples are shown as well as a constant fit over the whole range.	313
C.60 Trigger efficiencies for trigger bit 17 ((MUIDLL1_N1D  S1D)&BBCLL1(noVtx)) for single $W \rightarrow \mu$ candidates in the rapidity range $1.4 < \eta < 2.0$ as a function of $\phi$ . The efficiencies for ERT (blue), MPC (green), MinBias(red) and 1D (purple) triggered data samples are shown as well as a constant fit over the whole range. . . . .	314
C.61 Trigger efficiencies for trigger bit 24 (left, MUON_S_SG1&BBCLL1(noVtx)) and 25(right, MUON_N_SG1&BBCLL1(noVtx)) for single $W \rightarrow \mu$ candidates in the rapidity range $1.4 < \eta < 2.0$ as a function of $\phi$ . The efficiencies for ERT (blue), MPC (green), MinBias(red) and 1D (purple) triggered data samples are shown as well as a constant fit over the whole range. . . . .	315
C.62 Trigger efficiencies for trigger bit 24 (left, MUON_S_SG1&BBCLL1(noVtx)) and 25(right, MUON_N_SG1&BBCLL1(noVtx)) for single $W \rightarrow \mu$ candidates in the rapidity range $1.4 < \eta < 2.0$ as a function of $\phi$ . The efficiencies for ERT (blue), MPC (green), MinBias(red) and 1D (purple) triggered data samples are shown as well as a constant fit over the whole range. . . . .	316

C.63 Trigger efficiencies for trigger bit 22 (left, MUON_S_SG1_RPC3A&MUID_S1D) and 23(right, MUON_N_SG1_RPC3A&MUID_S1D) for single $W \rightarrow \mu$ candidates in the rapidity range $2.0 < \eta < 2.6$ as a function of $\phi$ . The efficiencies for ERT (blue), MPC (green), MinBias(red) and 1D (purple) triggered data samples are shown as well as a constant fit over the whole range. . . . .	317
D.1 Trigger efficiencies for trigger bit 17 (((MUIDLL1_N1D  S1D)&BBCLL1(noVtx))) for single $W \rightarrow \mu$ candidates in the rapidity range $1.4 < \eta < 2.0$ (left) and $2.0 < \eta < 2.6$ (right) as a function of the raw BBCnoVtx rate. The efficiencies for ERT (blue), MPC (green), MinBias(red) and 1D (purple) triggered data samples are shown as well as a constant fit over the whole range. . . . .	319
D.2 Trigger efficiencies for trigger bit 24 (left, MUON_S_SG1&BBCLL1(noVtx)) and 25(right, MUON_N_SG1&BBCLL1(noVtx)) for single $W \rightarrow \mu$ candidates in the rapidity range $1.4 < \eta < 2.0$ as a function of raw BBCnoVertex rate. The efficiencies for ERT (blue), MPC (green), MinBias(red) and 1D (purple) triggered data samples are shown as well as a constant fit over the whole range.	321
D.3 Trigger efficiencies for trigger bit 26 (MUON_S_SG1_RPC3_1_B  C, left) and 27 (MUON_N_SG1_RPC3_1_B  C, right) for single $W \rightarrow \mu$ candidates in the rapidity range $1.4 < \eta < 2.0$ as a function of raw BBCnovertex rate. The efficiencies for ERT (blue), MPC (green), MinBias(red) and 1D (purple) triggered data samples are shown as well as a constant fit over the whole range.	323
D.4 Total trigger efficiencies in the $W \rightarrow \mu$ candidates separated by arm and charge for various muon triggers as a function of rapidity. Those with substantial contributions are given in the Legend to the right for each arm including their average efficiencies and relative contributions. . . . .	324
D.5 Total trigger efficiencies in the $W \rightarrow \mu$ candidates separated by arm and charge for various muon triggers as a function of rapidity. Those with substantial contributions are given in the Legend to the right for each arm including their average efficiencies and relative contributions. . . . .	325
D.6 Total trigger efficiencies in the $W \rightarrow \mu$ candidates separated by arm and charge for various muon triggers as a function of rapidity. Those with substantial contributions are given in the Legend to the right for each arm including their average efficiencies and relative contributions. . . . .	326
D.7 Total trigger efficiencies in the $W \rightarrow \mu$ candidates separated by arm and charge for various muon triggers as a function of rapidity. Those with substantial contributions are given in the Legend to the right for each arm including their average efficiencies and relative contributions. . . . .	327
D.8 Total trigger efficiencies in the $W \rightarrow \mu$ candidates separated by arm and charge for various muon triggers as a function of rapidity. Those with substantial contributions are given in the Legend to the right for each arm including their average efficiencies and relative contributions. . . . .	328

E.1	Raw asymmetries $\epsilon_L$ for the Blue (blue symbols) and Yellow (orange symbols) beams and $\epsilon_{LL}$ (black symbols) for both arms and charges as a function of the pre-selection range. The combination of all rapidities in one bin after selecting the <b>sideband</b> $dw_{23}$ region is displayed. In addition the extracted signal to background ratios are displayed using the right-hand axis values. The green line displays the data-based extraction method while the magenta line represents the MC signal based extraction. . . . .	331
E.2	Raw asymmetries as a function of minimal $W_{ness}$ cut when splitting the data sample into three nearly equal luminosity bins of increasing BBC rate in the order of open triangles, open squares and open circles. Each plot displays one asymmetry for each arm and charge. The central $dw_{23}$ region has been selected. In addition the extracted signal to background ratios are displayed using the right-hand axis values. The green line displays the data-based extraction method while the magenta line represents the MC signal based extraction. . . . .	333
E.3	Student T scores and distribution when comparing the lot to medium and the low to high rate subset. . . . .	334
E.4	Raw asymmetries as a function of minimal $W_{ness}$ cut when splitting the data sample into three nearly equal luminosity bins of increasing run number in the order of open triangles, open squares and open circles. Each plot displays one asymmetry for each arm and charge. The central $dw_{23}$ region has been selected. In addition the extracted signal to background ratios are displayed using the right-hand axis values. The green line displays the data-based extraction method while the magenta line represents the MC signal based extraction. . . . .	336
E.5	Student T scores and distribution when comparing the lot to medium and the low to high run number subset . . . . .	337
E.6	Raw asymmetries $\epsilon_L$ for the Blue (blue symbols) and Yellow (orange symbols) beams and $\epsilon_{LL}$ (black symbols) for both arms and charges as a function of the minimal transverse momentum cut are displayed. In addition the extracted signal to background ratios are displayed using the right-hand axis values. The green line displays the data-based extraction method while the magenta line represents the MC signal based extraction. . . . .	339
E.7	Raw asymmetries $\epsilon_L$ for the Blue (blue symbols) and Yellow (orange symbols) beams and $\epsilon_{LL}$ (black symbols) for both arms and charges as a function of transverse momentum are displayed. The combination of all rapidities in one bin after selecting the central $dw_{23}$ region is displayed. In addition the extracted signal to background ratios are displayed using the right-hand axis values. The green line displays the data-based extraction method while the magenta line represents the MC signal based extraction. . . . .	340



# List of Tables

4.1	Some units describing the geometry of and data taken by PHENIX. . . . .	66
4.2	A summary of PHENIX hardware [32]. $e^\pm/\pi^\pm$ separation and $\pi/K$ separation requires the Time of Flight (ToF) working with PbGl and PbSc data. PbGl refers to “Lead Glass Scintillator” and PbSc refers to “Lead Scintillator”. The Muon Identifier (Muon ID, MuID) can help suppress hadrons by absorbing them in the iron layers. . . . .	67
4.3	The design characteristics of the RPCs [26] . . . . .	81
4.4	‘List of Triggers used in the 2013 run and description of hit requirements in various detectors. Some reminders about detector geometry: MUID has 5 gaps and last gap describes the furthest gap away from the collision that sees a hit. MuTr measures Sagita (amount of azimuthal bending of a track) in terms of number of MuTr strips. RPC has two stations - station 1 is closest to the collision, station 3 is further away. Station 1 has two “rings” of modules in $\theta$ (B, C). Station 3 has three rings (A, B, C)’ [33] . . . . .	93
5.1	A summary of vernier scans in run 12. Scans which proceed with the horizontal scan, followed by the vertical scan are denoted ‘H - V’, with the reverse order denoted similarly. Scan types are defined in Figure 5.1 . . . . .	98
5.2	The variables we use in the vernier analysis. Some variables are extracted directly from the data streams (such as the bbc-rate), while others are calculated from distributions of variables (such as the beam-width, $\sigma_{x,y}$ ). . .	99
5.3	Shown: the horizontal scan. BPM data compared to CAD planned steps for run 359711. Columns are from left to right, we see the CAD planned horizontal beam displacement, the bpm-measured horizontal beam displacement, $  CAD_x  -  BPM_x  $ (to account for polarity flips in bpm), the CAD planned vertical beam displacement, the bpm-measured beam displacement, $  CAD_y  -  BPM_y  $ , the total beam separation ( $\sqrt{BPM_x^2 + BPM_y^2}$ ) and the difference between the measured total separation and the CAD planned total separation. Nominally, CAD intends to hold one beam fixed, and scan the other beam. Rows are each scan step planned and measured for the run. .	106

5.4	Shown: the vertical scan. BPM data is compared to CAD planned steps for run 359711. Columns are from left to right, we see the CAD planned horizontal beam displacement, the bpm-measured horizontal beam displacement, $  CAD_x  -  BPM_x  $ (to account for polarity flips in bpm), the CAD planned vertical beam displacement, the bpm-measured beam displacement, $  CAD_y  -  BPM_y  $ , the total beam separation ( $\sqrt{BPM_x^2 + BPM_y^2}$ ) and the difference between the measured total separation and the CAD planned total separation. Nominally, CAD intends to hold one beam fixed, and scan the other beam. Rows are each scan step planned and measured for the run.	107
5.5	Data extracted from PRDFs.	110
5.6	The parameters characterizing the hourglass simulation are described. Though the normalization of the luminosity describing the final $z$ -vertex profile with a fixed offset depends on many parameters, only parameters shown actually effect the shape of the distribution.	138
6.1	Shown: the triggers sensitive to $W$ boson muonic decay [30]	157
7.1	The Basic Cuts used in the Run 13 analysis. lastGap refers to the last gap in the MUID which saw a $\mu$ candidate event. The fourth gap is the furthest penetration possible, therefore suggesting a high enough energy muon. Other parameters are described in Tables A.1, A.2, A.3, and A.4	176
7.2	Simulated sub processes in Run 13 including their generated event numbers as well as the corresponding luminosity and cross sections. An extensive analysis of the simulated data was undertaken to determine an appropriate k-factor.	178
7.3	South arm $W \rightarrow \mu^-$ fit results per analyzer [31]	205
7.4	A summary table from the results of the EULMF to the unbinned data set, summed to one $\eta$ bin per arm and charge.	209
8.1	From left to right, bunch 0 in the blue or yellow beam is filled with the leftmost polarization, with bunch 1 getting the next, and so on. The pattern repeats as soon as the end has been reached, until we get to the last filled bunch, with any empty bunch being ‘polarized’ as if it were not empty.	219
8.2	Shown: a division of the yields by arm, charge, and helicity combination, which is color-coded for the polarization of the blue and yellow beams. Yields contain a combination of signal and background muons. + represents positive helicity beam polarization relative to the blue beam’s momentum, - represents negative helicity, with * representing an unfilled bunch.	223
8.3	A summary of the sign convention when we consider rapidity with respect to the probe beam, as opposed to the rapidity of the PHENIX coordinate system. Column <b>Sign of <math>\eta</math></b> refers to the sign of $\eta$ of the observed muon track with respect to the probe beam.	225
A.1	Variables characterizing events overall	243

A.2	Muon tracker variables. Generally, this data set is indexed on a subevent level, where one event will contain all reconstructed muon tracks seen for that event.	244
A.3	A summary of the variables reconstructed from FVTX raw data [34].	244
A.4	RPC Track matching variables	245
A.5	$\eta$ dependent trigger efficiencies are calculated for the South arm in 20 $\eta$ bins. Each correction has both systematic and statistical error accounted for.	245
A.6	$\eta$ dependent trigger efficiencies are calculated for the North arm in 20 $\eta$ bins. Each correction has both systematic and statistical error accounted for.	246
A.7	A typical run from the 2013 data set, numbered with PHENIX's standard numbering scheme. Each trigger has a descriptive name hinting its composition (some triggers are actually constructed from trigger coincidences). Since PHENIX cannot record all data, we see the scale-down, the raw rate, and the live-time, which is basically a DAQ triggering efficiency.	247

# Chapter 1

## Introduction

Nuclear structure has been studied since the late 19th century, but a complete understanding of the proton's spin has eluded scientists. Early models of the proton structure such as the three valence quark model could accurately predict the charge and spin of the proton. When the spin contribution of the valence quarks was measured in 1988 [35], their contribution was found to be much less than the total spin of  $1/2$ . This event is known as the ‘proton spin crisis’ (Figure 1.1).

Although recent papers [36] have suggested that this ‘spin crisis’ (Figure 1.1) is simply due to mis-attribution of spin, most literature to date has focused on understanding how to model the proton with parton distribution functions, and the vast scientific consensus is that the EMC results published detailing the spin crisis in 1988 are valid.

Following the spin crisis, a major challenge in particle physics theory was to create a framework which could explain both the ‘valence-quark’ behavior of protons at some scattering energies, as well as predict the break down of that model and properly account for the proton’s spin. Global analyses [15] were undertaken to model the proton with probabilistic structure functions, incorporating scale-dependent structure. These global analyses require experimental data as a constraint for the structure function parameterization. One method of providing constraints is through the measurement of particle production asymmetries [37].

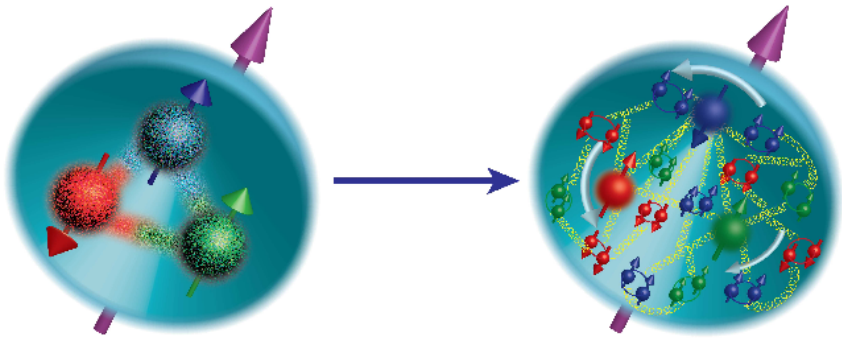


Figure 1.1: Left: the naïve quark model, while predicting the correct spin of the proton, does not bear fruit when the quark spin contribution is measured. Right: a more realistic cartoon of the proton as a composite of gluons, valence quarks and sea-quarks [1].

Structure functions can be used to calculate parton distribution functions, which describe the momentum fraction carried by partons in the proton. Parton distribution functions may describe either polarized or unpolarized partons. In global analyses, the parton distribution functions for quark polarization are calculated from the structure functions, and experimental data constrains these functions via the calculation of the asymmetry.

## 1.1 Scope and Objectives of This Work

This thesis seeks to measure the longitudinal asymmetry of the  $W \rightarrow \mu$  process in order to provide experimental data to constrain the polarized parton distribution functions characterizing the anti-quarks in the proton sea. Additionally, I present an analysis which characterizes the luminosity of the beams produced at the Relativistic Heavy Ion Collider (RHIC).

I begin by laying out the historical foundations of deep inelastic scattering, and the larger pursuit to understand the structure of matter in Chapter 2. Then, I describe the theoretical underpinnings of proton structure, for both unpolarized and polarized parton distribution functions in Chapter 3. Chapter 4 contains a description the experimental apparatus, the Relativistic Heavy Ion Collider (RHIC), and how it is used to carry out the data acquisition and facilitate this analysis. I will discuss the Vernier Analysis (Chapter 5), and how this relates to understanding the absolute luminosity delivered by RHIC

collisions—an important parameter needed to normalize any cross section measured experimentally at RHIC. Chapters 6-8 contains a discussion of the analysis of the data set taken by the Pioneering High Energy Nuclear Interaction Experiment (PHENIX) at RHIC in 2013. These chapters motivate the selection of analysis variables from the data set, the transformations applied to the data to extract our observable, the longitudinal asymmetry, and the calculation of the asymmetry itself. Finally, I will discuss the outlook and impact of these measurements in Chapter 9.

# Chapter 2

## History

### 2.1 The Phenomenon of Spin

Spin is a fundamental quantity possessed by all elementary particles. The word ‘spin’ is used to describe the property because particles which possess spin behave as though they have some kind of intrinsic hidden rotation, as if they were ‘spinning’. The dimension of spin is angular momentum. Spin is somewhat bizarre, because one does not observe anything physically spinning, although there are some phenomena (such as orbital angular momenta) which can be naively thought of as a ‘spinning system’. For quantum mechanical systems, the classical analogy breaks down since a system’s spin is a superposition of possible spin states. The role of spin in physics is of foundational importance, therefore physicists should strive to understand origin of spin in the building blocks of the visible universe—protons and neutrons.

Relativistic particles that possess non-zero spin are chiral (handed). The existence of Chirality has huge implications for how elementary particles can generate structure in matter itself [38]. In the case of the weak interaction, the presence of spin creates chiral spinors that break the left-right symmetry of weak coupling in matter. This symmetry breaking is exploited in this thesis to probe the spin of the proton sea.

The phenomena of spin also imposes rules for how ensembles of particles may exist in a potential. Particles with spin are fermions. Because these particles must obey Fermi-statistics, structure is observed in all the visible matter of the universe. Without spin, the world as we know it would collapse in on itself, making any kind of extended non-exotic structures which currently exist by virtue of the Pauli exclusion principal, impossible.

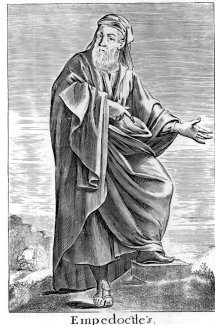
## 2.2 A Brief History of Relevant Physics

The study of spin is an outgrowth of the general study of matter. Models for matter, and the underlying structure of matter (in the modern sense), represent over a hundred years of experimental and theoretical efforts, and thousands of years of contemplating what makes up the universe.

Although indulgent on my part, I find it interesting and humbling to try and map out the path that humanity and science has trodden on its way to understanding the building blocks of the universe. To find the first time that humanity began to realize that our visible world is constructed from invisible, fundamental building blocks, we must travel back nearly 2,500 years into the past.

## 2.3 Ancient Foundations

Sometime between 490 - 370 BCE lived two philosophers, Empedocles (Figure 2.1a), and Democritus (Figure 2.1b). Both men lived approximately at the same time and made huge philosophical leaps in attempting to understand the nature of the visible world.



(a) Empedocles [39]



(b) Democritus [40]

Figure 2.1: Two Greek philosophers, who made important philosophical contributions our understanding of matter. Empedocles (Panel (a)), postulated the precursor to the elemental theory of matter[2] and Democritus (Panel (b)), postulated the precursor to the atomic theory of matter.

Democritus was part of a movement of thought which was first to make the intellectual jump that perhaps matter was not a continuum, but instead composed of ‘atomon’.

‘Atomon’ were thought to be small and indivisible particles building up all that is observable [41]. Empedocles made an equally important philosophical stride—he posited that matter must be composed of elemental primitives and that the properties of the primitives which build up matter, influence the properties of the bulk matter itself [2].

Although Empedocles’ ‘periodic table’ was only composed of Earth, Water, Fire, and Air, the idea that some unseen transmutation of elemental forces might generate observables in nature was an important step forward. This was the first time that humans considered that underlying structure in matter might influence the bulk properties of matter. Proto-scientists were beginning to generate models which derived our complicated observations from simpler forms.

## 2.4 The Scientific Revolution

Thanks to the mathematical foundations laid out by the minds of the Islamic Golden Age (8th century - 13th century), Europe was well poised to reignite the flames of scientific inquiry during the post Renaissance Scientific Revolution [42] (17th - 18th centuries), following a renewed interest the ideas of Greek philosophers after the dark ages.

The Scientific Revolution represented an unprecedented period of growth in science, thanks the foundations laid during the Italian Renaissance and emergence of British Empiricism [43].



(a) Galileo [44]



(b) Newton

Figure 2.2: Giants in the age of Empiricism, Newton (Panel (a)) and Galileo (Panel (b)) both made foundational contributions to Physics. Galileo lived in Italy, born in 1564 and dying in 1642. Newton lived in England from 1642 until his death in 1727

### 2.4.1 Galileo Galilei

Coming at the tail end of the Italian Renaissance, Galileo brought us into the age of Scientific Revolution.

While Galileo is best known for his work in Observational Astronomy, his importance to science extends beyond this. During his years in exile for his controversial views regarding the heliocentric universe, he produced some of his most important scientific work in kinematics [45]. What made this work remarkable is the care that Galileo took in merging mathematical modeling with well designed experimentation. This methodical approach to inquiry laid the foundation for the scientific method, which others would refine.

Galileo's formalization of the scientific method inexorably set science on a course to delving deep into the nature of matter and the laws of nature.

### 2.4.2 Isaac Newton

Fittingly born in the same year as Galileo's death, Isaac Newton would carry on Galileo's legacy of rigorous mathematical modeling mixed with experimentation. Perhaps no other scientist has touched so many different aspects of physics, from theories of propagation of light, to celestial mechanics, to mathematics, and kinematics.

Newton's Principia is arguably the most important scientific work ever published. It opened the doors of the universe in a way that nobody has since duplicated—Newtons' laws of motion are still taught in school today, and applied in real scientific contexts, providing the basis for the NASA space exploration program. Although Newton's models for motion have since been shown to be inaccurate at the smallest and largest scales, they still provide startlingly accurate predictions at intermediate scales.

One particularly prescient theory of Newton's was his corpuscular theory of light. Although not his most influential theory by far, the idea that an apparently continuous medium such as a beam of light might be made of small packets of energy (corpuscles) turned out to be partially right [46], and gained an interesting new context with the emergence of Quantum Mechanics in the early 20th century.

Newton's theories, and contributions to science are enormous, and have moved us deeper still into the underpinnings of matter. It would not be until roughly 200 years after his death, in the 19th century, that we finally can take the first steps into the world of the atomic, and sub-atomic: the world of the proton.

## 2.5 Atomic Theory

On the shoulders of giants such as Newton and Galileo, science finally came to know the tool which has been indispensable to modern particle physics: scattering. Rutherford and Thompson both carried out the most important scattering experiments in modern science. These experiments provided us with the first hints of a hidden, quantum world. It would not be until the 20th century that these important experiments would be fully contextualized with a theory of quantum scattering.

Scattering experiments offer a very powerful method where one uses a well known initial state of matter (typically in the form of a beam) and allows this beam to interact with an unknown configuration of matter. The final state of the target and scattered beam are measured. With a careful study of the kinematics of the scattered beam, one can create models that offer a peak into the structure of the target matter. As we journey down further in scale, matter begins to look quite different. In fact, the models we use are scale dependent, Figure 2.3. Thomson (Figure 2.8), and Rutherford (Figure 2.5) began to see matter as collections of atoms. Soon, nuclei were discovered to be divisible into protons and neutrons, which in turn were discovered to be composed of a sea of quarks and gluons.

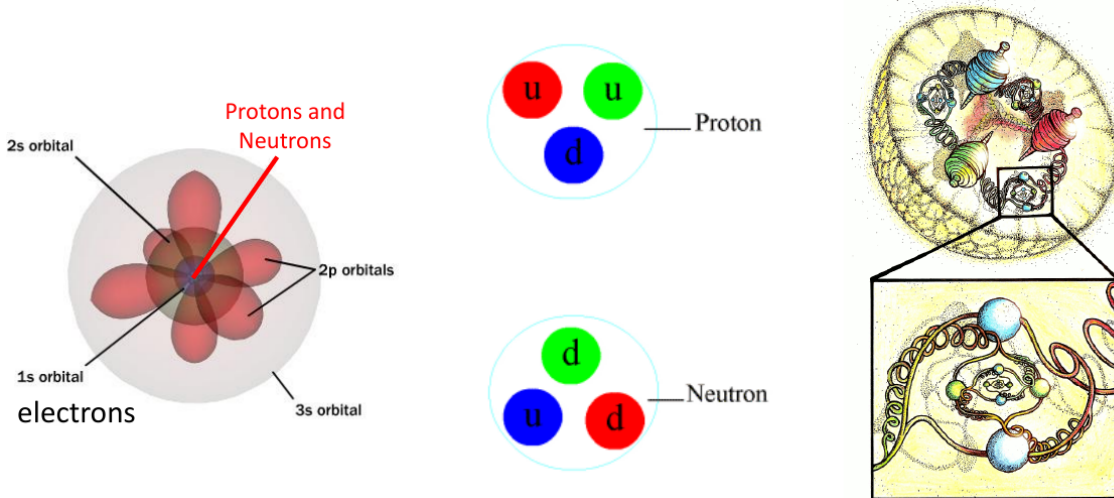


Figure 2.3: Matter at an atomic scale [3] (left), intermediate nuclear scale [4] (center), and the sub-nuclear partonic scale (right) [5]

### 2.5.1 John Dalton

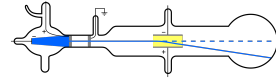
While many had postulated the existence of atoms, the first evidence based theory which suggested the existence of atoms was produced by John Dalton in the early 19th century. Dalton made an important conceptual leap to relate the existence of stoichiometric ratios in chemistry to the presence of small, individual functional units in his experiments with chemical reactions. Dalton's realization was only made possible due to his careful accounting of reactants in his experiments.

However, humanity had to wait for Einstein's 1905 theory on Brownian Motion to be experimentally verified by Jean Perrin to obtain the first limits on the mass and size of atoms that Dalton's atomic theory predicted [47].

### 2.5.2 J.J. Thompson



(a) J.J. Thomson [48]



(b) Cathode Ray Tube [49]

Figure 2.4: Left: J.J. Thomson, who showed that cathode ray tubes were in fact producing the first observed subatomic particle: the electron. Right: A cartoon of Thomson's cathode ray tube setup. Electrons would be deflected by a magnetic field, sent from cathode to anode.

Thomson (Figure 2.4) would discover that atoms are not the smallest indivisible piece of matter. In his landmark experiment, he used cathode ray scattering experiments to show that cathode rays were in fact subatomic particles. He showed these cathode rays were identical to particles given off by the photoelectric effect. He discovered that these were the same particles responsible for electric current. Scientists began to wonder: if atoms were not the smallest piece of matter, then perhaps atoms themselves might not be 'indivisible' as previously thought [50].

### 2.5.3 Ernest Rutherford

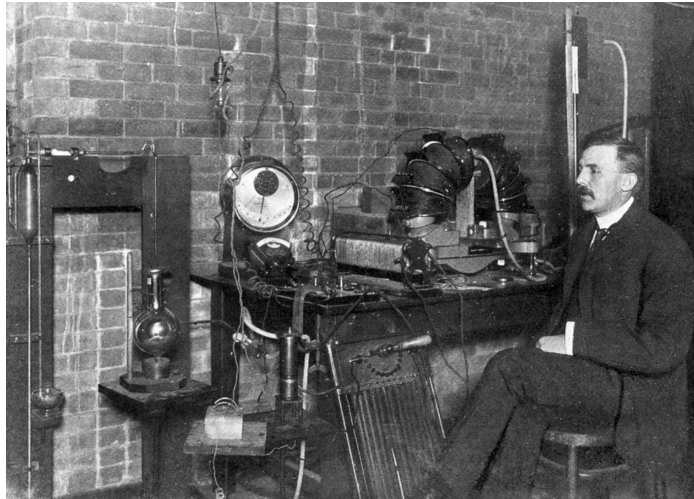


Figure 2.5: Ernest Rutherford, in his lab. [6]

Ernest Rutherford (Fig 2.5) was the first to show that atoms themselves had underlying structure and consisted of a small dense center. He had discovered the nucleus.

Rutherford's work with radioactivity was of fundamental importance. He discovered and classified both alpha-particle radioactivity and beta-particle radioactivity. Further studies into these types of nuclear radiation would unlock the nucleus of atoms through the work of future scientists.

After his discovery of the proton, Rutherford proposed a planetary model for the nucleus. While this model was eventually shown to be wrong, it shifted paradigms from the pudding model of atoms to the more familiar nucleus + electron model. This shift eventually led to the emergence of Quantum Mechanics.

Rutherford's work helped push us out of the cocoon of classical mechanics into the world of the quantum mechanics—scientists would soon find that the nucleus is not just a dense concentration of charge, but a probabilistic structure, with rich sub nuclear structure.

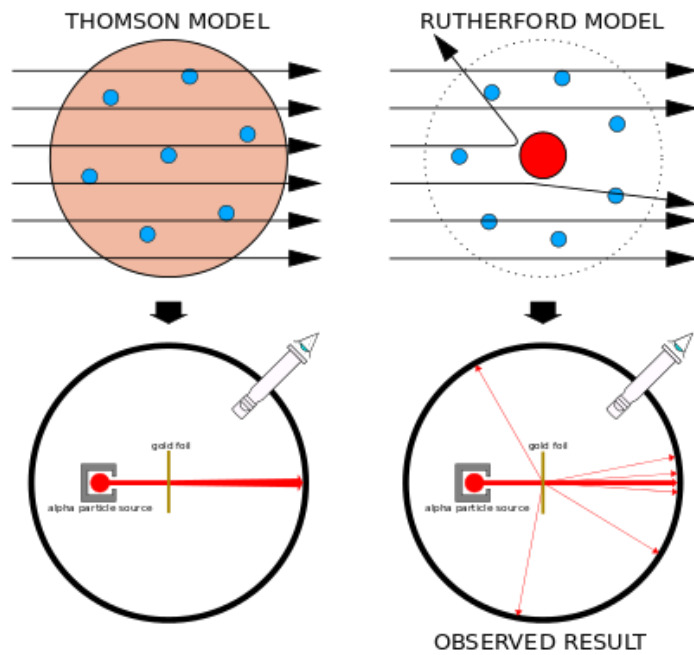


Figure 2.6: Ernest Rutherford's historic experiment, showing (top right) that atoms were composed of a small dense nucleus, in contrast to Thomson's 'pudding model' of homogeneous charge (top left). The experiment, (bottom left and right) contrast the expected results (bottom left) against the observed results (bottom right) [7].



Figure 2.7: The attendees of the Solvay Conference in Brussels, 1927 [8].

## 2.6 Early Quantum Theory

During Rutherford's time, experiments were already underway investigating modeling light as a wave phenomena. This was in contrast to Newton's (unverified) corpuscular theory of light. The argument whether light was wave-like or particle-like eventually lead to a classical field theory describing light as electromagnetic radiation. Max Planck proposed theories which required the quantization of light [51]. Einstein would show that light is indeed quantized into packets of energy in his analysis of the photoelectric effect. The nascent atomic theory of matter hinted at a hidden, quantized world.

At the 1927 Solvay Conference in Brussels(Figure 2.7) an unprecedented gathering of some of the most important figures in modern physics, built the foundations of what would become quantum mechanics. These scientists defined the nature and rules of quantum mechanics—the weird model which accommodates a wave-particle duality of matter.

It was found that not only light possesses this wave-particle duality, but also the particles that make up atoms. These models were formalized by Paul Dirac, David Hilbert and John Von-Neumann.

Further refinements and additions to quantum mechanics gave birth to quantum field theory. Early quantum models were very successful at describing static particles trapped in static potentials. Scientists could predict exactly observed atomic emission spectra. But, more work was needed to understand the relationship between electrical currents, light and magnetism. These concepts were all related by James Clerk Maxwell [52] in the latter half of the 19th century, but had yet to receive a quantum-treatment.

Dirac was first to create a model for describing the electron, its behavior in electromagnetic fields, and photon emission and absorption. Dirac's models were fully relativistic [53]. Dirac's model was so successful, that it would become the basis for what we now call quantum electrodynamics. Much of the mathematical formalism was reused to describe other field theories. Field Theory is the ultimate language used in modeling and describing the structure of matter—including the insides of a proton.



$$\left( \beta mc^2 + c \left( \sum_{n=1}^3 \alpha_n p_n \right) \right) \psi(x, t) = i\hbar \frac{\partial \psi(x, t)}{\partial t} \quad (2.1)$$

(b) The ‘Original Form’ of the Dirac Equation

(a) Paul Dirac, 1933 [54]

Figure 2.8: Paul Dirac, next to his original formulation of the Dirac Equation, describing the wave function for an electron with rest-mass  $m$ , in terms of its space-time coordinates. Dirac’s equation has been expressed free of any defined basis.

Dirac’s work successfully merged relativity into his wave equations describing the motion of particles. He additionally incorporated the spin (i.e. Dirac Spinors) of these particles. The inclusion of spin allowed for the most precise predictions ever to be made for hyperfine divisions in the atomic spectra [53].

In Dirac’s time, the proton was already known to reside in the enigmatic nucleus. However attempts to use Quantum Electrodynamics to describe the state of the

nucleus failed. It was clear that there was a very strong force holding together the positively charged protons of a nucleus. This force would have to be far stronger than the electromagnetic repulsion felt by the positively charged particles in such close proximity. Further complicating an understanding of the nucleus is the fact that as the length scale of probing decreases, the energies probed increase. This fundamentally makes the nucleus a relativistic object. Physics would once again forge ahead in attempting to understand the inner workings of the nucleus.

## 2.7 Early Particle Physics and The Eightfold Way

The hydrogen atom and its spectra was well-modeled with quantum mechanics by the end of the early 20th century. However, attempts to study Helium were not as successful. By 1932, when James Chadwick turned a beam of helium particles (at that time only known as  $\alpha$  particles) on a sample of Beryllium, he observed that neutral, non-ionizing, penetrating radiation was produced [55]. Photons were ruled out as possible candidates, leading to the discovery of the neutron. Protons and neutrons were hypothesized by Heisenberg to both be the same state of a new conceptual particle, the nucleon [56]. In the same year, Carl Anderson discovered the positron.

By 1934, Hideki Yukawa (Fig. 2.9) had created an effective field theory for interactions of ‘elementary particles’ (at this time, thought to be protons and neutrons). He predicted the existence of mesons, and wrote down an effective field theory which described how protons and neutrons bind together in the nucleus [57].

Though non-relativistic quantum mechanics was mostly complete by 1934, scientists were already hard at work incorporating relativistic corrections to the theory. Experiments with cosmic rays soon revealed the existence of muons and the first observation of mesons.

Three separate paths eventually lead to the development of particle accelerators. To date, these massive machines provide the best apparatus in physics to probe nuclear structure. These accelerators are an outgrowth of ever more intense Rutherford-style experiments. An array of technologies have supported this growth: Tandem Van-Der-Graaf generators, resonant acceleration techniques, RF linacs, and betatron accelerators [58].

By the 1950s a cornucopia of strange new particles had been discovered, both matter and antimatter. Neutrinos were proposed as a means of understanding ‘missing energy’ observed in some scattering experiments. Mesons such as Kaons ( $K$ ), Pions ( $\pi^+, \pi^-, \pi^0$ ), and Lambdas ( $\Lambda$ ) were well understood. Physicists were doing nuclear chemistry, attempting to work out how quickly some particles decayed, and what decays were allowed or forbidden. Science entered an age of nuclear alchemy.

“Strange” particles were discovered ( $K$  and  $\Lambda$ ), so called because in bevatron experiments, they were produced in great quantities, but were slow to decay, unlike the



Figure 2.9: Hideki Yukawa, the first Japanese Nobel Laureate and publisher of influential research on the theory of mesons, and other elementary particles [9].

faster  $\pi$  decay. Gell-Mann proposed that this strangeness in matter was due to a new quantum number (he called it ‘strangeness’). The name stuck [59], [60], [55].

The introduction of new conserved quantities and the vast proliferation of particles was an exciting puzzle for physicists to unravel. The subatomic world of the 1950s was confusing and complex. In his book, *The God Particle*, Leon Lederman recalled his adviser (Enrico Fermi) frustratedly remarking ‘Young Man, if I could remember the names of these particles, I would have been a botanist’. At this time the number of mesons and baryons that had been discovered were at least in the dozens, if not more.

While the use of particle accelerators were speeding along the scientists’ quest to understand structure of matter, one particular invention truly revolutionized the field—the bubble chamber (Figures 2.10 and 2.11).

The bubble chamber is essentially a large vat of supercritical fluid which could easily be caused to boil with small perturbations. This feature was exploited, by positioning a bubble chamber in a magnetic field (to cause charged tracks to bend) near the interaction point between a particle beam and a fixed target. The bubble chamber itself was sometimes the target—since a popular liquid to use was hydrogen.



Figure 2.10: An old bubble chamber, once used at Fermilab, [10]

Invented by Donald Glaser in 1952, the bubble chamber was ‘perfected’ by Luis Alvarez when he helped to develop a version which could be used with liquid hydrogen. Hydrogen was desirable as a target and medium due to its simple structure. This led to cleaner results, unlike the original medium Ether. Additionally, using hydrogen gave physicists a convenient way to directly probe the sub-nuclear structure of the simplest form of matter.



Figure 2.11: An example of the photographs taken with a Bubble Chamber, in 1973. In this picture, we see a  $300 \text{ GeV}$  proton producing particles as it travels through a hydrogen-filled bubble chamber at Fermilab [11].

Soon after the advent of bubble chambers, physicists were able to macroscopically image these new, exotic particles interacting with normal matter and decaying. Novel computer techniques were developed to analyze and catalog the massive influx of data.

A break-through came in 1961, when Gell-Mann and Nishijima recognized the underlying symmetry of the interactions taking place and created what would be known as ‘the eightfold way’. This theory created a scheme for organizing the observed baryons and mesons according to their properties in groupings called “octets”. These octets were in fact representations of the elements of members of the  $SU(3)$  group. Gell-Mann had discovered the underlying structure of flavor-symmetry between the three lightest quarks— $u$ ,  $d$ , and  $s$ .

Gell-Mann’s quark model soon made important predictions which were later verified, notably the existence of the  $\Omega^-$  mesons, the ground-state particle of the spin-3/2 decuplet, discovered at Brookhaven National Laboratory. Gell-Mann formalized his quark theory of matter in 1964, however, due to the unforeseen phenomena of color confinement, it would be several years before evidence of quarks composing baryons and mesons was directly obtained from deep inelastic scattering experiments.

This work directly led to the development of the quark model of matter and the foundation of what would become the foundation of the standard model of particles. To date, the standard model is the most successful theory describing particles and their interactions.

## 2.8 Deep Inelastic Scattering, Quantum Chromodynamics and The Parton Model

Deep inelastic scattering experiments (Figure 2.12) were a natural outgrowth of Rutherford’s experiment from the late 19th century. Rutherford’s scattering experiments can be modeled classically, by using a classical potential as a scattering source. One solves as usual using an impact parameter and potential as in central force problems. Rutherford’s experiments were considered generally ‘elastic’ because the target absorbed very little kinetic energy from the projectile, and no new particles were created from the kinetic energy of the projectile-target system.

By the late 20th century, scattering experiments became highly inelastic. Targets would absorb a lot of kinetic energy, sometimes so much that targets would break apart and the kinetic energy of the system would create particles.

Deep Inelastic scattering describes the process in which a high energy interaction occurs between a projectile (often a beam) and a target (a gas, or another beam). The process is akin to smashing to swiss-watches together to understand how the gears fit together in synchrony to tell time.

The interaction occurring between the target and the projectile can change the state of the projectile and generate matter due to the high energies involved. One can observe the state of the projectile and account for the matter which is created. If there are laws which govern how the state of the projectile changes or the kinds of matter that can be created, then we can run the clock backwards and reconstruct the initial state from the final state of the interaction. Alternatively, the goal of deep inelastic scattering may also be to simply measure and characterize the final state of an interaction, based on a known initial state. This process teaches us something about nuclear structure (or even partonic structure). In this way, one can also identify conserved quantities, which in turn suggest physical symmetries and help to build models.

One can think of an interaction of a beam and target in terms of a probability of interaction. One can mathematically ‘separate’ part of this interaction probability into a quantity called a ’cross-section’, often denoted as  $\sigma$  for a total cross section, or  $d\sigma$  for a differential cross section, or even  $\frac{d\sigma}{d\Omega}$  to refer to a differential cross section scattered into a solid angle. Understanding the cross-section of a process requires knowledge of the

luminosity (interactions per second, per unit area) of beam with respect to the target. Understanding Luminosity is of fundamental importance, and is discussed in Chapter 5.

A subcategory of deep inelastic scattering is 'Semi-Inclusive Deep-Inelastic Scattering'. This refers to a case where a beam (say a lepton, such as an electron) interacts inelastically with a point-like internal structure of a target particle, and a hadron is produced (such as a  $\pi^+$ ), which is then detected. Semi-Inclusive Deep-Inelastic scattering is then the process by which the scattered lepton and a specific hadron are measured in the final state of the interaction (but other particles that might be produced are neglected or ignored).

Nuclei are not elementary particles. They are built up from what we assume are fundamental particles. Deep inelastic scattering experiments slowly revealed that individual protons and neutrons are not elementary particles, but instead, composite particles. It is natural to assume that the properties of protons and neutrons are not 'fundamental' either, in that these properties must be emergent from the partonic substructure. In fact, the vast zoo of particles that were discovered in early inelastic scattering experiments, such as  $\pi$  or  $K$ , or any meson or baryon are not fundamental, but bound states of quarks and gluons.

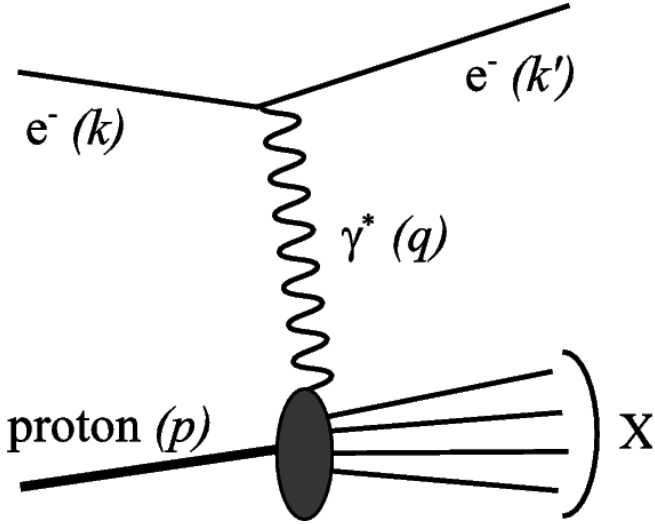


Figure 2.12: A schematic [12] of deep inelastic scattering, where the incoming electron inelastically scatters off the proton, producing results  $X$ , via virtual photon exchange,  $\gamma^*$ . The diagram is split into a perturbative portion (the electron) and a non-perturbative portion. Mathematically, we describe the interaction with kinematic variables summarized in Equations 3.1-3.3

By the 1970s, collaborations between Bjorken, Feynman, and others had produced a coherent partonic model which contained quarks and force-mediating gluons. The concept of Structure functions had been developed. Modified from Rutherford's original scattering formula, a new formalism to describe the cross section of deep inelastic scattering incorporated structure functions. Structure Functions provide a means to separate out the momentum exchange between target and projectile (via a virtual photon), and isolate this known process from the total interaction. The  $W_1$  and  $W_2$ , structure functions were defined to be experimentally measured quantities representing the electron-proton interaction [61].

This period of time, from 1970–1990 was truly the golden age of Deep Inelastic Scattering Experiments. The biggest laboratories responsible for data from this period were The European Organization for Nuclear Research (CERN), The Stanford Linear Accelerator Center (SLAC), and The German Electron Synchrotron (DESY). Thousands of ground-breaking papers were published, such as the CERN's European Muon Collaboration experiment which showed a measurement of the spin asymmetry and determination of the proton structure function  $g_1$  in muon-proton deep inelastic scattering [35].

The formalism of scattering theory continued to evolve during this booming period. Though the process of scattering itself has not changed since its inception in Rutherford’s lab, vast improvements in technology have allowed unprecedented scattering energies with high luminosity accelerators. We now can take measurements of particles and their properties with exquisite precision. The level of precision now possible is exemplified in Brookhaven National Laboratory’s E821 Muon ( $g$ -2) experiment—which measured the anomalous magnetic moment,  $g$ -2, of the muon to a precision of 7 parts in ten million [62].

With the advent of the structure function model, we began an era where matter ceased to be modeled as a simplistic bound-state of quarks, such as the valence quark model for the proton, and instead, complex clouds of quark and gluon interactions. The mathematics of scattering formalism had to change to accommodate the underlying physical distribution of partonic matter in baryons. Deep Inelastic Scattering continued to probe various portions of these structure functions, and the structure of the standard model began to come into focus, distilled into the relatively simple mathematical structure of group theory. The standard model is a gauge theory, which contains the internal symmetries of  $SU_c(3) \times SU_L(2) \times U_Y(1)$ , Figure 2.13. The Standard Model is said by some to be “complete” with the discovery of the Higgs Boson, yet for emergent phenomena such as proton spin, it does not provide a straightforward prediction.

## The Standard Model of Particle Physics

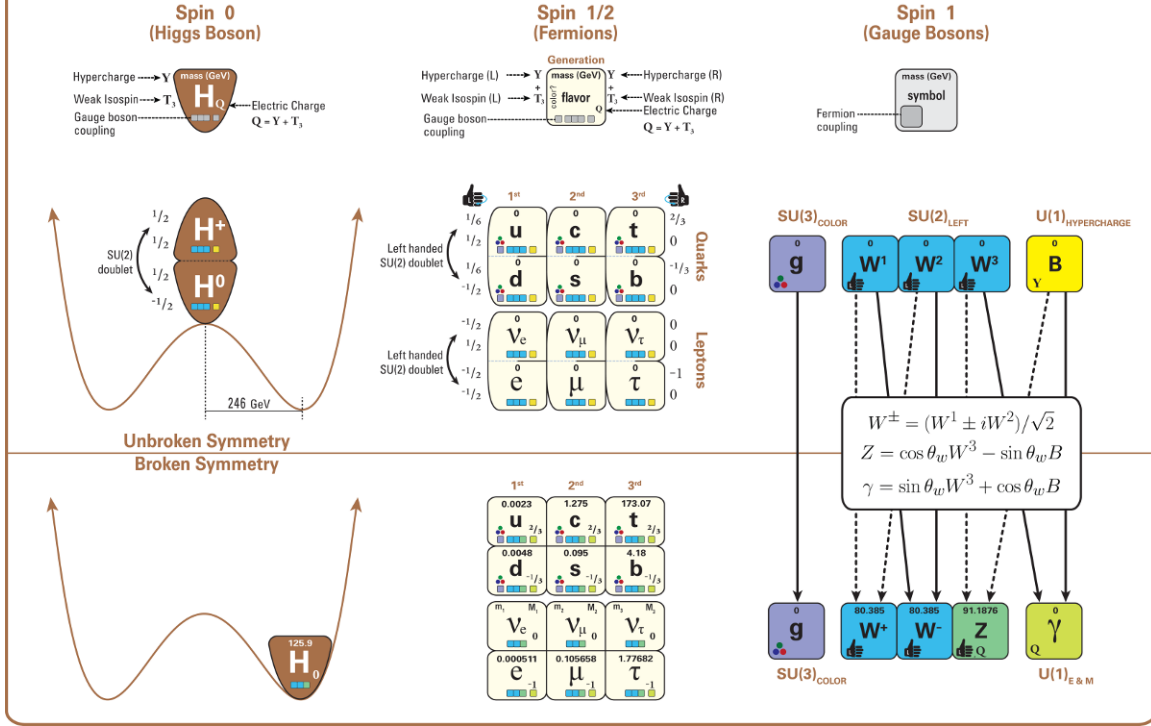


Figure 2.13: "This diagram displays the structure of the standard model (in a way that displays the key relationships and patterns more completely, and less misleadingly, than in the more familiar image based on a 4x4 square of particles). In particular, this diagram depicts all of the particles in the standard model (including their letter names, masses, spins, handedness, charges, and interactions with the gauge bosons – i.e. with the strong and electroweak forces). It also depicts the role of the Higgs boson, and the structure of electroweak symmetry breaking, indicating how the Higgs vacuum expectation value breaks electroweak symmetry, and how the properties of the remaining particles change as a consequence." [13].

## 2.9 Modern Deep Inelastic Scattering Experiments

Here, I hope to highlight the last 40 years or so of physics produced by deep inelastic scattering experiments. The boundaries of science are pushed by huge collaborations of men and women working together, starkly contrasting the lonely pursuits of a handful of scientists in 19th century laboratories.

This era of deep inelastic scattering has unearthed some of the most surprising and monumental discoveries in physics, from the recent discovery of the Higgs-particle, to the discovery that protons and neutrons are not fundamental particles at all, but are instead, highly relativistic balls of gluons.

SLAC Experiments (E80-E155) were some of the first experiments to probe the proton spin structure, operating from 1978-1999. SLAC pioneered the usage of spin asymmetries as a means of ruling out models for various parameterizations of quark structure functions, as well as provided important data constraining nuclear structure functions. SLAC's experiments focused on understanding the spin structure of the quarks (but not gluons) within protons.

The European Muon Collaboration at CERN was one of the first major international efforts to study the underlying structure of protons and neutrons with deep inelastic scattering. The collaboration produced scientific results from 1979 to 1997. The EMC's major contribution to our understanding of nuclear structure was to amass evidence which supported the parton model of protons and neutrons, as well as discovering the self-named ‘EMC effect’, which showed that the volume ‘occupied’ by quarks scales with heavier nuclei [63]. EMC also elucidated the effects of quark fragmentation and hadron production, DIS in the nuclear medium, and produced some of the first measurements of the spin structure of the proton. Most famously, the EMC originally published the ‘proton spin crisis’ in its first measurement of the proton spin structure function,  $g_1$  where it found the spin carried by the proton’s ‘valence quarks’ is significantly less than  $1/2$  [35].

CERN produced another collaboration which contributed to our understanding of nuclear structure, the Spin Muon Collaboration. SMC was active from 1993 to 1998 and used polarized beams of muons to interact with a spin polarized target (ammonia and later p-butanol). SMC measured virtual photon production asymmetries,  $A_1$ , in order to measure information about the proton spin structure function,  $g_1$  (discussed in detail in the following chapter).  $g_1$  gives access to the quark polarization of protons. Spin structure physics has

been explored at the COMPASS experiment since 2005. CERN’s work to understand the spin structure of the proton probed the contributions of both the quark, and gluons.

The German Electron Synchrotron (DESY) is Germany’s the premier accelerator science laboratory, and has been operating continuously since 1964. DESY’s primary experiments in deep inelastic scattering to understand nuclear structure have been underway since 1992. DESY operates several deep inelastic scattering experiments including ZEUS, HERA (H1 and H2) and HERMES. The scientific goals of the DESY institute as a whole are broad, since it represents Germany’s premier accelerator physics scientific effort. DESY hosts experiments in condensed matter physics and astrophysics, addition to its efforts in DIS. However, the portion of DESY’s research program devoted to spin structure seeks to understand both the quark and gluon contributions to proton spin.

Jefferson Laboratory (JLab) is an electron accelerator complex in Virginia specializing in the cutting edge of fixed target electron deep inelastic scattering experiments. Experiments in Hall A, B and C are all involved with studying both quark and gluon contributions to proton spin.

Finally, there is the Relativistic Heavy Ion Collider, and the experiment PHENIX. RHIC and PHENIX are discussed in detail in Chapter 4. This thesis presents an analysis of the data set recorded in 2013 by the PHENIX detector.

## Chapter 3

# Models and Associated Probes For Proton Spin Structure

With the advances made over the last half-century, we have come very close to obtaining a complete model describing the world around us. Rapid progress has been made in the last 40 years in the understanding of the structure of the nucleon. Protons and neutrons make up the majority of the mass in the visible universe—therefore understanding their nature completely is of fundamental importance to physics.

This thesis will discuss the experimental efforts of PHENIX to do something no other experiment has done—utilize the production of  $W$  Bosons as a direct probe of proton spin. Before specifics of this are discussed, lets first put proton spin into a larger context.

### 3.1 Modeling the Proton Structure

A constraint using particle accelerators to study any kind of nuclear structure is that one does not ever get to directly look at the innards of a proton, due to the phenomena of color confinement.

This means that one must deal with the process of how partons (quarks, gluons) fragment and decay after a proton proton collision in the final state. Additionally, the scale variance of the fundamental forces plays an important role.

The scale variance of the fundamental forces has large implications for the strong nuclear force, represented by the coupling constant  $\alpha_S$ . This constant scales with distance, and becomes highly non-perturbative at short distances. Models must differentiate be-

tween perturbative and non-perturbative processes. In perturbative models, the strategy is to write down a Hamiltonian or Lagrangian to describe a system, and then obtain predictions from the model by expanding in terms of a ‘small’ parameter. Then, predictions from the leading order, NLO,  $N^2\text{LO}$  or  $N^3\text{LO}$  are made and verified with data. Non perturbative models often cannot write down all possible processes which contribute to the overall Hamiltonian. Instead, non-perturbative models use structure functions which take the form of global fits to experimental data. The models can then make predictions through QCD evolution, which extrapolates the structure functions to other energy scales, which again are probed experimentally.

The internal degrees of freedom of the proton, and the small scales involved make models for the proton fall generally into non-perturbative regimes. The structure and distribution of partons and gluons in the nucleus is a scale-dependent phenomena. That is to say, if one take measurements at a lower energy, one may obtain a different distribution of partons and gluons at a higher energy. This scale dependence requires many measurements to be taken which probe different scales in order to properly constrain models for proton structure.

In order to properly model the non-perturbative structure of the proton, Factorization Theorems are used. Factorization provides a means to mathematically separate a probe interactions (such as electron-hadron scattering in DIS) into perturbative and non-perturbative parts (example, Figure 2.12). Represented as a blob in such diagrams, the non-perturbative aspect is the portion which is experimentally constrained.

### 3.1.1 Structure Functions

Given that the proton itself has so far been shown to be a non-perturbative object, the theoretical thrust is to create a probabilistic model for the proton structure that can subsequently used to how two colliding protons interact and generate particles. For each hadronic process, there is an associated structure function. The variables defined to describe the kinematics of deep inelastic scattering are (see Figure 2.12):

$$P \tag{3.1}$$

$$Q^2 \equiv -q^2 \tag{3.2}$$

$$x \equiv \frac{Q^2}{2P \cdot q} \tag{3.3}$$

$P$  is the total hadron momentum (in our case, the proton's momentum),  $Q^2$  is the momentum exchange between the proton and probe lepton, and  $x$  is the fraction of the total proton's momentum carried by the quark scattering with the lepton.  $q$ , in Equation 3.3 is four-momentum transferred from the lepton to the quark.

One can then write down structure functions in terms of these variables, choosing the decomposition consistent with Lorentz Structure:

$$F_1(x, Q^2) = \frac{1}{2} \sum_f e_f^2 (q_f(x) + \bar{q}(x)) \tag{3.4}$$

$$F_2(x, Q^2) = 2xF_1(x, Q^2) \tag{3.5}$$

The subscript,  $f$  refers to the quark flavors represented in the structure functions, with  $e_f$  referring to the charge of each quark being summed over (i.e.  $\pm \frac{1}{3}$  or  $\pm \frac{2}{3}$ ).  $q(x)$  refers to the parton distribution function associated with each quark flavor.

An integration over the momentum fraction,  $x$  of Equation 3.5 and the gluon structure function  $g(x)$  yields the familiar ‘valence quark’ structure of the proton, i.e. two up-quarks and one down quark, with remaining quark flavors  $q_h$  summing to zero:

$$\int_0^1 F_2(x, Q^2) + g(x) dx = \int_0^1 \left( x \sum_f e_f^2 (q_f(x) + \bar{q}(x)) \right) + g(x) dx \tag{3.6}$$

$$\int_0^1 (u(x) + \bar{u}(x) dx) dx = 2 \tag{3.7}$$

$$\int_0^1 (d(x) + \bar{d}(x) dx) dx = 1 \tag{3.8}$$

$$\int_0^1 (q_h(x) + \bar{q}_h(x) dx) dx = 0 \tag{3.9}$$

The rest of the world data on  $F_2(x, Q^2)$  is summarized in Figure 3.1

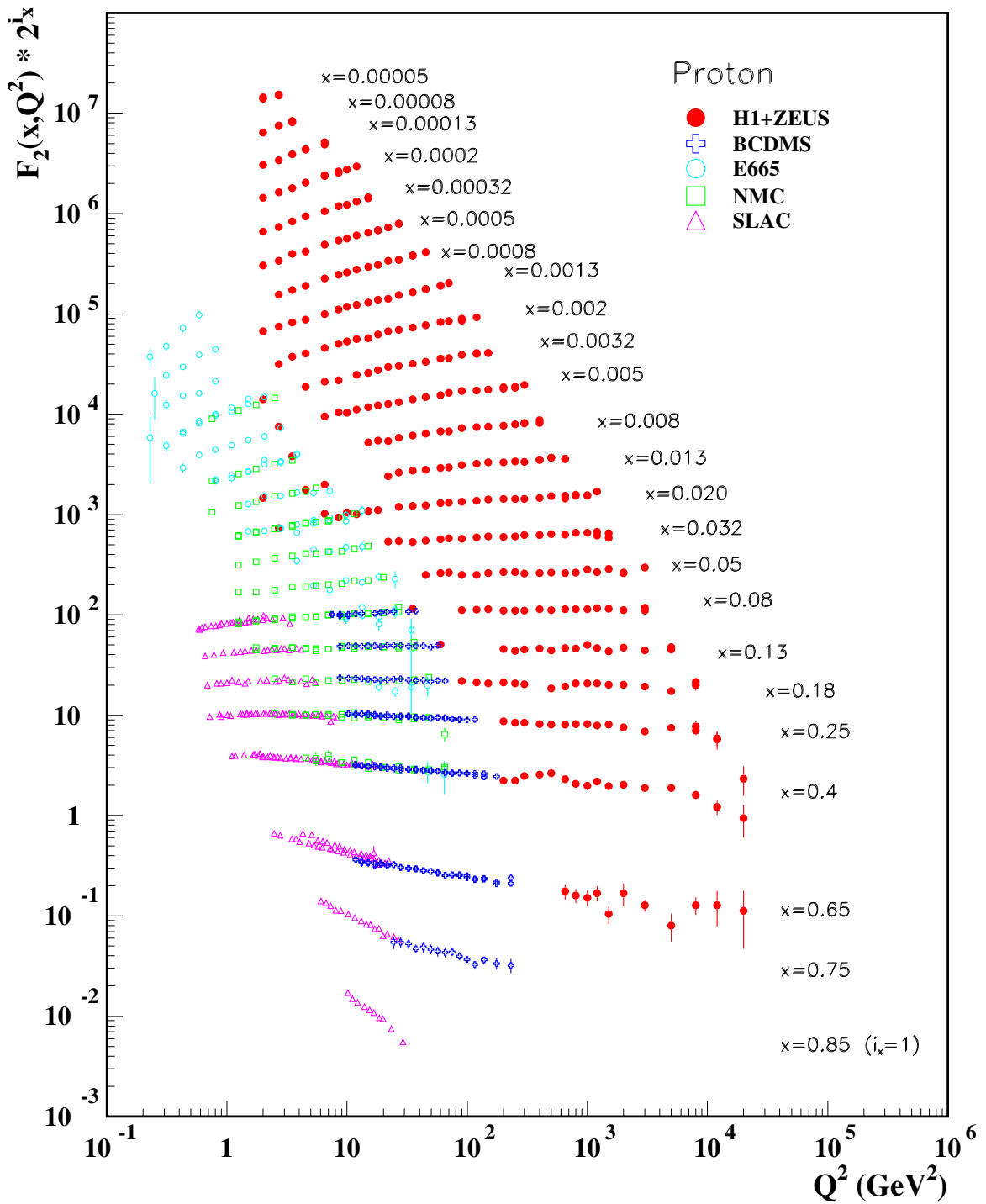


Figure 3.1: Shown: “the proton structure function,  $F_2^p$  measured in electromagnetic scattering experiments of electrons and positrons on protons” from experiments including H1+Zeus, BCDMS, E665, NMC and SLAC [14]

### 3.2 Parton Distribution Functions

From this dataset, the Parton Distribution Functions for any combination of  $x$  and  $Q^2$  may be extracted. Under this particular framework, DGLAP evolution equations are used to evolve PDFs observed at one  $Q^2$  to some other  $Q^2$  [64].

With QCD evolution, one can additionally undertake a global analysis, which effectively puts a constraint on Parton Distribution functions using ‘evolved projections’ of  $x$  and  $Q^2$  into the kinematic range of the experimental probes [65].

The world data on proton structure can be evolved with the DGLAP equations [66] to generate parton distribution functions representing the momentum fraction carried by various partons building up the proton, the summary of this is shown in Figure 3.2. As expected—the PDF for  $u$  is about twice as large as  $d$  indicating the valence structure of the proton at high- $x$  ( $> 0.1$ ).

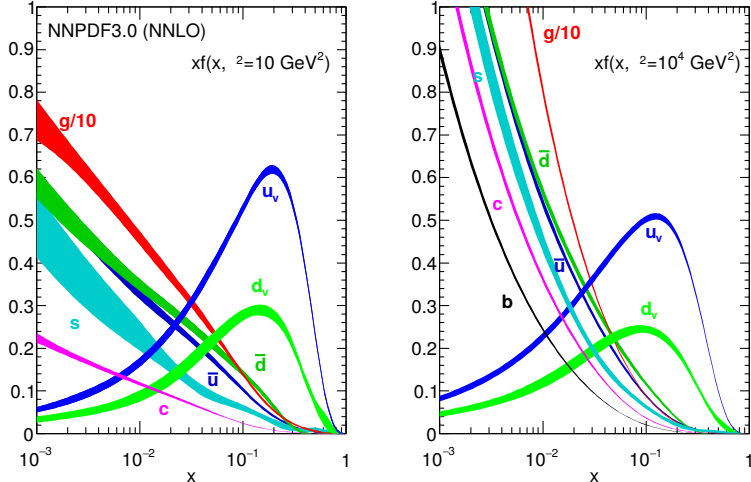


Figure 3.2: On the left is the NNPDF calculation of PDFs with world data (width is related to uncertainty) at 10 GeV, while 10 TeV is shown on the right. Note that at low  $x$ , the proton is dominated by gluons. [14].

While DIS, and Semi-Inclusive Deep Inelastic Scattering have provided a wealth of data on the proton’s internal structure, RHIC data can be used to undertake a complimentary analysis using hadron-hadron collisions, instead of hadron-lepton collisions. A

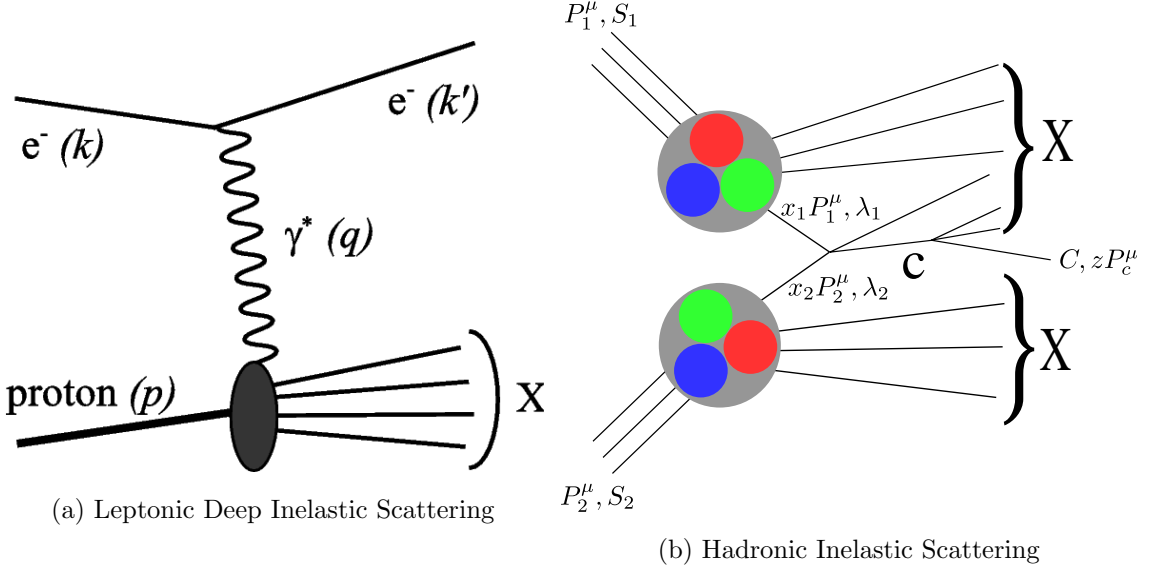


Figure 3.3: Deep Inelastic Scattering Process (Panel (a)) alongside Hadron-Hadron inelastic scattering (Panel (b)). In hadron inelastic scattering, one may try to select initial state with scattering between arbitrary partons in order to probe various proton structures.

similar picture to DIS can be drawn of hadron-hadron interactions to the DIS schematic, as seen in Figure 3.3.

Hadron-Hadron scattering can be a useful means to determine PDFs experimentally, but often intermediate states are not known and it is difficult to isolate a single PDF. Hadron-hadron scattering experiments provide an excellent source of data to constrain gluon PDFs.

### 3.2.1 Polarized Parton Distribution Functions

Polarized parton distributions are measured with the same methods discussed above—except the beam and/or target in the scattering formalism are spin-polarized. We can similarly write down the structure functions for polarized protons, in the same manner as  $F_1$  and  $F_2$ :

$$g_1 = \frac{1}{2} \sum_q e_q^2 (q^+(x) - q^-(x)) = \frac{1}{2} \sum_q e_q^2 \Delta q(x) \quad (3.10)$$

Here,  $e_q$  is the charge of the quark-flavor (i.e.,  $1/3e$ ,  $2/3e$ ), with the sum taken over all quark/anti-quark flavors. The  $q$  terms refer to the number density of each particularly

quark flavor associated with the “+” or “-” quark spin orientation (relative to the struck hadron), such that “+” refers to a parallel spin and “-” refers to an anti-parallel spin.  $g_1$  describes the longitudinal spin polarization of the nucleus, while  $g_2$  describes the transverse spin polarization of the nucleus. A knowledge of both longitudinal and transverse spin structure is necessary for a complete understanding of the three-dimensional structure of the proton.

The experimental tool for measurement of the spin structure of the proton is the ‘spin asymmetry’. The spin asymmetry is defined in terms of scattering cross-sections, therefore one may experimentally determine these cross sections, or calculate these cross sections from models. In particular, the asymmetry is directly proportional to the structure functions describing the proton:

$$A(x, Q^2) = \frac{\sigma^+ - \sigma^-}{\sigma^+ + \sigma^-} \quad (3.11)$$

$$\equiv \frac{g_1(x, Q^2)}{F_1(x, Q^2)} \quad (3.12)$$

With our knowledge of  $F_1$  from fits to the world’s data (Fig. 3.1), the asymmetry may provide a direct measurement of  $g_1$  [15]. With the discovery that the proton’s spin is not entirely carried by the valence quarks, one may construct additional spin-dependent parton distribution functions, and design experiments to measure and constrain them. Current knowledge of parton distribution functions is summarized in Figure 3.4 and 3.5.

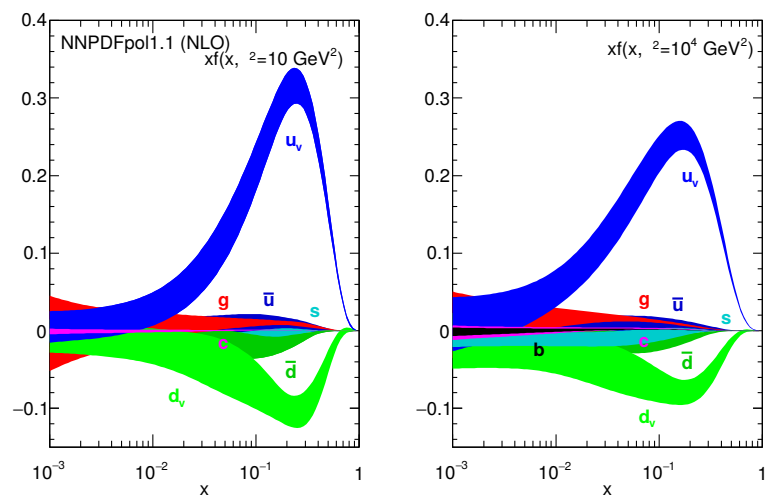


Figure 3.4: World data used to generate fits to predict the parton distribution functions of various quark flavors in the proton at 10 GeV (left) and 10 TeV (right) [14]

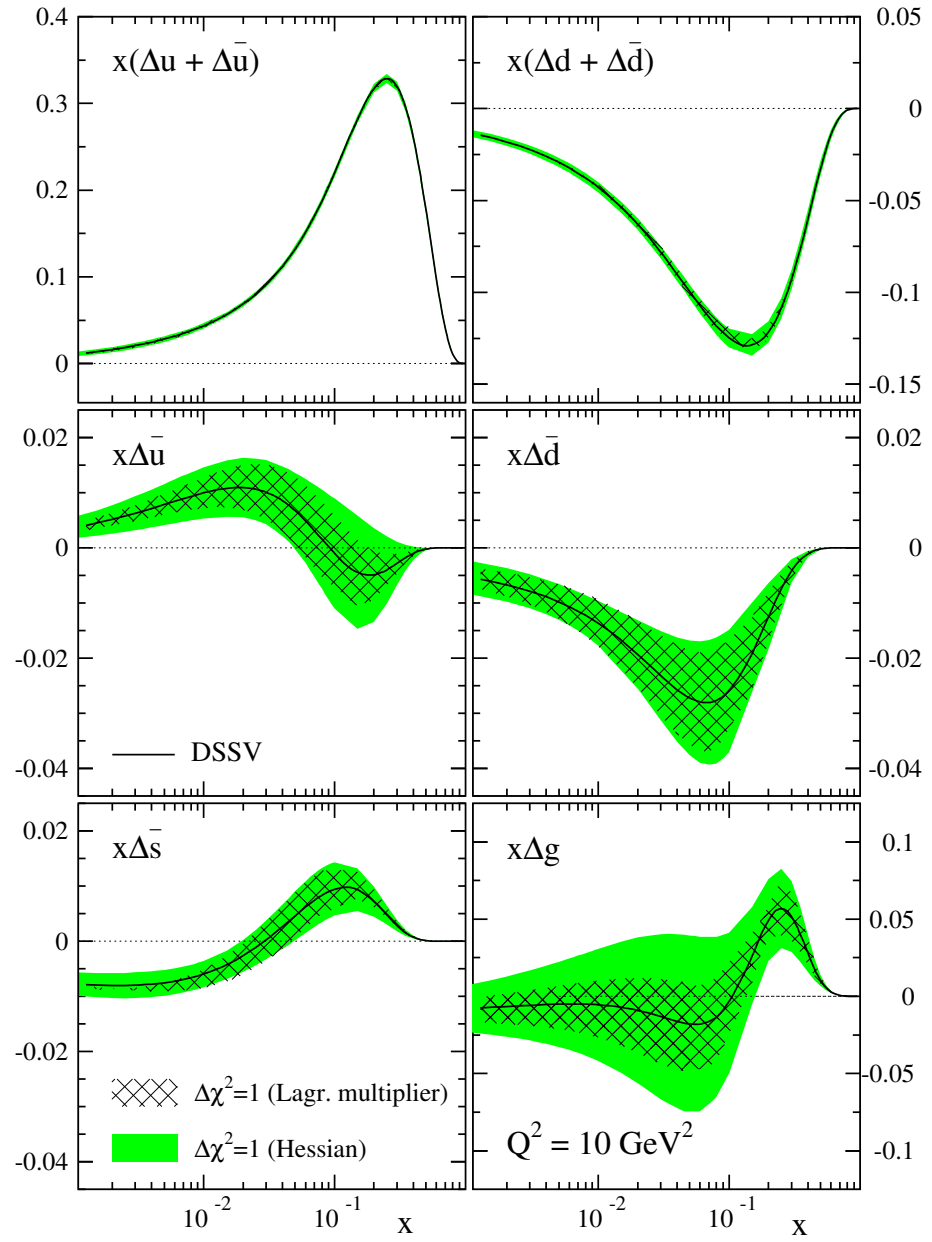


Figure 3.5: PDFs for polarized parton distribution functions shown at 10 GeV for quarks, anti-quarks, and gluons in the proton. The uncertainties for the gluon and anti-quark PDFs are quite large, warranting experimental investigation [15].

### 3.3 Proton Spin Decomposition with the Ellis-Jeffe Sum Rule

The spin contribution of the proton may be written as a sum of the various spin contributions using the polarized parton distribution functions. The particulars of the decomposition vary with the chosen gauge. Ellis-Jeffe produced a gauge invariant decomposition:

Gauge invariant Ellis-Jeffe

$$\langle P, \frac{1}{2} | \hat{J}_z | P, \frac{1}{2} \rangle = \frac{1}{2} = \frac{1}{2} \Delta \Sigma + L_q + J_g \quad (3.13)$$

and another, intuitive decomposition, in the infinite momentum gauge:

$$\langle P, \frac{1}{2} | \hat{J}_z | P, \frac{1}{2} \rangle = \frac{1}{2} = \frac{1}{2} \Delta \Sigma + L_q + \Delta g + L_g \quad (3.14)$$

The quark helicity distribution is subdivided into its flavor structure:

$$\Delta \Sigma = (\Delta u + \Delta \bar{u}) + (\Delta d + \Delta \bar{d}) + (\Delta s + \Delta \bar{s}) \quad (3.15)$$

As discussed earlier, there is a large uncertainty in the contribution of the anti-quarks to the proton spin which this work seeks to constrain.

### 3.4 The Spin Asymmetry: An Experimental Probe

The spin asymmetry is an important experimental probe into the longitudinal spin structure function,  $g_1$  from which one derives polarized parton distribution functions. At RHIC, hadron inelastic scattering is used to generate events from which asymmetries for various final-states are measured. The probes available at RHIC via hadronic deep inelastic scattering are summarized in Figure 3.6.

One potential pit-fall of using hadronic initial states in spin measurements is the issue of fragmentation. Fragmentation complicates the process of determining the initial state interaction and measuring the correct final state. For example, consider measuring a photonic decay from a final state. A  $p\pi^0$  can be produced as part of a specific initial state of interest, however  $\pi^0$ 's can be produced in a vast array of fragmentation processes, and all of them can decay to photons. It can be hard to isolate the parent interaction which produces the particles of interest.

Consider as a contrast, the production of the  $W$ . The  $W$  decay offers a clean probe free of fragmentation, useful for studying the polarization of anti-quark parton distribution functions. Specifically, due to the parity violating nature of the  $W$  decay,  $W$ 's will only couple to left handed particles and right handed anti-particles. Consider too the relativistic neutrino resulting from the  $W$  decay. Due to this, interactions producing a  $W$  boson necessarily have the helicity state in the initial state fixed. This makes the  $W$  boson an attractive candidate for studying the sea-quark polarization of the proton.

While all weak processes are mediated by the  $W/Z$  boson, real  $W$  production from  $q + \bar{q}$  interactions produce a clear Jacobean peak at central rapidities at the 510 GeV  $\sqrt{s}$  collision energy of interest (at PHENIX), and additionally can be identified at forward rapidities using statistical methods discussed in Chapter 7.

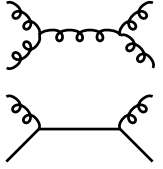
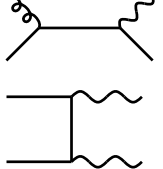
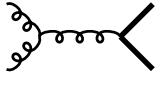
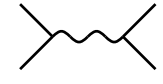
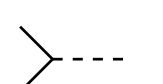
Reaction	Dom. partonic process	probes	LO Feynman diagram
$\vec{pp} \rightarrow \pi + X$	$\vec{g}\vec{g} \rightarrow gg$ $\vec{q}\vec{g} \rightarrow qg$	$\Delta g$	
$\vec{pp} \rightarrow \text{jet(s)} + X$	$\vec{g}\vec{g} \rightarrow gg$ $\vec{q}\vec{g} \rightarrow qg$	$\Delta g$	(as above)
$\vec{pp} \rightarrow \gamma + X$ $\vec{pp} \rightarrow \gamma + \text{jet} + X$ $\vec{pp} \rightarrow \gamma\gamma + X$	$\vec{q}\vec{g} \rightarrow \gamma q$ $\vec{q}\vec{g} \rightarrow \gamma q$ $\vec{q}\vec{q} \rightarrow \gamma\gamma$	$\Delta g$ $\Delta g$ $\Delta q, \Delta \bar{q}$	
$\vec{pp} \rightarrow DX, BX$	$\vec{g}\vec{g} \rightarrow c\bar{c}, b\bar{b}$	$\Delta g$	
$\vec{pp} \rightarrow \mu^+ \mu^- X$ (Drell-Yan)	$\vec{q}\vec{\bar{q}} \rightarrow \gamma^* \rightarrow \mu^+ \mu^-$	$\Delta q, \Delta \bar{q}$	
$\vec{pp} \rightarrow (Z^0, W^\pm)X$ $\vec{pp} \rightarrow (Z^0, W^\pm)X$	$\vec{q}\vec{\bar{q}} \rightarrow Z^0, \vec{q}'\vec{\bar{q}} \rightarrow W^\pm$ $\vec{q}'\vec{\bar{q}} \rightarrow W^\pm, q'\vec{\bar{q}} \rightarrow W^\pm$	$\Delta q, \Delta \bar{q}$	

Figure 3.6: A summary of the various probes for longitudinally polarized protons. The “**Reaction**” column summarizes the reaction observed experimentally. The “**Dom. partonic process**” column describes the dominant process at the partonic level. The “**probes**” column shows which proton spin structure can be measured with the reaction. Finally, the leading order Feynman diagram for the partonic process is drawn [16].

### 3.5 $W$ Production

Though the  $W$  can be created in collisions with the right ingredients and correct energy, the  $W$  decays that PHENIX seeks to measure are very special. The conditions of collision at the PHENIX interaction region provides enough energy to create real  $W$  Bosons from direct parton-parton interactions between protons. However, the energy is not sufficiently high enough to produce real  $W$  Bosons from secondary decay processes in amounts which would significantly dilute the primary source.

The standard model tells us that  $W$  production occurs through a pure vector-axial interaction. This implies that the helicity of the parents particles—in particular  $u + \bar{d} \rightarrow W^+$  and  $\bar{u} + d \rightarrow W^-$  are fixed, due to the relativistic final state neutrino, and the maximal parity violating nature of the interaction. To visualize the leading order of  $W$  production, with regards to the quark-sea element being probed, the leading order diagrams for the interaction are shown in Figure 3.7 [16]

We probe the polarized parton distribution functions representing quarks and anti-quarks by measuring the asymmetry of the decay products of the  $W$ , with respect to the helicities of the protons in the initial state.  $\Delta q$ , the polarized parton distribution function representing the quark contribution to proton spin (Equation 3.13) can be subdivided into further quark PDFs, Equation 3.15. The  $W$  boson decay provides a unique glimpse into specifically the anti-quark polarized parton distribution functions.

PHENIX collides polarized protons, but the polarization of one participant proton can be effectively ignored by summing over all polarization states for one of the two protons. With this assumption, one may construct a single spin asymmetry for colliding protons by counting difference in the number of positively and negatively polarized  $W$ 's produced in collisions, scaled by the total production:

$$A_L^W = \frac{1}{P} \times \frac{N_-(W) - N_+(W)}{N_-(W) + N_+(W)} \quad (3.16)$$

This extraction of this experimental probe is discussed in Chapter 7.

As seen earlier, in Section 3.2.1, one may write an asymmetry in terms of the scattering cross section for the process responsible for particle yields. These cross-sections were shown to be written in terms of polarized parton distribution functions. The full

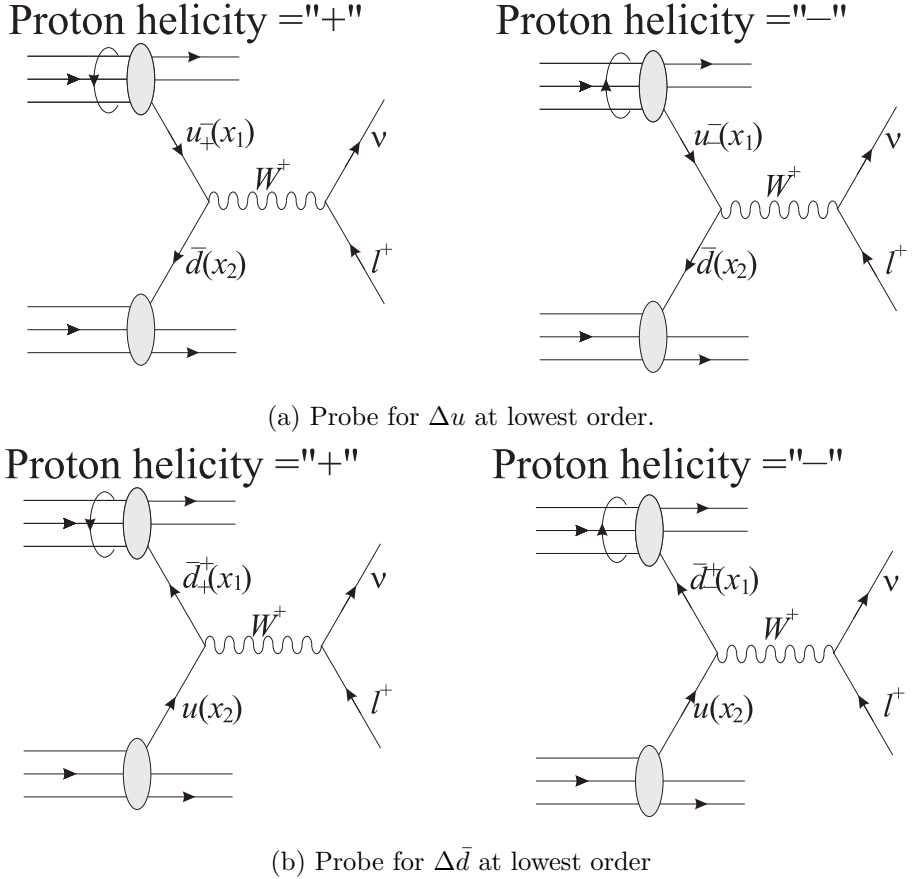


Figure 3.7: Real  $W^+$  production as produced at PHENIX. The helicity of the initial state fixes the helicity of the partonic participants due to the relativistic final state of the neutrino + the handedness of the  $W$ .  $x_1$  and  $x_2$  are the momentum fractions of the quarks participating from the participant partons [16].

expression of the theoretical asymmetries for this process are written in terms of the parton distribution functions, with implicit integration over  $x_1$  and  $x_2$ .

For  $W^+$  and  $u$ :

$$A_L^{W^+} = \frac{u_-(x_1)\bar{d}(x_2) - u_+(x_1)\bar{d}(x_2)}{u_-(x_1)\bar{d}(x_2) + u_+(x_1)\bar{d}(x_2)} \quad (3.17)$$

For  $W^+$  and  $\bar{d}$

$$A_L^{W^+} = \frac{\bar{d}_+(x_1)u(x_2) - \bar{d}_-(x_1)u(x_2)}{\bar{d}_+(x_1)u(x_2) + \bar{d}_-(x_1)u(x_2)} \quad (3.18)$$

Observationally, a superposition of 3.17 is seen and 3.18, which is expressed in Equation 3.19:

$$A_L^{W^+} = \frac{\Delta u(x_1)\bar{d}(x_2) - \Delta\bar{d}(x_1)u(x_2)}{u(x_1)\bar{d}(x_2) + (\bar{d})(x_1)u(x_2)} \quad (3.19)$$

For the case of  $W^-$ , we observe  $\bar{d}$  and  $u$ . For  $W^-$  and  $d$ :

$$A_L^{W^+} = \frac{d^-(x_1)\bar{u}(x_2) - d^+(x_1)\bar{u}(x_2)}{d^-(x_1)\bar{u}(x_2) - d^+(x_1)\bar{u}(x_2)} \quad (3.20)$$

For  $W^-$  and  $\bar{u}$

$$A_L^{W^+} = \frac{\bar{u}^+(x_1)d(x_2) - \bar{u}^+(x_1)d(x_2)}{\bar{u}^+(x_1)d(x_2) + \bar{u}^+(x_1)d(x_2)} \quad (3.21)$$

Observationally, the superposition of 3.20 and 3.21 is measured: Equation 3.22:

$$A_L^{W^-} = \frac{\Delta d(x_1)\bar{u}(x_2) - \Delta\bar{u}(x_1)d(x_2)}{d(x_1)\bar{u}(x_2) + (\bar{u})(x_1)d(x_2)} \quad (3.22)$$

Kinematics of the collision can simplify the equations even further [16]. Concretely, this is shown via integration over the momentum fractions,  $x_1$  and  $x_2$ , explicitly writing the W decay in terms of the scattering cross section for polarized proton collisions (a derivation reproduced from [25]):

$$\begin{aligned} d\sigma(p^\Rightarrow + p \rightarrow W^+ \rightarrow \ell + \nu_\ell) = & \\ \frac{K}{3} \int dx_1 dx_2 \sum_{i,j} & (q_i^\Rightarrow(x_1)\bar{q}_{j+}(x_2) + \bar{q}_{j+}^\Rightarrow(x_1)q_{i-}(x_2)) \\ & \times d\hat{\sigma}(q_i + \bar{q}_j \rightarrow W^+ \rightarrow \ell^+ + \nu_\ell) \end{aligned} \quad (3.23)$$

Similarly, we may write the interaction cross-section for the opposite helicity in the initial state:

$$\begin{aligned} d\sigma(p^\Leftarrow + p \rightarrow W^+ \rightarrow \ell + \nu_\ell) = & \\ \frac{K}{3} \int dx_1 dx_2 \sum_{i,j} & (q_i^\Leftarrow(x_1)\bar{q}_{j+}(x_2) + \bar{q}_{j+}^\Leftarrow(x_1)q_{i-}(x_2)) \\ & \times d\hat{\sigma}(q_i + \bar{q}_j \rightarrow W^+ \rightarrow \ell^+ + \nu_\ell) \end{aligned} \quad (3.24)$$

Assuming massless quarks, the helicity state of the quarks becomes identical to the chirality state. Then, substitute in the definition for polarized parton distribution functions  $\Delta q \equiv q_+^\Rightarrow - q_-^\Rightarrow$ , and sum over quark flavors. Strange quarks do not contribute:

$$\begin{aligned}
A_L(p^\Rightarrow + p \rightarrow W^+ \rightarrow \ell^+ + \nu_\ell) &= \frac{\int dx_1 dx_2 \sum_{i,j} (-\Delta q_i(x_1) \bar{q}_j(x_2) + \Delta \bar{q}_j(x_1) q_i(x_2)) \cdot d\hat{\sigma}}{\int dx_1 dx_2 \sum_{i,j} (q_i(x_1) \bar{q}_j(x_2) + \bar{q}_j(x_1) q_i(x_2)) \cdot d\hat{\sigma}} \\
&\approx \frac{\int dx_1 dx_2 (-\Delta u(x_1) \bar{d}(x_2) + \Delta \bar{d}(x_1) u(x_2)) \cdot d\hat{\sigma}}{\int dx_1 dx_2 (u(x_1) \bar{d}(x_2) + \bar{d}(x_1) u(x_2)) \cdot d\hat{\sigma}}
\end{aligned} \tag{3.25}$$

Since we have restricted ourselves to only the case for  $u\bar{d}$ ,  $A_L^{W+}$  is observed. Equation 3.25 is rewritten to reflect its rapidity dependence:

$$A_L^{W+}(y_\ell) = \frac{\int dx_1 dx_2 \left( -\Delta u(x_1) \bar{d}(x_2) (1 - \cos\hat{\theta})^2 + \Delta \bar{d}(x_1) u(x_2) (1 + \cos\hat{\theta})^2 \right)}{\int dx_1 dx_2 \left( (u(x_1) \bar{d}(x_2) (1 - \cos\hat{\theta})^2 + \bar{d}(x_1) u(x_2) (1 + \cos\hat{\theta})^2) \right)} \tag{3.26}$$

In this case, we follow the notational convention of [25] and  $\hat{\theta}$  in terms of the angle between the direction of momentum of the polarized proton and the lepton in the center of mass frame. Therefore, decoupling of  $\Delta u$  and  $\Delta \bar{d}$  is achieved at forward or backward rapidity. We may write  $A_L^{W-}(y_\ell)$  similarly:

$$A_L^{W-}(y_\ell) = \frac{\int dx_1 dx_2 \left( -\Delta \bar{u}(x_1) d(x_2) (1 - \cos\hat{\theta})^2 + \Delta d(x_1) \bar{u}(x_2) (1 + \cos\hat{\theta})^2 \right)}{\int dx_1 dx_2 \left( (\bar{u}(x_1) d(x_2) (1 - \cos\hat{\theta})^2 + d(x_1) \bar{u}(x_2) (1 + \cos\hat{\theta})^2) \right)} \tag{3.27}$$

With an understanding of the  $W$  process and ability to probe the helicity dependent parton distribution functions, the remaining challenge is to use RHIC and PHENIX to record this data set, discussed next!

## Chapter 4

# The Relativistic Heavy Ion Collider

### 4.1 Overview

While there have been many experiments which have performed deep inelastic scattering over the years, the experiments built around the Relativistic Heavy Ion Collider at Brookhaven National Laboratory are positioned to take advantage of this unique accelerator.

The Relativistic Heavy Ion Collider (RHIC) is the world's only intersecting ring particle accelerator which is capable of colliding polarized proton beams. The beams are differentiated with the mnemonic "Blue" and "Yellow" labels. The blue beam circulates clockwise when viewed from above the RHIC complex, the yellow beam circulates counter-clockwise. As is typical for intersecting ring experiments, the beams are bunched, with bunches of ions intersecting at designated intersection points, around which experiments are built. The filled bunches from the blue and yellow beams cross at a frequency of 106 nanoseconds. PHENIX's timing is set to correspond to the crossing rate of the blue and yellow beams. Because bunches always collide simultaneously, the blue beam timing clock is used as a matter of convention, though there are other timing clocks available for use. The bunches in the beams are numbered as a means of associating the bunch polarization configuration with the bunch crossing at each interaction region. This is necessary for any measurement which requires a knowledge of the initial polarization state of colliding hadrons (such as any spin physics measurement). This will be discussed more in the section of discussing the beam polarization at RHIC 4.3.

RHIC generally separates data taking into beam ‘fills’ which are uniquely numbered, and for which general data characterizing the machine state is logged in various databases and online logbooks. Logging is an important part of data quality assurance, but also plays a fundamental role in the physics. For example, the initial spin state of the colliding bunches is logged in databases, without which, spin analyses are impossible. The trigger configuration is recorded along with the rates associated with each trigger. Data logged into logbooks and databases characterizing a fill’s performance also plays an important forensic role with regards to solving issues which occurred during data taking, but were not immediately caught. Furthermore, because PHENIX is an international collaboration, this logged data is fundamentally important to communicating the state of the machine and data collection to the collaboration, as well as establishing a record of operations.

RHIC fills are composed of a unique population of bunched ions, circulating around the rings. During polarized fills, every bunch is polarized according to a planned polarization pattern. At the end of each fill, (typically 8 hours of collisions), the beam is dumped, and a new fill is generated. Experiments built around RHIC generally subdivide fills into ‘runs’, where a run is a period of time where the experiment is taking data during which there were no obvious machine malfunctions. When major issues occur during a run, data taking is interrupted until the problem is remedied, and the data is discarded. At PHENIX, runs are always segregated within a fill. No run will ever contain data from multiple fills, due to the additional complexity of potentially changing machine conditions, significant downtime between fills, and the potential of beam-dumps into sensitive high voltage enabled electronics.

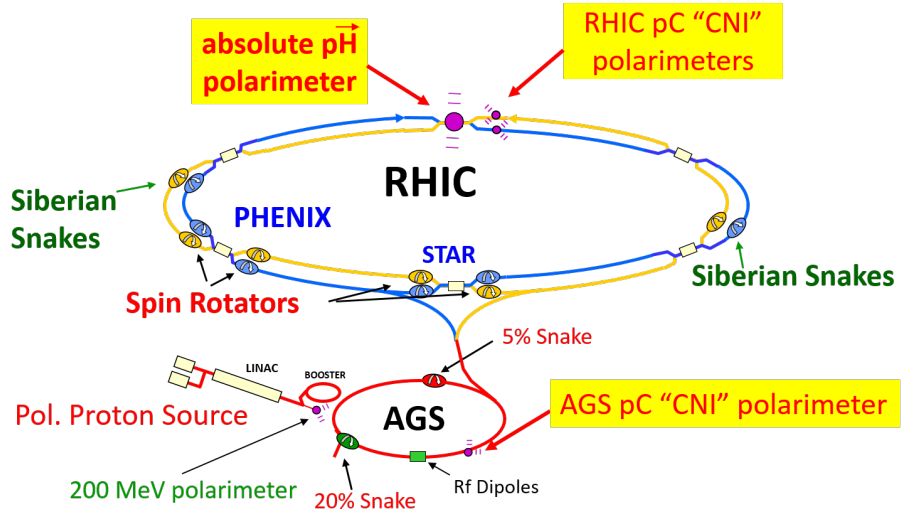
Scientists at RHIC have engineered many ingenious ways to create and maintain beam polarization (Section 4.3). Once this is accomplished, various probes can be constructed to probe processes which grant access to proton spin polarization (Figure 3.6). RHIC is a unique collider in that it is quite flexible. Beams may be transversely or longitudinally polarized, and a variety of ions may be used to fill the beams. To date, the various collision energies and beam ion species used are summarized in Figure 4.2 and Figure 4.3.

RHIC is an facility which has been built on top of previous accelerator experiments—a Linear Accelerator, a booster ring, and an Alternating Gradient Synchrotron, all of which now have been re-purposed to create the necessary beam injection conditions appropriate for

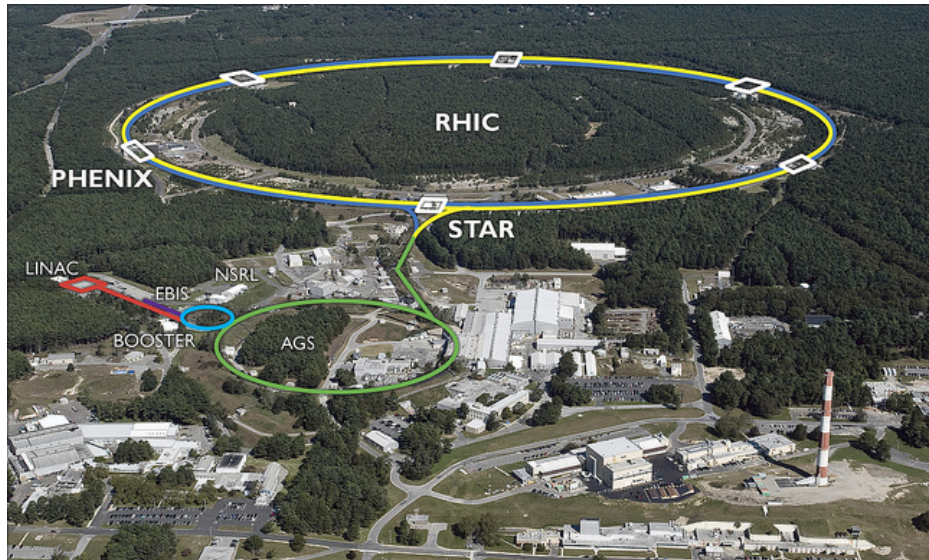
RHIC. Many experiments are still set up around various egress points along the acceleration chain, which are publicised on the Brookhaven National Laboratory website [www.bnl.gov](http://www.bnl.gov).

At the time of writing of this Thesis (Spring of 2016), there are two experiments which are actively taking data from collisions produced by RHIC: The Pioneering High Energy Nuclear Interaction Experiment (PHENIX, Section 4.4, Figure 4.5), and the Solenoidal Tracker at RHIC (STAR, Figure 4.5). STAR and PHENIX are complimentary to each other. PHENIX has a very high precision centrally covering Electromagnetic Calorimeter with other detectors engineered for precision measurements, but lacks full kinematic coverage. STAR has lower precision (with some measurement-dependent exceptions), but has the advantage of nearly full kinematic coverage around the beam intersection at its center.

RHIC's luminosity and beam polarization have been continuously improving (Figure 4.4) since RHIC was first turned on. As we will discuss later (Section 4.5), the increased luminosity observed in 2013, was maximally leveraged with upgrades to the PHENIX detector.



(a) Diagram of RHIC Accelerator Complex, (Figure from Kiyoshi Tanida)



(b) Aerial photograph of RHIC Complex [67]

Figure 4.1: A diagram of the acceleration process of RHIC is shown in the top panel, and aerial view is shown in thin the bottom panel. RHIC is nearly four miles in circumference and collides a variety of ions at center-of-mass energies between 5 GeV  $\sqrt{s}$  and 510 GeV  $\sqrt{s}$ .

RHIC operating modes and total integrated luminosity delivered to 6 experiments					
Run	species	total particle energy [GeV/nucleon]	calendar time in physics	total delivered luminosity	average store polarization, (H-jet)*
<b>Run-1</b> CY2000, FY2000 33.6 cryo-weeks	$^{197}\text{Au}^{79+} + ^{197}\text{Au}^{79+}$	27.9	3 shifts	$< 0.001 \mu\text{b}^{-1}$	—
	$^{197}\text{Au}^{79+} + ^{197}\text{Au}^{79+}$	65.2	5.3 weeks	$20 \mu\text{b}^{-1}$	—
<b>Run-2</b> CY2001/02, FY2001/02 40.7 cryo-weeks	$^{197}\text{Au}^{79+} + ^{197}\text{Au}^{79+}$	100.0	15.9 weeks	$258 \mu\text{b}^{-1}$	—
	$^{197}\text{Au}^{79+} + ^{197}\text{Au}^{79+}$ polarized p + p	9.8 100.2	2 shifts 8.3 weeks total, no continuous physics operation	$0.4 \mu\text{b}^{-1}$ $1.4 \text{ pb}^{-1}$	— 14%
<b>Run-3</b> CY2002/03, FY2003 30.4 cryo-weeks	d + $^{197}\text{Au}^{79+}$	100.7 + 100.0	10.2 weeks	$73 \text{ nb}^{-1}$	—
	polarized p + p	100.2	9.0 weeks total, no continuous physics operation	$5.5 \text{ pb}^{-1}$	34%
<b>Run-4</b> CY2003/04, FY2004 26.7 cryo-weeks	$^{197}\text{Au}^{79+} + ^{197}\text{Au}^{79+}$	100.0	12.0 weeks	$3.53 \text{ nb}^{-1}$	—
	$^{197}\text{Au}^{79+} + ^{197}\text{Au}^{79+}$ polarized p + p	31.2 100.2	9 days 6.1 weeks total, no continuous physics operation	$67 \mu\text{b}^{-1}$ $7.1 \text{ pb}^{-1}$	— 46%
<b>Run-5</b> CY2004/05, FY2005 31.4 cryo-weeks	$^{63}\text{Cu}^{29+} + ^{63}\text{Cu}^{29+}$	100.0	7.8 weeks	$42.1 \text{ nb}^{-1}$	—
	$^{63}\text{Cu}^{29+} + ^{63}\text{Cu}^{29+}$ polarized p + p	31.2 11.2 100.2	12 days 5 shifts 9.4 weeks	$1.5 \text{ nb}^{-1}$ $0.02 \text{ nb}^{-1}$ $29.5 \text{ pb}^{-1}$	— — 47%
<b>Run-6</b> CY2006, FY2006 21.2 cryo-weeks	polarized p + p	204.9	2 stores	$0.1 \text{ pb}^{-1}$	30%
	polarized p + p	100.2	13.1 weeks	$88.6 \text{ pb}^{-1}$	55%
	polarized p + p	31.2	12 days	$1.05 \text{ pb}^{-1}$	50%

Figure 4.2: Runs 1–3 at RHIC focused on commissioning work for experiments measuring collisions at RHIC. Work was mostly characterized by heavy-ion measurements related to understanding Quark-Gluon Plasma. The spin program began with Run 5. Table produced from data posted at the RHIC run page [17].

RHIC operating modes and total integrated luminosity delivered to 6 experiments						
Run	species	total particle energy [GeV/nucleon]	calendar time in physics	total delivered luminosity	average store polarization, (H-jet)*	
<b>Run-7</b> CY2006/07, FY2006 18.4 cryo-weeks	$^{197}\text{Au}^{79+} + ^{197}\text{Au}^{79+}$	100.0	12.8 weeks	7.25 nb <sup>-1</sup>	—	
	$^{197}\text{Au}^{79+} + ^{197}\text{Au}^{79+}$	4.6	3 shifts total, no continuous physics operation	small	—	
<b>Run-8</b> CY2007/08, FY2008 19.0 cryo-weeks	d + $^{197}\text{Au}^{79+}$	100.7 + 100.0	9.0 weeks	437 nb <sup>-1</sup>	—	
	polarized p + p	100.2	3.4 weeks	38.4 pb <sup>-1</sup>	44%	
	$^{197}\text{Au}^{79+} + ^{197}\text{Au}^{79+}$	4.6	3 shifts	small	—	
	polarized p + p	249.9	4.1 weeks	110 pb <sup>-1</sup>	34%	
<b>Run-9</b> CY2008/09, FY2009 22.0 cryo-weeks	polarized p + p	100.2	9.9 weeks	114 pb <sup>-1</sup>	56%	
	polarized pp2pp	100.2	3.5 days	0.6 nb <sup>-1</sup>	63%	
	$^{197}\text{Au}^{79+} + ^{197}\text{Au}^{79+}$	100.0	10.9 weeks	10.3 nb <sup>-1</sup>	—	
	$^{197}\text{Au}^{79+} + ^{197}\text{Au}^{79+}$	31.2	2.9 weeks	544 μb <sup>-1</sup>	—	
<b>Run-10</b> CY2009/10, FY2010 27.1 cryo-weeks	$^{197}\text{Au}^{79+} + ^{197}\text{Au}^{79+}$	19.5	1.8 weeks	206 μb <sup>-1</sup>	—	
	$^{197}\text{Au}^{79+} + ^{197}\text{Au}^{79+}$	3.85	4.6 weeks	4.23 μb <sup>-1</sup>	—	
	$^{197}\text{Au}^{79+} + ^{197}\text{Au}^{79+}$	5.75	1.4 weeks	7.8 μb <sup>-1</sup>	—	
	polarized p + p	249.9	9.7 weeks	166 pb <sup>-1</sup>	48%	
	$^{197}\text{Au}^{79+} + ^{197}\text{Au}^{79+}$	9.8	1.4 weeks	33.2 μb <sup>-1</sup>	—	
<b>Run-11</b> CY2010/11, FY2011 24.4 cryo-weeks	$^{197}\text{Au}^{79+} + ^{197}\text{Au}^{79+}$	100.0	6.4 weeks	9.79 nb <sup>-1</sup>	—	
	$^{197}\text{Au}^{79+} + ^{197}\text{Au}^{79+}$	13.5	8 days	63.1 μb <sup>-1</sup>	—	
	polarized p + p	100.2	4.4 weeks	74.0 pb <sup>-1</sup>	59%	
	polarized p + p	254.9	4.9 weeks	283 pb <sup>-1</sup>	52%	
<b>Run-12</b> CY2011/12, FY2012 22.9 cryo-weeks	$^{238}\text{U}^{92+} + ^{238}\text{U}^{92+}$	96.4	3.1 weeks	736 μb <sup>-1</sup>	—	
	$^{63}\text{Cu}^{29+} + ^{197}\text{Au}^{79+}$	99.9 + 100.0	5.4 weeks	27.0 nb <sup>-1</sup>	—	
<b>Run-13</b> CY2012/13, FY2013 17.0 cryo-weeks	polarized p + p	254.9	13.3 weeks	1.04 fb <sup>-1</sup>	53%	

Figure 4.3: Though RHIC is currently still running (as of May 9, 2016), I include runs here up to and including the run producing my data set (Run 13). An unprecedented 13.3 cryo-weeks of running was awarded to the W-Physics group. Table produced from data posted at the RHIC run page [17].

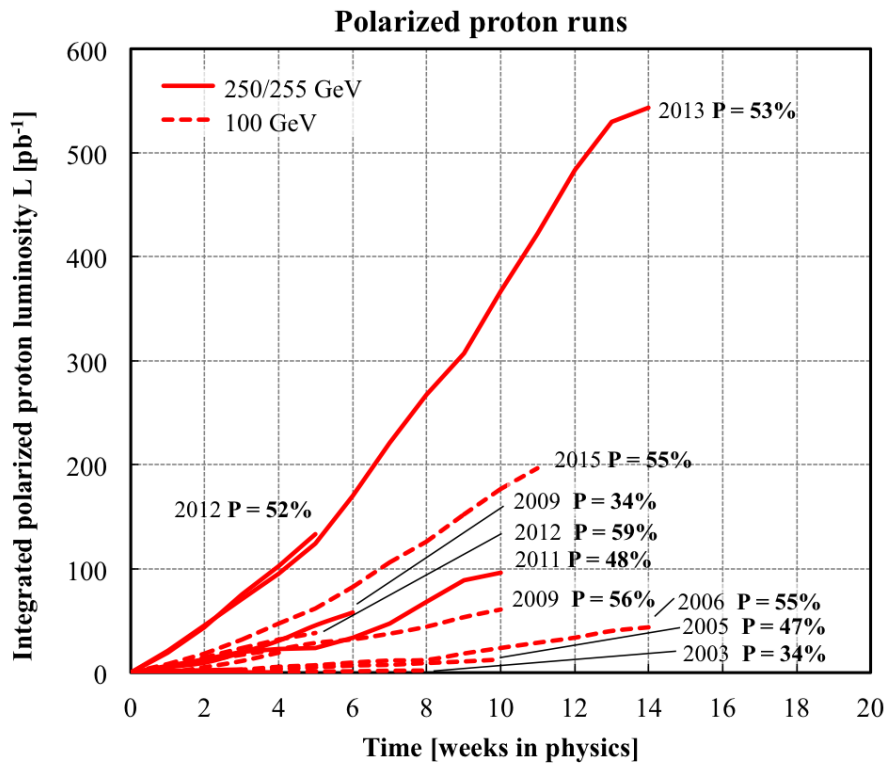


Figure 4.4: Upgrades to RHIC's electron lens have enabled massive improvements to luminosity—seen in the year 2013. The high luminosity was taken advantage of with an extra long proton+proton run. Figure obtained from [17]

#### 4.1.1 Experimental Apparatus

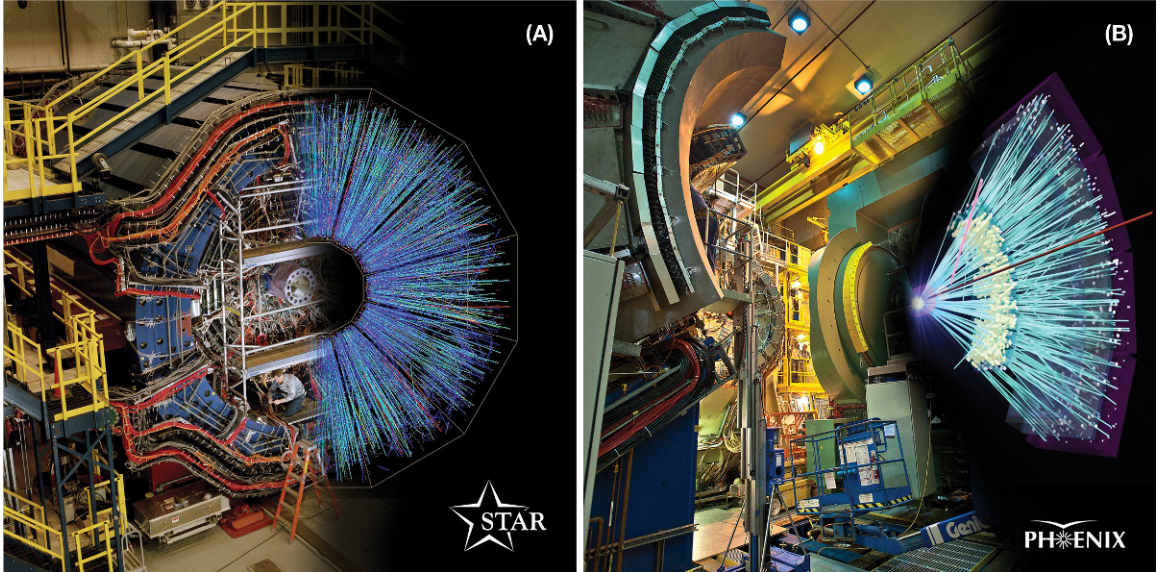


Figure 4.5: STAR (a) and PHENIX (b) with cutaways showing the event display for a heavy-ion collision as reconstructed by the detectors' electromagnetic calorimeters [18].

RHIC accelerates ions in a multi-stage process, summarized in Figure 4.1. The source of the beams is the **Electron Beam Ion Source**, built on top of a 200 MeV linear accelerator (Linac). Once ions are injected into the Linac, they travel to the **Booster Synchrotron**. At this stage, ions are accelerated with pulsed RF fields. After the beam of ions has been accelerated to nearly the speed of light, they are fed into the **Alternating Gradient Synchrotron** or AGS. At this time, ions are traveling at about  $0.37 c$ . By the time the ions leave the AGS, they are moving at  $0.997 c$ . When the ions have reached the appropriate injection energy (which is ion-species dependent), they are transferred to the **AGS-to-RHIC Line**, where a switching magnet pumps bunches of ions into either the counterclockwise circulating ring of RHIC, or the clockwise circulating ring of RHIC. The ions are accelerated here to maximum speed: each beam-ion travels a distance of 2.4 miles every 12.8 microseconds ( $0.99999 c$  at 510 GeV  $\sqrt{s}$  beam energy), for the duration of a physics-fill [68].

When the RHIC rings are filled with ions, the ions are bunched into rotating electromagnetic potentials called ‘buckets’. There are 360 beam-buckets in total, but typically

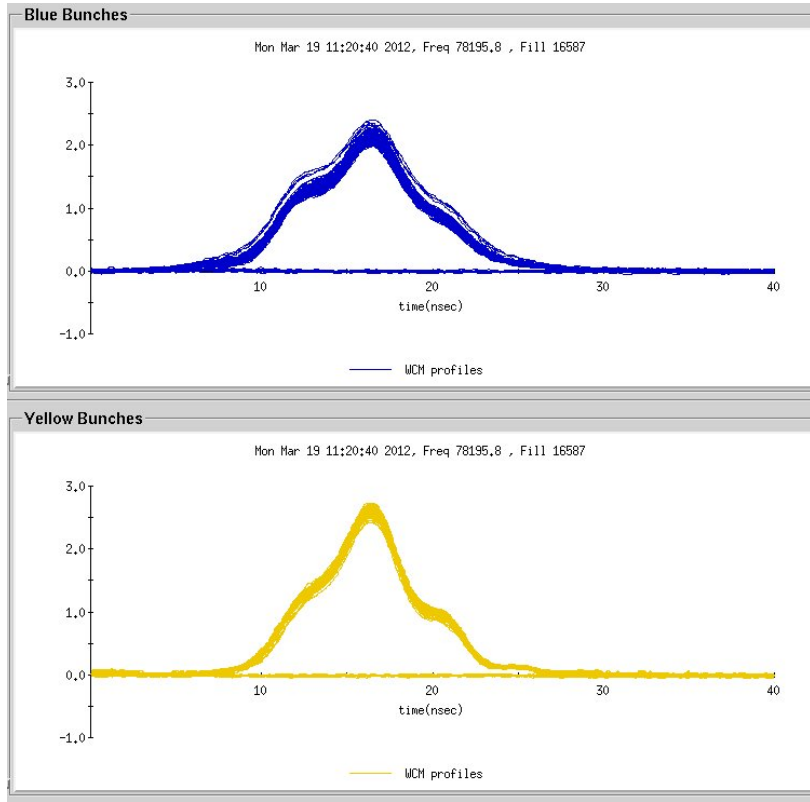


Figure 4.6: The longitudinal distribution of all bunches in a typical fill are overlaid. The bunches from the blue beam (top) and yellow beam (bottom) are shown for over a 40 nanosecond time period.

only a fraction are filled with ions. For this analysis, we took data with beams with 110 filled buckets. The sequence of beam buckets from one filled bunch to the next is referred to as a ‘bunch’—and are rather long - Figure 4.6. The bunch length is 12 meters longitudinally. The bunch width is quite narrow—with Gaussian geometry, it is between 150 mm and 300 mm depending on the beam energy. Understanding the beam bunch geometry is a crucial component to understanding total the total luminosity delivered by RHIC to PHENIX. A detailed presentation of beam dynamics with regards to luminosity will be presented in Chapter 5.

## 4.2 Production of Polarized Proton Beams

The production of polarized beams is crucial to the physics of this measurement—without polarized beams, no spin structure analysis can be done at RHIC. This is due to the fact that the helicity state of the protons in the initial state of any proton+proton collision can be connected to the final observed states in a way which provides information about the spin structure function, as was discussed in Section 3.

The production of polarized beams is a multistage process, and involves several experimental components. The importance of polarizing the beams is fully realized once polarized beams are collided at relatively high center of mass energies, where the beams behave less like polarized proton beams and more like polarized beams of quarks and gluons [69]. The beam is produced from a special polarized ion source, (OPPIS, Figure 4.7). Polarization is at its maximum immediately after transfer from OPPIS, and over the course of the acceleration through the various apparatuses described below, we work to maintain polarization by limiting and mediating depolarizing resonances, Figure 4.1. The exact details of beam injection and polarization management is presented in the RHIC Configuration Manual [20], with the relevant portions summarized here.

### 4.2.1 Polarized Injection

RHIC uses an optically pumped polarized ion source (OPPIS), Figure 4.7 to produce a polarized ion source greatly in excess of RHIC’s design intensity. This is used to our advantage, as the emittance of the beam can be lowered to create a highly collimated beam for physics use.

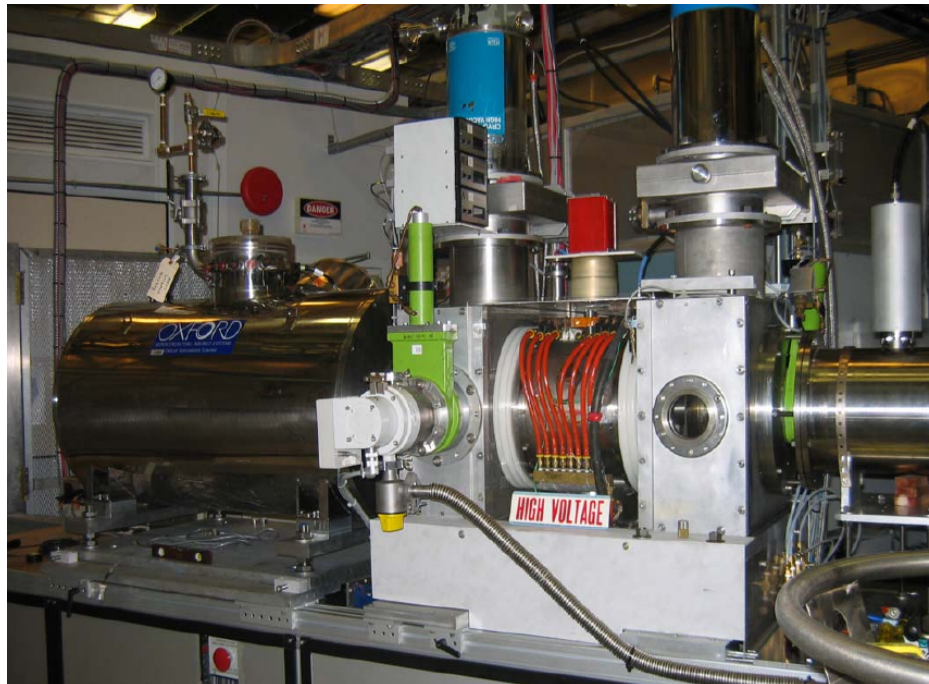
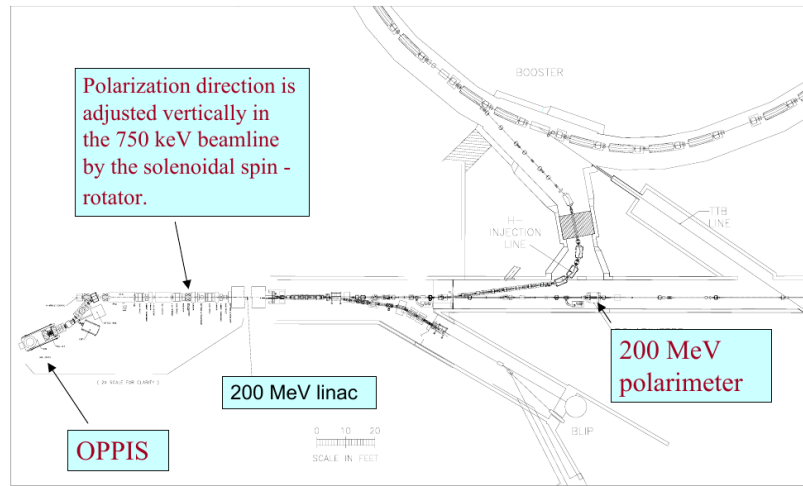


Figure 4.7: RHIC's optically pumped polarized ion source. Produces 0.5-1.0 mA current of polarized  $H^-$  ions. The optical pumping is pulsed at 400  $\mu$ s, [19]

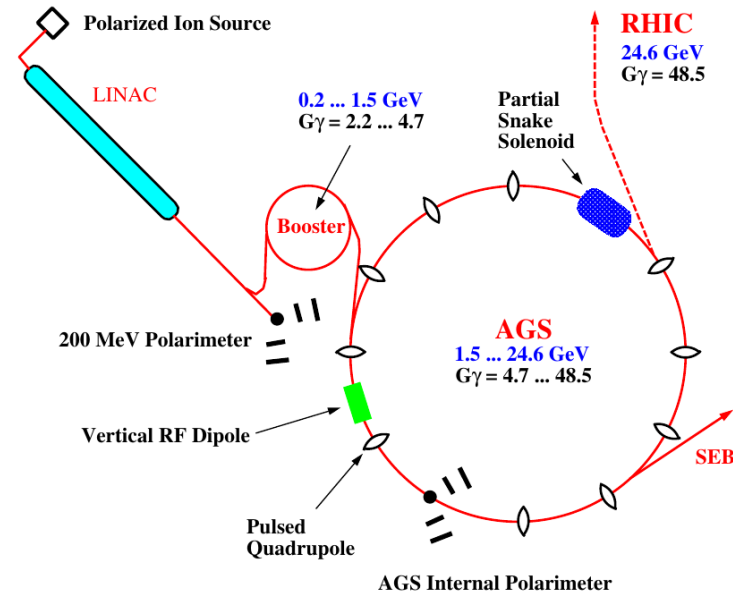
### 4.2.2 AGS to RHIC Transfer Line

Once ions have been optically pumped, we have a direct-current beam at approximately 80% polarization. This is accomplished using optically pumped Rubidium vapor. The polarized ions are then moved into the booster from the Linac, where some polarization is lost to spin precession, intrinsic to accelerating charged ions in a circular path. However, polarization is maintained, by matching the naturally occurring precession resonance due to circulating polarized beams to the orbiting frequency of the booster ring. The Siberian snakes (Section 4.3.1) at this stage serve to flip the ion spin by  $180^\circ$  such that the natural depolarization works to re-polarize the orbiting ions every full-turn. The full details of this procedure are described in Reference [20].

After the ions are sufficiently polarized and filled in the AGS, they are injected into the AGS to RHIC Transfer line, Figure 4.9. The beam is focused and fed through a switching magnet which must be timed with great precision in order to fill the blue and yellow beams with the appropriate polarization patterns. In fact, the precision is so great, that the Earth's curvature must be taken into account over this relatively short injection line. The entry point and exit point are bent ever-so-slightly due to the curvature of the Earth, with the entry point being bent at 12.51 mrad and the egress point being 12.46 mrad [20]. At the point of injection in the transfer line, the beam size, emittance, and polarization are measured.



(a) Technical schematic of Polarized Injection Line [19]



(b) Overhead view of Polarized Injection Line [20]

Figure 4.8: A view of the RHIC polarized injection system. Panel (a) shows a zoomed in technical view of the OPPIS to the booster. Panel (b) shows a zoomed out cartoon of the next step in the polarization injection system, including the AGS, and the feeder line to RHIC.

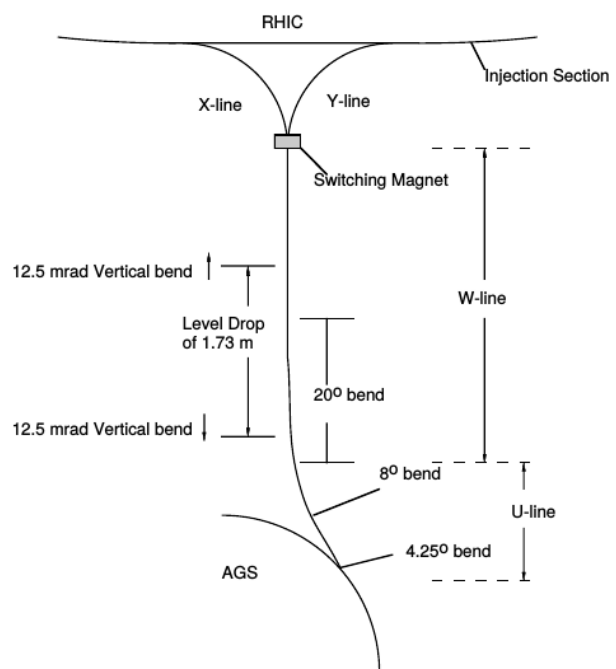


Figure 4.9: A schematic of the geometry of the AGS-to-RHIC transfer line [20].

## 4.3 Maintaining Beam Polarization

The creation of polarized beams is only half the battle. Depolarizing resonances in any particle beam are intrinsic in the design of any circulating beam particle accelerator—without intervention, after a few rotations, RHIC’s polarized beams would become unpolarized. RHIC applies several strategies in concert to correct for the largest of these depolarizing resonances, including beam orbit corrections, the Siberian Snakes, Betatron Tune Spreading, and sextupole magnetic depolarizing resonances.

### 4.3.1 Siberian Snakes

The Siberian Snakes are positioned at two locations on the RHIC ring. The most stable configuration of spin injected in RHIC is such that the spin axis is perpendicular to the plane of the accelerator ring. The Siberian snake is a helical magnet which forces the spin to rotate 180 degrees every half rotation. This special configuration of snakes (see Figure 4.1) ingeniously takes advantage of the rotational precision of the spin (a depolarizing resonance) to re-polarize the beam every half-orbit, by flipping the spin 180° every half orbit.

### 4.3.2 Spin Rotators

The spin rotators are located outside of experimental interaction regions around PHENIX and STAR. These superconducting dipole magnets rotate the spin of the beams onto a longitudinal (parallel with beam) axis—these magnets are important for any measurement (such as this one) requiring longitudinal spin polarization. Transverse spin polarization has also been used in RHIC operations to probe the transverse spin structure of protons. The transverse spin structure of the proton is a complementary and vital area of inquiry, but is not presented in this work.

### 4.3.3 Measuring Beam Polarization

The RHIC Collider-Accelerator Department provides several means of measuring the beam polarization over the course of the data taking period. PHENIX records special data collection runs which are used to determine the real beam polarization delivered to the detector, in a yearly analysis. This analysis is referred to “Local Polarimetry”, or “LPol”.



Figure 4.10: This cartoon illustrates one potential polarization pattern configuration of the beams as they collide at PHENIX’s interaction region. As beams are longitudinally rotated into position for collision, it is crucial to keep careful track of the magnet currents rotating the beams, as well as the overall polarization pattern.

The collider-accelerator department at RHIC will additionally measure polarization in via inelastic proton-carbon scattering in the Coulomb-Nuclear Interference (CNI) region. Relative polarization can be determined with to within 10% in only a few seconds of measurement.

Vertical polarization is determined through the calculation of the left and right particle production, with a known analyzing power ([20], Chapter 8):

$$P_B = \frac{1}{A_p} \frac{N_L - N_R}{N_L + N_R} \quad (4.1)$$

Where  $P_B$  is the beam polarization,  $N_L$  and  $N_R$  are the left-scattering produced particles, and right-scattering produced particles and  $A_p$  is the analyzing power, which can be calculated from first principals, and experimentally verified. Scattering takes place as a carbon filament is swept across the beam

Using a p-Carbon CNI polarimeter provides an economically viable way to measure beam polarization within the precision needed for the spin experiments.

#### 4.3.3.1 The Spin Monitor

The polarized proton beams at RHIC are not polarized uniformly. They are filled with a spin-pattern, a sequence of bunch polarizations which alternate the direction of the polarized spin for each bunch. During a RHIC run, it is crucial to keep track of the polarization patterns being collided at the PHENIX IR 4.10.

One of my major contributions to the PHENIX experiment was in the upkeep and development of the spin monitoring systems for the online data taking portions of the experiment, show in Figure 4.11.

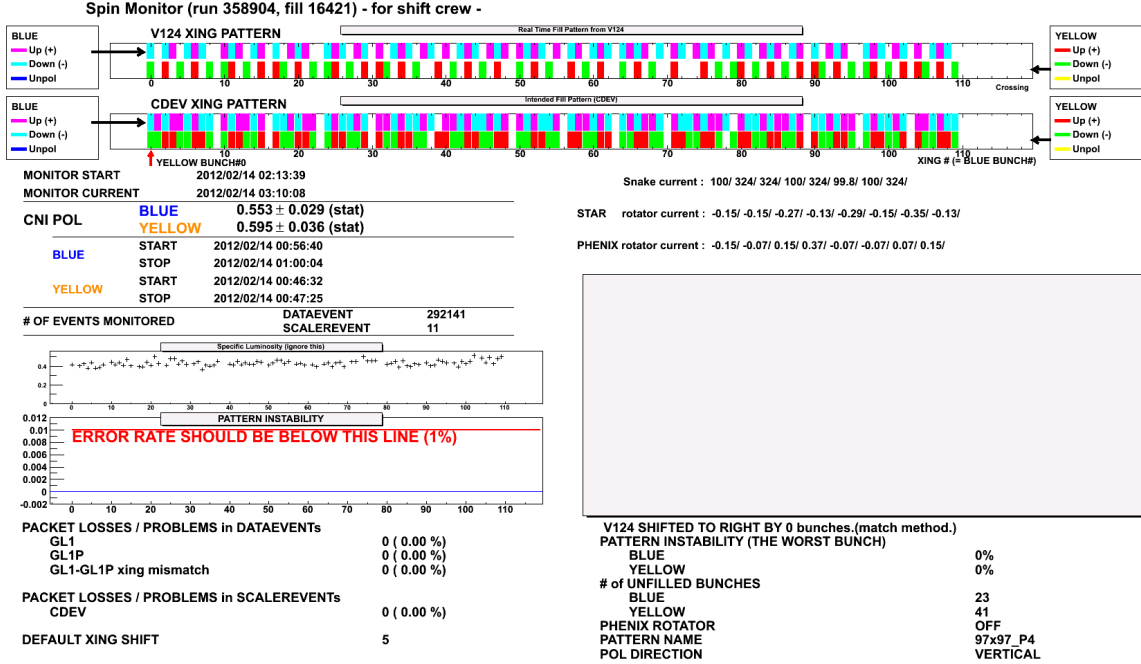


Figure 4.11: The shift-crew display output for the Spin Monitor. The upper panel shows the polarization of the blue and yellow beams, and other panels summarize information including magnet currents (needed to understand the spin orientation), issues with data packet loss, the recognized spin-pattern, as well as a large boxed area on the lower left where errors could be shown to the shift crew along with the proper response.

The spin monitor's purpose is to provide real-time feedback on the dipole magnets used to orient proton spin orientation prior to collision in addition to comparing the RHIC spin fill pattern against the measured spin pattern delivered to the PHENIX interaction region. This is discussed further, in the context of the calculation of the longitudinal asymmetry in Section 8.3.

## 4.4 The Pioneering High Energy Nuclear Interaction Experiment

The Pioneering High Energy Nuclear Interaction Experiment (PHENIX) is a synthesis of many smaller detectors: all of whom were commissioned for various physics goals; some of whom have been repurposed from their original application once their primary physics objective was completed. PHENIX has several major physics thrusts, which are discussed below.

Much of the PHENIX collaboration’s early published work focused on creating and studying quark gluon plasma in heavy ion collisions, but in following years spin papers came too. Major questions in physics that PHENIX set out to answer with its heavy-ion program include: color confinement, chiral symmetry restoration, thermal radiation of hot gasses, the QCD phase transition, strangeness and charm production, jet-quenching, and finally, QCD evolution [70].

One remaining physics goal of the PHENIX collaboration is to study the origins of proton spin. The PHENIX spin program ‘officially’ started with the RHIC upgrade to enable production of polarized proton beams.

The spin program came shortly after the 2001 commissioning run. The first polarized proton run was produced by RHIC for PHENIX in 2002, with 8.3 total weeks of data. Data was taken over several discrete periods, as RHIC was still being optimized for spin physics.

The purpose of the PHENIX spin program has been to understand the spin structure of the proton, and has historically utilized various particle production asymmetries (left-right and forward-backward) as an experimental probe for polarized parton distribution functions (as discussed in Chapter 3).

PHENIX studies the proton spin structure as modeled by the Ellis-Jeffe sum rule (Chapter 3). The PHENIX spectrometer is particularly well suited to studying gluon polarization,  $\Delta g$  and the anti-quark polarization,  $\Delta \bar{q}$ . Additionally, the ‘nature of parity non-conservation itself can be directly studied’ [71] using polarized beams, and spin asymmetries in collisions. This measurement requires a means of reconstructing jets, inclusive or leading particle production can be used as a proxy with some small asymmetry remaining.

The configuration of the PHENIX’s detectors changes from year to year, as part of planned upgrades. The configuration of the detector for the 2013 physics run is shown in Figure 4.12.

PHENIX makes use of many classic detectors, including Cherenkov light detectors, resistive plate chambers, electromagnetic calorimeters, silicon chip detectors, time of flight detectors, scintillation light detectors, cathode strip chambers, and proportional tube counters.

While all of these subsystems are interesting, and have produced excellent physics results, I will focus only on those pertinent to this analysis.

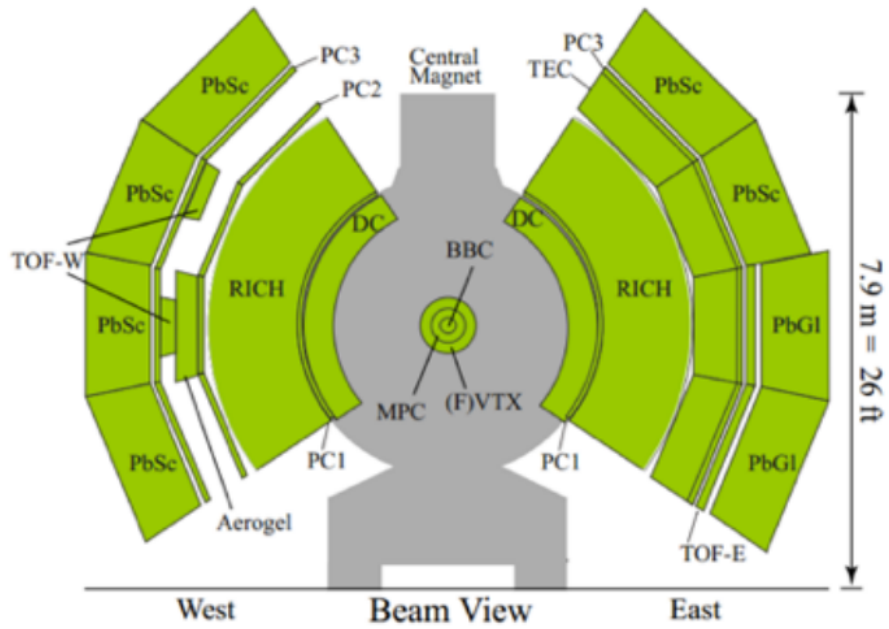
PHENIX is generally thought of as two ‘halves’ being comprised of two broadly defined ‘arms’—the forward Muon Arms, and the central arms. As the names suggest, the central arms cover the central rapidity range (close to  $y = 0$ ), whereas the Muon Arms cover larger rapidities and specialize in detecting muons. While both kinematic regions are used for heavy ion and spin physics analyses, this analysis exclusively uses the forward muon and the Beam Beam Counters. The majority of the central arms systems will not be discussed in detail in this thesis.

#### 4.4.1 Units

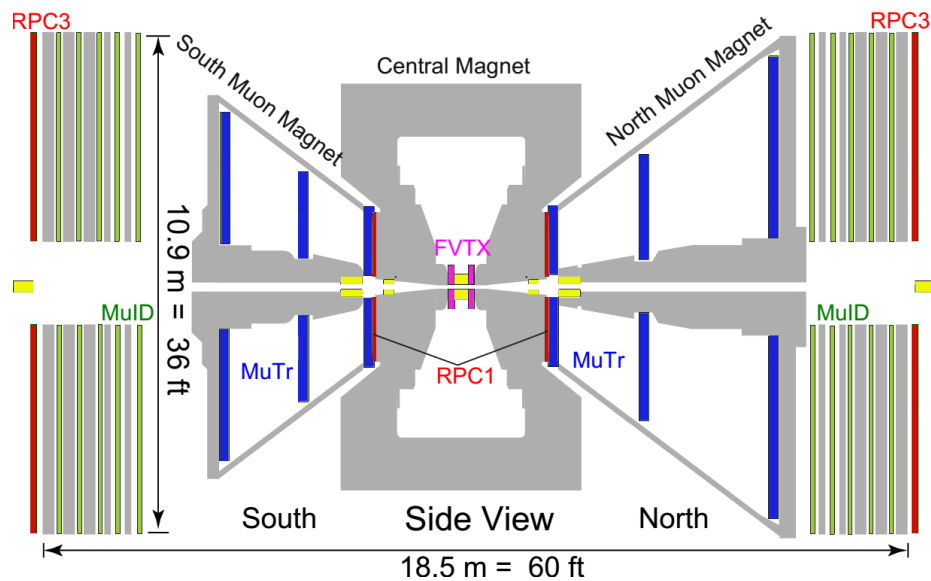
The data taken by PHENIX as well as the geometry of the detector can be characterized by various measurements and units. The data taken by the detector is shown relative to the PHENIX Coordinate System (Figure 4.13). Some accelerator-specific units are summarized in Table 4.1. The full description of the data taken by PHENIX is saved for Chapter 6.

A closely related analysis measures  $W \rightarrow e$  processes uses the central arms. As different arms are sensitive to different rapidity ranges, complimentary results are obtained from central and forward analyses. The central analysis is presented in references [65] and [72].

PHENIX also utilizes a complex data acquisition system (DAQ) which streams data from each detector, assembles this data into a labeled event, compresses and finally stores into a proprietary storage format. The work-flow of the DAQ is summarized in Figure 4.14.



(a) Central Arms



(b) Forward Muon Arms

Figure 4.12: Shown: The two main arms of the PHENIX Spectrometer. The central arms are shown via the beam-on view of PHENIX (a) and Forward Muon Arms are highlighted via the 90-degree rotated view (b). In both cases, the 2013 configuration is shown. The beams are brought into intersection at the geometric center of each figure (immediately between the BBCs)

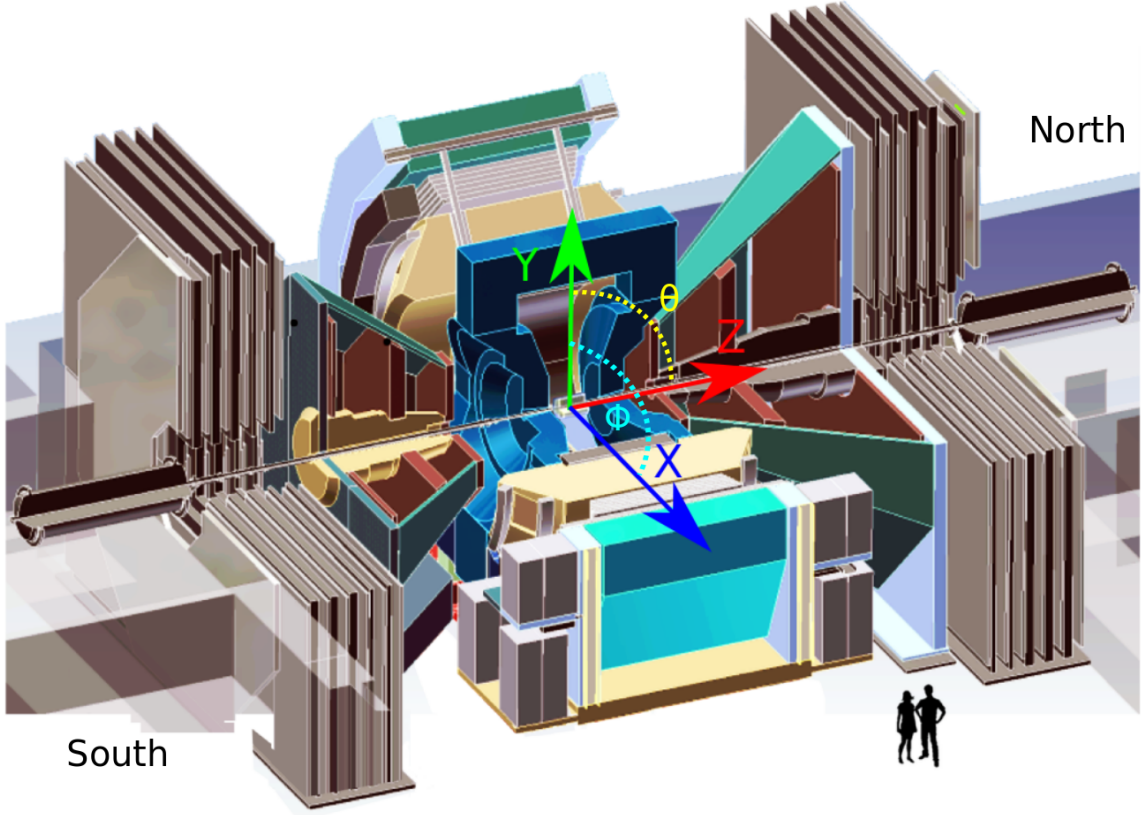


Figure 4.13: The PHENIX coordinate system is shown (RGB arrows) at the center of the nominal interaction point within PHENIX, the origin, in this quarter-cutaway drawing. The small black figures are actually miniaturized human beings, the PHENIX detector is very small—this is a full scale drawing of PHENIX. Shown: the  $x$ ,  $y$ , and  $z$  coordinates, as well as the azimuthal coordinate,  $\theta$  and polar coordinate  $\phi$  [21]

For each event, particles which interact with the detector material are transduced into electrical signals. The transduced signals are serialized into a detector-specific data stream, such that the state of the detector's excitation can be recorded and reconstructed later. This information is stored on the front-end-electronics modules (FEMs), and synchronized with timing information from the clock (ticks once every time there is a bunch crossing) and a Global Trigger decision, i.e. whether or not the right parts of the detector lit up to make this particular event worth keeping. If the detector triggering heuristics determine that an event is worthy of keeping, the uncompressed serialized information is sent to the DCMs (Data Collection Modules), where it is assembled into a packet, and then sent

Quantity	Definition	Description
$x, y, z$		Cartesian coordinates whose origin is at the center of the PHENIX detector
$\theta$	Polar coordinate relative to origin of PHENIX coordinate system defined by the positive z-axis and a reference point	
$\phi$	Polar coordinate relative to the origin of the PHENIX coordinate system, defining the angle between a reference point and the x-axis	
$v$		Speed of a particle
$c$		Speed of light
$E$		Relativistic energy of a particle
$p$	$(p_x, p_y, p_z, E)$	Total four-momentum of a particle
$y$	$\tanh^{-1}(v/c), \frac{1}{2}\ln\frac{E+p_zc}{E-p_zc}$	Spatial coordinate, rapidity, describing the hyperbolic angle difference between frames of reference in relative motion. When described in terms of the beam, it is the rapidity of the particle relative to the beam's center-of-mass frame.
$\eta$	$-\ln [\tan(\frac{\theta}{2})]$	Spatial coordinate describing the angle of a particle relative to the beam's center-of-mass frame.

Table 4.1: Some units describing the geometry of and data taken by PHENIX.

to the event builder (EvB). At the EvB, all packets originating from a common collision are assembled into an event. The event is compressed into a proprietary PRDF (PHENIX Raw Data File Format) format, and sent to the Buffer Boxes, a cache of high density local storage. Finally, this cached data is sent off to high density robotic magnetic tape storage on for ultra-stable and low-cost archival. Later, this data is copied to a computing cluster and reconstructed into ‘analysis-ready’ data structures, such as track reconstruction variables, event vertices and so-on. This is discussed in Chapter 6 and Chapter 7.

A complete summary of PHENIX detector subsystems (excluding the new Forward Vertex Detector, Silicon Vertex Detector, and Resistive Plate Chambers, which discussed separately) can be found in Table 4.2.

Element	$\eta$	$\phi$	Features
<b>Magnets</b>			
Central Magnet	$ \eta  < 0.35$	$360^\circ$	1.15 T
Muon Magnet North	$1.1 <  \eta  < 2.2$	$360^\circ$	0.72 T
Muon Magnet South	$1.1 <  \eta  < 2.4$	$360^\circ$	0.72 T
<b>Minimum Bias</b>			
Beam Beam Counter	$(3.1 <  \eta  < 3.9)$	$360^\circ$	Vertex Reconstruction
Zero Degree Calorimeter	$\pm 2mrad$	$360^\circ$	Minimum Bias Trigger
<b>Central Detectors</b>			
Drift Chambers	$ \eta  < 0.35$	$90^\circ \times 2$	Central $p$ and $n$
Pad Chambers	$ \eta  < 0.35$	$90^\circ \times 2$	Pattern Recognition
Ring Imaging Cherenkov	$ \eta  < 0.35$	$90^\circ \times 2$	Electron Identification
Time of Flight	$ \eta  < 0.35$	$45^\circ$	Hadron ID, $\sigma_T$
PbSc EMCAL	$ \eta  < 0.35$	$90^\circ, 45^\circ$	Calorimetry, photon, $e^\pm$
PbGl EMCAL	$ \eta  < 0.35$	$45^\circ$	$e^\pm, \mu^\pm$ separation at $p > 1GeV/c$ EM Shower $\alpha_{EM}$ $1GeV/c$
<b>Muon Arms</b>			
Muon Tracker South	$1.15 <  \eta  < 2.25$	$360^\circ$	North installation
Muon Tracker North	$1.15 <  \eta  < 2.44$	$360^\circ$	
Muon ID South	$1.15 <  \eta  < 2.25$	$360^\circ$	Steel absorbers, $\pi/K$
Muon ID North	$1.15 <  \eta  < 2.44$	$360^\circ$	""

Table 4.2: A summary of PHENIX hardware [32].  $e^\pm/\pi^\pm$  separation and  $\pi/K$  separation requires the Time of Flight (ToF) working with PbGl and PbSc data. PbGl refers to “Lead Glass Scintillator” and PbSc refers to “Lead Scintillator”. The Muon Identifier (Muon ID, MuID) can help suppress hadrons by absorbing them in the iron layers.

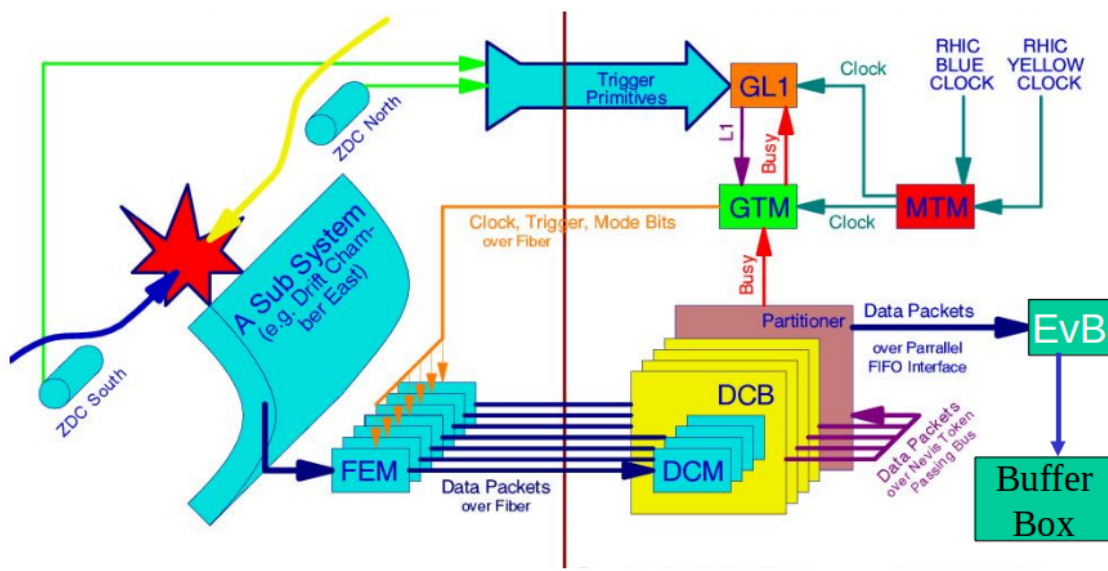


Figure 4.14: Shown: A flow chart summarizing the PHENIX DAQ [22].

#### 4.4.2 Subsystems

The major subsystems contributing to this work include the Muon Arms, the Beam Beam Counters (BBCs), and the Forward Vertex Detector, since the analysis is characterized by calculating the asymmetry for  $W \rightarrow \mu$  interactions, only muon reconstruction and identification is required. For the complimentary central arm analysis, the  $W \rightarrow e$  decay mode is explored.

##### 4.4.2.1 Beam Beam Counters

The Beam-Beam counters (BBCs, Figure 4.16) are photomultiplier tubes with scintillating lead-glass crystals. These detectors are situated 144 cm from either side of the nominal center of the PHENIX interaction region. The primary purpose of the BBCs is to provide the time of a beam-beam collision for triggering, and to measure the Z-Vertex of the collision (Figure 4.15).

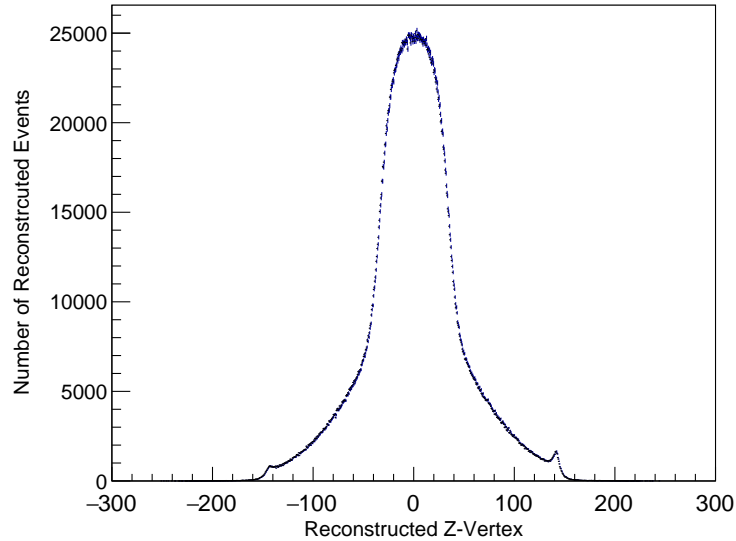


Figure 4.15: Here, we see a typical BBC z-vertex distribution for one run's worth of data, over a z-vertex range of -300 cm to 300 cm. The central peak is close to the nominal interaction point of  $z = 0$  cm. The peaks to the left and right (at  $\pm 144$  cm) are from collisions outside of the BBC.

When a collision occurs, each BBC measures the arrival time of the leading charged particles,  $T_S$  for the south BBC, and  $T_N$  for the north BBC (Figure 4.17). These times are defined as the average of times within the established timing window - each element of the BBC is capable of  $52\pm4$  ps, which is a factor of  $\tilde{2}500$  less than the bunch crossing rate (1 bunch every 106 ns) [73].

The Z-Vertex is determined from  $T_N$  and  $T_S$  as follows:

$$Z_{vertex} = c * (T_S - T_N)/2.0 \quad (4.2)$$

Note that a consequence of the way the z-vertex is calculated, when there are collisions occurring are outside of the BBCs (i.e.  $-144cm > z_{vertex}, z_{vertex} > 144cm$ ), the reconstructed z-vertex will either be at 144 cm or -144 cm. These events are removed with a vertex cut on the data.

The BBCs are used to record data with minimal bias towards any events containing a particular physics characteristic. This is important as a means for reconstructing the absolute abundance of particle production, which is crucial for determination of any inelastic scattering cross section and normalization of any cross-section of interesting scattering events. The Beam-Beam counters provide a measurement of vertex reconstruction by way of analyzing the time delay between triggering of the North and South BBCs. The delay window is then used to reconstruct the event vertex by assuming the impinging particles were traveling at near the speed of light, Figure 4.17.

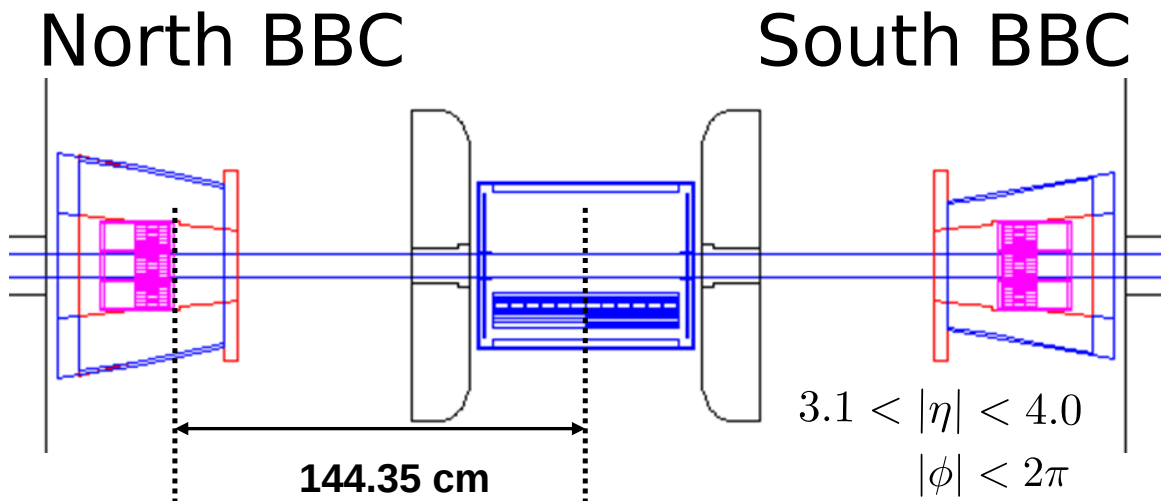


Figure 4.16: Shown: a schematic of the exact proportions of the detector as viewed alongside the beam pipe, along with the pseudorapidity and azimuthal coverage [23]

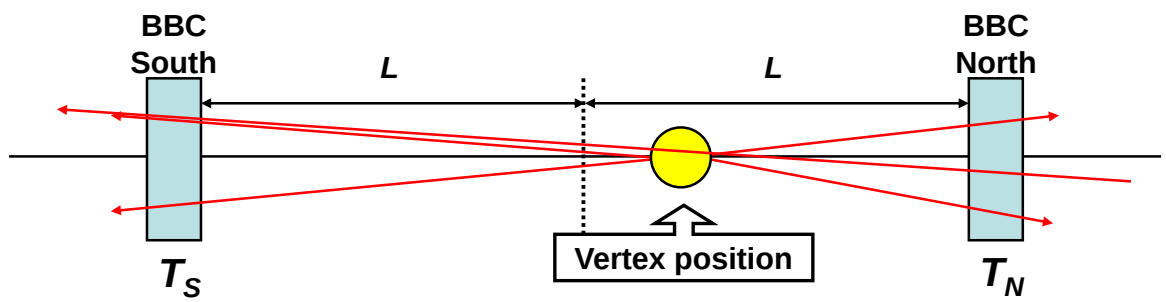


Figure 4.17: Showers from the primary event vertex impinge on the north and south BBC. The average timing of these particles are used to calculate  $T_N$  and  $T_S$ , allowing for the calculation of event z-vertex (Equation 4.2)

#### 4.4.2.2 Forward Vertex Detector

The Forward Vertex Detector (FVTX), Figure 4.18 is a silicon tracking detector, which enables detection of secondary event-vertices. Secondary vertex tracking provides additional information to improve the precision to the Muon Tracking system. As a result of this improvement, particles generated in decays occurring from those produced after the primary collision, but before interaction with detector bulk may be studied, or alternatively (as with this analysis) rejected.

For this analysis, the FVTX can provide an important additional layer of precision, because it can help to identify background-events which do not originate from the primary event vertex of a collision [24].

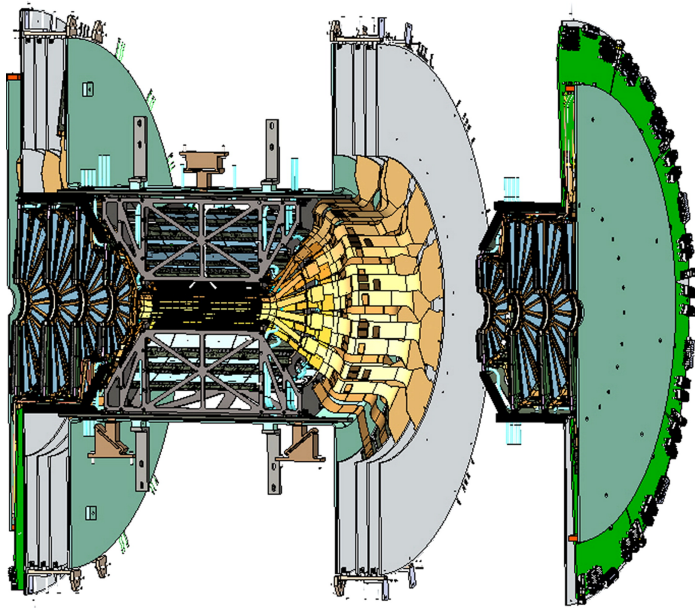


Figure 4.18: A schematic of the Forward Vertex Detector, showing the silicon chip layers (light blue wedges), and readout electronics (green). The FVTX was designed to mount directly onto the Silicon Vertex Detector (center) [24]. This configuration allows for a very high density of interleaved chips, in several layers, covering a maximum area around the beam pipe for detection of secondary vertex events. Secondary vertices are expected to occur rapidly after the primary vertex, making the region close to the primary vertex important real-estate to occupy.

#### 4.4.2.3 The Muon Arms

The Muon Arms are composed of several subsystems, including the Muon Tracker (MuTR, cathode strip chambers), the Muon Identifier (MuID, shielding and scintillation layers), and the Resistive Plate Chambers (RPC, bakelite gas gaps and azimuthal oriented capacitively coupled copper readout strips). The FVTX can be used to improve the track reconstruction, as discussed in Section 4.4.2.2.

The primary purpose of the Muon Tracker is to reconstruct momentum of muons in the forward kinematic region. The Muon Tracker has three cathode strip tracking planes with a volume of gas and an applied radial magnetic field. Each plane has two faces of tracking strips, for six total tracking readouts total. The arrangement of cathode strips makes the Muon Tracker very sensitive to the azimuthal dimension, but coarsely sensitive to the radial direction.

The three tracking stations of the Muon Tracker are utilized for momentum and charge identification. The Muon Tracker arms are sandwiched with resistive plate chambers. The MuID North and South are situated farthest from the beam interaction point on top of the Muon Trackers. The MuID identifies muons by suppressing hadronic background via absorption, by way of interleaving steel layers between Iarocci tubes. Muon tracks are reconstructed by matching the BBC event vertex with MuTR station hits using Kalman filter, and can even be matched with FVTX secondary vertices as a means of rejecting non  $W$  Boson decays. Prior to the Forward Upgrade (Section 4.5), the Muon Arms consisted solely of the Muon Tracker and the MuID.

The Muon Tracker North and South cover slightly different kinematic ranges, due to the physical dimensions of the PHENIX experimental hall. The North Arm covers a pseudorapidity range of  $-2.2 < \eta < -1.1$ , while the South Arm covers a pseudorapidity range of  $1.1 < \eta < 2.4$ . The muon trackers have full azimuthal coverage. The Muon Tracker is composed of three stations, subdivided into half-octants. The stations transduce impinging particle hits with cathode strip chambers, with the chambers being referred to as ‘gaps’. The cathode planes at each station are etched with radial strips. Each station additionally contains  $20\ \mu m$  gold plated anode wires and  $75\ \mu m$  gold plated copper-beryllium field wires. The inner edge and outer edge of the cathode planes are both used for signal readout. The cathode strips and anode wires are offset by approximately  $5^\circ$ . During signal readout, one can use the crossing location of the activated cathode and anode wires to

spatially locate the radial and transverse intersection point of a particle which crosses a tracking gap. The information from the crossing points along with the known magnetic field are used to reconstruct the arc made by a particle traversing the muon tracker planes [25], [74]. Information from the Muon Tracker is fed into the LL1 triggering decision, along with the MuID.

While the muon tracker provides the principal means of reconstructing the physical properties of the impinging particles, the MuID helps to reject hadronic background, and is used in the LL1 trigger. The MuID's Iarocci tubes are a special wire chamber, with a small wire is axially positioned inside of an Aluminum tube with gas fed through the tube. The central wire serves as an anode with the Aluminum tube serving as a cathode. As particles impinge on the tube, the gas is ionized, and the electric potential between the anode and cathode (4300-4500 V) creates a signal, which is read out from the anode wires. This process generates a  $\pm 20$  mV pulse, which is amplified and sent to a read-out card. The pulses are subsequently digitized and cached locally, before being sent to the LL1 trigger read-out, which has been programmed to trigger based on the desired threshold [25], [74].

The Muon Tracker has a radial magnetic field, leading to charged particles traversing the tracker to have a helical bend. The bend of this track is used to identify both the charge and momentum of the muon. This is suitable for lower energy muon tracks, such as muons coming from the  $J/\Psi$  decay, a di-muon process which characterizes the primary decay channel targeted in the original design.

The dimuons produced in  $J/\Psi$  decays have much lower energy than muons which decay from real  $W$  Boson production. To extend the muon tracker's usefulness into tracking these high energy muons, an upgrade to the triggering system was required to obtain adequate background rejection for the Forward  $W$  analysis. This cannot be done with offline analyses, because the rate of muon production from other sources is much higher than that of the  $W$  Boson decay source, and the PHENIX DAQ bandwidth ranges from 5-8 kHz, with other muonic processes potentially triggering the original muon trigger restrictively higher rates.

The Muon Arms were the subject of significant upgrades from 2011-2013. New front end electronics were added to improve triggering, in addition to a new detector subsystem: the RPC was added. The details of these upgrades are discussed in Section 4.5).

## 4.5 The Forward Upgrade

With the inception of the PHENIX spin program in 2004, one of the physics goals of PHENIX has been to constrain the sea-quark contribution to the total proton spin. To accomplish this, PHENIX needed to upgrade its detectors in order to trigger on W-genic muons (muons which come from the  $W$  Boson decay), due to the bandwidth constraints of the machine. While the overall sea-quark contribution to the proton spin is expected to be small, it is not expected to be uniformly zero.

Instead, the expectation is that the matter contribution to the quark sea is strongly positively polarized, while the antimatter contribution is strongly negatively polarized [16]. Measuring this polarization via the longitudinal asymmetry of W-genic muon production (Equation 3.16) is the means by which this is accomplished. Prior to the Forward  $\mu$  analysis, the only results from PHENIX constraining sea-quark polarization were produced from the Central  $W \rightarrow \mu$  analysis. To better constrain our models, we require lower uncertainty in the forward kinematic regime—thus, the Forward Upgrade.

The first data for this measurement was taken in 2009, and published in 2010 under [75], but only for central rapidities, where a clear signal peak could be found in the electron invariant mass spectrum at 40 GeV (half the rest mass of the  $W$  Boson). This made evaluating signal and background contribution and calculating asymmetries relatively straight-forward.

However, in forward kinematic region, it is very difficult to discriminate real  $W \rightarrow \mu$  from other sources  $X \rightarrow \mu$ . As one can observe in Figure 4.19, only at high  $p_T$  does the  $W$  Boson signal become dominant.

Figure 4.19 shows projected performance of the forward upgrade with regards to triggering on muonic processes. Panel (a) shows the momentum spectra of several muonic processes with the accepted trigger illustrating that the old electronics allow mostly low momentum muons. Panel (b) shows the original projection of the threshold after adding the new electronics. The old trigger relied solely on the MuID, which has good hadron rejection, but no momentum selectivity apart from the minimum momentum threshold needed to penetrate the layers of steel.

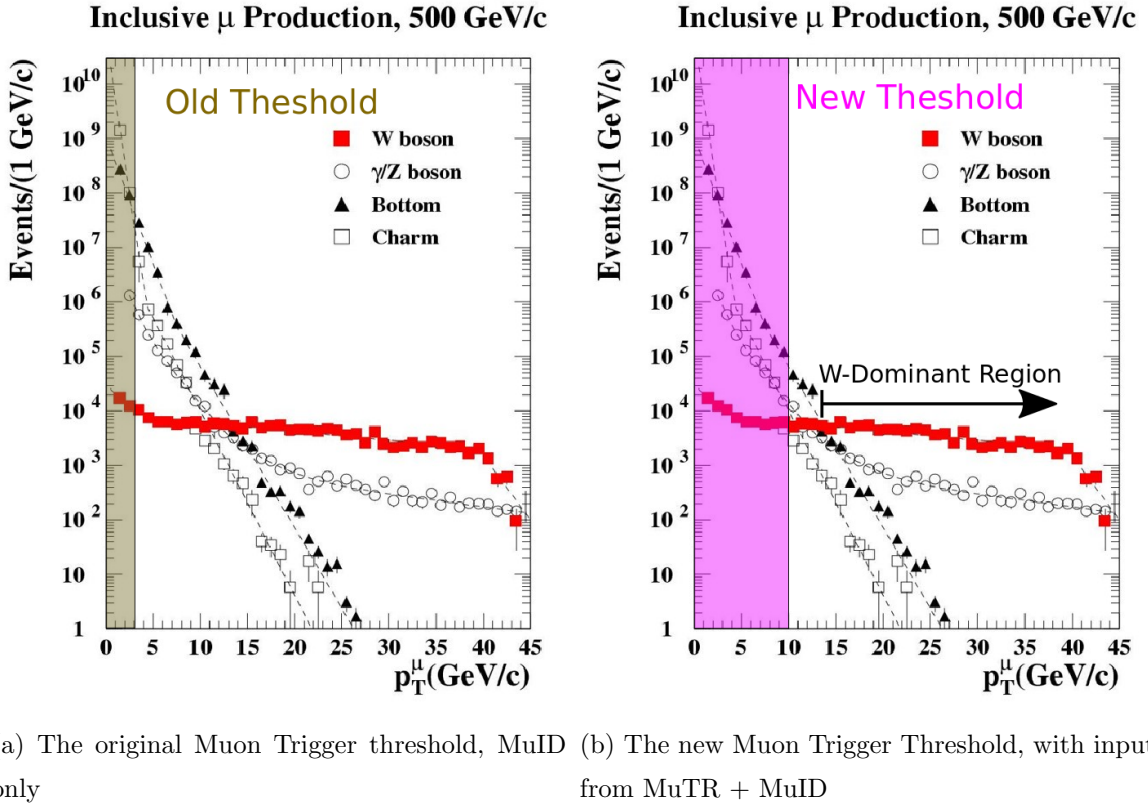
The Forward Upgrade to PHENIX increased the muon triggering threshold from about  $2\text{ GeV}$  to  $10\text{ GeV}$ , enough to insure that most muons produced from  $W$  Boson decays can be recorded, with much better background rejection.

#### 4.5.1 The Muon Tracker Electronics

Since the MuID will fire on Muons with a  $2.5\text{ GeV}$  momentum threshold, a high rate will be recorded, but biased toward non- $W$  events. With event rates in excess of 10 MHz, and the MuID trigger rate in excess of 20 kHz. Almost no  $W$  events would be recorded, even with scaling the archival rates of the MuID trigger. The signal would be totally suppressed. In addition, many of the events which trigger the MuID alone are ‘punch through’ hadrons, which are create a ‘fake’ muon signal. To combat this, the new trigger allows us to include Muon Tracker elements into the overall signal, such as track straightness, in order to obtain a much richer data set populated with a higher concentration of  $W$ -genic muon events. Background rejection factors in excess of 2000:1 were achieved. The new trigger schematic is summarized in Figure 4.20

Thus, before the Forward Upgrade, the Muon 1D trigger was insufficient. Additional absorber was installed at the nose-cone of the muon tracker to block these predominantly lower momentum hadronic particles.

To help with the setting an appropriate track momentum threshold, the addition the new Front End Electronics Modules replaced the existing muon tracker electronics to allow for the real-time calculation of pseudo-momentum to be fed into the trigger decision [26].



(a) The original Muon Trigger threshold, MuID only  
(b) The new Muon Trigger Threshold, with input from MuTR + MuID

Figure 4.19: Observing the simulated production of muon as a function of  $p_T$ , we can see that in the kinematic region of  $W$  production that the dominant sources of muons come from other processes. The new PHENIX muon trigger threshold is sensitive at 10 GeV/c and above. The threshold is still high enough that with other methods, we can record all events which come from the  $W$  Boson, with triggering, whereas with the old threshold, this was impossible.

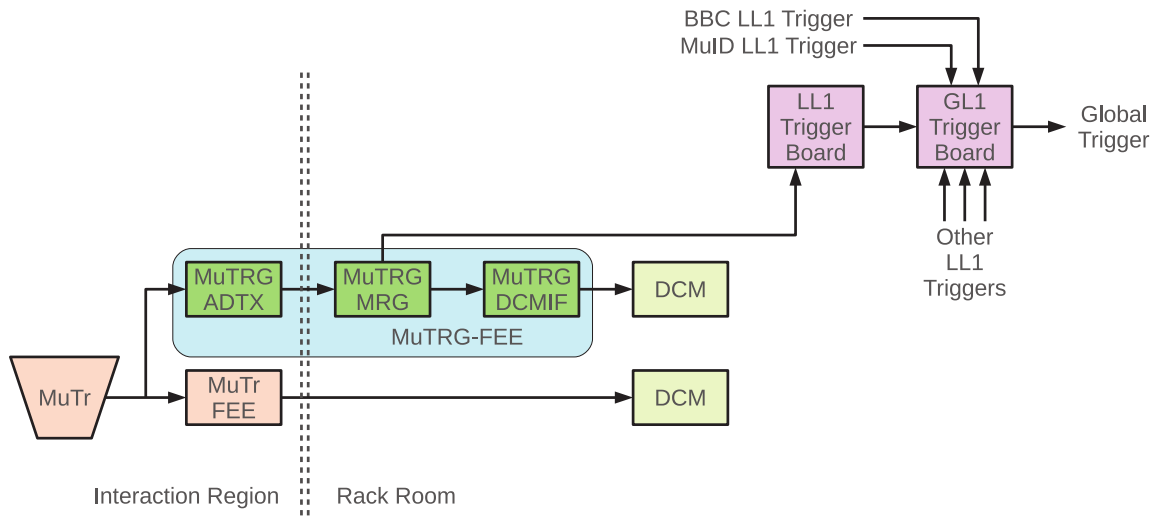


Figure 4.20: Shown: the muon trigger schematic layout, incorporating information from the Muon Tracker, and MuID. To the left of the dotted lines, we see the Muon Tracker, feeding information to both its front-end electronics module (MuTr FEE) and the analog-to-digital converter, in the MuID. The information is sent to the rack room, a small computing cluster which manages and assembles the data streaming in from the PHENIX interaction region [25].

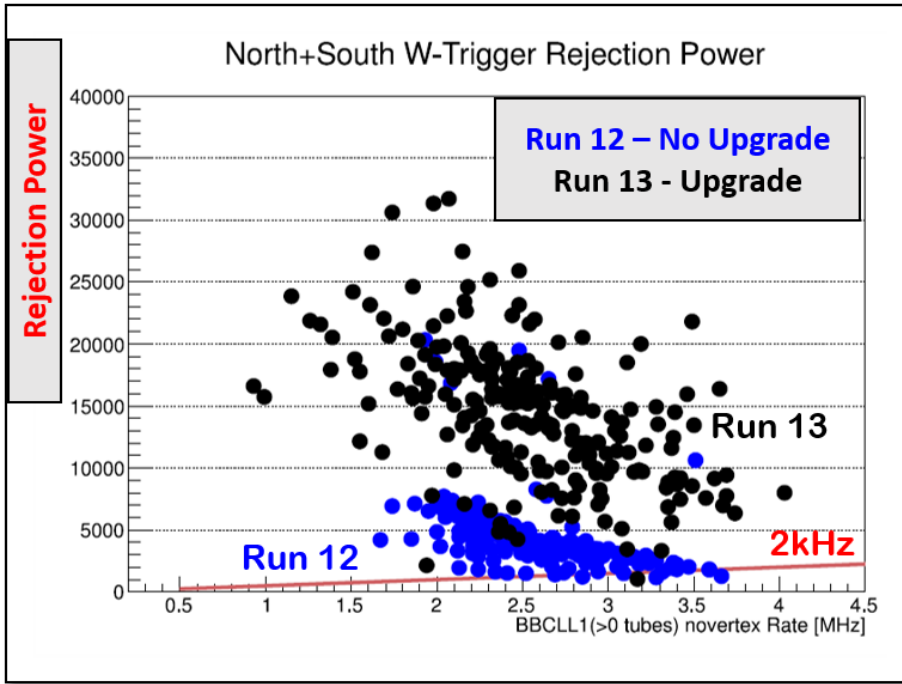


Figure 4.21: In 2013 with the final commissioning of the RPCs and the Forward Upgrade complete, we saw a dramatic increase in rejection power, as expected.

#### 4.5.2 The Resistive Plate Chambers

One of my major contributions to the PHENIX experiment was in the construction and testing of the RPCs at station 1 (closest to the beam interaction point at PHENIX), in 2012. An exploded view of the RPC is shown in Figure 4.23. The RPCs were a crucial part of the W-Physics muon trigger. One primary feature the presence of RPCs add to the PHENIX triggering system is timing resolution—2 nanoseconds (Table 4.3). This is crucial, because before the inclusion of RPCs, the only timing available was that offered by the BBCs and the Time of Flight detectors. The RPC provides local timing information, which allows the triggering system to record events which trigger the muon arm system, and not just the BBCs. This has the effect of significantly reducing backgrounds—by a factor greater than 6000 [26], Figure 4.21. The integration of the RPC timing information into the Muon Track information ensures that we can select the correct beam-bucket to associate with the muon track. This is necessary for this spin analysis, due to the distinct polarization associated with each beam bucket.

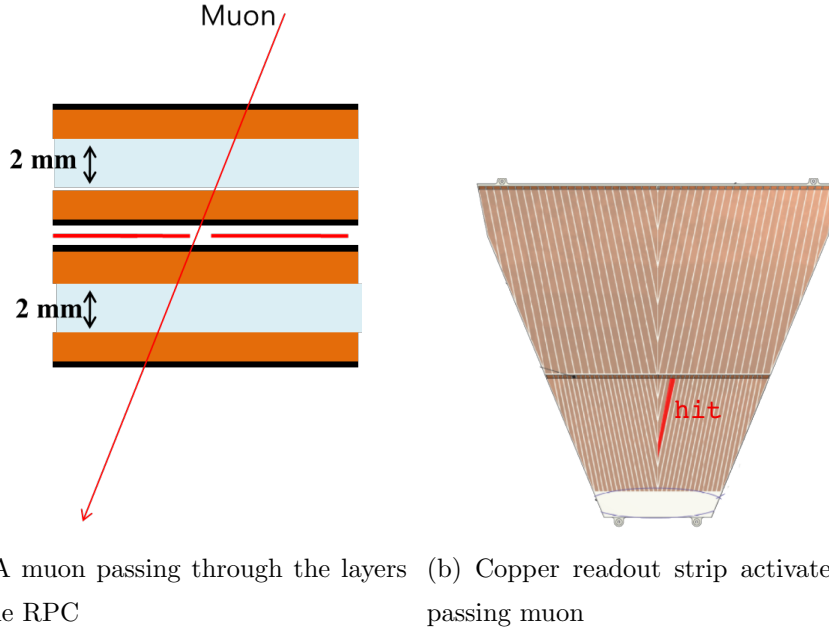


Figure 4.22: As a muon passes through the layers of the RPC (left), the gas in the bakelite gap is ionized. This charge migrates and collects near the highly resistive graphite coating. An image distribution is induced on the overlapping readout strip (right), which is passed along its own channel to the front-end electronics.

#### 4.5.2.1 Design

The design goal of the Resistive Plate Chambers is to provide accurate timing information at high speed in order to build a Trigger which can record  $W \rightarrow \mu$  events. RPCs were first implemented at the Large Hadron Collider at CERN, and their design was adopted for use at PHENIX both because of its high speed, and low cost. In Figure 4.23 the basic design is shown. The means of signal transduction is realized with the ionizing of gas inside a highly resistive chamber. The chamber is held at a large bias—at 8.5 kilovolts—such that any ionization will collect on the interior of the resistive chamber in a fixed and relatively static distribution in time, relative to time scales of triggering system timing, in millionths of a second. This charge distribution is read out with capacitively coupled copper readout strips into fast electronics (Figure 4.22). PHENIX requires that when triggered, 2 or fewer clusters (strips) in the RPCs are activated and that efficiency of the detector must be at least 95%. Additionally, the time resolution of the RPC hodoscope must be at least

2 nanoseconds, with a particle transduction rate of 500 Hz per square centimeter. These properties are summarized in Table 4.3 [26].

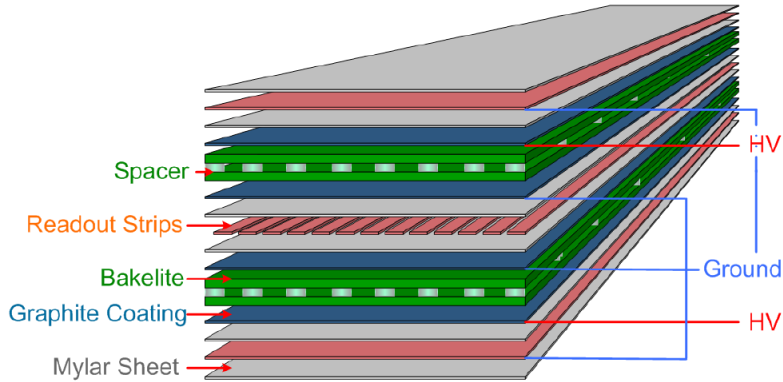


Figure 4.23: The individual layers of an RPC segment installed at PHENIX. A High Voltage bias is applied to the graphite coating on either side of bakelite gas-filled gaps. Readout strips are positioned between the two bakelite gaps. Finally, the entire double-gap structure is surrounded by a copper grounding cage, and wrapped in insulating mylar [26].

<b>Cluster Size</b>	<2 strips
<b>Efficiency</b>	>95% for MIP
<b>Time Resolution</b>	~2 nanoseconds
<b>Rate Capability</b>	0.5 kHz/cm <sup>2</sup>

Table 4.3: The design characteristics of the RPCs [26]

#### 4.5.2.2 Construction and Testing

Construction of the Resistive Plate Chambers took place in two stages over several years. Fabrication of the bakelite gas gaps was done overseas in Korea, and the aluminum chassis was manufactured in China. Pieces for the RPC 3 and RPC 1 were shipped to Brookhaven National Laboratory, where they were assembled and tested before being installed. The installation occurred over two years, with the first stage, the RPC 3, being



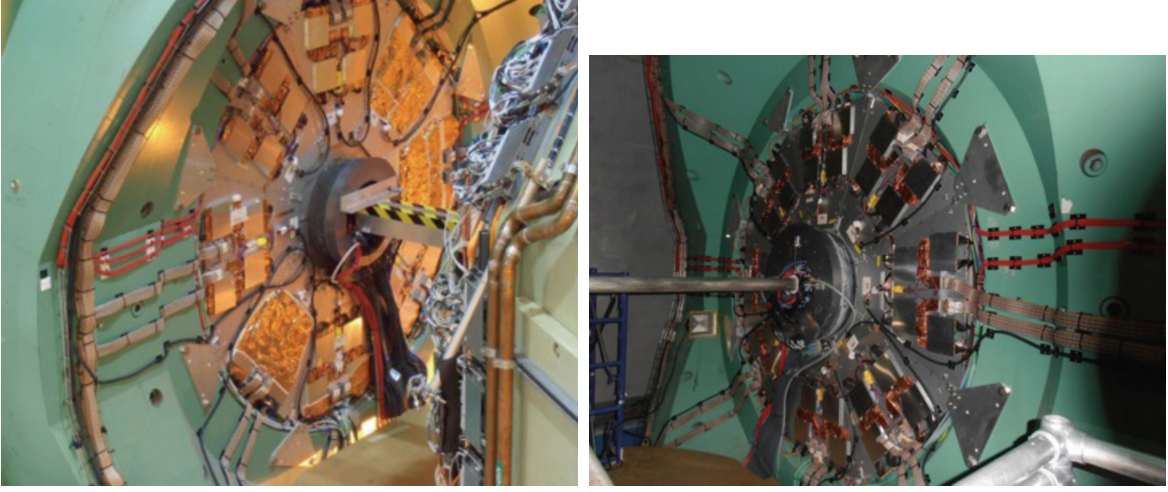
Figure 4.24: Two special tents inside building 912 at Brookhaven National Laboratory, built to house completed RPC octants and the laboratory used to construct and test the octants.

installed in 2011. The second stage, the RPC 1, was installed in 2012. After being fully commissioned, the capstone data set for W-Physics was taken in 2013, which is discussed in detail in Chapter 6.

The RPC 3 and RPC 1 construction efforts took place in a special clean-room built inside of the cavernous building 9-12 (Figure 4.24) at Brookhaven National Lab.

The RPCs are modular. The larger RPC 3 North and South were separated into 16 half octants, whereas the smaller RPC 1 North and South were separated into eight octants. Both North and South RPCs have the same full azimuthal coverage and match the pseudorapidity coverage of the arms on which they are installed.

The RPC 1 octants were installed directly on the nose-cone of the Muon Tracker, shown in Figure 4.25. Unlike to the RPC 3, the RPC 1 North and South are more compact, and are the exact same size.



(a) RPC Station 1, North

(b) RPC Station 1, South

Figure 4.25: The North RPC Station 1 is installed on the muon tracker nosecone (left). Similarly we see the installation of the south RPC Station 1 (right). The metal tube in the center is the beryllium beam pipe.

Each RPC1 octant was hand assembled, with components being tested at each stage of the construction, where relevant. The first stage of construction involved preparing the machined aluminum chassis. Mylar sheets were cut to fit the chassis baseplate, and secured to the aluminum with Kapton tape—chosen for robustness over high ranges of temperature as well as good electrical insulating properties. The chassis itself is not one machined piece, but is instead bolted together with machine screws 4.26. The chassis is continually cleaned of debris during the assembly process with methanol.

Double-sided tape is then added to the mylar sheeting, and foam is then placed down. Sections are removed from the foam to accommodate routing of the electrical hookup for setting the Bakelite gas-gaps to a high bias, Figure 4.27.

After the chassis has been prepared, the bakelite gas gaps are assembled. The gas gap itself (Figure 4.28, Figure 4.23), is composed of two layers of Bakelite, which are separated by small insulating spacers. The Bakelite is externally coated with graphite suspended in linseed oil to provide surfaces that can be held at a fixed voltage bias. The separation of the plates forms a chamber, which is sealed, and prepared for gas flow. Electrodes are attached to the linseed oil to allow for an applied voltage bias, and plastic nipples

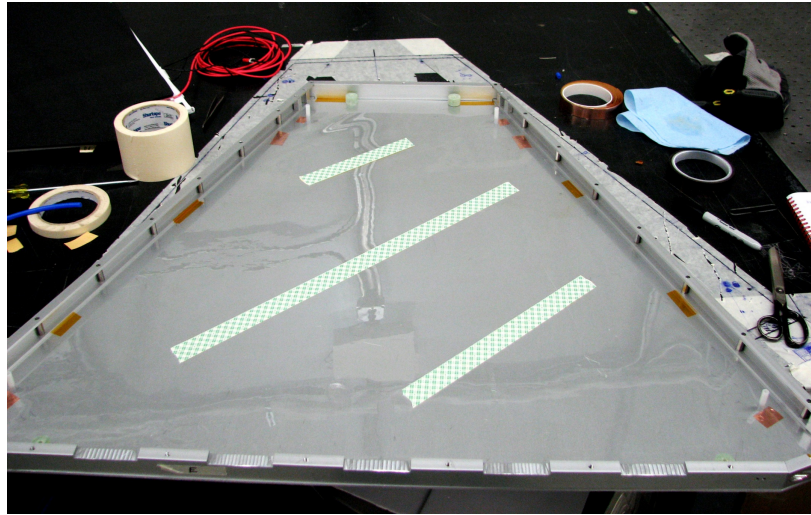


Figure 4.26: The chassis is prepared with insulating Kapton tape and mylar sheeting. The grooves along the bottom of the chassis are for routing cabling from the readout strips (shown later). The channels along the side of the chassis is for routing gas flow lines.

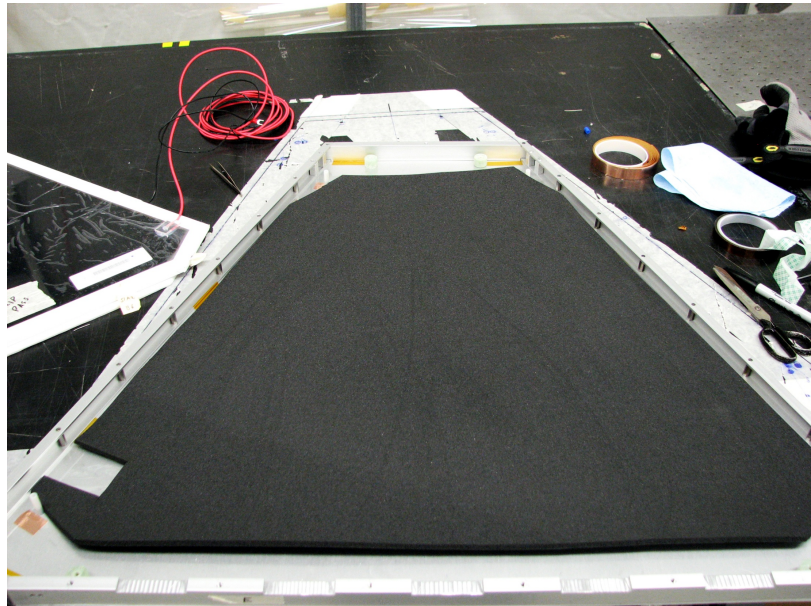


Figure 4.27: Foam shock insulation is added to the RPC 1 chassis.

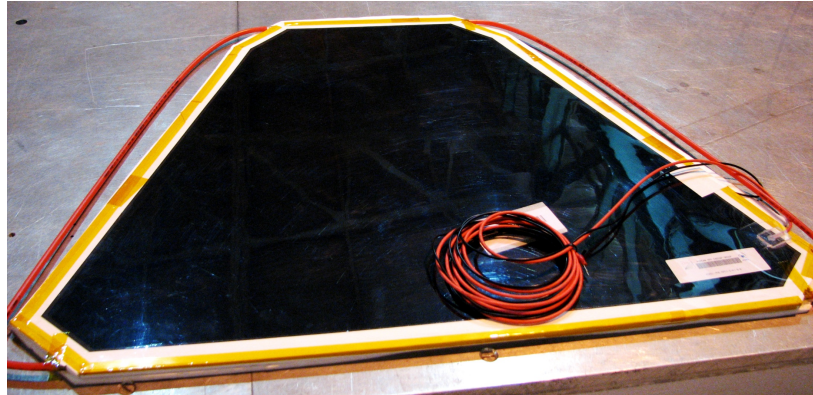


Figure 4.28: The assembled Bakelite gas gap, ready for leak/pop testing, followed by burn in.

are routed into the gap chamber allowing for gas flow. Tubes are cut to size and fixed to the gas chamber nipples, and then routed out down to the widest end of the RPC. These gas tubes are color coded—a different color for each Bakelite section in the RPC. The gas gaps are ‘leak’ and ‘pop’ tested at the assembly lab. This test involved pressurizing the gaps to 8.5 inches of water, and measuring pressure loss over a ten minute interval using Argon. Pressure losses less than 1 inch were acceptable. During pressurization, assemblers listened for an audible pop sound, which indicated one of the gap spacers had popped lose. Popping noises, or bad pressure retention would both result in the gas gap being discarded. Finally, before installing the gap, the gap was ‘burnt in’, a process where the gaps were filled with an isobutane gas mixture used for operations and then slowly voltage cycled to operating voltage over 24 hours.

After the bakelite gas gaps were sufficiently studied, they were installed into the chassis, Figure 4.29. The chassis was prepared for installation with the addition of a layer of copper foil, to create a Faraday cage around the sensitive bakelite gaps. Tabs are left on the copper foil, such that they could be folded around the inner gaps, but not around the gas lines. The bias cables and gas lines were routed through the chassis side channels.

Once the bottom gas gap was installed and secured, the copper readout strips were added, Figure 4.30. The strips are oriented such that two annuli of readout strips are created (azimuthally) when the RPC 1 is installed onto the nose cone of the muon trackers. The readout strips were designed this way to offer some rough radial tracking. The copper

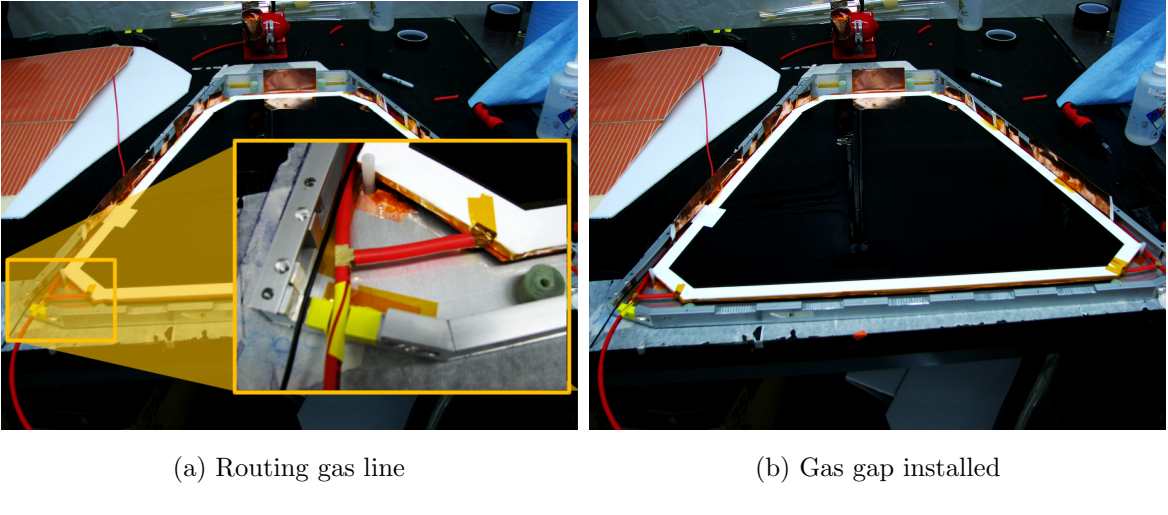


Figure 4.29: The egress port of the gas gap is carefully shielded with tape to prevent friction from causing tears, and routed out of the ports machined into the bottom of the chassis (right), with the final position of the first gap shown on the left.

readout strips are laminated with mylar, and each was soldered to its own channel. The channels were gathered and soldered onto PCB chips. The readout strips are laminated such that mounting holes in the laminate attach in the same way to each octant, for consistency.

Following the installation of the readout strips, the final two gas gaps were installed with their electronics and gas lines routed through the chassis similarly to the bottom gap, Figure 4.31.

Finally, the high voltage cables were grounded to the chassis and soldered to the relevant wires leading to the graphite electrodes on the outside of the Bakelite gas gaps. Wires, tubes, etc, were all fixed in place with Kaptan tape. The top of the chassis was screwed into place, and the front-end electronics were installed, with the copper readout chips plugging into the relevant FEM board. Ribbon cables were appropriately routed, and all electronics were encased in copper foil, and then additionally protected with the Aluminum chassis lid, Figure 4.32.

After assembly, the RPCs were subjected to a barrage of tests, using a cosmic ray test stand to measure clustering (Figure 4.33), designed to measure the activation threshold (combined with energy readings from scintillators above and below the test stand),

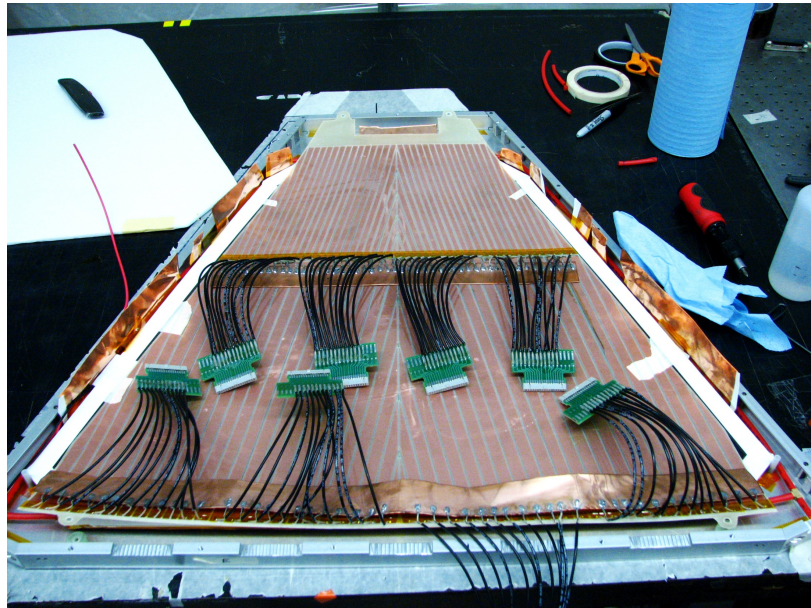


Figure 4.30: The copper readout strips are mounted to the chassis. Each readout strip is soldered to a copper wire, which in turn are gathered into readout chips.

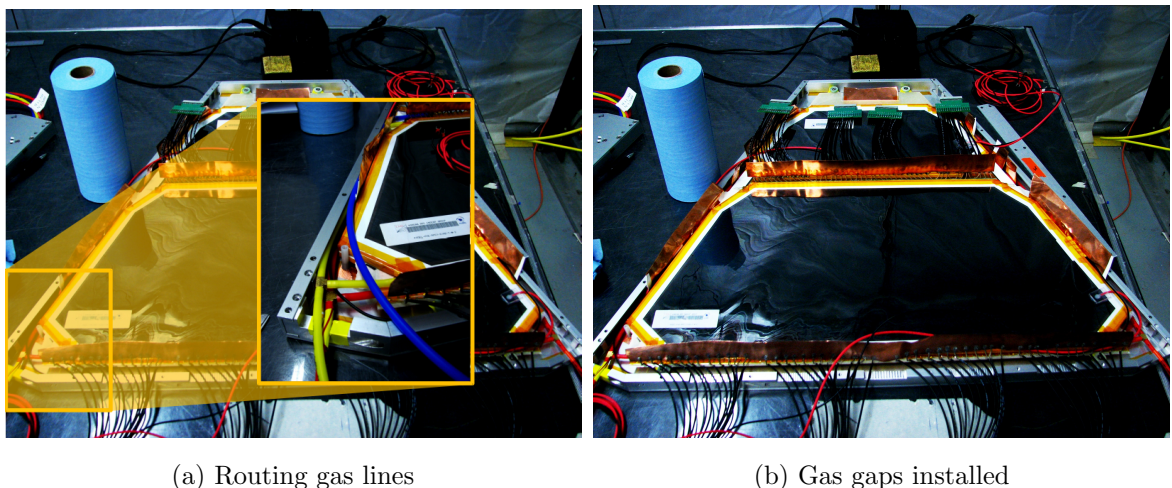


Figure 4.31: The final Bakelite gas gaps are installed on top of the copper readout strips. Gas lines are routed similarly to 4.29

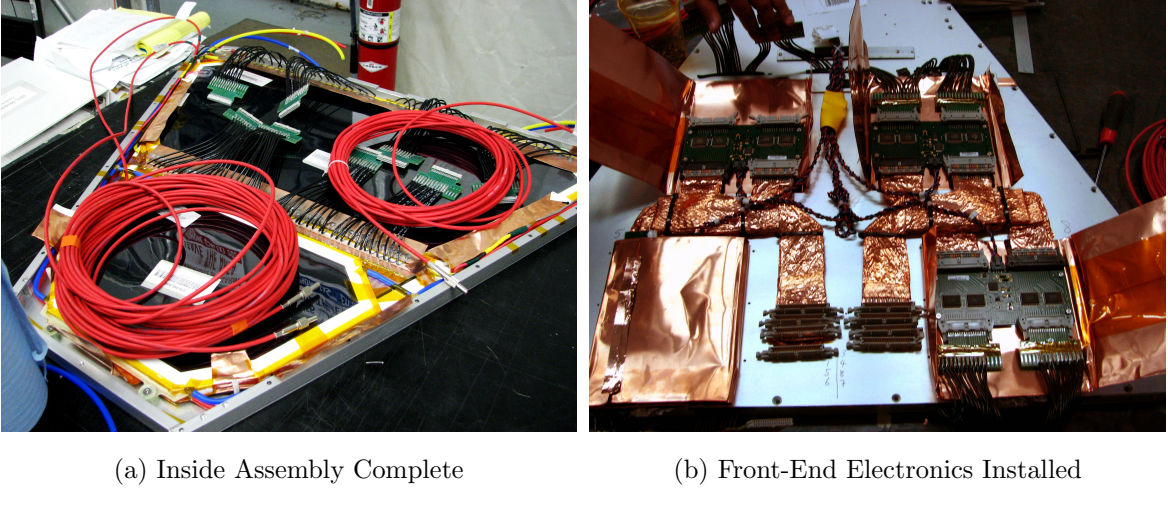


Figure 4.32: A completed RPC 1 octant, interior assembly complete, left, and the outer assembly completed on the right.

determine the average cluster size, and measure overall detector efficiency. The overall ohmic ‘dark-current’ was also measured.

#### 4.5.2.3 Performance

With the construction and installation of the RPCs and new Front End Electronics for the Muon Tracker, PHENIX was ready to take data for the  $W$  measurement by 2013. A dedicated run was taken, accumulating over  $200 pb^{-1}$  of data. All tolerances and design specifications for the upgrade were met.

#### 4.5.3 Triggering and Data Acquisition

The new triggering scheme incorporating the RPCs and the new FEEs is summarized in Figure 4.34, while the final configuration of the PHENIX detector after the forward upgrade is shown in Figure 4.35. As discussed, data was recorded at about 30% of the total PHENIX DAQ bandwidth over the 2013 polarized proton+proton run, which was sufficient to record enough  $W \rightarrow \mu$  events at forward rapidities to generate a statistically measurable sample. This speaks to the relative rarity of this event, as compared to other events—the overall collision rate for protons at  $510 GeV/c^2$  was as high as 10 MHz.

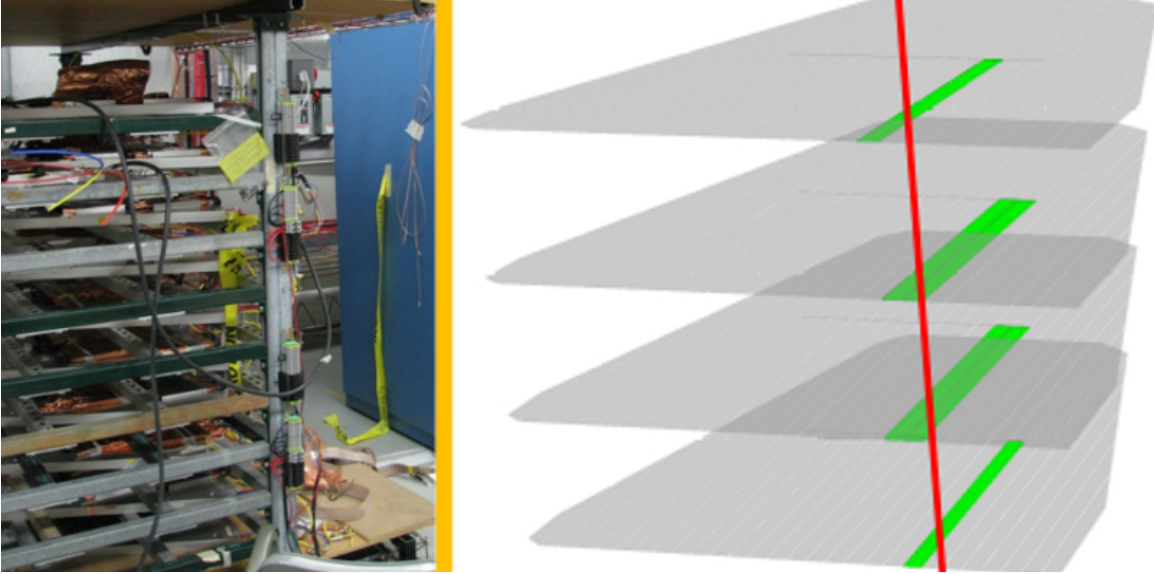


Figure 4.33: Left: the cosmic test stand setup. RPC octants were sandwiched between scintillators to run performance and efficiency tests. An example of the clustering due to a cosmic ray is shown on the right, with a particle (red) activating one or two strips per octant (activation shown in green).

#### 4.5.3.1 2013 Data Set Triggers

To learn about new physics, or to test models, one must devise a way to preferentially record ‘interesting’ data, since data recording bandwidth is limited. What constitutes an ‘interesting’ event of course depends on the physics goals of the data-taking period. For this analysis, ‘interesting’ means that for a given event, our forward trigger is telling us that there is a track which has been reconstructed that may originate from a  $W$  Boson decay. This decision must be made within the time scale of one beam crossing (106 nanoseconds), in order to inform the PHENIX DAQ whether or not to archive the data which is produced. This process is called ‘triggering’. The minimum bias trigger rate and pre-scale must be recorded, along with the pre-scales of other triggers, so as to reconstruct the relative abundance of events after the fact. Data is pre-scaled because the overall rates that triggers fire is much higher than the rate that data can be archived, such that not all events can be physically recorded. Once a trigger condition has been satisfied, all PHENIX subsystems will dump their data into the data stream. With respect to the  $W$  physics trigger pre-scales,

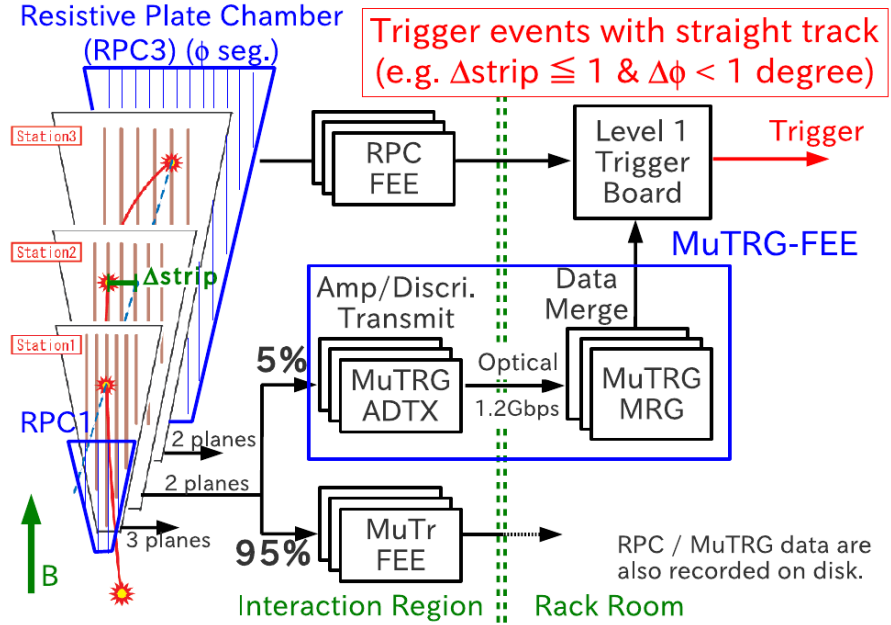


Figure 4.34: A schematic of the new muon trigger for recording  $W$  bosons [26]

the primary triggers were not scaled at all, which implies that every  $W$  physics event which triggered the PHENIX DAQ, was recorded.

The PHENIX DAQ can accommodate 32 different triggers. Any transduced signal by a part of the PHENIX spectrometer can, provided the front end electronics are fast enough, be fed into a global triggering decision. Thus, PHENIX, like other triggered particle physics experiment, can be arbitrarily configured to record a desired subset of data from the total data set.

Of the 32 triggers available, one is always set to ‘Noise’ (but not recorded) and another is set to ‘CLOCK’ which is timed to trigger every beam crossing. No bandwidth is reserved for these triggers for physics data taking, however some special runs are taken (such as the Vernier Scan, Chapter 5) where time-dependent beam dynamics need to be recorded (and reconstructed), in which case they are enabled. The noise trigger may be enabled for general QA (such as the Pedestal Scan), but again, is not enabled under normal operation.

When the DAQ records triggered data, there are three distinct ‘scalers’ which are recorded associated with each trigger. The ‘raw’ scaler counts the total number of times a trigger has been fired. The ‘live’ scaler counts the number of times a trigger fires, but only

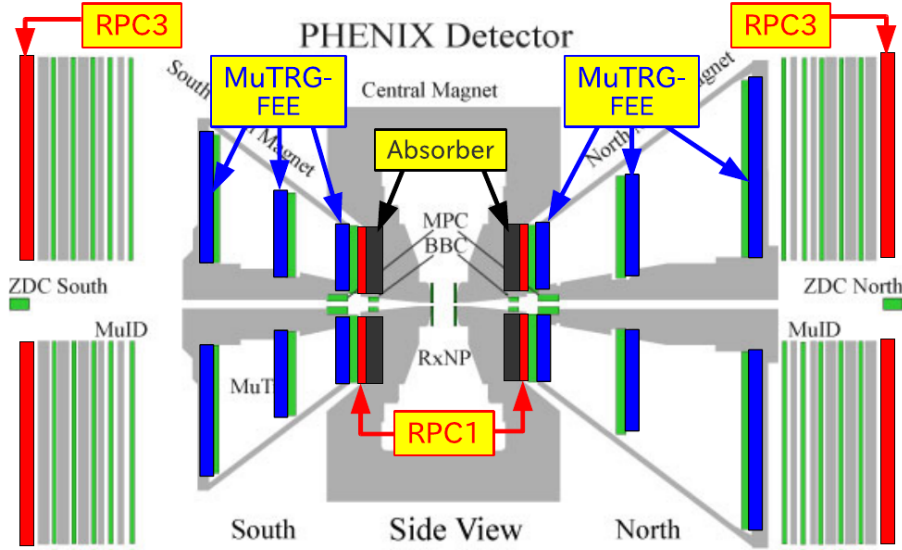


Figure 4.35: The position of the Front-End Electronics upgrades and new RPCs + Absorber are shown. Muon tracker stations are shown in blue (along with the front-end electronics). The RPCs sandwich the muon tracking stations and the MuID. The absorber material sits just inside of the Muon Arms, before the Forward Vertex Detectors and inner tracking stations of the muon tracker [26]

when the DAQ is not emitting a ‘busy’ signal. The DAQ is busy when all DAQ elements cannot accommodate any more bandwidth, and in this case, all events which might have been recorded are lost. This is unavoidable, but the DAQ is not flagged as busy often more than 90% of the time, by requirement. The percent of time the DAQ is flagged as ‘busy’ is called the live-time. The raw scaler count is related to the live time with:

$$LIVE\_SCALER = LIVE\_TIME \times RAW\_SCALER \quad (4.3)$$

Additionally, there is one final type of ‘scaler’, which is the ‘scaled scaler’. Scaled scalers represent the number of times a trigger has fired, divided by  $(1+TRIGGER\_PRESCALE)$ , corrected for live time. This represents the real number of events associated with a trigger which was recorded. Scaling is necessary to fill the PHENIX DAQ bandwidth with events which may be of interest to an analysis, while rejecting events that do not contribute to an analysis. The scalers can then be related:

$$SCALED\_SCALER = LIVE\_TIME \times \frac{RAW\_SCALER}{1 + TRIGGER\_PRESCALE} \quad (4.4)$$

There was one global physics trigger configuration used in the Run 13 data set, it was called ‘PP510Run13’. An example configuration is shown in Table 4.4. In the case of the  $W$  Analysis, the relevant physics triggers were recorded without pre-scale, indicating that most triggered  $W$  events were actually recorded.

Each physics trigger is stored as a 32-bit integer. This is a very special integer, because it does span the full range of possible 32-bit integers. A trigger with a bit-number of “2” means that the second binary digit of the trigger’s binary representation is flipped to “1” and the rest of the digits are “0”. In this way, one can easily store and check which triggers for a recorded event actually fired. Thus, an important variable called ‘trigscaled’ is created, to track which triggers which fired on a certain event by taking the bitwise-OR operation between all binary representations of triggers which fired for that event. While this integer records the total number of triggers fired, one must still account for the efficiency of triggers, which is discussed in Section 6.5.

For example, consider a simplified four-bit version of this scheme with four assigned trigger bits. Consider an event where the following triggers fired:

- Trigger 1 Fired: 0001
- Trigger 3 Fired: 0100
- Trigger 4 Fired: 1000

The boolean-OR bitwise comparison is then:

- Trigscaled: 1101

Note how we lost no information regarding which triggers fired for this event. We can recover later, in code, the trigger mix for every event by using bitwise-AND operations, so long as we know which triggers were assigned to which bit, and we have the trig-scaled number.

This bit-masked final number, ones and zeroes, is one of the crucial variables in all PHENIX data sets, and is discussed in Chapter 6 and Section 6.5. It is crucial to know

Trigger Descriptions			
Trigger Name	BBC	MUID	MuTr
			RPC
BBCCLL1(>0 tubes)	<30cm vertex	-	-
BBCCLL1(>0 tubes) narrowvtx	<15cm vertex	-	-
BBCCLL1(>0 tubes) novertex	any vertex	N  S lastGap >= 1 (N&S lastGap >= 1)    (N  S lastGap >= 2)	-
(MUIDLL1_N1D S1D)&BBCCLL1(noVtx)	any vertex	N  S lastGap >= 1 (N  S lastGap >= 2)	-
((MUIDLL1_N2D  S2D) (N1D&S1D))&BBCCLL1(noVtx)	any vertex	-	-
MUON_N_SG1&BBCCLL1(noVtx)	any vertex	-	N sagita <= 1
MUON_N_SG1_RPC3_1_B  C	-	-	N sagita <= 1
MUON_N_SG1_RPC3A&MUID_N1D	-	N lastGap >= 1	N sagita <= 1 N 3 A
MUON_S_SG1&BBCCLL1(noVtx)	any vertex	-	S sagita <= 1
MUON_S_SG1_RPC3_1_B  C	-	-	S sagita <= 1
MUON_S_SG1_RPC3A&MUID_S1D	-	S lastGap >= 1	S sagita <= 1 S 3 A
RPC1+RPC3_N	-	-	N (1 B  C)&(3 A  B  C)
RPC1+RPC3_S	-	-	S (1 B  C)&(3 A  B  C)
SG1+RPC1(C)&MUIDLL1_N  S	-	N  S	N  S sagita <= 1 N  S 1 C
SG3&MUID_1H_N  S	-	N  S lastGap >= 1 N  S lastGap >= 3	N  S sagita <= 3 N  S 3 A  B  C
SG3&RPC3&MUID_1D_N  S	-	N  S lastGap >= 1	N  S sagita <= 3 N  S 3 A  B  C

Table 4.4: ‘List of Triggers used in the 2013 run and description of hit requirements in various detectors. Some reminders about detector geometry: MUID has 5 gaps and last gap describes the furthest gap away from the collision that sees a hit. MuTr measures Sagita (amount of azimuthal bending of a track) in terms of number of MuTr strips. RPC has two stations - station 1 is closest to the collision, station 3 is further away. Station 1 has two “rings” of modules in  $\theta$  (B, C). Station 3 has three rings (A, B, C)’ [33]

which triggers fired for which event so that the original collision conditions, and therefore the physics, can be reconstructed. Since each detector subsystem may not have the same geometric acceptance, trigger acceptance, signal transduction hardware, triggering, while necessary for taking data, introduces severe bias into the data set. Knowledge of which triggers fire for each recorded event gives us the ability to correct for these kinds of biases to recover the original conditions of the data sample.

# Chapter 5

## The Vernier Analysis

### 5.1 Overview

The Vernier Scan Analysis is typically done every year. Its purpose is to calculate the absolute luminosity of collisions delivered to PHENIX’s interaction region (IR) by RHIC. Absolute luminosity is a necessary for the normalization of any cross-section. This chapter describes the process of carrying out the vernier analysis for the 2012 data set, but it was also carried out for the 2013 data set.

A vernier scan describes the process where, one beam is scanned across another beam held at several fixed positions. The purpose of this maneuver is to enable direct measurement of the transverse profile of the blue and yellow beam, which are assumed to be identical. The scanning serves a second purpose, in that, if one observes the distribution of event collision vertex (in  $z$ ), the shape of the distribution provides information about the value of the beam focusing parameter  $\beta^*$ , and the crossing angle  $\theta_{x\text{ing}}$  between the beams.

Measuring the transverse beam profile allows one to calculate from first principals the expected machine luminosity delivered to PHENIX,  $\mathcal{L}_{RHIC}$ . This luminosity is corrected for both the beam focusing effect, and the crossing angle. Neglecting to correct both effects will result in an underestimated luminosity, sometimes by as much as 20%.

The vernier scan also provides an opportunity to calculate the efficiency of the minimum bias BBC novertex trigger, which enables the BBCs to be used as a luminosity monitor for physics operations.

For the BBC trigger, we represent the relationship between  $\mathcal{L}$  and the cross section observed by the BBC as:

$$\mathcal{L}_{BBC} = \frac{R_{BBC}}{\sigma_{BBC}} \quad (5.1)$$

Where  $\mathcal{L}_{BBC}$  is the effective luminosity delivered to a specific BBC trigger,  $R_{BBC}$  is the live event rate of the BBC trigger, and  $\sigma_{BBC}$  is defined as the cumulative cross section of events measured by this trigger.

The absolute luminosity for a single bunch crossing is calculated:

$$\mathcal{L} = \frac{f_{bunch} N_b N_y}{2\pi\sigma_x\sigma_y} \quad (5.2)$$

Where  $\mathcal{L}$  is the absolute luminosity,  $f_{bunch}$  is the frequency of each individual bunch crossing,  $N_b, N_y$  are the bunch populations for the specific blue and yellow beam bunch, respectively, and  $\sigma_x, \sigma_y$  are the transverse widths of both bunches in the  $x$  and  $y$  directions (see the PHENIX coordinate system for more details on the origin of these measurements, Figure 4.13). We assume identical beam bunch distributions for the blue and yellow beams [76].

Filled bunches cross once every beam clock tick. Therefore, for 120 bunch fills (including filled and empty bunches), and the standard blue beam clock frequency,  $f_{clock}$ , of  $9.36MHz$ ,  $f_{bunch} \equiv f_{clock}/120 = 78kHz$ .

This work builds upon previous Vernier Analyses undertaken at PHENIX: [77], [78], [79], [76], and [80].

Global vernier scan characteristics are summarized in table 5.1. Each vernier scan is done slightly differently as a systematic check - beam scan order is varied, beam energy is varied, scan length and step length is varied, and scanning patterns are varied. These variations are not expected to produce changes in the final luminosity calculation.

Two different scanning patterns were used in Run 12, summarized in Figure 5.1. Scan Type 2 was previously used in past years prior to 2012, and is included in this year's set of scans as a consistency check. Type 2 scanning describes the pattern where beams begin maximally overlapped, and are gradually displaced to maximum displacement, brought into maximum overlap again, then gradually displaced in the opposite direction. Type 1 was used for the majority of the scans in 2012, and consists of beams beginning maximally overlapped, subsequently maximally displaced, and swept back through maximum over-

## Run 12 Scanning Patterns

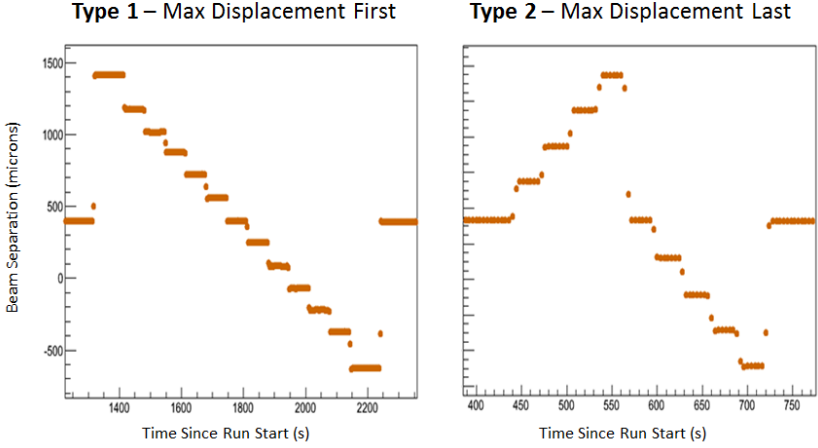


Figure 5.1: Left Panel: Type 1 scanning pattern. Right Panel: Type 2 scanning pattern. In both panels, we see the mean beam displacement as a function of time since the beginning of the vernier scan.

lap, continuing, and ending maximally displaced. The scan order does not effect the final luminosity, provided that beam losses over time are properly accounted for.

## 5.2 Variables and Calculations

Variables used in the Vernier Analysis are chosen because they characterize the dynamics of the beams intersecting in the PHENIX interaction region (IR). The goal in the vernier analysis is to calculate the effective detector cross section for our Beam Beam Counter, as well as the RHIC machine luminosity,  $\mathcal{L}_{RHIC}$ . We must also use a realistic model for highly relativistic collisions between two intersecting beams.

The basic equations, models and variables used in the analysis are summarized here. I will go into detail discussing the extraction of each parameter within relevant section.

The effective detector cross section can be expressed as:

$$\sigma_{BBC} = \frac{R_{max}\sigma_x\sigma_y}{N_y N_b \epsilon_{BBC}} \times K_{\beta^*} K_{\theta_{xing}} \quad (5.3)$$

with various parameters are defined in Table 5.2.

Run Number	Fill Number	Energy ( $GeV\sqrt{s}$ )	Scan Time (min)	Scan Pattern	Scan Order	Beam Scanned	Steps	Step Time (s)
359711	16444	200	41	Type 1	H - V	Blue	26	57.5
360879	16470	200	41	Type 1	H - V	Yellow	26	61.2
362492	16514	200	50	Type 1	V - H	Blue	26	62.3
364636	16587	510	58	Type 2	H - V	Yellow	18	21.7
365866	16625	510	53	Type 1	H - V	Blue	26	70.0
366605	16655	510	54	Type 1	H - V	Yellow	26	67.7
367138	16671	510	54	Type 1	H - V	Blue	26	68.65

Table 5.1: A summary of vernier scans in run 12. Scans which proceed with the horizontal scan, followed by the vertical scan are denoted ‘H - V’, with the reverse order denoted similarly. Scan types are defined in Figure 5.1

We use the standard relativistic intersecting beam model for colliding bunches [76], which is defined to be:

$$\mathcal{L} = \frac{n_{bunch} f_{bunch} N_B N_Y}{2\pi^2 \sigma_x \sigma_y \sigma z^2} \int \int e^{-\left(\frac{z^2}{\sigma_z^2} + \frac{c^2 t^2}{\sigma_z^2}\right)} c dt \quad (5.4)$$

The full summary of the variables either extracted or directly used in the vernier analysis are presented in Table 5.2.

Variable	Description
$\sigma_{x,y,z}$	bunch profile width obtained from vernier scan beam overlap in $x$ , $y$ , or $z$ directions.
$\sigma_z$	bunch profile width in $z$ -direction, i.e. $z$ -beam width.
$\dot{N}$	Live event rate for "BBCLL1(>0 tubes)" trigger
$R_{max}$	Maximum BBC Rate determined from maximum overlap of beams rate for "BBCLL1(>0 tubes)" trigger
$R_{MC}$	Multiple collisions rate
$\mathcal{L}_{RHIC}$	Absolute luminosity delivered to PHENIX IR from RHIC
$\sigma_{p+p}$	Inelastic scattering cross section of proton-proton collisions
$N_b^i, N_y^i$	Number of ions in bunch $i$ for the blue ( $b$ ) beam or yellow ( $y$ ) beam.
$f_{bunch}$	Frequency of a specific bunch crossing
$k_b$	Number of bunches filled in one of the beams (assume identical beams)
$\sigma_{BBC}$	Cross section of p+p collisions observed by BBC, uncorrected for efficiency
$\epsilon_{BBC}$	BBC efficiency
$n_{bunch}$	Number of filled bunches in the blue or yellow beam
$\beta^*$	Beam focusing parameter, which effectively reduces transverse beam width as a function of distance from PHENIX IR.
$\theta_{xring}$	Crossing angle in the X-Z plane of the blue and yellow beams at the intersection point in PHENIX
$K_{\beta^*}$	Multiplicative correction to luminosity due to beam focusing parameters, $\beta^*$
$K_{\theta_{xring}}$	Multiplicative correction to luminosity due to beam crossing angle.

Table 5.2: The variables we use in the vernier analysis. Some variables are extracted directly from the data streams (such as the bbc-rate), while others are calculated from distributions of variables (such as the beam-width,  $\sigma_{x,y}$ ).

## 5.3 Data Streams

PHENIX software and the overall DAQ structure were discussed in Chapter 4. The vernier analysis is only interested in understanding the frequency of minimum bias events, one does not do any physical event reconstruction beyond determining the event  $z$ -vertex. To characterize the vernier scan, the following data streams are used:

- PRDF Data (available on either 1 second intervals, or event-by-event basis)
  - GL1P-0: "BBCLL1(>0 tubes)"
  - GL1P-1: "CLOCK"
  - GL1P-2: "ZDCLL1Wide"
  - GL1P-3: "ZDCLL1Narrow"
  - event-sequence
  - ATP number
  - epoch time stamp
  - GL1 crossing ID (bunch number)
- BPM Data (available in four second intervals)
  - Sector 7 Blue Beam x position
  - Sector 7 Blue Beam y position
  - Sector 7 Yellow Beam x position
  - Sector 7 Yellow Beam y position
  - Sector 8 Blue Beam x position
  - Sector 8 Blue Beam y position
  - Sector 8 Yellow Beam x position
  - Sector 8 Yellow Beam y position
  - epoch time stamp
- WCM and DCCT Data (available every few seconds)
  - WCM population for each bunch

- DCCT beam current for blue beam
- DCCT beam current for yellow beam
- epoch time stamp associated with each field of WCM or DCCT data
- DST Data
  - BbcOut Node
    - \* BBC pmt tubes fired north
    - \* BBC pmt tubes fired south
    - \* BBC event z-vertex
  - ZdcOut Node
    - \* ZDC event z-vertex
  - TrigLvl1 Node
    - \* bitmasked triglive
    - \* bitmasked trigscaled
    - \* bitmasked trigraw
  - SpinDataEventOut Node
    - \* GL1P crossing ID
    - \* event-sequence
    - \* GL1P-0: "BBCLL1(>0 tubes)"
    - \* GL1P-1: "CLOCK"
    - \* GL1P-2: "ZDCLL1Wide"
    - \* GL1P-3: "ZDCLL1Narrow"

The vernier analysis is unique among various PHENIX analyses because it requires that data streams from RHIC machine sources and the PHENIX detector are synchronized. It is also unique in that the data set itself exhibits obvious time dependent behavior. This introduces interesting challenges, as PHENIX software generally does not provide tools to deal with time dependent data, and synchronization of PHENIX data with other RHIC data streams is infrequently done. PHENIX and RHIC data streams effectively live in entirely different software universes (post data production), so there is no guarantee of a common key which can be used to synchronize the data.

## 5.4 Beam Position Monitors

There are two beam position monitors BPM(s) located about 8 meters away from the PHENIX IR on either side (BPM sector 7, and BPM sector 8). The BPMs may be used to establish the relative separation of the blue and yellow beams, but are not good for establishing absolute beam position [81].

The BPM data obtained contains measurements of beam position over the course of an entire fill. The start and end run times recorded in the PHENIX run data base are used to isolate a chunk of BPM data corresponding to the vernier scan using epoch time. The BPM data set contains the following fields:

- epoch time
- blue beam, sector 7  $x$  position
- blue beam, sector 7  $x$  position
- blue beam, sector 8  $y$  position
- blue beam, sector 8  $y$  position
- yellow beam, sector 7  $x$  position
- yellow beam, sector 7  $x$  position
- yellow beam, sector 8  $y$  position
- yellow beam, sector 8  $y$  position

The beam position monitors are coupled capacitively to the beam pipe(Figure 5.2), with pick ups on the left and right of the pipe, and pickups above and below the pipe. Every four seconds, data is read out from the BPMs.

The method of BPM transduction of beam current to transverse beam position is described in Figure 5.2. The beam current, passing through the BPM, induces a time dependent voltage proportional to the derivative of the beam current itself. BPM electronics use a comparator circuit, and the readings from pickups situated around the beam pipe are used to determine the  $x$  and  $y$  beam positions. The absolute measurement of beam position

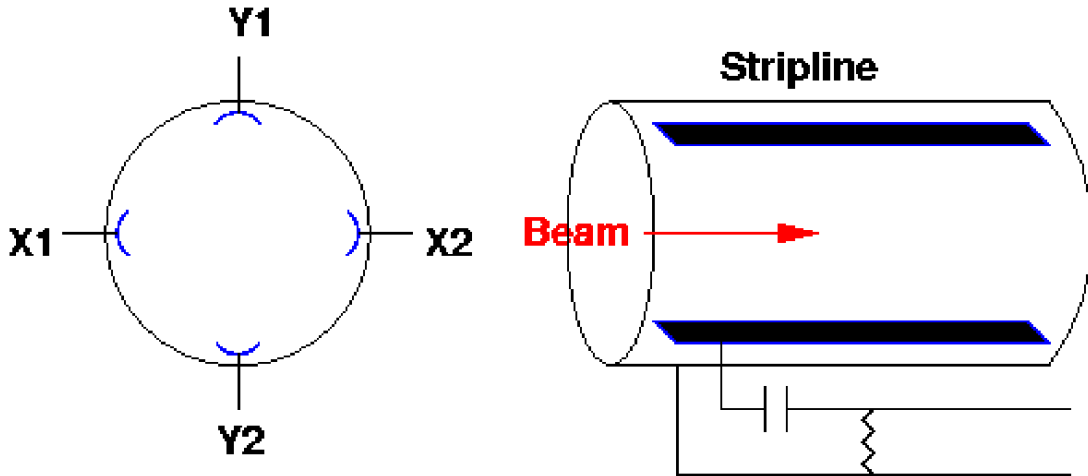


Figure 5.2: BPM electronics use a comparator circuit, and the readings from X1,2 and Y1,2 to determine the  $x$  and  $y$  beam positions.

is subject to offsets stemming from various effects, but the relative beam displacement is reliable [27]

The BPM data stream provides an  $x$  and  $y$  position, plus an epoch time stamp associated with the blue and yellow beams, from sector 7 and sector 8 BPMs. With this data, one can geometrically extrapolate the intersection of the blue and yellow beams respectively in the PHENIX IR plane, and then calculate the net separation between the two beams, Figure 5.3. Three parallel planes are defined, each plane perpendicular to the beam axis. One places the planes at Sector 7 BPM location, the PHENIX IR, and Sector 8 BPM location. The two BPM planes are equidistant from the PHENIX IR. One can geometrically solve for the equation for the line, given intersections at the BPM Sector 7 plane, and the BPM Sector 8 plane, and extrapolate the beams' intersection with the IR plane. From this intersection, one obtains the net beam displacement.

An example of the BPM data recorded during a vernier scan is shown in Figure 5.4, which shows the relative horizontal and vertical displacements of the beam at the PHENIX IR for run 359711.

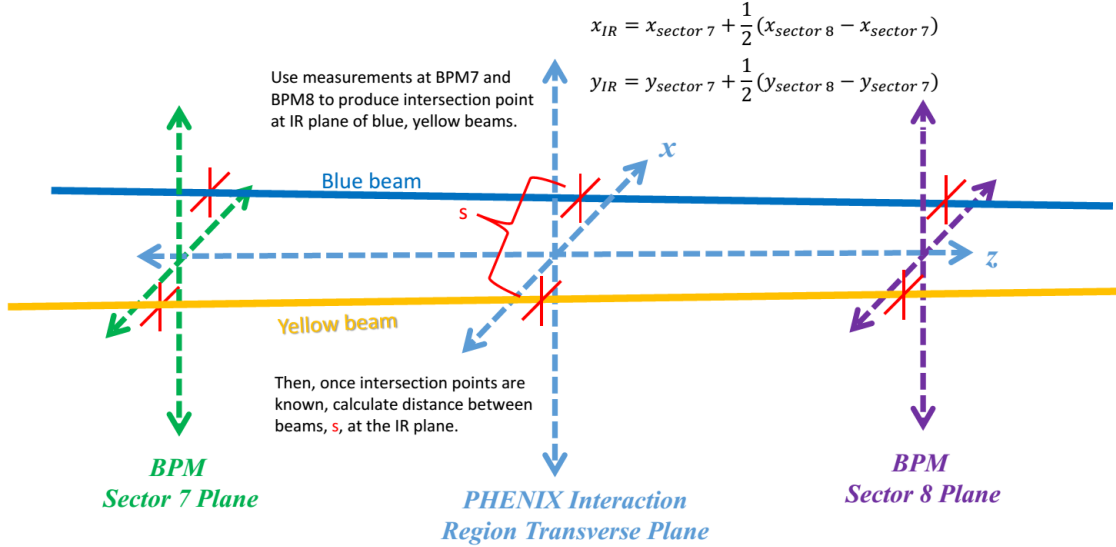


Figure 5.3: Shown: the geometric extrapolation of beam displacement at the IR plane.

One potential complication in using the BPM data is that the polarity of the data (whether or not the position monitored is positive or negative with respect to ‘0’) may at times flip. Additionally, the intended step pattern executed by the Collider-Accelerator department (CAD) may differ from the actual net displacements of the beam. As a study, one may compare the actual planned displacements, to the real measured displacements produced by the BPM. This can serve to identify the accuracy of CAD’s beam positioning, and whether or not a polarity shift occurred. An example of a vernier scan, as seen by the BPMs is shown in Table 5.3 (Horizontal Scan) and Table 5.4 (Vertical Scan).

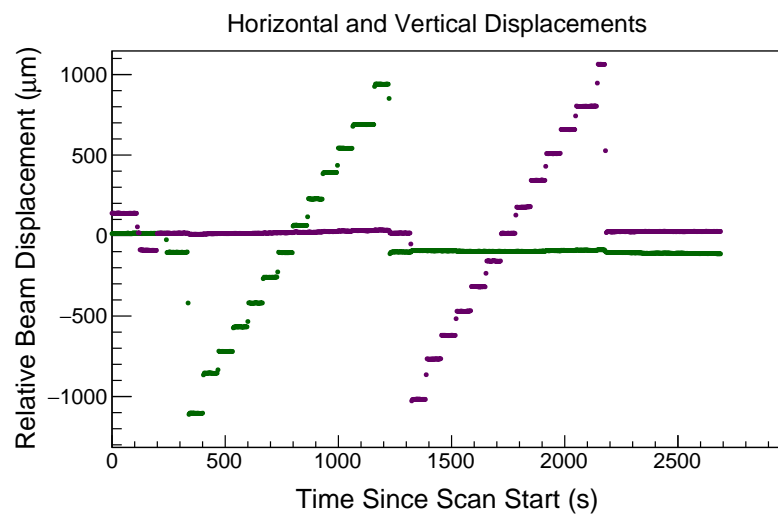


Figure 5.4: The horizontal scan is shown in green, with the vertical scan shown in purple. Note that relative scan displacements are shown in both the horizontal and vertical for the horizontal scan and vertical scan. In this case, the blue beam was scanned and the yellow beam was held fixed.

$CAD_x$ ( $10^{-6}m$ )	$BPM_x$ ( $10^{-6}m$ )	$\Delta_x$ (%diff)	$CAD_y$ ( $10^{-6}m$ )	$BPM_y$ ( $10^{-6}m$ )	$\Delta_y$ (%diff)	$BPM_{tot}$ ( $10^{-6}m$ )	$\Delta_{tot}$ (%diff)
-1000.00	-1103.61	(10 %)	0.00	8.07		1103.64	(10 %)
-750.00	-854.70	(14 %)	0.00	10.67		854.77	(14 %)
-600.00	-720.00	(20 %)	0.00	11.86		720.10	(20 %)
-450.00	-567.61	(26 %)	0.00	13.04		567.76	(26 %)
-300.00	-419.25	(40 %)	0.00	14.25		419.49	(40 %)
-150.00	-258.89	(73 %)	0.00	16.00		259.39	(73 %)
0.00	-106.14		0.00	17.32		107.55	
150.00	63.04	(58 %)	0.00	20.89		66.41	(56 %)
300.00	227.11	(24 %)	0.00	21.36		228.11	(24 %)
450.00	391.46	(13 %)	0.00	24.82		392.25	(13 %)
600.00	542.27	(10 %)	0.00	28.10		542.99	(10 %)
750.00	689.36	(8 %)	0.00	30.36		690.03	(8 %)
1000.00	940.39	(6 %)	0.00	34.04		941.01	(6 %)

Table 5.3: Shown: the horizontal scan. BPM data compared to CAD planned steps for run 359711. Columns are from left to right, we see the CAD planned horizontal beam displacement, the bpm-measured horizontal beam displacement,  $||CAD_x| - |BPM_x||$  (to account for polarity flips in bpm), the CAD planned vertical beam displacement, the bpm-measured beam displacement,  $||CAD_y| - |BPM_y||$ , the total beam separation ( $\sqrt{BPM_x^2 + BPM_y^2}$ ) and the difference between the measured total separation and the CAD planned total separation. Nominally, CAD intends to hold one beam fixed, and scan the other beam. Rows are each scan step planned and measured for the run.

$CAD_x$ ( $10^{-6}m$ )	$BPM_x$ ( $10^{-6}m$ )	$\Delta_x$ (%diff)	$CAD_y$ ( $10^{-6}m$ )	$BPM_y$ ( $10^{-6}m$ )	$\Delta_y$ (%diff)	$BPM_{tot}$ ( $10^{-6}m$ )	$\Delta_{tot}$ (%diff)
0.00	-93.96		-1000.00	-1017.07	(2 %)	1021.40	(2 %)
0.00	-94.75		-750.00	-767.29	(2 %)	773.11	(3 %)
0.00	-95.25		-600.00	-620.36	(3 %)	627.63	(5 %)
0.00	-97.21		-450.00	-470.18	(4 %)	480.12	(7 %)
0.00	-98.07		-300.00	-317.89	(6 %)	332.68	(11 %)
0.00	-98.00		-150.00	-158.64	(6 %)	186.47	(24 %)
0.00	-98.60		0.00	14.27		99.63	
0.00	-98.50		150.00	176.64	(18 %)	202.25	(35 %)
0.00	-97.36		300.00	343.18	(14 %)	356.72	(19 %)
0.00	-94.21		450.00	508.79	(13 %)	517.44	(15 %)
0.00	-92.67		600.00	658.70	(10 %)	665.19	(11 %)
0.00	-90.95		750.00	803.25	(7 %)	808.38	(8 %)
0.00	-88.57		1000.00	1063.50	(6 %)	1067.18	(7 %)

Table 5.4: Shown: the vertical scan. BPM data is compared to CAD planned steps for run 359711. Columns are from left to right, we see the CAD planned horizontal beam displacement, the bpm-measured horizontal beam displacement,  $||CAD_x| - |BPM_x||$  (to account for polarity flips in bpm), the CAD planned vertical beam displacement, the bpm-measured beam displacement,  $||CAD_y| - |BPM_y||$ , the total beam separation ( $\sqrt{BPM_x^2 + BPM_y^2}$ ) and the difference between the measured total separation and the CAD planned total separation. Nominally, CAD intends to hold one beam fixed, and scan the other beam. Rows are each scan step planned and measured for the run.

## 5.5 PHENIX Raw Data

The PHENIX raw data format (better known as PRDFs) are the form that recorded data takes immediately after being assembled into events, by the PHENIX DAQ. PRDF data is archived soon after being generated on the massive robotic tape file-system.

The trigger scalers representing the clock, BBC novertex trigger, BBC 30 cm cut trigger, and ZDCLL1 trigger are extracted from the PRDFFs.

PRDF data is hierarchical. It is first organized by event-type, and then organized by packet-type. Every packet has a header, which contains general information such as what the packet contains, and in what order that packet was received from the DAQ. Every packet recorded can be associated with a unique event-sequence number, which specifies roughly the order in which the event owning the packet was received by the DAQ. Within a given run number, an event-number is guaranteed to be unique. The complexity of the packet is limited by the bandwidth available to move data off PHENIX onto other storage, and the buffers/reconstruction ability of the front end electronics modules built onto PHENIX subsystems.

Generally, raw PHENIX data is too complex to use straight-away, because minimal to no reconstruction of physical properties for a certain event is done (and this varies by the constraints of each individual subsystem). However, for the vernier analysis, we are generally only interested in very simple properties of an event, all of which are completely available directly from the PRDF. This allows huge flexibility, as other than the libraries required to dump packet information from PRDFs headers, there are no dependencies for obtaining the data we need from PRDFs.

One constraint of using PRDFs as a primary data source is disk space. A normal physics run may be segmented into hundreds of PRDFs, each at 20 GB in size. However, because the event rates are on average quite low for a vernier scan, and because vernier scans typically do not last longer than 20 minutes, there are typically only five or six PRDFs needed to store an entire scan. The data extracted from PRDFs is summarized in table 5.5.

### 5.5.1 GL1-1P Scalers, ATP Number and Event Time Stamps

With the DAQ was described in Section 4.5.3), relevant discussion of the DAQ with regards to the Vernier Analysis is discussed here.

Over the course of the archiving process executed by the DAQ, the event is categorized by event type. For this analysis, we consider “DATAEVENT” event types and “SCALEREVENT” event types. When data is sent to the ATPs, one of the 64 distinct ATPs will receive each event, depending on which ATP is available to process an event. Each ATP tags the event it received with an ATP number  $0 \leq ATPNUMBER < 64$ , corresponding to the ATP which processed the event and given an epoch time-stamp. If one desires to use this time stamp, network latency must be corrected for.

Since time is synchronized between the ATPs via the network, there may be some latency, which causes a time-offset between the ATPs. However, this latency can be corrected for. Because of the large volume of data, several thousand events will arrive for processing simultaneously, so one can simply choose an ATP (I choose “0”) and correct all other time offsets of other ATPs relative to this time, such that a time offset is obtained in order to synchronize all epoch times to within one second accuracy for the entire data set.

Other data that are extracted from PRDFS (besides ATPNUMBER, EPOCHTIME, RUNNUMBER, and EVENTNUMBER) are BUNCHNUMBER, and the GL1-1P scalers.

GL1-1P Scalers are unique counters which may be programmed to track any arbitrary trigger. These counters count the number of ”live” triggers for each programmed triggers which occur between recorded events. Each time an event is recorded, the counter dumps the number of ”in between” triggers to the GL1P packet. For Run 12, the triggers programmed into the GL1-1P boards were:

- BOARD-ID: 0, ”BBCLL1(>0 tubes)”
- BOARD-ID: 1, ”CLOCK”
- BOARD-ID: 2, ”ZDCLL1Wide”
- BOARD-ID: 3, ”ZDCLL1Narrow”

To obtain a rate for these trigger scalers, we have two options:

1. Sum all scalers associated with a single EPOCHTIME to get that scaler’s per second rate
2. Take the ratio of a particular scaler to the ”CLOCK” scaler, converting to a rate using the clock frequency ( $9.36MHz$ ).

Both options must yield the same results, unless there are DAQ issues related to live time. Item 2 is the preferred method, since live-time effects are nullified by taking the ratio of two run scalers with the same live time, and all DAQ triggers should generally have the same livetime. Other analyses for Vernier data have suffered when the CLOCK scaler is not included in the GL1-1P board programming. In this case, option 1 is the only available option, and the live-time must be corrected using ratios of live to raw events for each scaler.

Source
Event Header
Packet 140008
Packet 140001

Table 5.5: Data extracted from PRDFs.

## 5.6 Beam Beam Counter Analysis

An example of the BBC GL1P scaler for Run 359711 is shown in Figure 5.5, shown alongside the CLOCK GL1P scaler. These scalers are summed into bins which time order the data. This is accomplished by ordering the events by the event sequence, which tags events in the order they were produced. Scalers are summed for every one-thousand events, and then divided, scaled by the overall CLOCK rate of 9.36 MHz, to produce the BBC event rate. Note that in the histograms, as the beams are displaced, more and more clock scalers are recorded, filling the bandwidth, with fewer BBC GL1P scalers. For maximal overlap, the inverse is true.

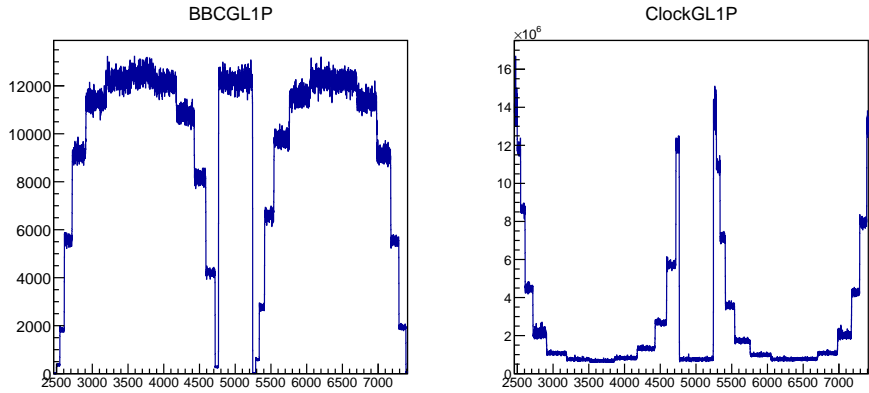


Figure 5.5: Left: the BBC GL1P scaler plotted as a time series, against an arbitrary time proxy. Right: the CLOCK GL1P scaler, plotted in the same way. Both distributions are histograms.

Note that in the event rate, clear divisions appear associated with beam displacements. When beams are displaced, the event rates drop, but when the beams are overlapped, the event rates increase. Combining the beam width data with the rate data is a crucial step in the vernier analysis which allows for the calculation of the beam width, described in Section 5.8. The BBC rates for Run 359711 are shown in Figure 5.6.

One can estimate the uncertainty associated with the BBC rate by observing the distribution of the rates around each step. This study is shown qualitatively in Figure 5.7, where one can observe histograms for each scan step of the BBC rate at that particular step. In practice, the average and RMS is extracted from each distribution.

BBC rates may be corrected for multiple collisions per bunch crossing. In measurements where overall particle yield is needed, this correction is vital, however, in our measurement, we care only about using rates to extract the beam width, as well as calculate the overall efficiency of the BBC trigger. Other analyses have found that while rates may change at maximum overlap by as much as 10%, it was shown to only affect the beam width by a factor of 1%.

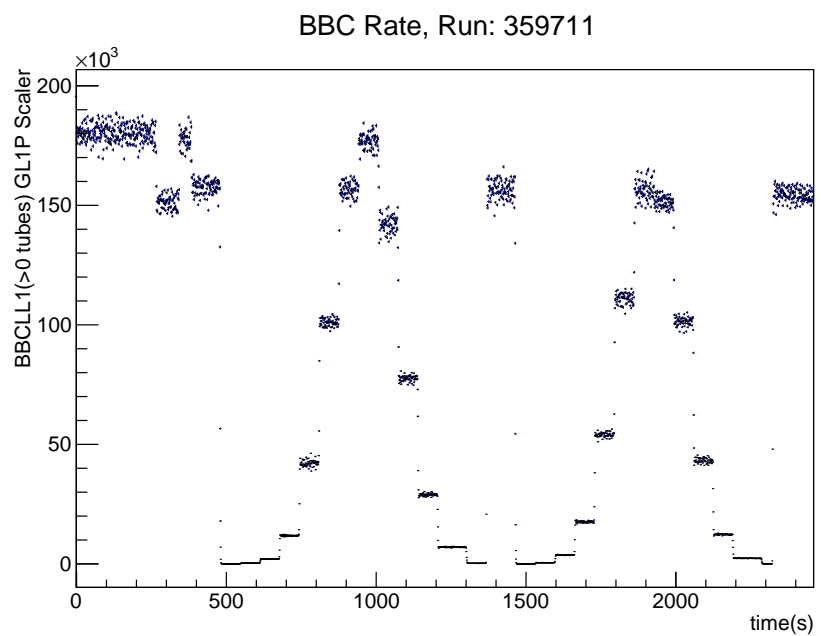


Figure 5.6: Shown: the BBC Rate as a function of time since scan start for Run 359711. The stepped distribution is due to changing beam overlap. The rates here are intrinsically live-time corrected, because they were generated from the ratio of the BBC GL1P scaler and the CLOCK scaler.

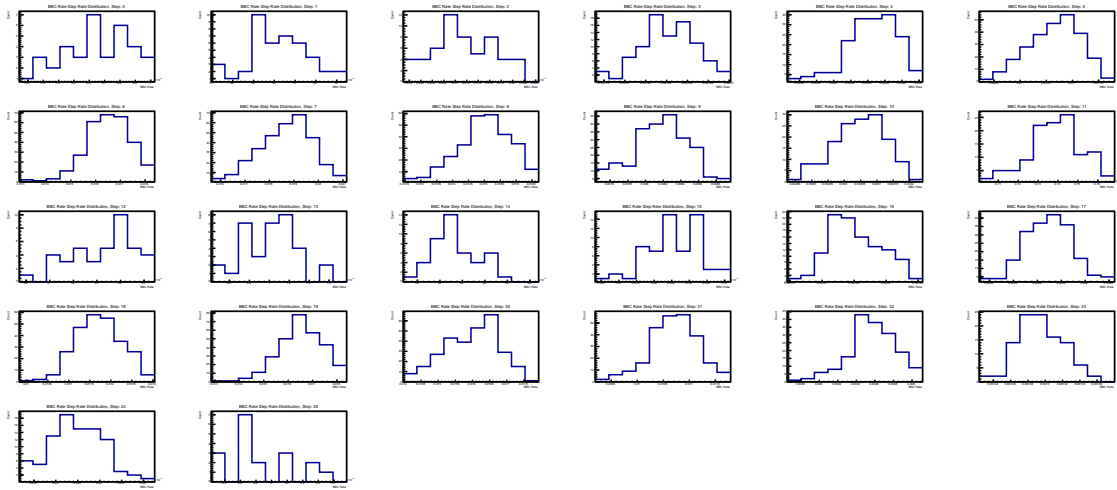


Figure 5.7: In each panel, the BBC rate distribution about a manually defined scan step is shown as a histogram. The horizontal is the rate, while the vertical is the number of times that a rate bin was observed in the data. From left to right, top to bottom, the scan steps are shown, starting at the chronologically first step in the top left, and ending with the chronologically last step in the bottom right.

### 5.6.1 BBC Efficiency

The efficiency of any detector element can be characterized by addressing the three following considerations:

1. **Geometric acceptance** (What is the size of the detector? Can particles impinging on the detector ‘miss’?)
2. **Physical detector properties** which limit response (i.e. does a transducing element operate according to some threshold which may not allow it to transduce every particle every time?)
3. **Trigger Efficiency**

For the BBCs, items 1 and 3 factor in heavily to its overall efficiency,  $\epsilon_{BBC}$ . The ZDC is used to calculate the efficiency of the BBC. This is possible because the geometric acceptance of the ZDC is relatively flat with respect to the geometric acceptance of the BBC, concerning particles which are produced from collisions between the BBCs at  $\pm 144cm$ . Schematically, this is shown in Figure 5.8. The geometric acceptance of a detector may be calculated as fraction of the total solid angle subtended by the detector as seen by an impinging particle from the event vertex:

$$BBC_{acc} = \frac{1}{4\pi} \left( \int_{\theta_1}^{\theta_2} \sin(\theta) d\theta \int_0^{2\pi} d\phi - \int_{\theta_3}^{\theta_4} \sin(\theta) d\theta \int_0^{2\pi} d\phi \right) \quad (5.5)$$

With the first terms in the integral to the left of the ‘-’ sign referring to the solid angle seen to the left, and the right referring to the solid angle seen to the right.

One can motivate the use of the ZDC as a calibrating detector for the BBCs with respect to acceptance by calculating the geometric acceptance of a particle at all possible event vertices for the BBC and ZDC, and confirming that the distribution is relatively flat for the ZDC, as seen in Figure 5.9.

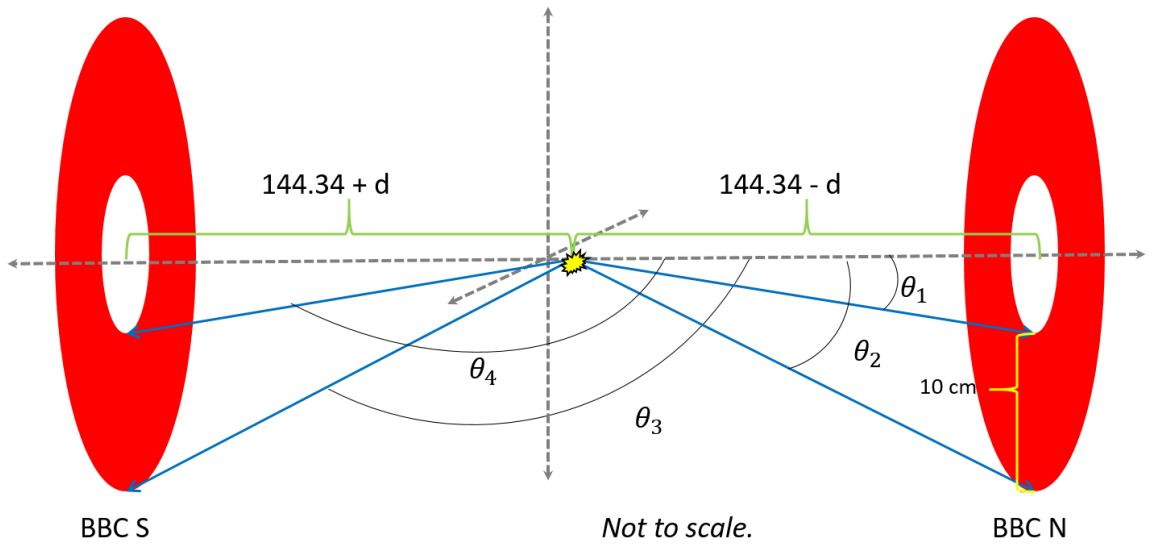


Figure 5.8: Shown on the left and right are annular cross-sections of the BBC north and south at  $\pm 144\text{cm}$ . The integration bounds in  $\theta$  (Eqtn 5.5) are labeled, with the distance relative to the BBC N and S labeled as  $d$ , with respect to the event collision vertex (the yellow sunburst). Scale is exaggerated to better show the angles.

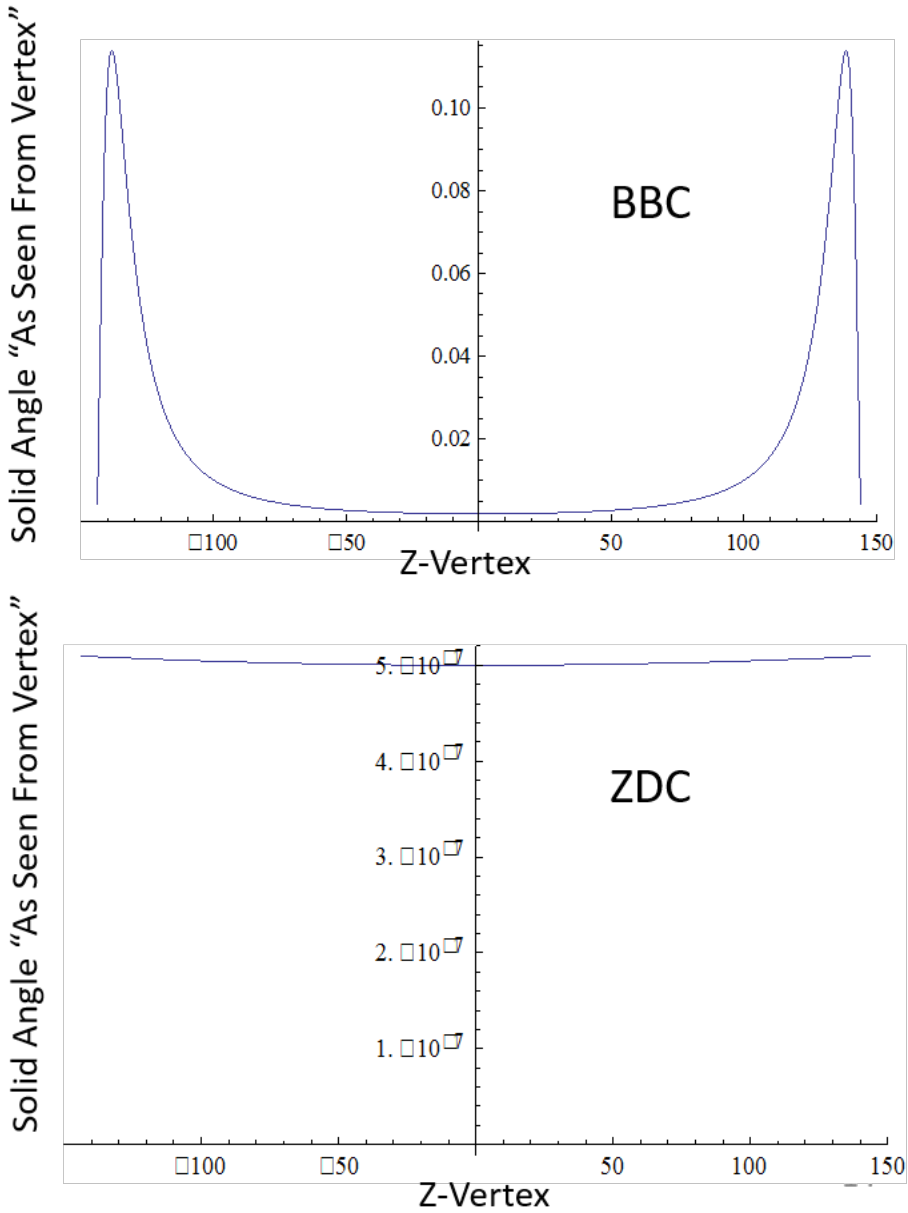


Figure 5.9: Top: the BBC solid angle as calculated for all possible solid angles within the BBC  $z$ -vertex sensitivity range. Bottom: the solid angle of the ZDC seen from an event vertex for all  $z$ -vertices over the BBC  $z$ -vertex range. Units on the vertical axis are arbitrary for this qualitative comparison.

### 5.6.2 Calculation of $\epsilon_{BBC}$

Analysis in this section focuses on Run 359711, though all scans are analyzed in a similar manner.

To obtain the BBC efficiency, we must integrate over the BBC trigger acceptance, while correcting this acceptance for any  $z$ -vertex dependence. We obtain the BBC trigger acceptance for the  $\pm 30\text{cm}$  BBC trigger using the BBC trigger with no vertex cut. First, histograms are generated, observing the yield of particles associated with various bins of  $z$ -vertex. We create two such histograms for the BBC measure trigger acceptance. The trigger acceptance is needed to determine the effective vertex cut of the BBC  $\pm 30\text{cm}$  trigger, which may not be precisely  $\pm 30\text{cm}$ .

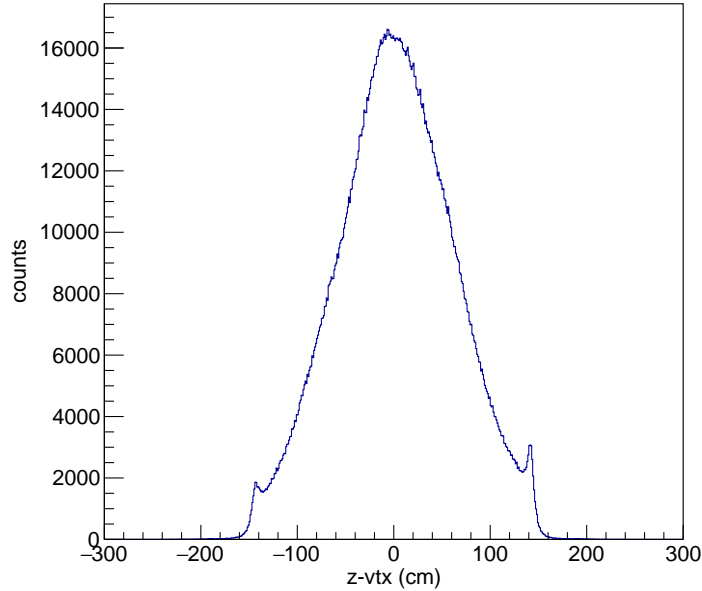
As the baseline, the no vertex cut  $z$ -vertex distribution is created, Figure 5.10a. Then, we fill another histogram only when both the no-vertex cut and  $\pm 30\text{cm}$  vertex trigger simultaneously fire, Figure 5.10b.

We then create the trigger acceptance plot, bin by bin, dividing the yields per bin of the no vertex distribution by those of the simultaneously triggered distribution. The resulting plot, Figure 5.11a is produced. From trigger acceptance, one can observe the derivative of the distribution, to pin point the turn-on position of the online vertex cut. We may observe the absolute value of the derivative of the trigger acceptance, which produces two Gaussian peaks centered at the exact locations of the trigger cut turn on 5.11b. In this case, for Run 359711, the true trigger turn on is determined to be events with  $z$ -vertices between -34.4 cm and 35.8 cm.

Since  $z$ -vertex yields may have some  $z$ -dependence due to geometric acceptance effects, this must be corrected. To do so, similar distributions of simultaneously triggered data are generated, however, in this case, we use the ZDC. In the same vein, the  $z$ -profile of events triggering the ZDC no vertex cut is generated, Figure 5.12a. Additionally,  $z$ -vertices are filled into a distribution conditionally, when there is a coincidence of the BBC no vertex cut trigger and the ZDC no vertex cut trigger (Figure 5.12b).

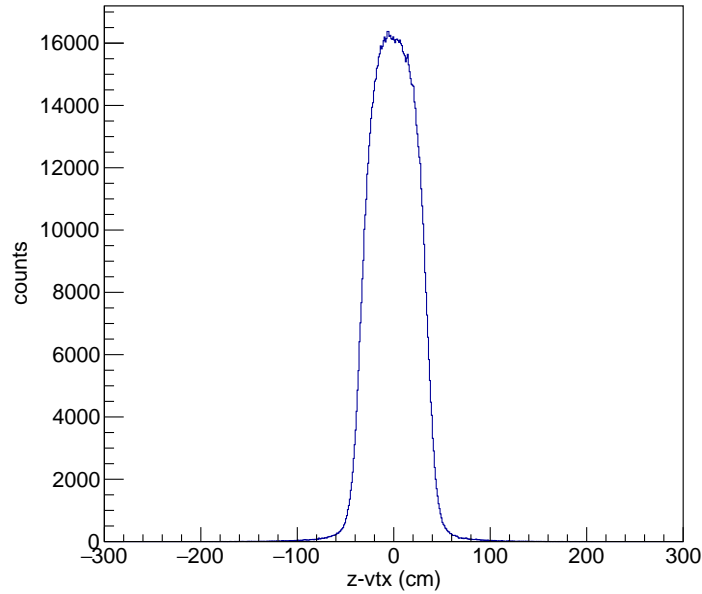
Finally, a distribution is formed in the same manner as the acceptance distribution earlier, only this time, this distribution is parameterized with a fit, Figure 5.13. The value

BBC Wide z-vtx Distribution Run: 359711



(a) BBC wide

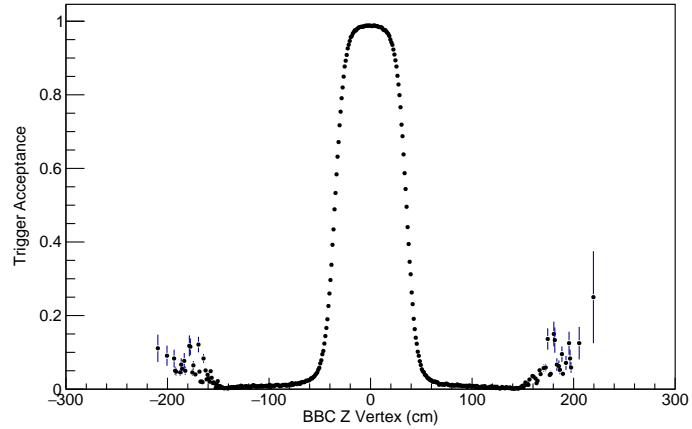
BBC Wide and Narrow Coincidence z-vtx Distribution Run: 359711



(b) BBC wide and narrow

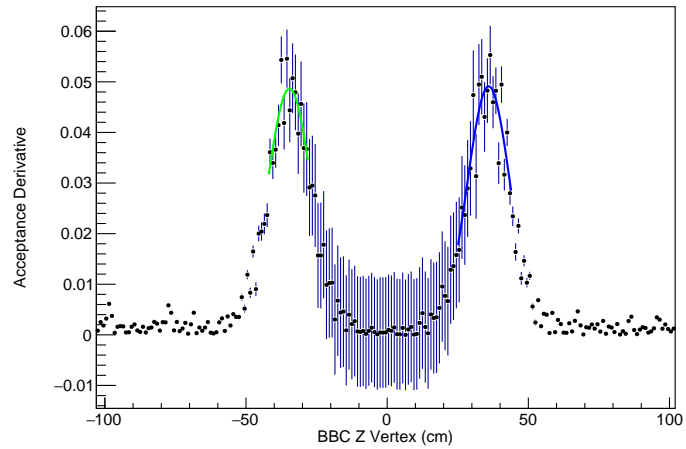
Figure 5.10: Panel(a): the  $z$ -vertex distribution for events that trigger the wide BBC trigger. Panel (b): the  $z$ -vertex distribution for events that trigger the BBC wide and narrow triggers.

BBCw&BBCnarrow/BBCw - Trigger Acceptance, Run: 359711



(a) Trigger Acceptance

First Derivative Trigger Acceptance, Run: 359711

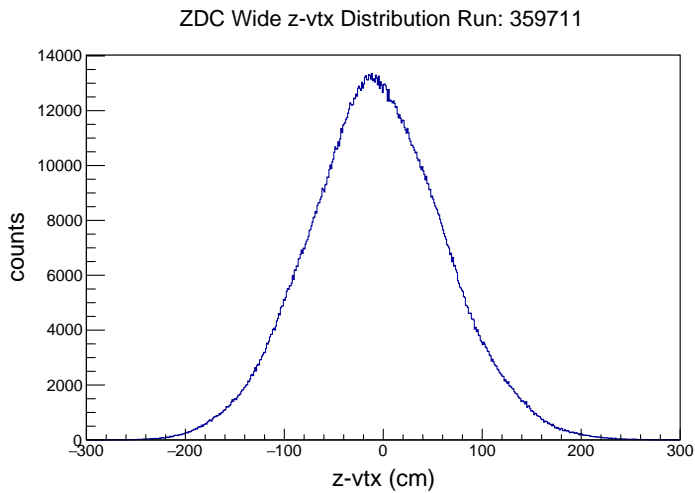


(b) Trigger Turn On

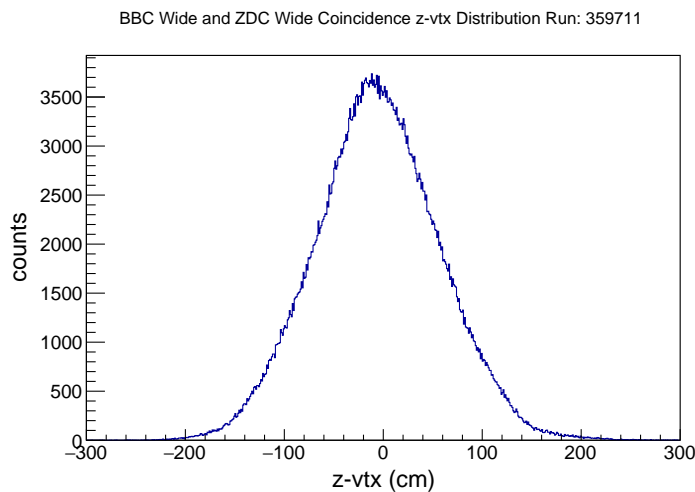
Figure 5.11: Panel (a) shows the trigger acceptance curve, produced from Figure 5.10. Panel (b) shows the absolute value of the derivative of (a), with two Gaussian fits to the peak, centered at -34.4 cm and 35.8 cm, representing the real trigger turn on.

of this fit represents the overall vertex dependence of the BBC no vertex trigger. The correction is applied as a scaling factor on each  $z$ -vertex bin of Figures 5.10a and 5.10b.

The final efficiency is calculated by summing the corrected yield of the simultaneously triggered BBC yields over the real trigger turn-on interval, and dividing by the total corrected yield over the full vertex range obtained from the BBC no vertex distribution. For the case of Run 359711,  $\epsilon_{BBC}$  was calculated to be 0.43.



(a) ZDC Wide  $z$ -vertex



(b) ZDC and BBC coincidence  $z$ -vertex

Figure 5.12: Panel (a) shows the wide ZDC  $z$ -vertex distribution, Panel (b) shows the distribution from trigger coincidences between the BBC wide and ZDC wide triggers.

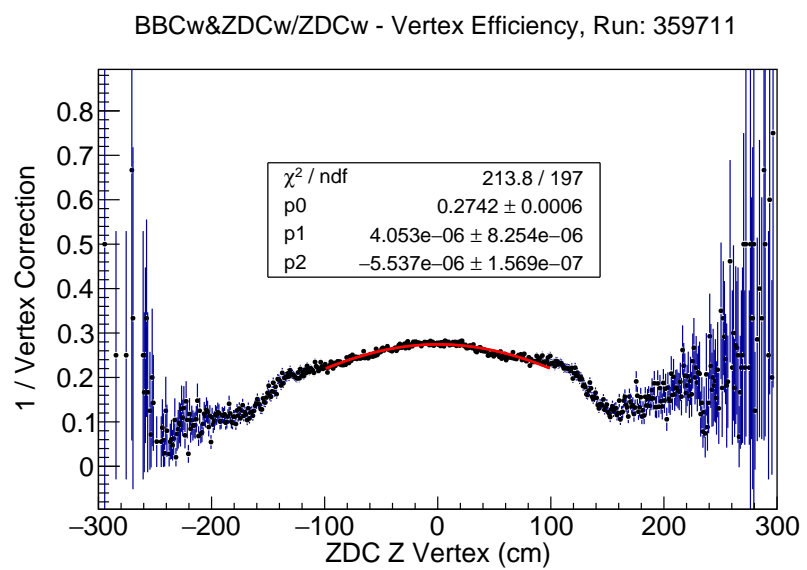


Figure 5.13: The BBC  $z$ -vertex correction is obtained from the ratio of BBC and ZDC to ZDC yields and fit with a quadratic polynomial. The resulting polynomial is used to correct the yields for the BBC coincidence and BBC wide distributions, before calculating the total efficiency.

## 5.7 Wall Current Monitor and Direct-Current Current Transformer

The wall current monitor (WCM, Figure 5.14) and direct-current current-transformers (DCCT, Figure 5.15) use induced image-charges in plates capacitively coupled to beam current to measure the total number of ions in the blue and yellow beams. Additionally, the WCM has timing sensitive enough to determine individual bunch populations. Since the DCCT is more accurate, it can be used to calibrate the overall values of bunch populations. The WCMs, because of their high frequency read out, can even measure the transverse profile of a single beam-bunch. This profile is necessary for accurate simulation of collision conditions. Simulations are required to obtain  $\beta^*$  and  $\theta_{x\text{ing}}$  through comparison with the data. This is discussed in Section 5.9.

Before the WCM data can be used to reckon the population of the beams, they must be calibrated with the DCCT data. We may calibrate using the following logic: if the WCM were to provide an accurate measurement of the beam current, then summing the WCM data over all bunches should yield the same population. However, since the DCCT is known to be more accurate, we may sum the WCM data, and normalize to the DCCT. The calibration proceeds as follows:

$$\text{let } \sum_{i=0}^N WCM_{true_{bunch_i}} = DCCT_{total} \quad (5.6)$$

$$\text{then } \frac{\sum_{i=0}^N WCM_{bunch_i}}{DCCT_{total}} = 1 \quad (5.7)$$

$$\therefore WCM_{true} = \frac{DCCT_{total}}{\sum_{i=0}^N WCM_{bunch_i}} \times WCM_{bunch_i} \quad (5.8)$$

$$\text{with } WCM_{calib} \equiv \frac{DCCT_{total}}{\sum_{i=0}^N WCM_{bunch_i}} \quad (5.9)$$

With  $WCM_{true}$  representing the ‘correct’ value for the WCM by assuming that the WCM and DCCT must yield the same number for the number of ions in the beam, a calibration constant is determined for the WCM. The calibration,  $WCM_{calib}$ , is applied individually for each matching time index in the time series data for WCM data and DCCT data.

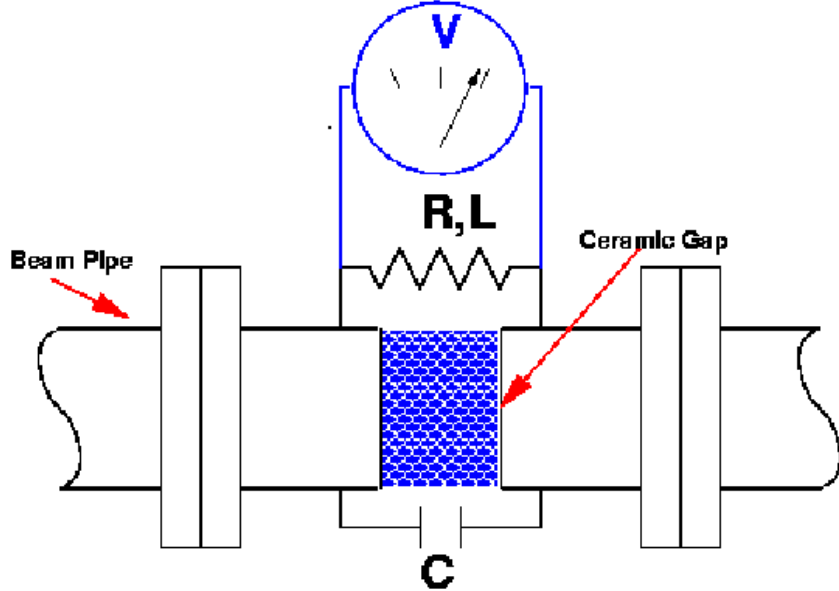


Figure 5.14: Shown: an insulating ceramic break in the beam pipe, which shunts image wall currents from the beam pipe into the electronics. Magnetic shielding excludes external magnetic fields. [27]

In addition to giving the total beam ion population, as well as the per-bunch beam ion population, the WCMs also allow us to estimate the rate of beam loss (Figure 5.16), which may impact the overall BBC rate over time. By taking the product of the blue and yellow beam current, and observing over the course of a run, one may fit this distribution linearly, and obtain the per-second percent loss of the beam ion population. Over the course of an entire vernier scan, this amounts to one percent or less losses, can can be neglected as a source of rate-loss.

Finally, we may observe the beam population per bunch using the calibrated WCM data Figure 5.17. Differences in bunch populations may be attributed to fluctuation in the way beams are filled, and do not effect the analyses generally, but should be visualized to determine if there are drastic fluctuations in beam population which could indicate other problems with the run.

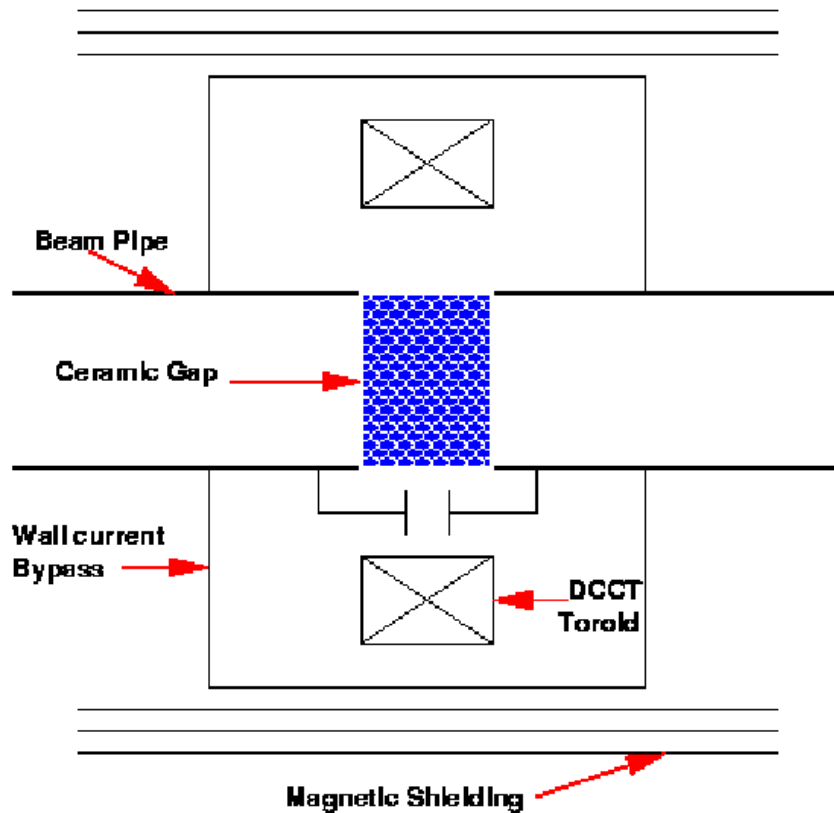


Figure 5.15: The wall current monitor uses an insulating ceramic break in the beam pipe similarly to the DCCT, which forces image wall currents through electronics which measure the current frequencies. The WCM is sensitive only to bunched beams, and can measure longitudinal profiles of bunches [27].

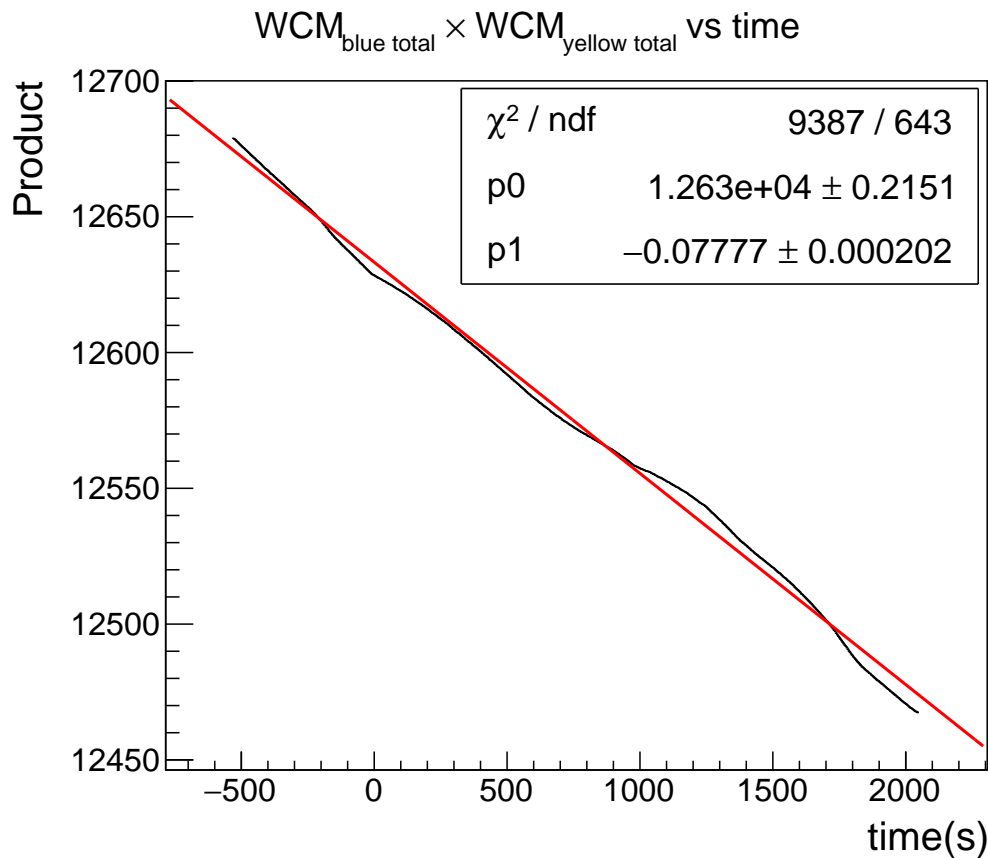


Figure 5.16: Shown: The product of the WCM blue and WCM yellow calibrated data describing the total beam ion distribution, as a function of time. This may be used to estimate the beam losses due to real ion loss, with the slope representing the per-second rate of luminosity loss. In all scans, this amounts to 1% or less for the duration of the scan.

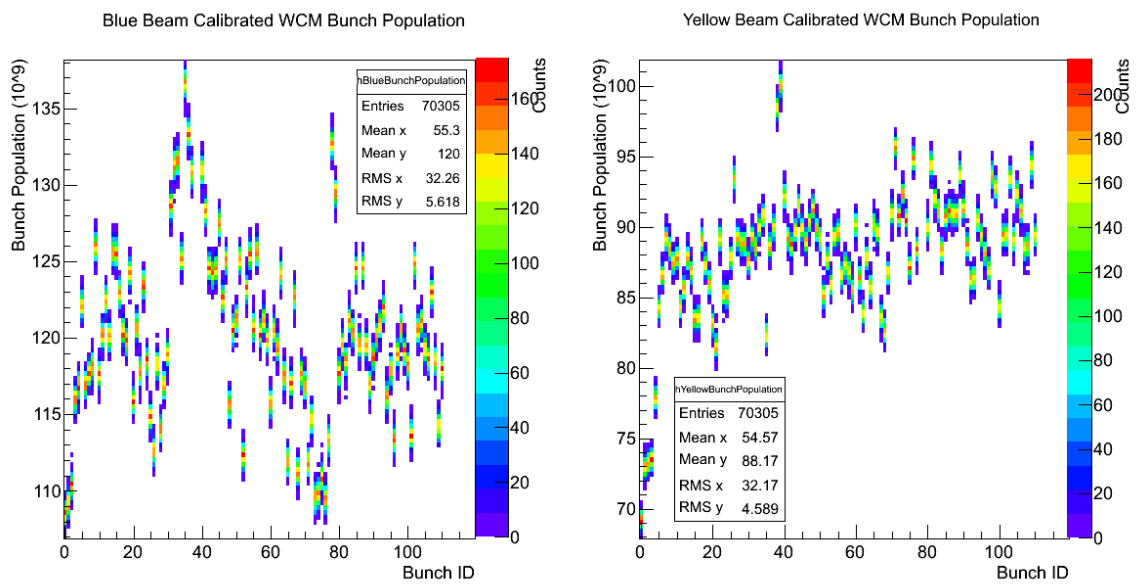


Figure 5.17: Distribution of WCM population, corrected by DCCT for each bunch for an example run. Left: blue beam. Right: yellow beam. For both figures, the horizontal axis represents the bunch number.

## 5.8 Beam Width Extraction

The BPM data (Section 5.4) and BBC rate data (Section 5.6) are combined to map out the convolution of the width of the blue and yellow beams. If the beams are identical in the transverse direction, then one may extract the beam width using these data sets. We assume that the transverse beam widths are identical.

The vernier scan itself is done to allow for the calculation of the beam width. As the beams are scanned through fixed beam displacements, one may correlate each scan step's beam displacement in  $x$  and  $y$  to the BBC rate. When these correlations are ordered by beam displacement, the resulting distribution traces out the beam width.

Additionally, although the beams are not guaranteed to maximally overlap, fitting the beam displacement versus the BBC rate allows us to determine what the BBC rate would be for maximal overlap. Thus, from this study, we recover  $\sigma_x$ ,  $\sigma_y$  and  $R_{MAX}$  (subject to correction for multiple collisions).

Consider the displacements extracted from the BPM data, Figure 5.4 and the BBC rate data, Figure 5.6. Note that the data follows a clear stepped pattern for both data sets. Though studies were done to recover the exact ‘step’ boundaries for these kinds of distributions, one may simply manually define the boundaries for each scan step by observing the distribution. So long as one is sufficiently far enough that the values for each step in the BPM and BBC are quiescent, one can define such boundaries. Then, the average position and rate is calculated for each step, plotted, and fit with a Gaussian distribution (the assumed transverse profile geometry), as in Figure 5.18 and Figure 5.19.

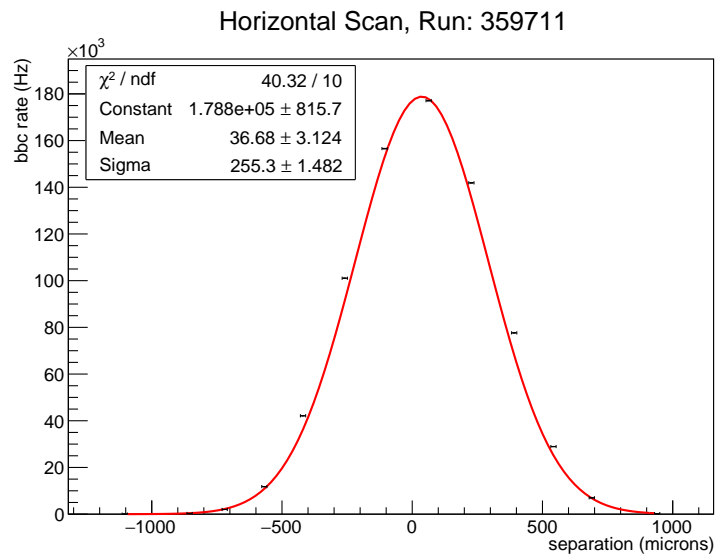


Figure 5.18: The horizontal beam width fit

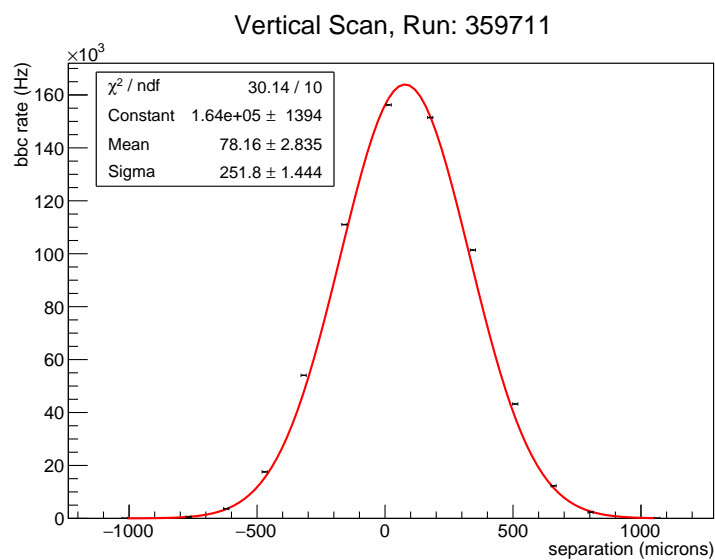


Figure 5.19: The vertical beam width fit

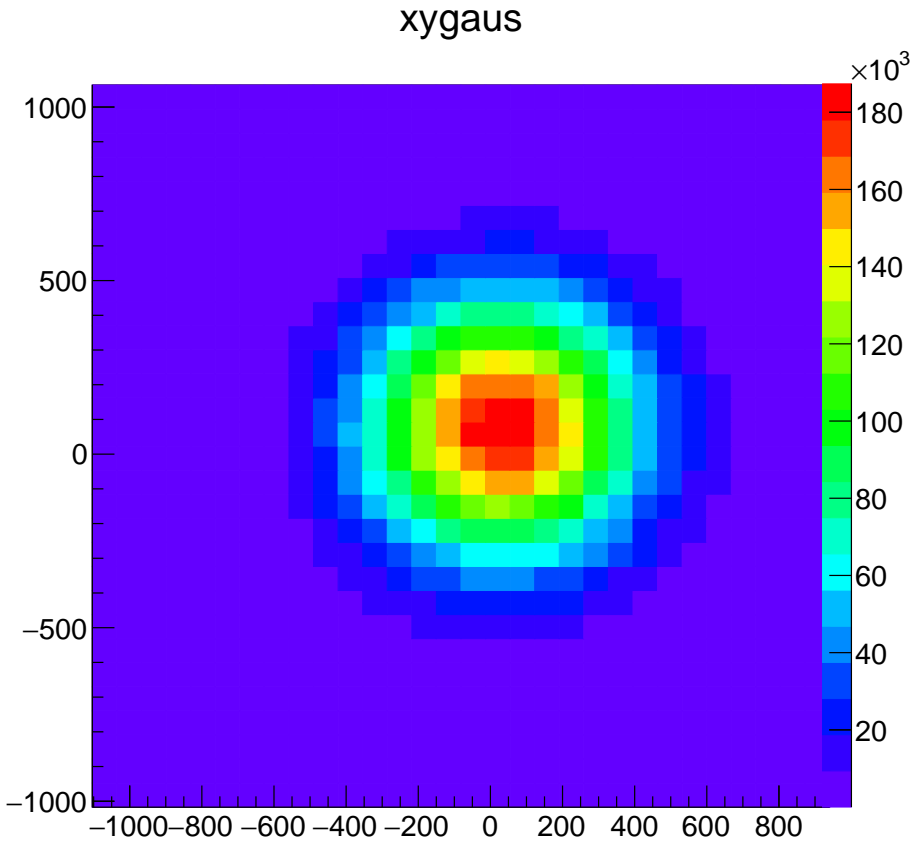


Figure 5.20: The simultaneous fit to the BBC rate vs beam displacement.

We obtain a horizontal beam width of 255 microns horizontally and 251 microns vertically. The horizontal fit shows a higher overall BBC rate, but the true rate can only be obtained from a simultaneous  $x$  and  $y$  fit with a two dimensional 2D Gaussian fit: Figure 5.20, and find that for run 359711, the true horizontal width is 254 microns with 251 vertically, closely matching the 1D case. Additionally, the overall max BBC rate,  $R_{MAX}$ , is found to be 188 kHz, which is typical for a lower luminosity run near the end of a fill, for 200 GeV beams. Rates are found to be higher for higher luminosities and higher beam energies. Additionally, at 510 GeV collision energies, the beam width drops to nearly 150 microns.

## 5.9 Determination of $\beta^*$ and $\theta_{xring}$

With the addition of a beam focusing parameter,  $\beta^*$ , and beam crossing angle,  $\theta_{xring}$ , the luminosity of intersecting ring particle accelerators can be boosted by a factor of nearly 20%. Since the vernier analysis seeks to calculate the real luminosity, it is important to characterize the amount that these parameters increase our luminosity. By observing PHENIX's zero-degree calorimeter's reckoning of the event vertex, at various beam displacements, one is granted access to observing the effects of these parameters.

In the model for beam luminosity discussed in Equation 5.2, we neglected to mention the importance of the  $z$ -dependent ion distributions in each bunch. In fact, beam bunches have a  $z$ -dependent component of their transverse ion distributions due to the  $\beta^*$  beam squeezing. If we could view the transverse beam width at various points along the bunch in the  $z$ -dimension, we would find that the transverse beam width varied as a function of  $z$ , Figure 5.21.

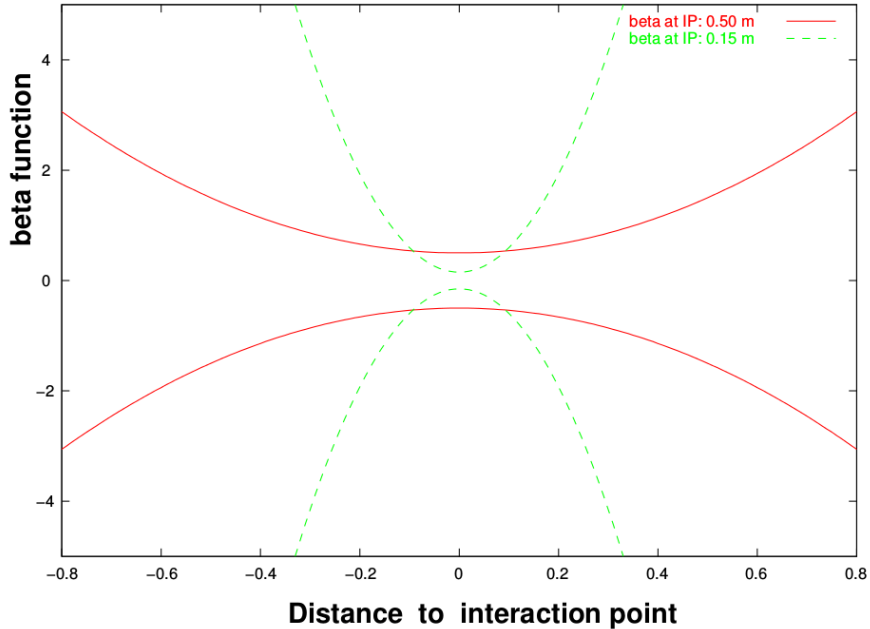


Figure 5.21: A cartoon is shown for various potential values of  $\beta^*$ , showing the squeezing transverse profile [28].

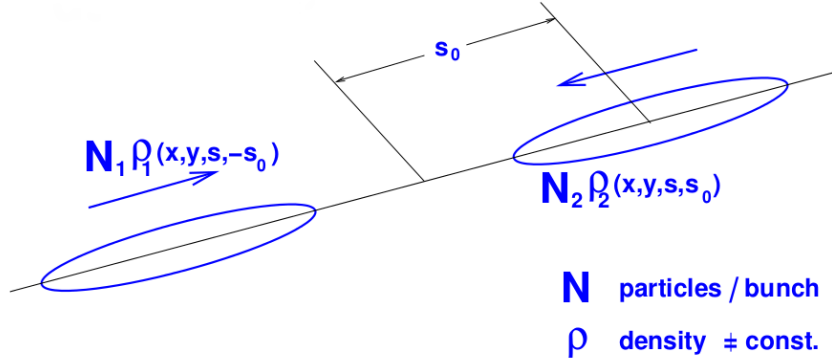


Figure 5.22: Shown: a simple bunch collision with no crossing angle or beam focusing with Gaussian bunch profiles in  $x,y$ , and  $z$ , [28].

A better model for the beam geometry without defining simple Gaussian geometry is defined:

$$\mathcal{L} = 2N_{blue}N_{yellow}f_{bunch}N_{bunch} \iiint_{-\infty}^{\infty} \rho_{blue}(x, y, z - ct_0)\rho_{yellow}(x, y, z + ct_0) dx dy dz dt \quad (5.10)$$

If the densities in equation 5.10 are simply Gaussian, the normalizations may be extracted from the integrand, and the integration can be performed analytically. This simple geometry is shown in Figure 5.22.

The simple normalized Gaussian beam profile for any single dimension,  $x_i, i = x, y, z$  may be written, and normalized as follows:

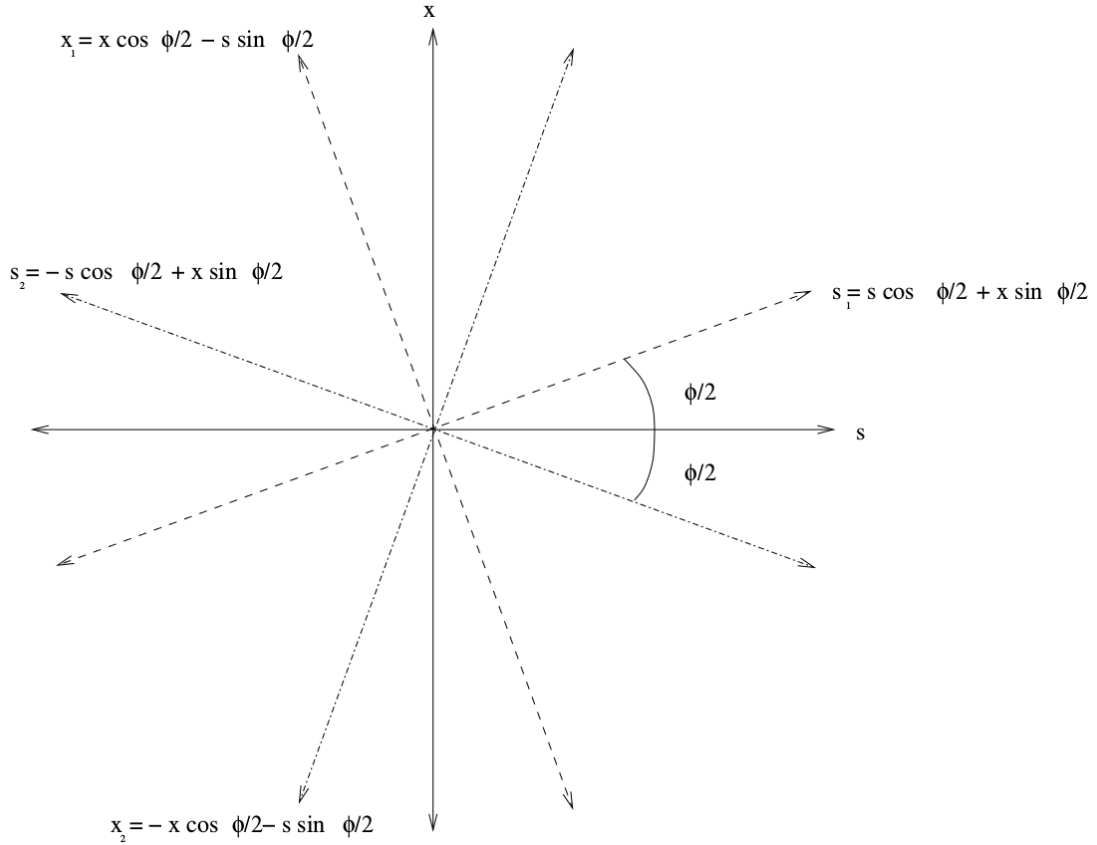
$$\rho(x_i) = \frac{e^{-\frac{(x_i - \mu)^2}{2\sigma_{x_i}^2}}}{\sigma_{x_i}\sqrt{2\pi}} \quad (5.11)$$

If all profiles are of this form, then the densities are separable, and we may perform the integration. However, higher order beam effects introduce complications which will prevent us from separating the densities, as well as performing the integration analytically.

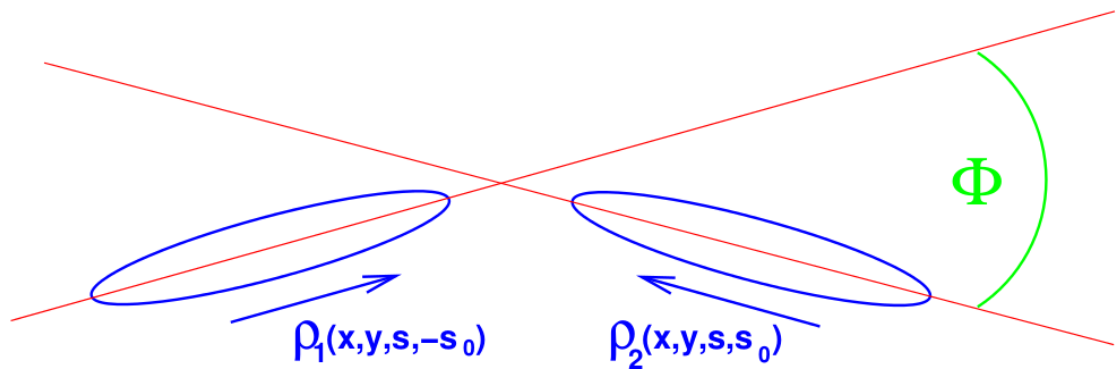
The beam crossing angle is assumed to occur only in the  $x-z$  plane. This assumption is motivated physically, as the RHIC accelerator is positioned such that the beams circulate in a path constrained to a flat plane.

One can apply transformations 5.23 to the basic Gaussian beam profile to generate the most realistic overlap integral. Once we have a form that is representative of the

real overlap conditions, we may integrate out the  $x$  and  $y$  degrees of freedom, leaving a distribution in  $z$  and  $t$ . This distribution is sampled randomly to create a simulated  $z$ -vertex profile. These transformations represent the effects of the crossing angle and the beta-squeeze at the PHENIX IR.



(a) Rotation to coordinates representing crossing angle [28]



(b) Bunches colliding at an angle [28]

Figure 5.23: Panel (a) shows the coordinate transformation applied to the bunch profiles which resulting in a crossing angle, with Panel (b) depicting the result.

The results of this rotation are described, assuming a small crossing angle, known to be within  $|\theta_{x\text{ing}}| < 2 \text{ mrad}$ :

$$x_{blue} \rightarrow x \cos \frac{\phi}{2} - z \sin \frac{\phi}{2} \quad (5.12)$$

$$z_{blue} \rightarrow z \cos \frac{\phi}{2} + x \sin \frac{\phi}{2} \quad (5.13)$$

$$x_{yellow} \rightarrow x \cos \frac{\phi}{2} + z \sin \frac{\phi}{2} \quad (5.14)$$

$$z_{yellow} \rightarrow z \cos \frac{\phi}{2} - x \sin \frac{\phi}{2} \quad (5.15)$$

$$\sin \frac{\phi}{2} \rightarrow \frac{\phi}{2} \quad (5.16)$$

$$\cos \frac{\phi}{2} \rightarrow 1 + \frac{\phi^2}{4} \quad (5.17)$$

with the beta squeeze transforming the profiles as:

$$\sigma_{x_i} \rightarrow \sigma_{x_i} \sqrt{1 + \left(\frac{z}{\beta^*}\right)^2} \quad (5.18)$$

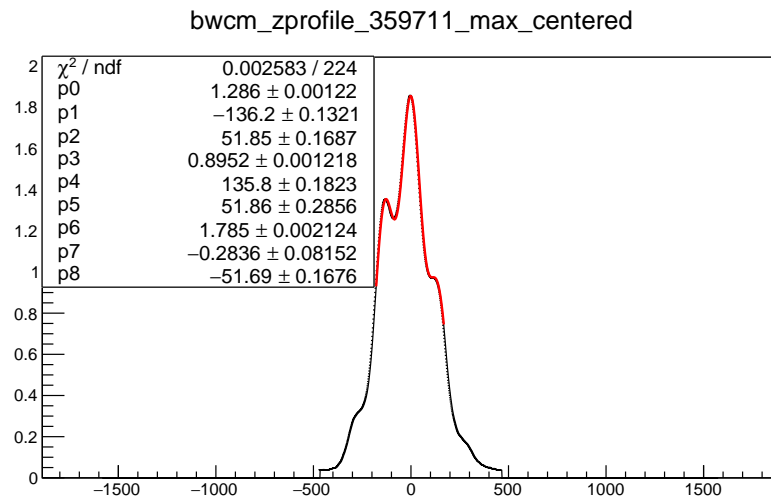
in the transverse directions.

With proper transformations applied to represent the beta squeeze and crossing angle, we may proceed with simulation, provided a realistic  $z$ -profile can be obtained. Fortunately, the WCM data provides such a profile, and one may fit this profile, as shown in Figure 5.24.

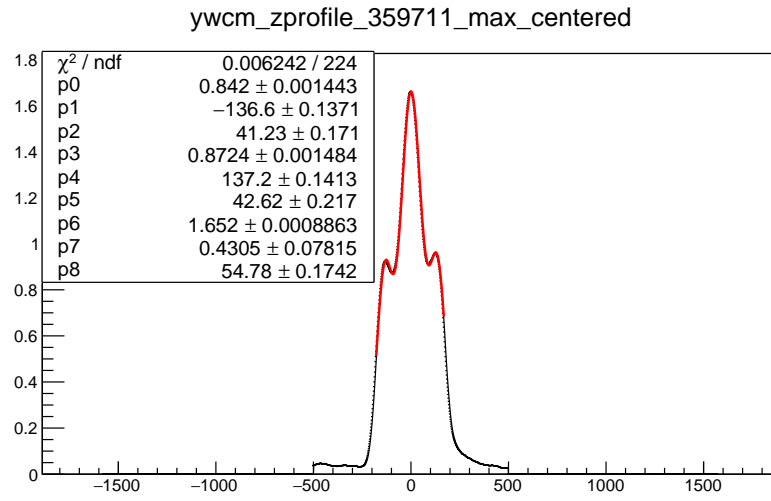
Under normal collision conditions, we expect a gaussian distribution in the  $z$ -vertex profile, as seen in Figure 5.25. This makes intuitive sense, if both beam profiles are even moderately Gaussian-shaped. Collisions are most likely when the densest part of the beam profile are overlapped, and beams are engineered to overlap maximally at  $z = 0$  in the PHENIX coordinate frame.

As the bunch becomes more diffuse towards the periphery, collisions may still occur, as the dense central region of each bunch overlaps with the less diffuse areas of the other bunch (visualized in Figure 5.26).

When beams are not maximally overlapped, one may observe the effects of both the beta squeeze and the crossing angle, collectively termed the ‘hourglass effect’. The term



(a) The blue beam profile



(b) The yellow beam profile

Figure 5.24: A parameterization of the blue beam profile in  $z$  is shown in Panel (a), with the yellow in panel (b). Included are the resulting fits by parameterizing the profiles with a triple-Gaussian fit, with parameters 2, 5 and 8 referencing the widths of the distributions.

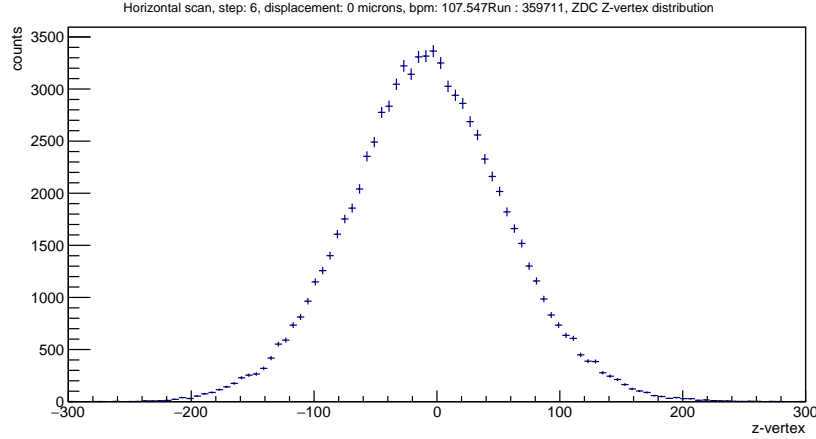


Figure 5.25: Shown: the ZDC  $z$ -vertex collision profile for beams colliding at maximum overlap.

refers to the shape of the zdc  $z$ -vertex profile associated with displaced beams, which looks like an hourglass turned on its side. This effect is most apparent at beam overlap relative to the total transverse beam width. One sees a double-peak structure, which is due to the  $\beta^*$  squeezing parameter and an asymmetry of peak-height which is due to the crossing angle, shown in Figure 5.27.

We cannot recover the parameters to the shape of this distribution with fitting, but we can simulate the collision conditions, and match the simulation to the data. To avoid the pitfalls of overtuning the simulation and recovering the wrong parameters of  $\beta^*$  and  $\theta_{x\text{ing}}$ , I developed a root-finding algorithm which performs a binary search over the parameter space of the simulation (described in Table 5.6) with the Multiple Collisions rate, the crossing angle, and the  $\beta^*$  parameters allowed to vary over a wide range.

Convergence in the simulation is tested by weighting the least-squares difference between the simulation and data by the uncertainty of the data for each  $z$ -vertex bin in the data sample. When the algorithm executes, a clear convergence of the least-squares residual is observed (Figure 5.28), indicating success. Schematically, the simulation is diagrammed in Figure 5.29. The algorithm is halted after fifteen iterations, which is typical of the

Parameter	Description
$\beta^*$	Beam focusing parameter which causes offset beams to follow a dual-peak structure
$\theta_{x\text{ing}}$	The beam crossing angle in the $x$ - $z$ plane relative to the PHENIX coordinate system. Causes an asymmetry in the observed peaks.
$R_{MC}$	Multiple collision rate. Causes scaling of the overall distribution towards the center, at $z = 0$ .
$\sigma_{x,y}$	Transverse beam widths. Along with the beam displacement, effects the threshold separation where $\beta^*$ and $\theta_{x\text{ing}}$ effects are obviously observed by eye
X,Y_OFFSET	The beam offset in the x and y directions. Along with the transverse beam width, these parameters effect the threshold where the hourglass effect can be observed by eye.

Table 5.6: The parameters characterizing the hourglass simulation are described. Though the normalization of the luminosity describing the final  $z$ -vertex profile with a fixed offset depends on many parameters, only parameters shown actually effect the shape of the distribution.

binary search, since each iteration halves the next step in the search domain and after fifteen iterations the step size changes are on the order of 1 part in 100,000.

With the binary search algorithm in place, we may now recover the value for  $\beta^*$ ,  $\theta_{x\text{ing}}$ , and  $R_{MC}$ . Examples of convergent distributions, along with the final best parameters characterizing the shape of the ZDC  $z$ -vertex profile are summarized in Figures 5.30 - 5.33. Though many parameters are shown alongside each simulation, the parameters listed outside of Table 5.6 do not effect the overall shape of the distribution, but can be used to calculate an overall luminosity associated with colliding beams at a fixed offset. Since the luminosity of interest is only when beams are overlapped maximally, these parameters are not used, but are kept for potential future cross-checks.

With a strategy to recover  $\beta^*$  and  $\theta_{x\text{ing}}$ , we may proceed with implementing the corrections for these effects to the total luminosity. This is done separately from the simulation, with the full form of the Luminosity being numerically integrated with all relevant parameters calculated or extracted from the data streams.

The effect of  $\beta^*$  is used to correct total luminosity according to:

$$L \sim \iiint \rho_{blue}(x, y, z, t) \dot{\rho}_{yellow}(x, y, z, y) dx dy dz dt \quad (5.19)$$

$$\rho(x, y, z, t) = \rho(x)\rho(y)\rho(z - ct) \quad (5.20)$$

$$\rho(x_i) = \frac{1}{\sigma(z)_{x_i} \sqrt{2\pi}} e^{-\left(\frac{x_i - x_0}{2\sigma(z)_{x_i}}\right)^2} \quad (x_1 = x, x_2 = y) \quad (5.21)$$

$$\sigma_{x_i}(z|_{z=0})^2 \left(1 + \left(\frac{z}{\beta^*}\right)^2\right) \quad (5.22)$$

$$K_{\beta^*} = \frac{\mathcal{L}_{\beta^* \rightarrow \infty}}{\mathcal{L}_{\beta^*}} \quad (5.23)$$

With Equation 5.23, the effect of  $\theta_{xing}$  used to correct total luminosity according to:

$$\rho(x) \rightarrow \rho(x + \alpha_x z) \quad (5.24)$$

$$\rho(y) \rightarrow \rho(y + \alpha_y z) \quad (5.25)$$

$$K_{\theta^*} = \frac{\mathcal{L}_{\alpha_i=0}}{\mathcal{L}_\alpha} \quad (5.26)$$

Where  $\alpha$ 's represent the crossing angle in the  $x-z$  plane or  $x-y$  plane, and the respective  $\mathcal{L}$ 's represent a calculation of the luminosity with or without the respective change to the bunch geometries  $\rho$ .

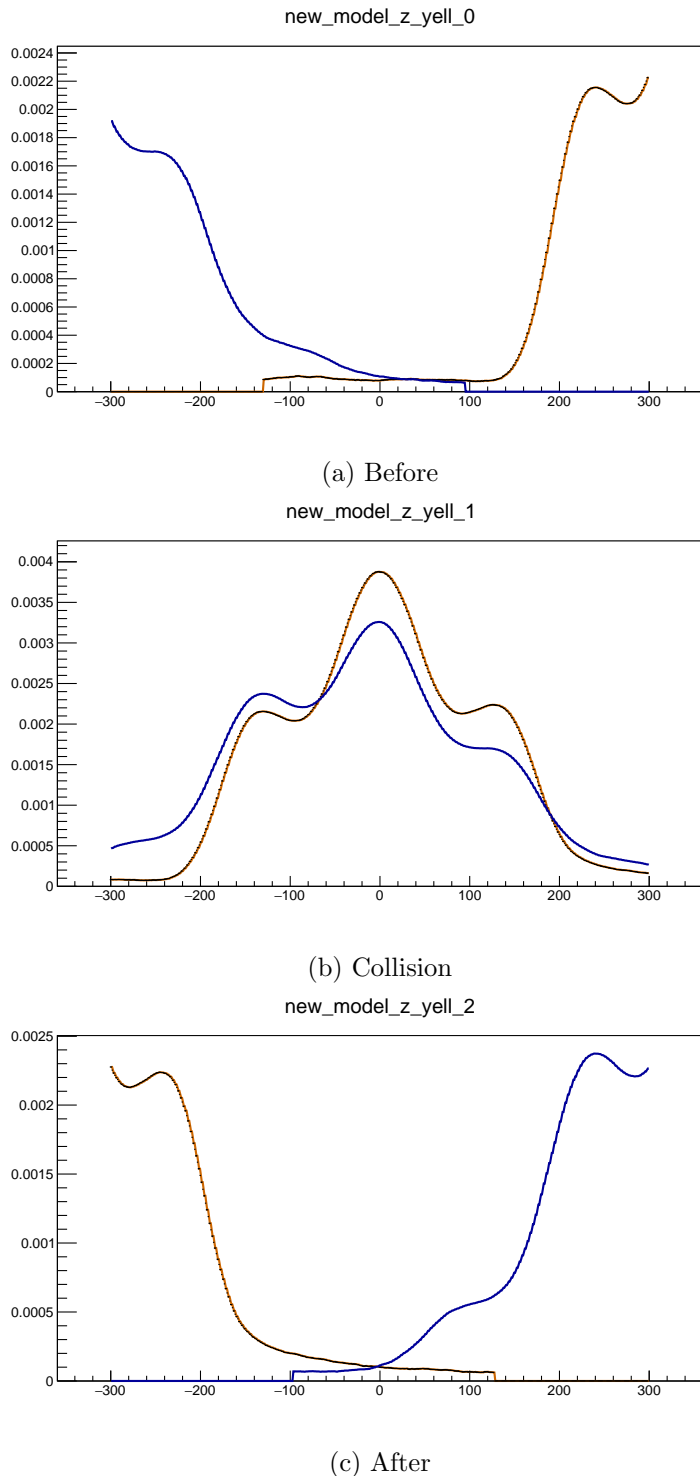


Figure 5.26: Shown: a cartoon of realistic beam profiles before (Panel (a)) collision, during collision (Panel (b)), and after collision (Panel(c)).

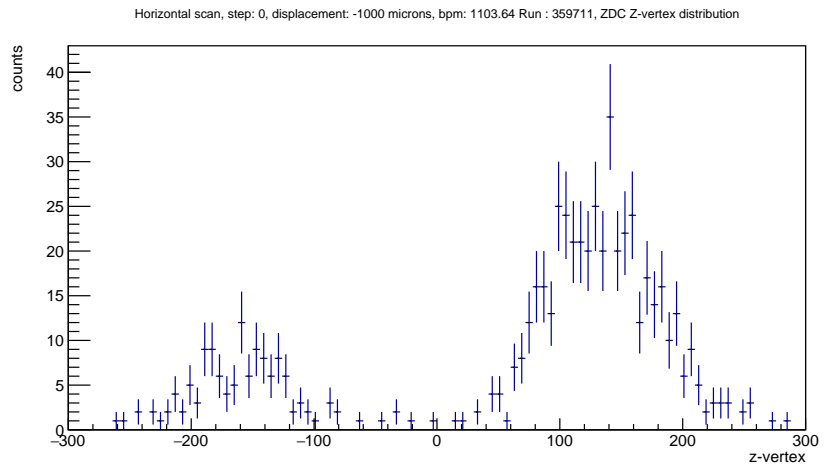


Figure 5.27: Shown: With a large displacement in the beams, the hourglass effect can be seen in the ZDC  $z$ -vertex profile.

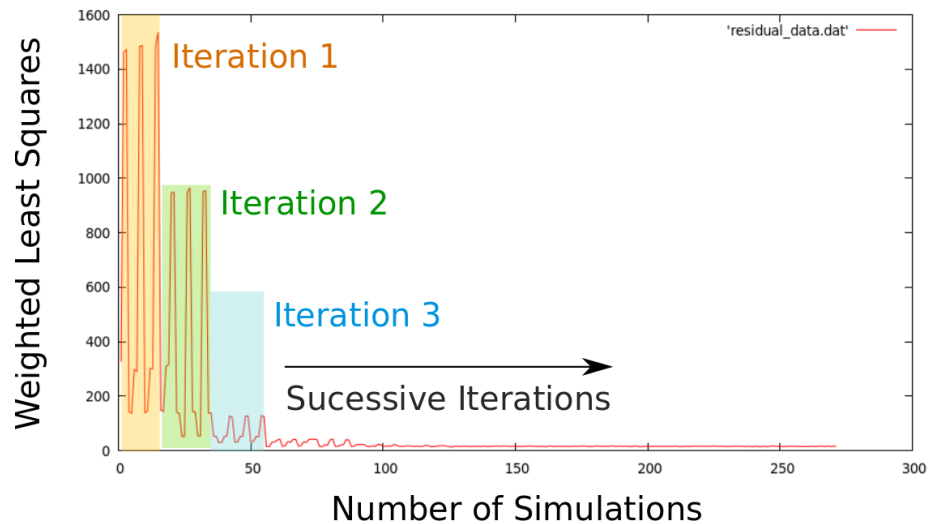


Figure 5.28: The least-squares residual is shown to be converging with each successive iteration of the algorithm. Modulation in the parameter within each iteration is a result of the binary search executing and finding the best set of parameters to keep for the next iteration.

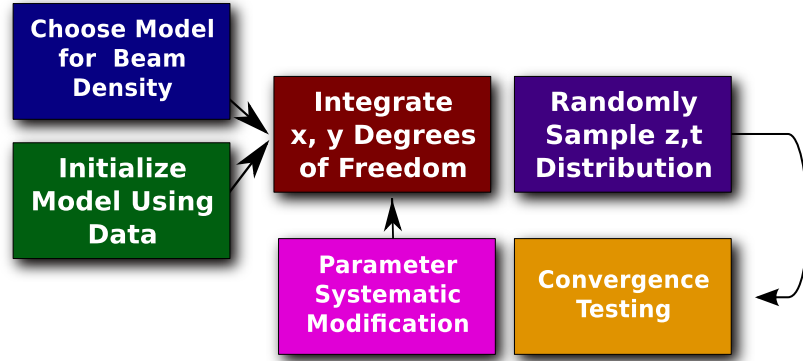


Figure 5.29: The schematic algorithm for the hourglass simulation.

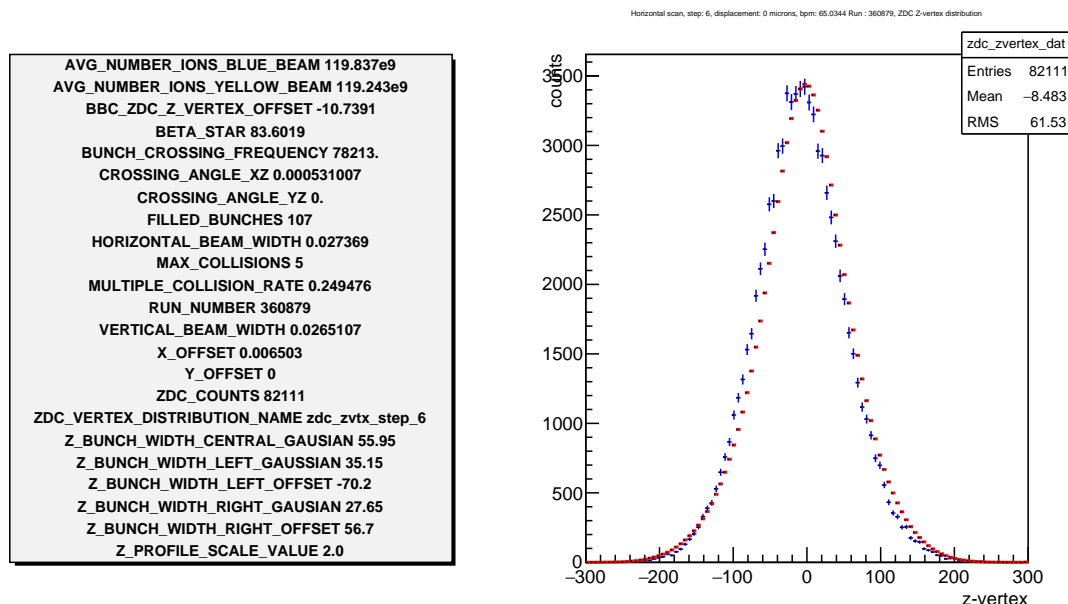


Figure 5.30: Shown: the convergence of the  $z$ -profile simulation after 15 iterations for a  $65 \mu\text{m}$  beam displacement.

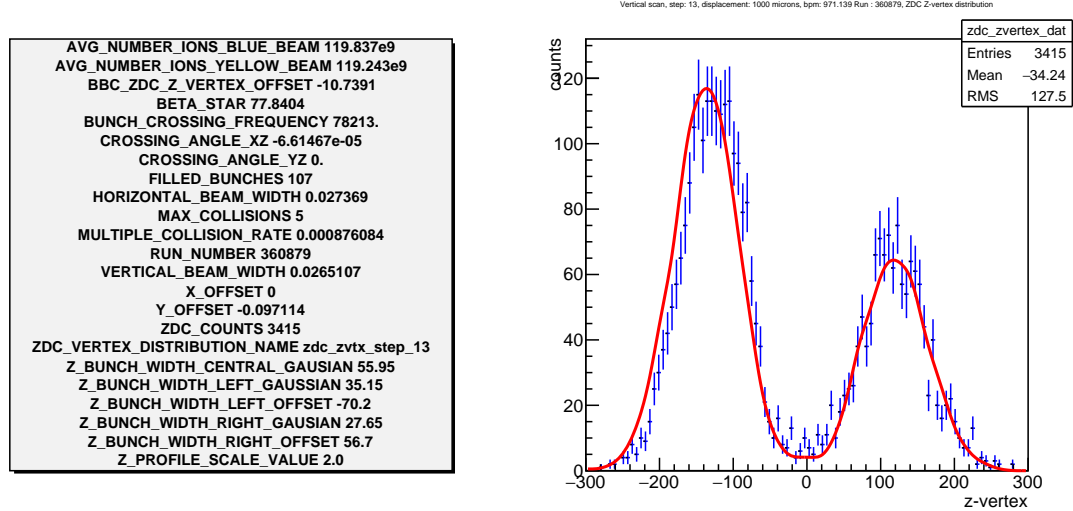


Figure 5.31: Shown: the convergence of the  $z$ -profile simulation after 15 iterations for a  $971 \mu\text{m}$  beam displacement.

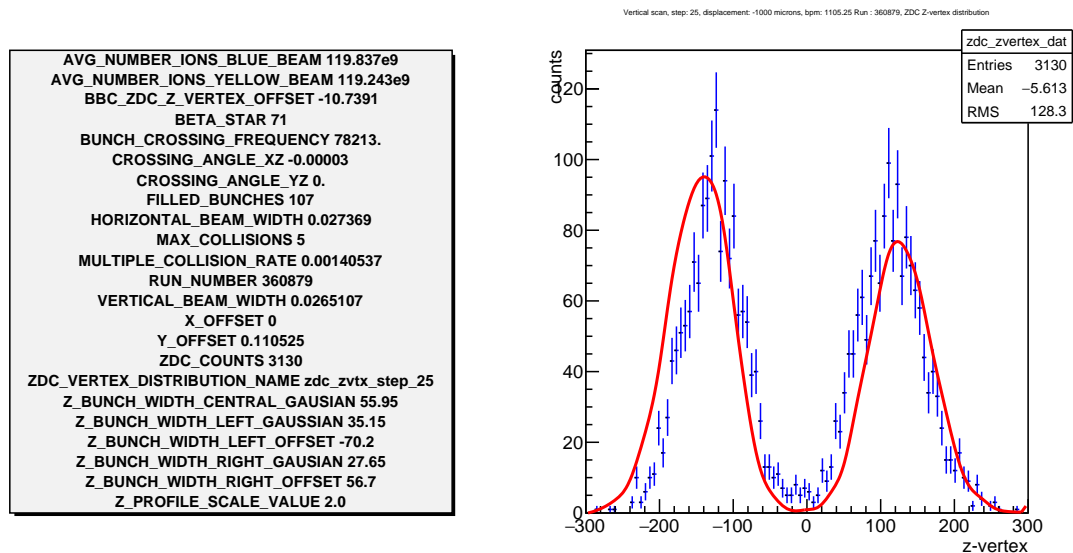


Figure 5.32: Shown: the convergence of the  $z$ -profile simulation after 15 iterations for a  $1105 \mu\text{m}$  beam displacement.

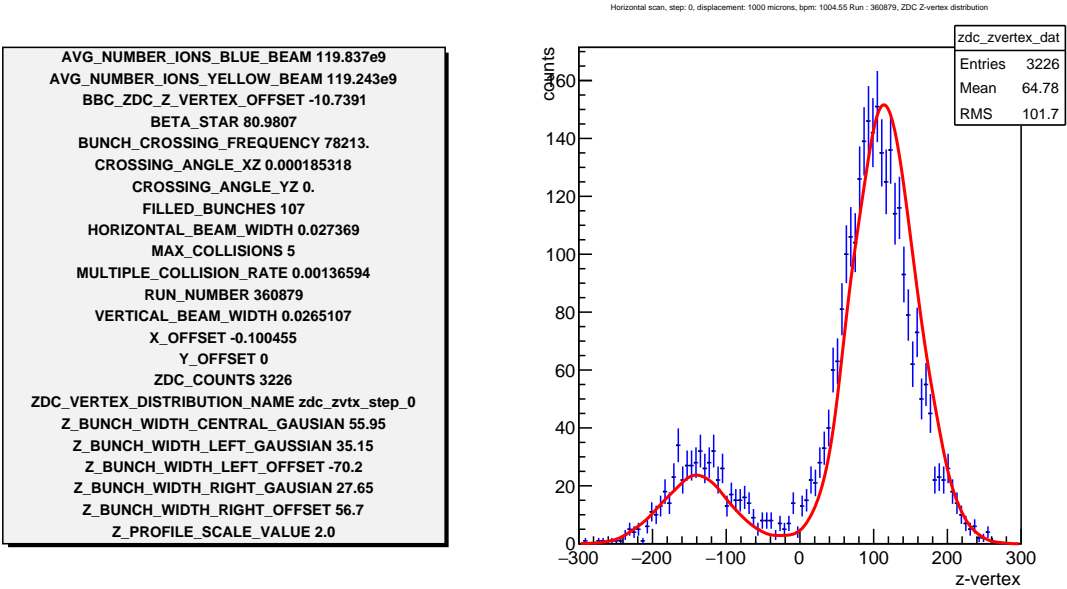


Figure 5.33: Shown: the convergence of the  $z$ -profile simulation after 15 iterations for a  $1004 \mu\text{m}$  beam displacement.

## 5.10 Outlook

Though this vernier analysis is nearly finished, some work remains. Although the analysis was shown for one litmus run, 359711, it must be repeated for all vernier scans in a given data taking year. Though the multiple collisions parameter can be recovered from Section 5.9, it may also be independently calculated, which has been presented in [82]. The correction, following [82], will be done and presented in the coming weeks following this dissertations' publication. The simulations presented in Section 5.9 are still being tuned, in order to determine the sensitivity of the outcome on variations in beam position, before the values for  $\beta^*$  and  $\theta_{xing}$  can be accepted as representative.

Additionally, the final luminosity must be calculated, along with  $\sigma_{BBC}$ . This chapter serves to summarize my work on the vernier analysis, as well as provide a synopsis of my methodology. The vernier analysis is an important analysis that must be done if one is to use the BBC as a luminosity monitor, with current analyses for the 2012, 2013, and 2015 data sets ongoing. to date, the most recent vernier analysis completed was in 2009 [76].

The final analysis of the 2012 data set will be presented in a PHENIX analysis note, which is currently being written.

Finally, the vernier analysis will impact the calculation of the absolute cross section of  $W$  production. This calculation is vital as a cross check to our understanding of the signal to background ratio estimation for  $W \rightarrow \mu$  events, presented in Section 7.4.

## Chapter 6

# Data Analysis

Although we have discussed in detail the theoretical motivations for the W physics program, as well as the machines producing the necessary collisions and recording data produced from these collisions, we have not yet addressed the form of the data set itself, and the substantial engineering it takes to extract the signal of interest out of that data set.

The relative abundance of the  $p + p \rightarrow W^\pm \rightarrow \mu^\pm + \nu$  signal events is rather low, compared to the other interactions which may take place when two protons collide.

The previous chapter how careful triggering is employed in order to ensure that any time this event does occur, it is recorded. This does not guarantee that *only* these events are recorded. Background events are still recorded much more frequently than signal events, even with the improved triggering. We collected  $271 \text{ pb}^{-1}$  of data (15.7 billion events, according to the PHENIX run database) from the 2013 dataset, but there are only 3086  $W \rightarrow \mu$  events, after cuts are made (see Chapter 7). Of this subset, assuming a signal to background ratio of 0.2 (this will be motivated and described in Section 7.4), we are left with only 617 ‘signal events’ out of 15.7 billion total events.

This leads to the substantial problem of extracting the appropriate physics events from the 15.7 billion event background.

PHENIX is a multipurpose detector, and has a long history of probing a variety of physics at a wide range of energy scales. The Muon Arms were originally designed for the reconstruction of much lower energy charmonium dimuon decays, and although the forward upgrade has allows us to collect most of the  $W \rightarrow \mu$  events as part of our total dataset, the task of differentiating very high energy muons from sources of background is challenging. Without a forward nose-cone calorimeter, or substantially more steel absorber in place, we

must resort to statistical methods to differentiate between signal events, and background events. This is described in Chapter 7

## 6.1 Raw Data to Reconstructed Parameters

Any time a PHENIX trigger condition is satisfied, all of the information recorded by the PHENIX spectrometer are read out from temporary on-detector memory, and fed into a data stream that eventually is archived as a ‘PHENIX Raw Data File Format’ or PRDFF.

PRDFF data is hierarchical, first being organized by event-type, and then organized by packet-type. There are many event types—‘DATAEVENTS’ typically carry the information relevant to a physics analysis, whereas other event-types carry very important QA information for determining the status of the RHIC apparatus, the beam, polarization, and PHENIX performance.

Every packet has a header, which contains general information such as what the packet contains, and in what order that packet was received. Every packet recorded can be associated with a unique event-sequence number, which specifies roughly the order in which the event owning the packet was received by the DAQ. Within a given run number, an event-number is guaranteed to be unique. The complexity of the packet is limited by the bandwidth available to move data off PHENIX onto other storage, and the buffers/reconstruction ability of the front end electronics modules built onto PHENIX subsystems. PHENIX archives data from the DAQ at a rate of approximately 700 Megabytes per second—or one compact disk.

Generally, raw PHENIX data is too complex to use straight-away, because minimal to no reconstruction of physical properties for a certain event is done, due to hardware limitations and time limitations—some of this raw data is often directly used in triggering decisions, which must be made once every 106 nanoseconds or faster (the bunch crossing frequency).

The raw data collected from PHENIX undergoes a process called “Data Production”, where physical parameters are reconstructed from the simpler raw data. Raw data could take any form—for example—which cathode strips were activated in an event in the muon tracker, or, the number of photons counted in a photomultiplier tube. This information is often combined with extensive survey information about the geometry of a given

detector, the known magnetic field in a detector, to reconstruct quantities such as momentum, or deposited energy.

Once reconstruction has finished in a Data Production, the data are then repackaged into ROOT files, often times internally structured into custom output objects which are associated with a specific detector. These output objects are simply custom C++ classes which have a serialization scheme, which have libraries and dictionaries compiled that allow for them to be serialized into ROOT’s file format.

For the purposes of this analysis, all data has been reconstructed and serialized into a specific type of output object called a ‘picoDST’ or even more concisely, ‘pDST’. This name, like many others in PHENIX has historical context: DST stands for ‘Data Summary Tape’ hearkening back to the days when data was stored primarily on magnetic tape (it is still archived on magnetic tape!), and ‘pico’ because of its relatively small disk-space requirement, compared to ‘nanoDST’ files or simply ‘DST’ files, which contain more granular information.

## 6.2 Choosing Analysis Variables

Even data reduced to the point of a pDST contains a rich and comprehensive array of features describing the data—far more than what was ultimately used in this analysis. This was largely pragmatic—one can characterize the data streaming from our detectors in many ways, and detectors themselves can be highly granular, with each functional piece of a detector producing a stream of data.

Rather than assuming from the outset that we know which variables will provide the most analyzing power, we observe a variety of data, and perform studies to determine which combination of variables offers the maximum analyzing power.

The only variables which are truly relevant to this analysis need to be relevant to understanding two questions:

1. *Is this reconstructed muon track the result of a real W Boson Decay?*
2. *What is the polarization of the two colliding protons for every recorded collision?*

To properly answer these questions, one needs to comprehensively understand what processes are capable of producing muons, as well as whether or not our detector can be ‘tricked’

by signals which look like muons, but really aren't. Secondly, there must be a means of recovering the proton spin polarization for each colliding bunch-pair.

The variables used in this analysis are summarized in Tables A.1,A.2, A.3 and A.4. When Cartesian coordinates are referenced, implicitly, the reference frame is the PHENIX Coordinate system (Figure 4.13).

### 6.3 Beam Polarization

Polarization recovery is relatively straight-forward. Each event is uniquely mapped to a specific colliding bunch (1,2,...,120). In turn , known ‘spin patterns’ are applied to each fill, which maps polarization direction to each bunch.

As discussed previously (Section 4.3), quality assurance apparatuses are in place to ensure the advertised spin pattern is the same as that delivered. Since polarization patterns do not typically change in a standard physics beam fill all that is needed is to associate a PHENIX run number, with a RHIC fill number, and then look up the spin pattern a database. If problems were found in the spin pattern during data taking, or later after scrutiny, the associated data is discarded. The overall beam polarization percentage is an important factor, which dilutes any spin asymmetry, but this is taken into account in the final spin database QA analysis [83], the results of which are summarized in Section 8.2.

We are left with the challenging task of differentiating between signal  $W \rightarrow \mu$  events from other  $X \rightarrow \mu$  events. This requires that we engineer features from the data set which are sensitive to the difference between signal and background. This task is challenging because the reconstruction characteristics of our detector make it difficult to differentiate between signal and background without employing sophisticated statistical models to sort our data set (Section 7.3).

### 6.4 Data Analysis

The thrust of the Data Analysis portion of this work is to separate the real W-genic muons from all other muon candidates. This requires some substantial feature engineering, creating statistical models, and a means of evaluating the performance of these statistical models. Validating our model can be difficult because since it requires a labeled data set. One way of model validation employs simulating the entire data set, thus providing every

muon track with a label, and applying the statistical model to this simulated data set. This analysis was presented in [31], lending confidence to our results.

#### 6.4.1 Variables Related to Likelihood Selection

In the first stage of the analysis, the variables used are: DG0, DDG0,  $DCA_r$ ,  $\chi^2$ ,  $Rpc1DCA$ ,  $Rpc3DCA$ ,  $fvtx_{dr \times d\theta}$ ,  $fvtx_{d\phi}$ , and  $fvtx_{cone}$ . These variables are all related to track reconstruction, and were chosen because they offer the most analyzing power in differentiating between signal events and background events. Schematically, the variables are described in Figure 6.1 and 6.2. These variables are chosen to be used in the Likelihood Event Selection, which is described in Section 7.3. Likelihood event selection us used as an secondary cut on data, after the basic cut, described in Section 7.1.

Muon tracks are reconstructed by essentially connecting the dots between ‘hits’ recorded at each station of the Muon Tracker. The lines connecting these hits are called ‘roads’. Following this, the roads and hits are used to generate a curve fit to the data, given knowledge of the muon tracker’s radial magnetic field. This curve, with knowledge of the Muon Trackers’ magnetic field, is used to obtain the charge and momentum of tracks. Subsequently, variables are constructed to describe the difference between the reconstructed curve, and the ‘connect the dots’ roads. The smaller these differences are, the more straight the track is, and as discussed, straightness points to higher momentum, which ultimately leads to labeling as a W-genic particle, if the momentum is in the correct range.

##### 6.4.1.1 DG0 and DDG0

As seen on the left of Figure 6.1, DG0 and DDG0 (Figure 6.3) are variables defined relative to the reconstructed muon track, and the road through the MUID. Concretely, the angle that the reconstructed track makes with the road at station 0 of the MUID defines DDG0, while the absolute distance between the track and road at MUID station 0 defines DG0. High momentum tracks, with less bend are correlated with both of these variables being small. Because DG0 and DDG0 are necessarily correlated, they require special treatment in the analysis, which is described fully in Section 7.3.

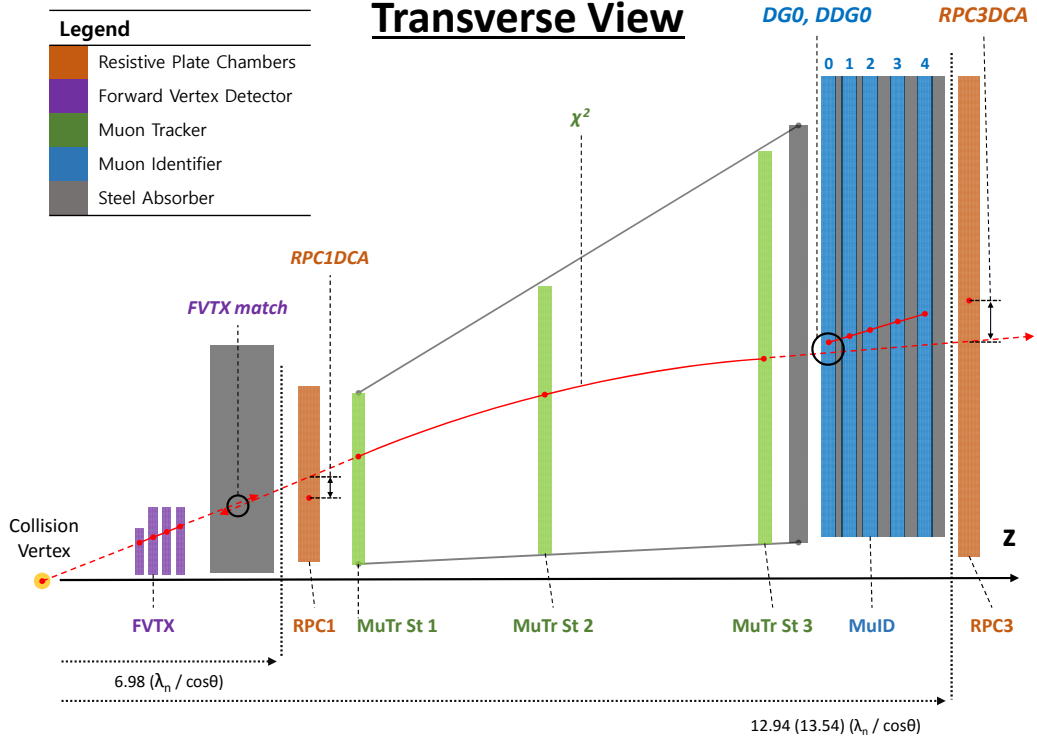


Figure 6.1: Shown: A transverse-view of the FVTX, RPCs, MuTR, and MUID, with variables engineered from track reconstruction (track shown as red arc from yellow collision point on left) [29]

#### 6.4.1.2 $DCA_r$ , $\chi^2$ , $DCA_z$

The ‘distance to closest approach’ ( $DCA_r$ ) and ‘distance of closest approach z’ ( $DCA_z$ ) are shown on the left of Figure 6.2.  $DCA_r$  is defined to be the distance between the reconstructed track and the beam axis in the transverse direction, measured at the collision vertex.  $DCA_z$  is defined similarly, except the relative distance interval is between the collision vertex and the track’s z-position at the point where  $DCA_r$  is evaluated. These distances are useful for evaluating the reconstructed track’s probable origin. The closer to the primary event vertex, the better, as the  $W$ -Boson is an interaction associated with the primary event vertex.  $\chi^2$  is the reduced chi-square associated with the quality of track fitting. The chi-square is the resulting parameter from the Kalman filter based on the

## Beam view

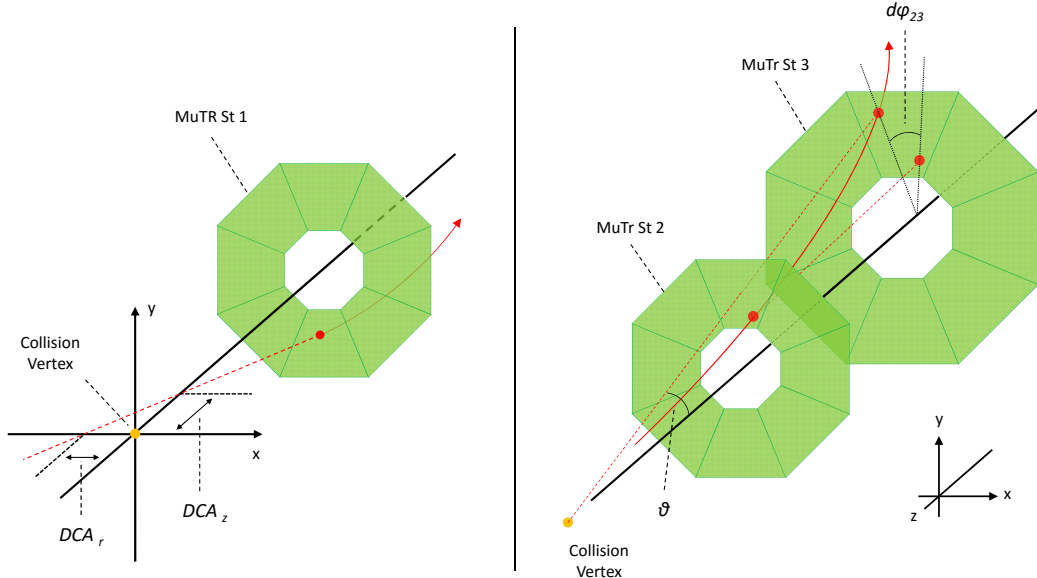


Figure 6.2: Shown: A beam-view of the MuTR tracking planes with additional variables engineered from track reconstruction [29].

'residuals between the measured coordinate of the cathode planes' of the Muon Tracker after taking into account position resolution and energy losses [25].

Because DCA<sub>r</sub> and  $\chi^2$  are correlated, they require special treatment in the analysis, which is described in Section 7.3. Grouped for correlation

### 6.4.1.3 RPC Variables

Rpc1DCA, Rpc3DCA refer to the distance of closest approach at RPC station 1 and station 3, of the linearly extrapolated track to the closest RPC strip associated with a hit-cluster on the RPC. These variables are shown at the position of the RPC1 and RPC3 in Figure 6.1.

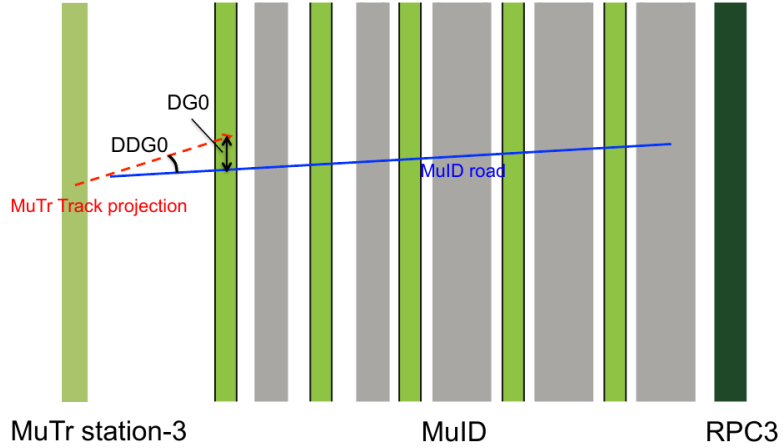


Figure 6.3: A schematic representation of track-matching variables DG0 and DDG0 at the intersection between the Muon Tracker and Muon Identifier [25].

#### 6.4.1.4 FVTX Tracking

The Forward Vertex Detector provides additional tracking information which can be used to identify events that originate from secondary decays, outside the primary event vertex.  $fvtx_{dr \times d\theta}$  is the product of two FVTX tracking variables,  $fvtx_{dr}$  and  $fvtx_{d\theta}$ . The product is taken to reduce the dimensionality of the variable set, because the two quantities are highly correlated. The FVTX hits are matched to the reconstructed Muon Track, with  $fvtx_{dr}$  representing the residual between the reconstructed FVTX track and the reconstructed Muon Tracker track in the transverse direction, with  $d\theta$  and  $d\phi$  representing the residuals of similar matching in the canonical  $\phi$  and  $\theta$  directions. These variables are summarized in Table A.3.

The tracking variables discussed above all characterize the reconstruction of muon tracks. These variables were chosen due to their sensitivity to differences in muon tracks likely resulting from  $W$ -Boson decays versus other sources. This is exploited by generating probability distributions associated with each variable in order to calculate the likelihood of a track originating from a signal event, or a background event, discussed in Section 7.3.

#### 6.4.2 Variables Related to Signal to Background Ratio Extraction

In the second phase of the analysis,  $dw_{23}$  and  $\eta$  are employed.  $dw_{23}$  is associated with the bending of the reconstructed muon track in the Muon Tracker volume, and is

referred to as “reduced azimuthal bending”. The distribution of  $\eta$  is expected to have distinct distribution, which differs based on the track source— $W$ -Boson decay, other real muons, and hadronic decays in the Muon Tracker volume which are reconstructed as muon tracks. Due to  $dw_{23}$  and  $\eta$  being both relatively uncorrelated to each-other, as well as the other variables, one can avoid biasing our statistical models by effectively over-weighting with correlated variables.

$dw_{13}$ ,  $dw_{23}$  are shown schematically in Figure 6.2 and are constructed from  $d\phi_{13}$ , and  $d\phi_{23}$ .  $d\phi_{ij}$  is taken as the azimuthal bending of the track between stations  $i$  and  $j$ .  $\phi_i$  is calculated from the  $x$  and  $y$  coordinates of tracks passing through Station  $i$  of the Muon Tracker:

$$\phi_i = \tan^{-1} \left( \frac{ySta_i}{xSta_i} \right) \quad (6.1)$$

$dw_{ij}$  is constructed from  $d\phi_{ij}$  as follows:

$$dw_{ij} = p_T \times \sin(\theta) \times d\phi_{ij} \quad (6.2)$$

Equation 6.2 is a proxy for the amount of bending of a track between stations  $i$  and  $j$ , which is strongly correlated to the momentum of the track.

A common theme amongst these variables is that they should help us distinguish between high momentum muon tracks from  $W$  Bosons, and other muon tracks. The procedure depends on the expectation that  $W$ -genic muon tracks are kinematically restricted to have a relatively narrow momentum distribution. Tracking variables can be used to partially differentiate between signal and background events.

In general,  $W$ -genic events will be mostly straight, geometrically, and so this constrains the values of variables such as  $DCA_r$  substantially, and other variables less so. Thus,  $dw_{23}$  should be a good discriminator, as it depends on  $p_T$  and the azimuthal bending of the charged tracks, due to the radial magnetic field in the MuTR.

Our secondary requirement of our variables is that they are relatively uncorrelated with each-other, to leave plenty of room for statistical modeling. Ultimately, a subset of the available tracking variables are used to carry out the analysis, in two stages. The correlation of variables for both data and simulation are summarized in Figure 7.2.

Since we are interested in recovering forward rapidity  $\mu+$  and  $\mu-$ , and backward rapidity  $\mu+$  and  $\mu-$  which result from  $W$ -Boson decay, we partition the dataset into these four categories, and perform the analysis on each category in parallel.

The data are further subdivided based on the available track matching variables for a given event. Not all tracking variables are available for every reconstructed track, because not all detectors have been triggered in the same way for every event. This is further discussed in Chapter 7.

## 6.5 Efficiencies

As discussed in Section 4.4.2 and Section 4.5.3, particles interact with detectors, and this interaction is transduced and used for either triggering and for reconstructing the properties of particles. Detectors, and triggers constructed from the transduced signals in detectors do not operate with 100% efficiency. A requirement for measuring cross-sections is to understand the efficiency of these triggers and detectors, so that properly normalized yields may be measured for various processes. The triggers used for the extraction of the  $W \rightarrow \mu$  process have been optimized to obtain the maximum signal yield within the bandwidth allocated to the DAQ, with minimal losses due to inefficient triggering. Due to the geometry of the detectors, the triggers used in this analysis are more efficient in some pseudo-rapidity ranges, and less in others. Additionally, the various triggers used for this particular analysis (Table 6.1) do not share the same rapidity coverage, so the calculation of the overall triggering efficiency is non-trivial. This analysis of detector and trigger efficiencies are reproduced from [30]. Additional related plots and tables are saved for Appendix C.

Bit Number	Trigger Name
9	SG3&MUID_1H_N  S
16	((MUIDLL1_N2D  S2D)  ((N1D&S1D))&BBCLL1(noVtx)
17	(MUIDLL1_N1D  S1D)&BBCLL1(noVtx)
18	RPC1+RPC3_S
19	RPC1+RPC3_N
20	SG3&RPC3&MUID_1D_N  S
21	SG1+RPC1(C)&MUIDLL1_N  S
22	MUON_S_SG1_RPC3A&MUID_S1D
23	MUON_N_SG1_RPC3A&MUID_N1D
24	MUON_S_SG1&BBCLL1(noVtx)
25	MUON_N_SG1&BBCLL1(noVtx)
26	MUON_S_SG1_RPC3_1_B  C
27	MUON_N_SG1_RPC3_1_B  C

Table 6.1: Shown: the triggers sensitive to  $W$  boson muonic decay [30]

## 6.6 Rate Dependence of Detector Response

## 6.7 MuID hit efficiency

In this analysis, there was a clear degradation of the MuID hit efficiency with respect to the beam luminosity. The MuID hit efficiency is calculated based on HV groups (described in 6.4). MuID tube efficiencies are assumed to be uniform within the same HV group. Figure 6.4 shows the structure of MuID HV groups. The MuID consists of five gaps per arm, and each arm has two planes (horizontal and vertical planes).

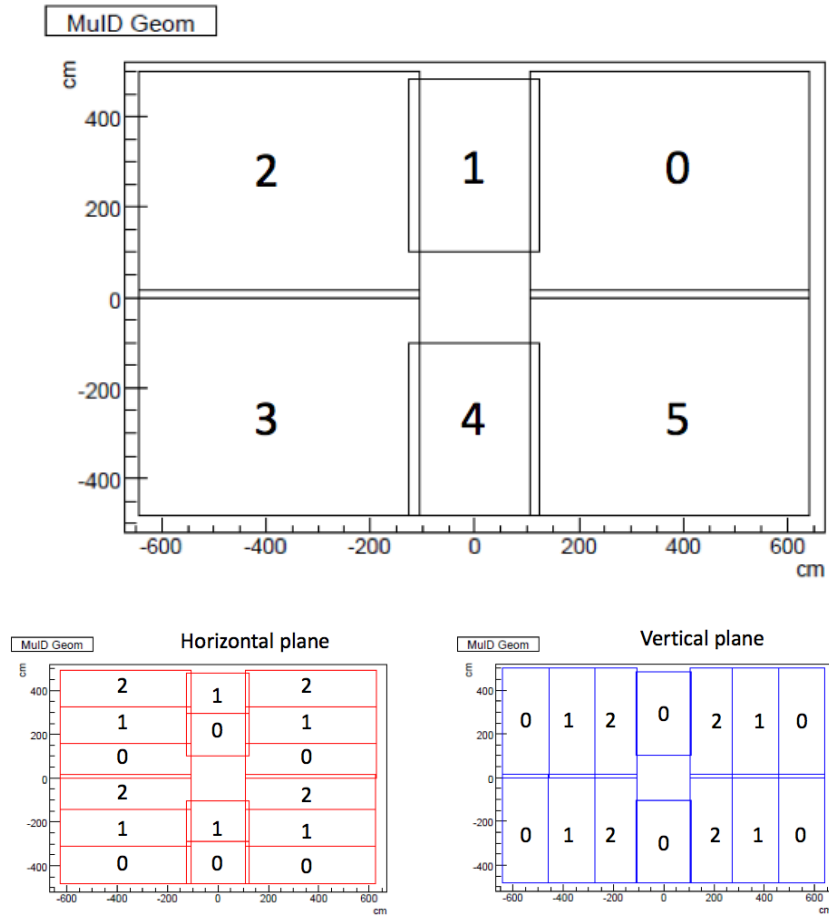


Figure 6.4: The top plot shows panel numbering scheme. Each plane has six panels. The bottom plots show the structure of hv groups for each horizontal and vertical plane [30].

The MuID hit efficiency is defined as:

$$\text{Efficiency}_{\text{iplane}} = \frac{\text{hit in iplane}}{\text{MuTr tracks which require MuID road finder and trigger emulator}} \quad (6.3)$$

The following cut is applied to select event samples:

- Distance between MuID road and MuTr track  $< 20.0 \text{ cm}$
- Absolute  $p_z > 1.3 \text{ GeV}/c$
- Hits in both planes in a gap

An example of the MuID hit efficiency is shown in Figure 6.5 here, with the remaining hit studies saved for the appendix from Figure C.1 to C.20. Hit efficiencies are calculated for data partitioned into north or south arm, positive or negative charges, for each gap and plane. In all cases, the efficiencies are compared between the 2011, 2012 and 2013 data sets.

## 6.8 MuTR Hit Efficiency

The MuTR hit efficiency requires some adjustment due to its discrepancy between stereo and non-stereo planes in the same gap. The total hit efficiency is redefined as the base efficiency used as one of the input parameters for PISA simulation. The other parameter is the asymmetry between widths of the MuTR planes, which comes from the charge difference between two cathode planes in a gap. The luminosity dependence of hit efficiency have been determined from the forward analyses in 2011 and 2012, and similar dependence is present in the 2013  $W \rightarrow \mu$  analysis. The method for recovering the hit efficiency developed for the 2011 and 2012 data sets is applied for this analysis as well. The hit efficiency is cross-checked by looking at the hit in each plane of MuTR directly. The details of the method used in this analysis are described in detail in [84].

To calculate MuTr hit efficiencies, one assumes uniform detector performance and symmetry between two planes in a gap. Two probabilities are defined,  $p_1$  and  $p_2$ .  $p_1$  characterizes the probability of a hit in one MuTr plane ‘OR’ another MuTr plane, while  $p_2$  characterizes the probability that one MuTR gap does ‘NOT’ have a hit ‘OR’ another gap does have a hit. Using these two probabilities, the gap and plane efficiencies are written:

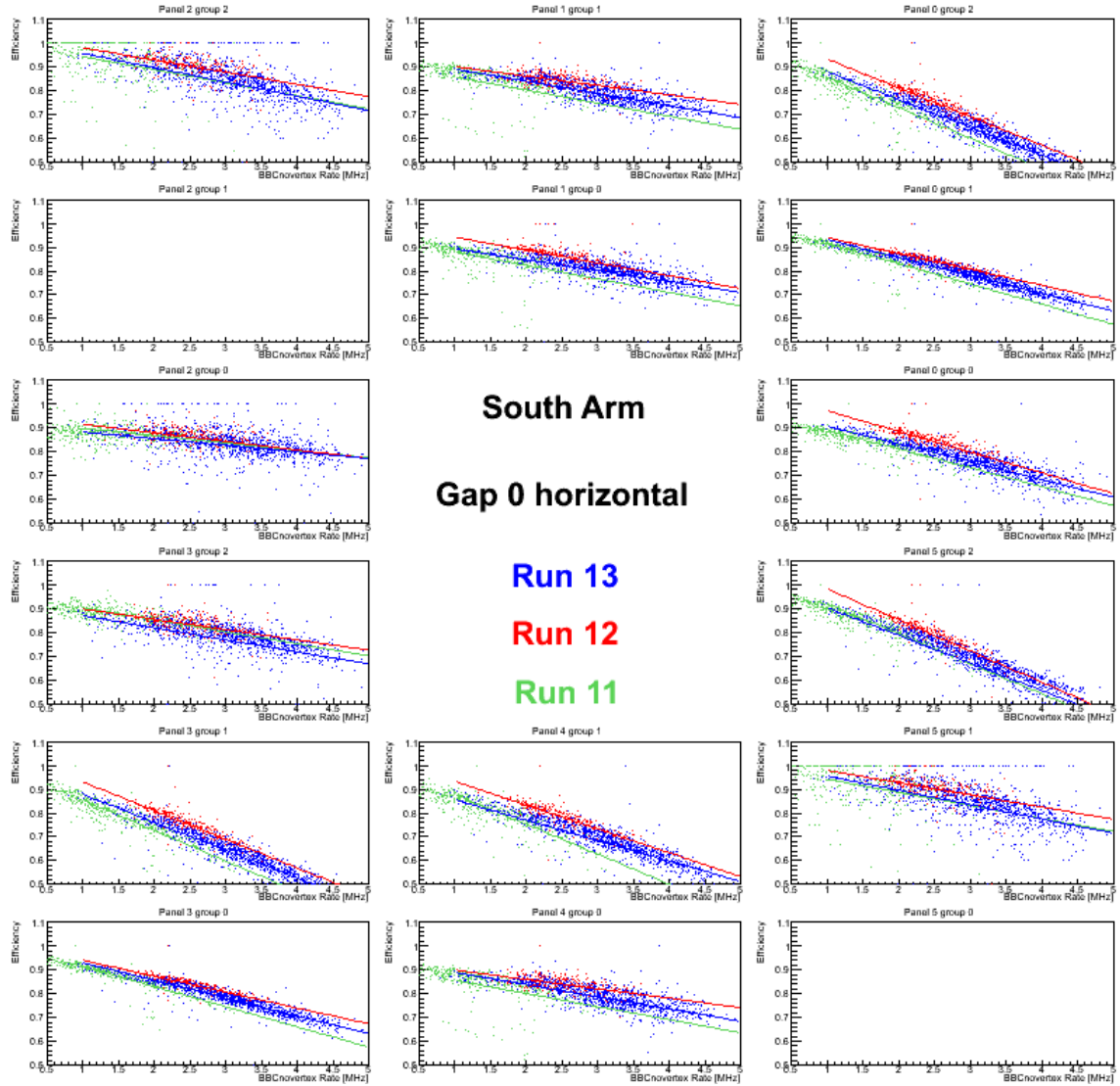


Figure 6.5: MuID hit efficiency of south gap0 horizontal plane, for the 2011 data set (green), the 2012 data set (red) and the 2013 data set (blue) [30].

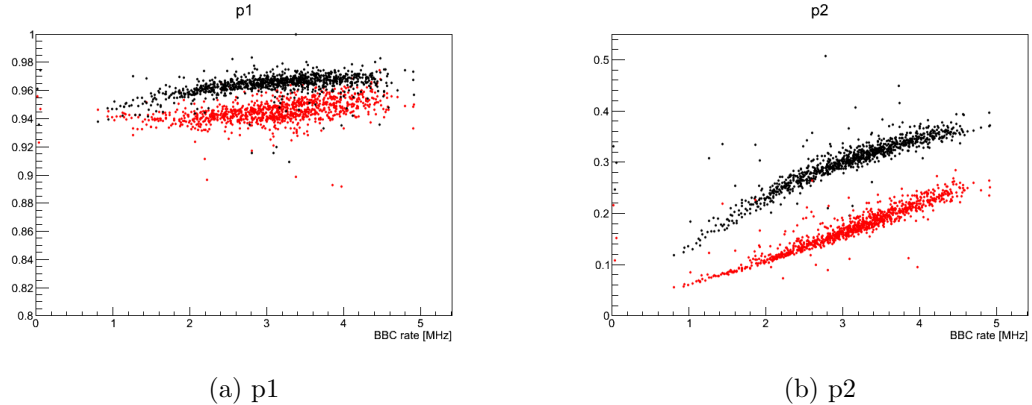


Figure 6.6: Panel (a): The probability to have OR hit in a gap. Panel (b): The probability that a gap does not have a hit in one plane when there is OR hit in a gap. Both: The red points are for south arm, and black points are for north arm in both plots [30].

$$P_k = {}_n C_k P_1^k (1 - P_1)^{n-k}, (0 \leq k \leq n) \quad (6.4)$$

$$P_i = \sum_{\frac{i}{2} \leq k \leq i} {}_n C_k P_1^k (1 - P_1)^{n-k} {}_k C_{2k-i} (1 - P_2)^{i-k} P_2^{2k-i}, (k = \text{integer}, k \leq n) \quad (6.5)$$

where  $k$  is the gap number, and  $n$  is the total number of gaps per arm. Binomial fitting is performed with the above equations with respect to the plane hit distribution to obtain the parameters  $p1$  and  $p2$ . Figure 6.6 shows run by run distributions of  $p1$  and  $p2$  as a function of the BBC(noVtx) trigger rate.

Gap efficiency is additionally defined to have hits in both planes and plane efficiency using the parameter  $p1$  and  $p2$ . The correlation between two efficiencies becomes weaker as the luminosity increases as shown in figure 6.7.

$$[b]\epsilon_{Gap} \equiv p_1(1 - p_2) \quad (6.6)$$

$$\epsilon_{Plane} \equiv p_1(1 - \frac{p_2}{2}) \quad (6.7)$$

The parameters, base efficiency and asymmetry width are obtained, and subsequently used to tune yields for simulations. These parameters, base efficiency and asymmetry width additionally depend on the rate of multiple collisions,  $\mu$ .

South Arm:

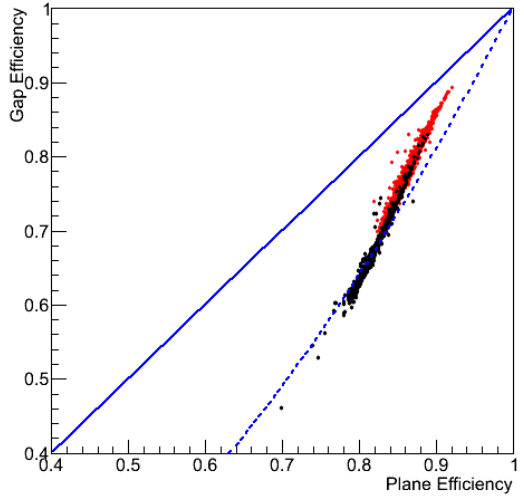


Figure 6.7: Shown: The correlation plots between gap efficiency and plane efficiency. The red points are for south arm, and black points are for north arm. The blue solid line indicates the full correlation, while the blue dashed line represents there is no correlation between two efficiencies [30]

- Base efficiency =  $0.9725 - 0.0526\mu + 0.0275\mu^2$
- Asymmetry width =  $0.3472 + 1.070\mu - 1.282\mu^2 + 3.213\mu^3$

North Arm:

- Base efficiency =  $0.9534 - 0.0084\mu - 0.1307\mu^2$
- Asymmetry width =  $0.4322 + 0.0355\mu + 3.763\mu^2 - 1.425\mu^3$

## 6.9 Single Muon Trigger Efficiencies

Reconstructed muon tracks above 16 GeV in the signal region ( $W_{ness} > 0.99$ ) are shown in Figure 6.8, with all muon tracks plotted, and additionally shown as relative yields in Figure 6.9.

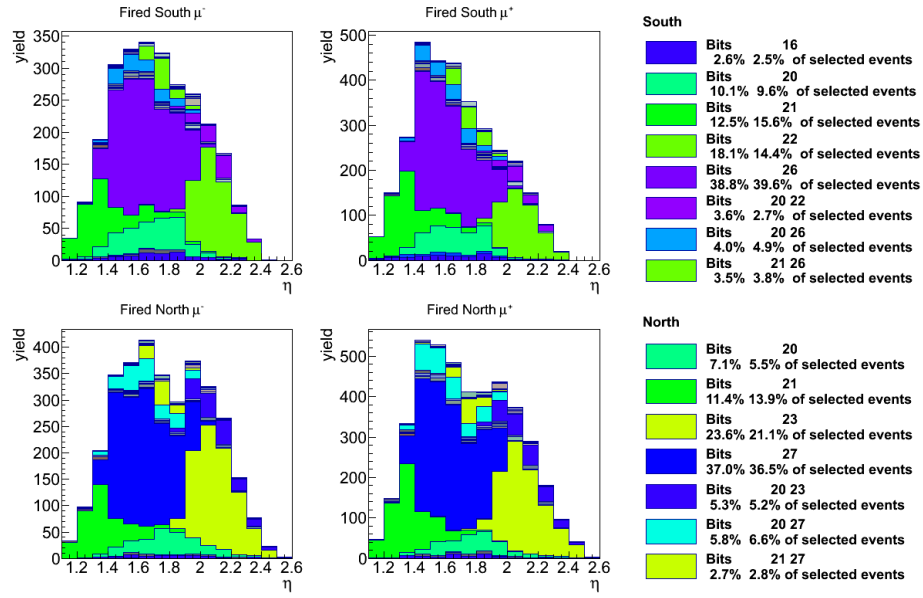


Figure 6.8: Shown: Absolute yields in the  $W \rightarrow \mu$  candidates separated by arm and charge for various muon triggers as a function of rapidity. Those with substantial contributions are given in the Legend to the right for each arm including their total fraction [30].

Apart from the primary physics trigger the (SG1 styled triggers, Table 6.1), other triggers also contribute significantly to the  $W$  candidate yield. These triggers are:

- Trigger bit 21 (referred to as the RPC1C trigger)
- Trigger bits 22 and 23 (referred to as the RPC3A trigger)
- Trigger bit 26 and 27 (referred to as the RPC13BC trigger)
- Trigger bit 20 (referred to as SG3RPC3)
- Trigger bit 15 (referred to as 2D)

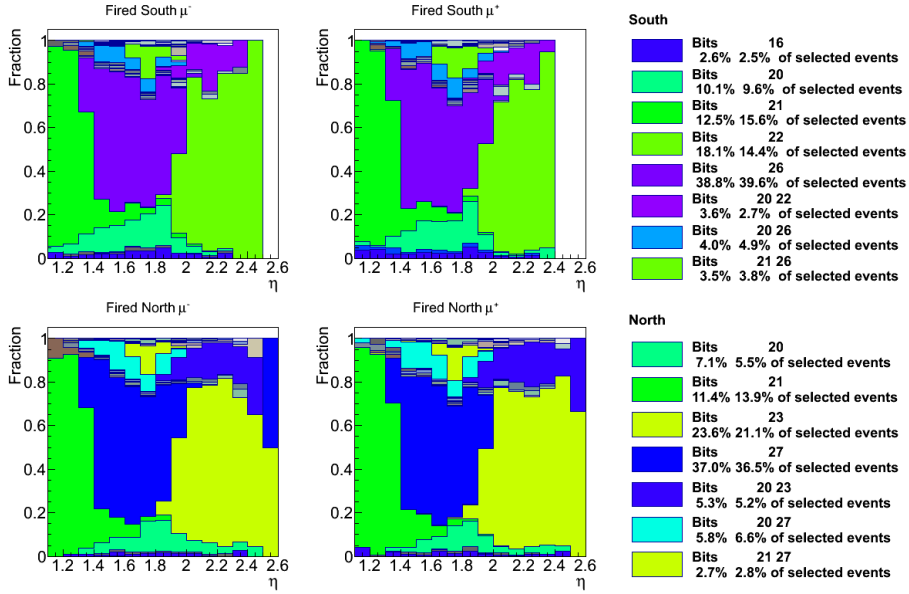


Figure 6.9: Shown: Relative yields in the  $W \rightarrow \mu$  candidates separated by arm and charge for various muon triggers as a function of rapidity. Those with substantial contributions are given in the Legend to the right for each arm including their total fraction [30].

Furthermore one clearly sees the effect of the different trigger acceptances related to the RPC1C, RPC13BC and RPC3A on the efficiency. As it is common for more than one muon trigger to fire after a collision, one cannot exclusively assign one trigger to that event. In order to obtain correct trigger efficiencies for such events, all possible muon trigger combinations are treated separately. The combinatorics of this process result in 86 different combinations for triggered events for a given muon candidate. Even so, the majority of triggered candidates come from single or double triggers as shown in Figures 6.8 and 6.9.

## 6.10 Reference data sets and method

In order to evaluate the trigger efficiencies for each of the trigger bit combinations mentioned above data samples not triggered by the triggers in question are needed. The most independent samples are those triggered either by triggers in the MPC, triggers in the ERT or Minimum Bias triggers. These various triggers do exist as separated streams on the Taxi and were thus directly used to evaluate the efficiencies.

The triggers used in the evaluation relate to:

Bit	Trigger Name	ERT	MPC	Minbias
0	BBCLL1(>0 tubes)	X	X	O
1	BBCLL1(>0 tubes) novertex	X	X	O
3	BBCLL1(noVtx)&(ZDCN  ZDCS)	X	X	O
4	BBCLL1(>0 tubes) narrowvtx	X	X	O
6	ERT_4x4b	O	X	X
7	ERTLL1_4x4a&BBCLL1(noVtx)	O	X	X
8	ERT_4x4c&BBCLL1(noVtx)	O	X	X
10	ERTLL1_E&BBCLL1(narrow)	O	X	X
12	MPC_B	X	O	X
13	MPC_A	X	O	X
14	MPC_C&ERT_2x2	X	O	X
15	(MPCS_C&MPCS_C)  (MPCN_C&MPCN_C)	X	O	X

where “O” corresponds to a matching trigger for that data set and “X” corresponds to a not matching trigger.

The trigger efficiencies for triggers which do not include the 1D triggers can be evaluated directly, while those including the 1D triggers additionally require the multiplication of the 1D efficiencies from the other samples. The corresponding 1D trigger efficiency is then applied when combining all triggers and efficiencies into a total trigger efficiency used for the  $W$  candidate data sample.

The extraction strategy compares for each trigger bit  $a$  in question the number of good candidate muon events with the particular trigger bit live with the total number of good candidate muon events in the particular data sample (Reference trigger):

$$\epsilon_{\text{Trigger}a} = \frac{(\text{muoncandidate})_{\text{Referencetrigger}} \&\& (\text{Triggeralive})}{(\text{muoncandidate})_{\text{Referencetrigger}}} . \quad (6.8)$$

The trigger efficiencies after the Basic Cut (Section 7.1) can still depend on muon rapidity,  $p_T$  and  $W$  likelihood ratio. Ideally a three-dimensional binning would properly address all those potential dependencies, but the statistics are not sufficient to evaluate the trigger efficiencies up to the high  $p_T$  and  $W$  likelihood ratios required for the final  $W$  selection. Therefore various aspects are studied in lower dimensional binning with slightly less stringent cuts. After, one extrapolates to the signal region. Different ways of extrapolating

to the region of interest will then be compared and systematic errors on the total trigger efficiencies will be assigned based on their comparison.

### 6.10.1 Rapidity Dependent Efficiencies

The first set of efficiency studies uses a fine rapidity binning of 15 equidistant bins with  $1.1 < |\eta| < 2.6$  and a minimum  $p_T$  of 5 GeV and a  $W_{ness}$  of above 0.9. The corresponding efficiency distributions separated by arm, charge and trigger. An example is shown in Figure 6.10(Trigger: (((MUIDLL1\_N2D||S2D)|(N1D&S1D))&BBCLL1(noVtx)), with remaining Figures produced in the Appendix from Figure C.21 - to Figure C.31. One sees, that the 1D trigger is mostly equally efficiency at all rapidities with maybe a hint of decreasing efficiencies at higher rapidities.

The same is true for the SG1 triggers (bits 24/25) which also have consistent efficiencies. The trigger bits 18 and 19 which are highly prescaled to reflect the combined acceptances of the RPC1 and the RPC3. Thus, bits 18 and 19 are only efficient from  $1.4|\eta|2.0$  and have decreasing efficiency for increasing rapidity. Also, the production triggers RPC13\_BC (bits 25/26) show the same rapidity dependence and are mostly efficient over  $1.4|\eta|2.0$ . The SG3RPC3 triggers have a flat efficiency above the acceptance edge of the RPC3 at around  $\eta \approx 1.4$ . This trigger is efficient without respect to  $W_{ness}$  cut, and therefore contributes a reasonable fraction of the  $W$  candidate events. The RPC1C trigger is only efficient in the RPC1 acceptance, at  $\eta < 1.4$  and conversely the RPC3A triggers are only efficient at  $\eta > 2$ .

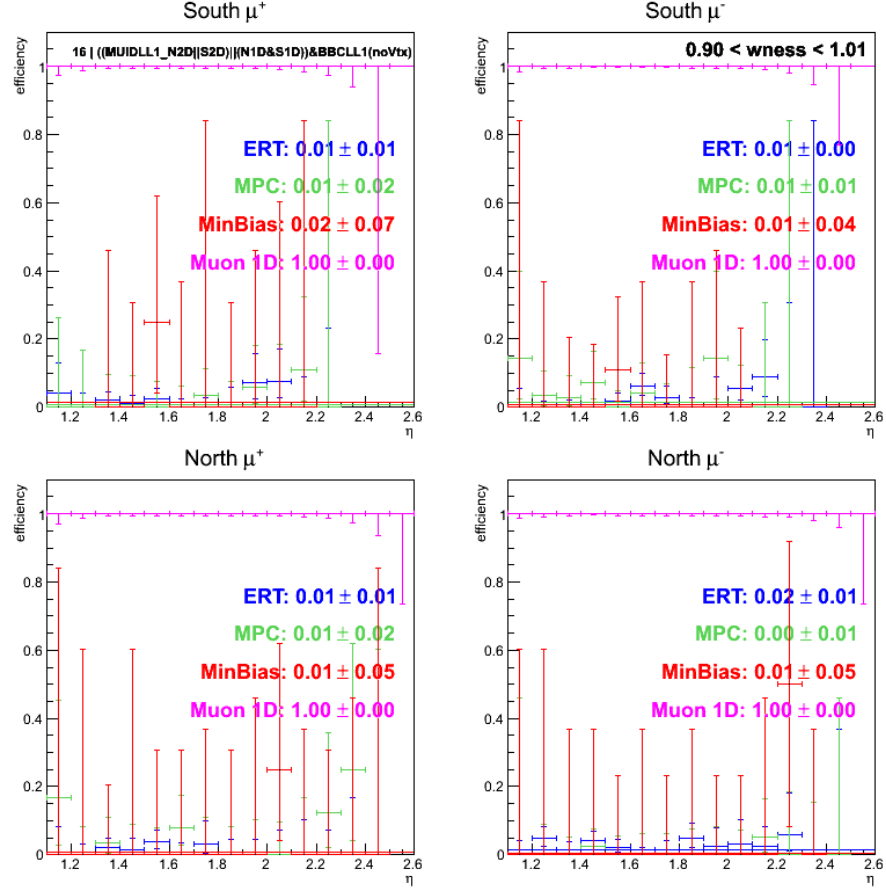


Figure 6.10: Shown: Trigger efficiencies for trigger bit 16 for single  $W \rightarrow \mu$  candidates with  $p_T$  above 5 GeV. The efficiencies for ERT (blue), MPC (green), MinBias(red) and 1D (purple) triggered data samples are shown as well as a constant fit over the whole range [30].

### 6.10.2 $p_T$ Dependent Efficiencies

To study  $p_T$  dependent efficiencies, no  $W_{ness}$  cut is applied, though data is binned in three rapidity bins,  $1.1 < \eta < 1.4$ ,  $1.4 < \eta < 2.0$  and  $2.0 < \eta < 2.6$ . Data is plotted as a function of  $p_T$ . As an example, Figure 6.11 is shown from this study, with remaining Figures C.21-C.45 shown in the appendix.

Additionally, fit results are shown alongside the efficiencies. The full  $p_T$  range is fitted with an error function and momentum above 10 GeV is fitted with a constant term. With no  $W_{ness}$  cut applied, the data is dominated by hadronic background. The results of the fits will later be used as lower limits of the total trigger efficiencies.

One sees very clear turn-on curves for nearly all triggers and rapidity ranges. However, some efficiencies seem to drop again at  $p_T$  above about 10 GeV. As a consequence the constant fits to this higher  $p_T$  region are generally lower than the plateau of the error function fit. The reason for this drop can be understood qualitatively as an effect from hadronic background mis-reconstructed as high  $p_T$  muons. As shown in [84], at high  $p_T$  the fake muons dominate. The hadronic background tends to create a signal in the MuTR which are associated with lower efficiencies and increased multiple scattering in the SG1 and RPC3 triggers. At  $p_T$  close to the thresholds of SG1 and related triggers the fraction of hadrons is still rather high, but they are much more likely to be correctly reconstructed at several GeVs and thus their signals are more likely to fire the SG1. In addition the majority of real muons can be also found at these intermediate momenta.

To summarize, the high momentum efficiencies seem to be lower due to the fake muon content and the plateau results just above the thresholds are more likely to correspond to actual muon efficiencies. However, once these fakes are removed via the  $W_{ness}$  cuts the actual efficiencies at high  $p_T$  are expected to rise to at least the plateau values.

When adding  $W_{ness}$  cuts, the high  $p_T$  sample is calculated to have a higher efficiency. An example is shown in Fig. 6.12 for comparison.

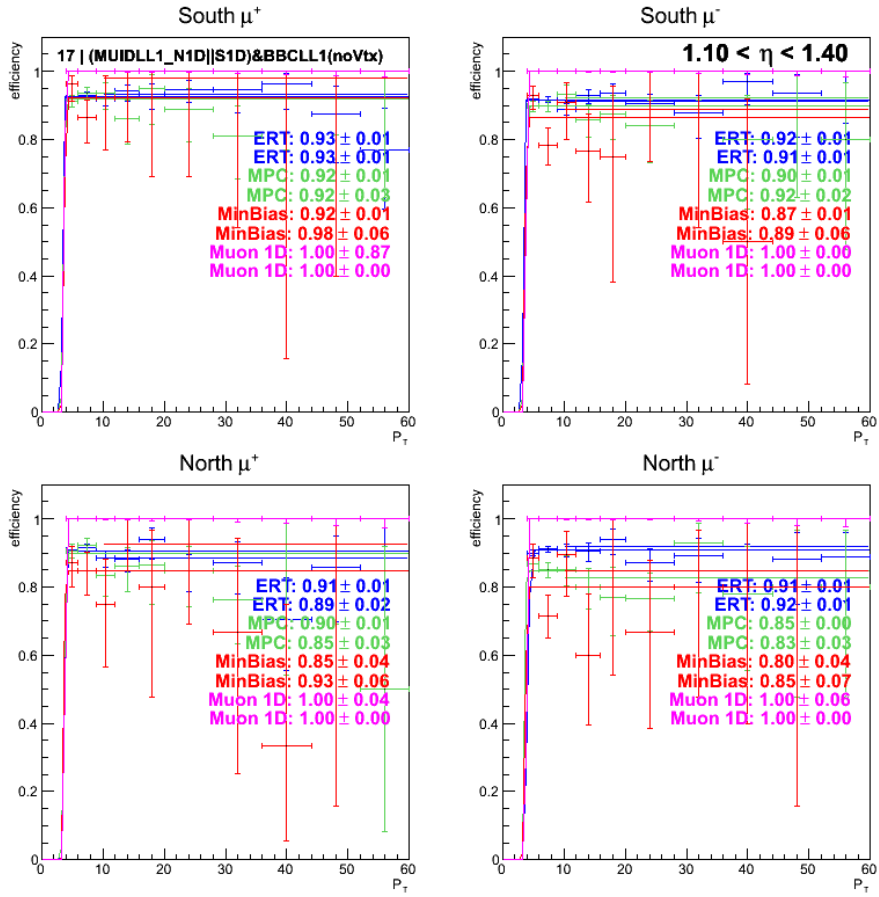


Figure 6.11: Trigger efficiencies for trigger bit 17 ( $((\text{MUIDLL1\_N1D} || \text{S1D}) \& \text{BBCLL1}(\text{noVtx}))$ ) for single  $W \rightarrow \mu$  candidates in the rapidity range  $1.1 < \eta < 1.4$  as a function of  $p_T$ . The efficiencies for ERT (blue), MPC (green), MinBias (red) and 1D (purple) triggered data samples are shown as well as a constant fit over the whole range [30].

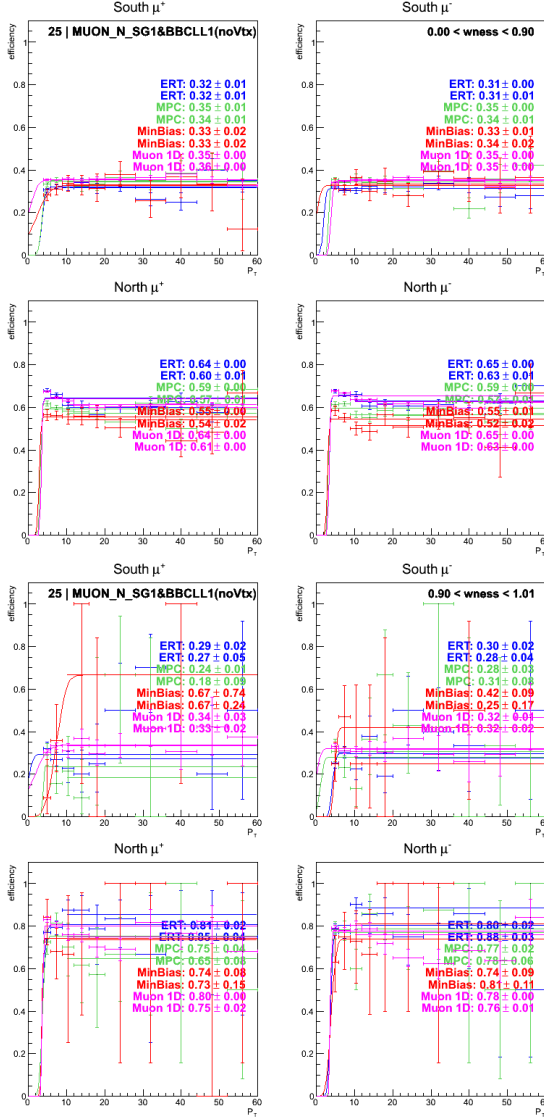


Figure 6.12: Left: Trigger efficiencies for trigger bit 25 (MUON\_N\_SG1&BBCLL1(noVtx)) for single  $W \rightarrow \mu$  candidates for the  $W_{ness}$  ranges  $0 \leq W_{ness} < 0.9$  (left plot) and  $W_{ness} > 0.9$ . Right: The triggers are shown as a function of  $p_T$ . The efficiencies for ERT (blue), MPC (green), MinBias (red) and 1D (purple) triggered data samples are shown as well as a constant fit over the whole range [30].

### 6.10.3 Efficiencies Versus $W_{ness}$

Next, the trigger efficiencies are evaluated as a function of the  $W_{ness}$  for  $p_T$  above 5 GeV and in three rapidity bins:  $1.1 < \eta < 1.4$ ,  $1.4 < \eta < 2.0$  and  $2.0 < \eta < 2.6$ . The data is partitioned in  $W_{ness}$  between 0, 0.1, 0.3, 0.5, 0.7, 0.9 and 1. Results are summarized in Figure 6.13, with remaining partitions presented in the appendix in Figures C.46 through C.59.

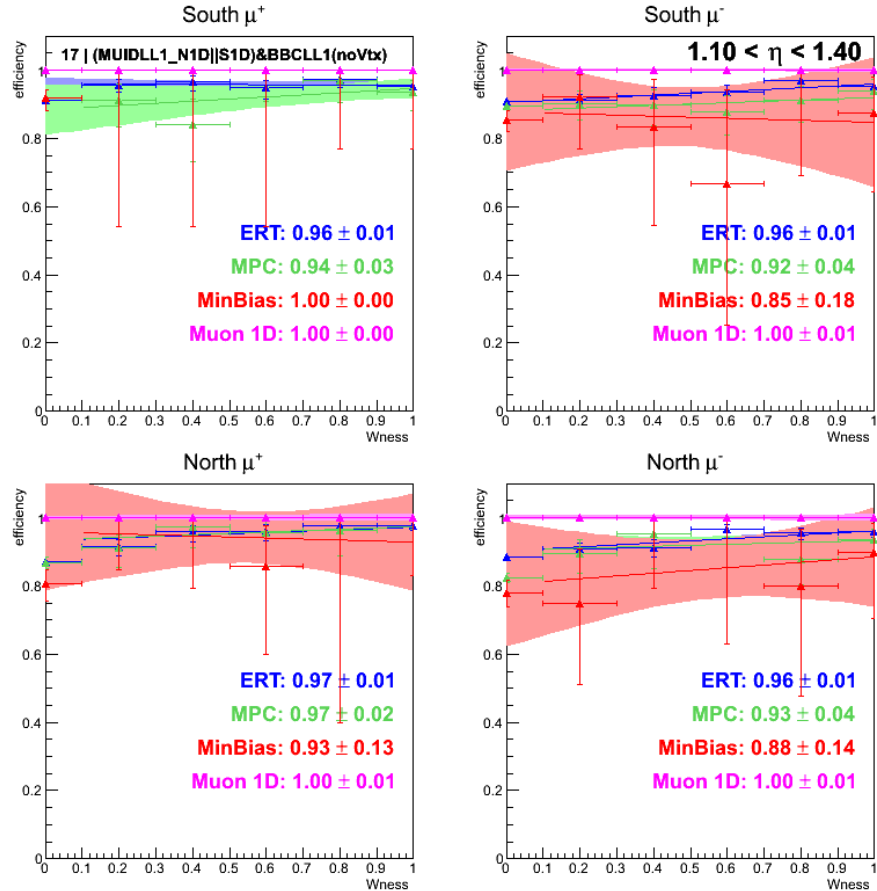


Figure 6.13: Trigger efficiencies for trigger bit 17 ((MUIDLL1\_N1D||S1D)&BBCLL1(noVtx)) for single  $W \rightarrow \mu$  candidates in the rapidity range  $1.1 < \eta < 1.4$  as a function of  $W_{ness}$ . The efficiencies for ERT (blue), MPC (green), MinBias (red) and 1D (purple) triggered data samples are shown as well as a constant fit over the whole range [30].

A linear fit for all but the first bin has been performed with the linear term constrained, such that the efficiency, together with the previously performed constant fit, never exceeds the allowed range between zero and unity. The total uncertainties of the fit including the covariance are also displayed and the efficiencies and errors in the target region at  $W_{ness} = 0.92$  have been evaluated. This value, and uncertainties will be the baseline of the overall trigger efficiency to be calculated.

Another extrapolation of the actual trigger efficiencies in the actual  $W_{ness}$  region can be obtained directly from the last bin from 0.9 to 1.0. Here, still some fake muons contribute, but their fraction is already substantially smaller and their other characteristics are already very similar to real high momentum muons, that this range can be trusted.

One can see in almost all triggers and data sets an increase in efficiency as the  $W_{ness}$  increases.

## 6.11 Total Trigger Efficiencies

The relative trigger contributions  $f_{trigger}$  of Fig. 6.9 were now combined with the trigger efficiencies for each individual trigger to obtain a total, rapidity dependent efficiency for each arm and charge. While the rapidity binning for the relative trigger contributions is finer, the efficiencies only in the aforementioned three rapidity bins were taken into account and multiplied with the corresponding relative fractions. In the case of the 1D triggered data sample the 1D trigger efficiency as average from the ERT and MPC data samples was multiplied for triggers which include the 1D. The total trigger efficiency per fine rapidity bin is calculated as follows:

$$\epsilon(arm, charge, \eta) = \sum_{trigger} \epsilon_{trigger}(arm, charge, matchingcoarse\eta bin) * f_{trigger}(arm, charge, \eta) . \quad (6.9)$$

Figure D.4 displays the total efficiencies and the breakdown into the individual trigger efficiencies in the total data sample. The several colors display the different data samples, with black showing the weighted average of all arm/charge partitions, with the individual contributions visible as a stack. The total efficiencies were evaluated based on the plateau value in the  $p_T$  dependent trigger efficiencies. Due to the large amount of fakes this total efficiency can be regarded as a low momentum limit of the total efficiencies.

The same is true even stronger in Fig. D.5 where the constant fit for  $p_T$  above 10 GeV was taken as individual efficiencies. As discussed above the corresponding efficiencies appear even lower due to the even higher fraction of fakes.

The more realistic total trigger efficiencies although with larger uncertainties can be found in Figs. D.6 and D.7, which were evaluated using either the highest  $W_{ness}$  bin or based on the extrapolation of the linear fit in  $W_{ness}$ . Both of these evaluations show substantially higher total efficiencies.

As the four arm/charge partitions show reasonably similar total efficiencies, the maximum differences to the average may serve as an estimate on the uncertainties.

For the total efficiencies used in the  $W$  signal to background evaluation as well as the total  $W$  cross section calculation, these two systematic uncertainties and the statistical uncertainties will be added in quadrature.

## Chapter 7

# Feature Engineering

The ultimate goal of ‘Feature Engineering’ is to clean and transform the data using heuristics and event tagging. Events are tagged to identify tracks which are likely to originate from signal sources, as separate from events which come from the background. Subsequently, the signal to background ratio can be calculated, which is needed to correct for background dilution present in the data set when the longitudinal asymmetry is calculated.

Even with the Forward Upgrade (Section 4.5), the data set is still composed mostly of background events. The primary constituents of the data set are muons from the following sources:

- **Hadronic Background**

- This hadronic background source is composed of hadrons which are produced at the primary event vertex, and then travel into the Muon Arms. The hadrons then decay into muons in the volume of the Muon Arms. The hit pattern from such decays is mis-reconstructed as high- $p_T$  muons originating at the primary event vertex. Though the probability of this scenario is small, the large number of hadrons results in a substantial background.

- **Muon Background**

- The muon background is composed of processes which produce real muons which fall into a similar kinematic regime of the W-genic muons. This contribution is separated from the signal data set with a combination of likelihood event tagging (Section 7.3) and an unbinned maximum likelihood fit (Section 7.4).

- **W Signal**

- These are the original muons from the  $W$  Boson decay, and carry information about the proton’s spin.

Likelihood event selection is applied in the first stage of event selection, where two classifications are considered for muon tracks. The first classification is ‘background’, which is composed of real muon background, and mis-reconstructed muon tracks originating from hadronic decay. The second classification is ‘signal’, which is composed of muons which have a high likelihood of having decayed from a  $W$ -Boson, alternatively referred to as ‘ $W$ -genic’ tracks. This process is described in Section 7.3.

The second stage of event selection differentiates the data set into three classifications—hadronic background, muon background and  $W$ -Boson decays. The recorded data set is used as a proxy for the hadronic background, while the  $W$  Boson and Muon Background contributions are modeled with a combination of simulation of tracks originating from the  $W$  Boson and Muon Background processes, as well as extrapolation from the data set. This is accomplished with a Maximum Likelihood Fit, described in Section 7.4.

In subsequent sections, I will provide a greater context for motivating the selection of analysis variables, which were introduced in Section 6.4.1. As this data set is dominated by background sources, the analysis relies heavily on simulations to estimate how signal  $\mu$  events might look like in the PHENIX detectors.

At the time of writing, simulation of hadronic background has not yet been incorporated into the analysis. This is because events which originate from punch through hadrons that mimic high  $p_T$  muons are quite rare, relative to other hadronic processes. Because of this rarity, trillions of events would need to be generated before a representative sample of hadronic background could be generated. Even if such simulations were produced, hadronic decays that mimic high  $p_T$  muons in PHENIX’s muon tracker are not understood with precision which rivals our understanding of the real muon background and  $W$  decay. Therefore, while the  $W \rightarrow \mu$  and muon background are simulated reliably, the data itself still provides the best proxy for hadronic background.

## 7.1 The Basic Cut

The basic cut aims to remove all events which are kinematically forbidden from resulting from a  $W$ -boson decay. Because the  $W$  boson must produce narrowly curved muons due to high momentum, one may remove tracks outside of a momentum threshold. The threshold is defined both in terms of the actual reconstructed momentum, as well as with respect to variables which are correlated to the amount of track bending.

The “Basic Cut” is defined:

Variable	Lower Bound	Upper Bound
DG0	0 <i>cm</i>	20 <i>cm</i>
DDG0	0.0 °	9.0 °
DCA <sub>r</sub>	0 <i>cm</i>	30.0 <i>cm</i>
$\chi^2$	0	20
$p$	5 <i>GeV/c</i>	250 <i>GeV/c</i>
$p_T$	16 <i>GeV/c</i>	60 <i>GeV/c</i>
MUID lastGap	Gap 4	*
Number of $\mu$ Tracks Per Event	N/A	1

Table 7.1: The Basic Cuts used in the Run 13 analysis. lastGap refers to the last gap in the MUID which saw a  $\mu$  candidate event. The fourth gap is the furthest penetration possible, therefore suggesting a high enough energy muon. Other parameters are described in Tables A.1, A.2, A.3, and A.4

With this cut, we reduce the background in our data by a factor of about 15,700—without worry of removing any events in that fall within the kinematic range of  $W$  Boson production. The basic cut reduces our data set from 15.7 billion events to about one million events.

## 7.2 Simulations

PHENIX has a rather well developed simulation framework, which uses the in-house built “PHENIX Integrated Simulation Application” (PISA) [85] custom simulation framework. The simulation framework models the entire  $12\text{m} \times 18\text{m} \times 18\text{m}$  volume of the PHENIX apparatus in detail, as well as all the various material properties of the apparatus. The software package uses GEANT as a basis, with PHENIX geometry build on top. PISA additionally encapsulates event-generators, a standalone geometry verification package, and the PHENIX offline analysis shell, in order to generate data that is completely compatible with PHENIX’s data packaging framework. PISA has since been integrated into a simulation work-flow with the standard-bearing PYTHIA event generation system.

The simulations were created by selecting the biggest sources of muon background produced at PHENIX as predicted by the Standard Model as well as the  $W$  Boson event. Events were generated until a large enough sample was accumulated to provide statistically significant distributions of simulated data.

The purpose of simulating the muon background and  $W$ -Signal is to generate probability distribution functions for the variables which have the largest analyzing power—i.e. ability to differentiate between signal and background.

After producing a simulated data set, the simulations for muon background were summed to produce a data set to represent what a data set composed only of these processes might look like. The yields of each process were normalized to represent the actual fraction of the total data set that each process contributed, which is summarized in Table 7.2. The simulation for the  $W$  Boson muon decay was treated similarly, but kept separate from the muon background.

Along with our proxy for the hadronic background, extracted from the real data set, we produce probabiltiy distribution functions for each variable used in the analysis in order to facilitate the likelihood event selection.

For the simulations, we consider the following processes: Open charm or charmonium refers to the bound state of the  $c\bar{c}$  quarks. The Onium muon background source refers to any process where a quark is in a bound-state with its own antiparticle, excluding  $c\bar{c}$  and  $b\bar{b}$  which is simulated separately. Open bottom refers to the bound state of  $b\bar{b}$  quarks.  $Z/d\gamma$  refers to the production and decay of the mixing between the Z-boson and virtual

photons. ONLY Z refers to Z production and decay. W is the signal event in this work. These processes are summarized in Table 7.2.

Reference Run 393888				
Process	k factor	$\sigma$ (mb)	# Events	$\mathcal{L}$ ( $fb^{-1}$ )
$c\bar{c}$	2.44	5.71e-01	5.85e+11	1.02
onium	0.415	1.35e-01	1.5e+11	1.11
$b\bar{b}$	1.83	7.30e-03	7.36e+09	1.01
ONLY Z	1.25	3.37e-07	1.73e+08	577.0
W	1.5	1.66e-06	3.38e+08	198.9
Z	1.25	1.02e-06	2.93e+08	61.2

Table 7.2: Simulated sub processes in Run 13 including their generated event numbers as well as the corresponding luminosity and cross sections. An extensive analysis of the simulated data was undertaken to determine an appropriate k-factor.

“

The simulations must additionally be weighted for trigger efficiency. To accomplish this, we weight events for each arm and charge with the associated trigger efficiency when constructing probability density functions representing the muon background. The trigger efficiencies generally manifest as  $\eta$  dependent functions—thus we bin the data into 20 separate  $\eta$  bins and calculate the efficiency associated with each bin. The bin ranges, and efficiency corrections are summarized in Table A.6 for the North arm, and Table A.5 for the South arm in the appendix.

The trigger efficiencies of the archived data is needed in order to correct the overall yields of events in the data-set, and is done by scaling the yield of a particular trigger with the efficiency. This analysis was presented in [31].

One can visualize the composition of the simulated data set by stacking the relative distributions of these variables. Observing the cross-sections of these variables as a function of  $p_T$ , allows one to see how the background composition varies with  $p_T$  (Figure 7.1).

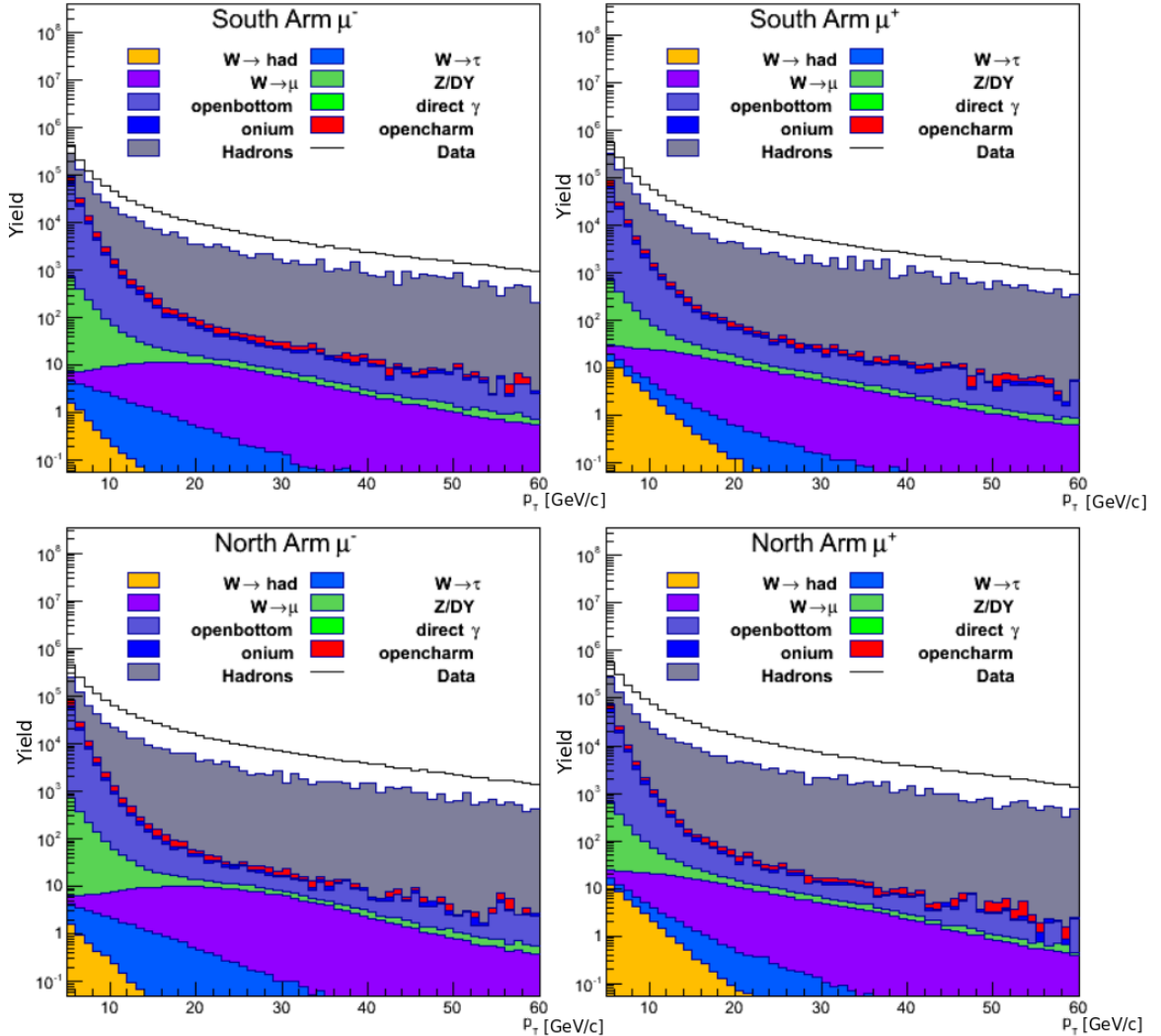


Figure 7.1: Shown: stacked cross-sections of all simulated processes as a function of  $p_T$ . All data shown has been created from the PISA+PYTHIA framework. Top Left: South  $\mu^-$ , Top Right: South  $\mu^+$ , Bottom Left: North  $\mu^+$ , Bottom Right: North  $\mu^-$  [31]

## 7.3 $W_{ness}$ : Likelihood Event Tagging

Recalling that the dataset into is already split into three main contributions: hadronic background, real muon background, and W-Signal, the next task is to formulate a means to separate signal from background.

Previous analyses have attempted to separate the muon spectrum into  $p_T$  bins, to estimate the composition, however, because the  $W \rightarrow \mu$  signal is so small in the forward kinematic regime, these methods are not viable, as there is no ‘visible’ cutoff in the spectrum associated with a invariant mass peak at half the mass of the  $W$  Boson.

High momentum  $\mu$  tracks are straight, with less bending than other  $\mu$  tracks. The kinematic variables describing track reconstruction have characteristically narrow distributions for our signal muons.

One can think of the study of the data set in terms of a classification problem. Bayes Theorem is at the foundation of a robust classification technique, known Naive Bayes. Using this technique to classify a data requires that one has a sample of labeled testing data to construct a model which can classify data into two or more classes. Care must be taken not over-train the classifier, or attempt to classify data which has been used in the subset of data to train the classifier. An example of over-training might be a case where one customizes the model by providing training data which is not representative of the real variation in the true data set, which artificially inflates the model’s accuracy when used on training data.

In this case, simulations serve as the training data, guaranteeing that there will be no overlap between the physical data produced, and the data used to train the classifier. Thus, a Naive Bayes Classifier is implemented (also known as Likelihood Selection) to label our data with two classes. Rather than labeling data with a binary classification, data is labeled with its likelihood of receiving a ‘signal’ classification.

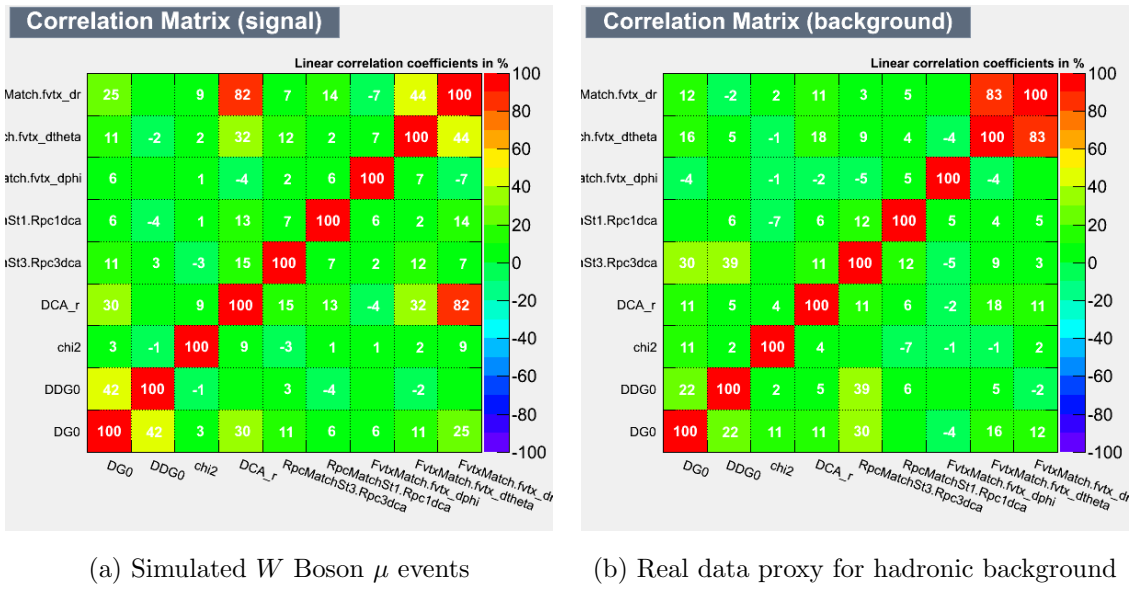
### 7.3.1 Naive Bayes Classification

There are many techniques available for classifying a collection of variables (a feature set) into categories. Naive Bayes is useful in cases where meaningful classification categories can be applied to feature sets, and labeled training data is available. One advantage of Naive Bayes is that after training the classifier, very large data sets can be classified, with little computational resources needed to store the classifier itself. A soft requirement

for Naive Bayes classification is that feature sets must not be correlated, since this can lead to over training. Originally used for classification of text documents, Naive Bayes is also able to handle numeric features whose distributions are known [86].

In this analysis, consider our track reconstruction variables as the ‘feature set’, and the classification of ‘signal’ or ‘background’ as the label.

In order to obtain the best performance from the classifier, without over-training, one must ensure that the variables used to determine a class are maximally uncorrelated. After early correlation studies were done on various possible observables, the variables used in this analyses were chosen. The variables which match this criteria are:  $DG_0$ ,  $DDG_0$ ,  $\chi^2$ ,  $fvtx$  variables,  $Rpc1DCA$ ,  $Rpc3DCA$ ,  $DCA_r$ , and  $DCA_z$ . The linear correlations between these variables are shown for both the data, and the simulated W-Signal in Figure 7.2.



(a) Simulated  $W$  Boson  $\mu$  events

(b) Real data proxy for hadronic background

Figure 7.2: In panel (a) Correlations are shown between kinematic variables, produced from the signal simulation. In panel (b) correlations are shown for the real data proxy for hadronic background. Variables that are correlated are combined in two dimensional probability distribution functions, i.e.  $DG_0$  and  $DDG_0$  and  $DCA_r$  and  $\chi^2$ .

As one can see from Figure 7.2,  $DG_0$  and  $DDG_0$  are slightly correlated, as are  $\chi^2$  and  $DCA_r$ . A Naive Bayes classifier may be constructed from the core of the familiar Bayes Theorem from probability and statistics. In our case, we understand Naive Bayes as a

conditional probability. Concretely, we consider a vector of features (i.e. our discriminating kinematic variables):

$$\mathbf{x} = (x_1, \dots, x_n) \quad (7.1)$$

and assume independence between each feature  $x_n$ . We then define the probability of a given classification,  $C_k$  (i.e. signal or background) given a set of features  $x_n$  (i.e. DCA<sub>r</sub>,  $\chi^2$  ...):

$$\mathcal{P}(C_k|x_1, \dots, x_n) \quad (7.2)$$

This conditional probability is defined in terms of Bayes Theorem:

$$\mathcal{P}(C_k|\mathbf{x}) = \frac{\mathcal{P}(C_k) \mathcal{P}(\mathbf{x}|C_k)}{\mathcal{P}(\mathbf{x})} \quad (7.3)$$

The terms here are defined as:

- $\mathcal{P}(C_k) \rightarrow$  prior probability
- $\mathcal{P}(\mathbf{x}|C_k) \rightarrow$  likelihood
- $\mathcal{P}(\mathbf{x}) \rightarrow$  overall probabiltiy

The probabilities described here are realized through constructing probability density functions from the data and simulations. The constraints for choosing PDFs to use represent the two lables are: (1) PDFs must be able to be meaningfully normalized, (2) PDFs associated with each label should have a unique enough shape to differentiate between either label, and (3) the PDFs should be uncorrellated.

The likelihood ratio is constructed using the posterior probability for each classification, which is defined as  $W_{ness}$ :

$$\lambda_{sig} = \prod_k \mathcal{P}(\mu_{sig}|C_k) \quad (7.4)$$

$$\lambda_{bak} = \prod_k \mathcal{P}(\mu_{bak}|C_k) \quad (7.5)$$

$$W_{ness} = \frac{\lambda_{sig}}{\lambda_{sig} + \lambda_{bak}} \quad (7.6)$$

Where  $\lambda_{sig}$  and  $\lambda_{bak}$  represent the total likelihoods that a given track is either signal, or background, constructed from the product of likelihoods calculated from each probability density function.

$\lambda$  is the final product of the component probability distribution functions:

$$\lambda = p(DG0, DDG0)p(\chi^2)p(DCA_r)p(RPC1/3DCA)p(fvtx_{dr})p(fvtx_{d\theta})p(fvtx_{d\phi}) \quad (7.7)$$

Note that the PDFs are composed by creating a histogram of the synonymous kinematic variable associated with the label of ‘signal’ or ‘background’. In the case of DG0 and DDG0, we use a 2D histogram to account for correlation, as well as  $DCA_r$  and  $\chi^2$ .

In order to construct probability distribution functions to use in this classification, one must select samples of labeled data representing each classification. The recorded data is used as a proxy for the ‘background’ labeled data set, and the simulation of the  $W$  boson decay is the ‘signal’ labeled data set. The  $W$  Boson signal at this stage of the analysis does not meaningfully change the shape of the PDFs extracted from the data. Even after the Basic Cut, the number of  $W$  Boson decay events is small relative to the hadronic and muon background (less than one part in 1000). The  $W$  Boson production cross section is precisely known—since the luminosity delivered to PHENIX is also known, the  $W$  Boson yield may be trivially estimated.

Not all recorded events contain valid tracking information for all tracks. For example, consider a muon track which was recorded due to a minimum bias trigger. When any trigger causes data to be recorded, there is no guarantee that all subsystems have been triggered, but all subsystems flush the data in their buffers to the archival data stream. This is not an error, each detector subsystem has an associated efficiency and acceptance. For example, with our example track, perhaps the physical process related to triggering a detector simply didn’t occur. One may correct account for all this when constructing PDFs. A selection process is superimposed such PDFs are constructed only from events (simulated or otherwise) containing valid data. Similarly, the selection process must also be preserved when looking up what PDFs to ultimately use in calculating the likelihood of an event being generated from a signal process. This process is represented in Figure 7.3.

Finally, once all PDFs have been constructed, following the selection process shown in Figure 7.3, one may loop over the simulated data set, and the recorded data set, and

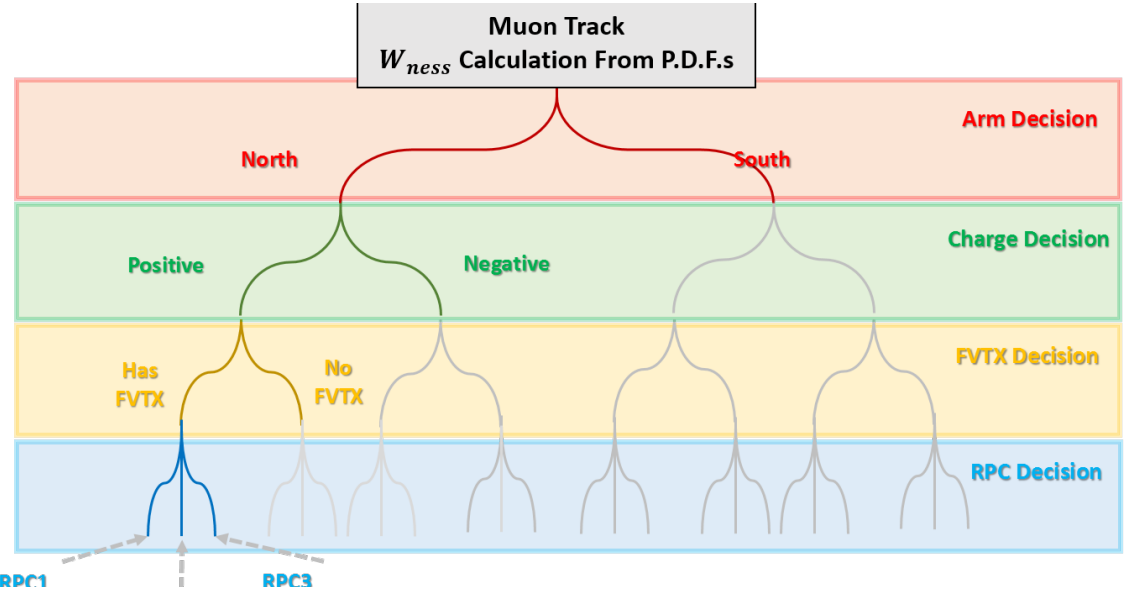


Figure 7.3: A cartoon of the decision tree to determine the PDF cocktail to use for quantifying the  $W_{ness}$  of a given track. The track's properties are used to traverse the tree, and select the cocktail contents.

perform the likelihood calculation for each muon track (Equation 7.6). The value of  $W_{ness}$  is stored for every track in the simulation and data as an engineered feature to be used in cuts.

In figures B.5-B.1, the probability distribution functions are shown for each arm and charge combination. In the figures, we represent the product of all probability functions which are used to tag an event as  $\lambda$  such that  $\lambda = \prod_k \mathcal{P}(\mu|C_k)$ . The 1D distributions are shown for all variables to highlight each variable's distribution, but recall that DG0 and DDG0 are combined into a 2D histogram in practice, along with  $DCA_r$  and  $\chi^2$ . As an example, the PDF for  $DCA_r$  (Figure 7.4) is shown, with the remaining PDFs included in the appendix.

After constructing PDFs, the  $W_{ness}$  is calculated for each muon track (Equation 7.6) contained in the recorded data set, and the simulated data set for the  $W$  Boson signal. The final distributions of  $W_{ness}$  are shown for signal simulation and the recorded data in Figure 7.5.

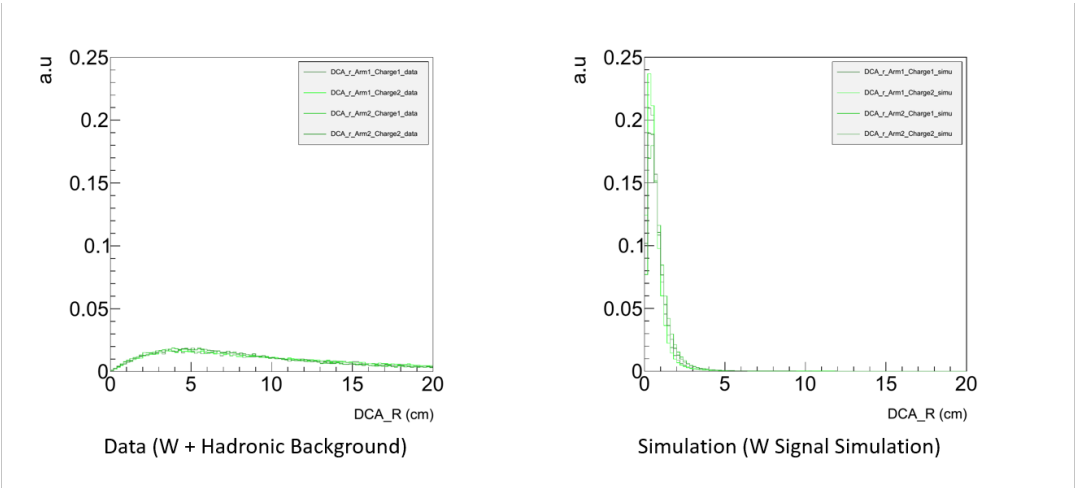


Figure 7.4: The left panel shows the distribution of  $DCA_r$ , the transverse distance of closest approach between the track and the event vertex, for each arm and charge, produced from the PHENIX data set, after the basic cut. The right panel the same distributions from a simulation of the  $W$ -Signal. Both panels have the arm and charge data partitions overlaid.

As seen in Figure 7.5, most of the simulated data falls in the high  $W_{ness}$  range while most of the physics data falls in the low  $W_{ness}$  range. The goal of the likelihood analysis is to tag the data with  $W_{ness}$  in order to apply cuts on the data based on the likelihood. The cut is applied such that background is removed with minimal reduction in signal. This is accomplished by applying successive  $W_{ness}$  cuts and choosing the cut which minimizes the reduction in potential signal events, summarized in Figure 7.6.

To obtain optimal  $W_{ness}$  cutoff, successive cuts in  $W_{ness}$  are made. The fraction of signal and background was compared at each cut. It is found that  $W_{ness} > 0.99$  (the likelihood of a track receiving the ‘signal’ label) is the optimum cutoff.  $W_{ness}$  cuts at 0.92 were also tested. Data below this threshold will represent the data population containing only background events, while data above this threshold represents the fraction of the data containing signal events.

Note that now with this reduced data set, one could simply assume that all remaining data is signal, and calculate an asymmetry, however, there is clearly still a lot of background present. Any background that is still present will dilute the longitudinal asymmetry in  $W$  production. Therefore, an unbinned maximum likelihood fit (Section 7.4)

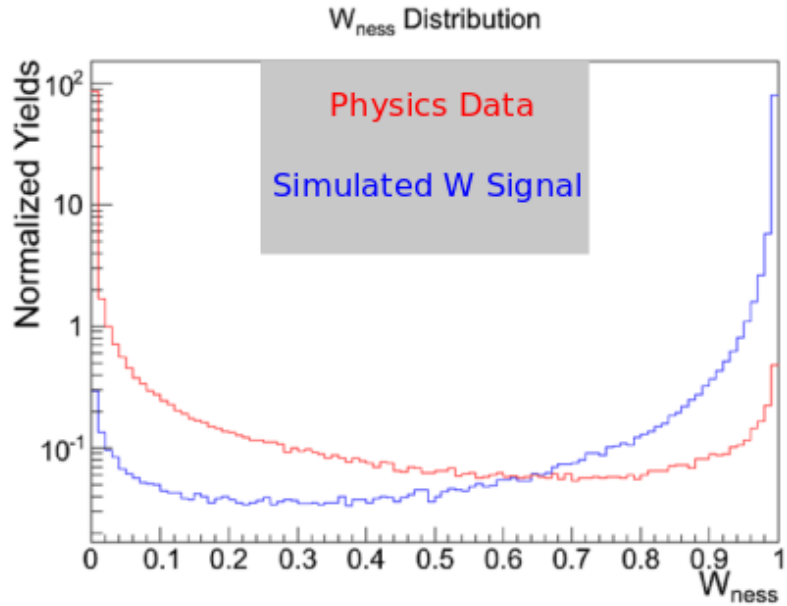


Figure 7.5: Distributions of  $W_{ness}$  are shown for the recorded data in red, and the simulated data in blue. Note that the vertical is plotted on a log scale. The two distributions have been normalized to total area.

is applied to the remaining data set, in order to estimate the residual background contribution. The result of the fit will estimate the residual fraction of Muon Background, Hadronic Background and W-genic muons in the data after applying the  $W_{ness}$  cut. The fit is applied over a domain of  $W_{ness}$ ,  $\eta$  and  $dw_{23}$ .

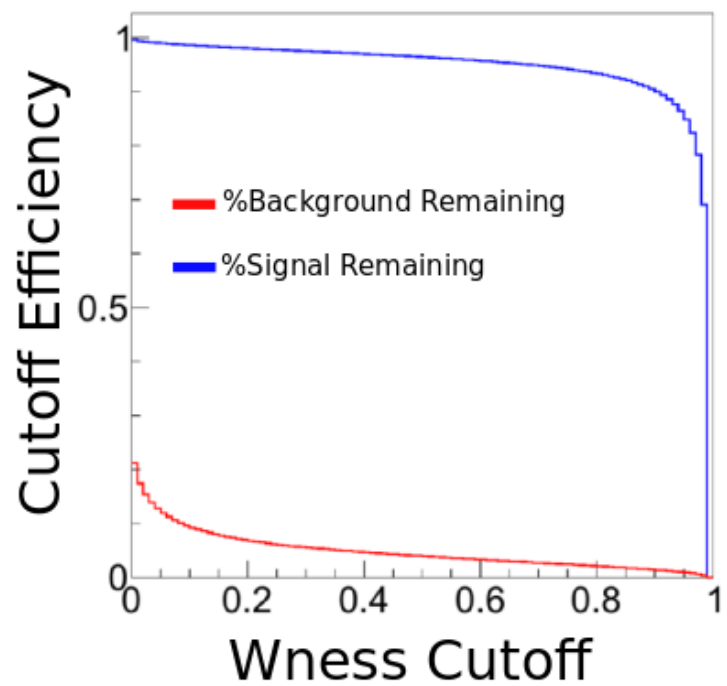


Figure 7.6: Shown: the fraction of signal and background remaining (vertical axis) in the total data set with successively higher cuts in  $W_{ness}$  (horizontal axis). The inflection point in the blue distribution is chosen as the optimal  $W_{ness}$  cut.

## 7.4 Extended Unbinned Maximum Likelihood Selection: The Signal to Background Ratio

### 7.4.1 Introduction

The goal of the Extended Unbinned Maximum Likelihood Fit (EULMF) is to extract the signal to background ratio, which in turn helps to estimate the background dilution in the measurement of the longitudinal asymmetry. The EULMF is a statistical method which relies on creating Probability Density Functions to represent the likelihood that a given track to originates from the muon background,  $W$  signal or hadronic background. However, this is distinct from the Likelihood Selection Method (Section 7.3) because rather than using likelihood to tag events, PDFs are fit to recorded data itself. After the fits, the overall composition of the recorded data remaining after the  $W_{ness}$  cut is estimated. Yields are obtained for three categories of data–Hadronic Background, Muon Background, and  $W$  signal.

The EULMF uses PDFs formed to represent  $dw_{23}$  and  $\eta$ .  $dw_{23}$  and  $\eta$  are uncorrelated, and are additionally uncorrelated from the PDFs used to calculate  $W_{ness}$ . This helps to avoid over-fitting, especially since  $W_{ness}$  is used explicitly to facilitate the extraction of the  $dw_{23}$  PDF representing the hadronic background.

The PDFs representing  $\eta$  and  $dw_{23}$  representing  $W$  signal are extracted directly from simulations. Additional care is needed for extracting the PDFs representing the Hadronic Background (Section 7.4.2). The shape of  $dw_{23}$  for hadronic background is extrapolated from the low  $W_{ness}$  portion of the recorded data into the signal region  $W_{ness} > 0.99$ .  $\eta$  has an unchanging shape with respect to  $W_{ness}$ , therefore its shape is extracted directly from the  $W_{ness} < 0.99$  portion of the recorded data. The details of extracting the hadronic background PDFs are discussed in Section 7.4.2.

When forming the PDFs representing  $dw_{23}$  and  $\eta$  for the Muon Background, the yields of each simulated process are weighted and added together to reflect the expected composition of the Muon Background in the recorded data. The details of extracting the PDFs from simulated data are discussed in Section 7.4.3.

With PDFs generated that representing Muon Background,  $W$  signal and the hadronic background, the EULMF is defined:

$$\mathcal{L}(\theta|X) \equiv \frac{n^N e^{-n}}{N!} \prod_{x_i \in X}^N \sum_c \frac{n_c}{n} p_c(x_i), ; \text{with } n = \sum_c n_c \quad (7.8)$$

where  $X$  is the sample of  $N$  total events  $x_i = (\eta_i, dw_{23i})$ , and  $\theta$  gives the parameters of the fit  $\theta = (n_{sig}, n_\mu, n_{had})$ .  $c$  is an index running over the three data types (muon background, hadronic background,  $W$  signal). In the fit, the Muon Background,  $n_\mu$ , is fixed to the expected yields of these processes according to the cross section of muon background processes, and machine luminosity. The remaining parameters are obtained from the fit ( $n_{sig}, n_{had}$ ) by minimizing the  $-\log(\mathcal{L}(\theta|X))$ . Due to the large integrated luminosity,  $277 pb^{-1}$ , of 2013's data set, the data was able to be partitioned evenly into three  $\eta$  bins:  $1.10 < \eta < 1.40$ ,  $1.40 < \eta < 1.80$  and  $1.80 < \eta < 2.60$ . The EULMF was performed with signal to background ratios evaluated and asymmetries calculated for each bin.

#### 7.4.2 Hadronic Background PDFs

The main analysis challenge for the EULMF is describing the shape of the hadronic background PDF associated with  $dw_{23}$ . Care must be taken here, since the data set ultimately contains the desired signal events. If one takes the data set in the signal region to be representative of the hadronic background's shape, signal events will be severely undercounted. The task of properly extrapolating  $dw_{23}$  is accomplished by observing the shape of  $dw_{23}$  at different  $W_{ness}$  values, and parameterizing the way that that its shape changes with increasing  $W_{ness}$ . This is qualitatively presented in Figures 7.7 and 7.8, where a  $dw_{23}$  is seen in the recorded data to slowly narrow as  $W_{ness}$  increases—contrasting with the simulated distribution which is uniformly narrow. This suggests that a broader  $dw_{23}$  is more associated with hadronic background. Conversely, the shape of  $\eta$  is not as sensitive to  $W_{ness}$ .

The  $W_{ness}$  dependence of  $dw_{23}$  is recovered by observing the shape of the variable at fixed slices of  $W_{ness}$ . Considering the shape of  $dw_{23}$  at a particular  $W_{ness}$  slice, an appropriate fit for the distribution is a coaxial double Gaussian, Figure 7.9.

The changing shape of  $dw_{23}$  as a function of  $W_{ness}$  is captured by observing how each of the parameters characterizing a coaxial double Gaussian fit vary with  $W_{ness}$ . Each parameter is plotted against  $W_{ness}$  for four distinct slices and coaxial Gaussian fits.

By observing the resulting distributions, a reasonable approximation of how each coaxial Gaussian parameter depends on  $W_{ness}$  is linear. Subsequent linear fits of the coax parameters vs  $W_{ness}$  fall within the parameters' uncertainty 7.10.

A full parameterization of  $dw_{23}$  as a function of  $W_{ness}$  is achieved by fitting the 2D data set of track-yield vs  $dw_{23}$  and  $W_{ness}$  with a two-dimensional function. While the width of  $dw_{23}$  as a function of  $W_{ness}$  has been shown to be well described as a coaxial double Gaussian, whose parameters depend linearly on  $W_{ness}$ , the overall height of the distribution must be parameterized as well. The shape of the  $W_{ness}$  histogram shown in Figures 7.7 and 7.8 suggests a quartic parameterization. The  $W_{ness}$  distributions are fit, results shown in Figure 7.11.

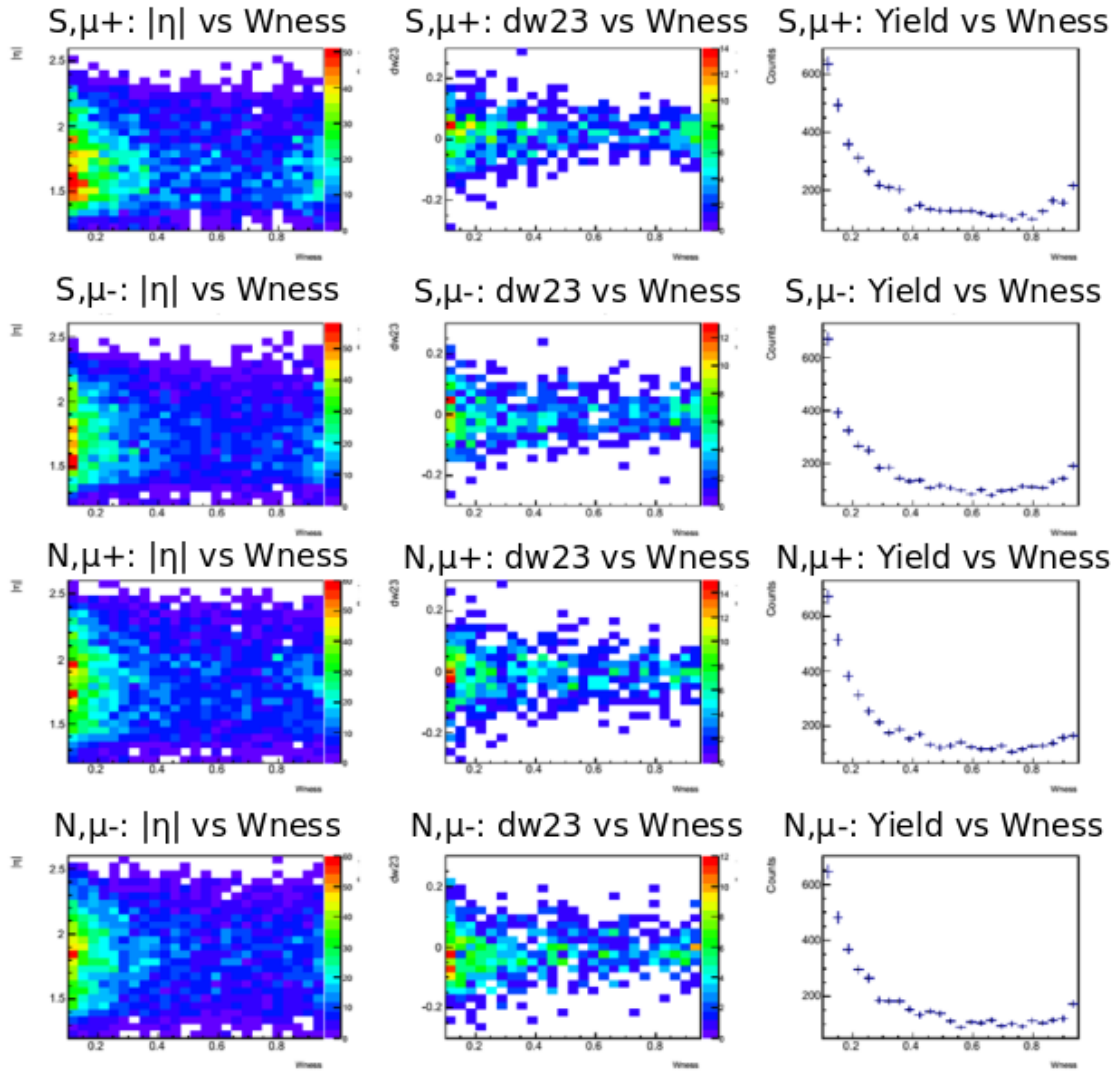


Figure 7.7: Shown: distributions of the recorded data set for  $dw_{23}$ ,  $\eta$  and  $W_{ness}$ . The first column shows  $\eta$  as a function of  $W_{ness}$ . The middle column shows  $dw_{23}$  as a function of  $W_{ness}$ , and the right column shows a histogram of the  $W_{ness}$  distribution. The rows all correspond to (top to bottom): North,  $\mu+$ , North  $\mu-$ , South  $\mu+$ , and North  $\mu-$ .

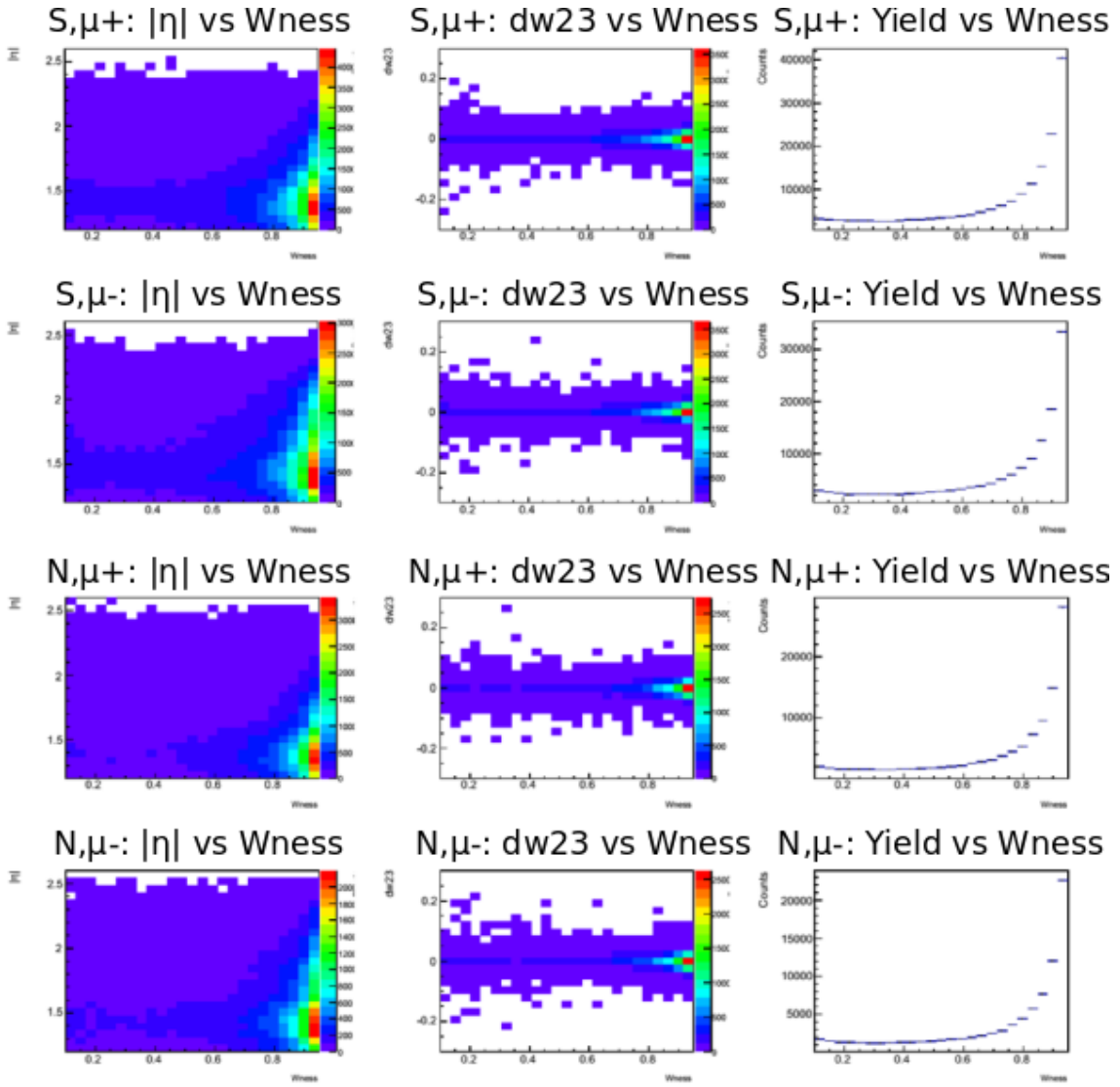


Figure 7.8: Shown: distributions of the simulated  $W$  signal data set for  $dw_{23}$ ,  $\eta$  and  $W_{ness}$ . The first column shows  $\eta$  as a function of  $W_{ness}$ . The middle column shows  $dw_{23}$  as a function of  $W_{ness}$ , and the right column shows a histogram of the  $W_{ness}$  distribution. The rows all correspond to (top to bottom): North,  $\mu+$ , North  $\mu-$ , South  $\mu+$ , and North  $\mu-$ .

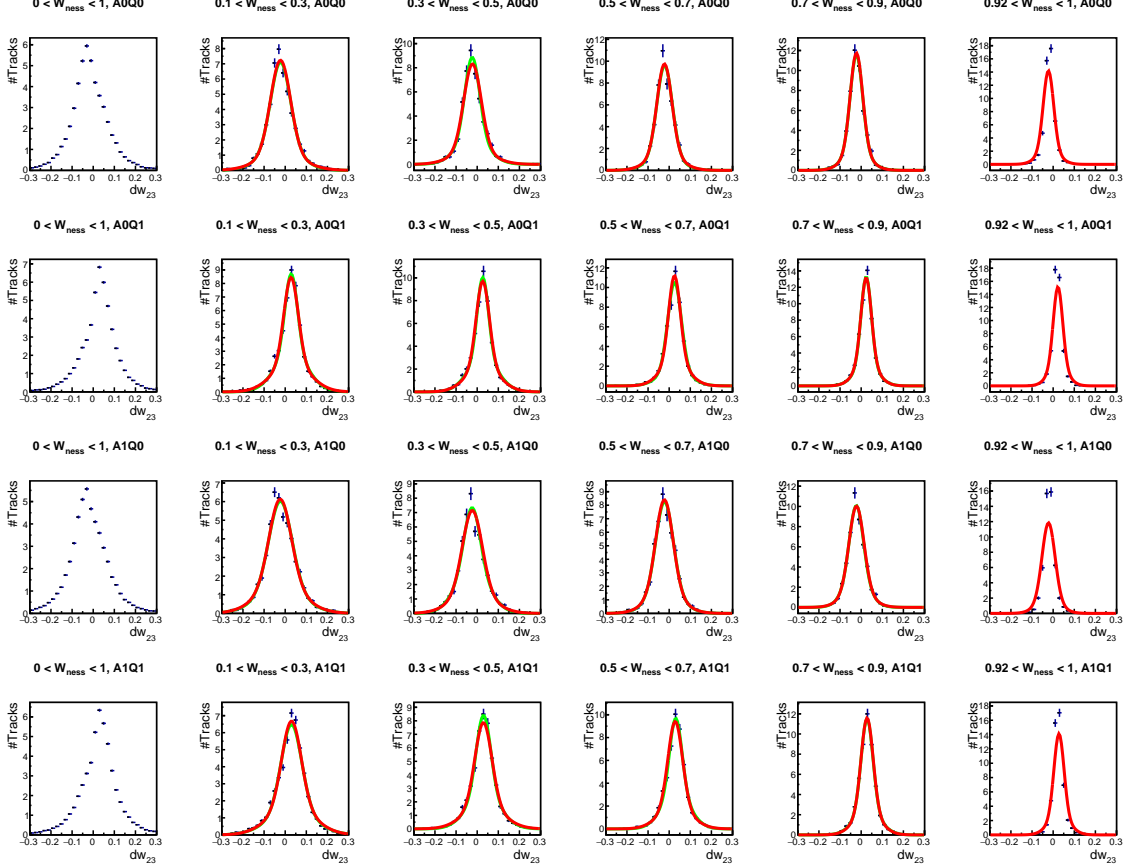


Figure 7.9: From left to right the columns show  $dw_{23}$  for the full  $W_{ness}$  range,  $0.1 < W_{ness} < 0.3$ ,  $0.3 < W_{ness} < 0.5$ ,  $0.5 < W_{ness} < 0.7$ ,  $0.7 < W_{ness} < 0.9$ . The columns show the extrapolated shape for  $W_{ness} > 0.99$ . The red curve shows the 1D projection of the total 2D parameterization of  $dw_{23}$  vs  $W_{ness}$  plotted on top of the green curves. The green curve shows the coaxial double Gaussian fit to a slice of  $dw_{23}$  in  $W_{ness}$ . The final column shows the projected shape of  $dw_{23}$  against the signal data region ( $W_{ness} > 0.99$ ). A0 and A1 refer to North or South arms, Q0 and Q1 refer to negatively or positively charged muons.

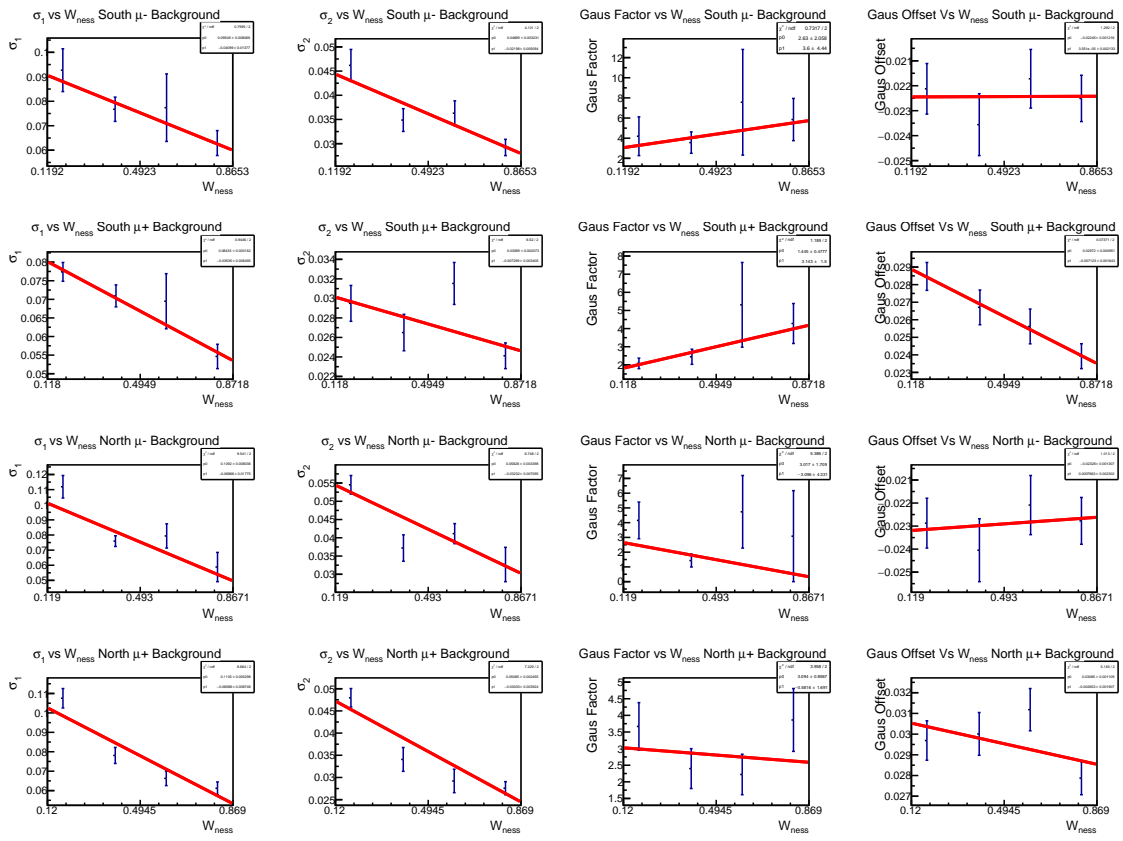


Figure 7.10: The four parameters from the co-axial Gaussian parameterization of  $dw_{23}$  as a function of  $W_{ness}$ . Rows are arm/charge, labeled on the left, while columns are co-axial Gaussian parameters, summarized in Equation 7.13

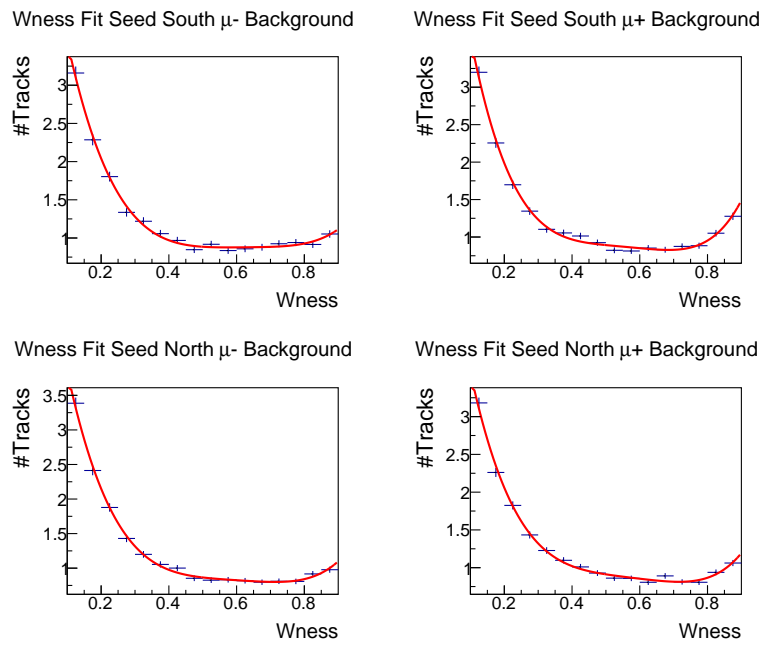


Figure 7.11: Shown: resulting fourth degree polynomial fit to the yield vs  $W_{ness}$  representing the hadronic background region  $0 < W_{ness} < 0.9$  of the real data.

#### 7.4.2.1 Final Parameterization of $dw_{23}$

With reasonable parameterization of our  $dw_{23}$  parameter as a function of  $W_{ness}$ , a 2D fit is performed which captures both the quartic dependence of the data set yield vs  $W_{ness}$  and the  $dw_{23}$  width dependence on  $W_{ness}$ .

The parameterization separated into quartic and coaxial Gaussian portions:

$$F(W_{ness}, dw_{23}) = f(W_{ness}) \times g(W_{ness}, dw_{23}) \quad (7.9)$$

$f(W_{ness})$  represents the fourth-degree polynomial dependence of yield vs  $W_{ness}$ :

$$f(W_{ness}) = P_8 + P_9 W_{ness} + P_{10} {W_{ness}}^2 + P_{11} + {W_{ness}}^3 + P_{12} + {W_{ness}}^4 \quad (7.10)$$

and  $g(W_{ness}, dw_{23})$  represents the changing width of the  $dw_{23}$  coaxial double Gaussian as a function of  $W_{ness}$ . The Parameters of the co-axial double Gaussian to vary linearly with  $W_{ness}$ :

$$\sigma_1 = P_1 + P_3 \times W_{ness} \quad C_g = P_6 + P_7 \times W_{ness} \quad (7.11)$$

$$\sigma_2 = P_4 + P_5 \times W_{ness} \quad \mu = P_0 + P_1 \times W_{ness} \quad (7.12)$$

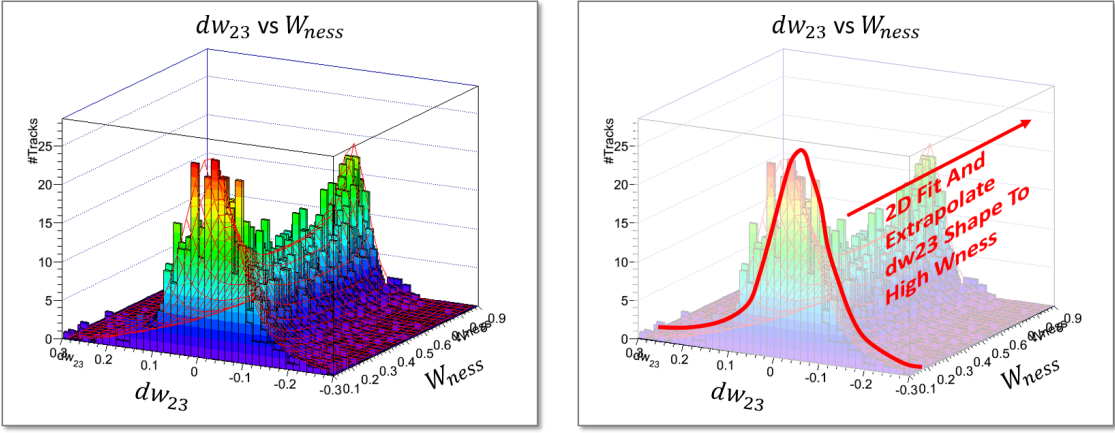
with  $g(W_{ness}, dw_{23})$  parameterized:

$$g(W_{ness}, dw_{23}) = C_w \times \left( \left( \frac{1}{\sqrt{2\pi}\sigma_1 + C_g \sqrt{2\pi}\sigma_2} \right) \times \left( e^{\frac{1}{2} \left( \frac{dw_{23}-\mu}{\sigma_1} \right)^2} + C_g e^{\frac{1}{2} \left( \frac{dw_{23}-\mu}{\sigma_2} \right)^2} \right) \right) \quad (7.13)$$

The full fit, (Eqtn. 7.9) is seeded using the parameters extracted from the 1D slices of  $dw_{23}$  in  $W_{ness}$ . The results of this fitting procedure are summarized in Figure 7.12.

Finally, the extrapolation of  $dw_{23}$  was reproduced and cross-checked by four independent analyzers. The distributions are in close agreement: Figure 7.13.

The PDF for the variable  $\eta$  representing the hadronic background was obtained by creating a histogram of the variable for events tagged with  $W_{ness} < 0.9$ .



(a) The final fit to  $dw_{23}$  vs  $W_{ness}$

(b) Cartoon of the extrapolation

Figure 7.12: Panel (a) shows a red wire-frame representing the resultant fit of to the  $dw_{23}$  vs  $W_{ness}$  distribution, against the lego-style real data distribution. Panel (b) shows the process of extrapolating the shape of  $dw_{23}$  from lower  $W_{ness}$  to the signal region to obtain the hadronic background PDF representing  $dw_{23}$ .

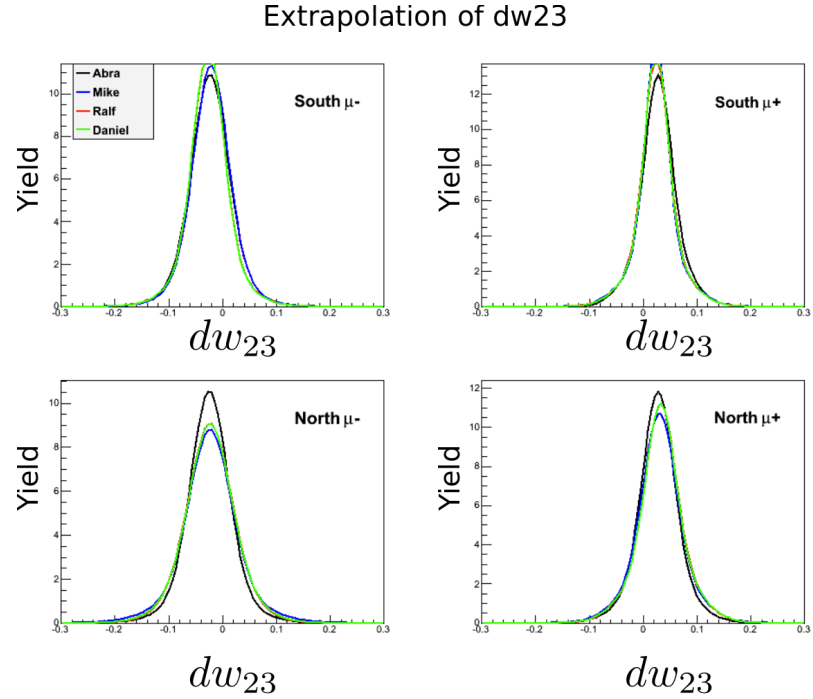


Figure 7.13: Shown: a comparison of four independent extrapolations of  $dw_{23}$  into the signal region [31].

### 7.4.3 Muon Background and W-Signal PDFs

Simulations are used to define the distributions  $dw_{23}$  and  $\eta$ , for PDFs representing both  $W$  signal and Muon Background processes.

As discussed in Section 7.2 and in the introduction to this Section (7.4.1), the Muon Background is modeled with simulations, which are summed to a representative PDF by scaling the simulated yields to match what is expected in the data set. Since the  $W$  signal is singular in source, no scaling is needed, as the PDFs are normalized before being used in any calculation.

#### 7.4.3.1 Multiple Collisions and Pile-Up

Simulations are produced using a reference run as a means of comparison. In the case of this analysis, the reference run used to seed simulations is 393888.

When events are generated for each muon process and added, they must be weighted for luminosity, cross section, k-factor and generated events to get an overall factor with which weight each individual distribution to generate the total ‘Muon Background’ distributions. For event generation, one must sum to obtain a sample consistent with the PHENIX sampled luminosity of  $277 pb^{-1}$ , which has been corrected for pile-up and multiple collisions.

The pile-up correction has been performed for all three  $W \rightarrow \mu$  and closely follows the procedure most recently detailed in [82]. For our luminosity detector, the BBC, one must consider that the BBC has a finite efficiency for the North and South subsystems, and therefore can mis-count the actual number of collisions.

Instead of calculating the efficiencies for a finite number of collisions in one crossing, it is easier to calculate the probability of not counting any collision. In an iterative procedure which generally converges after one or two iterations, the north (south) efficiencies  $k_N$ , ( $k_S$ ) were evaluated based on the true number of collisions per crossing  $\mu$ :

$$R_{BBC} = 1 - e^{-\mu \epsilon_{BBC}(1+k_N)} - e^{-\mu \epsilon_{BBC}(1+k_S)} + e^{-\mu \epsilon_{BBC}(1+k_N+k_S)} , \quad (7.14)$$

where  $R_{BBC}$  is the observed number of collisions per crossing and  $\epsilon_{BBC}$  is the overall BBC efficiency of 0.53, describing the fraction of the time the BBC will trigger on event, given that an event has occurred.

This way the actual average collisions rate can be evaluated for each run and the actual luminosity can then be obtained via the collision frequency ( $f_{coll} = 1/(106ns)$ ), the length of a run  $t$ , and its live fraction and the total BBC cross section (at 510 GeV:  $\sigma_{pp} = 61$  mb):

$$L_i = \frac{BBC_{live}}{BBC_{raw}} \times t \times f_{coll}/\sigma_{pp} . \quad (7.15)$$

Summing up all produced runs available, one obtains a total luminosity of 277 pb<sup>-1</sup>.

The actual number of collisions as well as the measured and true minimum bias collisions rates for each run are displayed in Fig. 7.14. One sees, that on average one has 0.74 collisions per crossing which motivates the reference run (393888) selection for the simulation, since this run had the same average collision rate.

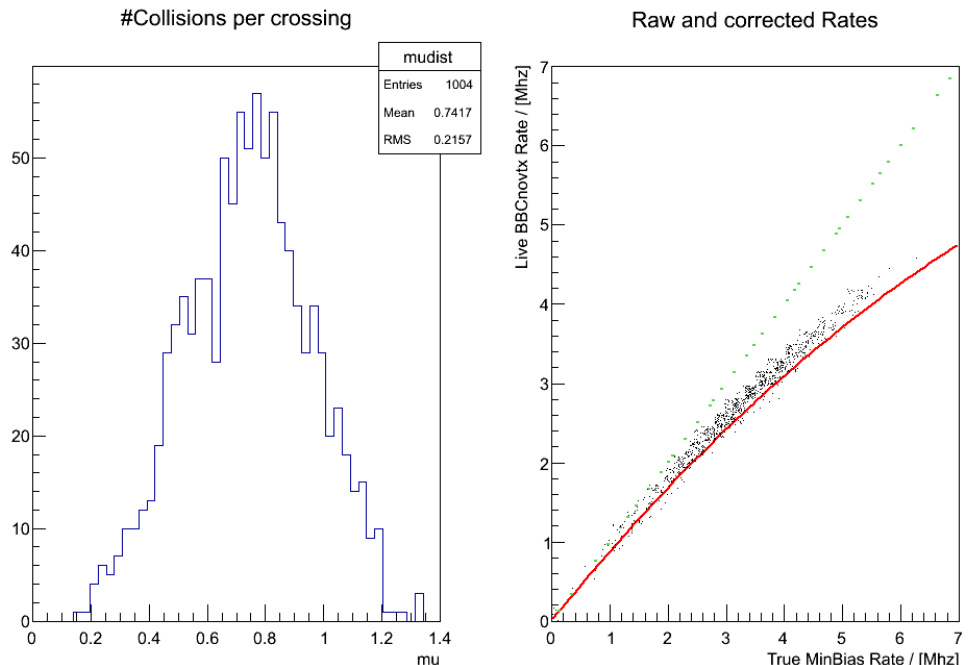


Figure 7.14: Left: distribution of number of collisions per crossing  $\mu$  for all runs available from the 2013 data set. Right: True and observed BBCnovotx live rates for all runs as a function of the true rate and calculated as described in the text. The green, dashed line represents a perfect accounting of true collisions, while the red curve takes the efficiencies of the two BBC sides into account [31].

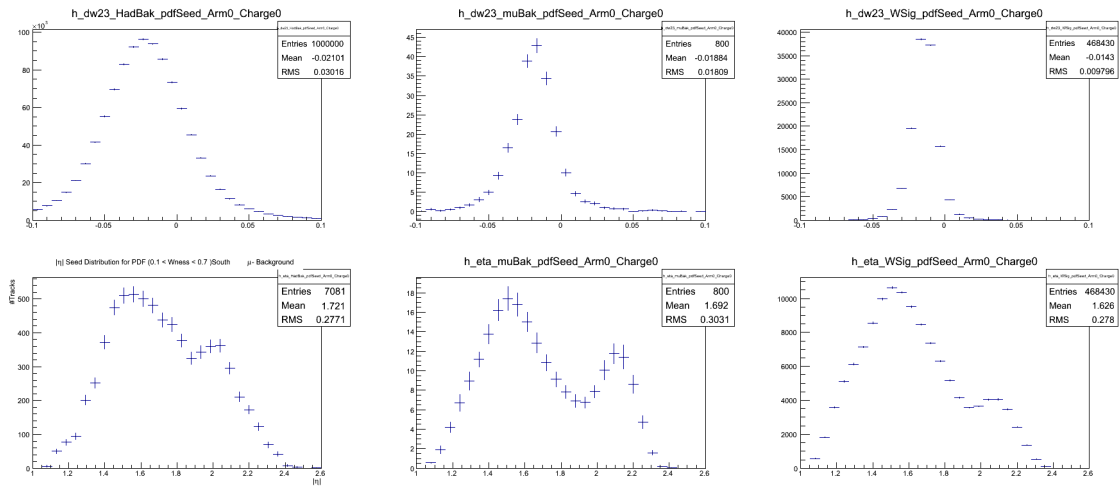


Figure 7.15: Left Column: The hadronic background PDFs, Middle Column: The Summed Muon Background PDFs, Right Column: The  $W$ -Signal PDF. For South Arm,  $\mu+$

#### 7.4.4 Final PDFs Used in EULMF

The PDFs which were used in the EULMF are summarized in Figures 7.15-7.18. The PDFs have been smoothed with a moving windowed-average algorithm to remove statistical fluctuations, with the overall shape apparently different for Hadronic Background, Muon Background and  $W$  signal.  $dw_{23}$ , as expected, has the narrowest distribution for the  $W$  signal PDFs, with the broadest width for the hadronic background.

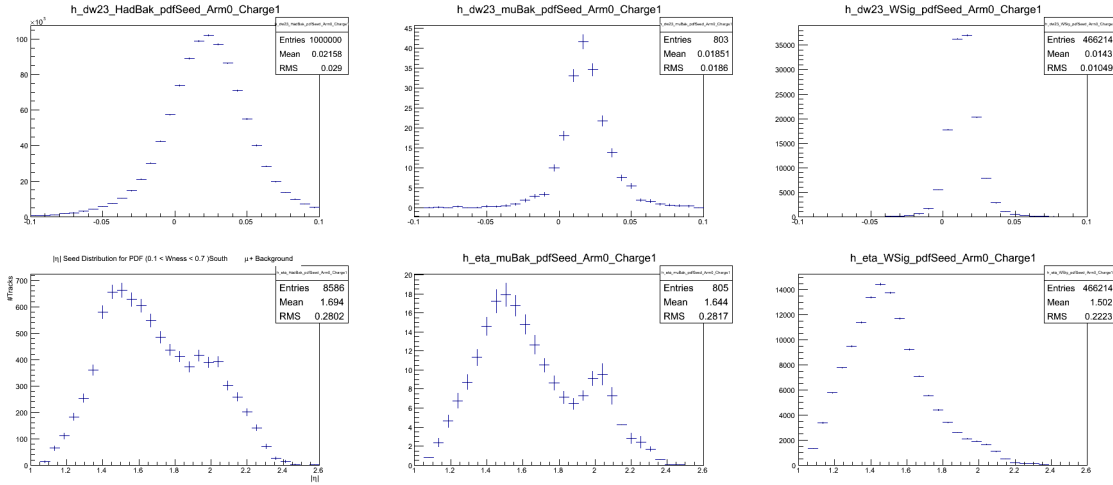


Figure 7.16: Left Column: The hadronic background PDFs, Middle Column: The Summed Muon Background PDFs, Right Column: The W-Signal PDF. For South Arm,  $\mu-$

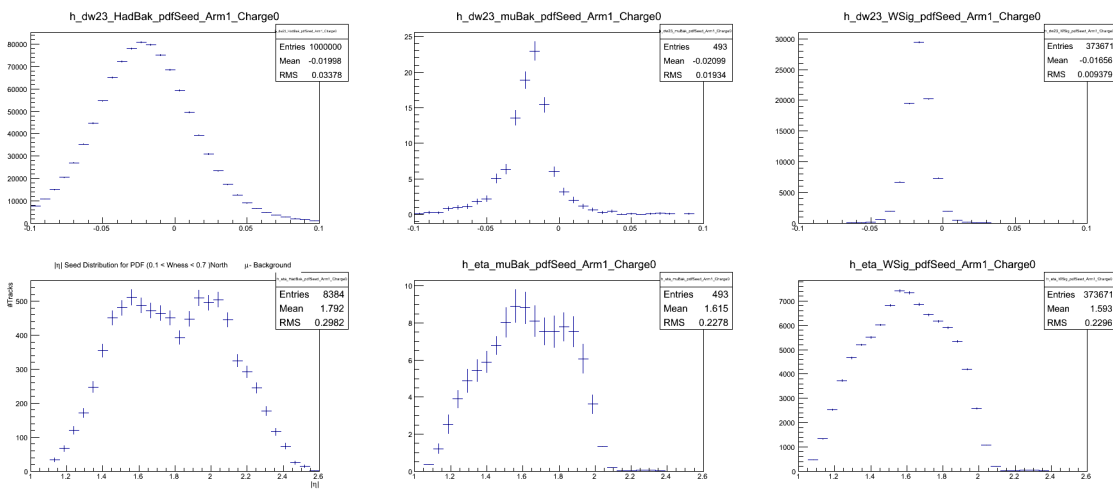


Figure 7.17: Left Column: The hadronic background PDFs, Middle Column: The Summed Muon Background PDFs, Right Column: The W-Signal PDF. For North Arm,  $\mu-$

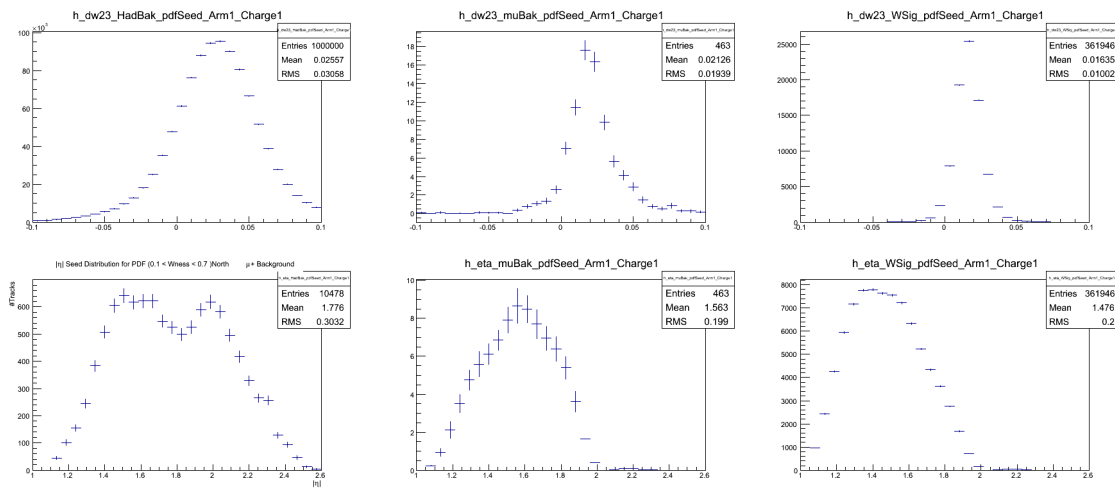


Figure 7.18: Left Column: The hadronic background PDFs, Middle Column: The Summed Muon Background PDFs, Right Column: The W-Signal PDF. For South Arm,  $\mu+$

#### 7.4.4.1 EULMF Fit Results

With all PDFs prepared, the EULMF is executed, and the resultant yields for the Hadronic Background + Muon Background (which was fixed) and the  $W$  signal are obtained. From these yields, the signal to background ratios with associated uncertainties are estimated. The results of the EULMF are shown in Figures 7.19-7.22.

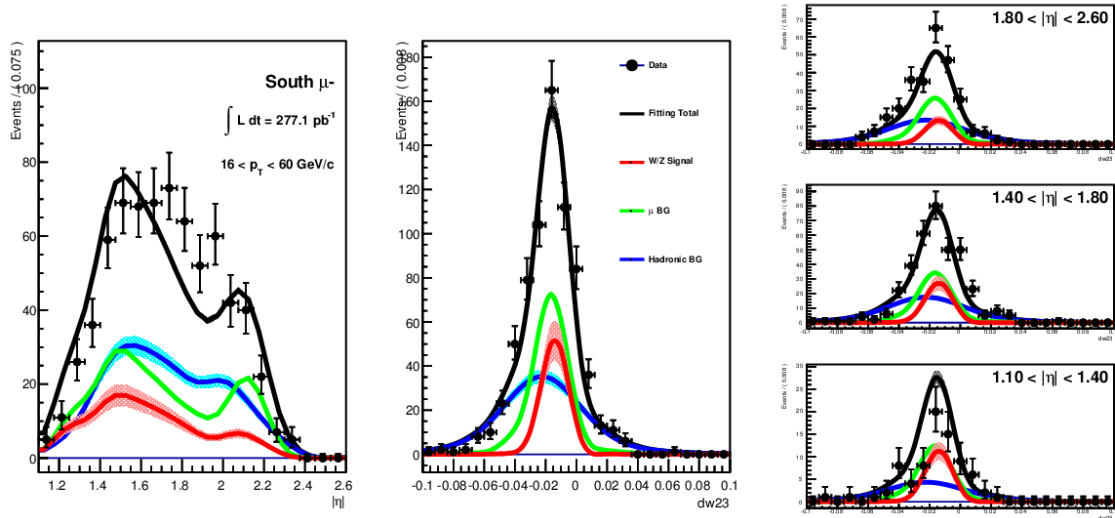


Figure 7.19: Here, we see the preliminary results of the EULMF for the 2013 Run. On the left,  $\eta$  is shown. In the middle,  $dw_{23}$ . On the right,  $dw_{23}$  is subdivided into the three standard  $\eta$  bins. In all cases, we see the unbinned data in black (with error bars), and the sum of the three fits in black. In Blue, we can see the fake-muon hadronic background. In Green, the muon background. In blue, we see the  $W$ -Signal result. The area under the curves represents the yield, relative to the total. Shown: South Arm,  $\mu-$  [31]

The signal to background ratio extraction is summarized and cross-checked among four independent analyses of the recorded data set. Each analyzer's result is presented alongside my result in Table 7.3, for the South Arm  $\mu-$  (the canonical cross check, among the analyzers).

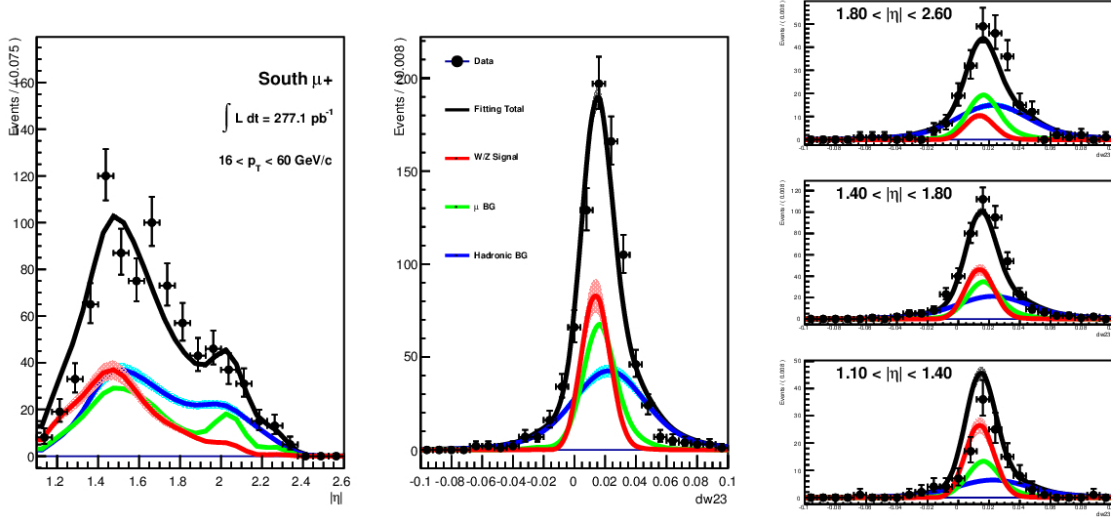


Figure 7.20: Here, we see the preliminary results of the EULMF for the 2013 Run. On the left,  $\eta$  is shown. In the middle,  $dw_{23}$ . On the right,  $dw_{23}$  is subdivided into the three standard  $\eta$  bins. In all cases, we see the unbinned data in black (with error bars), and the sum of the three fits in black. In Blue, we can see the fake-muon hadronic background. In Green, the muon background. In blue, we see the W-Signal result. The area under the curves represents the yield, relative to the total. Shown: South Arm,  $\mu^+$  [31]

---

South $\mu^-$				
Variable	Ralf	Daniel	Mike	Abraham
<b>Total events</b>	2032	2034	2022	2039
<b>Signal events</b>	$340^{+42.14}_{-41.42}$	$303^{+42.31}_{-41.59}$	$332^{+42.28}_{-41.58}$	$294^{+41.38}_{-41.38}$
<b>Hadron events</b>	$1424^{+53.57}_{-52.60}$	$1469^{+54.55}_{-53.59}$	$1433^{+53.97}_{-52.99}$	$1485^{+53.85}_{-53.85}$
<b>Muon events</b>	269	262	257	259
<b>Signal/BG</b>	$0.20^{+0.03}_{-0.03}$	$0.18^{+0.00}_{-0.00}$	$0.20^{+0.03}_{-0.03}$	$0.17^{+0.02}_{-0.00}$

---

Table 7.3: South arm  $W \rightarrow \mu^-$  fit results per analyzer [31]

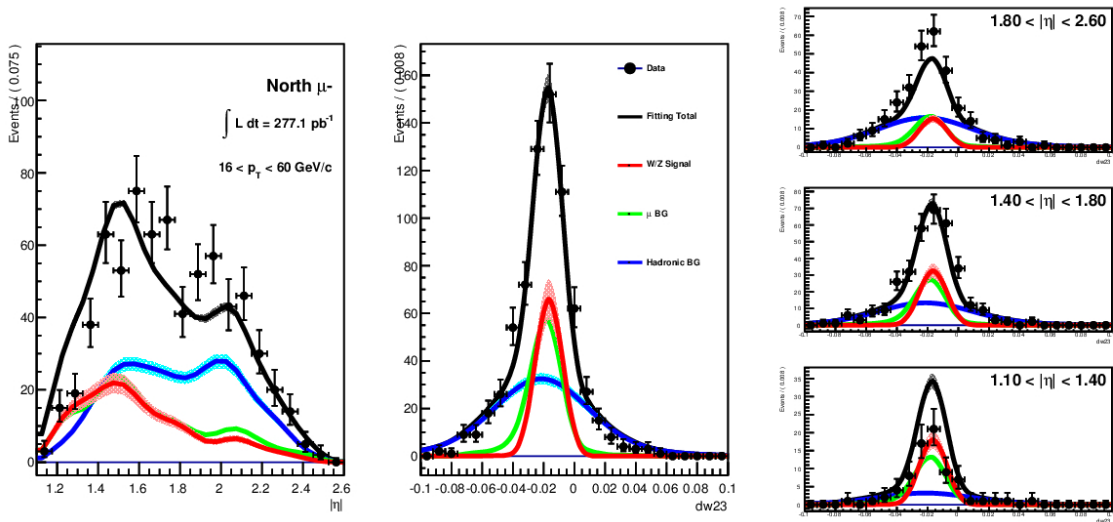


Figure 7.21: Here, we see the preliminary results of the EULMF for the 2013 Run. On the left,  $\eta$  is shown. In the middle,  $dw_{23}$ . On the right,  $dw_{23}$  is subdivided into the three standard  $\eta$  bins. In all cases, we see the unbinned data in black (with error bars), and the sum of the three fits in black. In Blue, we can see the fake-muon hadronic background. In Green, the muon background. In blue, we see the W-Signal result. The area under the curves represents the yield, relative to the total. Shown: North Arm,  $\mu-$  [31]

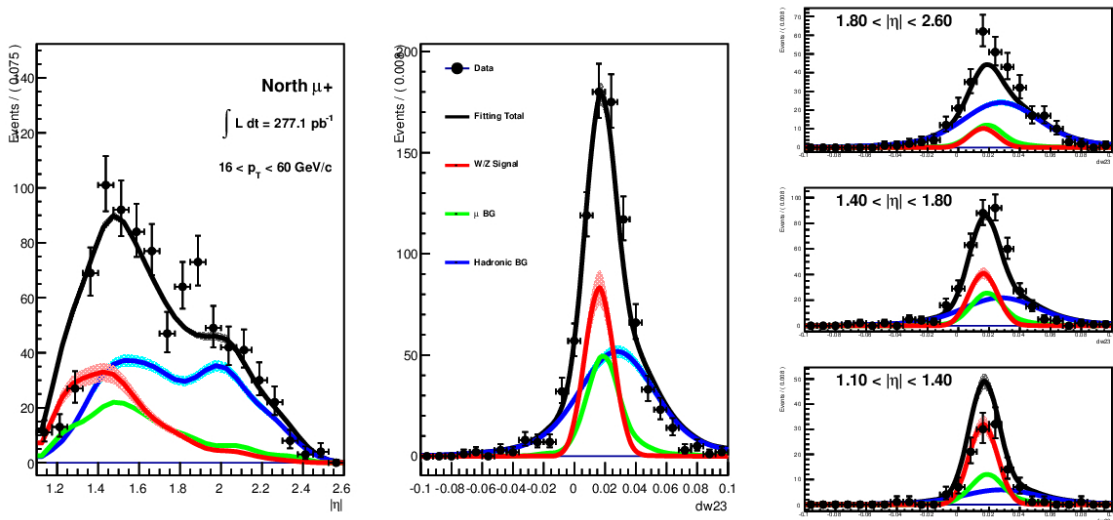


Figure 7.22: Here, we see the preliminary results of the EULMF for the 2013 Run. On the left,  $\eta$  is shown. In the middle,  $dw_{23}$ . On the right,  $dw_{23}$  is subdivided into the three standard  $\eta$  bins. In all cases, we see the unbinned data in black (with error bars), and the sum of the three fits in black. In Blue, we can see the fake-muon hadronic background. In Green, the muon background. In blue, we see the W-Signal result. The area under the curves represents the yield, relative to the total. Shown: North Arm,  $\mu^+$  [31].

For all data partitions, the signal to background ratio is presented in Table 7.4.

Arm	Charge	Total Events	Signal Events	Fake Muons	Muon Background	SBR
S	$\mu^-$	2023	$354^{+41.9714}_{-41.2598}$	$1448^{+53.6777}_{-52.7162}$	$2210^{+212103}_{-0.0263482}$	0.0258992
S	$\mu^+$	2468	$498^{+44.0941}_{-43.2297}$	$1767^{+57.046}_{-56.3006}$	$2030^{+252792}_{-0.0238242}$	0.0233755
N	$\mu^-$	2029	$370^{+34.4599}_{-33.7046}$	$1555^{+48.5042}_{-47.6586}$	$1040^{+223026}_{-0.0219055}$	0.0214353
N	$\mu^+$	2633	$505^{+37.9628}_{-37.2192}$	$2043^{+54.5676}_{-53.7571}$	$850^{+237312}_{-0.0189323}$	0.0185715

Table 7.4: A summary table from the results of the EULMF to the unbinned data set, summed to one  $\eta$  bin per arm and charge.

## 7.5 Systematic Tests

One of the rare advantages of this analysis was that I had the opportunity to undertake it in parallel with others, working as a team to accomplish goals. As a result, there were many complimentary systematic tests undertaken by others, summarized in Appendix E. These tests all confirm that the standardized checks for systematic problems with the analysis undertaken in many PHENIX spin analysis, do not yield any uncertainty to this analysis.

# Chapter 8

## Spin Analysis

### 8.1 Introduction

The overall goal of this analysis is to calculate the longitudinal asymmetry,  $A_L$ , for  $W \rightarrow \mu$  production. As discussed in Chapter 3,  $A_L$  is an important probe for the polarized parton distribution functions describing the quarks and anti-quarks of the proton sea-quark population.  $A_L$  provides an excellent probe in the case of the  $W$  interaction because of the parity violating nature of the interaction. The  $W^+$  interacts only with left handed quarks and right-handed anti-quarks, with respect to sea-quark interaction. This means that measurement of the  $W^+$  asymmetry gives direct access to the initial helicity state of  $u$  and  $\bar{d}$ , while  $W^-$  gives direct access to  $d$  and  $\bar{u}$ , and even then, the interaction is only permitted providing that either of the quarks are in an allowed initial helicity state.

$A_L$  can be written in terms of experimental yields for a process, or in terms of the scattering amplitudes of the  $W \rightarrow \mu$  process:

1. Write it in terms of the machine luminosity and the number of events of a particular type observed
2. Calculate the scattering amplitude for the process, and then the cross-section of the process. Write down the cross-section in terms of experimental observables.

Global fits have been carried by the DSSV analysis group [15] which predict the helicity distribution of various partons in the proton. These fits suffer from large uncertainties, which may be reduced via measurement of the asymmetry.

One measures this asymmetry, as discussed in item (1), and this measurement is then fed back into the models in order to reduce the degrees of freedom in the existing model reduce the uncertainty of the models' predictions.

The remaining task in this analysis, after an understanding of the signal to background ratio, and a means to estimate the real yields of the  $W$  signal event is to calculate asymmetries.

The Asymmetry Calculation relies on understanding the following items quantitatively:

1. What is the total beam polarization?
2. What is the polarization of the blue bunch, and yellow bunch at the time of each beam-beam interaction which generated a W-genic muon?
3. What is the total yield of  $\mu$ 's at forward and backward rapidity, for positive and negative charge?

$A_L$  is then calculated:

$$A_L = \frac{d\sigma^{\Rightarrow} - d\sigma^{\Leftarrow}}{d\sigma^{\Rightarrow} + d\sigma^{\Leftarrow}} \quad (8.1)$$

Where  $d\sigma$  is calculated as:

$$d\sigma = \frac{1}{\mathcal{L}} \dot{N}, \quad (8.2)$$

with  $\Rightarrow$  or  $\Leftarrow$  referring to tracks which come from positive( $\Rightarrow$ ) or negative( $\Leftarrow$ ) helicities relative to the initial proton polarization state.  $\mathcal{L}$  refers to the beam luminosity, a property of the colliding beams, and  $\dot{N}$  refers to the production rate of W-genic muons. This calculation is done for forward and backward rapidities for positively and negatively charged muons, with associated asymmetries calculated individually for each arm and charge. The asymmetries are then summed according to the charge of the parent  $W$  boson.

In practice, one does not need to calculate cross-sections for  $W \rightarrow \mu$  for the purposes of evaluating  $A_L$ . Only yields are needed, since in principal  $\mathcal{L}$  will be a common factor in all cross-sections and cancel out. This of course comes with major caveats— $\mathcal{L}$  only cancels out if the relative luminosity of each polarization condition is the same. Spin patterns are chosen in order to ensure this happens. This is verified by counting the number of polarization states observed, and ensuring that all states occur with the same frequency.

Experimentally, raw asymmetries, ( $\epsilon_L$ ), are constructed from muon yields in the same way as  $A_L$  but without correction for background dilution or beam polarization. With those factors applied, we may transform the raw asymmetry to the true longitudinal asymmetry. This is further discussed in Section 8.5.2

## 8.2 Measured Beam Polarization

Beam polarization is obtained from the p-Carbon scattering experiments done for every polarized fill. Because fills are eight hours each, several consecutive runs in the same fill will share the same spin pattern, but the overall polarization of the beam may change as a function of time due to depolarizing resonances. The data archived during these measurements is stored to a database, and an analysis, ‘spin database QA’, performs consistency checks to ensure that polarization patterns do not change over the course of a fill, and are consistent with the advertised polarization pattern. This study also produces the average beam polarization per run. The polarization of the beams are measured at the beginning and end of every fill. This was described in Section 4.3. The results of the polarization study and spin database QA are all stored in a PostgreSQL database, indexed by run number. The average percent polarization of the blue and yellow beams over the Run 13 run are summarized in Figure 8.1 and Figure 8.2.

The average beam polarization over the whole of Run 13 was well over 50% for the majority of the run, with a few poorly polarized runs. This is accounted for by calculating asymmetries for individual runs which are weighted by that run’s average polarization. It was found that the final asymmetry resulting from individual run weighting was the same using the average polarization for all runs. This indicates that the polarization for most of the recorded data was consistent. The average beam polarization for each run in the Run 13 data set is summarized in Figure 8.1, indicating a consistent, regular distribution. The average beam polarization is also visualized as a histogram to highlight the overall distribution of polarizations in the 2013 data set, Figure 8.2.

Beam Polarization For Run 13

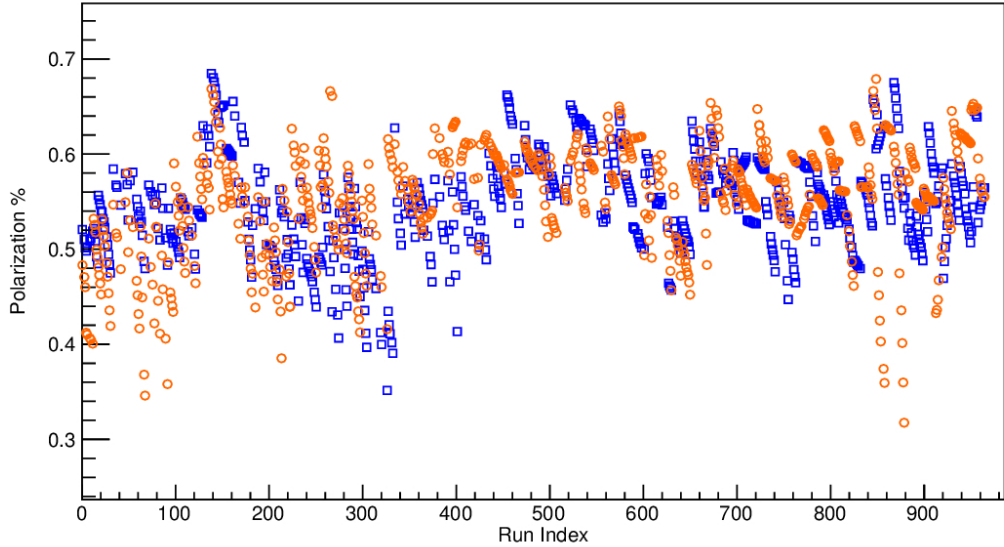
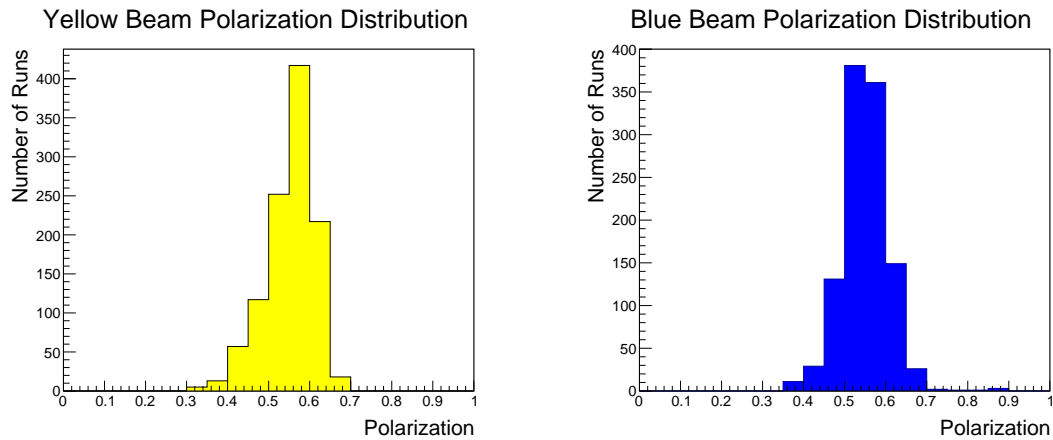


Figure 8.1: Shown: the average beam polarization per run over the course of the 2013 data set. All of the runs in the analysis were indexed from 0 to approximately 1000, and plotted in the order that they were taken. The blue open circles are from the blue beam, the yellow open circles are for the yellow beam.



(a) Distribution of Yellow Beam Polarization

(b) Distribution of Blue Beam Polarization

Figure 8.2: Panel (a) shows the yellow beam polarization distribution over all runs in the 2013 data taking period, with an average of about 55.27%. Panel (b) shows the blue beam similarly, with an average polarization of 55.08% polarization.

## 8.3 Spin Patterns

In the 2013 Run Period, I was in charge of the PHENIX spin quality assurance while the detector was actively taking data. As part of this work it was my job to maintain the monitoring software as well as confirm that physics fills were usable for spin physics analyses. The criteria for ‘usable’ in the context of live data taking QA is to confirm that the spin pattern filled into the beams is stable, and matches the advertised pattern. A spin pattern refers to the sequence of individual bunch polarizations (positive or negative) repeated through out the filled bunches of the blue and yellow beams. This live quality assurance monitoring is vital because we rely on knowing the spin patterns associated with each bunch-crossing to identify the initial helicity state of collisions, which is used in the asymmetry calculation.

PHENIX uses a numbering system identify which bunch in the blue beam collides with which bunch from the yellow beam. Blue bunch “0” collides with yellow bunch “0” at the PHENIX interaction point, by definition. There are bunches in the blue, and yellow beams which are left purposefully empty, which allows one to later reconstruct and confirm which bunches are colliding, since if a filled bunch collides with an empty bunch, there will be no collisions for that bunch crossing. PHENIX has a slight delay in its triggering electronics related to the time delay between the DAQ receiving the ‘begin run’ event and the first ‘data event’. This delay is exactly five bunch-crossings in length, so when data is reconstructed, recorded bunch crossing numbers in the data stream will be off by 5. Considering the BBC rate as a function of bunch crossing allows one to identify, and correct this crossing-shift, which is done in the offline spin data QA [83].

In the 2013 data taking period, RHIC provided sixteen different bunch patterns - the patterns were varied to help avoid any kind of systematic bias towards one bunch polarization over another. For the first half of the 2013 data period, each beam had two consecutive empty bunches, and a 10-bunch long empty ‘abort-gap’. The abort gap is canonically set to occur at bunch number 109-119 (indexing from 0). The consecutive empty bunches occurred at position 68 and 69 in the yellow beam, and 28 and 29 in the blue beam.

Bunch patterns P1-P8 were used in the first half of the data taking period, with P21-P28 being used in the second half of the data taking period in Run 2013. The spin

patterns were defined using repeated sub-patterns, repeated until the last bunch in a given beam is reached.

The patterns are designed to provide many permutations of bunch-bunch polarization conditions. The beams are transversely polarized: '+' is up and '-' is down during the fill, but the polarizations are rotated towards PHENIX (longitudinally) immediately before collision. The various collision conditions need to occur with the same relative frequency—so the patterns are designed to fulfill this requirement.

The polarization consistency is visualized in Figure 8.3, which shows, for all muon tracks after the basic cut, consistent fills. Additionally, if one counts the various permutations of spin patterns, i.e. ++, -+, +-, -, such that the left character is the blue polarization and the right character is the yellow polarization, one should expect to see very similar yields for each polarization combination, which is confirmed with Figure 8.4.

With consistent distributions of polarization seen for each arm/charge, one does not need to consider possible dilution of the asymmetry due to incorrect accounting for polarization. Even so, this check has been done, and is presented in the appendix.

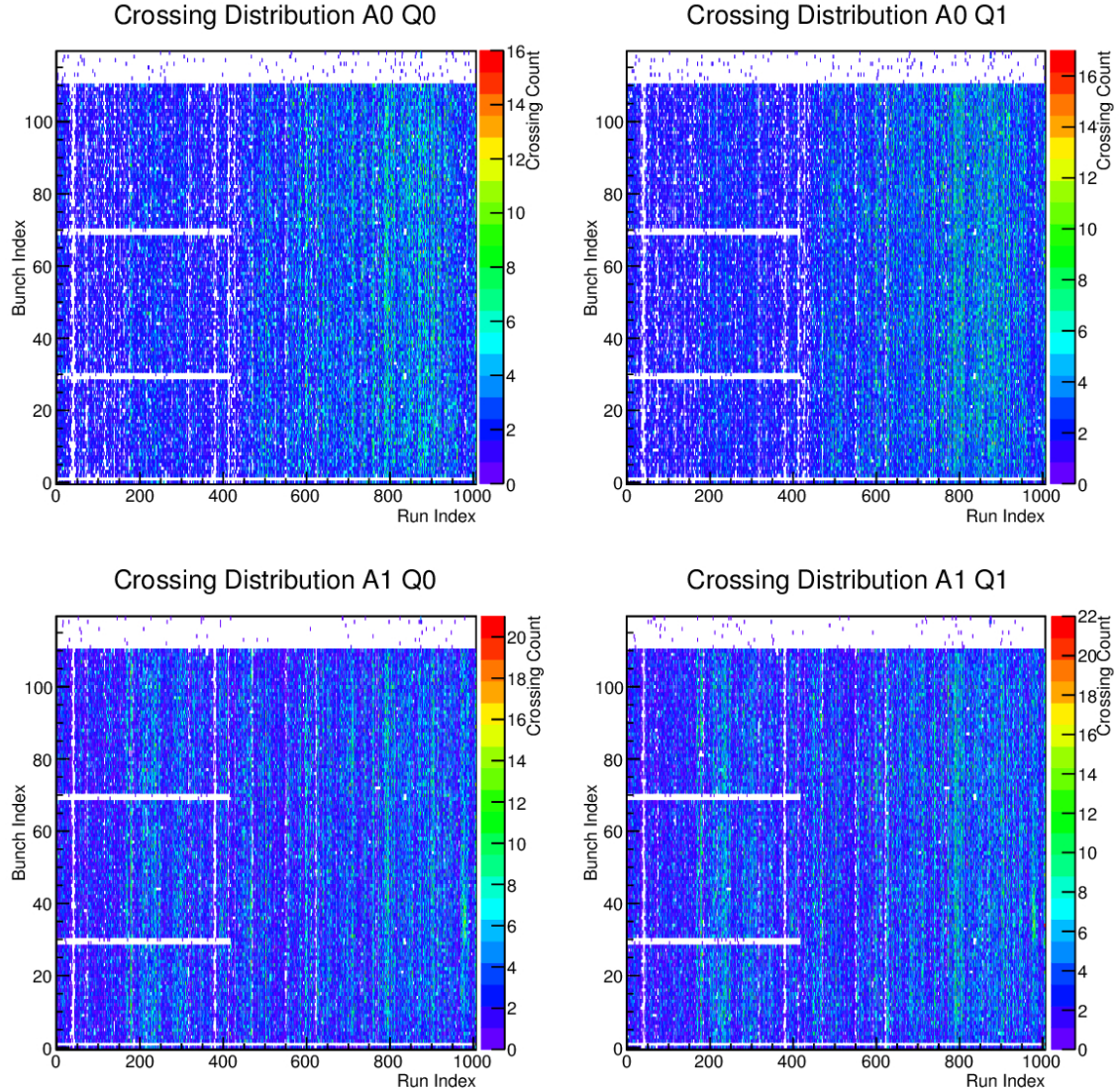


Figure 8.3: Shown: the crossing distribution for every run taken for the 2013 data set. We use the typical code for arm/charge. The top row is for the South Arm. The bottom row is for the North Arm. The left column is for negative charge, the right column is for positive charge. Note the characteristic empty abort gap, as well as the change from  $109 \times 109$  colliding bunches to  $111 \times 111$  colliding bunches about 1/3 of the way through the data taking period.

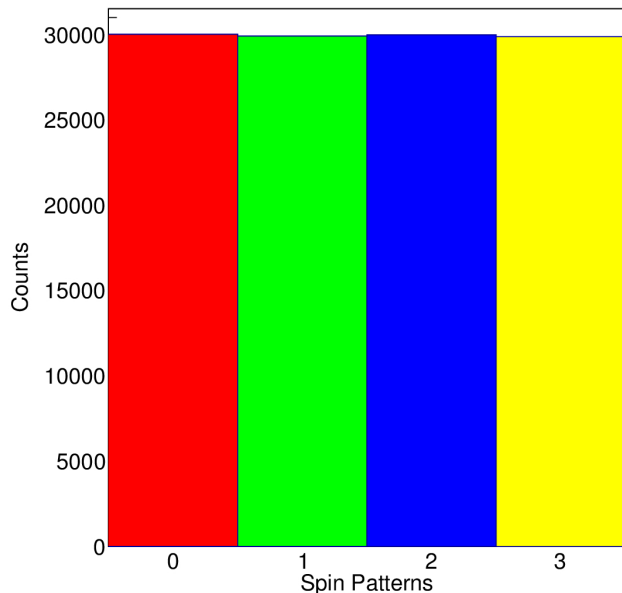


Figure 8.4: Shown: the yield for various crossing combinations as taken from the dataset itself, rather than the database. We see a very consistent distribution between the various possible crossing patterns. In this case, the horizontal axis is the crossing pattern code— $0:++$ ,  $1:-+$ ,  $2:+-$ ,  $3:--$ . Any slight difference between yields for each pattern is well below our experimental precision.

Pattern	Blue Pattern	Yellow Pattern
P1	++-- +--+ +--- ++-	++++ ---- +--+ -
P2	--++ --++ --++ +	+++- ---+ ++ -
P3	+--+ ++-- ++--	-- -- +--+ -- +
P4	--++ --++ --++ +	-- -- +--+ -- +
P5	+--+ ---- ++++ -	+--+ +--+ +--
P6	+--+ ---- ++++ -	--++ --++ --++ +
P7	-- -- ++++ -- --	+--+ +--+ +--
P8	-- -- ++++ -- --	--++ --++ --++ +
P21	+--+ ++-- ++--	--++ ++-- ++-- +
P22	+--+ ++-- ++--	+--+ -- -- +--+ -
P23	--++ --++ --++ +	--++ ++-- ++-- +
P24	--++ --++ --++ +	+--+ -- -- +--+ -
P25	--++ ---- ++++ --	+--+ +--+ +--
P26	--++ ---- ++++ --	--++ +--+ --++ +
P27	+-- --++ --++ +	+-- +--+ +--
P28	+-- --++ --++ +	--++ --++ +--

Table 8.1: From left to right, bunch 0 in the blue or yellow beam is filled with the leftmost polarization, with bunch 1 getting the next, and so on. The pattern repeats as soon as the end has been reached, until we get to the last filled bunch, with any empty bunch being ‘polarized’ as if it were not empty.

## 8.4 Muon Yields

Calculating  $A_L$  requires obtaining yields for positive and negative rapidity muons for all arm and charge conditions associated with the  $W \rightarrow \mu$  signal process.

Yields are obtained in the signal region by applying the  $W_{ness}$  cut to the recorded data set (cut events with  $W_{ness} < 0.99$ ), sorted into arm, charge, and pseudorapidity bin. Each yield is then corrected for the signal to background ratio, obtained from Section 7.4. The final muon yields are summarized in Table 8.5 (south arm, three eta bins), and Table 8.6 (north arm, three eta bins).

Though there was enough integrated luminosity to separate data into six total eta bins over the full rapidity range of the PHENIX muon arms, as a consistency check to previous analysis which only had enough statistics for two  $\eta$  bins, one forward, and one backward for  $A_L^{W+}$ , I have also included data matching previous binning, Table 8.2.

With the extraction of the yields and confirmation that the beam polarization is well behaved, the asymmetries are calculated and corrected for the signal to background dilution, and the beam polarization. Any non-vanishing asymmetry with such corrections represents actual physical asymmetries.

South Arm				
Charge	Helicity	$ \eta $	Range	$\mu$ Yield
-1	++	1.1 < $ \eta $ < 1.4		12
-1	++	1.4 < $ \eta $ < 1.8		67
-1	++	1.8 < $ \eta $ < 2.6		63
-1	-+	1.1 < $ \eta $ < 1.4		21
-1	-+	1.4 < $ \eta $ < 1.8		99
-1	-+	1.8 < $ \eta $ < 2.6		49
-1	+--	1.1 < $ \eta $ < 1.4		19
-1	+--	1.4 < $ \eta $ < 1.8		76
-1	+--	1.8 < $ \eta $ < 2.6		58
-1	--+	1.1 < $ \eta $ < 1.4		14
-1	--+	1.4 < $ \eta $ < 1.8		68
-1	--+	1.8 < $ \eta $ < 2.6		57
-1	**	1.1 < $ \eta $ < 1.4		0
-1	**	1.4 < $ \eta $ < 1.8		0
-1	**	1.8 < $ \eta $ < 2.6		0
+1	++	1.1 < $ \eta $ < 1.4		28
+1	++	1.4 < $ \eta $ < 1.8		94
+1	++	1.8 < $ \eta $ < 2.6		50
+1	-+	1.1 < $ \eta $ < 1.4		26
+1	-+	1.4 < $ \eta $ < 1.8		96
+1	-+	1.8 < $ \eta $ < 2.6		41
+1	+--	1.1 < $ \eta $ < 1.4		22
+1	+--	1.4 < $ \eta $ < 1.8		124
+1	+--	1.8 < $ \eta $ < 2.6		47
+1	--+	1.1 < $ \eta $ < 1.4		26
+1	--+	1.4 < $ \eta $ < 1.8		97
+1	--+	1.8 < $ \eta $ < 2.6		66
+1	**	1.1 < $ \eta $ < 1.4		0
+1	**	1.4 < $ \eta $ < 1.8		0
+1	**	1.8 < $ \eta $ < 2.6		0

Figure 8.5: Shown: the South arm's yields for each helicity combination of colliding protons, with the polarization of the blue beam and yellow beams color coded in column 2. These yields represent all muons observed in the signal region, and are a combination of signal and background muons. + represents positive helicity beam polarization relative to the blue beam's momentum, - represents negative helicity, with \* representing an unfilled bunch.

North Arm				
Charge	Helicity	$ \eta $	Range	$\mu$ Yield
-1	++	1.1 < $ \eta $ < 1.4		18
-1	++	1.4 < $ \eta $ < 1.8		76
-1	++	1.8 < $ \eta $ < 2.6		57
-1	-+	1.1 < $ \eta $ < 1.4		14
-1	-+	1.4 < $ \eta $ < 1.8		63
-1	-+	1.8 < $ \eta $ < 2.6		56
-1	+-	1.1 < $ \eta $ < 1.4		13
-1	+-	1.4 < $ \eta $ < 1.8		74
-1	+-	1.8 < $ \eta $ < 2.6		61
-1	--	1.1 < $ \eta $ < 1.4		19
-1	--	1.4 < $ \eta $ < 1.8		63
-1	--	1.8 < $ \eta $ < 2.6		65
-1	**	1.1 < $ \eta $ < 1.4		0
-1	**	1.4 < $ \eta $ < 1.8		0
-1	**	1.8 < $ \eta $ < 2.6		0
+1	++	1.1 < $ \eta $ < 1.4		24
+1	++	1.4 < $ \eta $ < 1.8		96
+1	++	1.8 < $ \eta $ < 2.6		60
+1	-+	1.1 < $ \eta $ < 1.4		30
+1	-+	1.4 < $ \eta $ < 1.8		95
+1	-+	1.8 < $ \eta $ < 2.6		64
+1	+-	1.1 < $ \eta $ < 1.4		27
+1	+-	1.4 < $ \eta $ < 1.8		68
+1	+-	1.8 < $ \eta $ < 2.6		64
+1	--	1.1 < $ \eta $ < 1.4		33
+1	--	1.4 < $ \eta $ < 1.8		99
+1	--	1.8 < $ \eta $ < 2.6		56
+1	**	1.1 < $ \eta $ < 1.4		0
+1	**	1.4 < $ \eta $ < 1.8		0
+1	**	1.8 < $ \eta $ < 2.6		0

Figure 8.6: Shown: the North arm's yields for each helicity combination of colliding protons, with the polarization of the blue beam and yellow beams color coded in column 2. These yields represent all muons observed in the signal region, and are a combination of signal and background muons. + represents positive helicity beam polarization relative to the blue beam's momentum, - represents negative helicity, with \* representing an unfilled bunch.

<b>Arm</b>	<b>Charge</b>	<b>Helicity</b>	$\mu$	<b>Yield</b>
S	-1	++		142
S	-1	-+		169
S	-1	+−		153
S	-1	−−		139
S	-1	**		0
S	+1	++		172
S	+1	-+		163
S	+1	+−		193
S	+1	−−		189
S	+1	**		0
N	-1	++		151
N	-1	-+		133
N	-1	+−		148
N	-1	−−		147
N	-1	**		0
N	+1	++		180
N	+1	-+		189
N	+1	+−		159
N	+1	−−		188
N	+1	**		0

Table 8.2: Shown: a division of the yields by arm, charge, and helicity combination, which is color-coded for the polarization of the blue and yellow beams. Yields contain a combination of signal and background muons. + represents positive helicity beam polarization relative to the blue beam's momentum, - represents negative helicity, with \* representing an unfilled bunch.

## 8.5 Calculation of $\epsilon_L$ and $A_L$ for $W \rightarrow \mu$

With an understanding of beam polarization and the signal to background ratio, the asymmetries are calculated. One first proceeds the calculation of the raw asymmetry,  $\epsilon_L$ , directly from the raw muon yields, and subsequently corrects for dilution from background events and beam polarization to obtain the true longitudinal asymmetry,  $A_L$ .

### 8.5.1 Defining $A_L^{W\pm}$ , $A_{LL}^{W\pm}$

There is a lot of language and terminology inherited from previous work in Deep Inelastic Scattering Experiments and the models developed to characterize the results of these experiments. One such concept is the idea of a ‘probe’ particle, and a ‘target’ particle. In DIS experiments, especially those designed to study proton polarization, there is typically a high energy electron beam impinging on a spin polarized gas target. Asymmetries were then defined in terms of scattering cross sections, where the polarization of the beam (or probe) and target were known.

For the case of RHIC, this formalism must be translated to describe an intersecting ring collider. Since final state of the  $W \rightarrow \mu$  is measured, and the initial polarization state of the colliding protons is known, one may adopt the formalism, assigning one proton to the ‘probe’ and the other to the ‘target’. Our convention is to take the polarized proton as our target, and then assume the other proton is our ‘probe’, subsequently summing over the various probe polarizations. In this way, the asymmetries are measured in  $W$  boson production.

To describe the asymmetry intuitively: the longitudinal asymmetry for  $W$  boson production refers to the difference in  $W$  Boson production for two different initial-state proton polarizations. Mathematically, this is formalized by normalizing this total difference in production with the total production of  $W$  Bosons from both polarization states. Because we may treat the blue beam as the probe *or* the target (similarly with the yellow beam), one must take care, because the helicity of the initial state protons is defined as positive or negative relative to the probe beam’s momentum. Therefore, because PHENIX records and labels data according to its coordinate system, the sign of pseudorapidity might switch based on which beam is the probe, and which beam of the target, when calculating asymmetries. This convention is summarized in Table 8.3. The convention can be summarized as “when

is a factor of -1 applied to the rapidity measured with respect to the PHENIX coordinate system”.

Arm	Charge	Probe Beam	Target Beam	Sign of $\eta$
N	$\mu^+$	Blue	Yellow	$+\eta$
N	$\mu^-$	Blue	Yellow	$+\eta$
S	$\mu^+$	Blue	Yellow	$-\eta$
S	$\mu^-$	Blue	Yellow	$-\eta$
N	$\mu^+$	Yellow	Blue	$-\eta$
N	$\mu^-$	Yellow	Blue	$-\eta$
S	$\mu^+$	Yellow	Blue	$+\eta$
S	$\mu^-$	Yellow	Blue	$+\eta$

Table 8.3: A summary of the sign convention when we consider rapidity with respect to the probe beam, as opposed to the rapidity of the PHENIX coordinate system. Column **Sign of  $\eta$**  refers to the sign of  $\eta$  of the observed muon track with respect to the probe beam.

It is very important to stick with our convention, as it allows us to combine the results of the raw asymmetries, to obtain a full description for  $A_L^{W\pm}$ , since  $W^\pm$  may decay into forward, or backward rapidities. Proceeding with the asymmetry calculation, with our conventions defined:

For any fixed rapidity bin, we write down the Single Spin Asymmetry, for  $W^\pm \rightarrow \mu$  production:

$$A_L = \frac{d\sigma^{\Rightarrow} - d\sigma^{\Leftarrow}}{d\sigma^{\Rightarrow} + d\sigma^{\Leftarrow}} \quad (8.3)$$

Recall from earlier that  $\Leftarrow$  refers to the negative helicity condition of the probe proton, while  $\Rightarrow$  refers to the negative helicity positive helicity of the probe proton. The helicity states of the target proton are summed over. The double spin asymmetry,  $A_{LL}$ , is defined similarly:

$$A_{LL} = \frac{d\sigma^{\Rightarrow\Rightarrow} - d\sigma^{\Leftarrow\Leftarrow}}{d\sigma^{\Rightarrow\Rightarrow} + d\sigma^{\Leftarrow\Leftarrow}} \quad (8.4)$$

$A_{LL}$  is calculated as a positivity constraint [37] in order restrict the allowed domain for spin observables.  $A_{LL}$  gives access to the product of quark and anti-quark polarizations, which is an important systematic effect which providing a constraint on the quark polarization. In this case the helicity states of the probe and target proton are indicated with  $\Rightarrow$  and  $\Leftarrow$ , with the left-hand arrow referring to the probe, and the right-hand arrow referring to the target.

With the required elements ready to calculate our asymmetries, the muon yields, beam polarization, the signal to background ratio, and the rapidity convention, the asymmetries are calculated.

Yields for the south arm are denoted:

$$\left\{ n_{(++)}^S, n_{(+-)}^S, n_{(-+)}^S, n_{(--)}^S \right\} \quad (8.5)$$

and north arm:

$$\left\{ n_{(++)}^N, n_{(+-)}^N, n_{(-+)}^N, n_{(--)}^N \right\} \quad (8.6)$$

With the + and – signs indicating the polarization of the beams, (left sign refers to blue polarization, right sign refers to yellow polarization). Implicitly, these yields are taken with respect to an  $\eta$  bin.

### 8.5.2 Calculating $A_L^{W\pm}$ , $A_{LL}^{W\pm}$

The asymmetries are calculated:

#### Single Spin Asymmetries

##### Polarized Blue Probe, Yellow Target, $\eta > 0$ w.r.t. Probe

$$\epsilon_{L,N}^{\eta>0} = \frac{\sigma^{\Rightarrow} - \sigma^{\Leftarrow}}{\sigma^{\Rightarrow} + \sigma^{\Leftarrow}} \rightarrow \frac{\left( n_{(++)}^N + n_{(+-)}^N \right) - \left( n_{(-+)}^N + n_{(--)}^N \right)}{\left( n_{(++)}^N + n_{(+-)}^N \right) + \left( n_{(-+)}^N + n_{(--)}^N \right)} \quad (8.7)$$

##### Polarized Blue Probe, Yellow Target, $\eta < 0$ w.r.t Probe

$$\epsilon_{L,S}^{\eta<0} = \frac{\sigma^{\Rightarrow} - \sigma^{\Leftarrow}}{\sigma^{\Rightarrow} + \sigma^{\Leftarrow}} \rightarrow \frac{\left( n_{(++)}^S + n_{(+-)}^S \right) - \left( n_{(-+)}^S + n_{(--)}^S \right)}{\left( n_{(++)}^S + n_{(+-)}^S \right) + \left( n_{(-+)}^S + n_{(--)}^S \right)} \quad (8.8)$$

**Polarized Yellow Probe, Blue Target,  $\eta > 0$  w.r.t Probe**

$$\epsilon_{L,S}^{\eta>0} = \frac{\sigma^{\Rightarrow} - \sigma^{\Leftarrow}}{\sigma^{\Rightarrow} + \sigma^{\Leftarrow}} \rightarrow \frac{\left(n_{(++)}^S + n_{(-+)}^S\right) - \left(n_{(+ -)}^S + n_{(--)}^S\right)}{\left(n_{(++)}^S + n_{(-+)}^S\right) + \left(n_{(+ -)}^S + n_{(--)}^S\right)} \quad (8.9)$$

**Polarized Yellow Probe, Blue Target,  $\eta < 0$  w.r.t Probe**

$$\epsilon_{L,N}^{\eta<0} = \frac{\sigma^{\Rightarrow} - \sigma^{\Leftarrow}}{\sigma^{\Rightarrow} + \sigma^{\Leftarrow}} \rightarrow \frac{\left(n_{(++)}^N + n_{(-+)}^N\right) - \left(n_{(+ -)}^N + n_{(--)}^N\right)}{\left(n_{(++)}^N + n_{(-+)}^N\right) + \left(n_{(+ -)}^N + n_{(--)}^N\right)} \quad (8.10)$$

**Double Spin Asymmetries**

**$A_{LL}$  North Arm**

$$\epsilon_{LL,N} = \frac{\sigma^{\Rightarrow\Rightarrow} - \sigma^{\Leftarrow\Leftarrow}}{\sigma^{\Rightarrow\Rightarrow} + \sigma^{\Leftarrow\Leftarrow}} \rightarrow \frac{\left(n_{(++)}^N + n_{(--)}^N\right) - \left(n_{(+ -)}^N + n_{(-+)}^N\right)}{\left(n_{(++)}^N + n_{(--)}^N\right) + \left(n_{(+ -)}^N + n_{(-+)}^N\right)} \quad (8.11)$$

**$A_{LL}$  South Arm**

$$\epsilon_{LL,S} = \frac{\sigma^{\Rightarrow\Rightarrow} - \sigma^{\Leftarrow\Leftarrow}}{\sigma^{\Rightarrow\Rightarrow} + \sigma^{\Leftarrow\Leftarrow}} \rightarrow \frac{\left(n_{(++)}^S + n_{(--)}^S\right) - \left(n_{(+ -)}^S + n_{(-+)}^S\right)}{\left(n_{(++)}^S + n_{(--)}^S\right) + \left(n_{(+ -)}^S + n_{(-+)}^S\right)} \quad (8.12)$$

In all cases,  $\epsilon$  refers to the raw asymmetry, i.e. an asymmetry which has not been corrected for dilution due to background contamination of the yields, or dilution due to less than 100% beam polarization.

The correction for either dilution is straight-forward:

$$A_L^{\eta>0} = \frac{D^N}{P_B} \epsilon_{L,N}^{\eta>0} = \frac{D^S}{P_Y} \epsilon_{L,S}^{\eta>0} \quad (8.13)$$

$$A_L^{\eta<0} = \frac{D^N}{P_B} \epsilon_{L,N}^{\eta<0} = \frac{D^S}{P_Y} \epsilon_{L,S}^{\eta<0} \quad (8.14)$$

$$A_{LL} = \frac{D^N}{P_B P_Y} \epsilon_{LL,N} = \frac{D^S}{P_B P_Y} \epsilon_{LL,S} \quad (8.15)$$

### 8.5.3 Preliminary Results

My analysis group earned PHENIX preliminary status for these results in October of 2015. The results were submitted for collaboration review, and were judged worthy of showing at conferences

The calculated asymmetries are shown in three  $\eta$  bins per arm in Figure 8.7. The asymmetries calculated for comparison with the previous  $\eta$  binning contention are shown in Figure 8.8. The signal to background ratios and yields were calculated from the signal region,  $W_{ness} > 0.99$ .

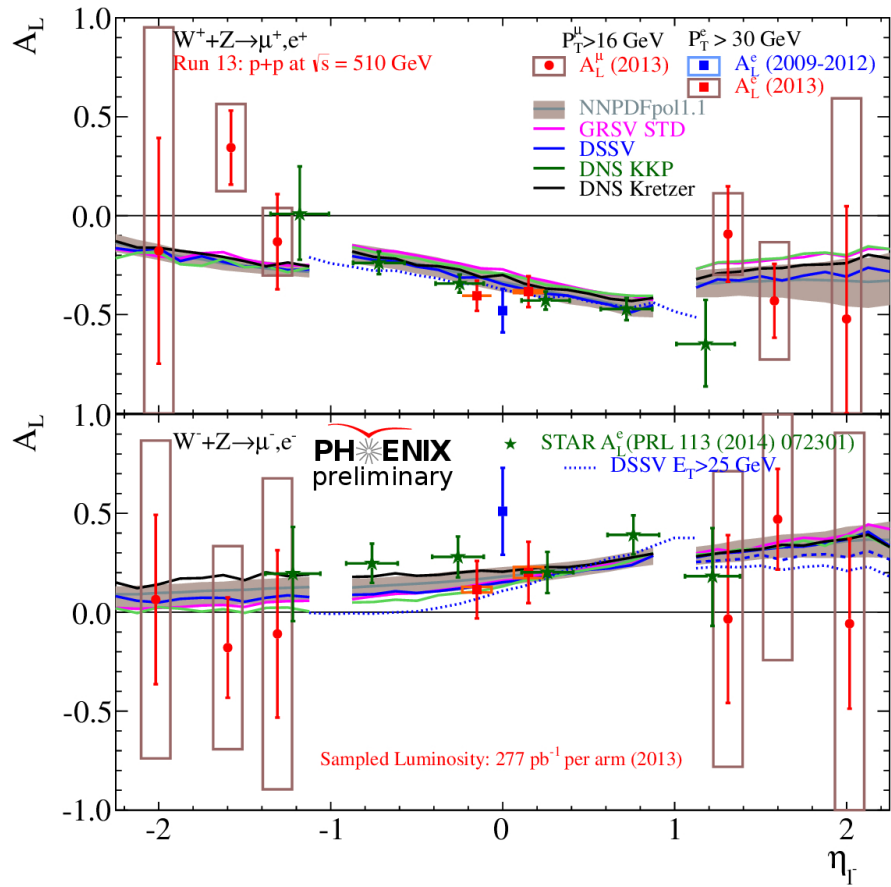


Figure 8.7: Shown: the preliminary longitudinal single spin asymmetries for three distinct bins in  $\eta$  per Muon Arm. The red boxed points represent the measured asymmetry from the 2013 analysis. The green points show the central rapidity asymmetries produced from STAR in 2014, with the blue points showing PHENIX's central asymmetries from 2009-2012. The colored curves are superimposed predicted asymmetries. The top panel shows results for the  $W^+$  process, with the bottom panel showing results for the  $W^-$  process.

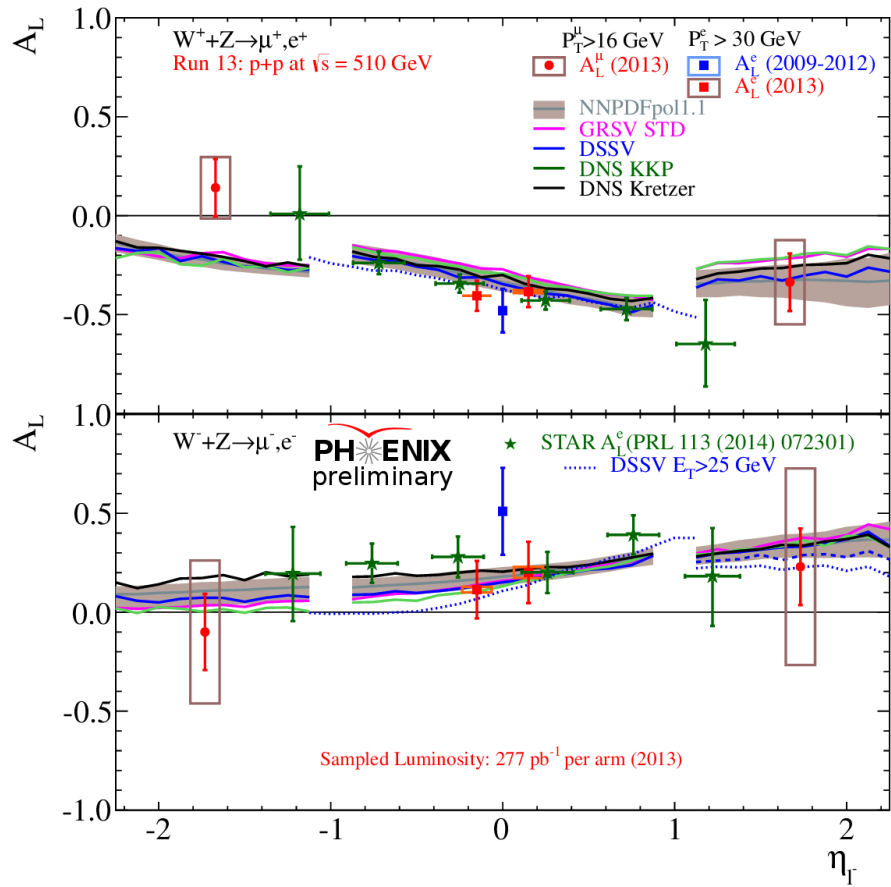


Figure 8.8: Shown: the preliminary longitudinal single spin asymmetries for two distinct bins in  $\eta$  per Muon Arm. The red boxed points represent the measured asymmetry from the 2013 analysis. The green points show the central rapidity asymmetries produced from STAR in 2014, with the blue points showing PHENIX's central asymmetries from 2009-2012. The colored curves are superimposed predicted asymmetries. The top panel shows results for the  $W^+$  process, with the bottom panel showing results for the  $W^-$  process.

## Chapter 9

# Discussion and Conclusion

The PHENIX results on the Asymmetry put an important constraint on the polarized parton distribution functions, and spin contributions of the sea-quarks to the total proton spin. Due to the vanishing asymmetries found in this analysis, we now know that with:

$$A_L(x, Q^2) = \frac{\sigma^+ - \sigma^-}{\sigma^+ + \sigma^-} \quad (9.1)$$

$$\equiv \frac{g_1(x, Q^2)}{F_1(x, Q^2)} \quad (9.2)$$

$$\approx 0 \quad (9.3)$$

that the sea quarks must contribute very little to the proton's total spin. We additionally know, with good constraints on the contributions from the valence quarks, that the majority of the proton spin must reside in the gluons and the angular momentum of the proton.

The task of building a RHIC and a PHENIX is truly monumental. The fact that particle physics can even be done in the first place, is absolutely astounding to me—the amount of infrastructure, technical expertise, collaboration, financial and intellectual capital needed to build such an enormous and precise machine is something that is very difficult to communicate.

Subsequent experiments such as the new Electron Ion Collider, which will be completed in coming years will be able to measure these contributions with much higher precision.

# Bibliography

- [1] a. Accardi, J. L. Albacete, M. Anselmino, N. Armesto, E. C. Aschenauer, A. Bacchetta, D. Boer, W. K. Brooks, T. Burton, N. B. Chang, W. T. Deng, A. Deshpande, M. Diehl, A. Dumitru, R. Dupré, R. Ent, S. Fazio, H. Gao, V. Guzey, H. Hakobyan, Y. Hao, D. Hasch, R. Holt, T. Horn, M. Huang, A. Hutton, C. Hyde, J. Jalilian-Marian, S. Klein, B. Kopeliovich, Y. Kovchegov, K. Kumar, K. Kumerički, M. A. C. Lamont, T. Lappi, J. H. Lee, Y. Lee, E. M. Levin, F. L. Lin, V. Litvinenko, T. W. Ludlam, C. Marquet, Z. E. Meziani, R. McKeown, A. Metz, R. Milner, V. S. Morozov, A. H. Mueller, B. Müller, D. Müller, P. Nadel-Turonski, A. Prokudin, V. Ptitsyn, X. Qian, J. W. Qiu, M. Ramsey-Musolf, T. Roser, F. Sabatié, R. Sassot, G. Schnell, P. Schweitzer, E. Sichtermann, M. Stratmann, M. Strikman, M. Sullivan, S. Taneja, T. Toll, D. Trbojevic, T. Ullrich, R. Venugopalan, S. Vigdor, W. Vogelsang, C. Weiss, B. W. Xiao, F. Yuan, Y. H. Zhang, L. Zheng, H. Paukkunen, A. Prokudin, V. Ptitsyn, X. Qian, J. W. Qiu, M. Ramsey-Musolf, T. Roser, F. Sabatié, R. Sassot, G. Schnell, P. Schweitzer, E. Sichtermann, M. Stratmann, M. Strikman, M. Sullivan, S. Taneja, T. Toll, D. Trbojevic, T. Ullrich, R. Venugopalan, S. Vigdor, W. Vogelsang, C. Weiss, B. W. Xiao, F. Yuan, Y. H. Zhang, and L. Zheng. Electron Ion Collider: The Next QCD Frontier - Understanding the glue that binds us all. *arXiv preprint*, page 164, 2012.
- [2] Herbert S. Long. The Unity of Empedocles' Thought. *The American Journal of Philology*, 70(2):142–158, 1949.
- [3] Craig Freudenrich. Combined Atomic Orbital, 2001.
- [4] Manisearch. scale\_of\_matter, 2010.
- [5] Marco Stratmann. Spin physics at rhic - a theoretical overview. Technical report, 2009.
- [6] Arthur Steward Eve. *Rutherford: Being the Life and Letters of the Rt. Hon. Lord Rutherford, O. M.* The University Press, 1939.
- [7] Kurzon. Diagram Illustratng Geiger-Marsden Experiment, 2014.
- [8] Bruxelles Benjamin Croupie. Participants of the 5th Solvay Congress. Technical report, 1927.
- [9] Wikimedia. Hideki Yukawa. *The Mainichi Graphic*, sep 1952.

- [10] FNAL. Fermi National Lab Bubble Chamber, 2005.
- [11] ENERGY.GOV. Bubble Chamber Tracks, 1973.
- [12] Ddn2. Electron Proton Deep Inelastic Scattering, 2008.
- [13] Latham Boyle. standard\_model\_complete, 2014.
- [14] J Beringer, J.-F. Arguin, R M Barnett, K Copic, O Dahl, D E Groom, C.-J. Lin, J Lys, H Murayama, C G Wohl, W.-M. Yao, P A Zyla, C Amsler, M Antonelli, D M Asner, H Baer, H R Band, T Basaglia, C W Bauer, J J Beatty, V I Belousov, E Bergren, G Bernardi, W Bertl, S Bethke, H Bichsel, O Biebel, E Blucher, S Blusk, G Brooijmans, O Buchmueller, R N Cahn, M Carena, A Ceccucci, D Chakraborty, M.-C. Chen, R S Chivukula, G Cowan, G D'Ambrosio, T Damour, D de Florian, A de Gouv  a, T DeGrand, P de Jong, G Dissertori, B Dobrescu, M Doser, M Drees, D A Edwards, S Eidelman, J Erler, V V Ezhela, W Fettscher, B D Fields, B Foster, T K Gaisser, L Garren, H.-J. Gerber, G Gerbier, T Gherghetta, S Golwala, M Goodman, C Grab, A V Gritsan, J.-F. Grivaz, M Grunewald, A Gurtu, T Gutsche, H E Haber, K Hagiwara, C Hagmann, C Hanhart, S Hashimoto, K G Hayes, M Heffner, B Heltsley, J J Hern  ndez-Rey, K Hikasa, A H  cker, J Holder, A Holtkamp, J Huston, J D Jackson, K F Johnson, T Junk, D Karlen, D Kirkby, S R Klein, E Klemp, R V Kowalewski, F Krauss, M Kreps, B Krusche, Y V Kuyanov, Y Kwon, O Lahav, J Laiho, P Langacker, A Liddle, Z Ligeti, T M Liss, L Littenberg, K S Lugovsky, S B Lugovsky, T Mannel, A V Manohar, W J Marciano, A D Martin, A Masoni, J Matthews, D Milstead, R Miquel, K M  nig, F Moortgat, K Nakamura, M Narain, P Nason, S Navas, M Neubert, P Nevski, Y Nir, K A Olive, L Pape, J Parsons, C Patrignani, J A Peacock, S T Petcov, A Piepke, A Pomarol, G Punzi, A Quadt, S Raby, G Raffelt, B N Ratcliff, P Richardson, S Roesler, S Rolli, A Romaniouk, L J Rosenberg, J L Rosner, C T Sachrajda, Y Sakai, G P Salam, S Sarkar, F Sauli, O Schneider, K Scholberg, D Scott, W G Seligman, M H Shaevitz, S R Sharpe, M Silari, T Sj  strand, P Skands, J G Smith, G F Smoot, S Spanier, H Spieler, A Stahl, T Stanev, S L Stone, T Sumiyoshi, M J Syphers, F Takahashi, M Tanabashi, J Terning, M Titov, N P Tkachenko, N A T  rnqvist, D Tovey, G Valencia, K van Bibber, G Venanzoni, M G Vinctor, P Vogel, A Vogt, W Walkowiak, C W Walter, D R Ward, T Watari, G Weiglein, E J Weinberg, L R Wiencke, L Wolfenstein, J Womersley, C L Woody, R L Workman, A Yamamoto, G P Zeller, O V Zenin, J Zhang, R.-Y. Zhu, G Harper, V S Lugovsky, and P Schaffner. Review of Particle Physics. *\Textbackslash Prd*, 86(1):1526, jul 2012.
- [15] Daniel De Florian, Rodolfo Sassot, Marco Stratmann, and Werner Vogelsang. Extraction of spin-dependent parton densities and their uncertainties. *Physical Review D - Particles, Fields, Gravitation and Cosmology*, 80(3):1–25, 2009.
- [16] Christine Aidala and Et Al. Research Plan for Spin Physics at RHIC. *report to DOE*, 2005.
- [17] Wolfram Fischer. RHIC Run Overview, 2016.

- [18] Karen Walsh and Peter Genzer. BNL Newsroom — Hot Nuclear Matter Featured in Science, 2012.
- [19] Brookhaven National Laboratory and Anatoli Zelenski. Towards 100% polarization in the Optically-Pumped Polarized Ion Source at RHIC. Technical report, Brookhaven National Laboratory, 2007.
- [20] RHIC, I. Alekseev, C. Allgower, M. Bai, and Et Al. Configuration Manual Polarized Proton Collider at RHIC. *Configuration Manual*, (January), 2006.
- [21] PHENIX Collaboration. PHENIX Drawings.
- [22] John Haggarty, Martin Purschke, Chris Pinkenburg, and Ed Desmond. PHENIX Shift Duties, 2016.
- [23] Tomoaki Nakamura. Introduction to PHENIX Beam Beam Counter ( BBC ) Purpose of PHENIX BBC. Technical report, 2002.
- [24] C. Aidala, L. Anaya, E. Anderssen, A. Bambaugh, A. Barron, J. G. Boissevain, J. Bok, S. Boose, M. L. Brooks, S. Butsyk, M. Cepeda, P. Chacon, S. Chacon, L. Chavez, T. Cote, C. Dagostino, A. Datta, K. Deblasio, L. Delmonte, E. J. Desmond, J. M. Durham, D. Fields, M. Finger, C. Gingu, B. Gonzales, J. S. Haggerty, T. Hawke, H. W. Van Hecke, M. Herron, J. Hoff, J. Huang, X. Jiang, T. Johnson, M. Jonas, J. S. Kapustinsky, A. Key, G. J. Kunde, J. Kurtz, J. Labounty, D. M. Lee, K. B. Lee, M. J. Leitch, M. Lenz, W. Lenz, M. X. Liu, D. Lynch, E. Mannel, P. L. McGaughey, A. Meles, B. Meredith, H. Nguyen, E. Obrien, R. Pak, V. Papavassiliou, S. Pate, H. Pereira, G. D N Perera, M. Phillips, R. Pisani, S. Polizzo, R. J. Poncione, J. Popule, M. Prokop, M. L. Purschke, A. K. Purwar, N. Ronzhina, C. L. Silva, M. Slune??ka, R. Smith, W. E. Sondheim, K. Spendier, M. Stoffer, E. Tennant, D. Thomas, M. Tom???ek, A. Veicht, V. Vrba, X. R. Wang, F. Wei, D. Winter, R. Yarema, Z. You, I. Younus, A. Zimmerman, and T. Zimmerman. The PHENIX forward silicon vertex detector. *Nuclear Instruments and Methods in Physics Research, Section A: Accelerators, Spectrometers, Detectors and Associated Equipment*, 755:44–61, 2014.
- [25] Hideyuki Oide. *Measurement of longitudinal spin asymmetry in production of muons from W / Z boson decays in polarized p + p collisions at s = 500 GeV with the PHENIX detector at RHIC*. PhD thesis, 2012.
- [26] Yoshinori Fukao. Forward upgrade for  $\langle i \rangle W \langle /i \rangle$  physics at the RHIC-PHENIX experiment. *Journal of Physics: Conference Series*, 295:012165, 2011.
- [27] Dave Kawall. How To Measure Absolute Luminosity. Technical report, RIKEN-BNL Research Center, University of Massachusetts Amherst, 2005.
- [28] Werner Herr and Bruno Muratori. Concept of luminosity. *CAS - CERN Accelerator School: Intermediate Course on Accelerator Physics, Zeuthen, Germany*, 2(3):361–378, 2003.
- [29] Chong Kim. Kinematic Variables Schematic, 2016.

- [30] Ralf Seidl, Francesca Giordano, Daniel Jumper, Michael Beaumier, Richard Hollis, and Abraham Meles. Run 13 W Analysis. 2014.
- [31] Ralf Seidl, Francesca Giordano, Daniel Jumper, Michael Beaumier, Richard Hollis, and Abraham Meles. Run 13 W Analysis. 2014.
- [32] K. Adcox, S. S. Adler, M. Aizama, N. N. Ajitanand, Y. Akiba, H. Akikawa, J. Alexander, A. Al-Jamel, M. Allen, G. Alley, R. Amirikas, L. Aphecetche, Y. Arai, J. B. Archuleta, J. R. Archuleta, R. Armendariz, V. Armijo, S. H. Aronson, D. Autrey, R. Averbeck, T. C. Awes, B. Azmoun, A. Baldissari, J. Banning, K. N. Barish, A. B. Barker, P. D. Barnes, J. Barrette, F. Barta, B. Bassalleck, S. Bathe, S. Batsouli, V. V. Baublis, A. Bazilevsky, R. Begay, J. Behrendt, S. Belikov, R. Belkin, F. G. Bellaiche, S. T. Belyaev, M. J. Bennett, Y. Berdnikov, S. Bhaganatula, J. C. Biggs, A. W. Bland, C. Blume, M. Bobrek, J. G. Boissevain, S. Boose, H. Borel, D. Borland, E. Bosze, S. Botelho, J. Bowers, C. Britton, L. Britton, M. L. Brooks, A. W. Brown, D. S. Brown, N. Bruner, W. L. Bryan, D. Bucher, H. Buesching, V. Bumazhnov, G. Bunce, J. Burward-Hoy, S. A. Butsyk, M. M. Cafferty, T. A. Carey, J. S. Chai, P. Chand, J. Chang, W. C. Chang, R. B. Chappell, L. L. Chavez, S. Chernichenko, C. Y. Chi, J. Chiba, M. Chiu, S. Chollet, R. K. Choudhury, T. Christ, T. Chujo, M. S. Chung, P. Chung, V. Cianciolo, D. J. Clark, Y. Cobigo, B. A. Cole, P. Constantin, R. Conway, K. C. Cook, D. W. Crook, H. Cunitz, R. Cunningham, M. Cutshaw, D. G. D'Enterria, C. M. Dabrowski, G. Danby, S. Daniels, A. Danmura, G. David, A. Debraine, H. Delagrange, J. DeMoss, A. Denisov, A. Deshpande, E. J. Desmond, O. Dietzsch, B. V. Dinesh, J. L. Drachenberg, O. Drapier, A. Drees, R. du Rietz, A. Durum, D. Dutta, K. Ebisu, M. A. Echave, Y. V. Efremenko, K. El Chenawi, M. S. Emery, D. Engo, A. Enokizono, K. Enosawa, H. En'yo, N. Ericson, S. Esumi, V. A. Evseev, L. Ewell, O. Fackler, J. Fellenstein, T. Ferdousi, J. Ferrierra, D. E. Fields, F. Fleuret, S. L. Fokin, B. Fox, Z. Fraenkel, S. Frank, A. Franz, J. E. Frantz, A. D. Frawley, J. Fried, J. P. Freidberg, E. Fujisawa, H. Funahashi, S. Y. Fung, S. Gadrat, J. Gannon, S. Garpmann, F. Gastaldi, T. F. Gee, R. Gentry, T. K. Ghosh, P. Giannotti, A. Glenn, A. L. Godoi, M. Gonin, G. Gogiberidze, J. Gosset, Y. Goto, R. Granier de Cassagnac, S. V. Greene, V. Griffin, M. Grosse Perdekamp, S. K. Gupta, W. Guryn, H. A. Gustafsson, T. Hachiya, J. S. Haggerty, S. Hahn, J. Halliwell, H. Hamagaki, R. H. Hance, A. G. Hansen, H. Hara, J. Harder, G. W. Hart, E. P. Hartouni, A. Harvey, L. Hawkins, R. S. Hayano, H. Hayashi, N. Hayashi, X. He, N. Heine, F. Heistermann, S. Held, T. K. Hemmick, J. M. Heuser, M. Hibino, J. S. Hicks, R. Higuchi, J. C. Hill, T. Hirano, D. S. Ho, R. Hoade, W. Holzmann, K. Homma, B. Hong, A. Hoover, T. Honaguchi, C. T. Hunter, D. E. Hurst, R. Hutter, T. Ichihara, V. V. Ikonnikov, K. Imai, M. Inaba, M. S. Ippolitov, L. Davis Isenhower, L. Donald Isenhower, M. Ishihara, M. Issah, V. I. Ivanov, B. V. Jacak, G. Jackson, J. Jackson, D. Jaffe, U. Jagadish, W. Y. Jang, R. Jayakumar, J. Jia, B. M. Johnson, J. Johnson, S. C. Johnson, J. P. Jones, K. Jones, K. S. Joo, D. Jouan, S. Kahn, F. Kajihara, S. Kametani, N. Kamihara, Y. Kamyshkov, A. Kandasamy, J. H. Kang, M. R. Kann, S. S. Kapoor, J. Kaputinsky, K. V. Karadjev, V. Kashikhin, S. Kato, K. Katou, H. J. Kehayias, M. A. Kelley, S. Kelly, M. Kennedy, B. Khachaturov, A. V. Khanzadeev, A. Khomutnikov, J. Kikuchi, D. J. Kim, D. W.

Kim, G. B. Kim, H. J. Kim, S. Y. Kim, Y. G. Kim, W. W. Kinnison, E. Kistenev, A. Kiyomichi, C. Klein-Boesing, S. Klinksiek, L. Kluberg, H. Kobayashi, V. Kochetkov, D. Koehler, T. Kohama, B. G. Komkov, M. L. Kopytine, K. Koseki, L. Kotchenda, D. Kotchetkov, Iou A. Koutcheryaev, A. Kozlov, V. S. Kozlov, P. A. Kravtsov, P. J. Kroon, C. H. Kuberg, L. G. Kudin, M. Kurata-Nishimura, V. V. Kuriatkov, K. Kurita, Y. Kuroki, M. J. Kweon, Y. Kwon, G. S. Kyle, J. J. LaBounty, R. Lacej, J. G. Lajoie, J. Lauret, A. Lebedev, V. A. Lebedev, V. D. Lebedev, D. M. Lee, S. Lee, M. J. Leitch, M. Lenz, W. Lenz, X. H. Li, Z. Li, B. Libby, M. Libkind, W. Liccardi, D. J. Lim, S. Lin, M. X. Liu, X. Liu, Y. Liu, Z. Liu, E. Lockner, N. Longbotham, J. D. Lopez, R. Machnowski, C. F. Maguire, J. Mahon, Y. I. Makdisi, V. I. Manko, Y. Mao, S. Marino, S. K. Mark, S. Markacs, D. G. Markushin, G. Martinez, X. B. Martinez, M. D. Marx, A. Masaike, F. Matathias, T. Matsumoto, P. L. McGaughey, M. C. McCain, J. Mead, E. Melnikov, Y. Melnikov, W. Z. Meng, M. Merschmeyer, F. Messer, M. Messer, Y. Miake, N. M. Miftakhov, S. Migluolio, J. Milan, T. E. Miller, A. Milov, K. Minuzzo, S. Mioduszewski, R. E. Mischke, G. C. Mishra, J. T. Mitchell, Y. Miyamoto, A. K. Mohanty, B. C. Montoya, A. Moore, T. Moore, D. P. Morrison, G. G. Moscone, J. M. Moss, F. Mühlbacher, M. Muniruzzaman, J. Murata, M. M. Murray, M. Musrock, S. Nagamiya, Y. Nagasaka, J. L. Nagle, Y. Nakada, T. Nakamura, B. K. Nandi, J. Negrin, J. Newby, L. Nikkinen, S. A. Nikolaev, P. Nilsson, S. Nishimura, A. S. Nyanin, J. Nystrand, E. O'Brien, P. O'Conner, F. Obenshain, C. A. Ogilvie, H. Ohnishi, I. D. Ojha, M. Ono, V. Onuchin, A. Oskarsson, L. Österman, I. Otterlund, K. Oyama, L. Paffrath, A. P T Palounek, C. E. Pancake, V. S. Pantuev, V. Papavassiliou, S. F. Pate, T. Peitzmann, R. Petersen, A. N. Petridis, C. H. Pinkenburg, R. P. Pisani, P. Pitukhin, T. Plagge, F. Plasil, M. Pollack, K. Pope, R. Prigl, M. L. Purschke, A. K. Purwar, J. M. Qualls, S. Rankowitz, G. Rao, R. Rao, M. Rau, I. Ravinovich, R. Raynis, K. F. Read, K. Reygers, G. Riabov, V. G. Riabov, Y. G. Riabov, S. H. Robinson, G. Roche, A. Romana, M. Rosati, E. V. Roschin, A. A. Rose, P. Rosnet, R. Roth, R. Ruggiero, S. S. Ryu, N. Saito, A. Sakaguchi, T. Sakaguchi, S. Sakai, H. Sako, T. Sakuma, S. Salomone, V. M. Samsonov, W. F. Sandhoff, L. Sanfratello, T. C. Sangster, R. Santo, H. D. Sato, S. Sato, R. Savino, S. Sawada, B. R. Schlei, R. Schleuter, Y. Schutz, M. Sekimoto, V. Semenov, R. Seto, Y. Severgin, A. Shajii, V. Shangin, M. R. Shaw, T. K. Shea, I. Shein, V. Shelikhov, T. A. Shibata, K. Shigaki, T. Shiina, T. Shimada, Y. H. Shin, I. G. Sibiriak, D. Silvermyr, K. S. Sim, J. Simon-Gillo, M. Simpson, C. P. Singh, V. Singh, W. Sippach, M. Sivertz, H. D. Skank, S. Skutnik, G. A. Slege, D. C. Smith, G. D. Smith, M. Smith, A. Soldatov, G. P. Solodov, R. A. Soltz, W. E. Sondheim, S. Sorensen, I. Sourikova, F. Staley, P. W. Stankus, N. Starinsky, S. Steffens, E. M. Stein, P. Steinberg, E. Stenlund, M. Stepanov, A. Ster, J. Stewering, W. Stokes, S. P. Stoll, M. Sugioka, T. Sugitate, J. P. Sullivan, Y. Sumi, Z. Sun, M. Suzuki-Nara, E. M. Takagui, A. Taketani, M. Tamai, K. H. Tanaka, Y. Tanaka, E. Taniguchi, M. J. Tannenbaum, V. I. Tarakanov, O. P. Tarasenkova, J. D. Tepe, R. Thern, J. H. Thomas, J. L. Thomas, T. L. Thomas, W. D. Thomas, G. W. Thornton, W. Tian, R. Todd, J. Tojo, F. Toldo, H. Torii, R. S. Towell, J. Tradeski, V. A. Trofimov, I. Tserruya, H. Tsuruoka, A. A. Tsvetkov, S. K. Tuli, G. Turner, H. Tydesjö, N. Tyurin, S. Urasawa, A. Usachev, T. Ushiroda, H. W. van Hecke, M. van

- Lith, A. A. Vasiliev, V. Vasiliev, M. Vassent, C. Velissaris, J. Velkovska, M. Velkovsky, W. Verhoeven, L. Villatte, A. A. Vinogradov, V. I. Vishnevskii, M. A. Volkov, W. von Achen, A. A. Vorobyov, E. A. Vznuzdaev, M. Vznuzdaev, J. W. Walker, Y. Wan, H. Q. Wang, S. Wang, Y. Watanabe, L. C. Watkins, T. Weimer, S. N. White, B. R. Whitus, C. Williams, P. S. Willis, A. L. Wintenberg, C. Witzig, F. K. Wohn, K. Wolniewicz, B. G. Wong-Swanson, L. Wood, C. L. Woody, L. W. Wright, J. Wu, W. Xie, N. Xu, K. Yagi, R. Yamamoto, Y. Yang, S. Yokkaichi, Y. Yokota, S. Yoneyama, G. R. Young, I. E. Yushmanov, W. A. Zajc, C. Zhang, L. Zhang, Z. Zhang, and S. Zhou. PHENIX detector overview. *Nuclear Instruments and Methods in Physics Research, Section A: Accelerators, Spectrometers, Detectors and Associated Equipment*, 499(2-3):469–479, 2003.
- [33] Daniel Jumper. *The Proton's Longitudinal Spin Structure Studied Through the Weak Interaction in PP Collisions*. PhD thesis, University of Illinois Urbana Champange, 2016.
  - [34] Abraham Meles. *Measurement of longitudinal spin asymmetry in production of muons from W / Z boson decays in polarized p + p collisions at s = 500 GeV with the PHENIX detector at RHIC*. PhD thesis, 2012.
  - [35] J Ashman, Others, B Badelek, G Baum, I G Bird, A W Edwards, and T Walcher. A Measurement Of The Spin Asymmetry And Determination Of The Structure Function  $g_1$  In Deep Inelastic Muon-Proton Scattering. *Phys. Lett. B*, 206(2):364–370, 1988.
  - [36] Bogdan Povh and Thomas Walcher. The end of the nucleon-spin crisis. 2016.
  - [37] Zhong Bo Kang and Jacques Soffer. General positivity bounds for spin observables in single particle inclusive production. *Physical Review D - Particles, Fields, Gravitation and Cosmology*, 83(11):1–8, 2011.
  - [38] Stanley J. Brodsky, John Ellis, and Marek Karliner. Chiral symmetry and the spin of the proton. *Physics Letters B*, 206(2):309–315, 1988.
  - [39] Thomas Stanley. The History of Philosophy, 1655.
  - [40] Hendrick ter Brugghen. Democritus, 1628.
  - [41] Richard W. Baldes. 'Divisibility' and 'Division' in Democritus. *Apeiron: A Journal for Ancient Philosophy and Science*, 12(1):1–12, 1978.
  - [42] Konstantinos Alexakos and Wladina Antoine. The Golden Age of Islam and Science Teaching: Teachers and students develop a deeper understanding of the foundations of modern science by learning about the contributions of Arab-Islamic scientists and scholars. *The Science Teacher*, 72(3):36–39, 2005.
  - [43] Fraser Cowley. *A Critique of British Empiricism*. MacMillan, 1968.
  - [44] Ottavio Leoni. Galileo Galilei, Portrait in Crayon by Leoni, 1624.

- [45] A. Rupert Hall. Galileo and the Science of Motion. *The British Journal for the History of Science*, 2(3):185–199, 1965.
- [46] Roger H. Stuewer. A Critical Analysis of Newton’s Work on Diffraction. *Isis*, 61(2):188–205, 1970.
- [47] Gary Patterson. Jean Perrin and the triumph of the atomic doctrine. *Endeavour*, 31(2):50–53, jun 2007.
- [48] George Thomson. J. J. Thomson, 1956.
- [49] Kurzon. Diagram of JJ Thomson’s Experiment With Cathod Rays, 2010.
- [50] Nobel Media. J.J. Thomson - Biographical, 2014.
- [51] M Planck. On the law of the energy distribution in the normal spectrum. *Ann. Phys*, 4:1–11, 1901.
- [52] J. Clerk Maxwell. A Dynamical Theory of the Electromagnetic Field [J]. *Philosophical Transactions of the Royal Society of London*, 155(January):459–512, 1865.
- [53] P. A. M. Dirac. The Quantum Theory of the Electron. *Proceedings of the Royal Society A: Mathematical, Physical and Engineering Sciences*, 117(778):610, 1928.
- [54] Nobel Foundation. Paul Dirac, 1933.
- [55] Frank Krauss. History of Particle Physics. Technical report, Institute for Particle physics Phenomenology, University of Durham, Durham, 2015.
- [56] W Heisenberg. Production of Mesons as a Shock Wave Problem Visual description of a shock wave. pages 1–17, 1952.
- [57] H. Yukawa, S. Sakata, and M. Taketani. On the interaction of elementary particles. III. *Progress of Theoretical Physics Supplement*, 1(Received):24–45, 1955.
- [58] Pj Bryant. A brief history and review of accelerators. *Cern European Organization for . . . ,* 1994.
- [59] M. Gell-Mann. Isotopic spin and new unstable particles. *Physical Review*, 92(3):833–834, 1953.
- [60] M. Gell-Mann. The interpretation of the new particles as displaced charge multiplets. *Il Nuovo Cimento Series 10*, 4(1 Supplement):848–866, 1956.
- [61] Michael Riordan. The Discovery of Quarks. 1992.
- [62] GW Bennett, B Bousquet, HN Brown, G Bunce, RM Carey, P Cushman, GT Danby, PT Debevec, M Deile, H Deng, SK Dhawan, VP Druzhinin, L Duong, FJM Farley, GV Fedotovich, Fe Gray, D Grigoriev, M Grosse-Perdekamp, A Grossmann, MF Hare, DW Hertzog, X Huang, VW Hughes, M Iwasaki, K Jungmann, D Kawall, Bi Khazin, F Krienen, I Kronkvist, A Lam, R Larsen, YY Lee, I Logashenko, R McNabb, W Meng,

JP Miller, WM Morse, D Nikas, CJG Onderwater, Y Orlov, CS Ozben, JM Pailey, Q Peng, CC Polly, J Pretz, R Prigl, G zu Putlitz, T Qian, Si Redin, O Rind, BL Roberts, N Ryskulov, YK Semertzidis, P Shagin, YuM Shatunov, Ep Sichtermann, E Solodov, M Sossong, LR Sulak, A Trofimov, P von Walter, and A Yamamoto. Measurement of the Negative Muon Anomalous Magnetic Moment to 0.7 ppm. 2004.

- [63] J.J. Aubert, G. Bassompierre, K.H. Becks, C. Best, E. Böhm, X. de Bouard, F.W. Brasse, C. Broll, S. Brown, J. Carr, R.W. Clift, J.H. Cobb, G. Coignet, F. Combley, G.R. Court, G. D'Agostini, W.D. Dau, J.K. Davies, Y. Déclais, R.W. Dobinson, U. Dosselli, J. Drees, A.W. Edwards, M. Edwards, J. Favier, M.I. Ferrero, W. Flauger, E. Gabathuler, R. Gamet, J. Gayler, V. Gerhardt, C. Gössling, J. Haas, K. Hamacher, P. Hayman, M. Henckes, V. Korbel, U. Landgraf, M. Leenen, M. Maire, H. Minssieux, W. Mohr, H.E. Montgomery, K. Moser, R.P. Mount, P.R. Norton, J. McNicholas, A.M. Osborne, P. Payre, C. Peroni, H. Pessard, U. Pietrzik, K. Rith, M. Schneegans, T. Sloan, H.E. Stier, W. Stockhausen, J.M. Thénard, J.C. Thompson, L. Urban, M. Villers, H. Wahlen, M. Whalley, D. Williams, W.S.C. Williams, J. Williamson, and S.J. Wimpenny. The ratio of the nucleon structure functions  $F_2^N$  for iron and deuterium. *Physics Letters B*, 123(3):275–278, 1983.
- [64] Guido Altarelli. QCD Evolution Equations For Parton Densities - Scholarpedia, 2009.
- [65] Ciprian Gal. *Measuring the anti-quark contribution to the proton spin using parity violating W production in polarized proton proton collisions*. PhD thesis, Stony Brook University, 2014.
- [66] John Ellis and Robert Jaffe. Sum rule for deep-inelastic electroproduction from polarized protons. *Physical Review D*, 9(5):1444–1446, 1974.
- [67] Brookhaven National Laboratory. RHIC Complex, 2011.
- [68] RHIC. RHIC — Accelerator Complex, 2016.
- [69] I. Alekseev, C. Allgower, M. Bai, Y. Batygin, L. Bozano, K. Brown, G. Bunce, P. Cameron, E. Courant, S. Erin, J. Escallier, W. Fischer, R. Gupta, K. Hatanaka, H. Huang, K. Imai, M. Ishihara, A. Jain, A. Lehrach, V. Kanavets, T. Katayama, T. Kawaguchi, E. Kelly, K. Kurita, S. Y. Lee, A. Luccio, W. W. MacKay, G. Mahler, Y. Makdisi, F. Mariam, W. McGahern, G. Morgan, J. Muratore, M. Okamura, S. Peggs, F. Pilat, V. Ptitsin, L. Ratner, T. Roser, N. Saito, H. Satoh, Y. Shatunov, H. Spinka, M. Syphers, S. Tepikian, T. Tominaka, N. Tsoupas, D. Underwood, A. Vasiliev, P. Wanderer, E. Willen, H. Wu, A. Yokosawa, and A. N. Zelenski. Polarized proton collider at RHIC. *Nuclear Instruments and Methods in Physics Research, Section A: Accelerators, Spectrometers, Detectors and Associated Equipment*, 499(2-3):392–414, 2003.
- [70] Shoji Nagamiya. PHENIX Experiment at RHIC. *Nuclear Physics A*, 566:287c–298 c, 1994.
- [71] PHENIX Collaboration and N. Saito. Spin Physics with the PHENIX Detector System. *Nuclear Physics A*, 638:575–578, 1998.

- [72] PHENIX Collaboration. Measurement of parity-violating spin asymmetries in W production at midrapidity in longitudinally polarized p+p collisions. page 8, 2015.
- [73] M. Allen, M. J. Bennett, M. Bobrek, J. B. Boissevain, S. Boose, E. Bosze, C. Britton, J. Chang, C. Y. Chi, M. Chiu, R. Conway, R. Cunningham, A. Denisov, A. Deshpande, M. S. Emery, A. Enokizono, N. Ericson, B. Fox, S. Y. Fung, P. Giannotti, T. Hachiya, A. G. Hansen, K. Homma, B. V. Jacak, D. Jaffe, J. H. Kang, J. Kapustinsky, S. Y. Kim, Y. G. Kim, T. Kohama, P. J. Kroon, W. Lenz, N. Longbotham, M. Musrock, T. Nakamura, H. Ohnishi, S. S. Ryu, A. Sakaguchi, R. Seto, T. Shiina, M. Simpson, J. Simon-Gillo, W. E. Sondheim, T. Sugitate, J. P. Sullivan, H. W. Van Hecke, J. W. Walker, S. N. White, P. Willis, and N. Xu. PHENIX inner detectors. *Nuclear Instruments and Methods in Physics Research, Section A: Accelerators, Spectrometers, Detectors and Associated Equipment*, 499(2-3):549–559, 2003.
- [74] Andrew S. Hoover. The PHENIX Muon Spectrometer and Charmonium Production at RHIC Particle Physics at RHIC. Technical report, New Mexico State University, 2003.
- [75] A. Adare, S. Afanasiev, C. Aidala, N. N. Ajitanand, Y. Akiba, R. Akiimoto, J. Alexander, H. Al-Taani, K. R. Andrews, A. Angerami, K. Aoki, N. Apadula, E. Appelt, Y. Aramak, R. Armendariz, E. C. Aschenauer, T. C. Awes, B. Azmoun, V. Babintsev, M. Bai, B. Bannier, K. N. Barish, B. Bassalleck, A. T. Basye, S. Bathe, V. Baublis, C. Baumann, A. Bazilevsky, R. Belmont, R. Bennett, A. Berdnikov, Y. Berdnikov, D. S. Blau, J. S. Bok, K. Boyle, M. L. Brooks, H. Buesching, V. Bumazhnov, G. Bunce, S. Butsyk, S. Campbell, A. Caringi, C. H. Chen, C. Y. Chi, M. Chiu, I. J. Choi, J. B. Choi, R. K. Choudhury, P. Christiansen, T. Chujo, O. Chvala, V. Cianciolo, Z. Citron, B. A. Cole, Z. Conesa del Valle, M. Connors, M. Csanad, T. Cs org, S. Dairaku, A. Datta, G. David, M. K. Dayananda, A. Denisov, A. Deshpande, E. J. Desmond, K. V. Dharmawardane, O. Dietzsch, A. Dion, M. Donadelli, L. D Orazio, O. Drapier, A. Drees, K. A. Drees, J. M. Durham, A. Durum, Y. V. Efremenko, T. Engelmore, A. Enokizono, H. En’yo, S. Esumi, B. Fadem, D. E. Fields, M. Finger, Jr., F. Fleuret, S. L. Fokin, J. E. Frantz, A. Franz, A. D. Frawley, Y. Fukao, T. Fusayasu, I. Garishvili, A. Glenn, M. Gonin, Y. Goto, R. Granier de Cassagnac, N. Grau, S. V. Greene, M. Grosse Perdekamp, T. Gunji, L. Guo, H. A. Gustafsson, J. S. Haggerty, K. I. Hahn, H. Hamagaki, J. Hamblen, J. Hanks, R. Han, E. Haslum, R. Hayano, T. K. Hemmick, T. Hester, X. He, J. C. Hill, R. S. Hollis, W. Holzmann, K. Homma, B. Hong, T. Horaguchi, Y. Hori, D. Hornback, S. Huang, T. Ichihara, R. Ichimiya, H. Iinuma, Y. Ikeda, K. Imai, M. Inaba, A. Iordanova, D. Isenhower, M. Ishihara, M. Issah, A. Isupov, D. Ivanischev, Y. Iwanaga, B. V. Jacak, PHENIX: J. Jia, X. Jiang, B. M. Johnson, T. Jones, K. S. Joo, D. Jouan, J. Kamin, S. Kaneti, B. H. Kang, J. H. Kang, J. Kapustinsky, K. Karatsu, M. Kasai, D. Kawall, A. V. Kazantsev, T. Kempel, A. Khanzadeev, K. M. Kijima, B. I. Kim, D. J. Kim, E. J. Kim, J. S. Kim, Y. J. Kim, Y. K. Kim, E. Kinney, A. Kiss, E. Kistenev, D. Kleinjan, P. Kline, L. Kochenda, B. Komkov, M. Konno, J. Koster, D. Kotov, A. Kral, G. J. Kunde, K. Kurita, M. Kurosawa, Y. Kwon, G. S. Kyle, R. Lacey, Y. S. Lai, J. G. Lajoie, A. Lebedev, D. M. Lee,

J. Lee, K. B. Lee, K. S. Lee, S. R. Lee, M. J. Leitch, M. A. L. Leite, P. Lichtenwalner, S. H. Lim, L. A. Linden Levy, A. Litvinenko, H. Liu, M. X. Liu, X. Li, B. Love, D. Lynch, C. F. Maguire, Y. I. Makdisi, A. Malakhov, V. I. Manko, E. Mannel, Y. Mao, H. Masui, M. McCumber, P. L. McGaughey, D. McGlinchey, C. McKinney, N. Means, M. Mendoza, B. Meredith, Y. Miake, T. Mibe, A. C. Mignerey, K. Miki, A. Milov, J. T. Mitchell, Y. Miyachi, A. K. Mohanty, H. J. Moon, Y. Morino, A. Morreale, D. P. Morrison, T. V. Moukhanova, T. Murakami, J. Murata, S. Nagamiya, J. L. Nagle, M. Naglis, M. I. Nagy, I. Nakagawa, Y. Nakamiya, K. R. Nakamura, T. Nakamura, K. Nakano, J. Newby, M. Nguyen, M. Nihashi, R. Nouicer, A. S. Nyanin, C. Oakley, E. O'Brien, C. A. Ogilvie, K. Okada, M. Oka, A. Oskarsson, M. Ouchida, K. Ozawa, R. Pak, V. Pantuev, V. Papavassiliou, B. H. Park, I. H. Park, S. K. Park, S. F. Pate, H. Pei, J. C. Peng, H. Pereira, V. Peresedov, D. Yu. Peressounko, R. Petti, C. Pinkenburg, R. P. Pisani, M. Proissl, M. L. Purschke, H. Qu, J. Rak, I. Ravinovich, K. F. Read, K. Reygers, V. Riabov, Y. Riabov, E. Richardson, D. Roach, G. Roche, S. D. Rolnick, M. Rosati, S. S. E. Rosendahl, P. Rukoyatkin, B. Sahlmueller, N. Saito, T. Sakaguchi, V. Samsonov, S. Sano, M. Sarsour, T. Sato, M. Savastio, S. Sawada, K. Sedgwick, R. Seidl, R. Seto, D. Sharma, I. Shein, T. A. Shibata, K. Shigaki, H. H. Shim, M. Shimomura, K. Shoji, P. Shukla, A. Sickles, C. L. Silva, D. Silvermyr, C. Silvestre, K. S. Sim, B. K. Singh, C. P. Singh, V. Singh, M. Slunečka, R. A. Soltz, W. E. Sondheim, S. P. Sorensen, I. V. Sourikova, P. W. Stankus, E. Stenlund, S. P. Stoll, T. Sugitate, A. Sukhanov, J. Sun, J. Szklai, E. M. Takagui, A. Takahara, A. Taketani, R. Tanabe, Y. Tanaka, S. Taneja, K. Tanida, M. J. Tannenbaum, S. Tarafdar, A. Tarannenko, E. Tenant, H. Themann, D. Thomas, M. Togawa, L. Tomášek, M. Tomášek, H. Torii, R. S. Towell, I. Tserruya, Y. Tsuchimoto, K. Utsunomiya, C. Vale, H. W. van Hecke, E. Vazquez-Zambrano, A. Veicht, J. Velkovska, R. Vértesi, M. Virius, A. Vossen, V. Vrba, E. Vznuzdaev, X. R. Wang, D. Watanabe, K. Watanabe, Y. Watanabe, F. Wei, J. Wessels, S. N. White, D. Winter, C. L. Woody, R. M. Wright, M. Wysocki, Y. L. Yamaguchi, R. Yang, A. Yanovich, J. Ying, S. Yokkaichi, J. S. Yoo, G. R. Young, I. Younus, Z. You, I. E. Yushmanov, W. A. Zajc, A. Zelenski, S. Zhou, and L. Zolin. Cross Section and Parity Violating Spin Asymmetries of  $W^{+/-}$  Boson Production in Polarized p+p Collisions at  $\sqrt{s}=500$  GeV. page 6, 2010.

- [76] Amaresh Datta and Dave Kawall.  $\sigma$  BBC using Vernier Scans for 500 GeV pp Data in Run09. 2010.
- [77] S. Belikov, G. Bunce, M. Chiu, B. Fox, Y. Goto, T. Kawabata, N. Saito, M. Tannenbaum, and K. A. Drees. Determination of the Absolute Luminosity for the Proton-Proton Data at 200 GeV Recorded by PHENIX during RHIC Run-02. 2003.
- [78] A Bazilevsky, R Bennett, A Deshpande, Y Goto, D Kawall, and J Seele. Absolute luminosity determination using the vernier scan technique : Run4 6 Analysis and preliminary results at  $s = 62 . 4$  GeV. 2007.
- [79] R Bennett, A Bazilevsky, A Deshpande, and Y Goto. Absolute luminosity determination using the vernier scan technique : Run5 6 analysis and final results at. 2008.

- [80] A Drees. Analysis of Vernier Scans during the PP2PP run in 2009 ( pp at 100 GeV / beam ). 2011.
- [81] A Drees. Analysis of Vernier Scans during RHIC Run-13 ( pp at 255 GeV / beam ). 13:1–18, 2013.
- [82] Scott Justin Wolin, Mickey Chiu, Matthias Grosse-perdekamp, and Justin Wolin. New Ideas on Relative Luminosity Determination in Run09 500 GeV Polarized Proton Collisions. 2014.
- [83] Mike Beaumier, Ciprian Gal, Minjung Kim, Sanghwa Park, R Seidl, and Inseok Yoon. Run 13 Spin Database Quality Assurance. Technical report, 2014.
- [84] R Seidl, H Oide, R Hollis, and M Sarsour. Run 11 W cross section and asymmetry analysis. 2012.
- [85] Charles F Maguire, Anita Trivedi, Andrew Rose, S Victoria Greene, Timothy Miller, Phool Chand, Ajit Mohanty, R K Choudhury, and S S Kapoor. PISA : The PHENIX Experiment Simulation Packages For the PHENIX collaboration. Technical report, Vanderbilt, Maguire1997, 1997.
- [86] Michael Collins. The Naive Bayes Model, Maximum-Likelihood Estimation, and the EM Algorithm. pages 1–21, 2013.

## Appendix A

# Tables of Variables Used in Analysis

Name	Description
Run_Number	A unique number identifying a run in a RHIC fill for PHENIX
Evt_Number	A unique number within a single run identifying the approximate order an event was taken.
Evt_bbcZ	The event z-vertex calculated by the BBC
triggerbit	The result of a bit-wise ‘OR’ applied to all 32-bit trigger bits which fired
clockcross	The bunch number of the two colliding bunches [0 – 119]. Required to look up the spin polarization, along with Run_Number

Table A.1: Variables characterizing events overall

Name	(Unit) Description
Evt_Nmu	The number of muon tracks reconstructed for a given event
charge	$(\pm e)$ The charge associated with a reconstructed muon track
$p_z$	(GeV) The z-momentum associated with the muon track
$p$	(GeV) The total momentum of a charged track
$\chi^2$	The result of the Kalman fitter reconstructing the track
lastGap	The last gap in the Muon Tracker which was activated (there are 4)
$\eta$	The rapidity of the track
$\phi$	(rad) The azimuthal position angle the track makes relative to the x-axis
DG0	(cm) A Track matching variable (matching between MuID and MuTR) associated with the MuID road, at MuID station 3.
DDG0	(degree) The opening angle between the MuID track road, and the MuTr projection onto the MuID
xSta <sub>i</sub>	(cm) The x-coordinate of the track at Station i, $i \in 1, 2, 3$ of the MuTr
ySta <sub>i</sub>	(cm) The y-coordinate of the track at Station i, $i \in 1, 2, 3$ of the MuTr
$\phi_i$	(rad) The angle the track makes with Station i, $i \in 1, 2, 3$ , i.e.: $\phi_i = \tan^{-1} \left( \frac{x_1}{y_1} \right)$
$\theta$	(rad) Azimuthal angle of track, $\tan^{-1} \left( \frac{p_T}{p_z} \right)$
DCA <sub>z</sub>	(cm) Distance of closest approach between the z-vertex positions extracted by projecting the MuTR track z-vertex back to the BBC z-vertex
DCA <sub>r</sub>	(cm) Distance of closest approach between the track and beam axis

Table A.2: Muon tracker variables. Generally, this data set is indexed on a subevent level, where one event will contain all reconstructed muon tracks seen for that event.

Name	Description
$fvtx_{d\phi}$	The $\phi$ residual between MuTR track and FVTX track
$fvtx_{d\theta}$	The $\theta$ residual between the MuTR track and FVTX track
$fvtx_{dr}$	The radial residual between the MuTR track and the FVTX track
$fvtx_{conebits}$	The number of FVTX clusters inside a cone around the track defined by: $0.04rad < dR < 0.52rad$ where $dR = \sqrt{d\eta^2 + d\phi^2}$

Table A.3: A summary of the variables reconstructed from FVTX raw data [34].

Name	Description
RpcMatchSt1	Distance of closest approach between projected MuTR track onto the RPC 1 and the closest hit cluster on RPC 1
RpcMatchSt3	Distance of closest approach between projected MuTR track onto the RPC 3 and the closest hit cluster on RPC 3

Table A.4: RPC Track matching variables

South Arm				
$\eta_{min}$	$\eta_{min}$	$\mu^- \pm stat \pm sys$	$\mu^+ \pm stat \pm sys$	
1.10	1.17	$0.27912 \pm 0.00297 \pm 0.10243$	$0.30607 \pm 0.00423 \pm 0.01108$	
1.17	1.25	$0.40422 \pm 0.01642 \pm 0.04811$	$0.43125 \pm 0.01717 \pm 0.26702$	
1.25	1.32	$0.27958 \pm 0.00056 \pm 0.05539$	$0.36619 \pm 0.00925 \pm 0.07316$	
1.32	1.40	$0.26563 \pm 0.00542 \pm 0.02485$	$0.25312 \pm 0.00349 \pm 0.04927$	
1.40	1.48	$0.39802 \pm 0.00497 \pm 0.07770$	$0.34295 \pm 0.00306 \pm 0.03127$	
1.48	1.55	$0.43156 \pm 0.00633 \pm 0.17060$	$0.37567 \pm 0.00248 \pm 0.03644$	
1.55	1.62	$0.34831 \pm 0.00309 \pm 0.03720$	$0.40246 \pm 0.00546 \pm 0.04605$	
1.62	1.70	$0.33043 \pm 0.00280 \pm 0.09227$	$0.40219 \pm 0.00472 \pm 0.05637$	
1.70	1.77	$0.33152 \pm 0.00318 \pm 0.11668$	$0.30805 \pm 0.00360 \pm 0.03644$	
1.77	1.85	$0.34710 \pm 0.00633 \pm 0.00918$	$0.38565 \pm 0.00439 \pm 0.04295$	
1.85	1.92	$0.32448 \pm 0.00404 \pm 0.14670$	$0.30118 \pm 0.00418 \pm 0.10071$	
1.92	2.00	$0.31461 \pm 0.00714 \pm 0.01799$	$0.31263 \pm 0.00545 \pm 0.01643$	
2.00	2.07	$0.64632 \pm 0.01161 \pm 0.23329$	$0.63252 \pm 0.01040 \pm 0.10507$	
2.07	2.15	$0.60582 \pm 0.00565 \pm 0.05569$	$0.67335 \pm 0.01245 \pm 0.05630$	
2.15	2.22	$0.45058 \pm 0.00697 \pm 0.45101$	$0.69619 \pm 0.01247 \pm 0.65623$	
2.22	2.30	$0.45185 \pm 0.01358 \pm 0.36032$	$0.51436 \pm 0.01288 \pm 0.43781$	
2.30	2.38	$0.43890 \pm 0.07336 \pm 0.34632$	$0.61623 \pm 0.06221 \pm 0.62209$	
2.38	2.45	$0.00000 \pm 0.25000 \pm 0.00000$	$0.00000 \pm 0.25000 \pm 0.00000$	
2.45	2.52	$0.00000 \pm 0.25000 \pm 0.00000$	$0.00000 \pm 0.25000 \pm 0.00000$	
2.52	2.60	$0.00000 \pm 0.25000 \pm 0.00000$	$0.00000 \pm 0.25000 \pm 0.00000$	

Table A.5:  $\eta$  dependent trigger efficiencies are calculated for the South arm in 20  $\eta$  bins. Each correction has both systematic and statistical error accounted for.

<b>North Arm</b>				
$\eta_{min}$	$\eta_{max}$	$\mu^- \pm stat \pm sys$	$\mu^+ \pm stat \pm sys$	
1.10	1.17	$0.56285 \pm 0.03834 \pm 0.32882$	$0.52850 \pm 0.01938 \pm 0.36163$	
1.17	1.25	$0.67803 \pm 0.02249 \pm 0.13431$	$0.49546 \pm 0.00261 \pm 0.16304$	
1.25	1.32	$0.69537 \pm 0.01551 \pm 0.03465$	$0.63287 \pm 0.01285 \pm 0.08350$	
1.32	1.40	$0.39864 \pm 0.00724 \pm 0.02330$	$0.38435 \pm 0.00762 \pm 0.11954$	
1.40	1.48	$0.52102 \pm 0.00750 \pm 0.05014$	$0.49573 \pm 0.00698 \pm 0.03733$	
1.48	1.55	$0.48068 \pm 0.00498 \pm 0.11579$	$0.48874 \pm 0.00357 \pm 0.08063$	
1.55	1.62	$0.54113 \pm 0.00860 \pm 0.04895$	$0.50041 \pm 0.00659 \pm 0.05165$	
1.62	1.70	$0.45140 \pm 0.00822 \pm 0.05718$	$0.46948 \pm 0.00755 \pm 0.09718$	
1.70	1.77	$0.43203 \pm 0.00547 \pm 0.04976$	$0.40722 \pm 0.00546 \pm 0.07957$	
1.77	1.85	$0.42141 \pm 0.00815 \pm 0.04366$	$0.44450 \pm 0.00628 \pm 0.04575$	
1.85	1.92	$0.37946 \pm 0.00620 \pm 0.01766$	$0.37183 \pm 0.00700 \pm 0.01848$	
1.92	2.00	$0.37499 \pm 0.00782 \pm 0.05026$	$0.40156 \pm 0.00678 \pm 0.02291$	
2.00	2.07	$0.51268 \pm 0.00547 \pm 0.10416$	$0.60041 \pm 0.00973 \pm 0.21212$	
2.07	2.15	$0.56990 \pm 0.00614 \pm 0.14507$	$0.58276 \pm 0.01392 \pm 0.25179$	
2.15	2.22	$0.60527 \pm 0.01524 \pm 0.10354$	$0.60766 \pm 0.00425 \pm 0.23618$	
2.22	2.30	$0.70200 \pm 0.01678 \pm 0.25233$	$0.45067 \pm 0.01008 \pm 0.24192$	
2.30	2.38	$0.48294 \pm 0.00294 \pm 0.12663$	$0.54157 \pm 0.02109 \pm 0.06230$	
2.38	2.45	$0.47814 \pm 0.02338 \pm 0.42026$	$0.42606 \pm 0.03092 \pm 0.25031$	
2.45	2.52	$0.61788 \pm 0.14438 \pm 0.61788$	$0.29673 \pm 0.06686 \pm 0.04941$	
2.52	2.60	$0.00000 \pm 0.25000 \pm 0.00000$	$0.15630 \pm 0.15630 \pm 0.18223$	

Table A.6:  $\eta$  dependent trigger efficiencies are calculated for the North arm in 20  $\eta$  bins. Each correction has both systematic and statistical error accounted for.

Name	Scale Down	Raw Trigger Rate	Livetime
BBCLL1(>0 tubes)	31141	1921013.65	0.89
BBCLL1(>0 tubes) novertex	6732	3196505.83	0.89
ZDCLL1wide	6227	370696.78	0.9
BBCLL1(noVtx)&(ZDCN  ZDCS)	6396	1498978.93	0.9
BBCLL1(>0 tubes) narrowvtx	4070	925279.35	0.89
ZDCNS	4411	233334.89	0.89
ERT_4x4b	0	93.22	0.88
ERTLL1_4x4a&BBCLL1(noVtx)	0	490.47	0.89
ERT_4x4c&BBCLL1(noVtx)	1	2191.87	0.9
SG3&MUID_1H_N  S	95	14830.21	0.88
ERTLL1_E&BBCLL1(narrow)	1	1039	0.9
CLOCK	46765	9388833.68	0.89
MPC_B	0	263.11	0.89
MPC_A	0	1511.4	0.89
MPC_C&ERT_2x2	0	189.37	0.9
(MPCS_C&MPCS_C) (MPCN_C&MPCN_C)	0	10.19	0.63
((MUIDLL1_N2D  S2D)   (N1D&S1D))&BBCLL1(noVtx)	0	260.64	0.63
(MUIDLL1_N1D  S1D)&BBCLL1(noVtx)	55	20196.39	0.87
RPC1+RPC3_S	359	23841.89	0.9
RPC1+RPC3_N	539	72270.55	0.9
SG3&RPC3&MUID_1D_N  S	2	5526.47	0.86
SG1+RPC1(C)&MUIDLL1_N  S	0	146.32	0.86
MUON_S_SG1_RPC3A&MUID_S1D	0	31.27	0.89
MUON_N_SG1_RPC3A&MUID_N1D	0	74	0.84
MUON_S_SG1&BBCLL1(noVtx)	2697	323237.99	0.9
MUON_N_SG1&BBCLL1(noVtx)	11128	1095764.77	0.9
MUON_S_SG1_RPC3_1_B  C	0	66.32	0.89
MUON_N_SG1_RPC3_1_B  C	0	173.57	0.88

Table A.7: A typical run from the 2013 data set, numbered with PHENIX’s standard numbering scheme. Each trigger has a descriptive name hinting its composition (some triggers are actually constructed from trigger coincidences). Since PHENIX cannot record all data, we see the scale-down, the raw rate, and the live-time, which is basically a DAQ triggering efficiency.

## Appendix B

# Additional Figures

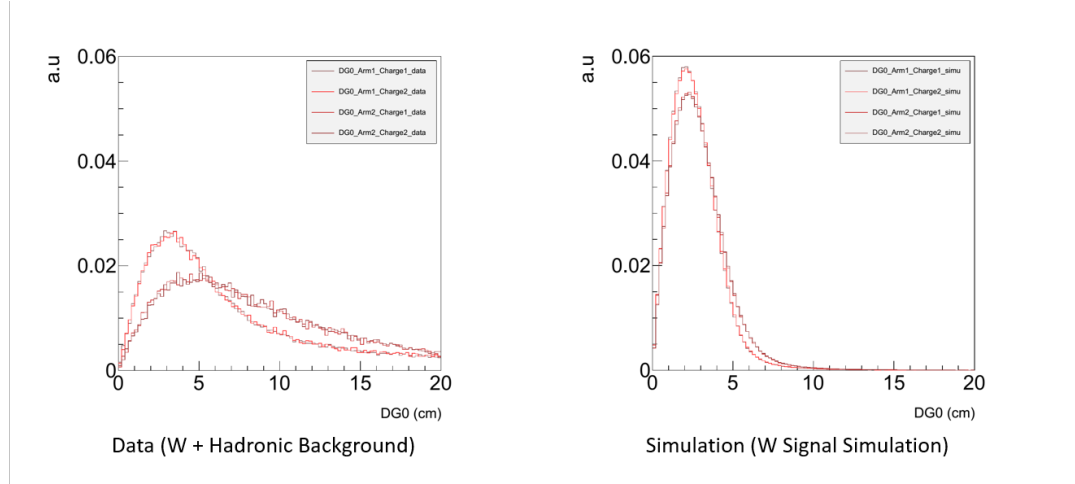


Figure B.1: The left panel shows the distribution of DG0, the linear distance between the reconstructed muon track and the road through station zero of the MUID, for each arm and charge, produced from the PHENIX data set, after the basic cut. The Right panel shows the same distributions from a simulation of the W-Signal. Both panels have the arm and charge data partitions overlaid.

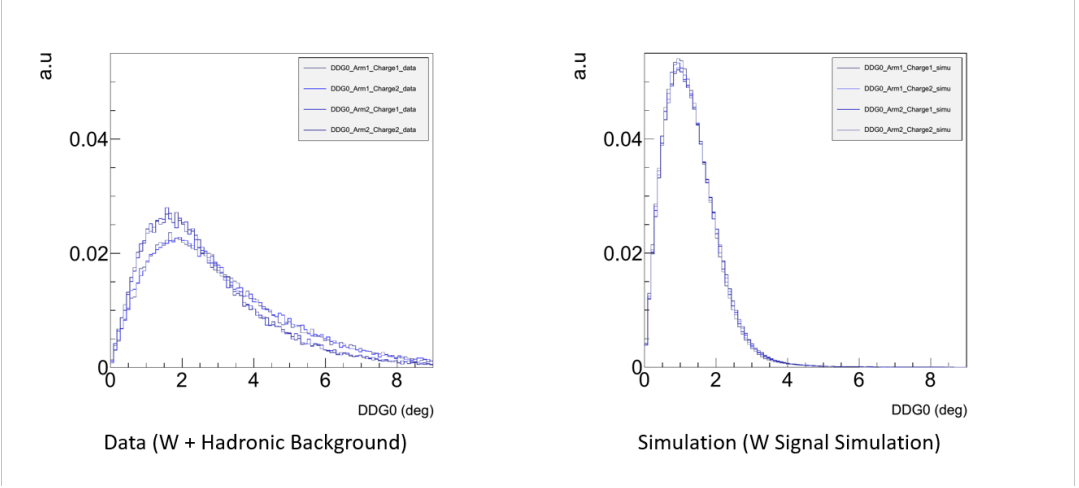


Figure B.2: The left panel shows the distribution of DDG0, the opening angle between the reconstructed muon track and the road to station 0 of the MUID, for each arm and charge, produced from the PHENIX data set, after the basic cut. The right panel shows the same distributions from a simulation of the W-Signal. Both panels have the arm and charge data partitions are overlaid.

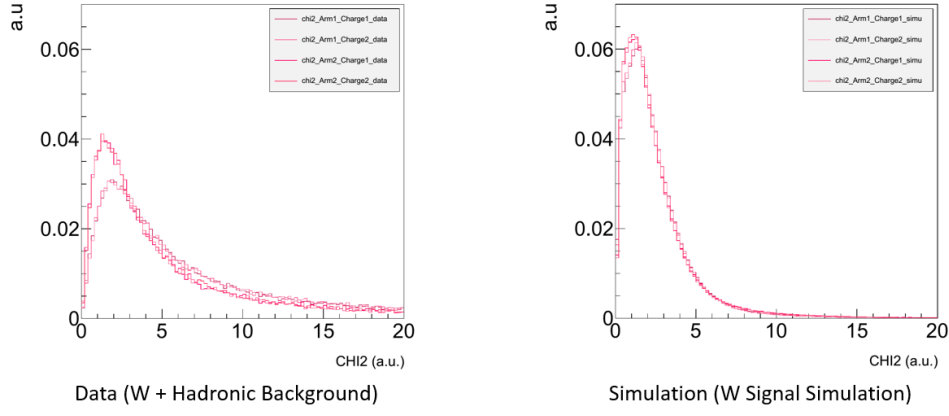


Figure B.3: The left panel shows the distribution of  $\chi^2$ , the reduced  $\chi^2$  residual from track reconstruction, for each arm and charge, produced from the PHENIX data set, after the basic cut. The right panel shows the same distributions from a simulation of the W-Signal. Both panels have the arm and charge data partitions overlaid.

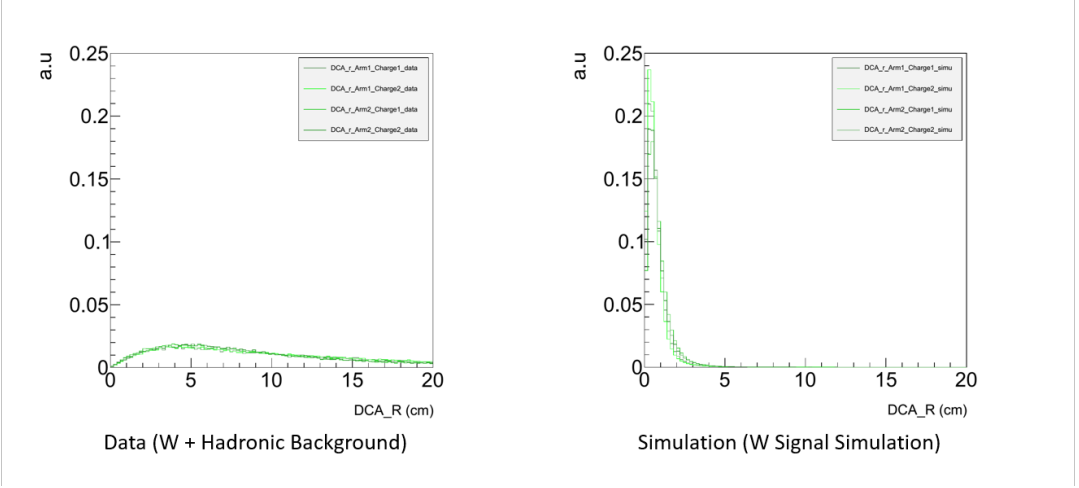


Figure B.4: The left panel shows the distribution of  $DCA_r$ , the transverse distance of closest approach between the track and the event vertex, for each arm and charge, produced from the PHENIX data set, after the basic cut. The right panel the same distributions from a simulation of the W-Signal. Both panels have the arm and charge data partitions overlaid.

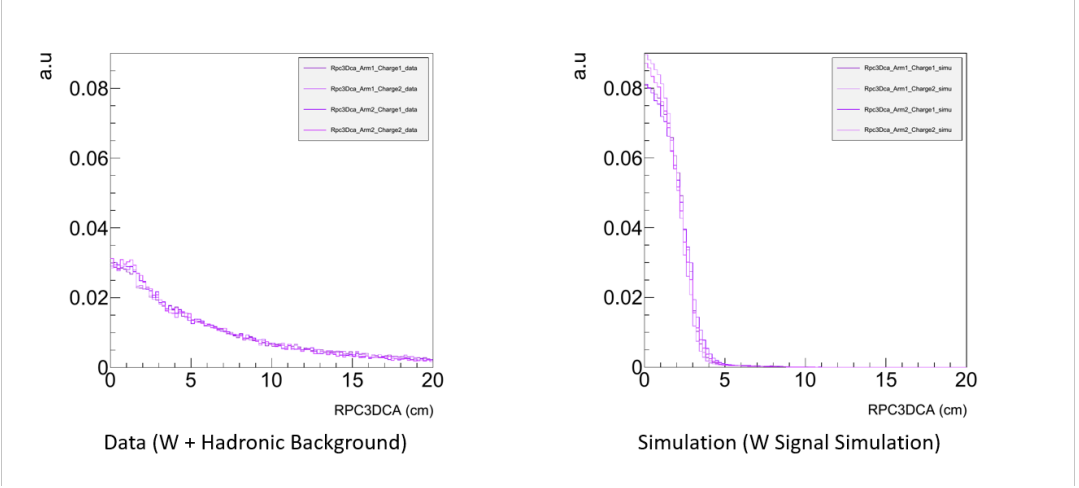


Figure B.5: The left panel shows the distribution of  $\text{Rpc3dca}$ , the distance of closest approach between the reconstructed muon track and the RPC3 hit cluster, for each arm and charge, produced from the PHENIX data set, after the basic cut. The right panel shows the same distributions from a simulation of the W-Signal. Both panels show the arm and charge data partitions overlaid.

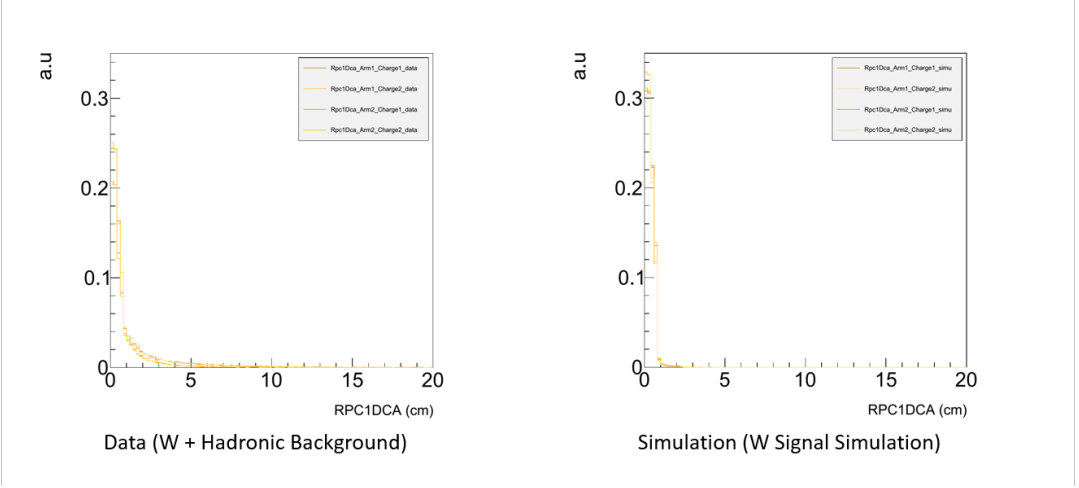


Figure B.6: The left panel shows the distribution of  $\text{Rpc1dca}$ , the distance of closest approach between the reconstructed muon track and the RPC1 hit cluster, for each arm and charge, produced from the PHENIX data set, after the basic cut. The right panel shows the same distributions from a simulation of the W-Signal. Both panels show the arm and charge data partitions overlaid.

## **Appendix C**

# **Trigger Efficiency Studies**

The work here is reproduced for reference from [30].

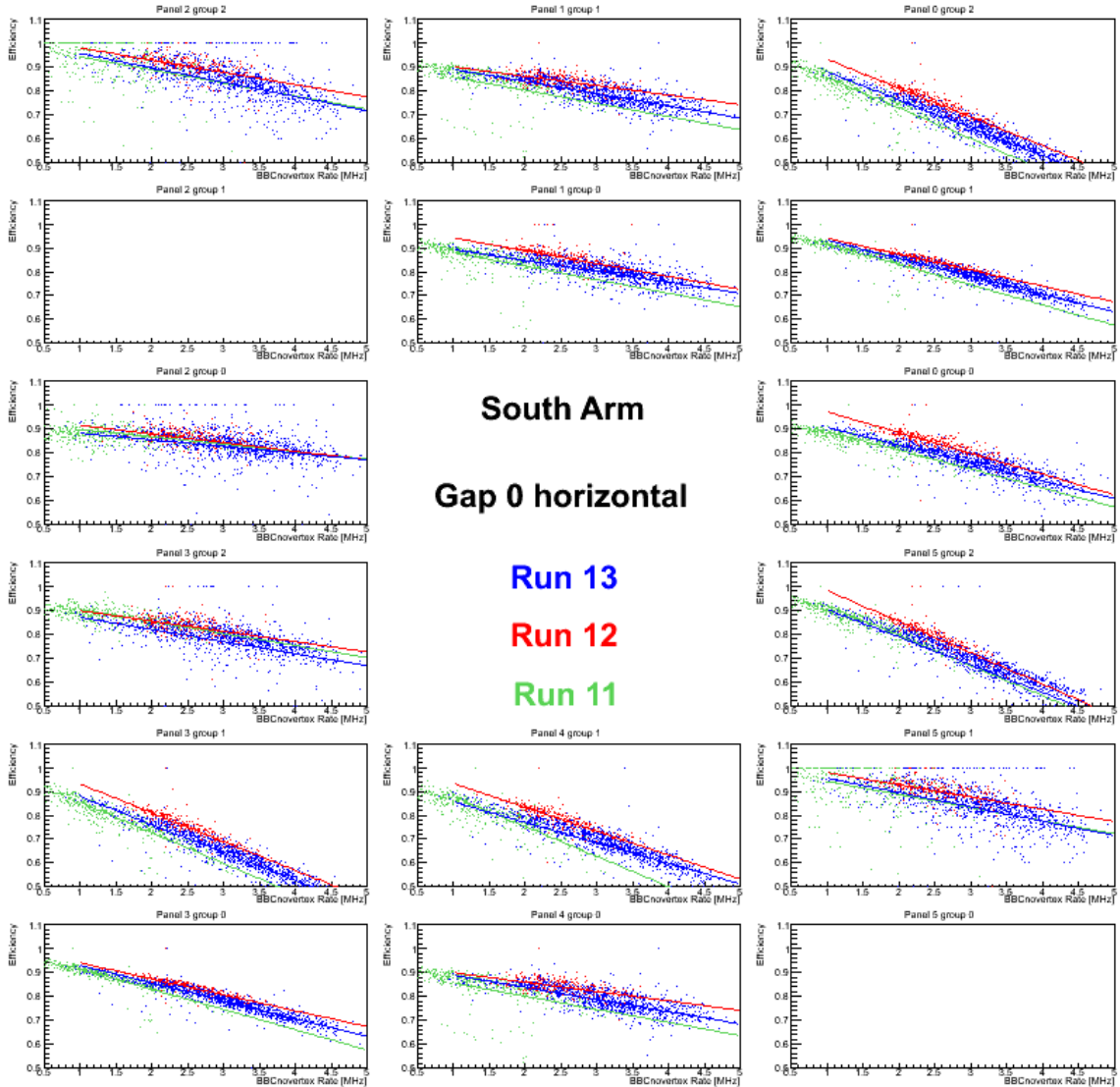


Figure C.1: MuID hit efficiency of south gap0 horizontal plane, for run11 (green), run12 (red) and run13 (blue).

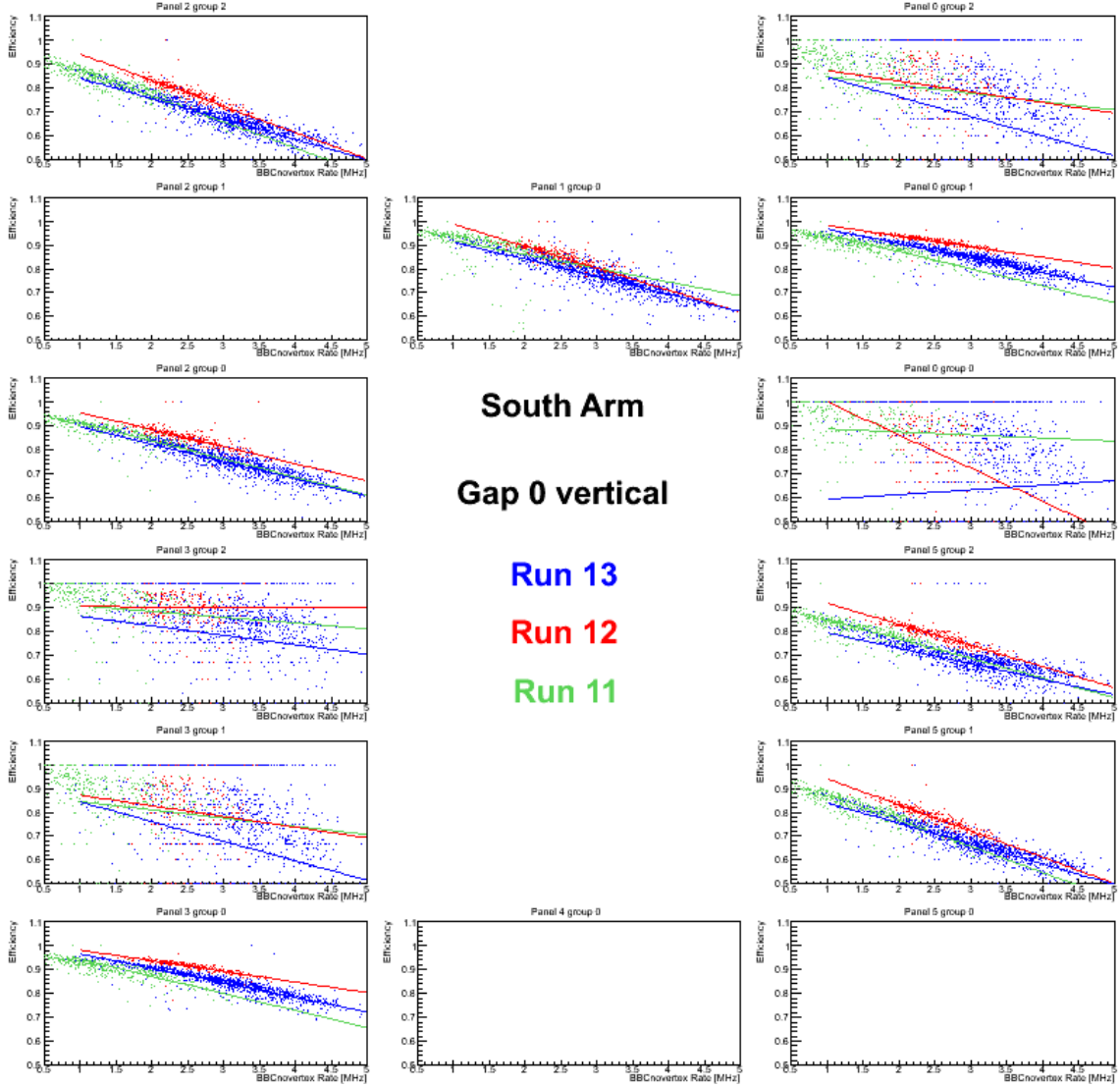


Figure C.2: MuID hit efficiency of south gap0 vertical plane, for run11 (green), run12 (red) and run13 (blue).

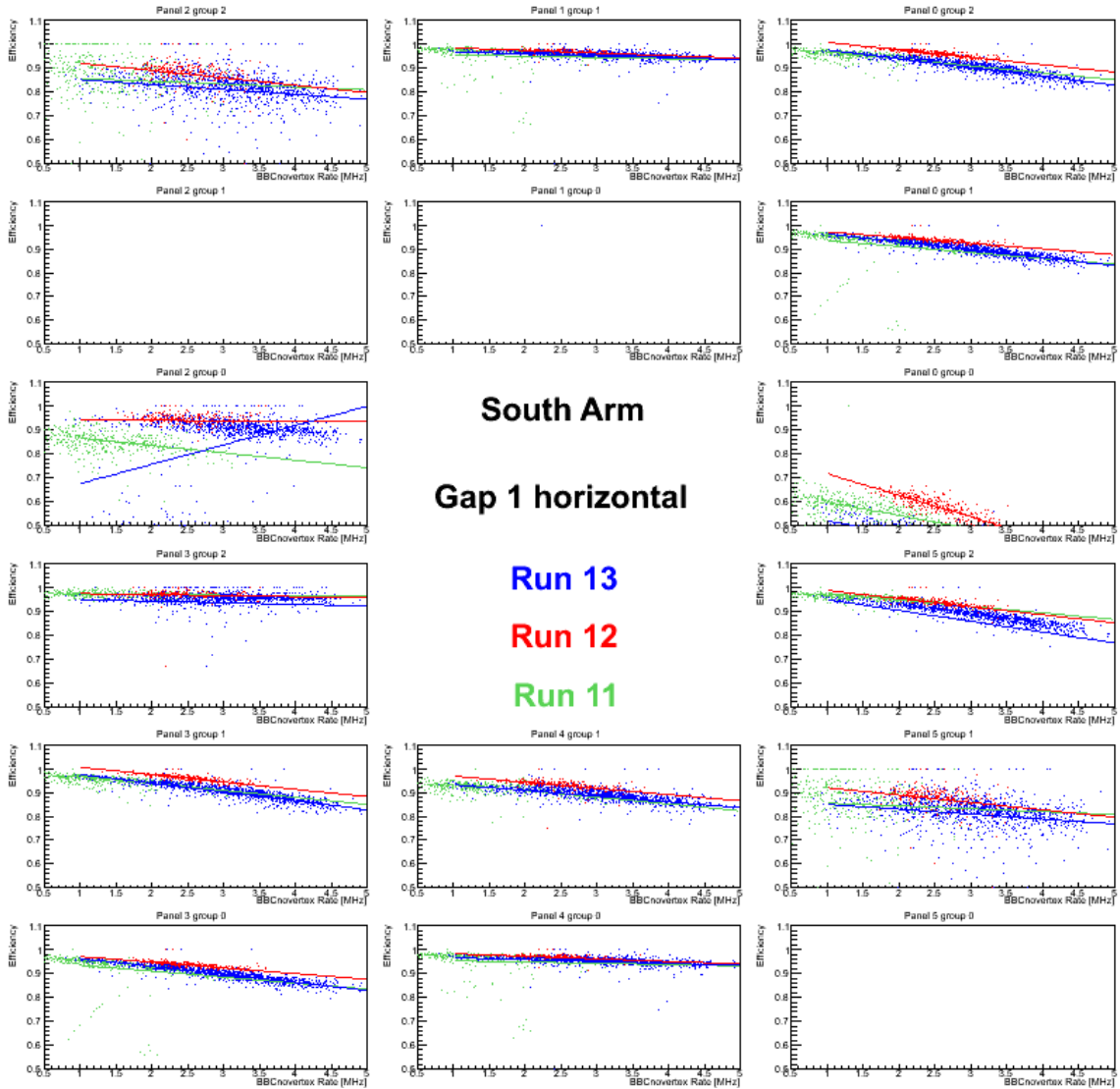


Figure C.3: MuID hit efficiency of south gap1 horizontal plane, for run11 (green), run12 (red) and run13 (blue).

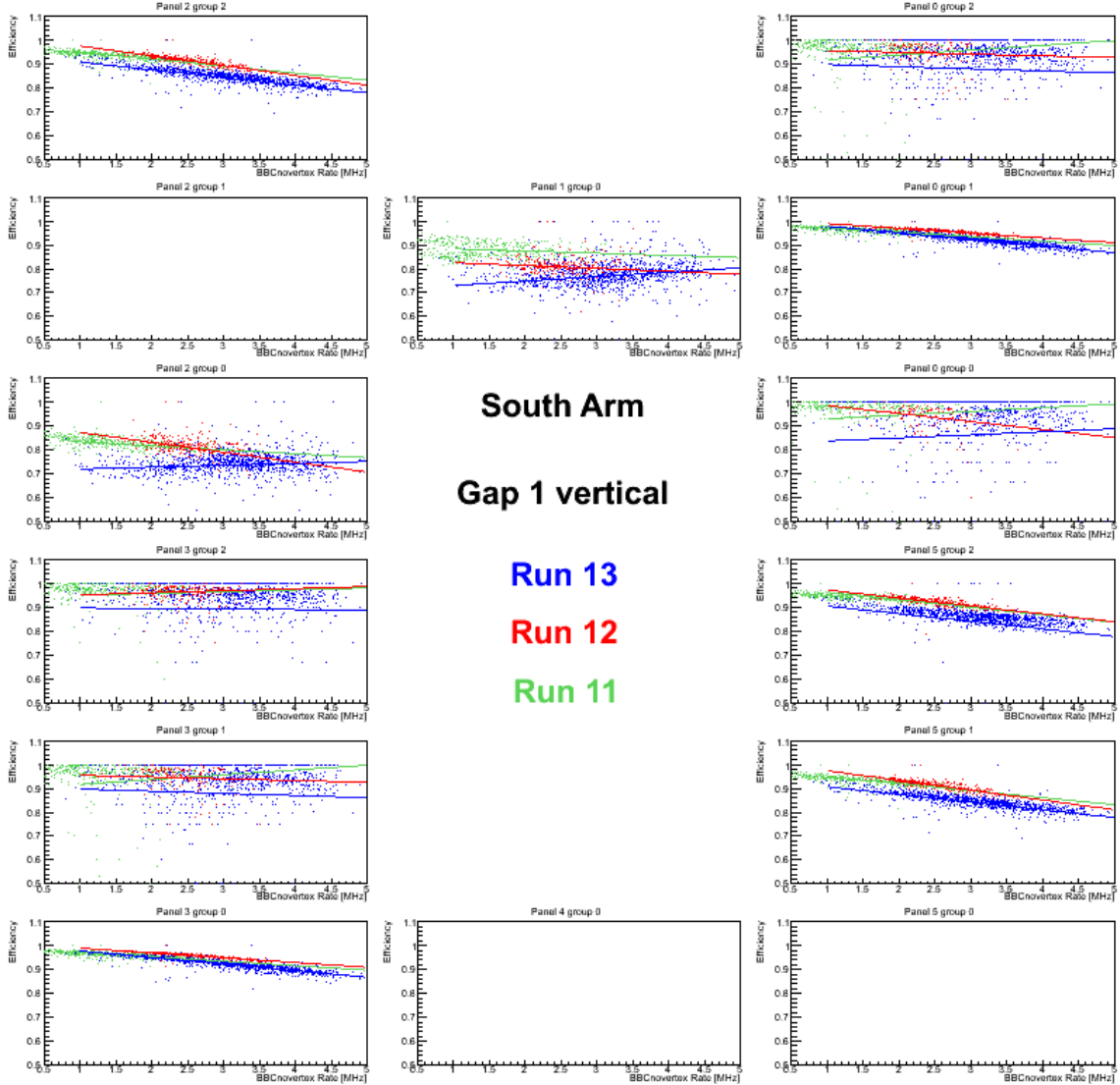


Figure C.4: MuID hit efficiency of south gap1 vertical plane, for run11 (green), run12 (red) and run13 (blue).

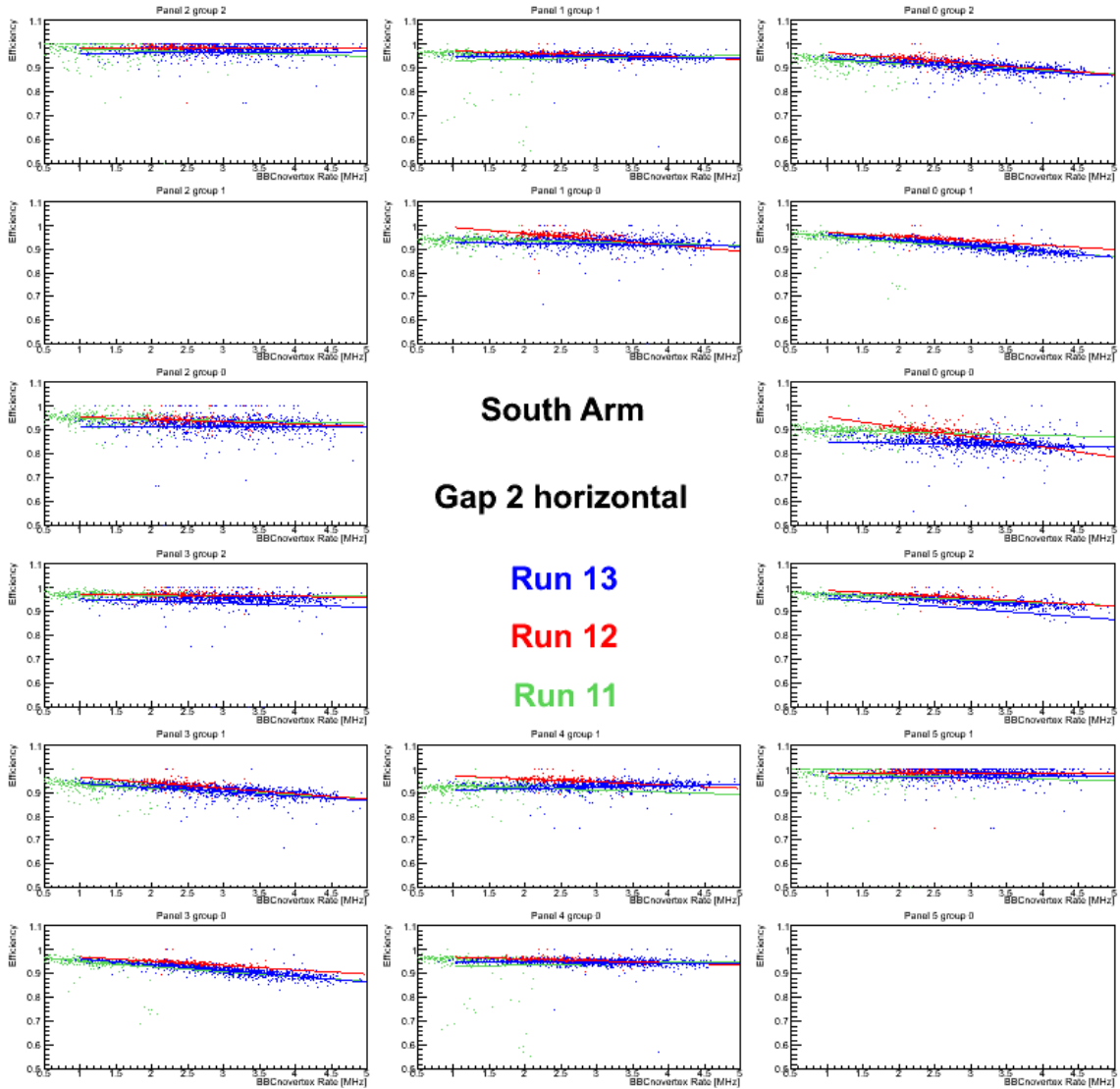


Figure C.5: MuID hit efficiency of south gap2 horizontal plane, for run11 (green), run12 (red) and run13 (blue).

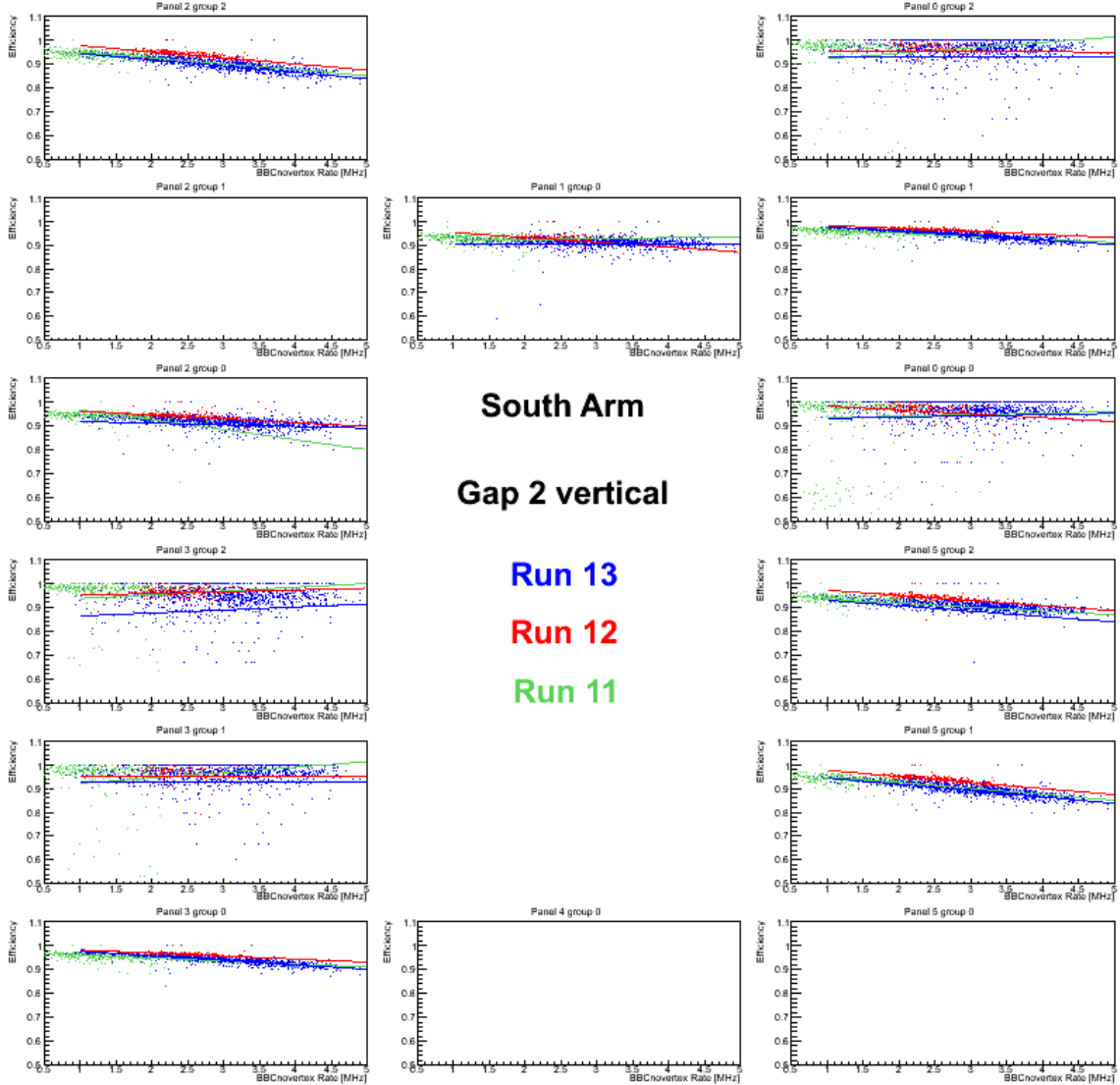


Figure C.6: MuID hit efficiency of south gap2 vertical plane, for run11 (green), run12 (red) and run13 (blue).

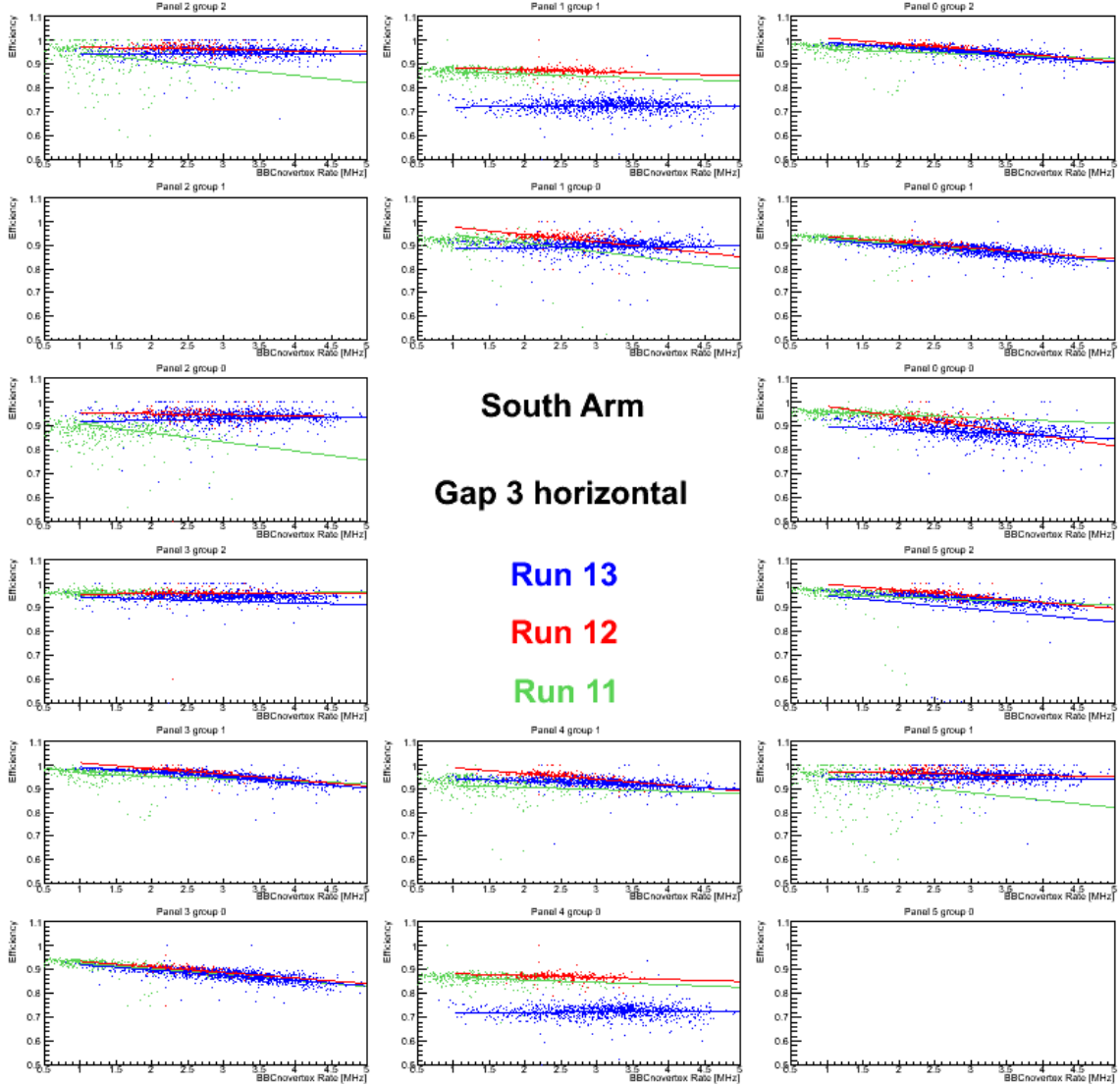


Figure C.7: MuID hit efficiency of south gap3 horizontal plane, for run11 (green), run12 (red) and run13 (blue).

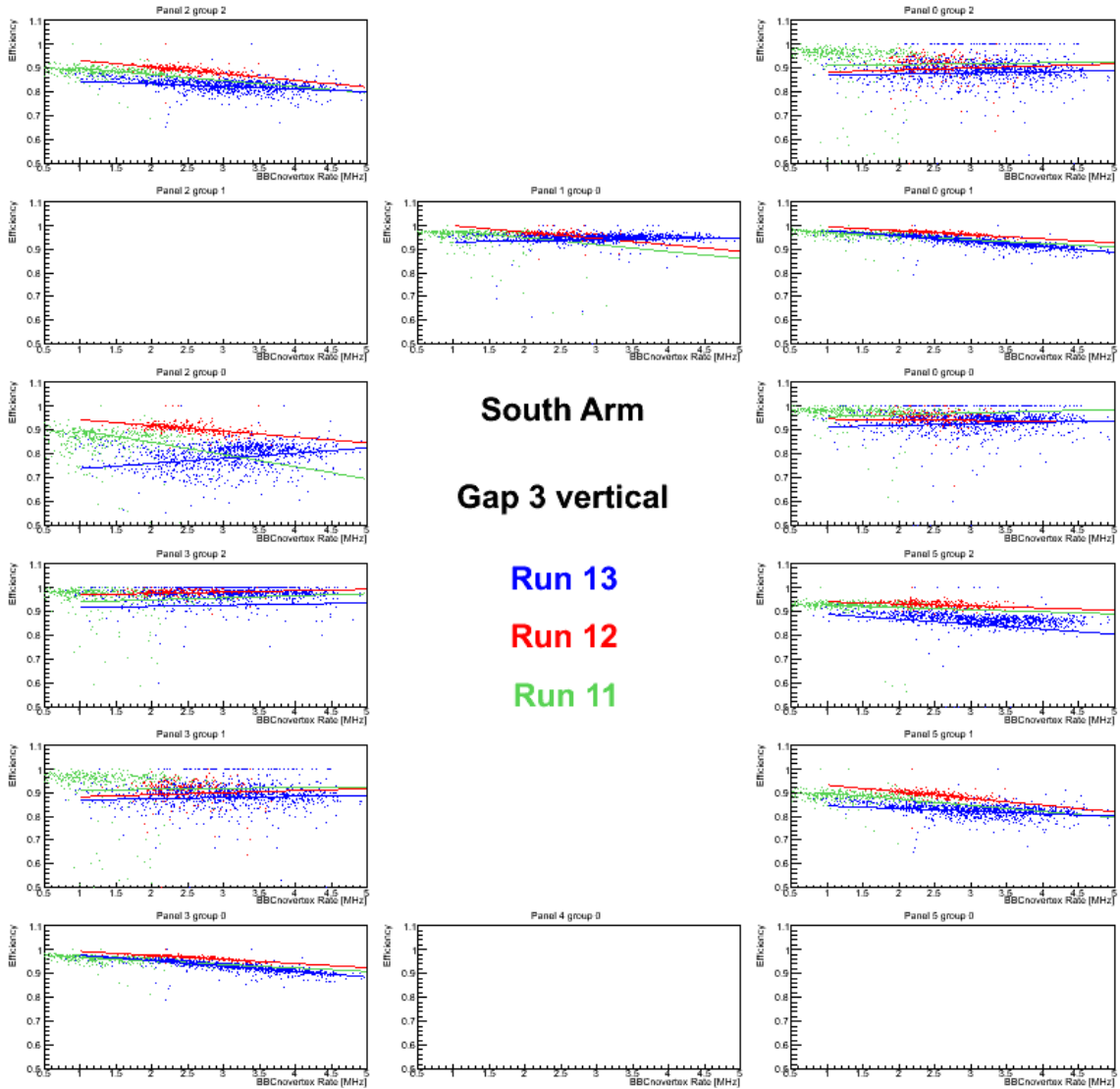


Figure C.8: MuID hit efficiency of south gap3 vertical plane, for run11 (green), run12 (red) and run13 (blue).

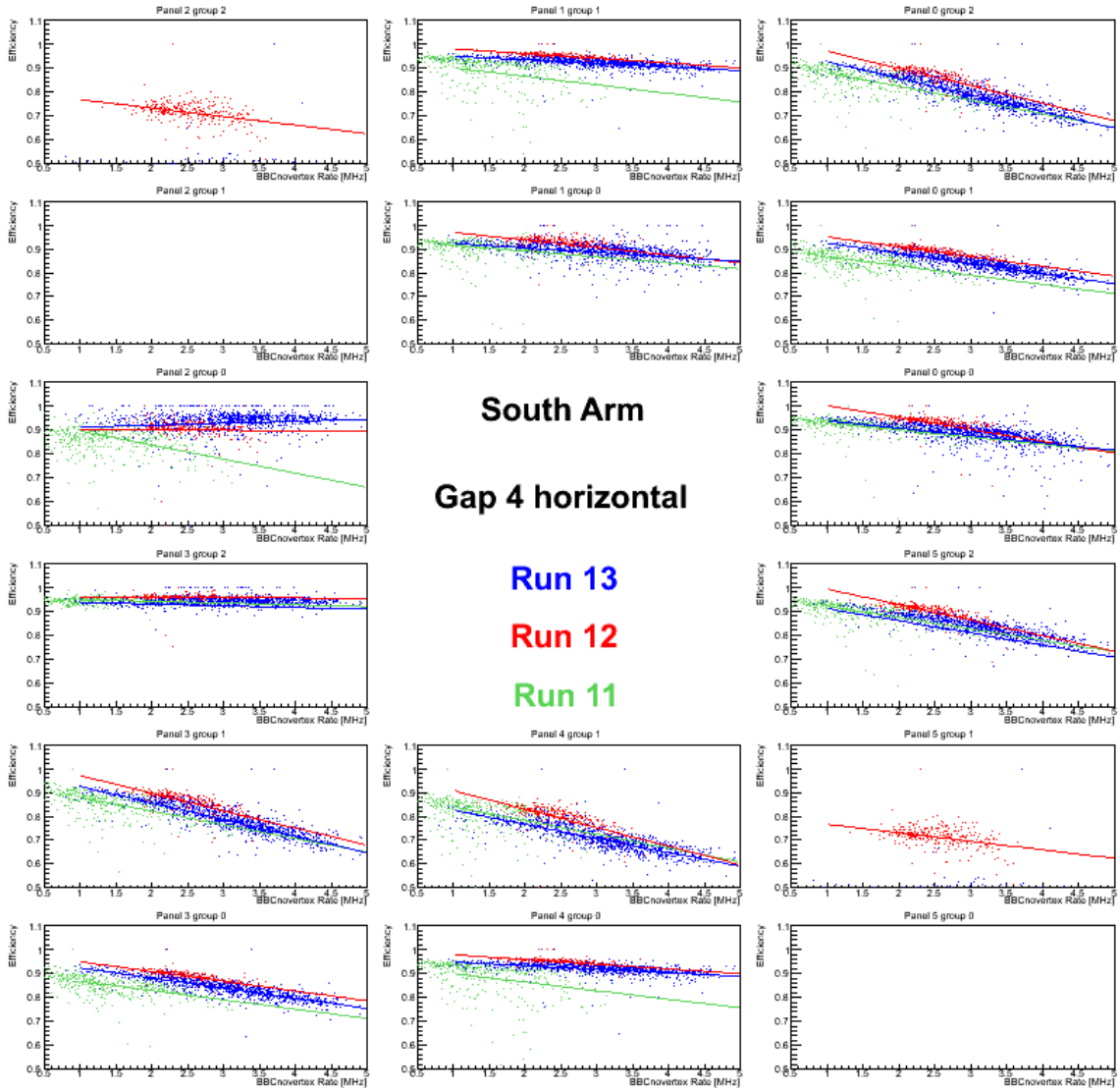


Figure C.9: MuID hit efficiency of south gap4 horizontal plane, for run11 (green), run12 (red) and run13 (blue).

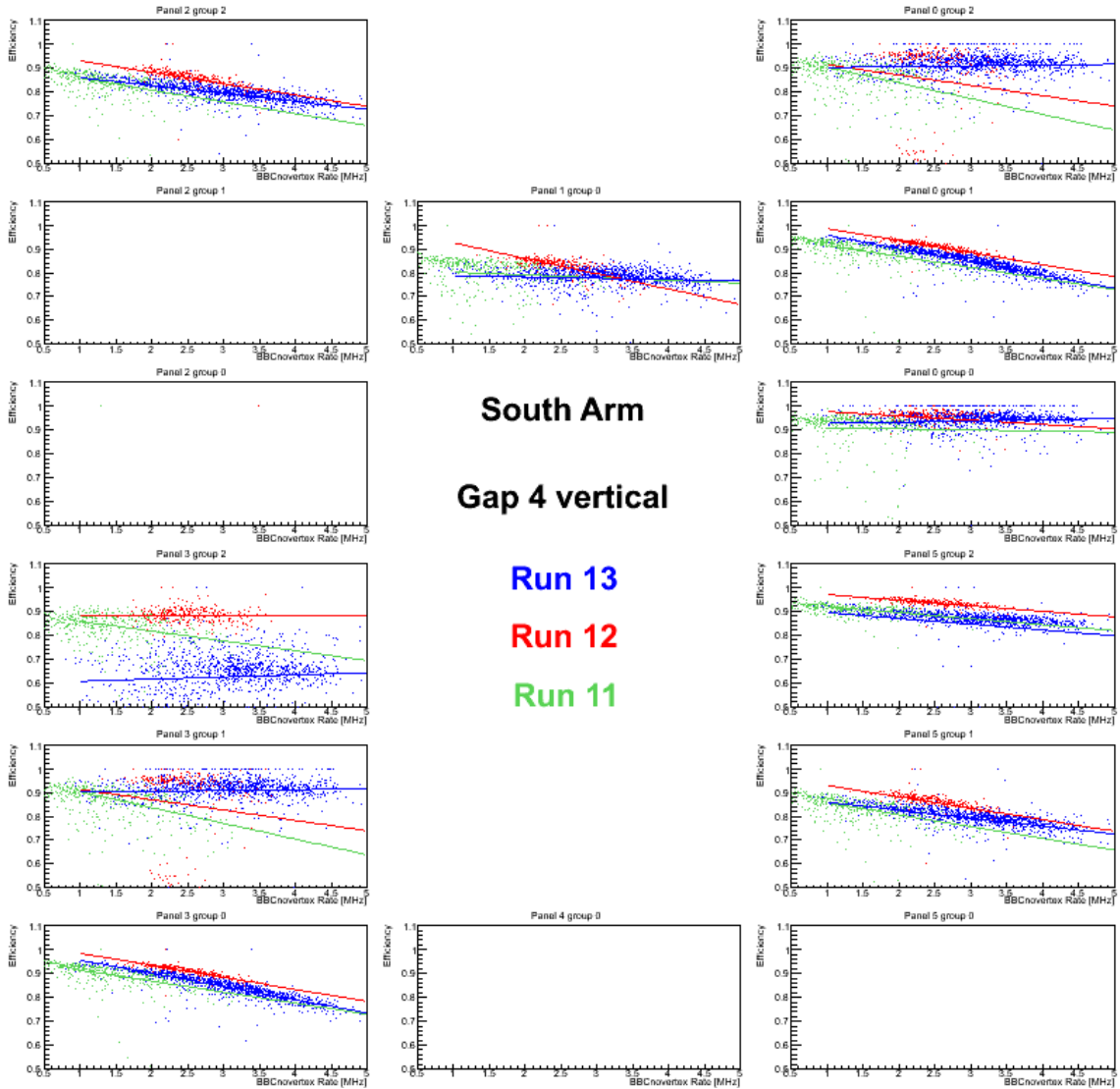


Figure C.10: MuID hit efficiency of south gap4 vertical plane, for run11 (green), run12 (red) and run13 (blue).

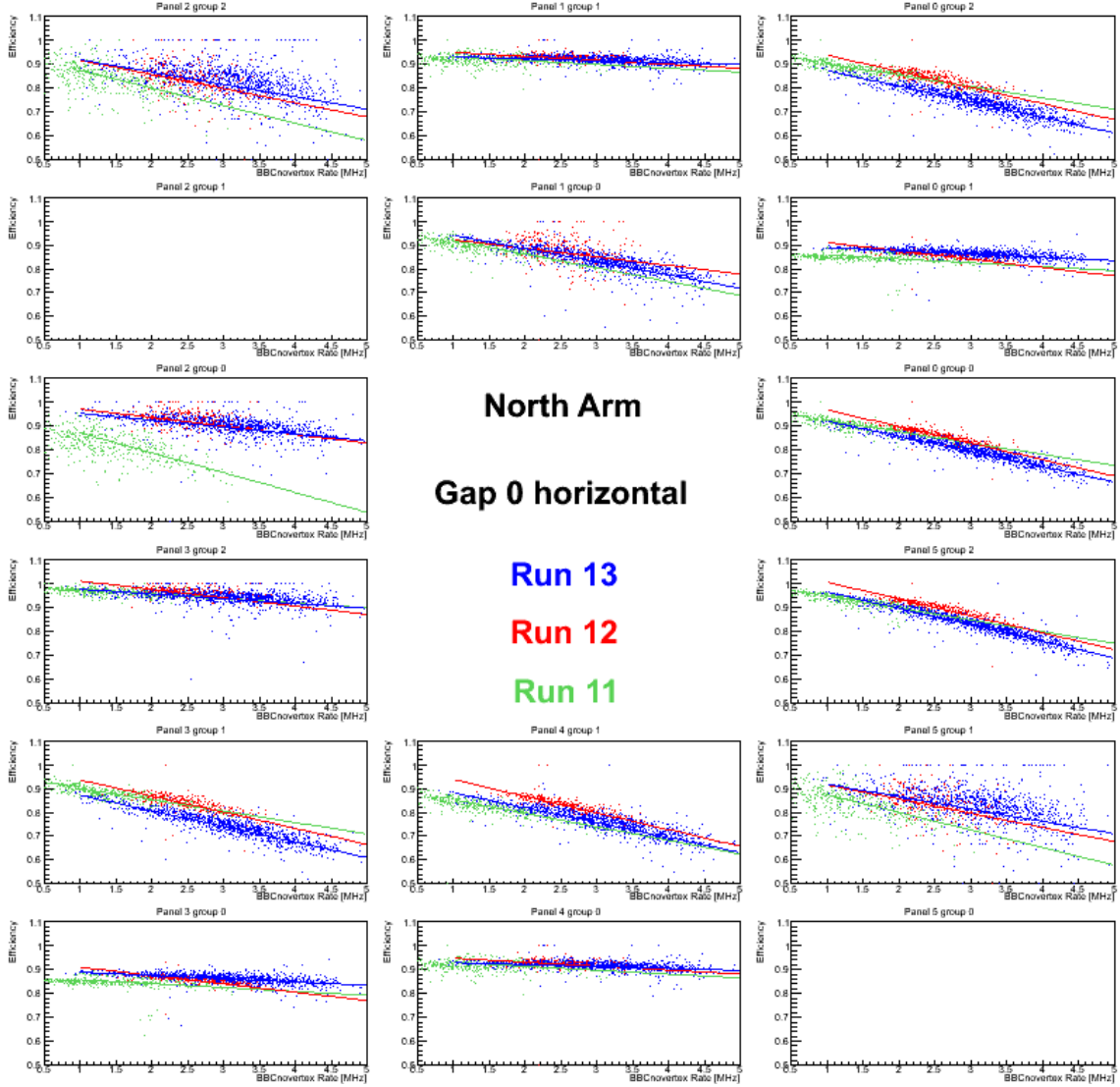


Figure C.11: MuID hit efficiency of north gap0 horizontal plane, for run11 (green), run12 (red) and run13 (blue).

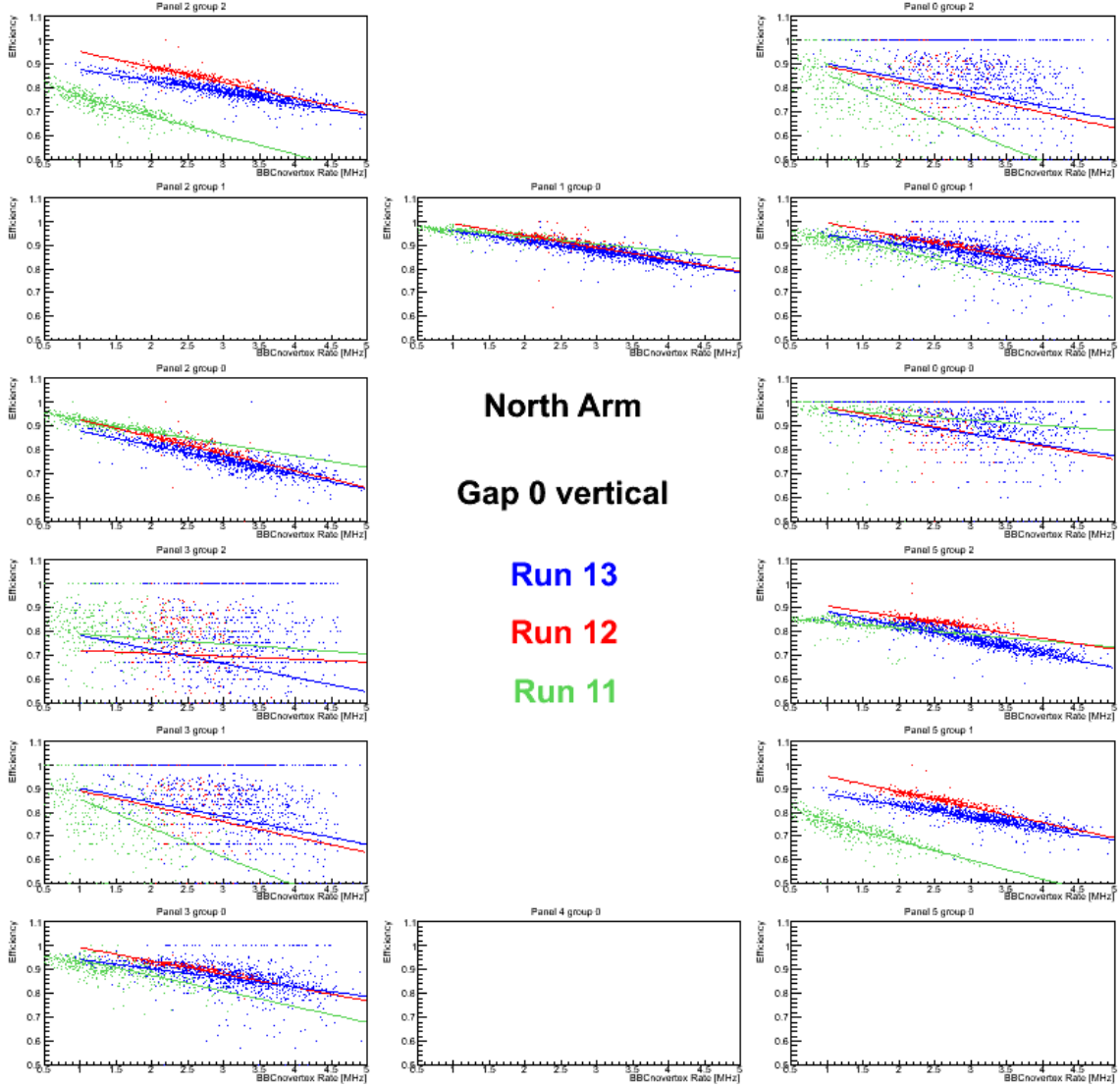


Figure C.12: MuID hit efficiency of north gap0 vertical plane, for run11 (green), run12 (red) and run13 (blue).

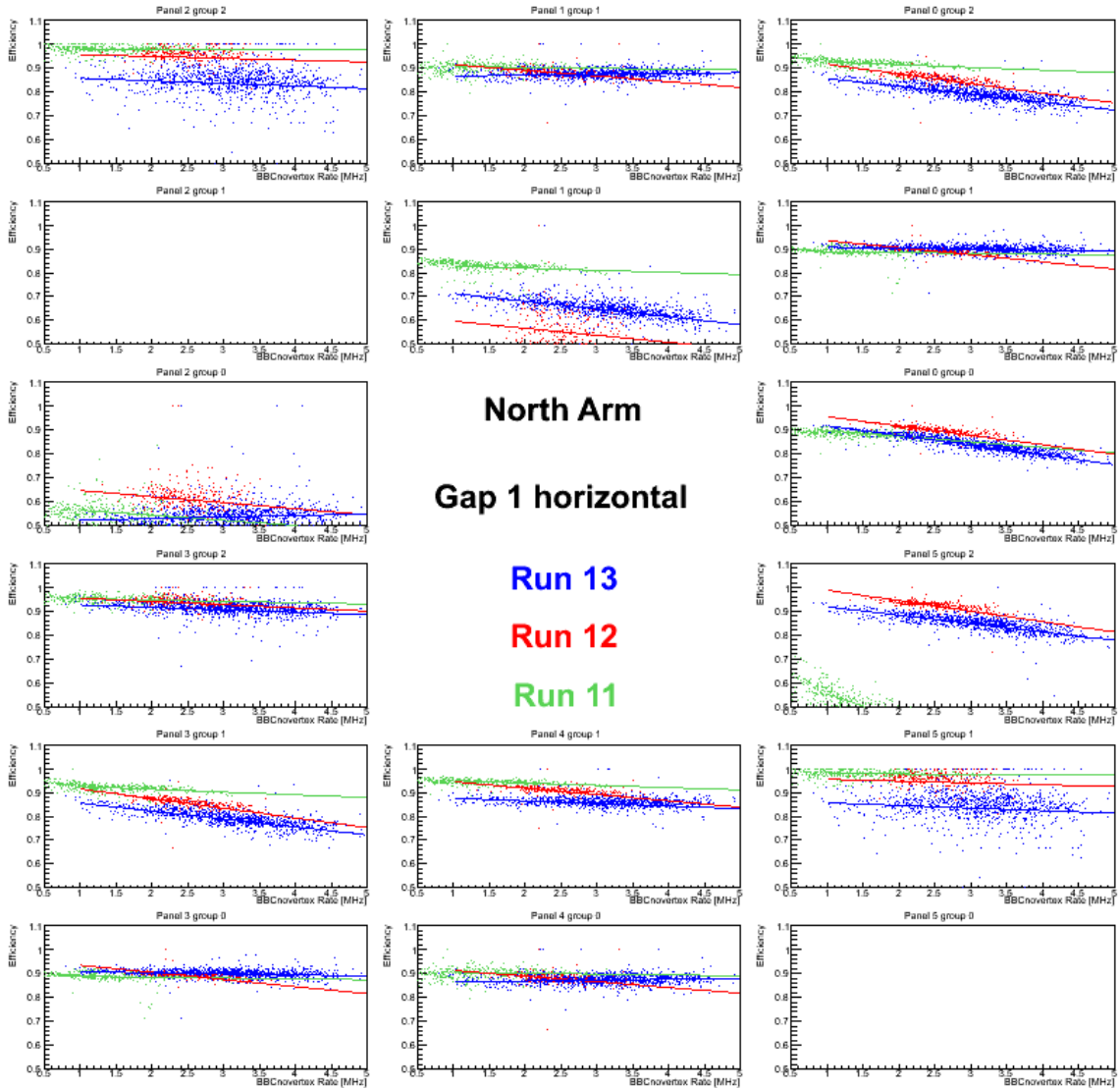


Figure C.13: MuID hit efficiency of north gap1 horizontal plane, for run11 (green), run12 (red) and run13 (blue).

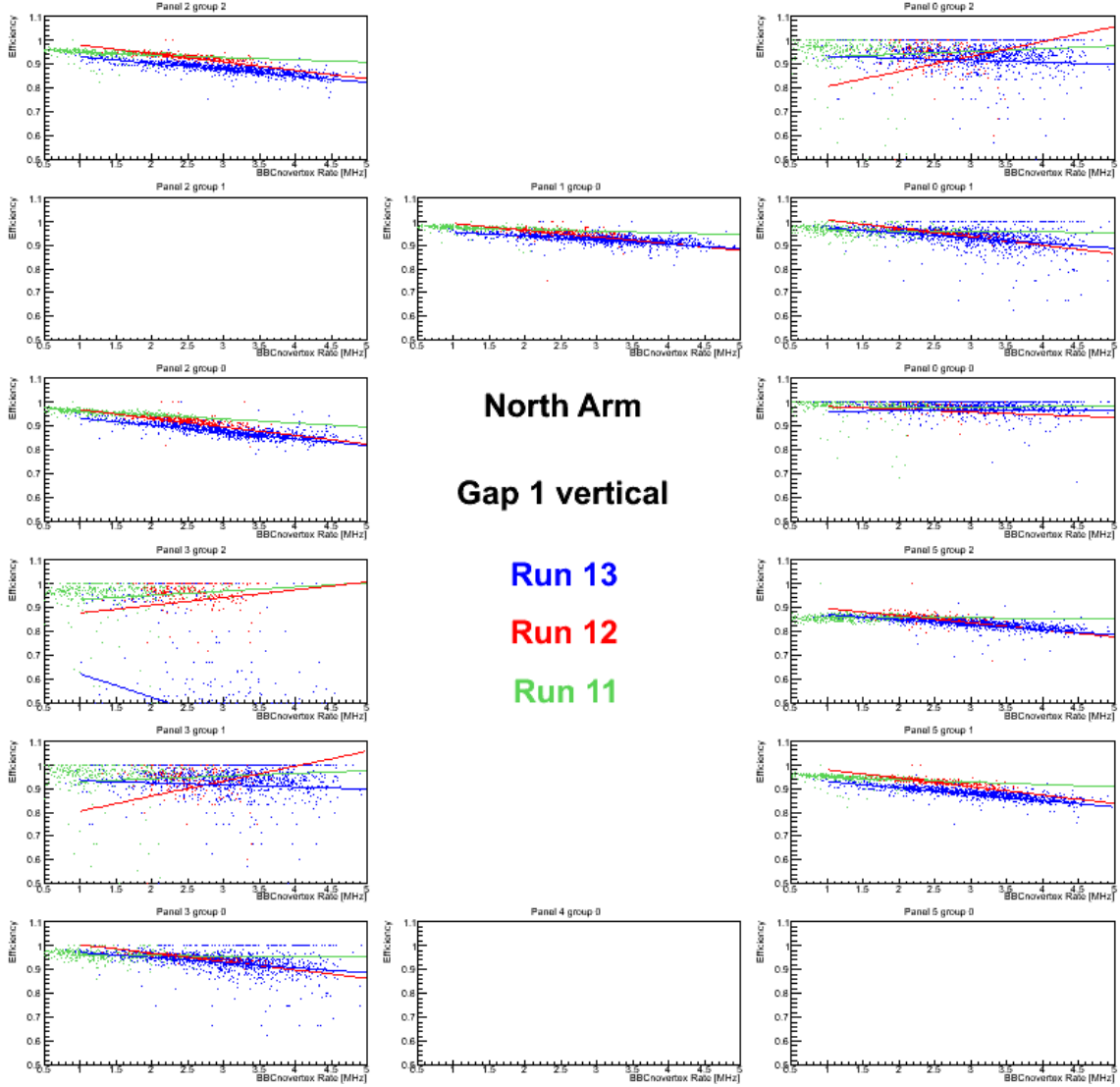


Figure C.14: MuID hit efficiency of north gap1 vertical plane, for run11 (green), run12 (red) and run13 (blue).

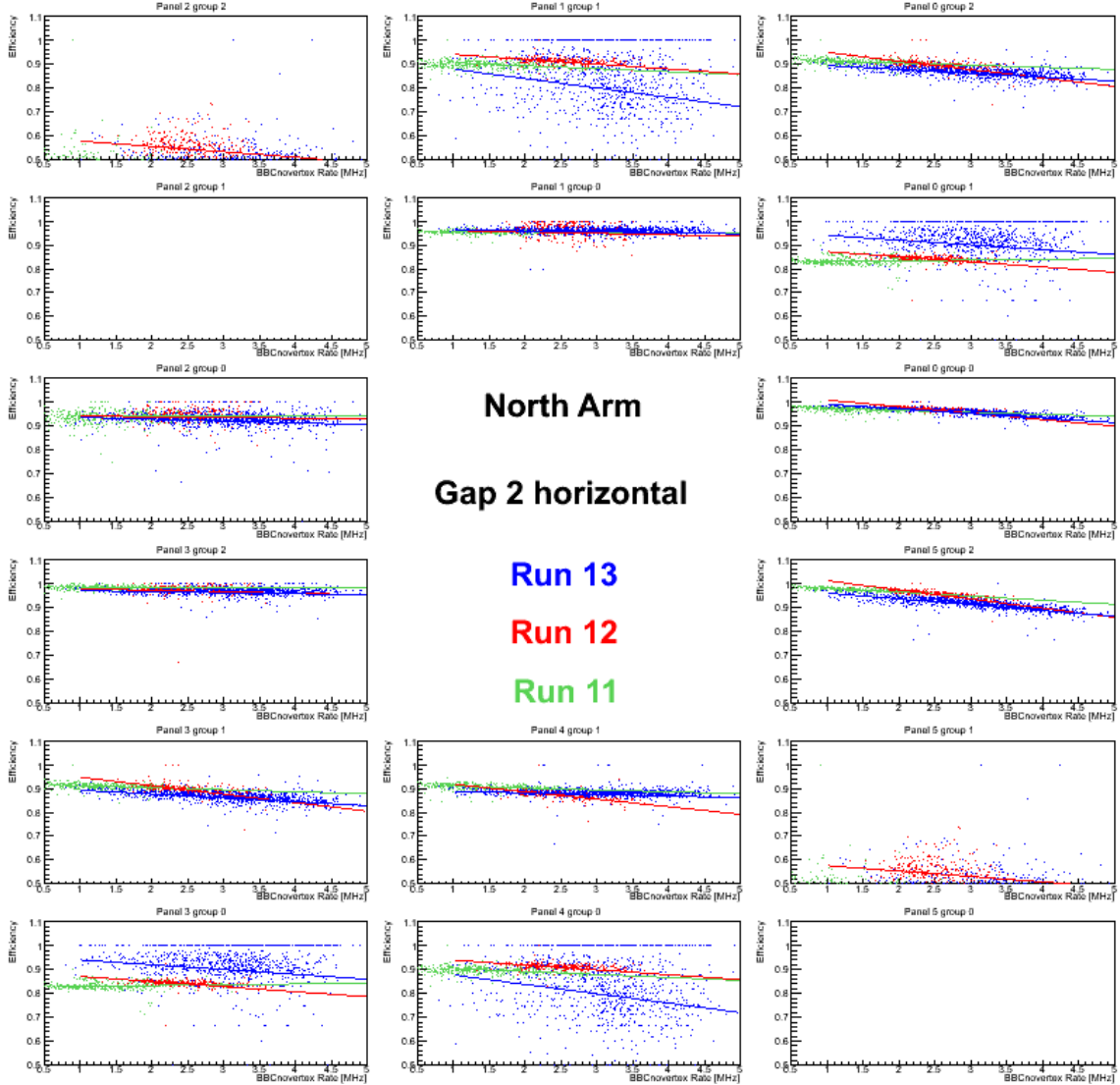


Figure C.15: MuID hit efficiency of north gap2 horizontal plane, for run11 (green), run12 (red) and run13 (blue).

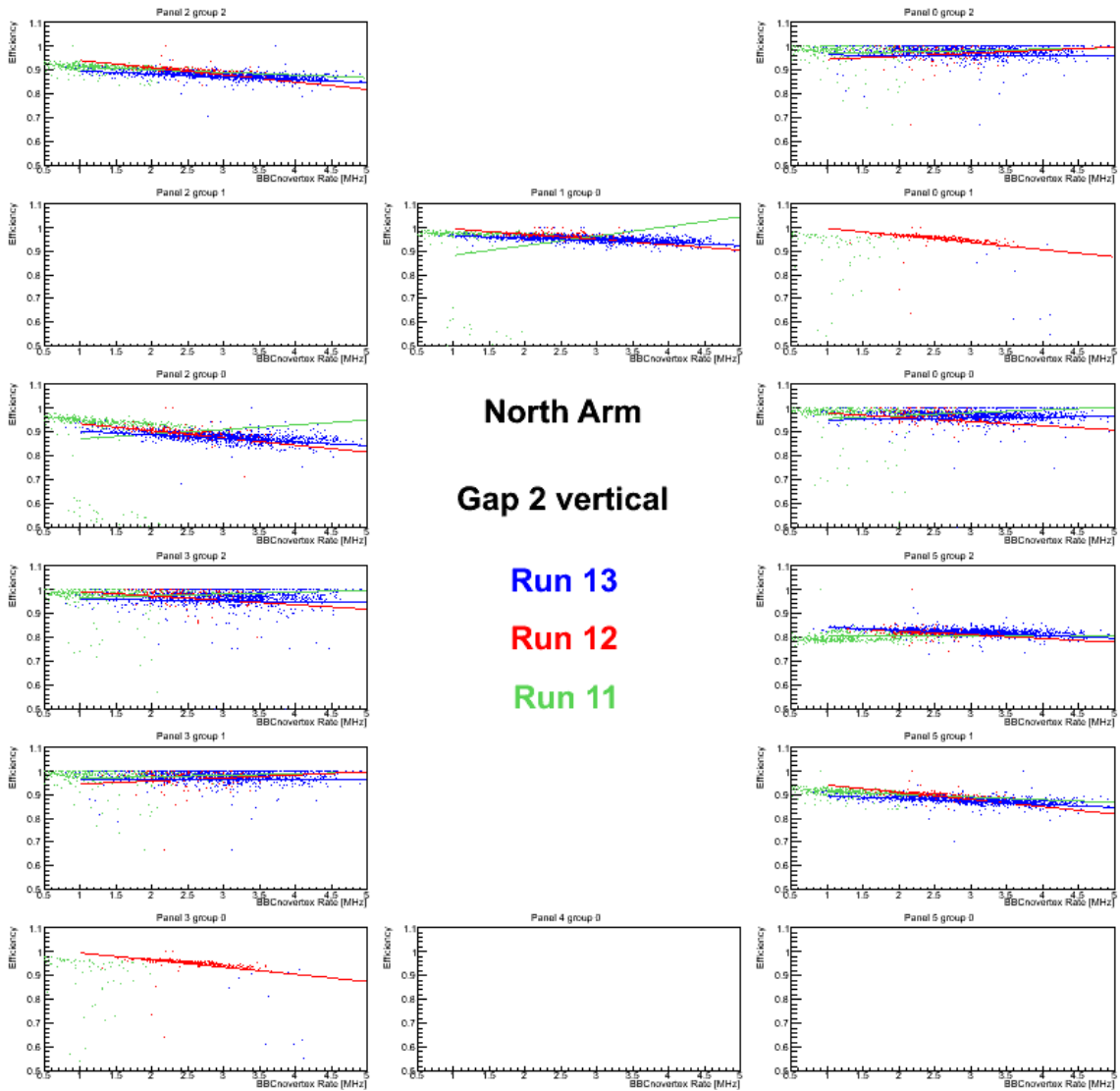


Figure C.16: MuID hit efficiency of north gap2 vertical plane, for run11 (green), run12 (red) and run13 (blue).

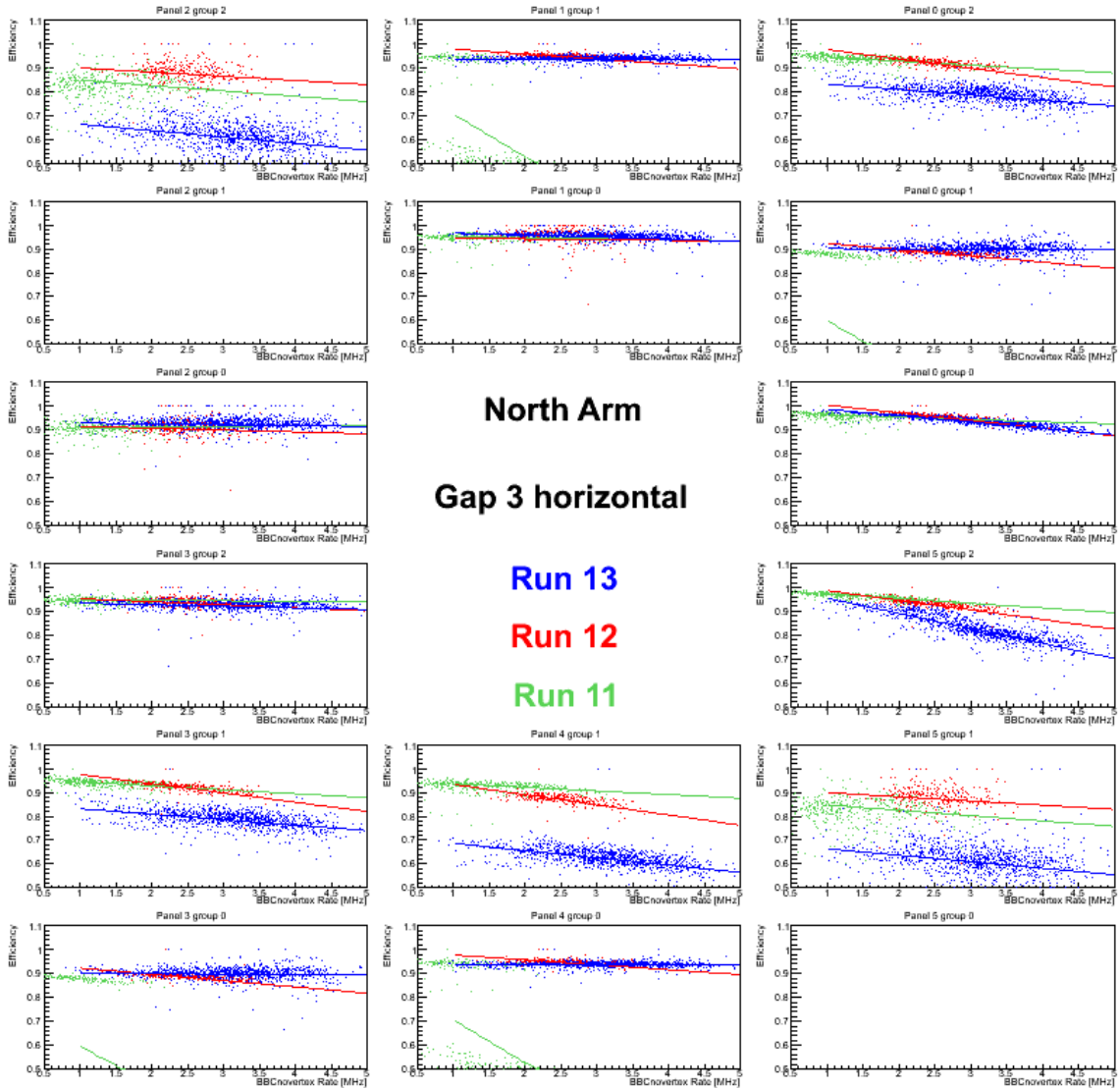


Figure C.17: MuID hit efficiency of north gap3 horizontal plane, for run11 (green), run12 (red) and run13 (blue).

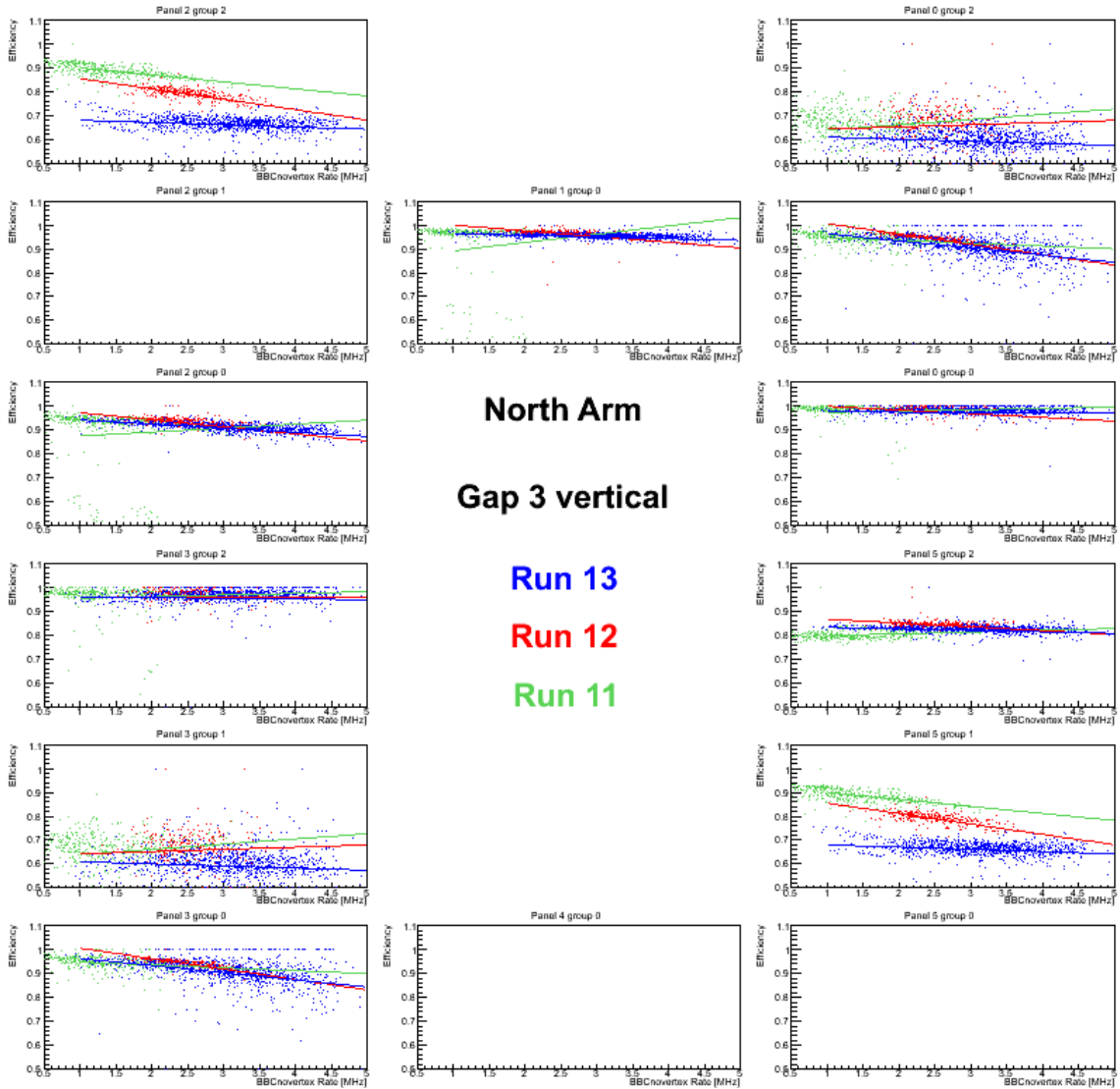


Figure C.18: MuID hit efficiency of north gap3 vertical plane, for run11 (green), run12 (red) and run13 (blue).

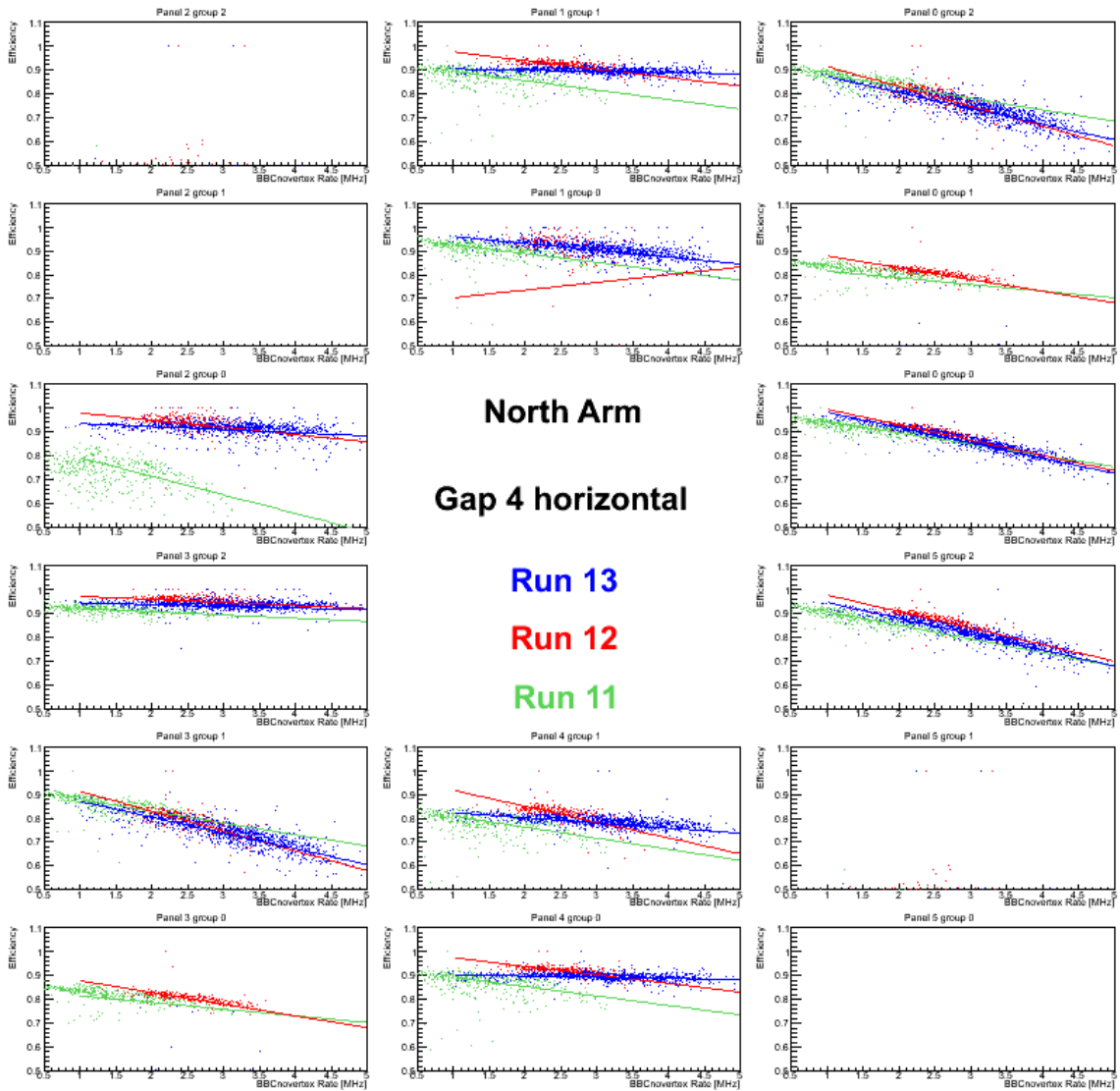


Figure C.19: MuID hit efficiency of north gap4 horizontal plane, for run11 (green), run12 (red) and run13 (blue).

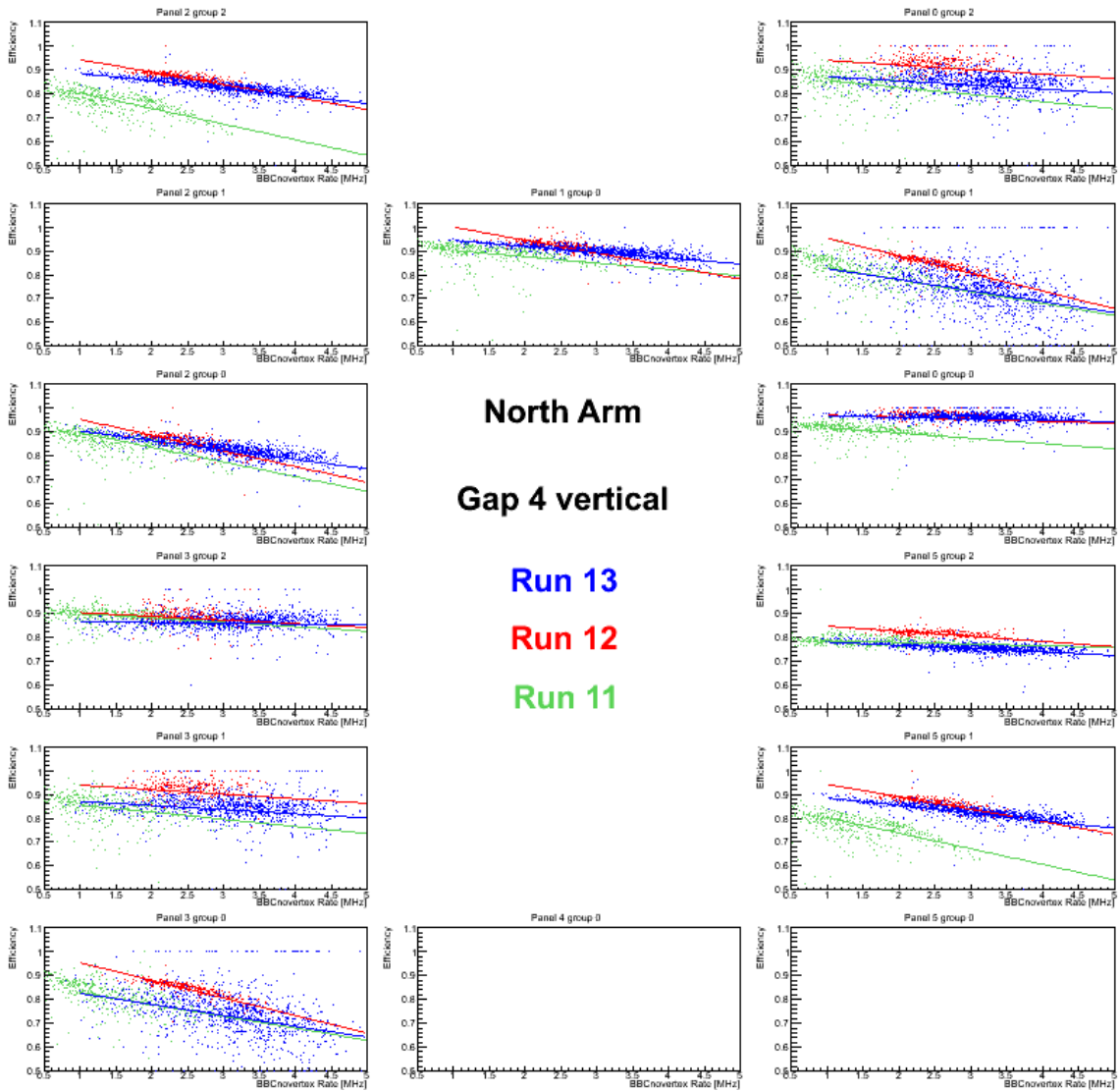


Figure C.20: MuID hit efficiency of north gap4 vertical plane, for run11 (green), run12 (red) and run13 (blue).

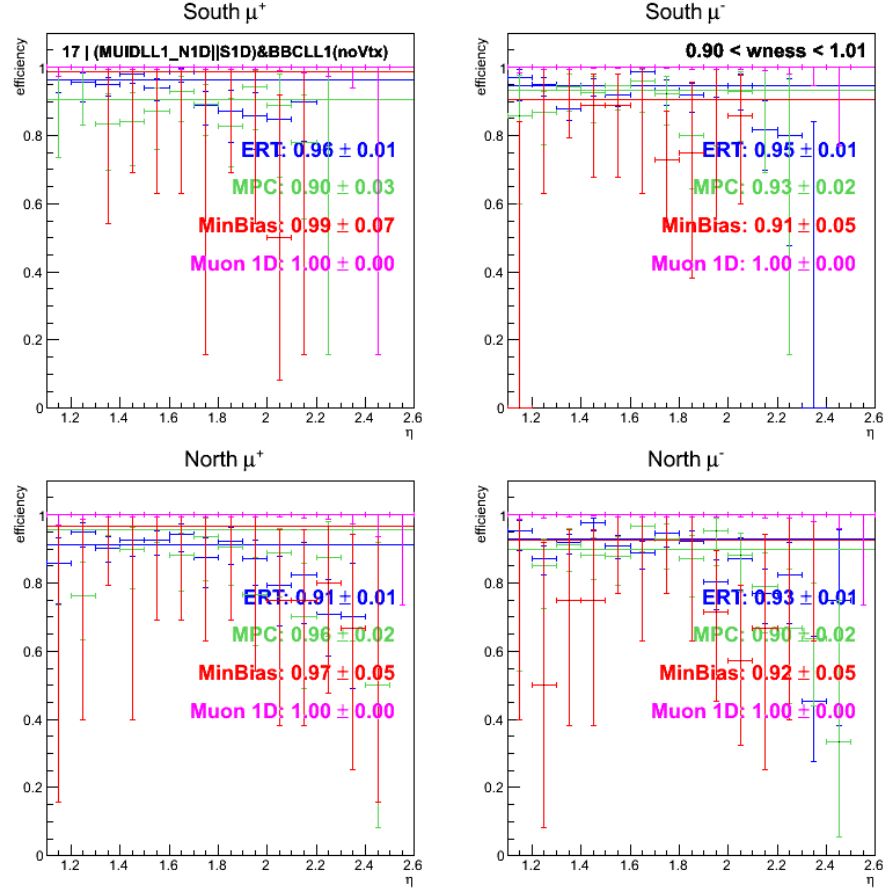


Figure C.21: Trigger efficiencies for trigger bit 17 ( $((\text{MUIDLL1\_N1D} \parallel \text{S1D}) \& \text{BBCLL1}(\text{noVtx}))$ ) for single  $W \rightarrow \mu$  candidates with transverse momenta above 5 GeV. The efficiencies for ERT (blue), MPC (green), MinBias (red) and 1D (purple) triggered data samples are shown as well as a constant fit over the whole range.

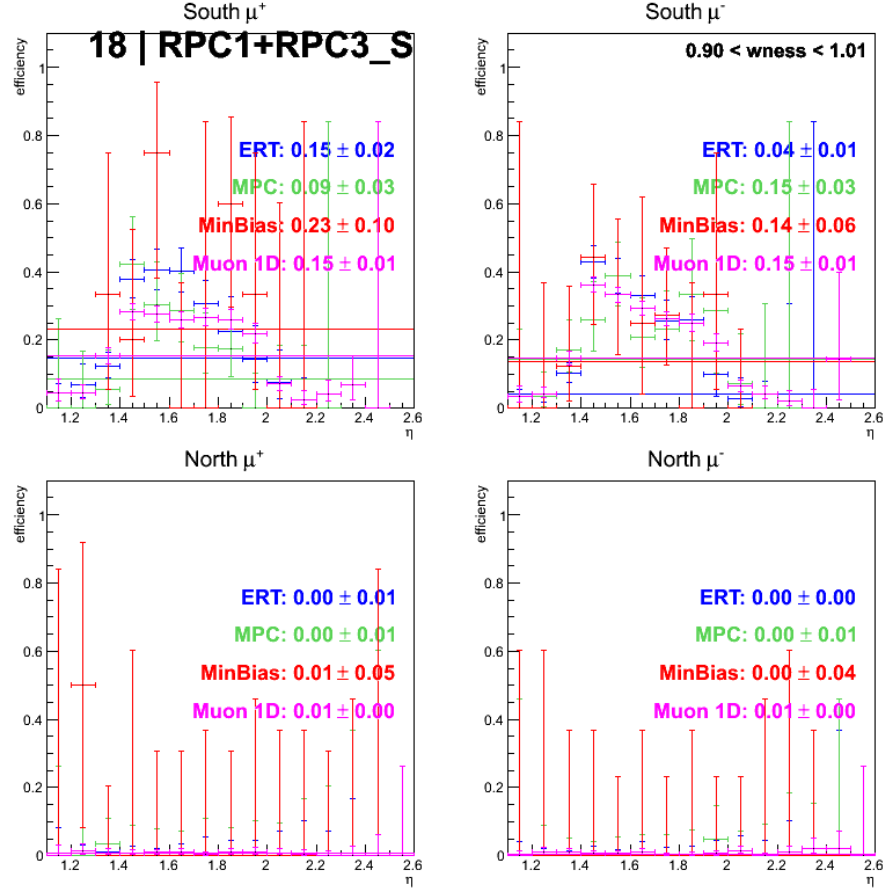


Figure C.22: Trigger efficiencies for trigger bit 18 (RPC1+RPC3\_S) for single  $W \rightarrow \mu$  candidates with transverse momenta above 5 GeV. The efficiencies for ERT (blue), MPC (green), MinBias(red) and 1D (purple) triggered data samples are shown as well as a constant fit over the whole range.

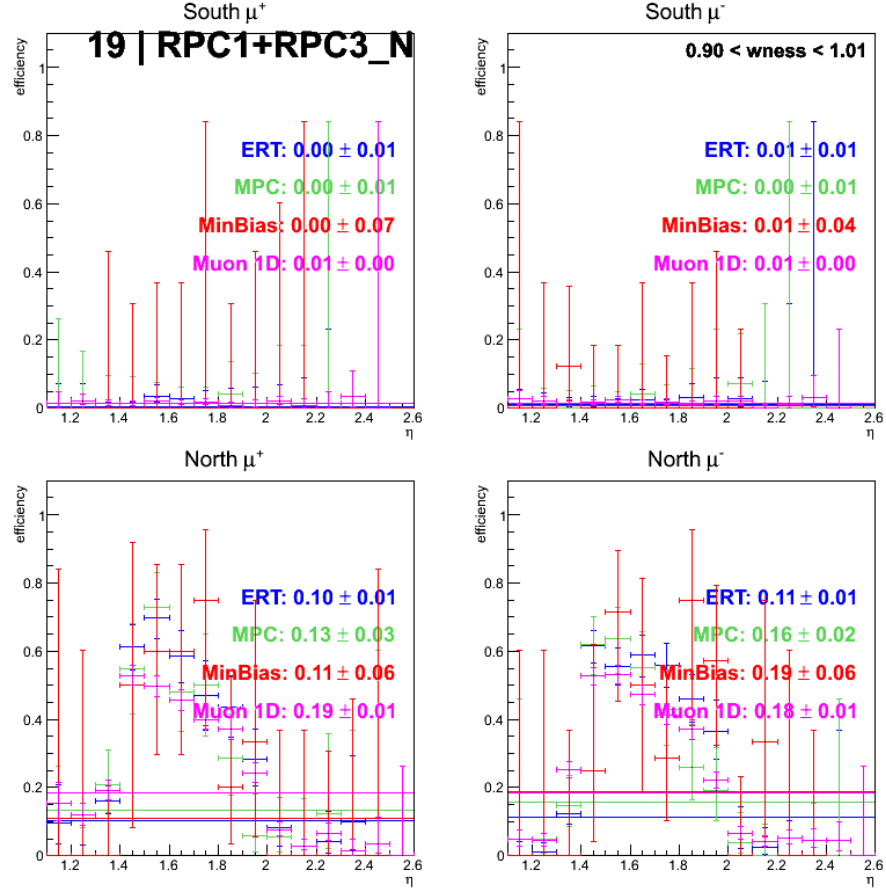


Figure C.23: Trigger efficiencies for trigger bit 19 (RPC1+RPC3\_N) for single  $W \rightarrow \mu$  candidates with transverse momenta above 5 GeV. The efficiencies for ERT (blue), MPC (green), MinBias(red) and 1D (purple) triggered data samples are shown as well as a constant fit over the whole range.

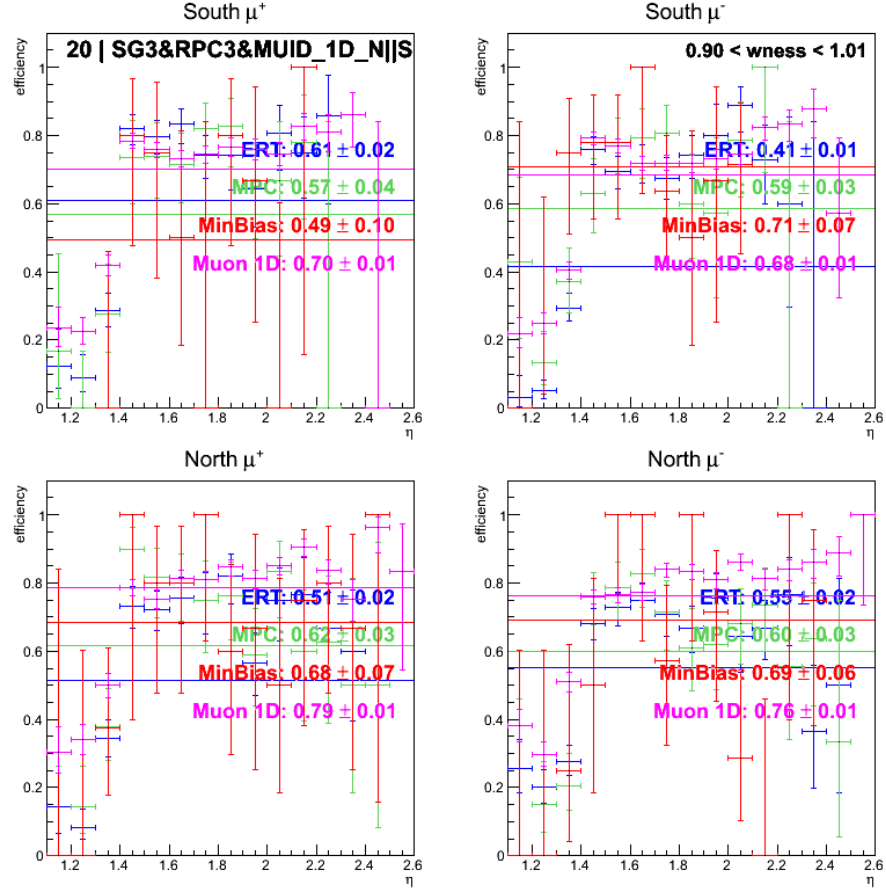


Figure C.24: Trigger efficiencies for trigger bit 20 (SG3&RPC3&MUID\_1D\_N||S) for single  $W \rightarrow \mu$  candidates with transverse momenta above 5 GeV. The efficiencies for ERT (blue), MPC (green), MinBias(red) and 1D (purple) triggered data samples are shown as well as a constant fit over the whole range.

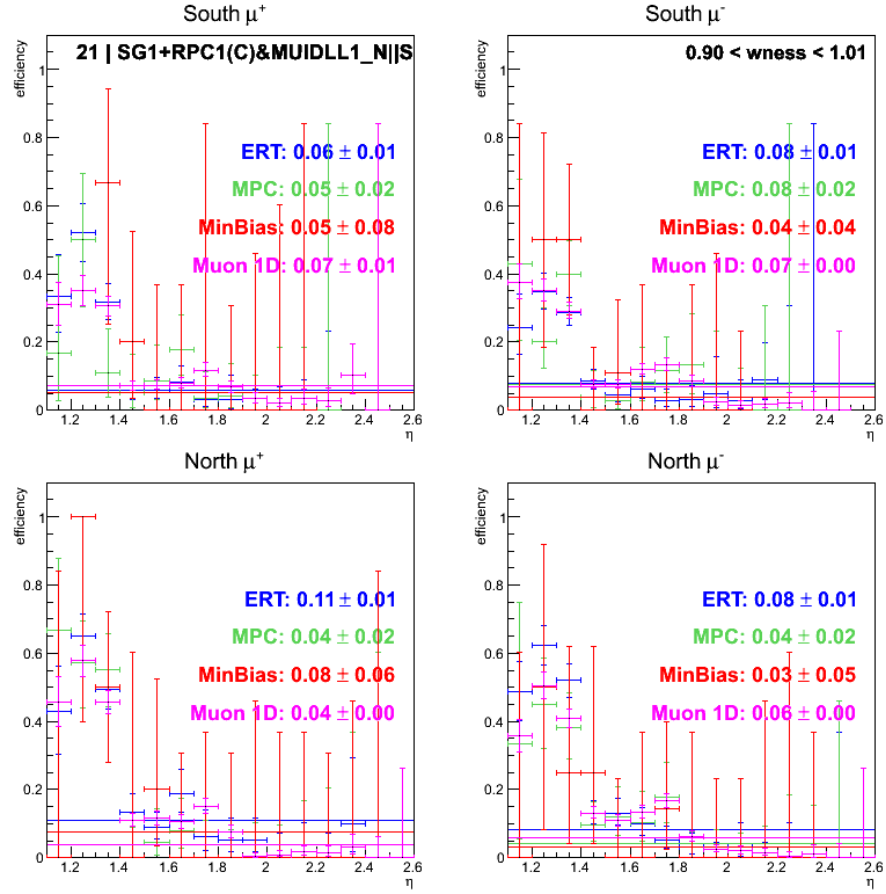


Figure C.25: Trigger efficiencies for trigger bit 21 (SG1+RPC1(C)&MUIDLL1\_N||S) for single  $W \rightarrow \mu$  candidates with transverse momenta above 5 GeV. The efficiencies for ERT (blue), MPC (green), MinBias(red) and 1D (purple) triggered data samples are shown as well as a constant fit over the whole range.

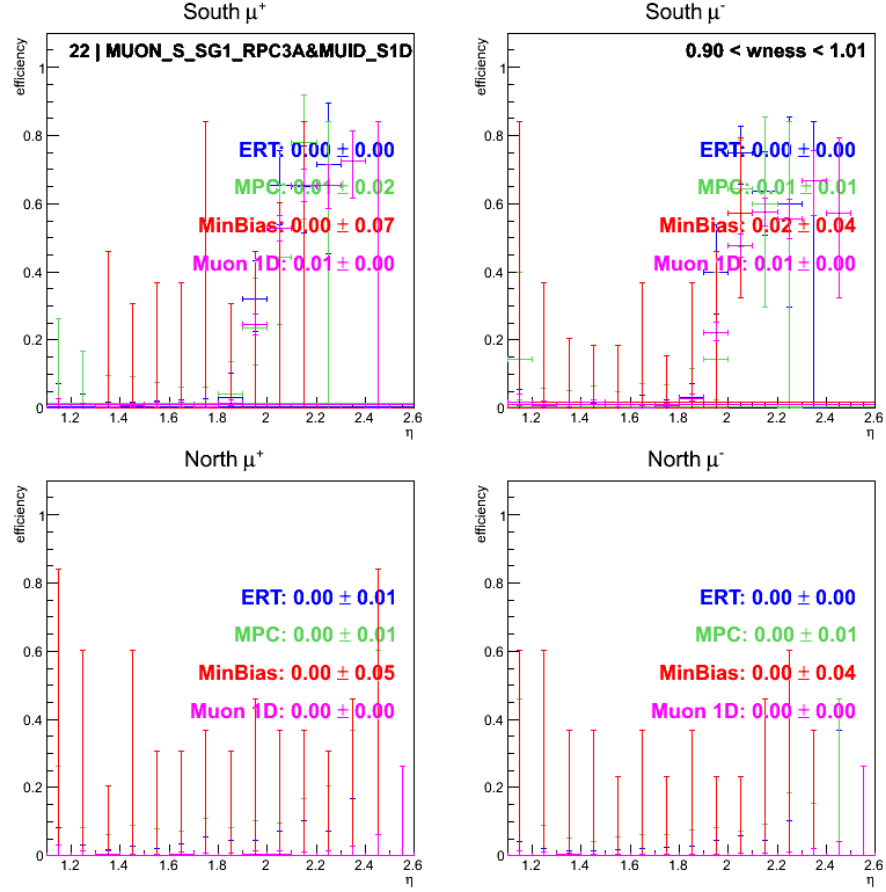


Figure C.26: Trigger efficiencies for trigger bit 22 ( MUON\_S\_SG1\_RPC3A&MUID\_S1D) for single  $W \rightarrow \mu$  candidates with transverse momenta above 5 GeV. The efficiencies for ERT (blue), MPC (green), MinBias(red) and 1D (purple) triggered data samples are shown as well as a constant fit over the whole range.

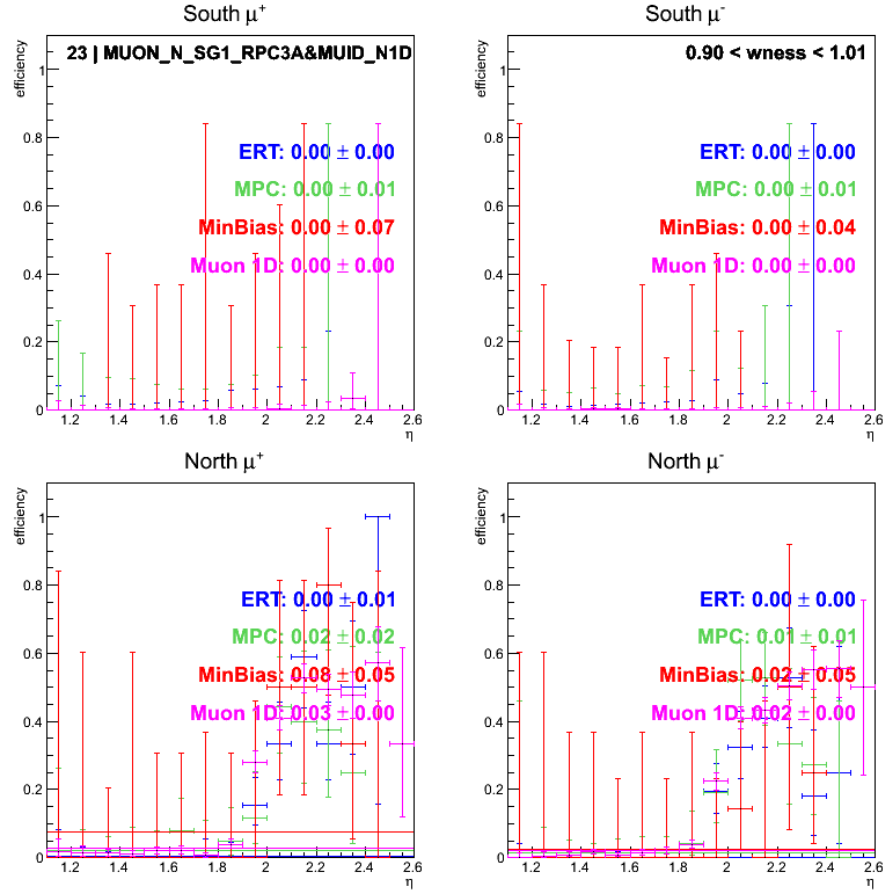


Figure C.27: Trigger efficiencies for trigger bit 23 ( MUON\_N\_SG1\_RPC3A&MUID\_N1D) for single  $W \rightarrow \mu$  candidates with transverse momenta above 5 GeV. The efficiencies for ERT (blue), MPC (green), MinBias(red) and 1D (purple) triggered data samples are shown as well as a constant fit over the whole range.

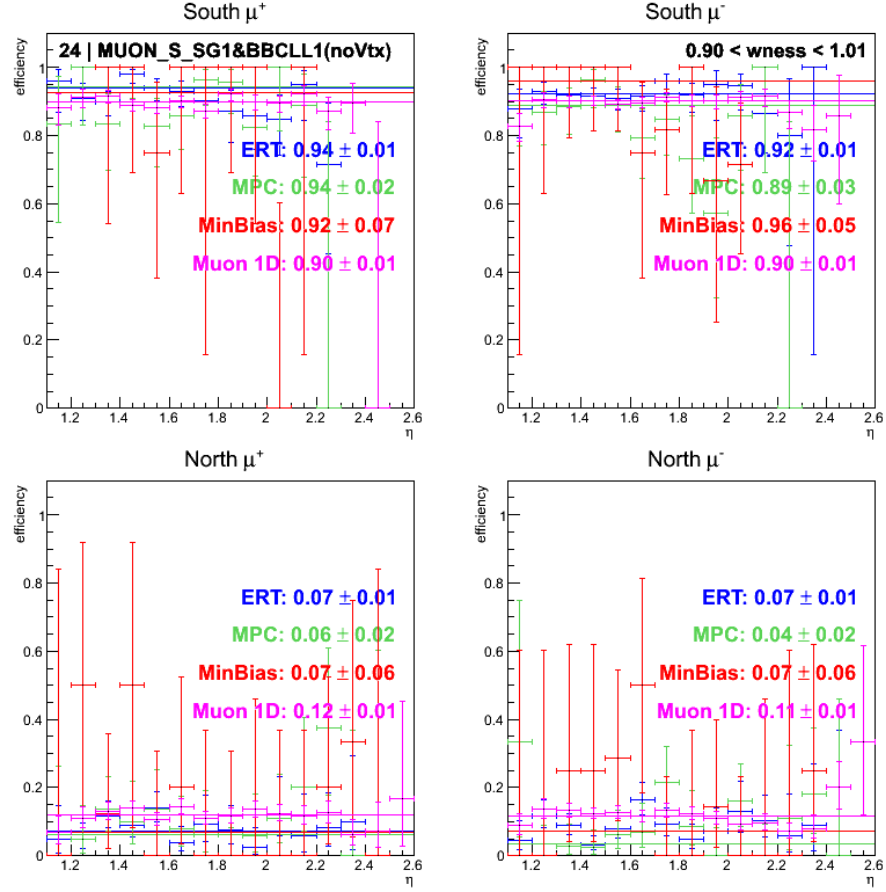


Figure C.28: Trigger efficiencies for trigger bit 24 (MUON\_S\_SG1&BBCLL1(noVtx)) for single  $W \rightarrow \mu$  candidates with transverse momenta above 5 GeV. The efficiencies for ERT (blue), MPC (green), MinBias (red) and 1D (purple) triggered data samples are shown as well as a constant fit over the whole range.

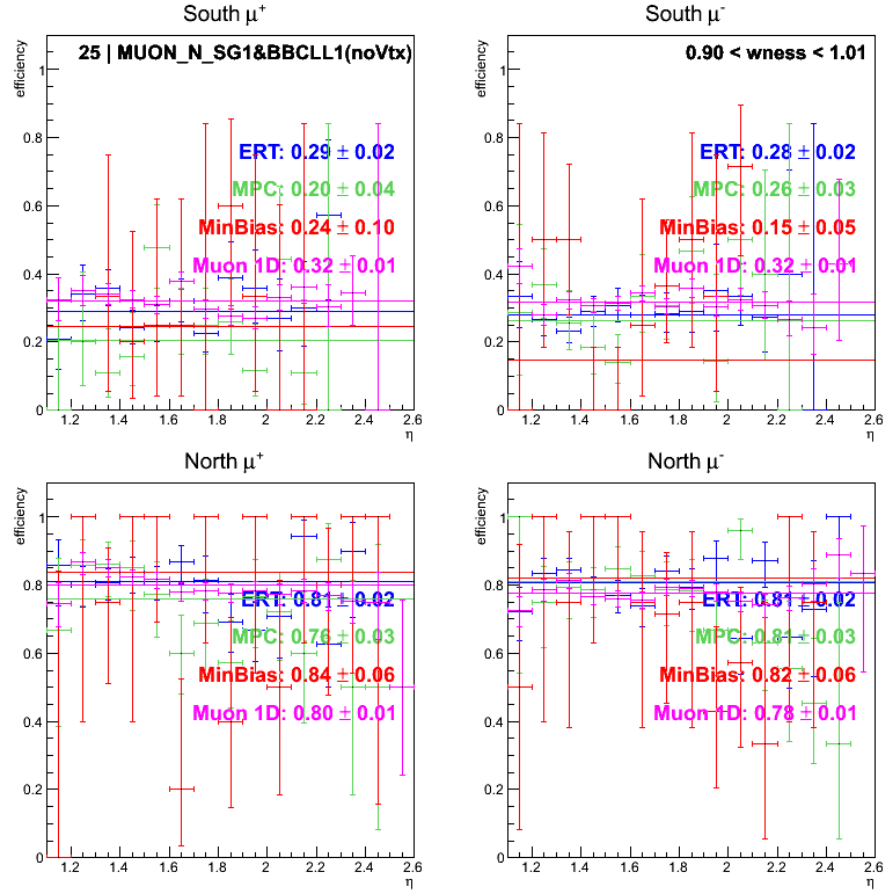


Figure C.29: Trigger efficiencies for trigger bit 25 (MUON\_N\_SG1&BBCLL1(noVtx)) for single  $W \rightarrow \mu$  candidates with transverse momenta above 5 GeV. The efficiencies for ERT (blue), MPC (green), MinBias (red) and 1D (purple) triggered data samples are shown as well as a constant fit over the whole range.

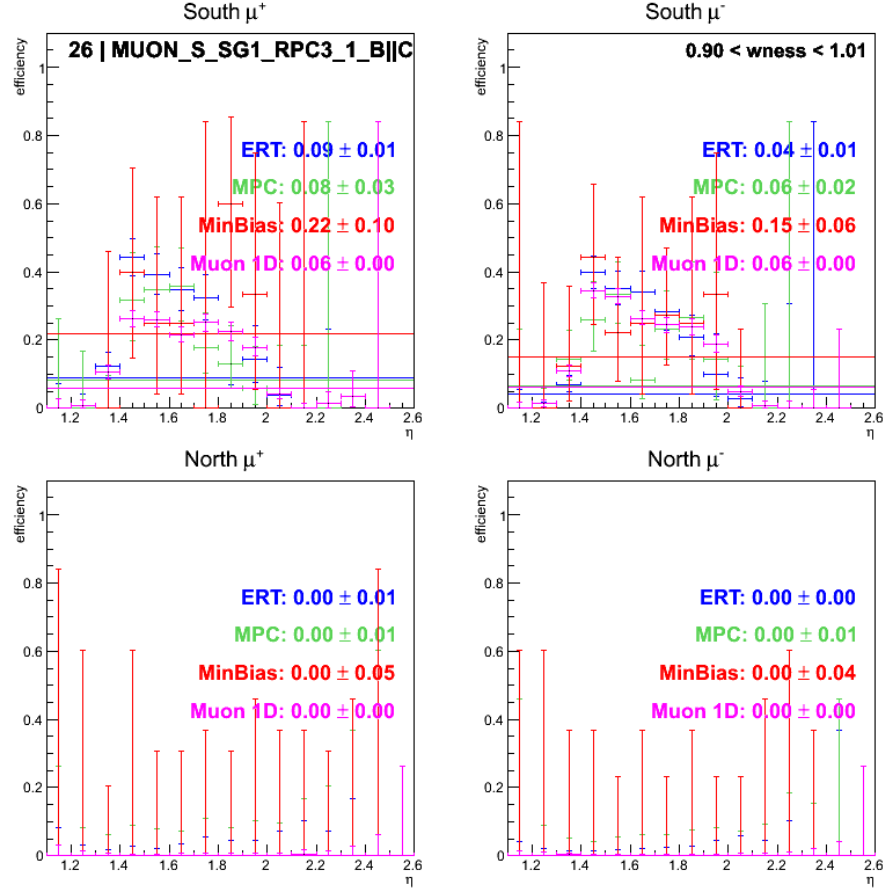


Figure C.30: Trigger efficiencies for trigger bit 26 (MUON\_S\_SG1\_RPC3\_1\_B||C) for single  $W \rightarrow \mu$  candidates with transverse momenta above 5 GeV. The efficiencies for ERT (blue), MPC (green), MinBias (red) and 1D (purple) triggered data samples are shown as well as a constant fit over the whole range.

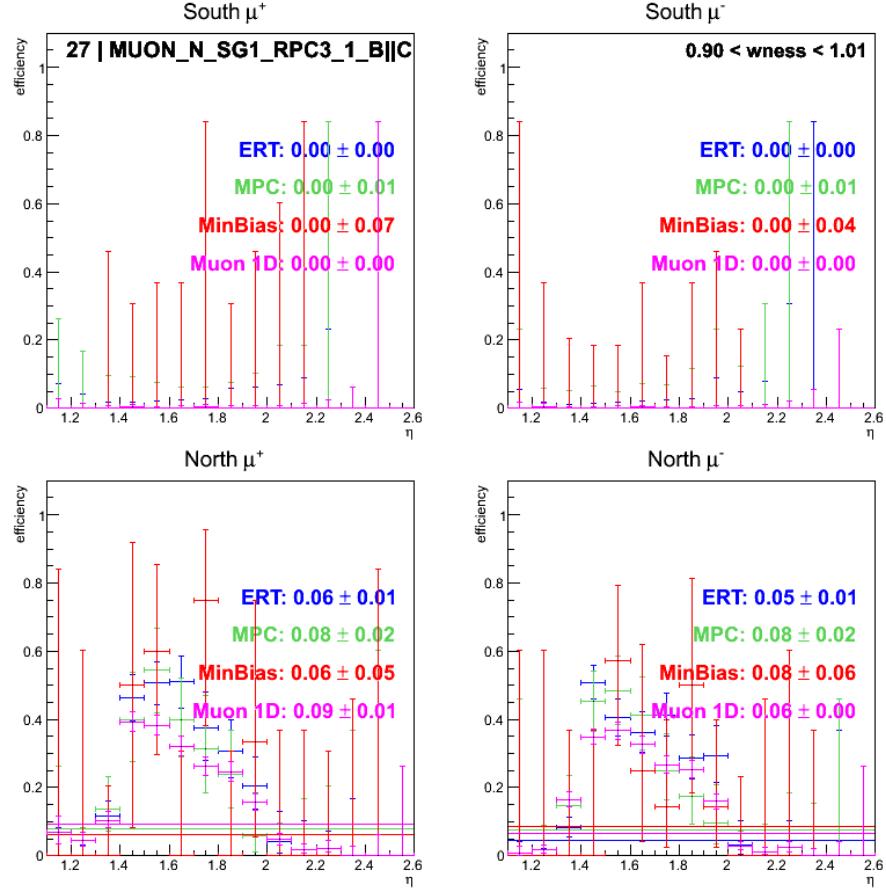


Figure C.31: Trigger efficiencies for trigger bit 27 (MUON\_N\_SG1\_RPC3\_1\_B||C) for single  $W \rightarrow \mu$  candidates with transverse momenta above 5 GeV. The efficiencies for ERT (blue), MPC (green), MinBias (red) and 1D (purple) triggered data samples are shown as well as a constant fit over the whole range.

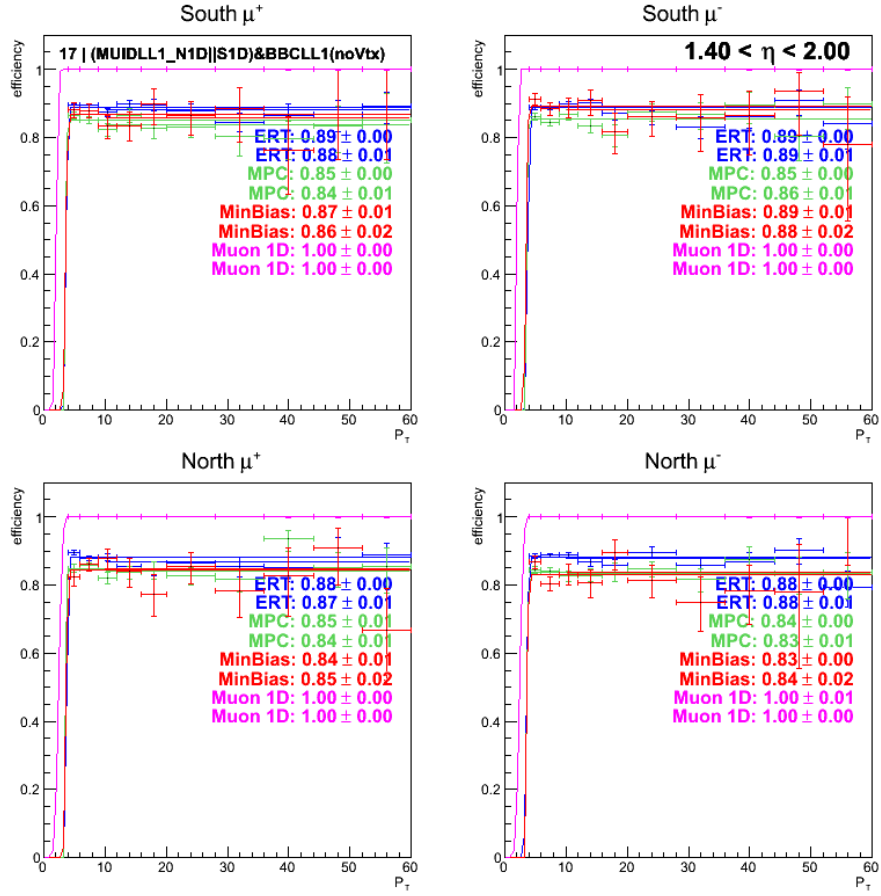


Figure C.32: Trigger efficiencies for trigger bit 17 ( $((\text{MUIDLL1\_N1D} \parallel \text{S1D}) \& \text{BBCLL1}(\text{noVtx}))$ ) for single  $W \rightarrow \mu$  candidates in the rapidity range  $1.4 < \eta < 2.0$  as a function of transverse momentum. The efficiencies for ERT (blue), MPC (green), MinBias (red) and 1D (purple) triggered data samples are shown as well as a constant fit over the whole range.

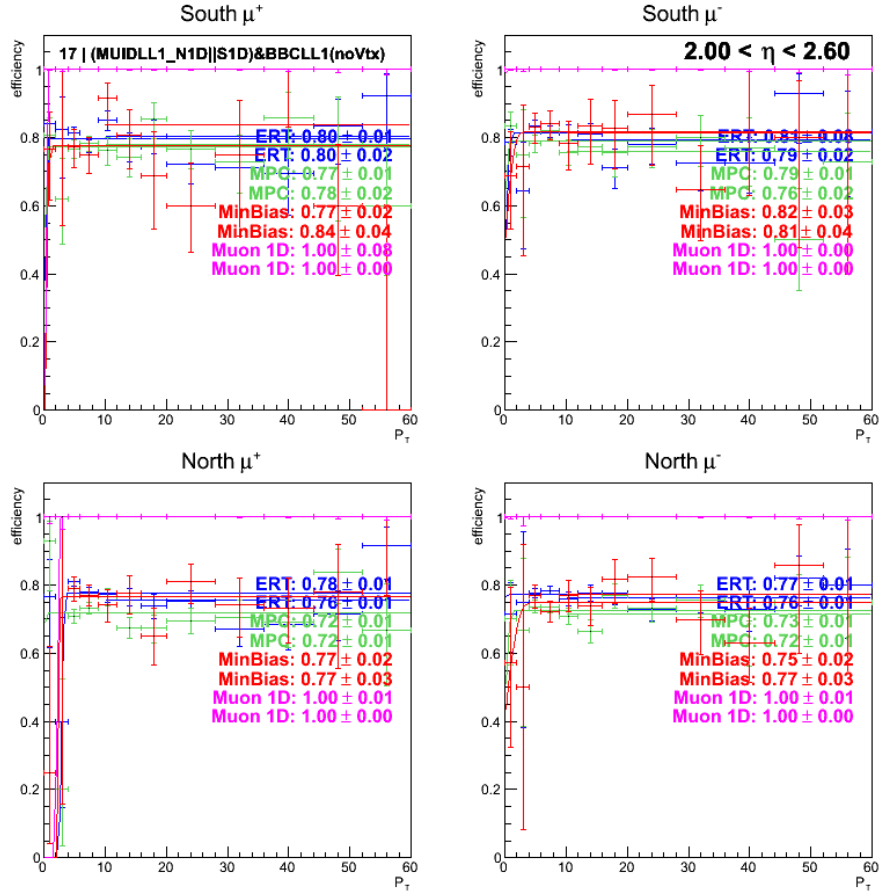


Figure C.33: Trigger efficiencies for trigger bit 17 ( $(\text{MUIDLL1\_N1D} \parallel \text{S1D}) \& \text{BBCLL1}(\text{noVtx})$ ) for single  $W \rightarrow \mu$  candidates in the rapidity range  $2.0 < \eta < 2.6$  as a function of transverse momentum. The efficiencies for ERT (blue), MPC (green), MinBias (red) and 1D (purple) triggered data samples are shown as well as a constant fit over the whole range.

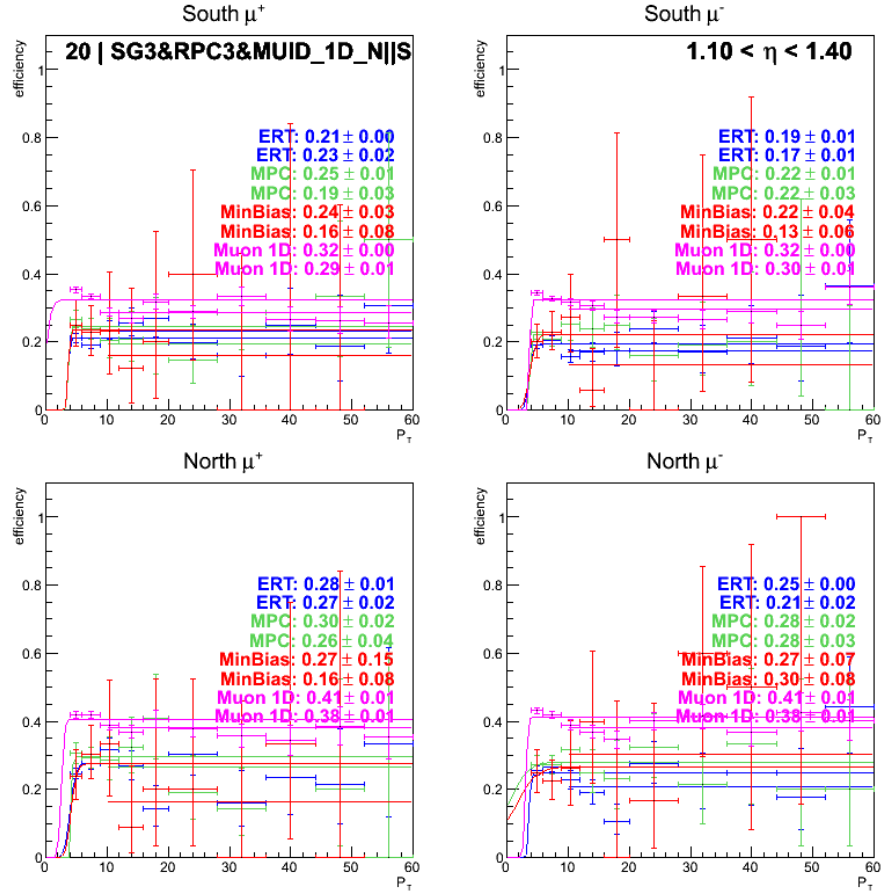


Figure C.34: Trigger efficiencies for trigger bit 20 (SG3&RPC3&MUID\_1D\_N||S) for single  $W \rightarrow \mu$  candidates in the rapidity range  $1.1 < \eta < 1.4$  as a function of transverse momentum. The efficiencies for ERT (blue), MPC (green), MinBias (red) and 1D (purple) triggered data samples are shown as well as a constant fit over the whole range.

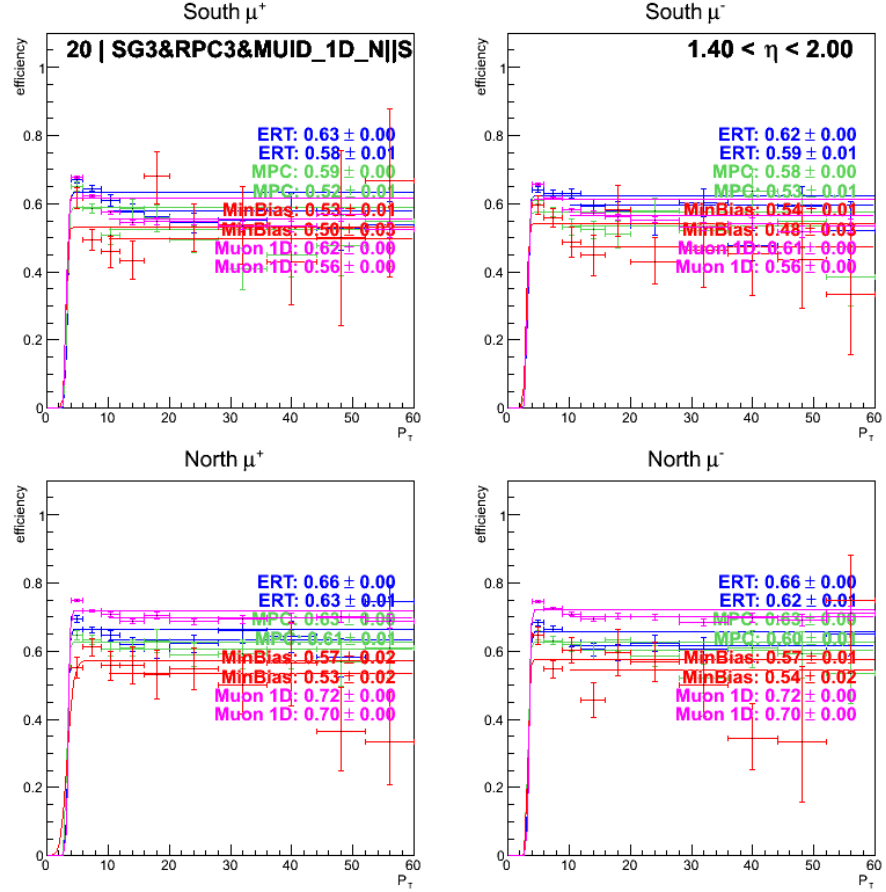


Figure C.35: Trigger efficiencies for trigger bit 20 (SG3&RPC3&MUID\_1D\_N||S) for single  $W \rightarrow \mu$  candidates in the rapidity range  $1.4 < \eta < 2.0$  as a function of transverse momentum. The efficiencies for ERT (blue), MPC (green), MinBias (red) and 1D (purple) triggered data samples are shown as well as a constant fit over the whole range.

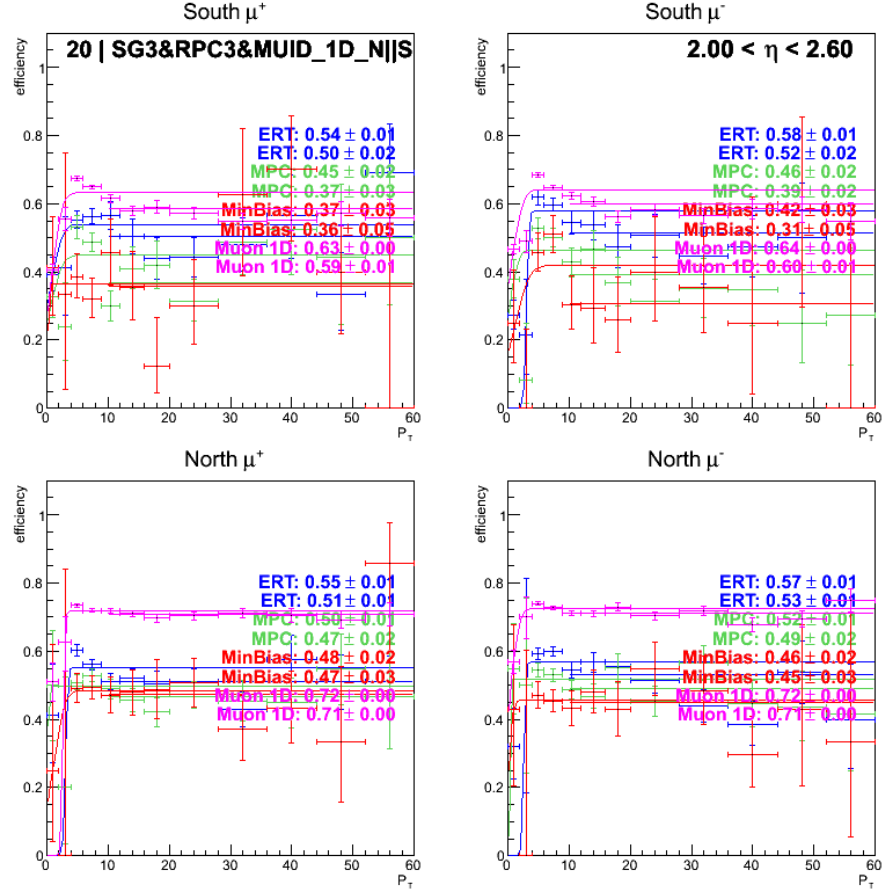


Figure C.36: Trigger efficiencies for trigger bit 20 (SG3&RPC3&MUID\_1D\_N||S) for single  $W \rightarrow \mu$  candidates in the rapidity range  $2.0 < \eta < 2.6$  as a function of transverse momentum. The efficiencies for ERT (blue), MPC (green), MinBias(red) and 1D (purple) triggered data samples are shown as well as a constant fit over the whole range.

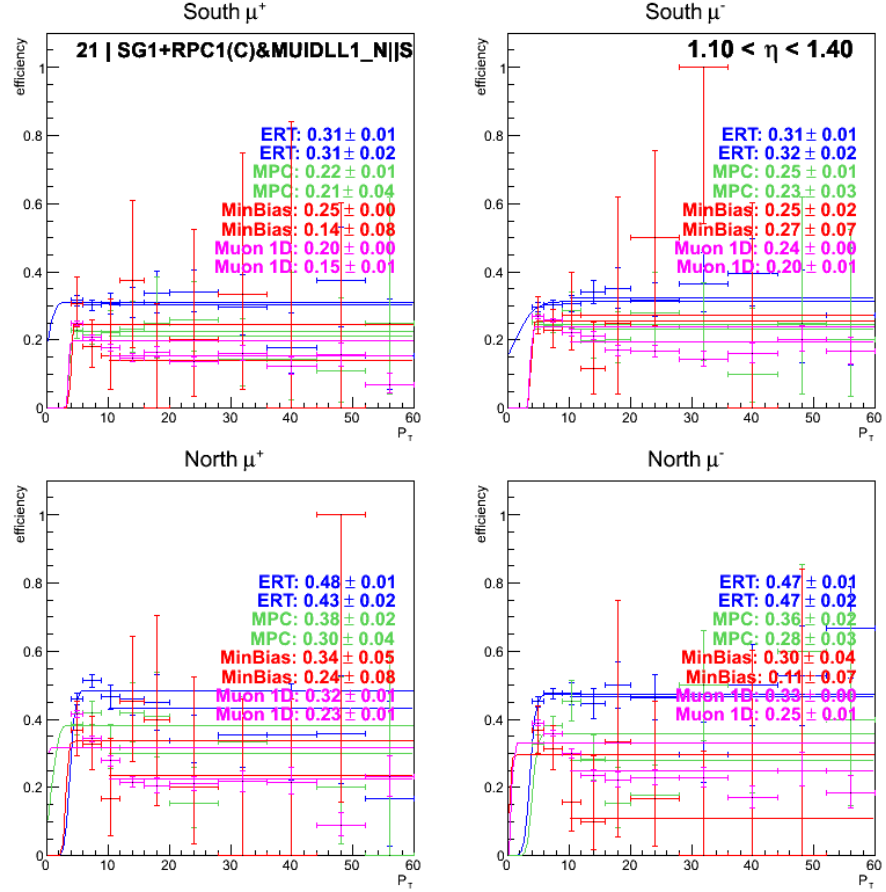


Figure C.37: Trigger efficiencies for trigger bit 21 (SG1+RPC1(C)&MUIDLL1\_N||S) for single  $W \rightarrow \mu$  candidates in the rapidity range  $1.1 < \eta < 1.4$  as a function of transverse momentum. The efficiencies for ERT (blue), MPC (green), MinBias(red) and 1D (purple) triggered data samples are shown as well as a constant fit over the whole range.

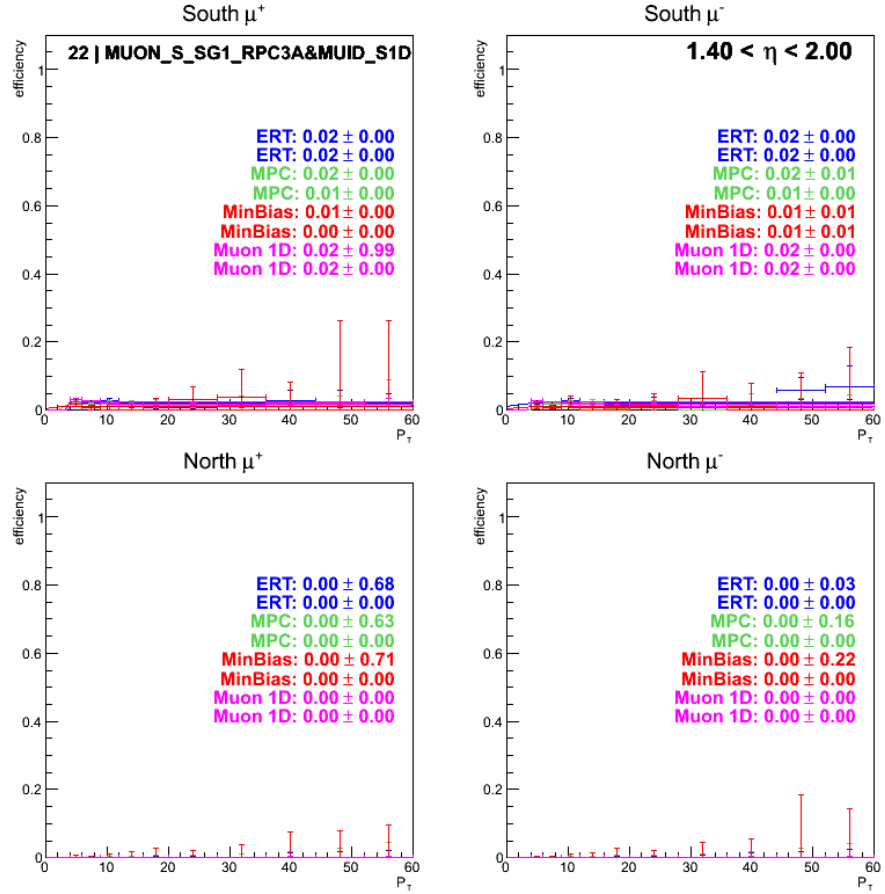


Figure C.38: Trigger efficiencies for trigger bit 22 ( MUON\_S\_SG1\_RPC3A&MUID\_S1D) for single  $W \rightarrow \mu$  candidates in the rapidity range  $1.4 < \eta < 2.0$  as a function of transverse momentum. The efficiencies for ERT (blue), MPC (green), MinBias(red) and 1D (purple) triggered data samples are shown as well as a constant fit over the whole range.

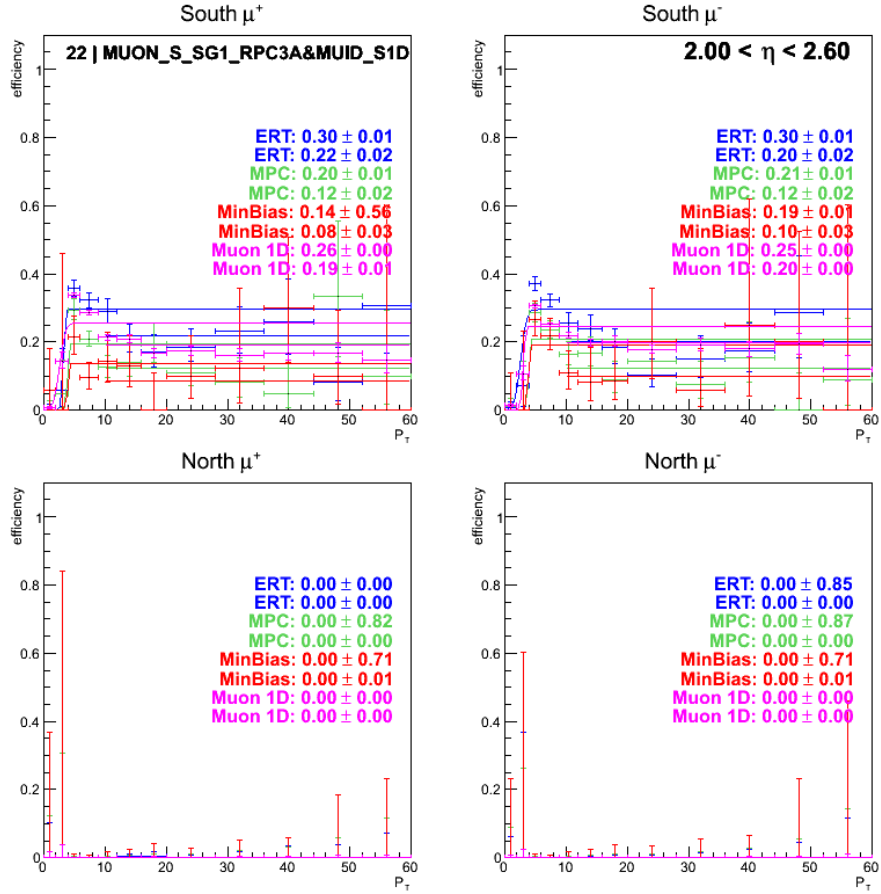


Figure C.39: Trigger efficiencies for trigger bit 22 ( MUON\_S\_SG1\_RPC3A&MUID\_S1D) for single  $W \rightarrow \mu$  candidates in the rapidity range  $2.0 < \eta < 2.6$  as a function of transverse momentum. The efficiencies for ERT (blue), MPC (green), MinBias(red) and 1D (purple) triggered data samples are shown as well as a constant fit over the whole range.

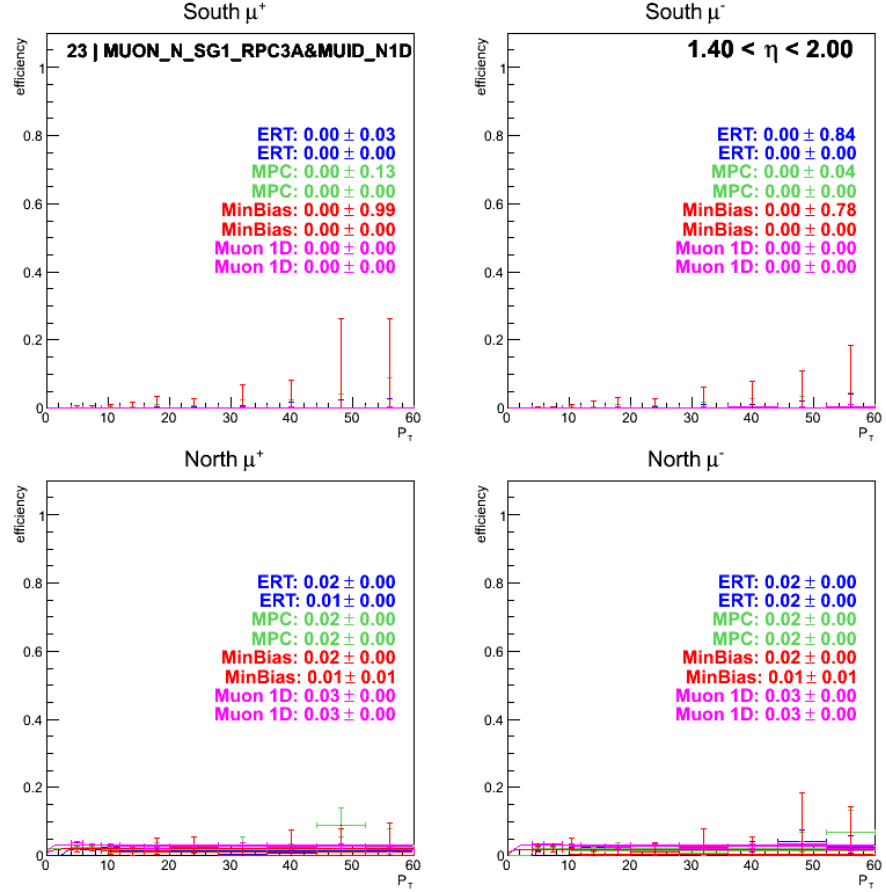


Figure C.40: Trigger efficiencies for trigger bit 23 ( MUON\_N\_SG1\_RPC3A&MUID\_N1D) for single  $W \rightarrow \mu$  candidates in the rapidity range  $1.4 < \eta < 2.0$  as a function of transverse momentum. The efficiencies for ERT (blue), MPC (green), MinBias(red) and 1D (purple) triggered data samples are shown as well as a constant fit over the whole range.

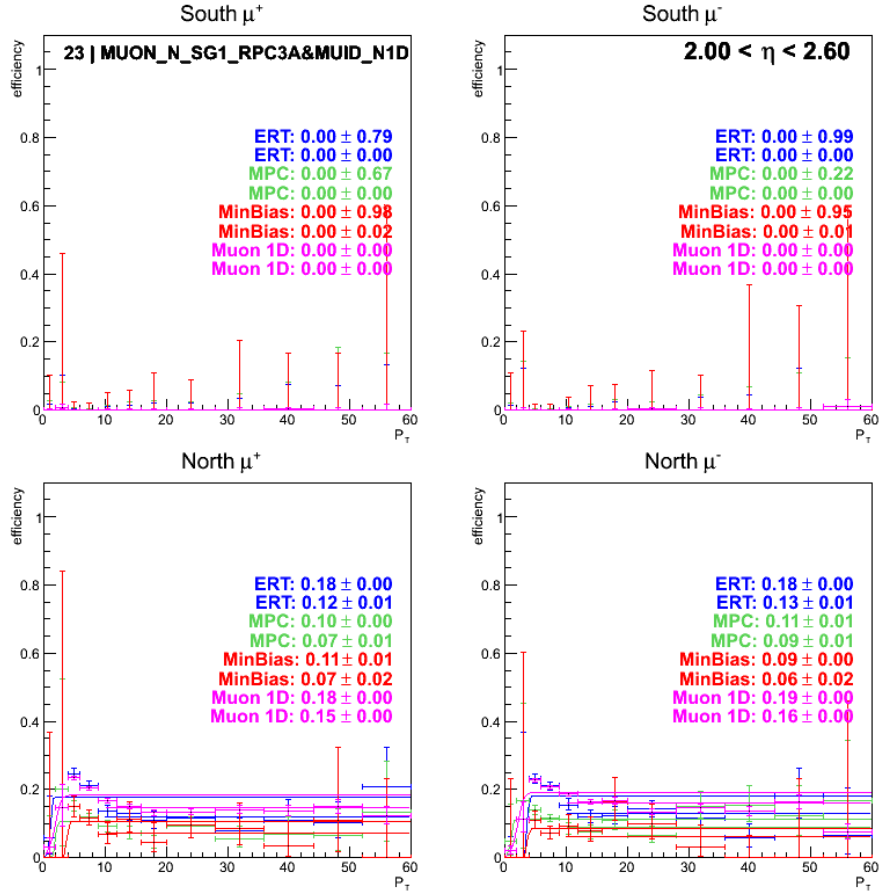


Figure C.41: Trigger efficiencies for trigger bit 23 ( MUON\_N\_SG1\_RPC3A&MUID\_N1D) for single  $W \rightarrow \mu$  candidates in the rapidity range  $2.0 < \eta < 2.6$  as a function of transverse momentum. The efficiencies for ERT (blue), MPC (green), MinBias(red) and 1D (purple) triggered data samples are shown as well as a constant fit over the whole range.

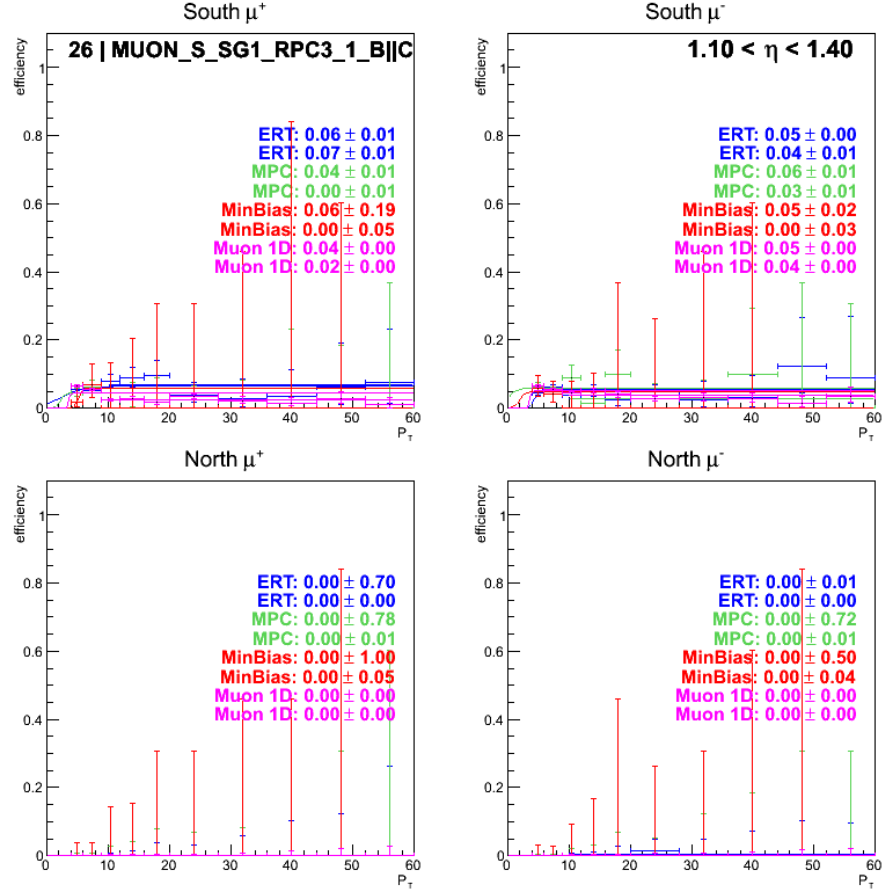


Figure C.42: Trigger efficiencies for trigger bit 26 (MUON\_S\_SG1\_RPC3\_1\_B||C) for single  $W \rightarrow \mu$  candidates in the rapidity range  $1.1 < \eta < 1.4$  as a function of transverse momentum. The efficiencies for ERT (blue), MPC (green), MinBias(red) and 1D (purple) triggered data samples are shown as well as a constant fit over the whole range.

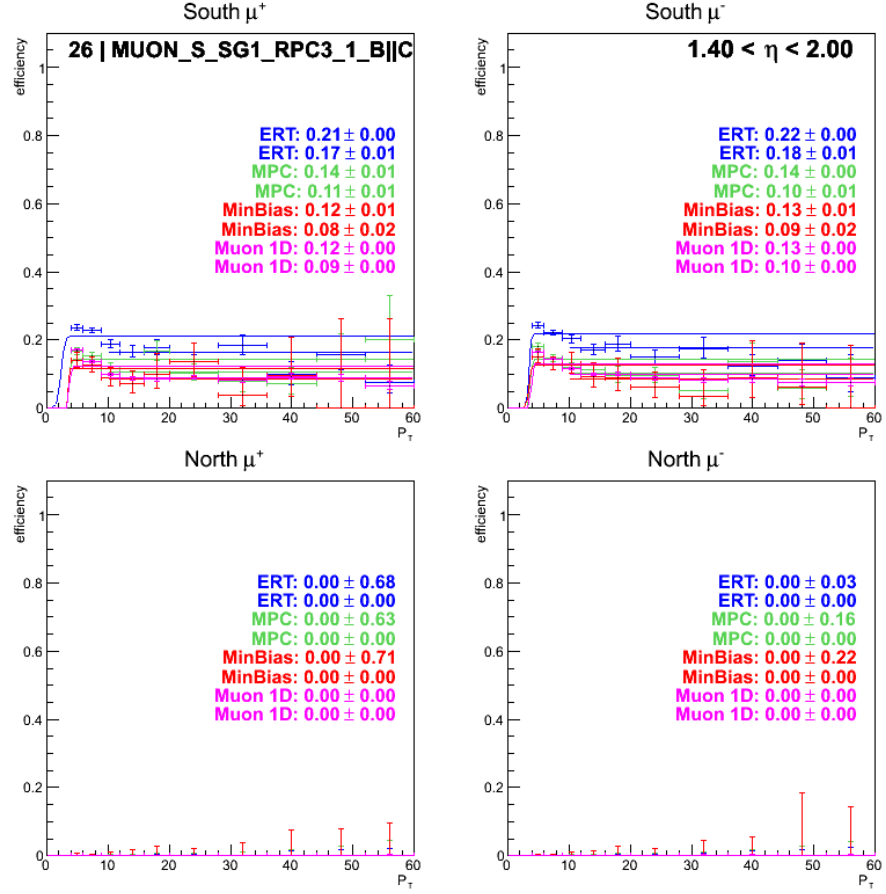


Figure C.43: Trigger efficiencies for trigger bit 26 (MUON\_S\_SG1\_RPC3\_1\_B||C) for single  $W \rightarrow \mu$  candidates in the rapidity range  $1.4 < \eta < 2.0$  as a function of transverse momentum. The efficiencies for ERT (blue), MPC (green), MinBias (red) and 1D (purple) triggered data samples are shown as well as a constant fit over the whole range.

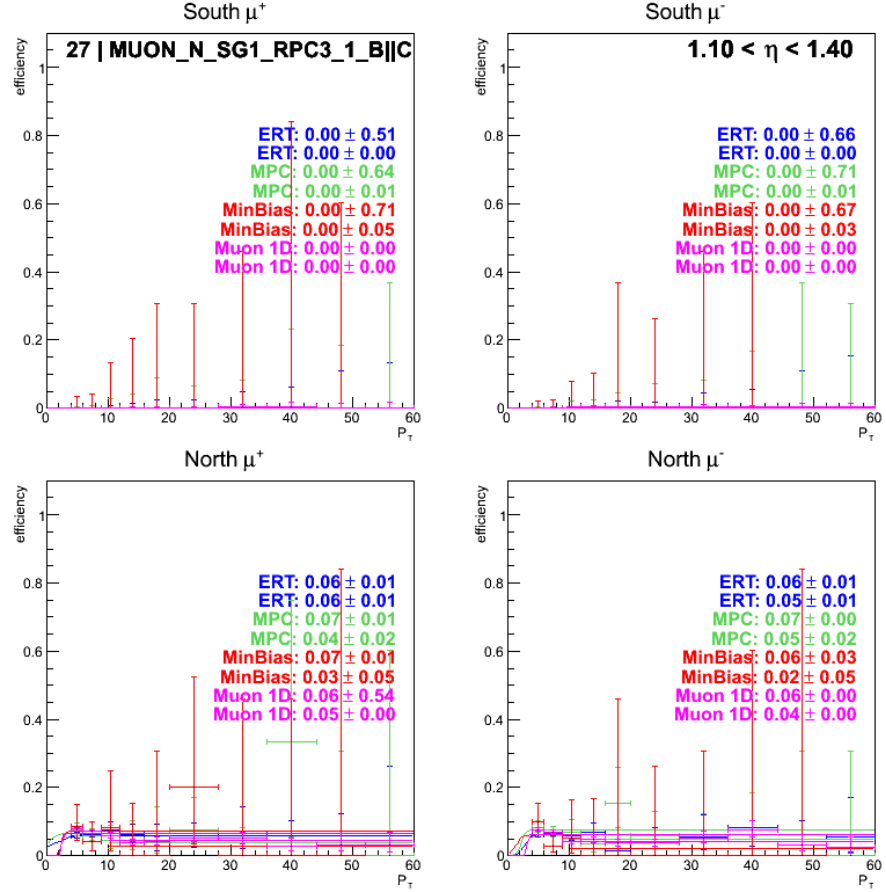


Figure C.44: Trigger efficiencies for trigger bit 27 (MUON\_N\_SG1\_RPC3\_1\_B||C) for single  $W \rightarrow \mu$  candidates in the rapidity range  $1.1 < \eta < 1.4$  as a function of transverse momentum. The efficiencies for ERT (blue), MPC (green), MinBias(red) and 1D (purple) triggered data samples are shown as well as a constant fit over the whole range.

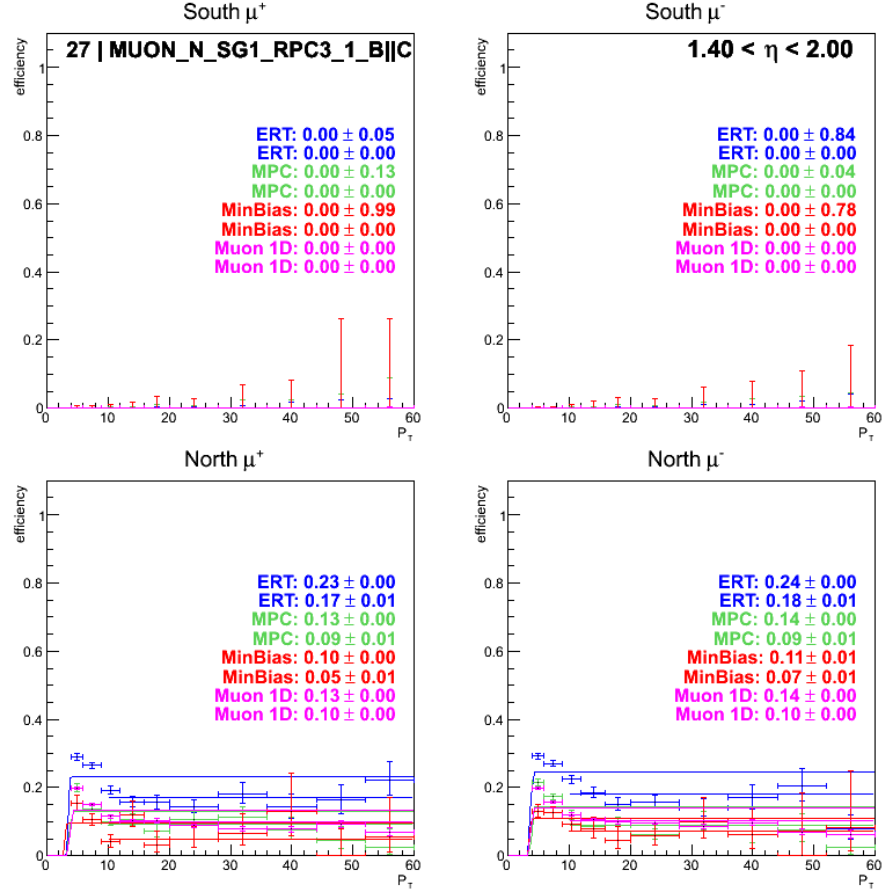


Figure C.45: Trigger efficiencies for trigger bit 27 (MUON\_N\_SG1\_RPC3\_1\_B||C) for single  $W \rightarrow \mu$  candidates in the rapidity range  $1.4 < \eta < 2.0$  as a function of transverse momentum. The efficiencies for ERT (blue), MPC (green), MinBias (red) and 1D (purple) triggered data samples are shown as well as a constant fit over the whole range.

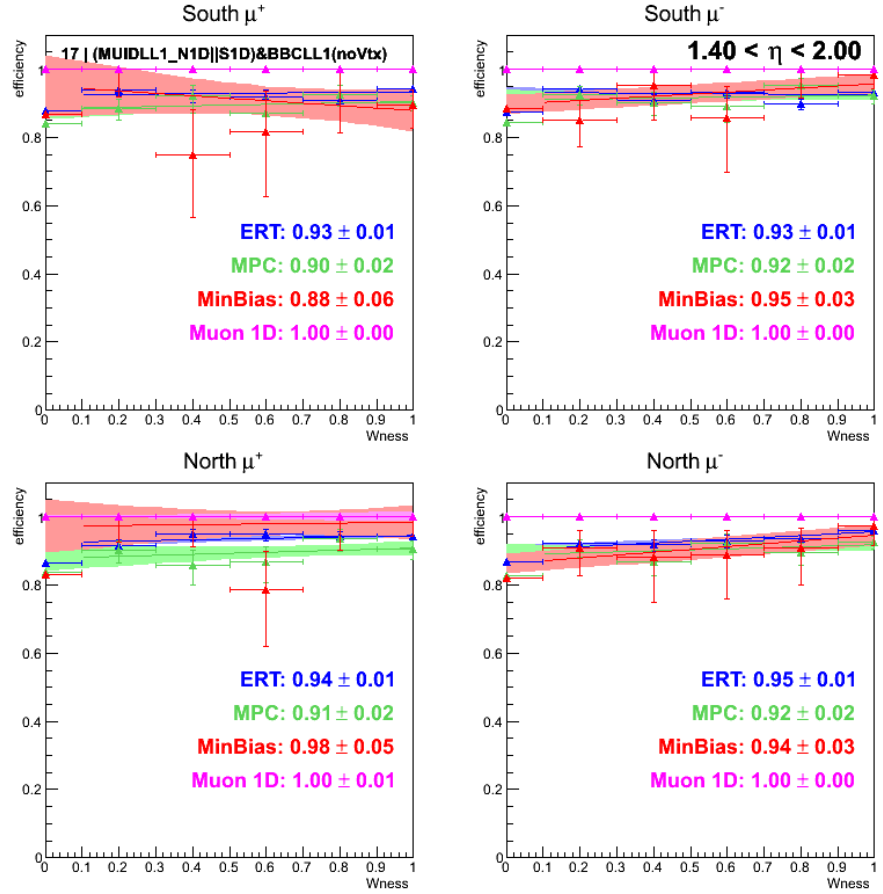


Figure C.46: Trigger efficiencies for trigger bit 17 ( $((\text{MUIDLL1\_N1D} \parallel \text{S1D}) \& \text{BBCLL1}(\text{noVtx}))$ ) for single  $W \rightarrow \mu$  candidates in the rapidity range  $1.4 < \eta < 2.0$  as a function of  $W_{ness}$ . The efficiencies for ERT (blue), MPC (green), MinBias (red) and 1D (purple) triggered data samples are shown as well as a constant fit over the whole range.

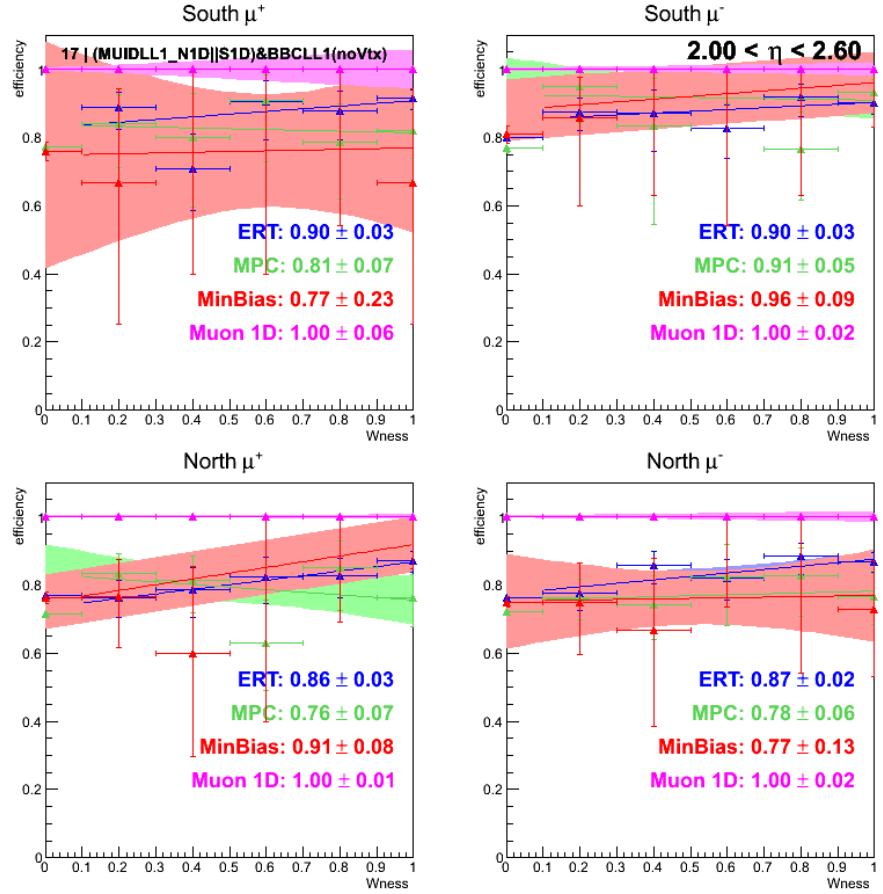


Figure C.47: Trigger efficiencies for trigger bit 17 ( $((\text{MUIDLL1\_N1D} || \text{S1D}) \& \text{BBCLL1}(\text{noVtx}))$ ) for single  $W \rightarrow \mu$  candidates in the rapidity range  $2.0 < \eta < 2.6$  as a function of  $W_{ness}$ . The efficiencies for ERT (blue), MPC (green), MinBias(red) and 1D (purple) triggered data samples are shown as well as a constant fit over the whole range.

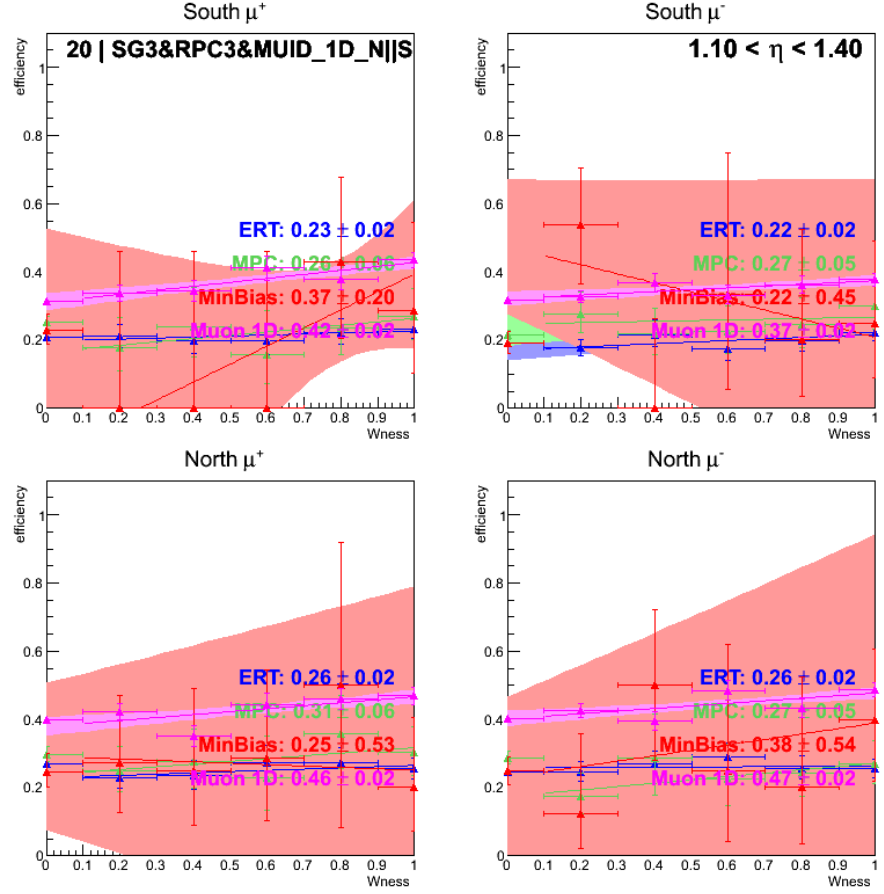


Figure C.48: Trigger efficiencies for trigger bit 20 (SG3&RPC3&MUID\_1D\_N||S) for single  $W \rightarrow \mu$  candidates in the rapidity range  $1.1 < \eta < 1.4$  as a function of  $W_{ness}$ . The efficiencies for ERT (blue), MPC (green), MinBias (red) and 1D (purple) triggered data samples are shown as well as a constant fit over the whole range.

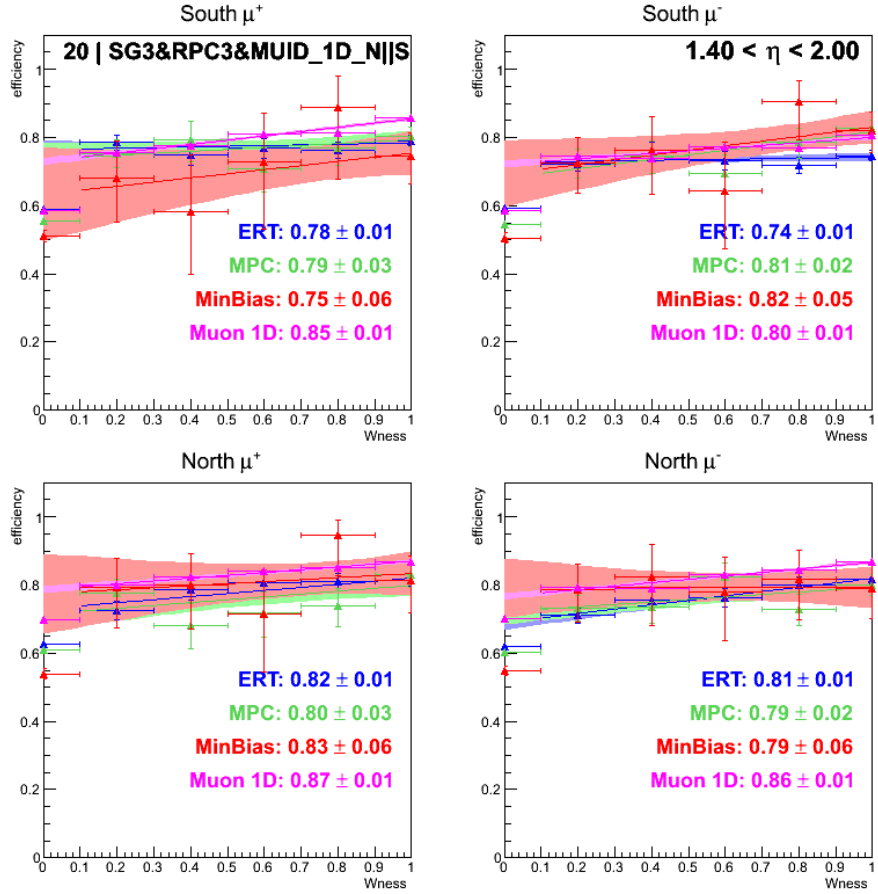


Figure C.49: Trigger efficiencies for trigger bit 20 (SG3&RPC3&MUID\_1D\_N||S) for single  $W \rightarrow \mu$  candidates in the rapidity range  $1.4 < \eta < 2.0$  as a function of  $W_{ness}$ . The efficiencies for ERT (blue), MPC (green), MinBias (red) and 1D (purple) triggered data samples are shown as well as a constant fit over the whole range.

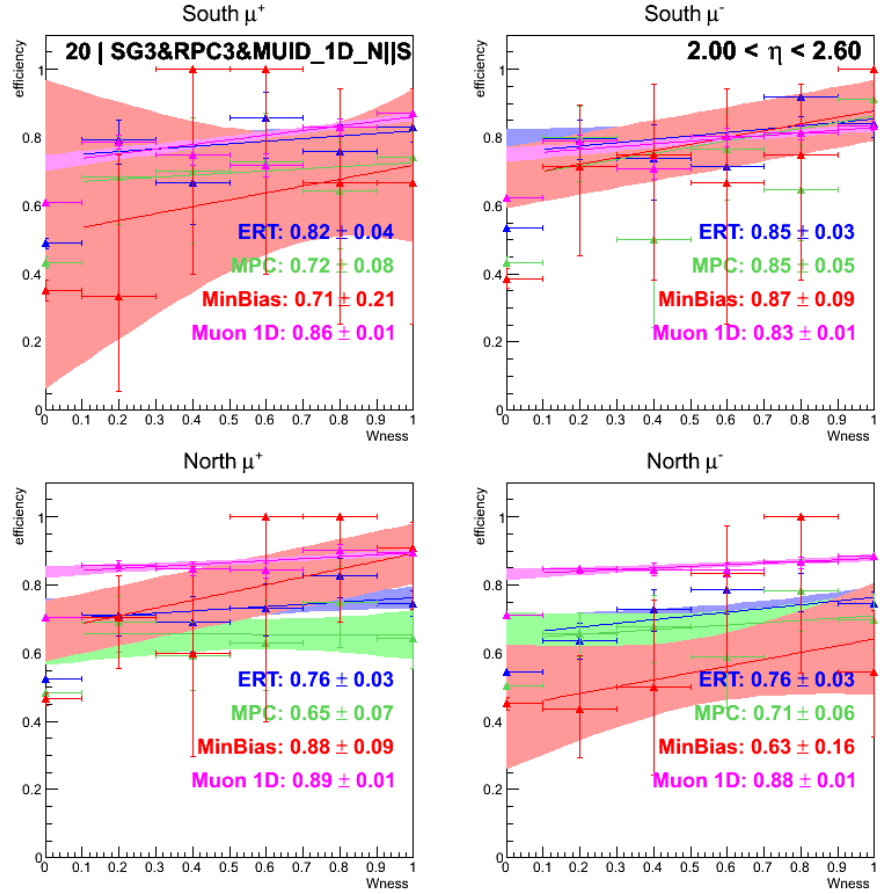


Figure C.50: Trigger efficiencies for trigger bit 20 (SG3&RPC3&MUID\_1D\_N||S) for single  $W \rightarrow \mu$  candidates in the rapidity range  $2.0 < \eta < 2.6$  as a function of  $W_{ness}$ . The efficiencies for ERT (blue), MPC (green), MinBias (red) and 1D (purple) triggered data samples are shown as well as a constant fit over the whole range.

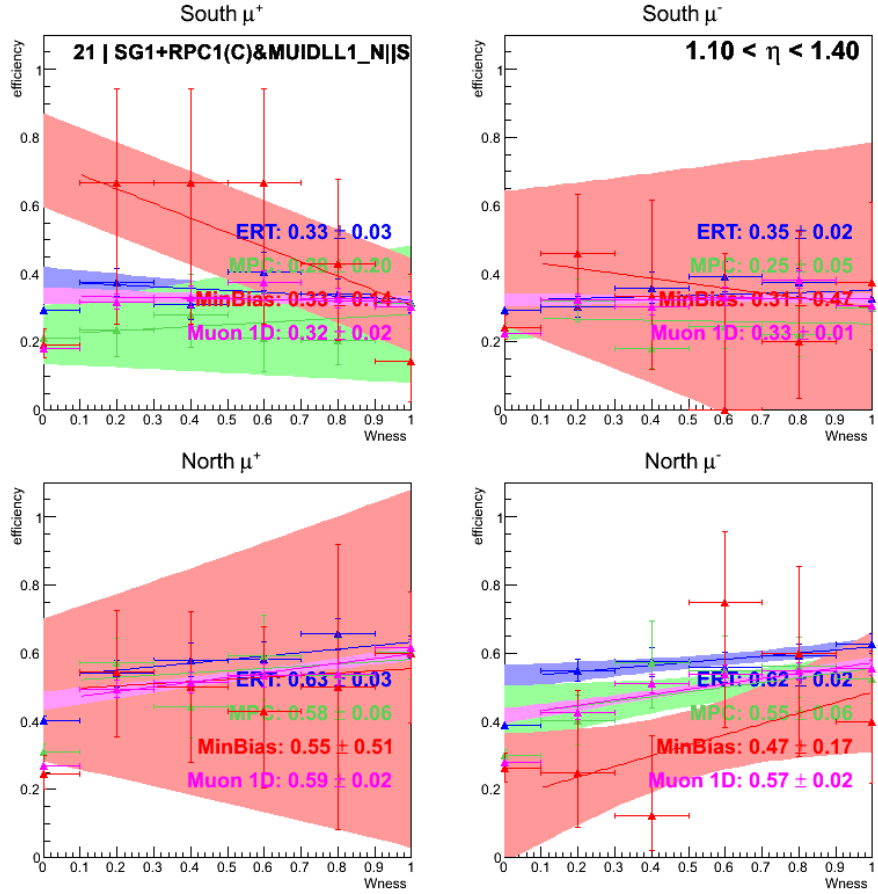


Figure C.51: Trigger efficiencies for trigger bit 21 (SG1+RPC1(C)&MUIDLL1\_N||S) for single  $W \rightarrow \mu$  candidates in the rapidity range  $1.1 < \eta < 1.4$  as a function of  $W_{ness}$ . The efficiencies for ERT (blue), MPC (green), MinBias(red) and 1D (purple) triggered data samples are shown as well as a constant fit over the whole range.

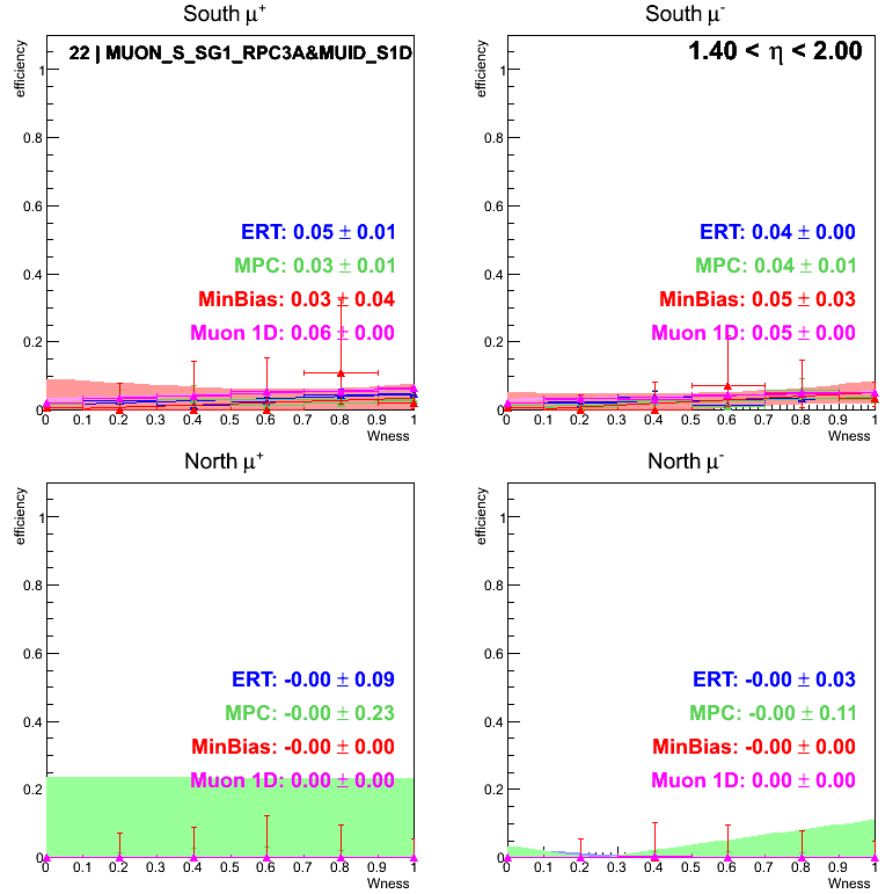


Figure C.52: Trigger efficiencies for trigger bit 22 ( MUON\_S\_SG1\_RPC3A&MUID\_S1D) for single  $W \rightarrow \mu$  candidates in the rapidity range  $1.4 < \eta < 2.0$  as a function of  $W_{ness}$ . The efficiencies for ERT (blue), MPC (green), MinBias(red) and 1D (purple) triggered data samples are shown as well as a constant fit over the whole range.

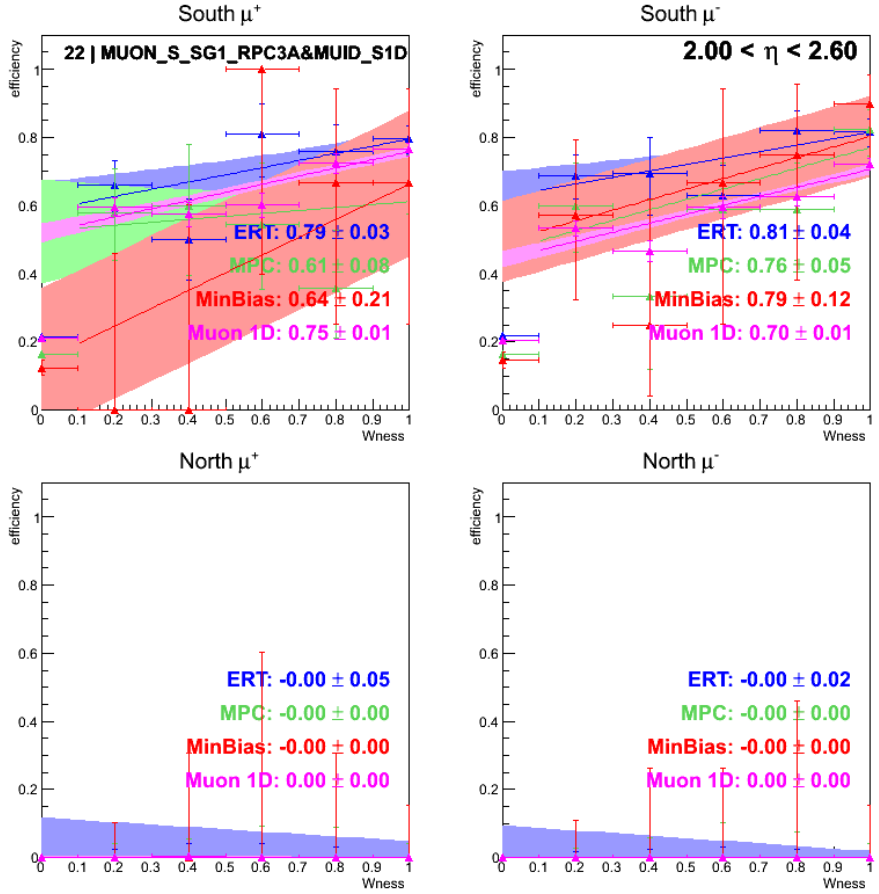


Figure C.53: Trigger efficiencies for trigger bit 22 ( MUON\_S\_SG1\_RPC3A&MUID\_S1D) for single  $W \rightarrow \mu$  candidates in the rapidity range  $2.0 < \eta < 2.6$  as a function of  $W_{ness}$ . The efficiencies for ERT (blue), MPC (green), MinBias(red) and 1D (purple) triggered data samples are shown as well as a constant fit over the whole range.

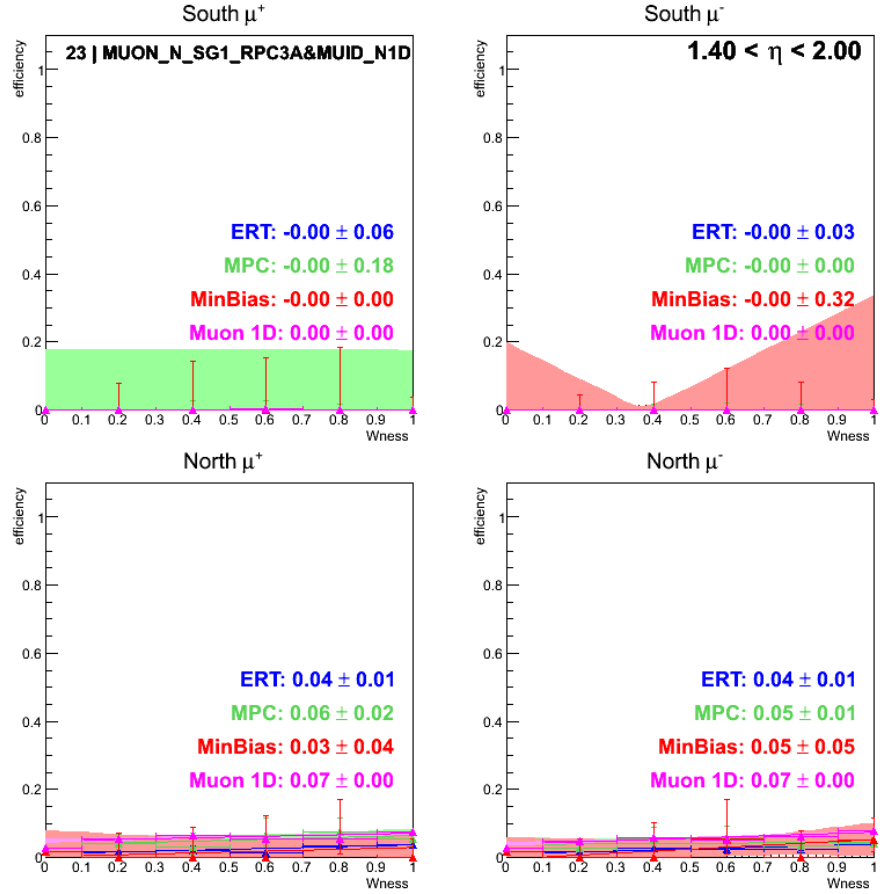


Figure C.54: Trigger efficiencies for trigger bit 23 ( MUON\_N\_SG1\_RPC3A&MUID\_N1D) for single  $W \rightarrow \mu$  candidates in the rapidity range  $1.4 < \eta < 2.0$  as a function of  $W_{ness}$ . The efficiencies for ERT (blue), MPC (green), MinBias(red) and 1D (purple) triggered data samples are shown as well as a constant fit over the whole range.

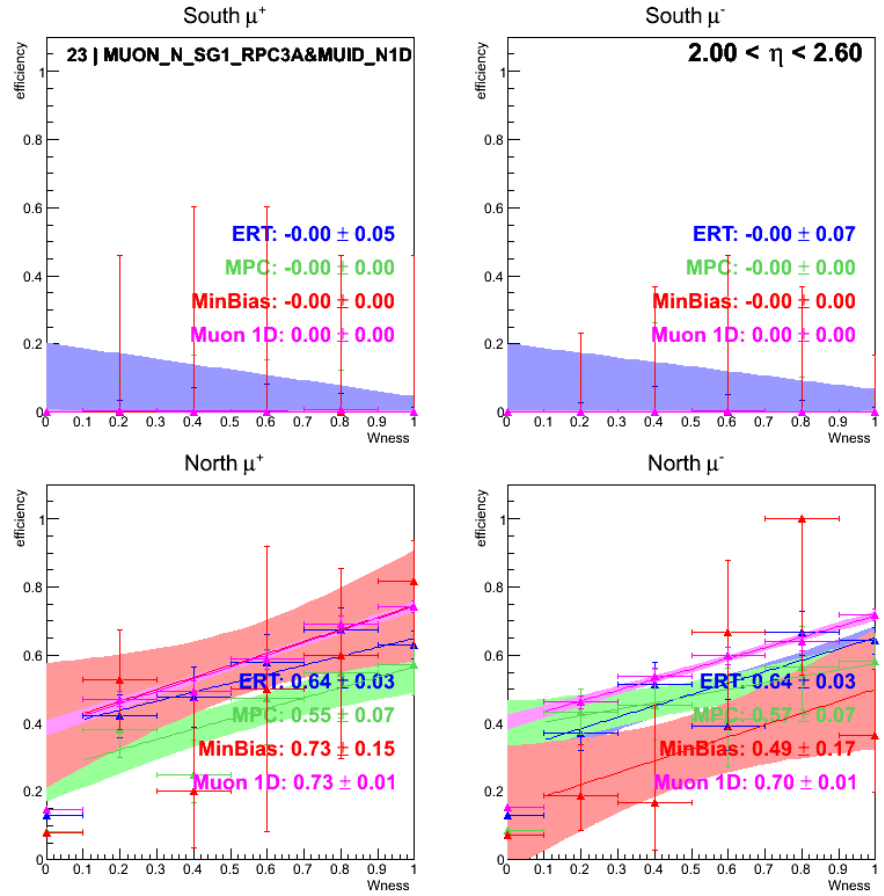


Figure C.55: Trigger efficiencies for trigger bit 23 ( MUON\_N\_SG1\_RPC3A&MUID\_N1D) for single  $W \rightarrow \mu$  candidates in the rapidity range  $2.0 < \eta < 2.6$  as a function of  $W_{ness}$ . The efficiencies for ERT (blue), MPC (green), MinBias(red) and 1D (purple) triggered data samples are shown as well as a constant fit over the whole range.

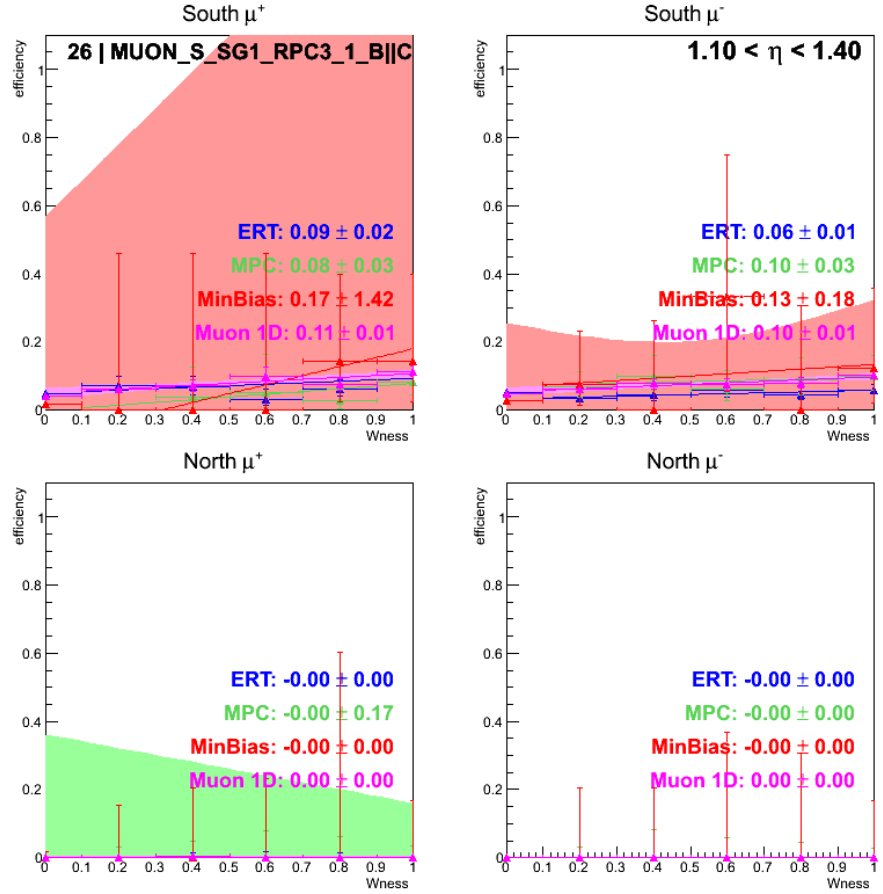


Figure C.56: Trigger efficiencies for trigger bit 26 ( $MUON\_S\_SG1\_RPC3\_1\_B||C$ ) for single  $W \rightarrow \mu$  candidates in the rapidity range  $1.1 < \eta < 1.4$  as a function of  $W_{ness}$ . The efficiencies for ERT (blue), MPC (green), MinBias(red) and 1D (purple) triggered data samples are shown as well as a constant fit over the whole range.

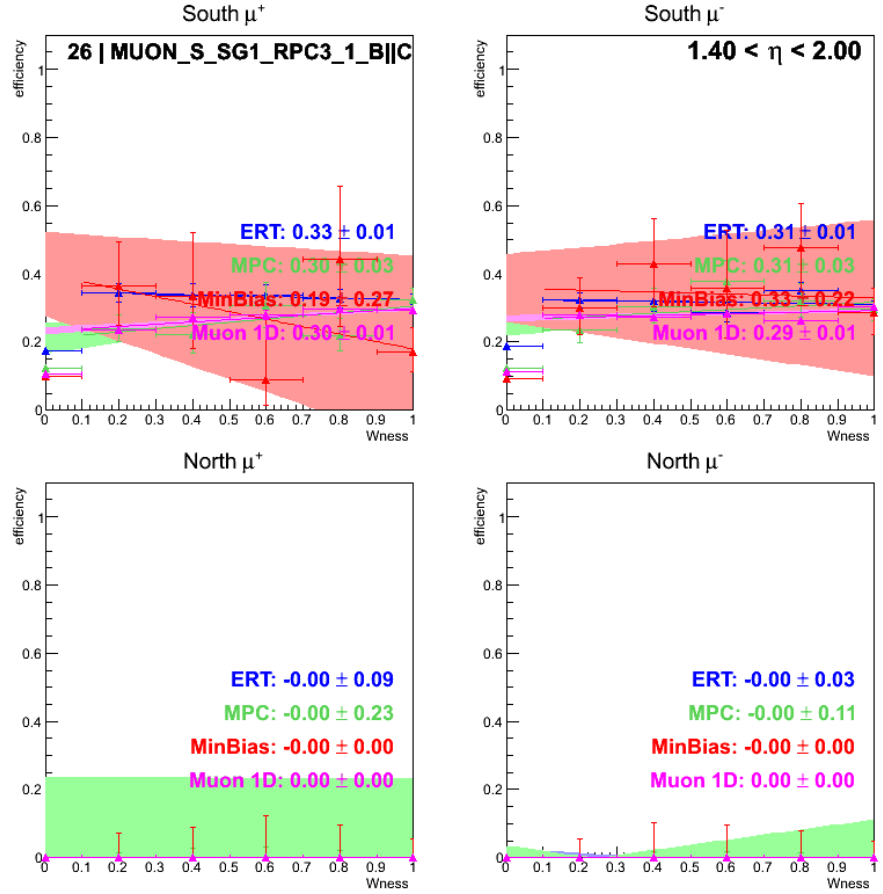


Figure C.57: Trigger efficiencies for trigger bit 26 (MUON\_S\_SG1\_RPC3\_1\_B||C) for single  $W \rightarrow \mu$  candidates in the rapidity range  $1.4 < \eta < 2.0$  as a function of  $W_{ness}$ . The efficiencies for ERT (blue), MPC (green), MinBias(red) and 1D (purple) triggered data samples are shown as well as a constant fit over the whole range.

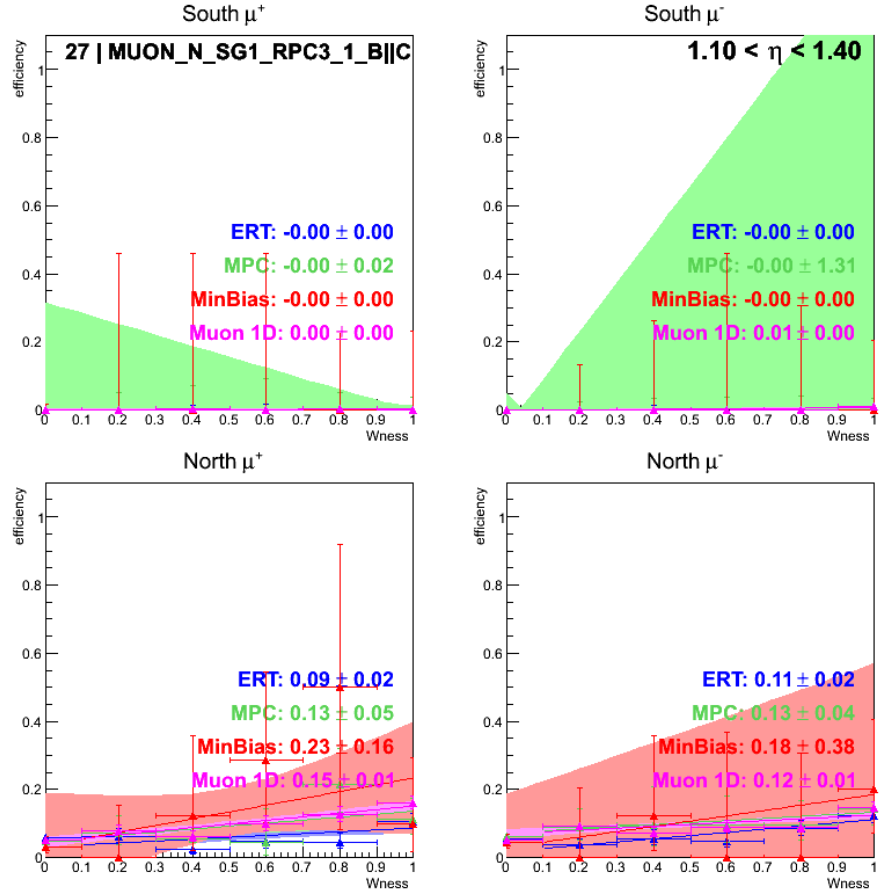


Figure C.58: Trigger efficiencies for trigger bit 27 (MUON\_N\_SG1\_RPC3\_1\_B||C) for single  $W \rightarrow \mu$  candidates in the rapidity range  $1.1 < \eta < 1.4$  as a function of  $W_{ness}$ . The efficiencies for ERT (blue), MPC (green), MinBias (red) and 1D (purple) triggered data samples are shown as well as a constant fit over the whole range.

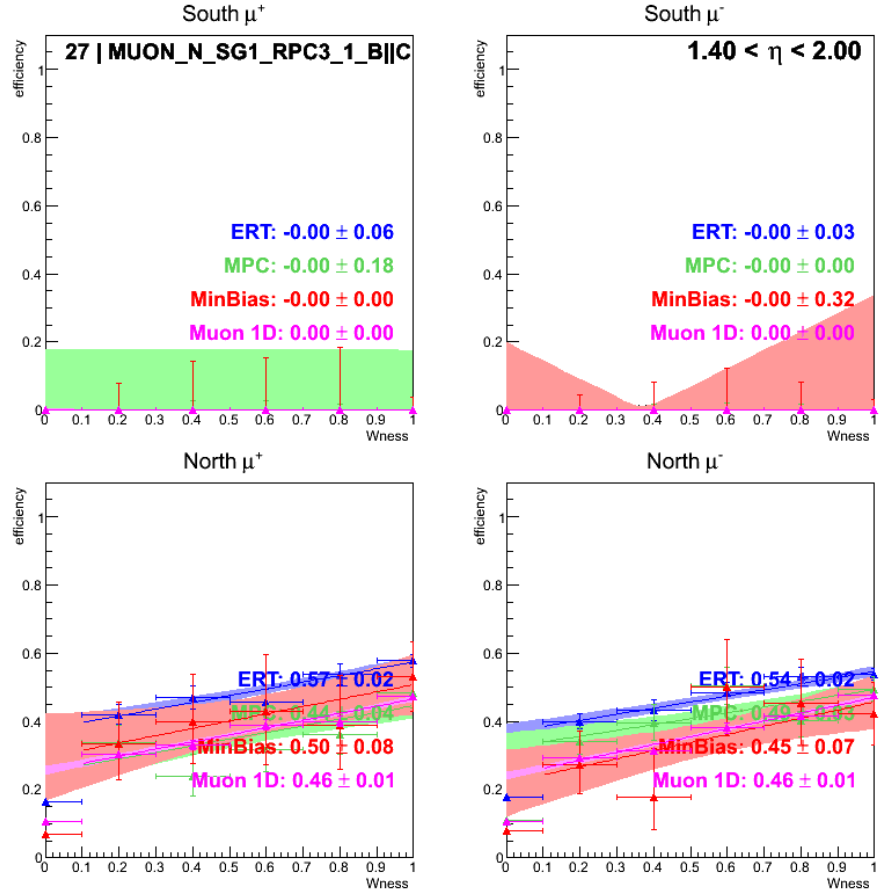


Figure C.59: Trigger efficiencies for trigger bit 27 (MUON\_N\_SG1\_RPC3\_1\_B||C) for single  $W \rightarrow \mu$  candidates in the rapidity range  $1.4 < \eta < 2.0$  as a function of  $W_{ness}$ . The efficiencies for ERT (blue), MPC (green), MinBias(red) and 1D (purple) triggered data samples are shown as well as a constant fit over the whole range.

#### C.0.4 Azimuthal Dependence of Trigger Efficiencies

While azimuthal dependence of trigger efficiencies are typically averaged over, there is still value in observing any potential azimuthal dependence. To mimic the half-octant structure of the Muon Tracker and the RPCs, 16 bins were assigned based on the PHENIX coordinate system. Here only the most striking results will be shown. Most importantly a clear  $\phi$  dependence was observed in the South 1D triggers at intermediate rapidities as seen in Figure C.60.

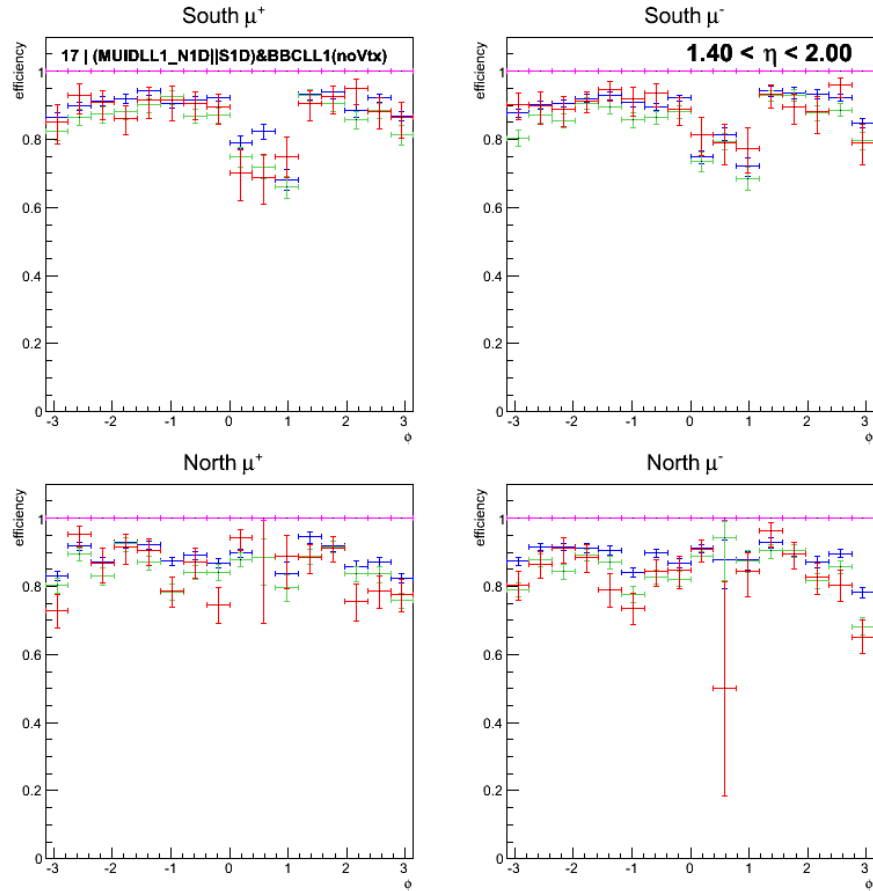


Figure C.60: Trigger efficiencies for trigger bit 17 ( $((\text{MUIDLL1\_N1D} \parallel \text{S1D}) \& \text{BBCLL1}(\text{noVtx}))$ ) for single  $W \rightarrow \mu$  candidates in the rapidity range  $1.4 < \eta < 2.0$  as a function of  $\phi$ . The efficiencies for ERT (blue), MPC (green), MinBias (red) and 1D (purple) triggered data samples are shown as well as a constant fit over the whole range.

The SG1 triggers alone, bits 24 and 25 show a homogeneous efficiency as a function of rapidity. Only some fluctuations are visible in the South arm for SG1S triggers as displayed in Fig. C.61.

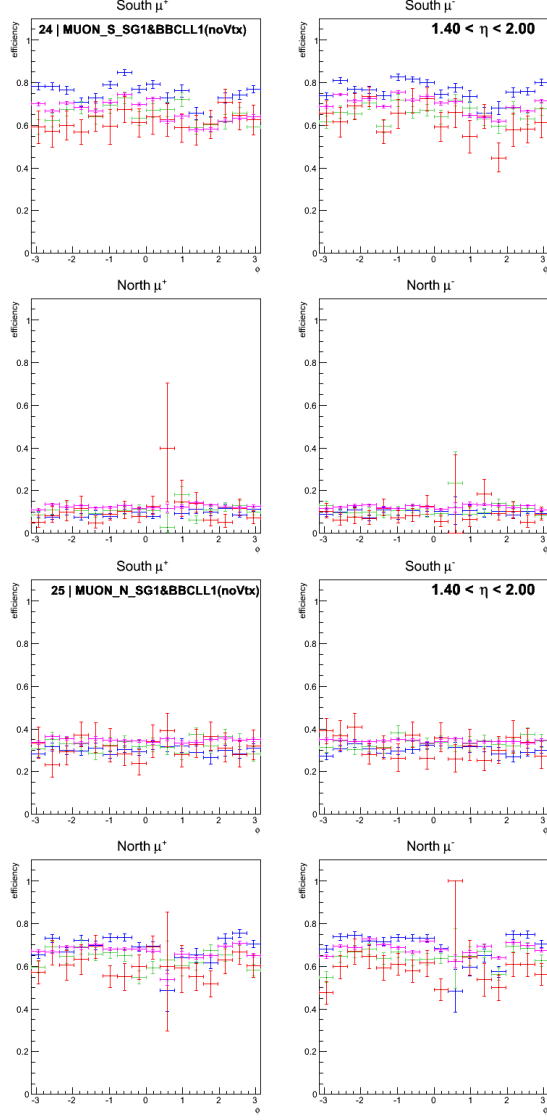


Figure C.61: Trigger efficiencies for trigger bit 24 (left, MUON\_S\_SG1&BBCLL1(noVtx)) and 25(right, MUON\_N\_SG1&BBCLL1(noVtx)) for single  $W \rightarrow \mu$  candidates in the rapidity range  $1.4 < \eta < 2.0$  as a function of  $\phi$ . The efficiencies for ERT (blue), MPC (green), MinBias(red) and 1D (purple) triggered data samples are shown as well as a constant fit over the whole range.

The RPC1+3 triggers alone, bits 18 and 19 also show generally a rather homogeneous efficiency as a function of rapidity. However, two half-octants in the North seem to be substantially less efficient as displayed in Fig. C.62.

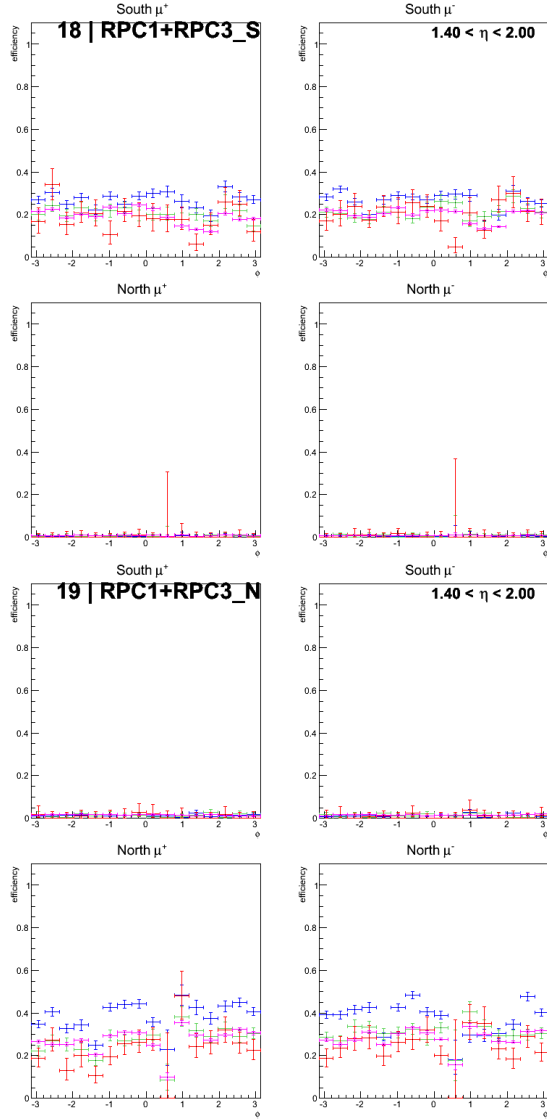


Figure C.62: Trigger efficiencies for trigger bit 24 (left, MUON\_S\_SG1&BBCLL1(noVtx)) and 25(right, MUON\_N\_SG1&BBCLL1(noVtx)) for single  $W \rightarrow \mu$  candidates in the rapidity range  $1.4 < \eta < 2.0$  as a function of  $\phi$ . The efficiencies for ERT (blue), MPC (green), MinBias(red) and 1D (purple) triggered data samples are shown as well as a constant fit over the whole range.

Comparing the 1C and 3A triggers the lack of statistics makes it difficult to determine, whether this drop of efficiency is related to the RPC1 or 3, but the drop at positive  $\phi$  seems to be visible also in the North 3A triggers, see Figs. C.63.

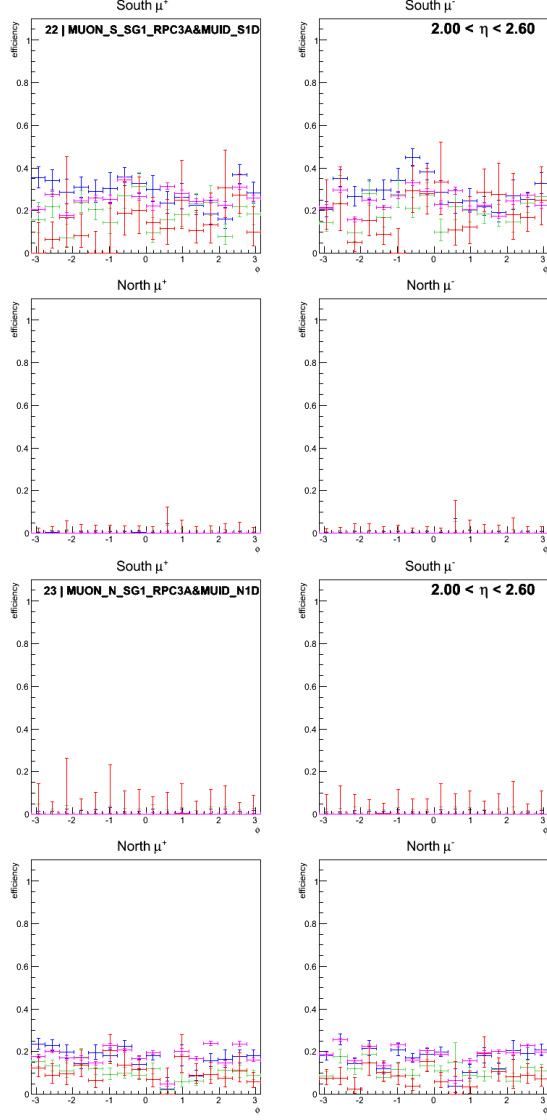


Figure C.63: Trigger efficiencies for trigger bit 22 (left, MUON\_S\_SG1\_RPC3A&MUID\_S1D) and 23(right, MUON\_N\_SG1\_RPC3A&MUID\_S1D) for single  $W \rightarrow \mu$  candidates in the rapidity range  $2.0 < \eta < 2.6$  as a function of  $\phi$ . The efficiencies for ERT (blue), MPC (green), MinBias(red) and 1D (purple) triggered data samples are shown as well as a constant fit over the whole range.

## Appendix D

# Rate Dependence of Trigger Efficiencies

The rate dependence is of muon production triggers is again mostly included in the overall trigger efficiencies as long as the sampled raw rates are not too different between the ERT, MPC, MinBias and 1D triggers. They might explain some of the differences seen between those triggers samples, as for example the 1D, ERT and MPC triggers might sample preferably at lower rates where their prescales are smaller. However, these effects are only higher order effects taken care of by assigning differences between reference samples as systematic uncertainty on the overall trigger efficiency.

Nevertheless it is of interest to see, whether the different triggers in the  $W$  candidate event sample do behave differently as a function of rate. It has been shown before, that the 1D trigger in the setting in Run 11 and 12 (pp) does show declining efficiencies as the collision rates increase. This behavior can be confirmed in Run13 as shown in Fig. D.1.

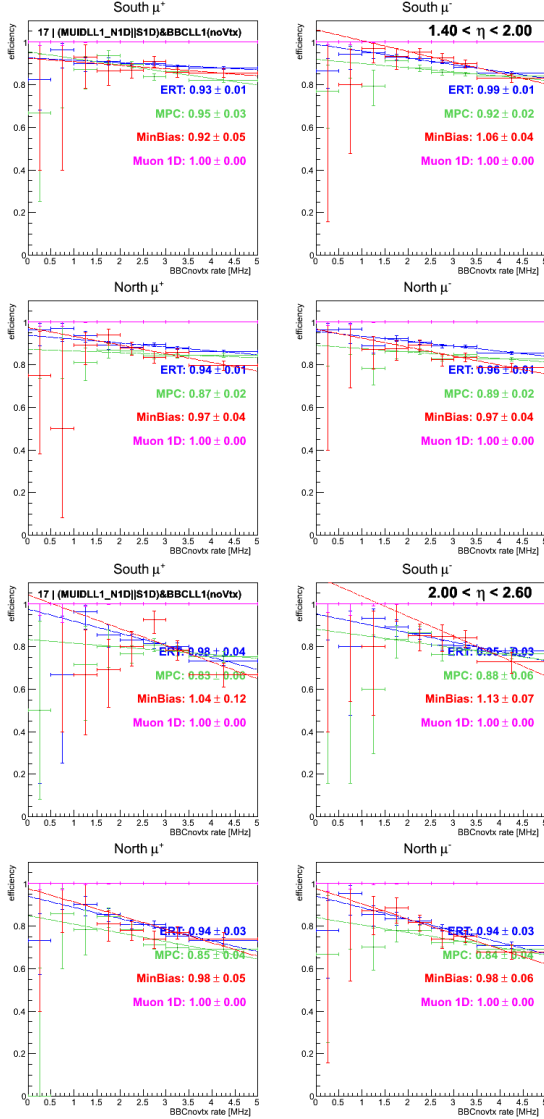


Figure D.1: Trigger efficiencies for trigger bit 17 (((MUIDLL1\_N1D||S1D)&BBCLL1(noVtx))) for single  $W \rightarrow \mu$  candidates in the rapidity range  $1.4 < \eta < 2.0$  (left) and  $2.0 < \eta < 2.6$  (right) as a function of the raw BBCnovtx rate. The efficiencies for ERT (blue), MPC (green), MinBias (red) and 1D (purple) triggered data samples are shown as well as a constant fit over the whole range.

What is a little surprising, is that there exist some triggers whose efficiencies increase as a function of rate, for example the SG1 triggers as shown in Fig. D.2 for the intermediate rapidity range, but high and low rapidities behave similar. Apparently the trigger rejections drop and more and more candidate tracks are picked up by this trigger including tracks in the wrong arm for which the efficiencies are initially zero but with slopes that are much steeper as for the actually triggered arm.

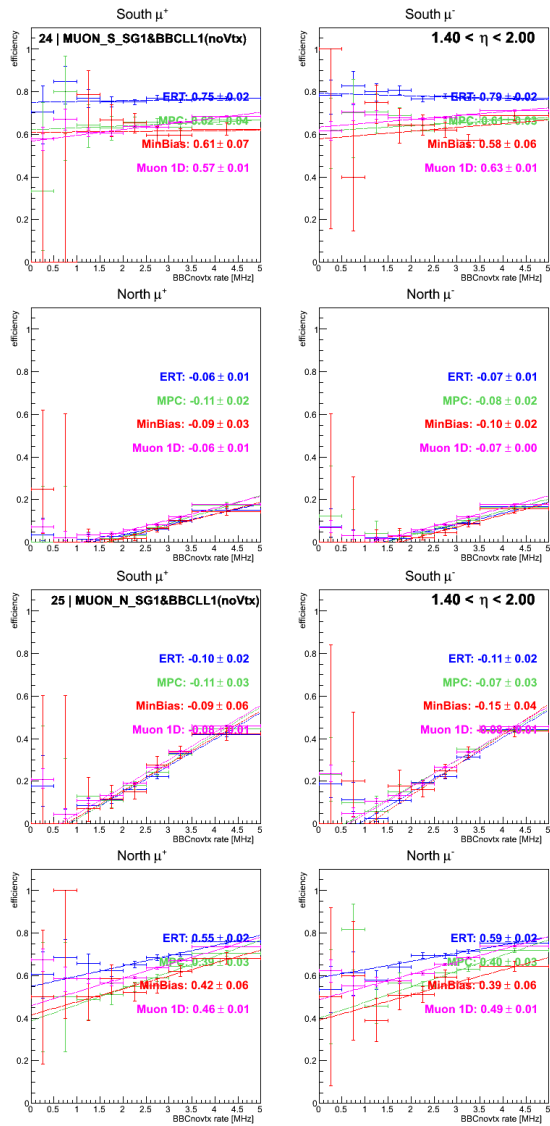


Figure D.2: Trigger efficiencies for trigger bit 24 (left, MUON\_S\_SG1&BBCLL1(noVtx)) and 25(right, MUON\_N\_SG1&BBCLL1(noVtx)) for single  $W \rightarrow \mu$  candidates in the rapidity range  $1.4 < \eta < 2.0$  as a function of raw BBCnovertex rate. The efficiencies for ERT (blue), MPC (green), MinBias(red) and 1D (purple) triggered data samples are shown as well as a constant fit over the whole range.

This rising SG1 behavior is then somewhat mirrored in some of the other triggers related to SG1 with the exception of the North RPC13\_BC trigger where the trigger efficiency is nearly flat or slightly falling, see Fig. D.3 as well as some other triggers in relation to the RPCs.

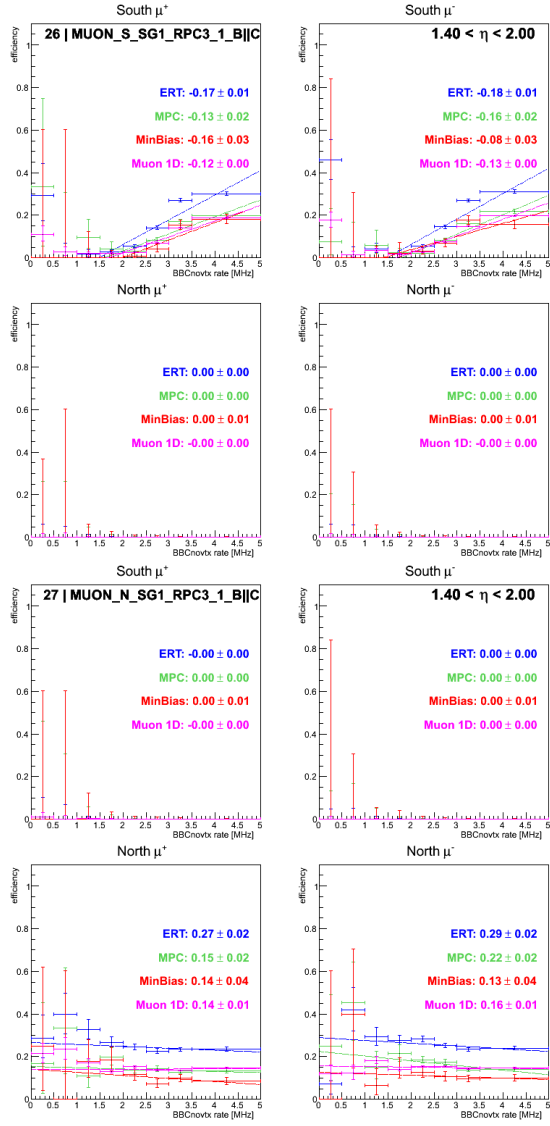


Figure D.3: Trigger efficiencies for trigger bit 26 (MUON\_S\_SG1\_RPC3\_1\_B||C, left) and 27 (MUON\_N\_SG1\_RPC3\_1\_B||C, right) for single  $W \rightarrow \mu$  candidates in the rapidity range  $1.40 < \eta < 2.00$  as a function of raw BBCnovertex rate. The efficiencies for ERT (blue), MPC (green), MinBias(red) and 1D (purple) triggered data samples are shown as well as a constant fit over the whole range.

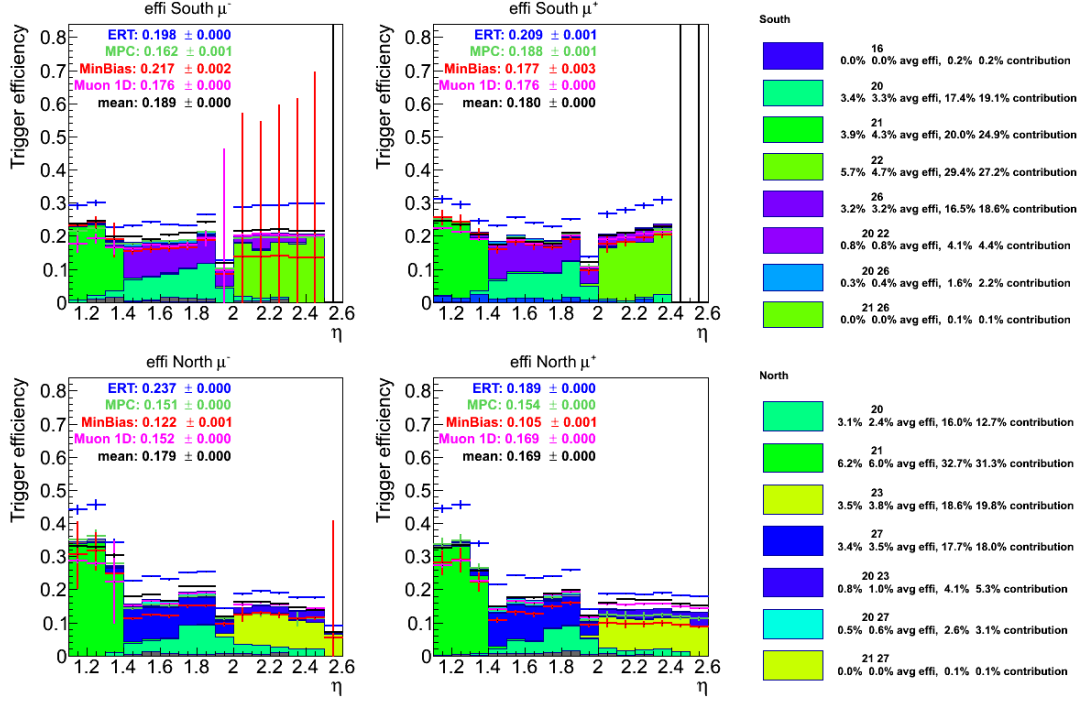


Figure D.4: Total trigger efficiencies in the  $W \rightarrow \mu$  candidates separated by arm and charge for various muon triggers as a function of rapidity. Those with substantial contributions are given in the Legend to the right for each arm including their average efficiencies and relative contributions.

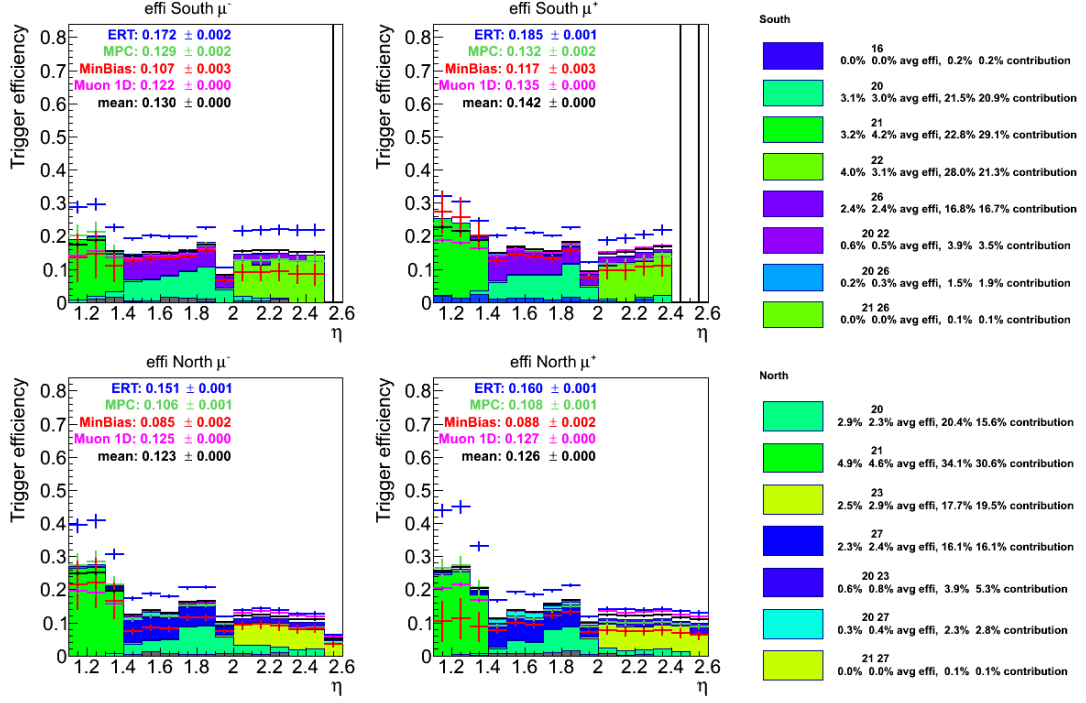


Figure D.5: Total trigger efficiencies in the  $W \rightarrow \mu$  candidates separated by arm and charge for various muon triggers as a function of rapidity. Those with substantial contributions are given in the Legend to the right for each arm including their average efficiencies and relative contributions.

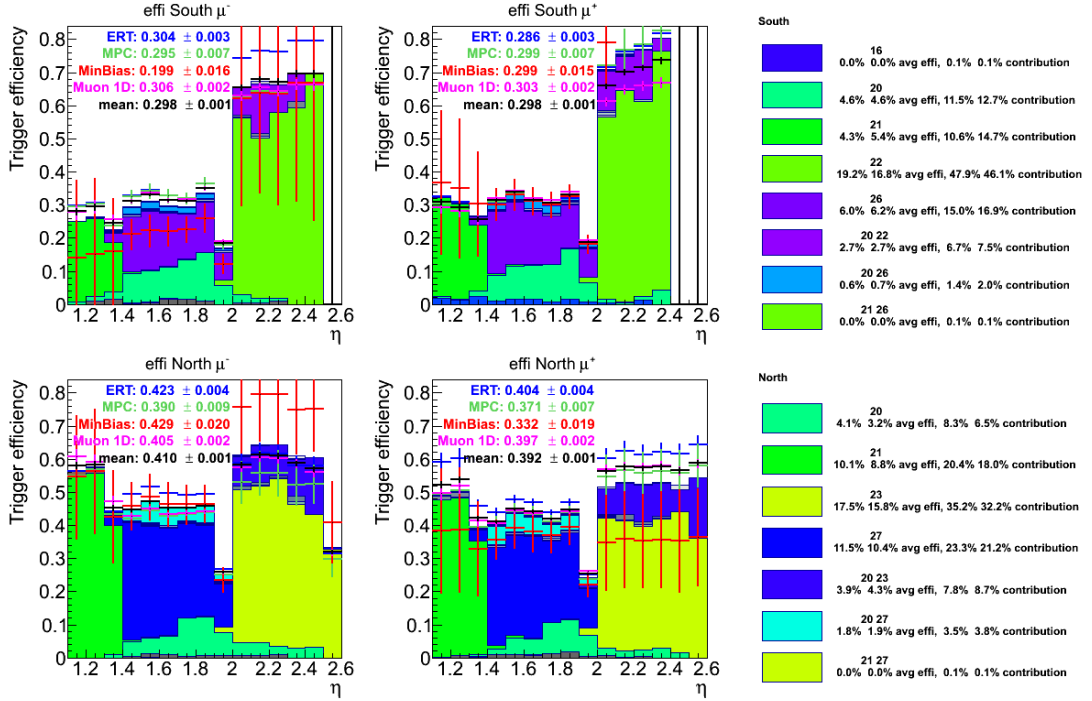


Figure D.6: Total trigger efficiencies in the  $W \rightarrow \mu$  candidates separated by arm and charge for various muon triggers as a function of rapidity. Those with substantial contributions are given in the Legend to the right for each arm including their average efficiencies and relative contributions.

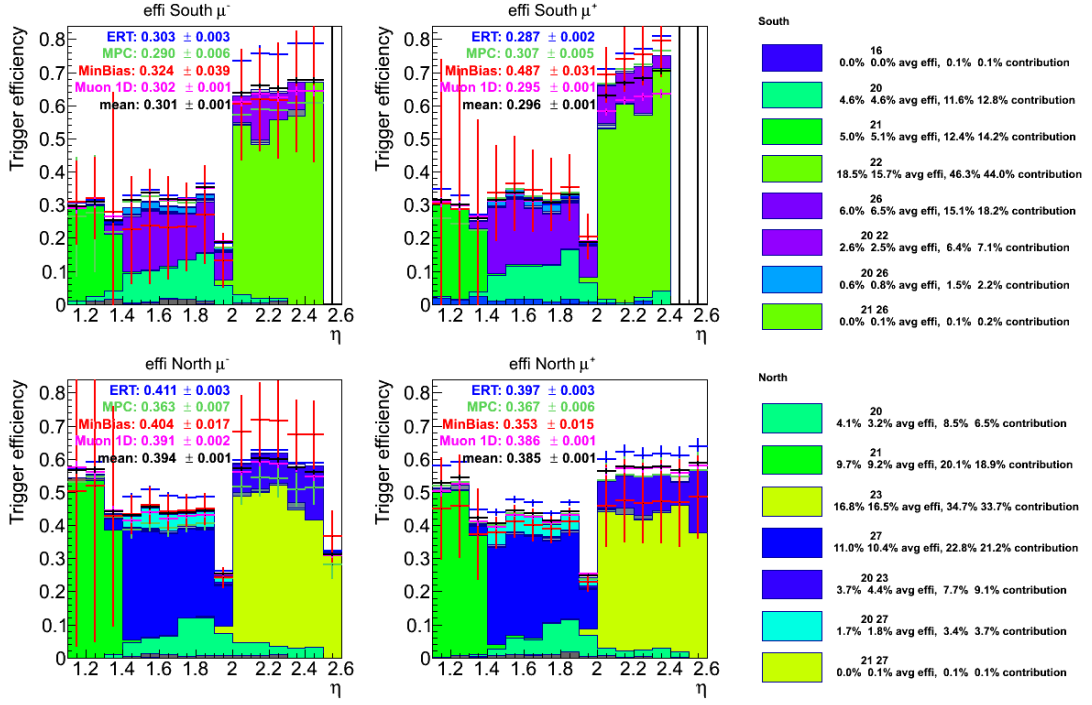


Figure D.7: Total trigger efficiencies in the  $W \rightarrow \mu$  candidates separated by arm and charge for various muon triggers as a function of rapidity. Those with substantial contributions are given in the Legend to the right for each arm including their average efficiencies and relative contributions.

As a potential alternative the high  $W_{ness}$  ( $W_{ness} > 0.92$ ), eta dependent efficiencies are taken for the total eta dependent efficiencies as shown in Fig. D.8. As those require smaller minimum  $p_T$ , their efficiencies are mostly slightly smaller than those obtained in Fig. D.7, but their finer eta binning takes the varying trigger acceptances better into account and discontinuities such as seen at around rapidities of 2 (due to the overlapping 13\_BD and 3A acceptances) disappear. Both values are given below as final results and are both used when applying them to the muon background simulations or to extract cross sections.

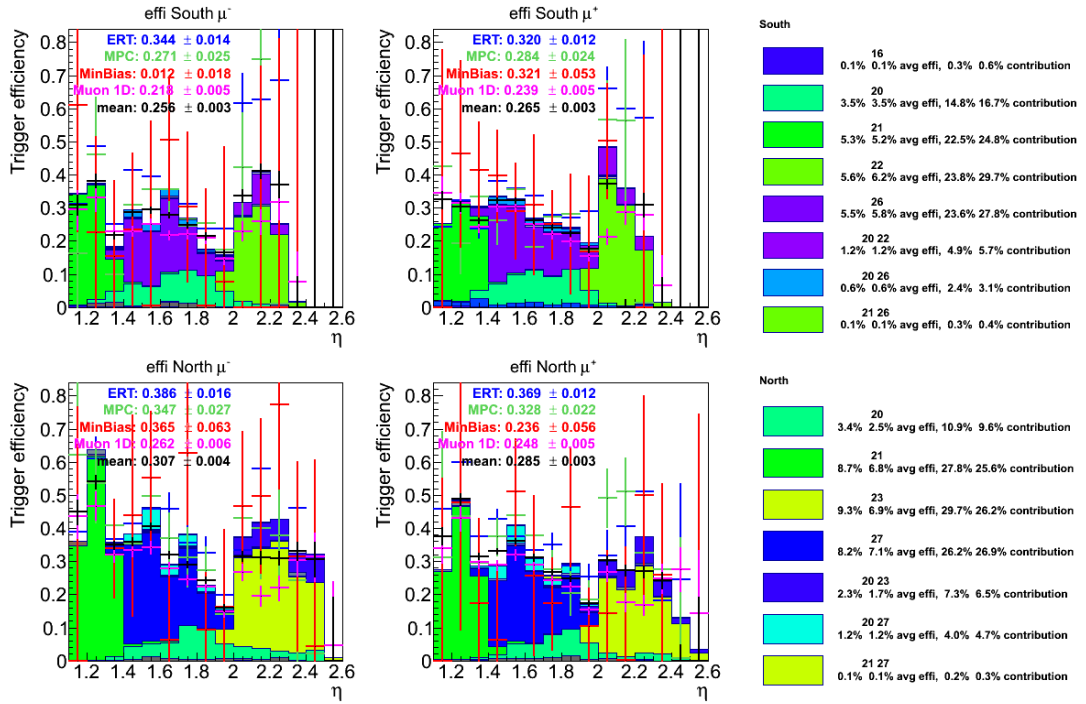


Figure D.8: Total trigger efficiencies in the  $W \rightarrow \mu$  candidates separated by arm and charge for various muon triggers as a function of rapidity. Those with substantial contributions are given in the Legend to the right for each arm including their average efficiencies and relative contributions.

## Appendix E

# Systematic Studies— $A_L$

Systematic studies have been done to study the reconstruction of the single spin asymmetries, and the sensitivity of this reconstruction to various potential systematic effects. These studies are reproduced from [31]

### E.1 Combined systematic studies

Using the data-based signal to background extraction in the way introduced in [25] the resulting background corrected asymmetries are significantly inconsistent with any of the parameterizations. The up and down quark polarizations are generally well enough known, as are the W kinematics, that there is little doubt in the asymmetries mostly related to them, namely the forward  $W^- \rightarrow \mu^-$  asymmetries and the backward  $W^+ \rightarrow \mu^+$  asymmetries. It seems therefore much more likely, that either a statistical fluctuation or analysis error creates the resulting discrepancies. When taking the signal to background values at face value a statistical fluctuation is essentially excluded, however, if there is a significant overestimation of these ratios it could still be possible.

In order to understand the origins of the data parameterization discrepancy better we are studying the asymmetries and the signal to background ratios as a function of various relevant variables. In most cases the background corrected asymmetries as well as the signal to background ratios are displayed together to give a better idea of the impact on the background. Either the data-based or W-MC based signal to background ratios are displayed and used to see the difference it makes.

### **E.1.1 Asymmetries as function of W selection and deflection angular bands**

As the asymmetry calculation only uses the  $dw_{23}$  region with supposedly W support the whole region and the inverse selection are also of interest. As the inverse region is expected to be dominated by more background its asymmetries should be closer to zero as only the W/Z production gives parity violating asymmetries. However, it seems, that while statistical uncertainties are generally larger the asymmetries have a tendency to be nonzero in particular also the double spin asymmetries. This could either be an indication of remaining signal in the sidebands or some remaining background asymmetries. The Asymmetries in the  $dw_{23}$  sidebands can be seen in Figs. E.1

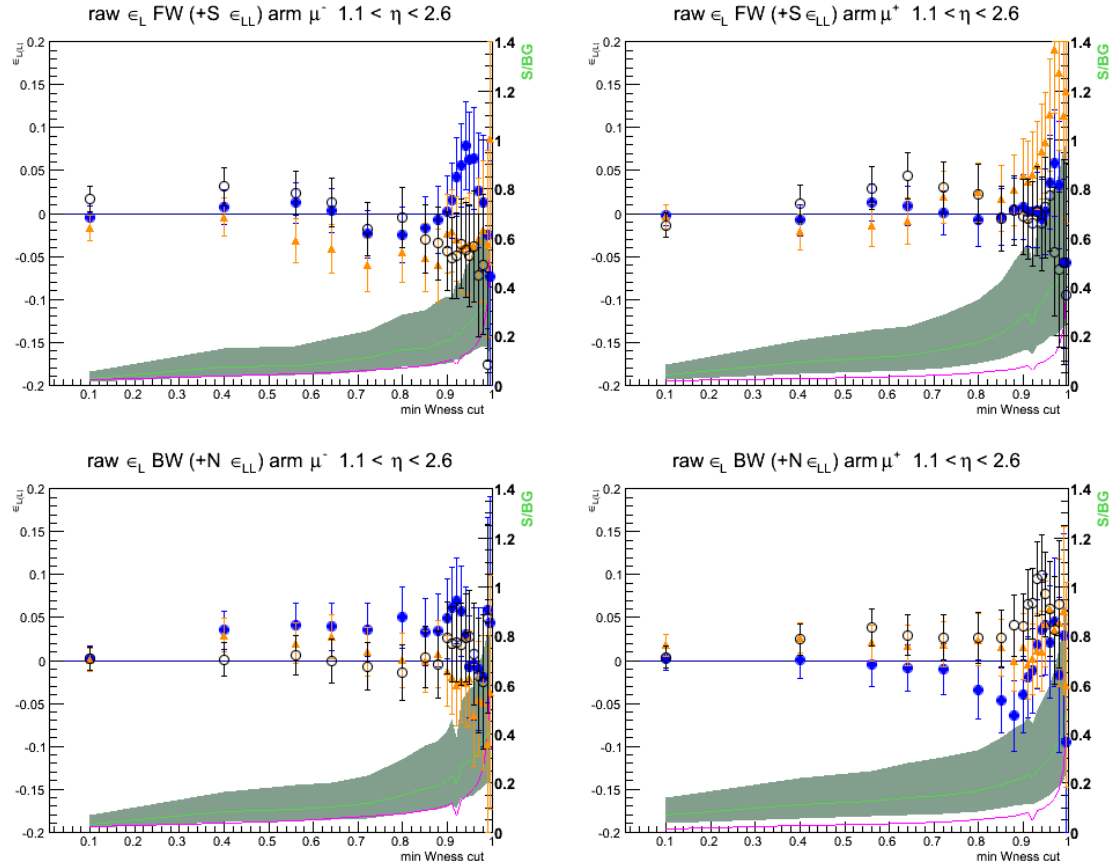


Figure E.1: Raw asymmetries  $\epsilon_L$  for the Blue (blue symbols) and Yellow (orange symbols) beams and  $\epsilon_{LL}$  (black symbols) for both arms and charges as a function of the pre-selection range. The combination of all rapidities in one bin after selecting the **sideband**  $dw_{23}$  region is displayed. In addition the extracted signal to background ratios are displayed using the right-hand axis values. The green line displays the data-based extraction method while the magenta line represents the MC signal based extraction.

### **E.1.2 Asymmetries and Signal to BG ratio as a function of rate, time and transverse momentum range**

Another important test is whether the asymmetries show any kind of rate or run dependence effect. For this purpose the data was split up into three rapidity ranges with about equal luminosity: The multi-collision parameters were chosen as 0, 0.69, 0.83, 2. Naively a rate dependent effect would result in a certain ordering of the asymmetries with either increasing or decreasing asymmetries as the rates increase. All the asymmetries as a function of minimum  $W_{ness}$  cut are displayed in Fig. E.2. Out of the 12 different asymmetries ( arm x charge x singe,double spin asymmetry) a few display such a behavior while the majority appears to be randomly distributed between the different rates.

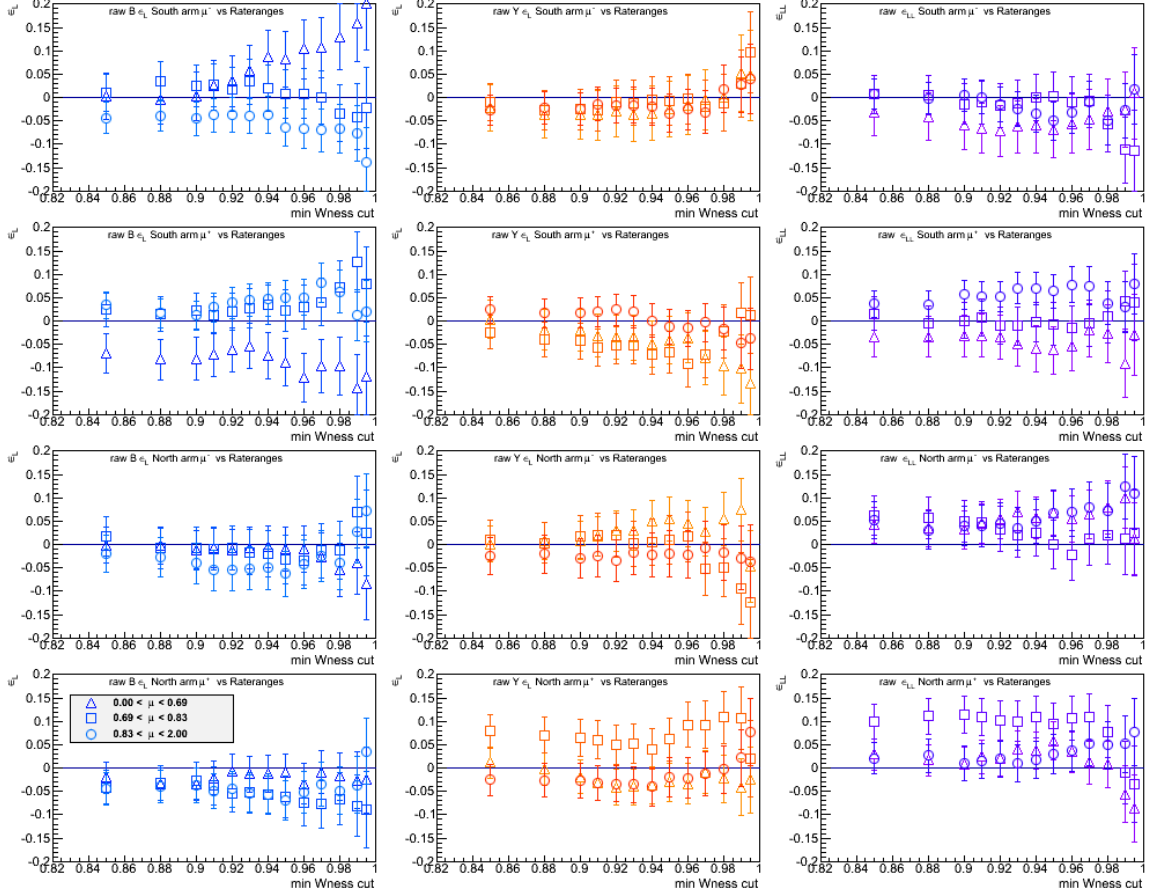


Figure E.2: Raw asymmetries as a function of minimal  $W_{ness}$  cut when splitting the data sample into three nearly equal luminosity bins of increasing BBC rate in the order of open triangles, open squares and open circles. Each plot displays one asymmetry for each arm and charge. The central  $dw_{23}$  region has been selected. In addition the extracted signal to background ratios are displayed using the right-hand axis values. The green line displays the data-based extraction method while the magenta line represents the MC signal based extraction.

A t-test between low and high to intermediate rates was performed and the distribution is given in Fig. E.3. The amount of larger differences is on the order expected for statistical fluctuations around an average value and therefore one can conclude, that no obvious rate dependent effect is visible.

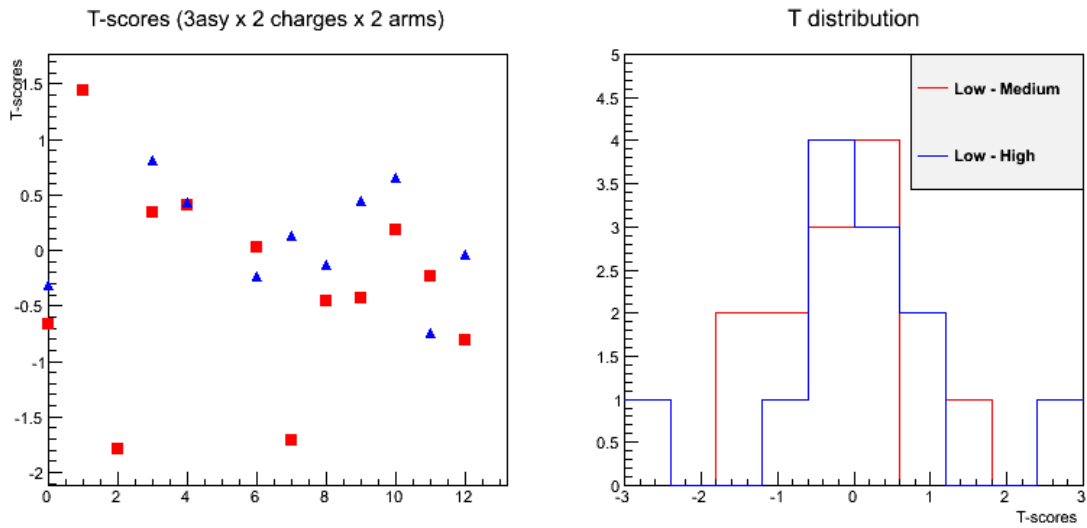


Figure E.3: Student T scores and distribution when comparing the lot to medium and the low to high rate subset.

Similarly, the run dependence was studied in three range bins from 0, 392276, 395770, 399000. While some correlation with the rates is likely, it should be mostly washed out as the collision rates decrease within fills. With the run dependence it would be possible to see, if time dependent detector or accelerator related effects bias the results in some way. The resulting asymmetries can be seen in Fig. E.4 and the corresponding t-test between low, high and mid run ranges is given in Fig. E.5. Again, while some asymmetries show a range dependence the overall distribution of differences as consistent with fluctuations only.

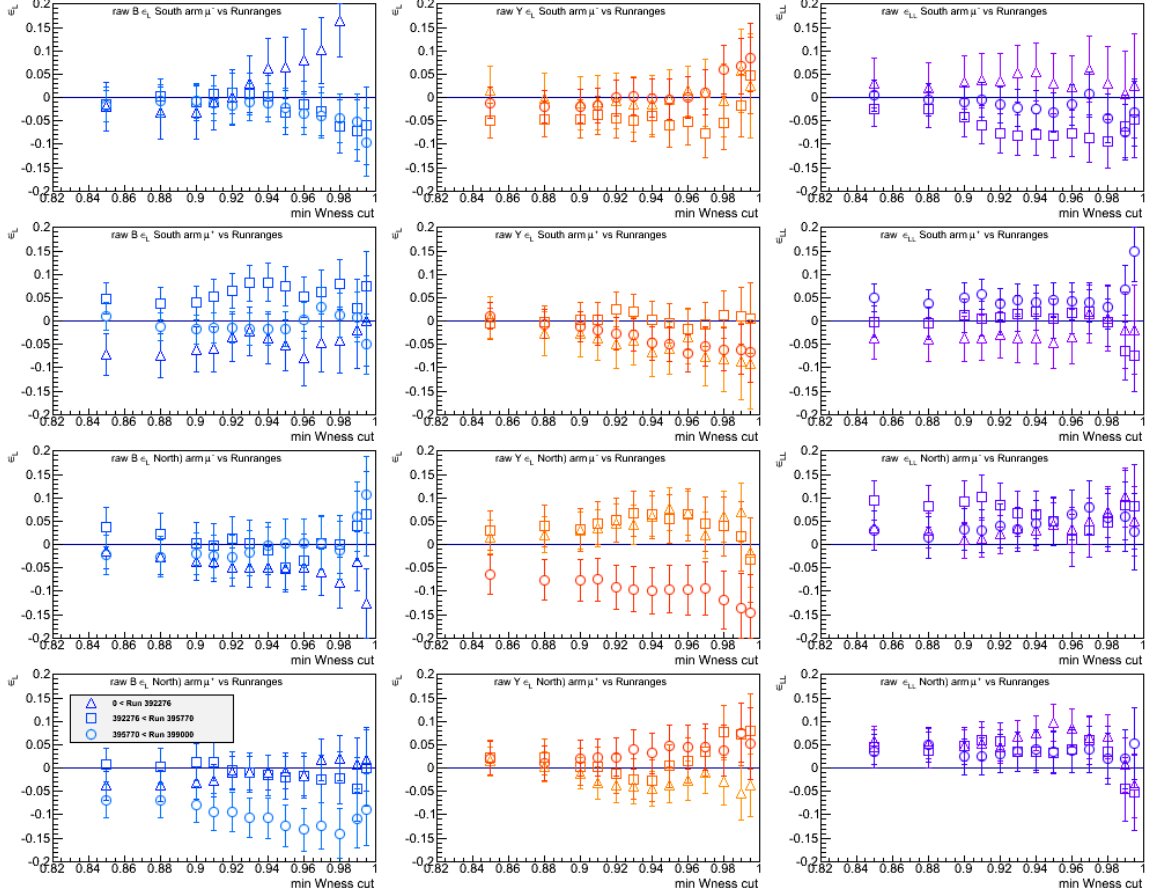


Figure E.4: Raw asymmetries as a function of minimal  $W_{ness}$  cut when splitting the data sample into three nearly equal luminosity bins of increasing run number in the order of open triangles, open squares and open circles. Each plot displays one asymmetry for each arm and charge. The central  $dw_{23}$  region has been selected. In addition the extracted signal to background ratios are displayed using the right-hand axis values. The green line displays the data-based extraction method while the magenta line represents the MC signal based extraction.

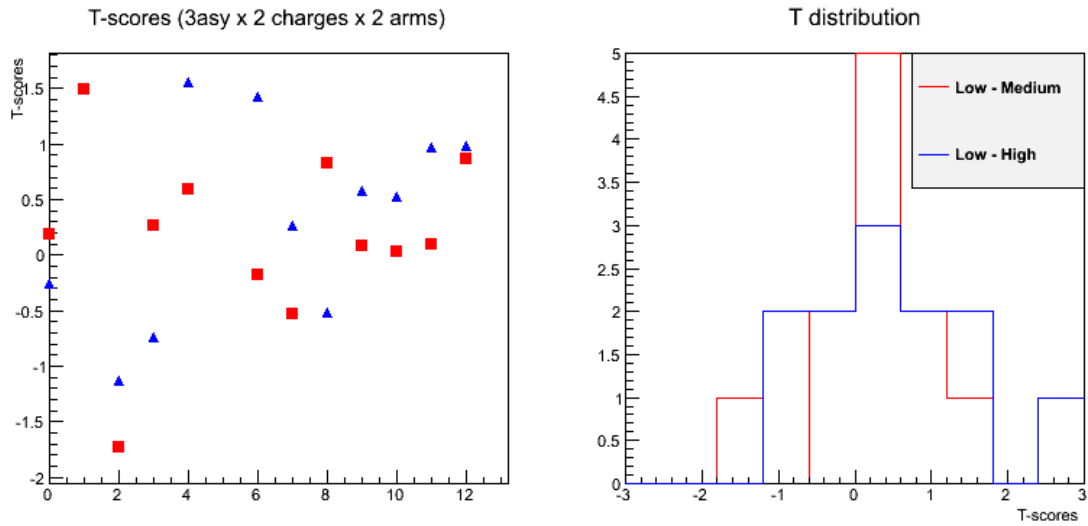


Figure E.5: Student T scores and distribution when comparing the lot to medium and the low to high run number subset

Another test is the dependence on the minimum transverse momentum cut or the transverse momentum range selected. As mentioned earlier in this analysis note the W and Z decay muons dominate at larger transverse momenta while at lower transverse momenta even more dilution from other muon processes and fake hadrons contribute. As a consequence any asymmetry should be largely diluted and start to appear as the minimum transverse momentum cut is increased. Such a behavior can be seen in Fig. E.6 where essentially all asymmetries are consistent with zero at low transverse momenta and then increase in some of the cases. What appears different than expectation is the signal to background ratio obtained from the fits. The signal to background ratios from the fits seem to be not increasing while the MC based signal to background ratios show the expected behavior.

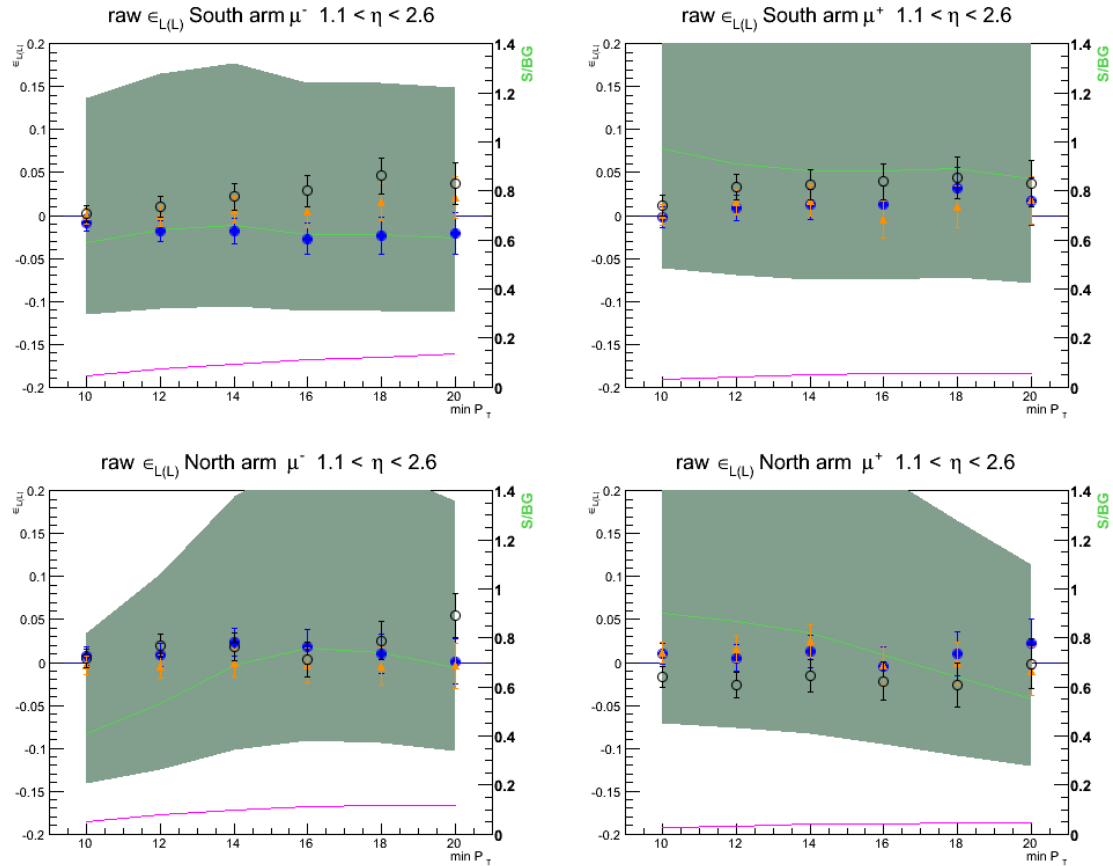


Figure E.6: Raw asymmetries  $\epsilon_L$  for the Blue (blue symbols) and Yellow (orange symbols) beams and  $\epsilon_{LL}$  (black symbols) for both arms and charges as a function of the minimal transverse momentum cut are displayed. In addition the extracted signal to background ratios are displayed using the right-hand axis values. The green line displays the data-based extraction method while the magenta line represents the MC signal based extraction.

The asymmetries in ranges of transverse momenta are shown in Fig. E.7. After small initial asymmetries they are mostly consistent at intermediate transverse momentum ranges and only seem to change again at transverse momenta of around 18. The signal-to-background distribution is again unexpected as obtained from the fits while it is more consistent with expectations in the MC based extraction.

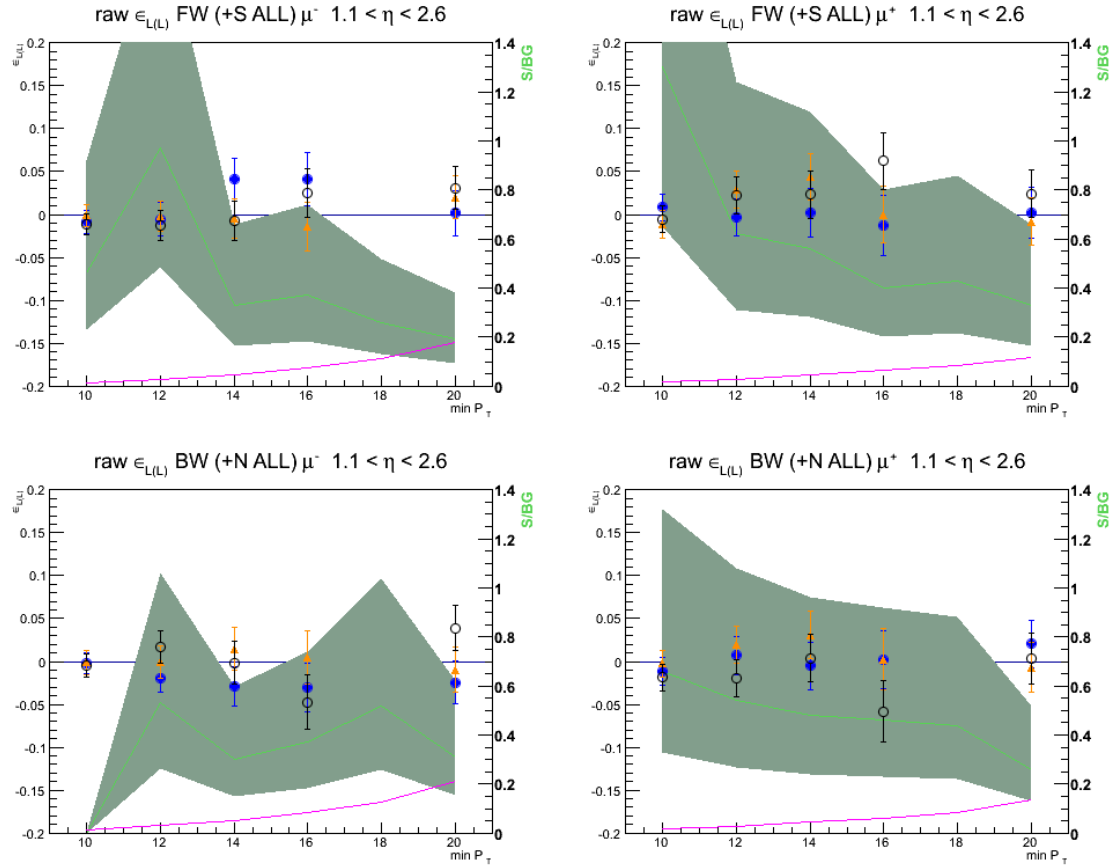


Figure E.7: Raw asymmetries  $\epsilon_L$  for the Blue (blue symbols) and Yellow (orange symbols) beams and  $\epsilon_{LL}$  (black symbols) for both arms and charges as a function of transverse momentum are displayed. The combination of all rapidities in one bin after selecting the central  $dw_{23}$  region is displayed. In addition the extracted signal to background ratios are displayed using the right-hand axis values. The green line displays the data-based extraction method while the magenta line represents the MC signal based extraction.

### E.1.3 Addition of artificial MC-based signal and asymmetries

Another type of test uses the generated signal MC and includes a fraction of it into the data set before calculating asymmetries and signal to background ratios. In order to do so, crossings are assigned randomly to the MC such, that a certain set of asymmetries can be generated. As an initial test only constant asymmetries were generated. Not any asymmetries can be physically created as the yields in the 4 helicity combinations need to be non-negative. The double spin asymmetries need to be within a certain range of the other two. The initial asymmetries created were 40% and 10% for the negative generated muons and -20% and -30% for the positive generated muons while no double spin asymmetries were generated.

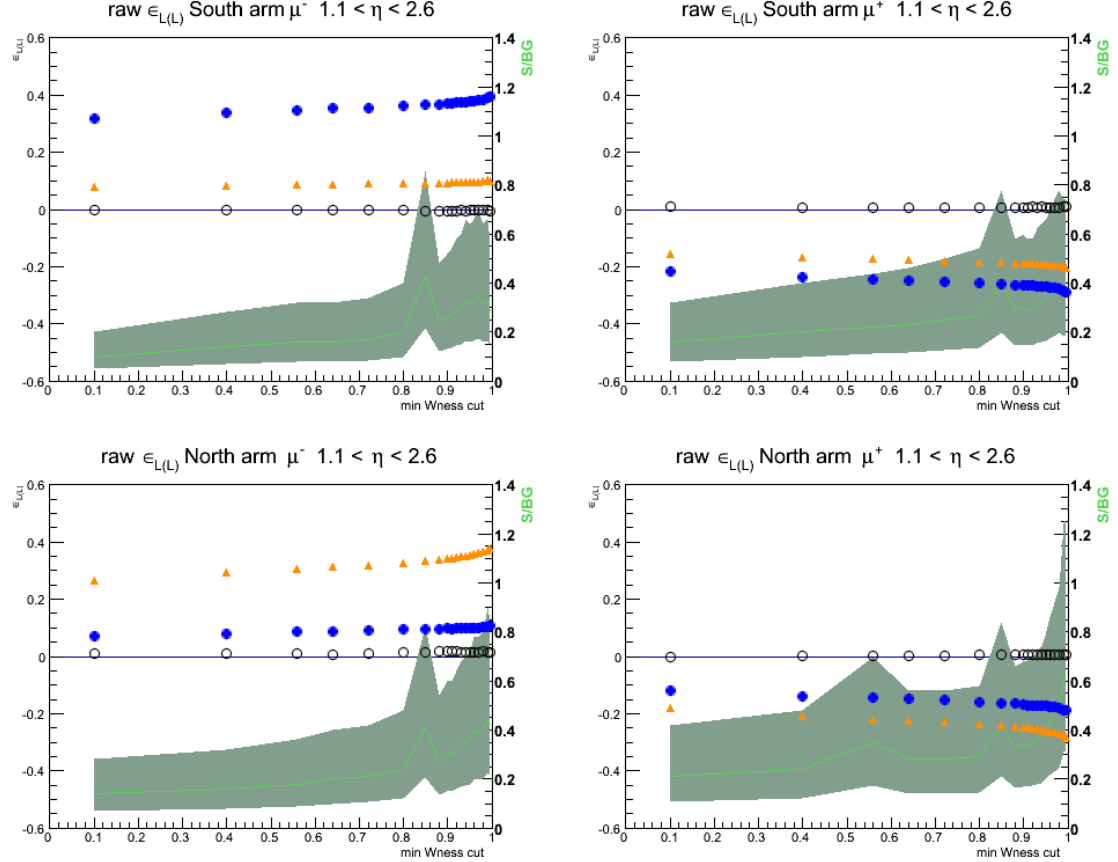


Figure E.8: Raw asymmetries  $\epsilon_L$  for the Blue (blue symbols) and Yellow (orange symbols) beams and  $\epsilon_{LL}$  (black symbols) for both arms and charges as a function of the minimum  $W_{ness}$  cut are displayed with a fixed signal MC addition of  $20 \text{ fb}^{-1}$ . The combination of all rapidities in one bin after selecting the central  $dw_{23}$  region is displayed. In addition the extracted signal to background ratios are displayed using the right-hand axis values. The green line displays the data-based extraction method while the magenta line represents the MC signal based extraction.

The resulting asymmetries and signal-to-background ratios are displayed in Fig. E.8 for an MC admixture of  $20 \text{ fb}^{-1}$  as a function of the minimum  $W_{ness}$  cut. One can see, that with increasing minimum  $W_{ness}$  the resulting asymmetries begin to increase as expected while the generally fall short of the generated asymmetries. In Fig. E.9 the asymmetries and signal-to-background ratios are displayed as a function of the MC admixture. Also the background corrected asymmetries are displayed which should return the generated asymmetries with the exception of the actual signal based asymmetries in the actual data. As one can see, the asymmetries are not properly recovered especially at low admixtures. While part of it could be coming from the Physics asymmetries its contribution should be small. Again, using the MC based signal to background ratios seem to better recover the generated asymmetries.

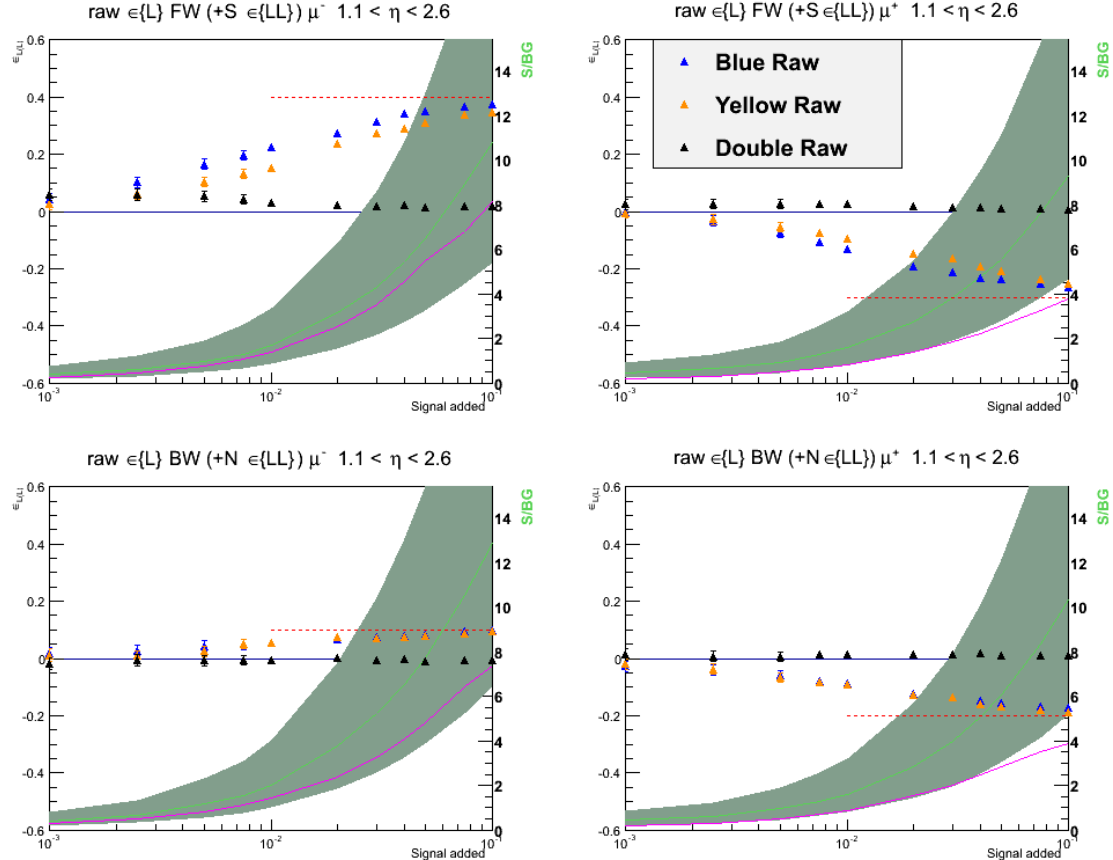


Figure E.9: Raw asymmetries  $\epsilon_L$  for the Blue (blue symbols) and Yellow (orange symbols) beams and  $\epsilon_{LL}$  (black symbols) for both arms and charges as a function of the total Signal MC added are displayed. The combination of all rapidities in one bin after selecting the central  $dw_{23}$  region is displayed. In addition the extracted signal to background ratios are displayed using the right-hand axis values. The green line displays the data-based extraction method while the magenta line represents the MC signal based extraction. The background corrected asymmetries using either the fit based S/BG values (downward open triangles) or old extraction (upward open triangles) are also displayed.

#### E.1.4 Checking the relative luminosities between patterns

In the previous evaluation of the asymmetries we were implicitly assuming that we took the same luminosity for every spin pattern. To make sure this is the case, we explicitly counted the scalers from the spin Data Base from the entry ScalerBbcNoCut for each spin pattern and we found the following:

Spin Pattern (Blue, Yellow)	
+1, +1	5.29+11
-1, +1	5.28e+11
+1, -1	5.29e+11
-1, -1	5.29e+11.

As can be seen in the previous table, there is only a 0.2% difference between the luminosity of the spin patterns, so the previous assumption that there are no differences in luminosities between spin patterns is safe. As a double check, we rescaled the yield for each spin pattern according to the scalers just reported, and as expected no significant differences were observed in the combined asymmetries, as shown in figure E.10.

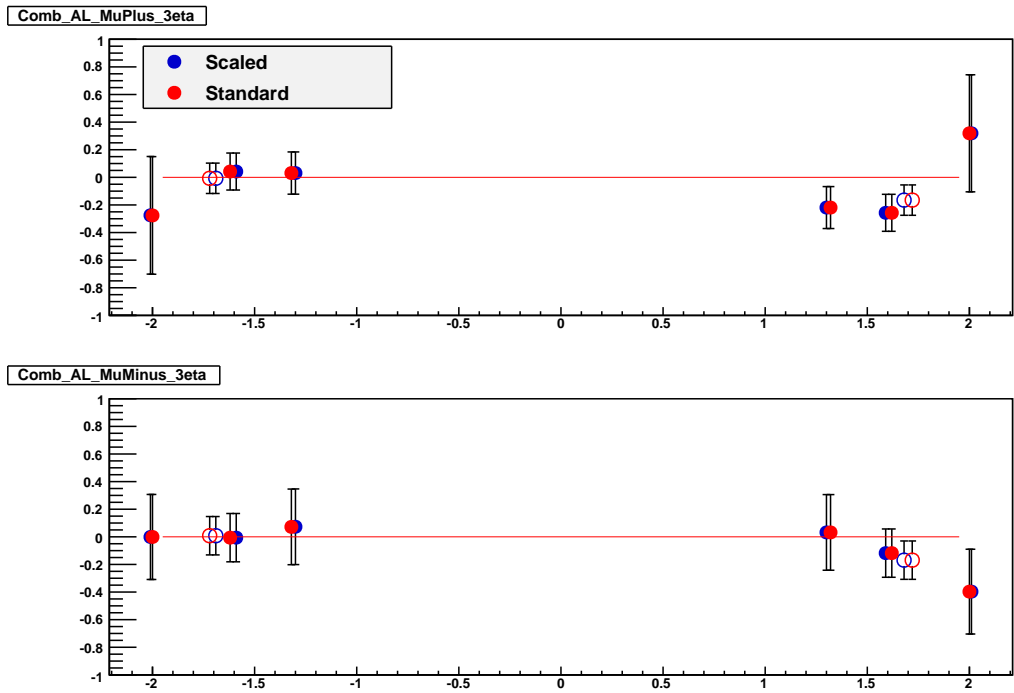


Figure E.10: Comparison between the combined asymmetries with (in blue) and without (in red) the yield rescaling by the relative luminosity of each spin pattern.